

**Book of Abstracts
of the 38th Solid Mechanics Conference
Warsaw, Poland, August 27–31, 2012**

Edited by:

**Ryszard Pęcherski
Jerzy Rojek
Piotr Kowalczyk**

**Institute of Fundamental Technological Research (IPPT)
Polish Academy of Sciences**

38th Solid Mechanics Conference

Warsaw, Poland, August 27–31, 2012

organized by

Institute of Fundamental Technological Research (IPPT) *and* Committee on Mechanics
POLISH ACADEMY OF SCIENCES

Scientific Committee

J. Badur	M. Kleiber	A. Nowicki	B. Skoczeń
M. Basista	W. Kosiński	P. Perzyna	K. Sobczyk
A. Borkowski	Z. Kotulski	H. Petryk	S. Stupkiewicz
T. Burczyński	Z. Kowalewski	R. Pęcherski	G. Szefer
K. Dems	J. Kubik	W. Pietraszkiewicz	J. Tejchman
P. Dłużewski	T. Łodygowski	M. Pietrzyk	A. Tylikowski
W. Gutkowski	Z. Mróz	B. Raniecki	K. Wiśniewski

Organizing Committee

R. Pęcherski (<i>Chairman</i>)	M. Nowak, P. Tazowski (<i>Managing assistants</i>)
J. Rojek (<i>Scientific Secretary</i>)	U. Czubacka (<i>Secretary</i>)

Thematic Sessions and their Organizers

Biomechanics	(<i>T. Lekszycki, P.J. Prendergast</i>)
Computational Aspects of Solid Mechanics	(<i>T. Burczyński, E. Oñate</i>)
Continuum Mechanics, Elasticity and Plasticity (in memory of Jan Rychlewski)	(<i>K. Kowalczyk-Gajewska, P. Lipinski, P. Perzyna</i>)
Experimental Mechanics	(<i>Z. Kowalewski, A. Rusinek</i>)
Fracture, Damage and Fatigue of Materials	(<i>J. Fernández-Sáez, Z. Nowak</i>)
Geomechanics	(<i>Z. Mróz, S. Pietruszczak, J. Tejchman</i>)
Micromechanics, Interfaces and Multi-Scale Modelling	(<i>J. Schröder, S. Stupkiewicz</i>)
Nonlinear and Stochastic Dynamics	(<i>R. Iwankiewicz, Z. Kotulski</i>)
Shells and Plates	(<i>W. Pietraszkiewicz, K. Wiśniewski</i>)
Smart Materials and Structures	(<i>C. Boller, J. Holnicki-Szulc</i>)
Structural Mechanics, Optimization and Reliability	(<i>K. Dems, R. Stocki</i>)

Copyright © by Institute of Fundamental Technological Research (IPPT)
of the Polish Academy of Sciences

Front cover by Marcin Nowak

Print: Zakład Graficzny Uniwersytet Warszawski, zam. 758/2012

Produced from camera-ready copies supplied by the authors

Warsaw 2012

Preface

This volume contains abstracts of papers accepted for presentation at the 38th Solid Mechanics Conference (SolMech 2012) held in Warsaw, August 27–31, 2012.

The series of Solid Mechanics Conferences have been organized by the Institute of Fundamental Technological Research since 1953. The conferences have maintained high scientific standard and served as a forum for exchange of ideas and research information. Traditionally, a set of invited plenary lectures have been presented at the Conferences by outstanding researchers. The aim of the meetings is to bring together the researchers from different countries and to create them the possibilities for the presentation of scientific results from a wide area of solid mechanics.

During this Conference, nine invited plenary lectures are going to be delivered. The Conference is organized into eleven Thematic Sessions with 13 keynote lectures and contributing oral presentations:

- Shells and Plates (23 presentations)
- Continuum Mechanics, Elasticity and Plasticity (Special Session in Memory of Jan Rychlewski) (21 presentations)
- Computational Aspects of Solid Mechanics (18 presentations)
- Experimental Mechanics (17 presentations)
- Micromechanics, Interfaces and Multi-Scale Modelling (14 presentations)
- Smart Materials and Structures (11 presentations)
- Fracture, Damage and Fatigue of Materials (11 presentations)
- Structural Mechanics, Optimization and Reliability (9 presentations)
- Biomechanics (6 presentations)
- Geomechanics (5 presentations)
- Nonlinear and Stochastic Dynamics (3 presentations)

On behalf of the Scientific and Organizing Committees of the 38th Solid Mechanics Conference (SolMech 2012) I wish all participants and accompanying persons an inspiring and enjoyable stay in Warsaw.

Ryszard Peçhowski

Warsaw, August 2012

Contents

Invited Plenary Lectures

- 2 *D. Mohr*
Multi-Axial Static and Dynamic Experiments to Investigate the Effect of Stress Triaxiality and Lode Angle on Ductile Fracture
- 4 *S. Stupkiewicz, H. Petryk*
Interfacial Energy Effects in Micromechanical Modelling of Shape Memory Alloys
- 6 *D. Weichert*
On Recent Progress in Limit and Shakedown Analysis
- 8 *W. Pietraszkiewicz*
Resultant Thermodynamics of Shells
- 10 *E. Oñate, M.A. Celigueta, S.R. Idelsohn, F. Salazar, A. Larese, R. Rossi*
Advances in the Particle Finite Element for Multidisciplinary Problems in Solid Mechanics
- 12 *F. Scarpa*
Auxetics: From Foams to Composites and Beyond
- 13 *F. dell'Isola*
Contact Interactions in Generalized N-Th Gradient Continua: Mathematical Foundations and a View to the Applications
- 14 *S. Mercier, N. Jacques, A. Molinari*
Effect of Inertia on Multiple Necking and on Dynamic Failure of Ductile Materials
- 16 *Z.L. Kowalewski*
Interdisciplinary Methods for Creep Damage Assessment of Materials Subjected to Creep and Fatigue

Biomechanics

- 20 *J.F. Ganghoffer, G. Maurice*
Bone Remodeling Based on Surface Growth. Theory and Numerics (*keynote lecture*)
- 22 *K. Czechowicz, J. Badur, K. Narkiewicz*
Assessing Arterial Flow Parameters to Measure the Influence of Blood Flow on Arterial Walls
- 24 *Sz. Hernik, P. Sulich*
Modeling of Fracture in Cortical Bone Using the Gurson–Tvergaard Model
- 26 *A. Jakubowicz, M. Pietrzyk*
Deformation of Red Blood Cells

-
- 28 *E. Postek, F. Dubois, R. Mozul*
Modeling of a Collection of Tensegrity Particles with a Non Smooth Discrete Element Method
- 30 *K. Szajek, M. Wierszycki, T. Łodygowski*
Multiobjective Optimization of Two-Component Implantology System
- 32 *G. Wróblewski*
Modeling of the Lateral Traumas of the Human Skull

Computational Aspects of Solid Mechanics

- 36 *J. Jaśkowiec, P. Pluciński, R. Putanowicz, A. Stankiewicz, A. Wosatko, J. Pamin*
Formulation and FEM Implementation of Nonlinear Thermo-Mechanical Coupling (*keynote lecture*)
- 38 *A. Pereira*
Elastoplastic Analysis by an Automatic and Adaptive BEM–FEM Coupling Strategy (*keynote lecture*)
- 40 *P. Baranowski, J. Małachowski, Ł. Mazurkiewicz, K. Damaziak*
Constitutive Rubber Material Models Comparison Studies in Quasi-Static Loading
- 42 *T. Bednarek, P. Kowalczyk*
Adaptive Estimation of Penalty Factors in Contact Modelling
- 44 *M. Cieszko, T. Bednarek, A. Stusznik*
A Flow of the Nonwetting Liquid Through Unsaturated Porous Layer
- 46 *O. Denina*
On Determination of the Elastic Properties of Heterogeneous Rods
- 48 *A. Długosz, T. Burczyński*
Evolutionary Multiobjective Optimization of Microactuators
- 50 *S. Fialko*
Parallel Sparse Incomplete Cholesky Conjugate Gradient Solver for Multi-Core Computers
- 52 *A. Genoese, A. Genoese, A. Bilotta, G. Garcea*
Mathematical Modeling of Thin-Walled Beams and FEM Applications
- 54 *M. German, J. Pamin*
Modelling of Corrosion Interface in RC Cross-Section
- 56 *A. Hashemian, H. Shodja*
Treatment of an Inhomogeneous Inclusion with the Augmented Corrected Collocation Method
- 58 *M. Leindl, E.R. Oberaigner*
Fracture Mechanics Analysis of a Cylindrical Sample Loaded by Time-Dependent Heating
- 60 *E. Majchrzak*
The General Boundary Element Method for Dual Phase Lag Model of Microscale Heat Transfer
- 62 *A.D. Miedzińska, T. Niezgoda*
Metal Foam Structure Finite Element Modelling Based on Computed Tomography

- 64 *B. Mochnacki, J. Dziatkiewicz*
Microscale Heat Transfer. Comparison of Numerical Solutions Using Two-Temperature Model and Dual Phase Lag Model
- 66 *A. Perduta, R. Putanowicz*
Automatic Generation of Benchmark Problems for Stress Analysis FEM Programs Using Manufactured Solutions Method
- 68 *K. Wawrzyk, P. Kowalczyk*
Modified Contact Search Algorithm for Sheet Metal Forming
- 70 *B. Wcisto, J. Pamin*
Gradient-Enhanced Damage Model for Large Deformations of Elastic-Plastic Materials

Continuum Mechanics, Elasticity and Plasticity (Special Session in Memory of Jan Rychlewski)

- 74 *K. Nalepka*
Specification of Interatomic Potentials by Symmetry (*keynote lecture*)
- 76 *E. Bulgariu*
On a Backward in Time Thermo-Microstretch Problem
- 78 *H. Egner, W. Egner*
Modelling of Thermo-Viscoplastic Coupling in AISI L6 Steel
- 80 *F. Fournier Dit Chabert, A. Gaubert, A. Longuet, S. Quilici*
Calibration and Validation of a Constitutive Model for Single Crystal Nickel Based Superalloys
- 82 *A. Fukalov, A. Kutergin, A. Zaitsev*
Exact Analytical Solutions to Problems on Equilibrium State of Elastic Anisotropic Heavy Bodies with Central and Axial Symmetry and Their Applications to Geomechanical Problems
- 84 *M. Hycza-Michalska*
Mechanical State Simulation Research of Hydromechanical Forming Processes of Nickel Superalloys
- 86 *W. Kosiński, P. Perzyna*
On the Principle of Stationary Action for Dissipative Solids with Thermo-Mechanical Couplings
- 88 *K. Kowalczyk-Gajewska*
Influence of Grain Shape on the Overall Behaviour of Incompressible Polycrystals
- 90 *A. Milenin, M. Kopernik, I. Tsukrov*
Sensitivity Analysis of Micro-Scale Model of TiN / Substrate in Nanoindentation Test
- 92 *Z. Nowak, T. Frąś, M. Nowak, R. Pęcherski*
Analysis of the Forming Processes Accounting for Asymmetry of Elastic Range
- 94 *Z. Nowak, P. Perzyna*
The Identification Procedure for the Constitutive Model of Elasto-Viscoplasticity Describing the Behaviour of Nanocrystalline Titanium
- 96 *J. Ostrowska-Maciejewska, K. Kowalczyk-Gajewska*
Third Order Tensors: Their Properties and Application to Coupled Problems

-
- 98 *H.M. Shodja, A. Khorshidi*
Reformulation of 3D Elasticity Equations Based on Orthogonal Tensor Spherical Harmonics
- 100 *B. Skoczeń*
Accelerated Shakedown in Two-Phase Structures Caused by the Plastic Strain Induced Phase Transformation
- 102 *W. Sumelka*
Fractional Viscoplasticity
- 104 *M. Svanadze*
Mathematical Problems in the Full Coupled Theory of Double-Porosity Materials
- 106 *P. Szeptyński, J. Ostrowska-Maciejewska, R. Pęcherski*
Extension of the Rychlewski Limit State Criterion Accounting for the Asymmetry of Elastic Range
- 108 *M. Tkocz, J. Pawlicki, F. Grosman*
Flow Stress in Unconventional Metal Forming Processes
- 110 *T. Wegner, D. Kurpisz*
Energy-Based Model of Nonlinear Elastic Orthotropic Material on the Example of Car's Tarpaulin
- 112 *R. Zaera, J.A. Rodríguez-Martínez, D. Rittel*
Modeling the Strain Induced Martensitic Transformation under Impact and its Influence on the Taylor–Quinney Coefficient
- 114 *G. Ziętek, Z. Mróz*
Thermomechanical Model for Austenitic Steel with Martensitic Transformation Induced by Temperature and Stress Variation

Experimental Mechanics

- 118 *M. Nishida, H. Watanabe, N. Fukuda, H. Ito*
Evaluation of Dynamic Properties of PLA/PBAT Polymer Alloys Using Tensile Split Hopkinson Bar (*keynote lecture*)
- 120 *S. Dodla, A. Bertram*
Investigation of Microstructural Influences on the Mechanical Properties of Cu–Ag Eutectic Alloy
- 122 *T. Frąś, R. Pęcherski, A. Rusinek*
Experimental Investigations of the Influence of Moderate Strains and Strain Rates on the Yield Surface of Ofhc Copper
- 124 *D. Inoshita, S. Yamanaka, T. Iwamoto*
A Study on Strain Rate Sensitivity of Transformation Behavior of on Trip Steel by Capturing Change in Impedance
- 126 *M. Kneć, T. Sadowski*
Influence of Aluminum Alloy Surface Treatments and Curing Temperature for Bonding Strength and Strain Concentration
- 128 *Z. Kowalewski, Z. Nowak, W. Moćko*
Direct Impact Compression Test of Tantalum — Experimental Investigation and Model Identification

- 130 *Z.L. Kowalewski, T. Szymczak*
Variations of Stress State Components During Step Cyclic Loading of Power Plant Steel
- 132 *J. Loya, J. Fernández-Sáez*
Fracture Properties Determination on Pmma Beams in Three-Point Bending Tests
- 134 *K. Makowska, Z.L. Kowalewski, J. Szelążek*
Structural and Mechanical Properties Estimated by Means of Ultrasonic Technique
- 136 *W. Moćko, Z.L. Kowalewski*
Mechanical Properties of Selected Aluminium Alloys at Wide Range of Strain Rates
- 138 *W. Oliferuk, K. Kochanowski, Z. Płochocki, A. Adamowicz*
Determination of Thermal Diffusivity of Austenitic Steel Using Pulsed Infrared Thermography
- 140 *W. Oliferuk, M. Maj, K. Zembrzycki*
Distribution of Energy Storage Rate in Area of Strain Localization During Tension of Austenitic Steel
- 142 *M. Rośkiewicz, T. Smal*
Research on Durability of Adhesive Composites with Regard to Expedient Repair of Technical Objects
- 144 *H.-D. Rudolph*
Electro-Optical Measuring System Model 200XY
- 146 *A. Rutecka, Z.L. Kowalewski, K. Pietrzak, L. Dietrich, K. Makowska, J. Woźniak, M. Kostecki, W. Bochniak, A. Olszyna*
AlMg/SiC Metal Matrix Composite under Fatigue and Creep Conditions
- 148 *A.M. Stręk*
Yield Criteria and Their Verification for Metal Foams
- 150 *J. Tabin*
Quality Optimization of Strain Measurement Path Included in the Experimental Cryogenic Stand for Tensile Testing at Ultra-Low Temperatures

Fracture, Damage and Fatigue of Materials

- 154 *J. Fernández-Sáez, E. Giner, D. Fernández-Zúñiga, J.A. Loya, A. Fernández-Canteli*
Some Results on Three-Dimensional Effects in Mode I Fracture Problems (*keynote lecture*)
- 156 *P. Perzyna*
Multiscale Constitutive Modelling of the Influence of Anisotropy Effects on Fracture Phenomena in Inelastic Solids (*keynote lecture*)
- 160 *G. Altmeyer*
Prediction of Material Instability by Linear Stability Method. Application to Elasto-Viscoplastic Media
- 162 *M. Białas*
Progressive Frictional Delamination of an Infinite Elastic Film on a Rigid Substrate due to in-Plane Point Loading
- 164 *K. Bizoń*
The Use of Magnetic Methods for the Evaluation of the Degree of Fatigue Degradation of Cast Steel LII500 Exemplified by Drive Wheels of Locomotive EU07

- 166 *H. Egner, M. Ryś, B. Skoczeń*
Modeling of Interaction Between Damage and Phase Transformation in Two-Phase Materials at Cryogenic Temperatures
- 168 *A. Kaczyński, B. Monastyrskyy*
On the 3D Thermoelastic Problem for an Anticrack Subjected to a Uniform Heat Flow in the Inclusion Plane
- 170 *F. Laengler, T. Mao, A. Scholz*
Creep-Fatigue Reliability of High Temperature Materials Applied in Turbine Housings of Turbochargers
- 172 *D. Lumelskyy, J. Rojek, R. Pęcherski, F. Grosman, M. Tkocz*
Numerical Studies of Formability of Pre-Stretched Steel Sheet
- 174 *M. Nowak, Z. Nowak, R. Pęcherski, M. Potoczek, R. Śliwa*
On the Geometry and Compressive Strength of Ceramic Foams

Geomechanics

- 178 *S. Pietruszczak, E. Haghghat*
Assessment of Slope Stability in Cohesive Soils due to a Rainfall (*keynote lecture*)
- 180 *R. Balevičius, Z. Mróz*
Modeling of the Combined Slip and Finite Sliding in a Frictional Contact Interaction of Spherical Particles: Static and Dynamic Response
- 182 *J. Kozicki, J. Tejchman*
Discrete Simulations of Quasi-Static Triaxial and Biaxial Compression for Sand Using DEM
- 184 *D. Leśniewska, M. Niedostatkiewicz, J. Tejchman*
Experimental Study on Shear Localization in Granular Materials Within Combined Strain and Stress Field
- 186 *R. Staroszczyk*
Steady Axially-Symmetric Polar Ice Sheet Flow with Evolving and Recrystallizing Fabric

Micromechanics, Interfaces and Multi-Scale Modelling

- 190 *M. Wojciechowski, M. Lefik, D.P. Boso*
Functionally Graded Composites: Numerical Modeling with Finite Element Method and Artificial Neural Network (*keynote lecture*)
- 192 *J. Bajolek, S. Philippon, K. Huynen, J. Salat, P. Lipinski*
Development of a Passive Heat Dissipation System Using Phase Change Materials Associated with Open Cell Metal Foams
- 194 *M. Cieszko*
Continuum Description of Quasistatic Capillary Transport of Liquid in Unsaturated Porous Materials
- 196 *M. Cieszko, P. Gadzała, Z. Szczepański, M. Kempński*
Determination of Pore Space Structure of Autoclaved Aerated Concrete Based on 3D μ ct Images and Mercury Porosimetry

- 198 *A. Javili, A. McBride, P. Steinmann*
Thermomechanical Solids with Energetic Material Interfaces
- 200 *B. Kuczma, M. Kuczma*
Adhesive Joints in Composite Beams of Steel and Concrete — Modelling, Experiment and Computer Simulation
- 202 *J. Lengiewicz, S. Stupkiewicz*
Micromechanical Study of Frictional Anisotropy in Rough Elastic Contacts
- 204 *M. Maździarz, K. Nalepka, Z. Szymański, J. Hoffman, S. Kret, S. Kucharski, P. Nalepka*
Atomistic Model of Decohesion of Copper–Corundum Interface
- 206 *Sz. Nosewicz, J. Rojek, K. Pietrzak, M. Chmielewski, D. Kaliński, R. Kačianauskas*
Discrete Element Modelling of Solid State Sintering Process of Metal–Ceramic Composite
- 208 *I. Pączelt, Z. Mróz*
Thermomechanical Analysis of Steady State Wear Problems for Monotonic and Periodic Contact Sliding Motion
- 210 *V. Rimša, S. Pilkavičius, R. Kačianauskas, J. Rojek*
Investigation of the Normal Contact Between Two Spherical Particles with Interface Material
- 212 *L. Scheunemann, J. Schröder, D. Balzani, D. Brands*
Construction of Statistically Similar RVEs for 3D Microstructures
- 214 *Y. Uetsuji, H. Kuramae, K. Tsuchiya*
Two-Step Homogenization Simulation of Polycrystalline Piezoelectric Materials
- 216 *T.G. Zieliński*
Concurrence of the Micro-Scale Calculation and Inverse Identification of Parameters Used for Modelling Acoustics of Porous Media

Nonlinear and Stochastic Dynamics

- 220 *D. Yurchenko, A. Naess, P. Alevras*
Rotational Motion of a Stochastic Non Linear Mathieu Equation under White Noise and Narrowband Excitation (*keynote lecture*)
- 222 *R. Iwankiewicz*
Generalized Moment Equations Technique for Dynamic Systems under Non-Poisson Impulses: Approach Based on Integro-Differential Chapman–Kolmogorov Equations
- 224 *P. Koziol, T. Krzyżyński*
Wavelet Analysis of a Dynamic Response of a Beam Resting on a Nonlinear Foundation

Shells and Plates

- 228 *K. Wiśniewski, E. Turska*
On Shell Elements Derived from Hu–Washizu Functional (*keynote lecture*)
- 230 *G. Avalishvili, M. Avalishvili*
On Two-Dimensional Models of Thermoelastic Shells in the Framework of Lord–Shulman Nonclassical Theory of Thermoelasticity

-
- 232 *M. Barski, A. Muc*
Buckling of the Composite Plates with Holes Subjected to Uniaxial and Biaxial Compression
- 234 *S. Bauer, E. Voronkova, L. Karamshina*
The Stress–Strain State of a Three-Layered Spherical Shell under Normal Pressure
- 236 *N. Chinchaladze*
Harmonic Vibration of a Cusped Plate in the Zero Approximation of Vekua’s Hierarchical Models
- 238 *S.V. Derezin, L.M. Zubov*
Relaxation of Residual Stresses in a Nonlinearly Elastic Plate
- 240 *A. Ermakov*
The Models of Nonclassical Anisotropic Spherical Shells
- 242 *G. Formica, M. Lembo, P. Podio-Guidugli*
Exact Levinson-Type Solutions for Multilayered Plates
- 244 *A. Girchenko, H. Altenbach, V.A. Eremeyev*
Instability of a Piezoelectric Helical Shell under Electrical Field
- 246 *J. Kaplunov, D.A. Prikazchikov*
An Asymptotic Model for the Konenkov Wave
- 248 *S. Karczmarzyk*
Local Model of Free Vibration of a Multilayered Sandwich Strip with Some Specific Fastening of Two Parallel Edges
- 250 *L.G. Kocsán*
hp Finite Element Model for Cylindrical Shells Using First-Order Stress Functions
- 252 *A.M. Kolesnikov*
The Finite Inflation of an Elastic Curved Tube with Noncircular Cross Section
- 254 *G. Mikhasev, A. Sheiko*
Governing Equations for Multi-Walled Carbon Nanotube Derived from Orthotropic Flügge Shell Theory and Nonlocal Elasticity
- 256 *G. Milani, A. Tralli*
Recent Developments in Computational Methods for Masonry Shells
- 258 *R. Nedin, A. Vatulyan*
Determination of Plane Heterogeneous Prestress Field in Plate
- 260 *A.D. Nguyen, M. Stoffel, D. Weichert*
Modeling of Shock Wave-Loaded Plates Using a Gradient-Enhanced Damage Model
- 262 *M. Serpilli, F. Krasucki, G. Geymonat*
A Second Gradient Reissner–Mindlin Plate Model via the Asymptotic Expansions Method
- 264 *A. Tobota, J. Karliński, A. Niechajowicz, P. Kaczyński*
Experimental and Numerical Studies of Foam-Filled Circular Tubes
- 266 *B. Tóth*
Dual-Mixed hp Finite Element Model for Elastodynamic Problems of Cylindrical Shells
- 268 *R. Winkler*
Low-Order Membrane and Shell Elements: The Assumed Central Strain Method and its Relation to Enhanced and Mixed Methods

- 270 Cz. Woźniak, J. Jędrzyak, B. Michalak
Vibrations of Periodically Stratified Unbounded Thick Plates
- 272 Cz. Woźniak, M. Wągrowaska, O. Szlachetka
A Model of a Thick Functionally Graded Laminated Plate with Interlaminar Defects

Smart Materials and Structures

- 276 G. Mikułowski, R. Wiszowaty, J. Holnicki-Szulc
Piezoelectric Actuation of a Pneumatic Adaptive Shock Absorber (*keynote lecture*)
- 278 J.M. Bajkowski, R. Zalewski, M. Pyrz
Modeling of a Sandwich Beam with Underpressure Granular Structure
- 280 J. Holnicki-Szulc, C. Graczykowski, P. Pawłowski, I. Ario
High Performance Valve for Adaptive Pneumatic Impact Absorbers
- 282 J. Kaleta, D. Lewandowski, M. Królewicz, M. Przybylski, P. Zajac
Magnetorheological Composites Based on Thermoplastic Matrices. Manufacture, Modelling, Experiment
- 284 P. Kędziora, A. Muc
Optimal Piezoelectric Location for Composite Structures
- 286 M. Kharrat, M.N. Ichchou, O. Bareille, W. Zhou
Defect Detection and Sizing in Pipes Using Torsional Guided Waves
- 288 G. Knor, J. Holnicki-Szulc
Numerical Modeling of Hardening and Cooling of Concrete Structures
- 290 K. Kulasiński, E.A. Pieczyska, H. Tobushi, K. Takeda
TiNi SMA Subjected to Compression — Thermomechanical Effects Investigated with IR Technique
- 292 K. Mitsui, K. Takeda, H. Tobushi, N. Levintant-Zayonts, S. Kucharski
Influence of Nitrogen Ion Implantation on Deformation and Fatigue Properties of TiNi Shape-Memory Alloy Wire
- 294 Ł. Nowak, T.G. Zieliński
Active Vibroacoustic Control of Beams and Plates with General Boundary Conditions
- 296 K. Takeda, H. Tobushi, E.A. Pieczyska
Creep Behavior under Stress-Controlled Subloop Loading in TiNi Shape Memory Alloy

Structural Mechanics, Optimization and Reliability

- 300 T. Garbowski, A. Knitter-Piątkowska, D. Jaśkowska
Stochastic Model Reduction Techniques Applied to Inverse Problems in Structural Engineering (*keynote lecture*)
- 302 B. Bochenek, K. Tajs-Zielińska
Cellular Automata as Efficient Generator of Optimal Topologies
- 304 M. Chen, A. Hachemi, D. Weichert
Shakedown Limit Loads for Periodic Heterogeneous Structural Elements

-
- 306 *J. Hou, Ł. Jankowski, J. Ou*
Online Local Structural Health Monitoring Using the Substructure Isolation Method
- 308 *J. Kang, A. Becker, W. Sun*
Implementation of Optimization Techniques in Determining Elastic-Plastic and
Visco-Plastic Properties from Instrumented Indentation Curves
- 310 *A. Knitter-Piątkowska, T. Garbowski, A. Garstecki*
Structural Damage Detection Through Wavelet Decomposition and Soft Computing
- 312 *R. Lammering, F. Dirksen, M. Rösner*
Design and Analysis of Compliant Mechanisms with Flexure Hinges
- 314 *F. Lisowski*
The Optimal Design of Bolted Connections by Applying Finite Element Method
- 316 *E. Postek, C. Caliendo, P.M. Latino*
Numerical Model of AlN-Based Bulk Acoustic High-Frequency Resonators
- 318 **Index of Authors**

Invited Plenary Lectures

MULTI-AXIAL STATIC AND DYNAMIC EXPERIMENTS TO INVESTIGATE THE EFFECT OF STRESS TRIAXIALITY AND LODE ANGLE ON DUCTILE FRACTURE

Dirk Mohr

*Solid Mechanics Laboratory (CNRS-UMR 7649), Department of Mechanics,
École Polytechnique, Palaiseau, France*

*Impact and Crashworthiness Laboratory, Department of Mechanical Engineering,
Massachusetts Institute of Technology, Cambridge MA, USA*

Recent experimental results have stimulated the development of Lode angle dependent fracture models. This talk provides an overview on new techniques for the experimental characterization of the effect of stress state on ductile fracture. Different types of flat specimens with selected cut-outs are discussed to characterize the effect of stress state on ductile fracture. An optimized butterfly-shaped specimen as well as a modified Lindholm specimen are presented for fracture testing under combined loading in dual actuator systems. Special emphasis is placed on the accuracy of a hybrid experimental-numerical approach which makes use of digital image correlation and finite element analysis to determine the local loading history all the way to the onset of ductile fracture. Examples are shown to elucidate the importance of reliable ductile fracture experiments to come up with physically-sound ductile fracture models for low stress triaxialities. In addition, a new SHPB tensile testing technique is presented to determine the effect of stress state under dynamic loading conditions.

The effect of strain-rate and stress-state on the ductile fracture of Advanced High Strength Steel (AHSS) sheets is determined using a hybrid experimental-numerical technique. Experiments under static loading conditions have demonstrated that both the effect of the stress-triaxiality and Lode angle have a strong influence on the apparent ductility of AHSS sheets. The so-called basic fracture testing program consisting of notched tensile specimens with different notch radii and a tensile specimen with a central hole is therefore performed for dynamic loading conditions. A newly-developed tensile testing device is employed in conjunction with a modified split Hopkinson pressure bar system to perform the dynamic experiments. The material parameters of the underlying rate-dependent plasticity model are identified through an inverse calibration method. Based on the recorded force-time histories and the DIC displacement-time measurements, finite element simulations are performed to determine the local stress and strain state history within the specimen gage section up to the point of onset of fracture. In addition to uniaxial experiments for pre-necking strain rates of up to $10^3/s$, equi-biaxial punch experiments are performed for equivalent plastic strain rates ranging from $10^{-3}/s$ to $10^3/s$. It is found that the ductility of the tested TRIP and DP steels increases as a function of strain rate. A rate-dependent phenomenological fracture model is therefore proposed to account for both the effect of strain-rate and stress-state on the onset of ductile fracture.

Keywords: ductile fracture, strain rate, stress triaxiality, lode angle

INTERFACIAL ENERGY EFFECTS IN MICROMECHANICAL MODELLING OF SHAPE MEMORY ALLOYS

S. Stupkiewicz, H. Petryk

Institute of Fundamental Technological Research (IPPT), Warsaw, Poland

1. Introduction

Shape memory alloys (SMA) exhibit spectacular effects, such as pseudoelasticity and shape memory effect, which are exploited in many advanced practical applications. These effects are associated with martensitic phase transformation induced by temperature changes or mechanical loading. At the microscale, the transformation proceeds by formation and evolution of complex martensitic microstructures at multiple length scales. Understanding these multiscale phenomena is crucial for development of reliable predictive models of SMA behaviour, hence significant research efforts have been spent in the last two decades on micromechanical modelling of shape memory alloys, martensitic microstructures, and related phenomena.

As mentioned above, martensitic transformation in SMA is a multiscale phenomenon. Evolution of the corresponding microstructures is thus associated with formation and propagation of interfaces at multiple scales. For instance, evolving laminated microstructures are typical for stress-induced martensitic transformations [1].

It is well known that size effects are governed by size-dependent interfacial energy contributions. Modelling of size effects in SMA requires thus consideration of the interfacial energy contributions at various scales of martensitic microstructures. This lecture will present an overview of the related aspects of the mechanics of martensitic microstructures.

2. Microstructured interfaces and interfacial energy

An interface between austenite and twinned martensite is a typical example of a microstructured interface where the local incompatibility of transformation strains is accommodated by elastic microstrains in a thin transition layer along the interface. The associated interfacial energy of elastic microstrains is, in fact, a bulk energy at a suitably fine scale, and it is interpreted as an interfacial energy at a higher scale, which corresponds to a kind of scale transition. The problem is that this interfacial energy cannot be measured directly, so that theoretical predictions seem to be the only alternative. A micromechanical framework for prediction of the elastic micro-strain energy and morphology of the transition layer at the austenite–twinned martensite interface has recently been developed in [2, 3, 4].

3. Incremental energy minimization

Formation of microstructure can be explained by minimization of non-convex free energy. However, consideration of the bulk energy contributions alone leads to infinitely fine microstructures. It is well known that characteristic length scales are introduced by size-dependent interfacial energy contributions, which allows prediction of characteristic dimensions of the microstructure.

Evolution of microstructure is associated not only with changes in the free energy but also with dissipation. A relevant evolution rule can be derived from the criterion of stability and takes the form of minimization of the incremental energy supply to the thermodynamic system, including the rate-independent dissipation [5]. The incremental energy minimization approach is fairly general; however, it requires a certain symmetry restriction to be imposed on the state derivative of the dissipation function [5, 6]. The interfacial energy contributions to the free energy and dissipation can be included in this framework in a natural way [6, 7].

In a related recent study of stability of equilibrium of evolving laminates [8], it is shown that a homogenized phase-transforming laminate with no length scale exhibits a localization instability. However, for laminates of finite spacing, the evolving laminates are stabilized by the elastic micro-strain energy at the boundary of the localization zone.

4. Size effects in SMA polycrystals

Applications of the general framework discussed above include a study of the pseudoelastic response of an idealized CuAlNi polycrystal [7] and a study of the grain-size effect on the macroscopic response of NiTi shape memory alloy [9]. It is demonstrated that quantitative evaluation of size effects is possible without introducing any artificial length-scale parameters. In particular, the effect of grain size on the stress-strain response and hysteresis width can be studied quantitatively, and the characteristic dimensions of the microstructure, e.g., martensite plate thickness and spacing, can be predicted.

References

- [1] S. Stupkiewicz. *Micromechanics of Contact and Interphase Layers*. Springer, Berlin Heidelberg New York, 2007.
- [2] G. Maciejewski, S. Stupkiewicz, and H. Petryk. Elastic micro-strain energy at the austenite-twinned martensite interface. *Arch. Mech.*, 57:277–297, 2005.
- [3] S. Stupkiewicz, G. Maciejewski, and H. Petryk. Low-energy morphology of the interface layer between austenite and twinned martensite. *Acta Mater.*, 55:6292–6306, 2007.
- [4] S. Stupkiewicz, G. Maciejewski, and H. Petryk. Elastic micro-strain energy of austenite-martensite interface in NiTi. *Modelling Simul. Mater. Sci. Eng.*, 20:035001, 2012.
- [5] H. Petryk. Incremental energy minimization in dissipative solids. *C. R. Mecanique*, 331:469–474, 2003.
- [6] H. Petryk and S. Stupkiewicz. Interfacial energy and dissipation in martensitic phase transformations. Part I: Theory. *J. Mech. Phys. Solids*, 58:390–408, 2010.
- [7] H. Petryk, S. Stupkiewicz, and G. Maciejewski. Interfacial energy and dissipation in martensitic phase transformations. Part II: Size effects in pseudoelasticity. *J. Mech. Phys. Solids*, 58:373–389, 2010.
- [8] H. Petryk and S. Stupkiewicz. Instability of equilibrium of evolving laminates in pseudo-elastic solids. *Int. J. Non-Linear Mech.*, 47:317–330, 2012.
- [9] S. Stupkiewicz and H. Petryk. Grain-size effect in micromechanical modelling of hysteresis in shape memory alloys. *ZAMM*, 90:783–795, 2010.

ON RECENT PROGRESS IN LIMIT AND SHAKEDOWN ANALYSIS

D. Weichert

Institute of General Mechanics, RWTH-Aachen University, Germany

Abstract

To determine limit states of mechanical structures has always been one of the most important design issues in mechanical and civil engineering and long before modern computational tools had been available, engineering scientists and mathematicians have developed methods to deal with this question. For this, most important is to identify failure mechanisms in their particular technical context, to model them and to understand the structural evolution leading to the according limit state.

Among the large variety of scenarios, we deal here exclusively with failure caused directly by inelastic material behaviour, concentrating on ductile metal or metal-like materials. From methodological point of view, only so-called Direct Methods, in particular Limit- and Shakedown Analysis are considered. Limit Analysis, applicable only in the case of monotone loading is considered as particular case of Shakedown analysis, valid for variable loads with not deterministically given loading histories.

In this lecture a state-of-the-art presentation of Direct Methods in this sense is given focusing on the extension of range of validity of the path making theorems by Melan (1936, 1938) and Koiter (1956). On the theoretical side, it is shown how Melan's theorem has been adapted to more sophisticated material models than the linear elastic-ideal plastic or unlimited linear kinematical hardening models. Besides thermo-mechanical loading these generalisations include more general forms of hardening, soil-type material laws, material damage and periodic composites.

Another issue addressed in this talk is the transmission of the theoretical achievements into the modern world of numerical methods: Despite the highly powerful statements of the theorems, no widespread use has been made of them in the past in practical engineering. This somewhat paradoxical situation is essentially caused by the ways how solutions are constructed when using these theorems. The tremendous progress in computer science and optimisation techniques however allows overcoming the obstacles and ways have been found to bridge the gap between Direct Methods and popular computational software based on step-by-step methods.

Finally, results from various fields of engineering are presented in order to illustrate the practical interest of the methodology. The lecturer will not fail to give a short historical overview honouring in particular the outstanding contribution by Polish scientists in this field and to highlight open questions and topics of ongoing and future research.

References

- [1] E. Melan (1936). Theorie statisch unbestimmter Systeme aus idealplastischem Baustoff, *Sitzber. Akad. Wiss., Wien, Abt. IIA*, 1936, 145, 195-218.
- [2] E. Melan (1938). Zur Plastizität des räumlichen Kontinuums, *Ing. Arch.*, 1938, **9**, 116-126
- [3] W. T. Koiter (1956). A new general theorem on shakedown of elastic-plastic structures. *Proc. Kon. Ned. Akad. Wet.*, **B59**, 24-34.
- [4] W. T. Koiter (1960). General theorems for elastic-plastic solids. In 'Progress in Solid Mechanics', eds. Sneddon, J. N. and Hill, R., **1**, North Holland, Amsterdam, 165-221.
- [5] J. A. König (1987). *Shakedown of Elastic-Plastic Structures*, Elsevier, Amsterdam.

-
- [6] D. A. Gokhfeld and O. F. Cherniavsky (1980). *Limit analysis of structures at thermal cycling*, Sijthoff & Noordhoff, Alpen aan den Rijn, The Netherlands.
 - [7] G. Maier (1969). Shakedown theory in perfect elastoplasticity with associated and nonassociated flow-laws: a finite element, linear programming approach. *Meccanica*, **4**, 250-260.
 - [8] G. Maier (1970). A matrix structural theory of piecewise-linear plasticity with interacting yield planes. *Meccanica*, **5**, 55-66.
 - [9] Sawczuk (1969). Evaluation of upper bounds to shakedown loads for shells. *J. Mech. Phys. Solids*, **17**, 291-301.
 - [10] Sawczuk (1989). *Mechanics and Plasticity of Structures*, PWN, Ellis Horwood Limited.
 - [11] M. Źyczkowski (1981). *Combined Loadings in the Theory of Plasticity*, Polish-Scientific Publ.
 - [12] Z. Mróz, D. Weichert and S. Dorosz eds. (1995). *Inelastic Behaviour of Structures under Variable Loads*, Kluwer Academic Publishers, Dordrecht.
 - [13] D. Weichert and J. Gross-Weege (1988). The numerical assessment of elastic-plastic sheets under variable mechanical and thermal loads using a simplified two-surface yield condition. *Int. J. Mech. Sci.*, **30**, 757-767.
 - [14] G. Maier, J. Pastor, A.R.S. Ponter, D. Weichert (2003). Direct Methods of Limit and Shakedown Analysis, in: *Comprehensive Structural Integrity*, Elsevier-Pergamon.
 - [15] D. Weichert, A.R.S. Ponter eds. (2008). *Limit States of Materials and Structures*, Springer.

RESULTANT THERMODYNAMICS OF SHELLS

W. Pietraszkiewicz

Institute of Fluid-Flow Machinery, PAFci, Gdańsk, Poland

1. Introduction

Non-linear two-dimensional (2D) models of shell thermodynamics formulated on the shell base surface M are usually developed by two main approaches: 1) the so-called direct 2D approach, and 2) the one derived from 3D continuum thermodynamics. We briefly review some known approaches to 2D shell thermodynamics. It is noted that the basic 2D relations and physical interpretation of their ingredients vary substantially throughout the literature. In particular, in the derived approach one usually expands all 3D field into series of thickness coordinate and then assumes some kinematic, dynamic, and/or thermal constraints to make the 2D shell relations simpler and more convenient for applications. In all cases errors of such 2D shell relations are practically indefinable.

2. Refined resultant approach

Simmonds [1,2] proposed to apply direct through-the-thickness integration of 3D laws of rational thermodynamics [3] and derived corresponding resultant 2D laws of shell thermodynamics. But in [4] it was noted that the resultant balance of energy, when expressed through the resultant fields, is incomplete. Some part of 3D mechanical power following from self-equilibrated distributions across thickness of the stresses, body forces and boundary tractions cannot be accounted by the through-the-thickness integration. Hence, an additional surface stress power called an interstitial working was added in [4] to the resultant balance of energy and then transferred by appropriate transformation into the resultant entropy inequality. The so refined resultant 2D balances of linear momentum, angular momentum, energy and 2D entropy inequality formulated on M may be regarded as direct implications of corresponding 3D laws of rational thermodynamics [3] based on the Clausius-Duhem inequality. In the Lagrangian description these local laws satisfied on any part $\Pi \subset M$ are

$$(1) \quad \begin{aligned} \text{Div } N + \rho f &= \dot{l}, \quad \text{Div} + \text{ax} (NF^T - FN^T) + \rho c = \dot{k} + \dot{y} \times l, \\ \rho \dot{\varepsilon} - (N E^\circ + M K^\circ + \text{Div } w) - (\rho r - \text{Div } q) &= 0, \\ -\rho \dot{\psi} - \rho \dot{\theta} \eta + N E^\circ + M K^\circ + \text{Div } w - \rho \theta s - \frac{1}{\theta} q \cdot g + \theta \text{Div } s &\geq 0. \end{aligned}$$

In (1), N and M are the referential resultant 2D stress and couple-stress tensors, ε, η, ψ and q are the resultant 2D internal energy, entropy, free energy and heat flux vector, E° and K° are the co-rotational time derivatives of 2D strain and bending tensors, w, s and s are the 2D interstitial working vector, extra surface heat supply and extra surface entropy supply vector, respectively, θ is the mean referential surface temperature, and other surface fields in (1) are described in [4].

The kinematic structure of the resultant shell thermodynamics is identical to the one of Cosserat surface, with the deformed position vector y and rotation tensor Q of M as independent kinematic variables of shell motion. The structure of resultant laws (1) containing the extra surface field s and divergences of vector fields w, q , reminds somewhat the one of local laws of 3D extended thermodynamics.

3. Constitutive equations

In the 2D BVP partly described by (1), the three fields $\mathbf{y}, \mathbf{Q}, \theta$ defined on M are the independent thermo-kinematic field variables, the eight fields $\Sigma \equiv (\mathbf{N}, \mathbf{M}, \boldsymbol{\varepsilon}, \boldsymbol{\eta}, \mathbf{q}, \mathbf{w}, s, \dot{s})$ are to be specified by material constitutive equations, while the 2D linear momentum \mathbf{l} and angular momentum \mathbf{k} by kinetic constitutive equations. If one allows the fields Σ to depend on histories of $\mathbf{y}, \mathbf{Q}, \theta$ only locally through the first time derivatives at time t and through the first surface gradients at any $x \in M$, then the corresponding constitutive assumption would be

$$(2) \quad \Sigma(x, t) = \hat{\Sigma}_{\kappa}(\mathbf{E}, \mathbf{K}, \text{Grad}\mathbf{E}, \text{Grad}\mathbf{K}, \dot{\mathbf{E}}, \dot{\mathbf{K}}, \theta, \dot{\theta}, \mathbf{G}),$$

where κ is the reference placement, $(\mathbf{N}, \mathbf{M}, \mathbf{E}, \mathbf{K}) = \mathbf{Q}^T(\mathbf{N}, \mathbf{M}, \mathbf{E}, \mathbf{K})$ and \mathbf{G} is the second surface gradient of θ .

Following Coleman and Noll [5] it is recognized that the entropy inequality (1)₄ plays the role of a restriction placed on allowable forms of the response functions $\hat{\Sigma}_{\kappa}$ in every thermomechanical process compatible with the resultant 2D balance laws (1)₁₋₃. As a result, it is found that $\boldsymbol{\psi} = \hat{\boldsymbol{\psi}}_{\kappa}(\mathbf{E}, \mathbf{K}, \theta)$, with the same structure of $\hat{\boldsymbol{\varepsilon}}_{\kappa}$ and $\hat{\boldsymbol{\eta}}_{\kappa}$, equilibrium parts of stress measures $\mathbf{N}^E = \boldsymbol{\psi}_{,\mathbf{E}}, \mathbf{M}^E = \boldsymbol{\psi}_{,\mathbf{K}}$, while for dynamic parts $\mathbf{N}^D = \mathbf{N} - \mathbf{N}^E, \mathbf{M}^D = \mathbf{M} - \mathbf{M}^E$ and other fields we obtain the following restriction:

$$(3) \quad \begin{aligned} & \mathbf{N}^D \dot{\mathbf{E}} + \mathbf{M}^D \dot{\mathbf{K}} - \rho \theta \dot{s} - \frac{1}{\theta} (\mathbf{q} - s_{,\theta}) + \frac{1}{\theta} s_{,g} \mathbf{G} + \text{tr} \left(\frac{1}{\theta} s_{,G} \circ \mathbf{G} \right) \\ & + \text{tr}(\mathbf{w}_{,\mathbf{E}} \circ \text{Grad}\mathbf{E}) + \text{tr}(\mathbf{w}_{,\mathbf{K}} \circ \text{Grad}\mathbf{K}) + \text{tr}(\mathbf{w}_{,\text{Grad}\mathbf{E}} \text{Grad}^2\mathbf{E}) + \text{tr}(\mathbf{w}_{,\text{Grad}\mathbf{K}} \text{Grad}^2\mathbf{K}) \geq 0. \end{aligned}$$

Here \circ and \cdot are intrinsic double-dot tensor multiplications of various-order tensors. In case of thermoelastic shells the above restriction can be further simplified.

Explicit forms of material constitutive equations can be constructed by further requiring material frame-indifference and material symmetry. Kinetic constitutive equations for \mathbf{l} and \mathbf{k} are constructed using heuristic arguments.

Resultant 2D thermodynamics has been applied, for example, to problems of phase transitions in shells, [6].

Acknowledgement The author was supported by the Polish Ministry of Science and Education with the grant N506 254 237.

References

- [1] J.G. Simmonds (1984). The nonlinear thermodynamical theory of shells: Descent from 3-dimensions without thickness expansion. In: E.L. Axelrad and F.A. Emmerling (eds.), *Flexible Shells*, 1-11. Springer-Verlag, Berlin.
- [2] J.G. Simmonds (2011). A classical nonlinear thermodynamic theory of elastic shells based on a single constitutive assumption, *J. Elast.*, DOI 10.1007/s10659-010-9293-2.
- [3] C. Truesdell (1984). *Rational Thermodynamics*, 2nd ed. Springer-Verlag, New York.
- [4] W. Pietraszkiewicz (2011). Refined resultant thermomechanics of shells, *Int. J. Engng. Sci.*, **49**, 1112-1124.
- [5] B.D. Coleman and W. Noll (1963). The thermodynamics of elastic materials with heat conduction and viscosity, *Arch. Rational Mech. Anal.*, **13**, 167-178.
- [6] V.A. Eremeyev and W. Pietraszkiewicz (2011). Thermomechanics of shells undergoing phase transitions, *J. Mech. Phys. Sol.*, **59**, 1395-1412.

ADVANCES IN THE PARTICLE FINITE ELEMENT FOR MULTIDISCIPLINARY PROBLEMS IN SOLID MECHANICS

E. Oñate^{1,2}, *M.A. Celigueta*¹, *S.R. Idelsohn*^{*}, *F. Salazar*¹, *A. Larese*¹ and *R. Rossi*¹
¹ *International Center for Numerical Methods in Engineering (CIMNE), Barcelona, Spain*

^{*} *ICREA Research Professor at CIMNE*

² *Universitat Politècnica de Catalunya (UPC), Barcelona, Spain*

1. Introduction

We present recent advances in the Particle Finite Element Method (PFEM) [1-3] for solving multidisciplinary problems in solid mechanics.

In the PFEM the fluid and the solid domains are modelled using an *updated Lagrangian formulation*. That is, all variables in the fluid and solid domains are assumed to be known at all the nodes in the *current configuration* at time t . The new set of variables in both domains are sought for in the *next or updated configuration* at time $t + \Delta t$. A mesh connecting the nodes (particles) is regenerated *at each time step* in order to solve the governing equations for both the fluid and solid problems in the standard FEM fashion. The nodes discretizing the fluid and solid domains are treated as *material particles* which motion is tracked during the transient solution. This is useful to model the separation of fluid particles from the main fluid domain in a splashing wave, or soil particles in a bed erosion problem, and to follow their subsequent motion as individual particles.

An advantage of the Lagrangian formulation is that the convective terms disappear from the fluid equations. The difficulty is however transferred to the problem of adequately moving the mesh nodes. We use a mesh regeneration procedure based on an extended Delaunay tessellation [1].

The PFEM is particularly suited for multidisciplinary coupled problems in mechanics such as fluid-structure interactions with large motions of the free surface and splashing of waves, heterogeneous fluid mixtures accounting for large deformations of the fluid and thermal coupling, and solid domains with multiple frictional contacts, surface erosion and material fragmentation [1-3].

2. Basic steps of the PFEM

1. The starting point at each time step is just the collection (cloud) of points in the fluid and solid domains. For instance ${}^n C$ denotes the cloud at time $t = t_n$ (Figure 1).
2. Identify the boundaries for both the fluid and solid domains defining the analysis domain ${}^n V$. The Alpha Shape method is used for the boundary definition [1].
3. Discretize the fluid and solid domains with a finite element mesh ${}^n M$.
4. Solve the coupled Lagrangian equations of motion for the fluid and the solid domains using a staggered scheme. Compute the variables in both domains at the next (updated) configuration.
5. Move the mesh nodes of the fluid and solid domain to a new position ${}^{n+1} C$. Ignore the mesh.
6. Go back to step 1 and repeat the solution process for the next time step to obtain ${}^{n+2} C$.

The quality of the numerical solution depends on the discretization chosen as in the standard FEM. Adaptive mesh refinement techniques can be used to improve the solution.

The PFEM is particularly suited for treating frictional-contact situations between deformable and rigid bodies in water. The PFEM can also be applied for modeling bed erosion due to water forces, as well as transport and deposition of sediment particles [2,3].

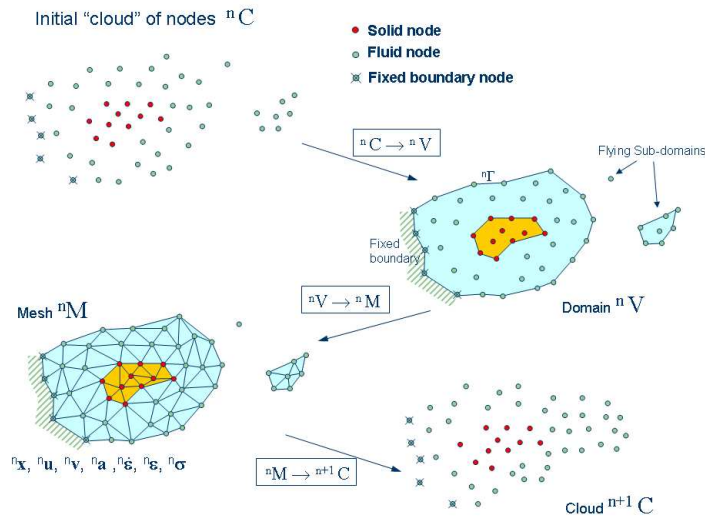


Figure 1: Scheme of steps to follow the motion of a continuum containing fluid and a solid subdomains using PFEM

The paper presents advances in the PFEM for solving multidisciplinary coupled problems in solid mechanics such as: a) the interaction between multiple bodies which are floating or submerged in a fluid account for FSI; b) the stability of structures under the action of waves; c) the modelling of the burning and melting of objects, d) transport of sediments in fluids and e) simulation of excavation and tunnelling processes [4], among others (Figure 2).

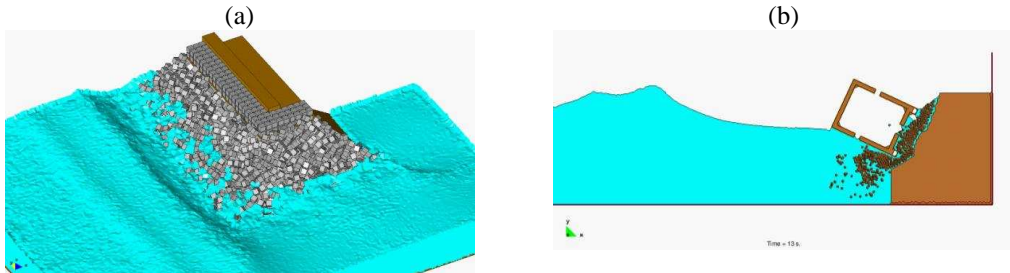


Figure 2: PFEM applications. (a) Waves acting on breakwater. (b) Falling of a solid in water due to erosion and failure of adjacent soil

6. References

- [1] E. Oñate, S.R. Idelsohn, F. Del Pin and R. Aubry (2004). The particle finite element method. An overview, *Int. J. Comput. Methods*, **1** (2), 267-307.
- [2] E. Oñate, M.A. Celigueta and S.R. Idelsohn (2006). Modeling bed erosion in free surface flows by the particle finite element method. *Acta Geotecnica*, **1** (4), 237-252.
- [3] E. Oñate, M.A. Celigueta, S.R. Idelsohn, F. Salazar and B. Suárez (2011). Possibilities of the particle finite element method for fluid–soil–structure interaction problems. *Computational Mechanics*, **48**, 307-318.
- [4] J.M. Carbonell, E. Oñate and B. Suárez: Modeling of ground excavation with the Particle Finite Element Method. *Journal of Engineering Mechanics (ASCE)* 136(4), (2010), 455-463.

AUXETICS: FROM FOAMS TO COMPOSITES AND BEYOND***Fabrizio Scarpa****Department of Aerospace Engineering**Advanced Composites Centre for Innovation and Science (ACCIS)**Dynamics and Control Research Group (DCRG)**Bristol Centre for Nanoscience and Quantum Information (NSQI)**Queens Building, Room # 0111, BS8 1TR Bristol, UK*

The term auxetic comes from the Greek auxetos: "which can expand". With this term we indicate a class of materials and structures exhibiting negative Poisson's ratio behaviour and, more generally, "negative material" properties (negative thermal expansion, stiffness, mass). Negative Poisson's ratio implies that a solid expands in one or more directions when it is tensioned along a specific one and, conversely, shrinks when compressed. In this lecture we will outline all recent developments in the field of auxetic materials, stretching from bulk sandwich applications in aerospace, to the more recent nano-structures with references to both experimental and modelling issues.

CONTACT INTERACTIONS IN GENERALIZED N-TH GRADIENT CONTINUA: MATHEMATICAL FOUNDATIONS AND A VIEW TO THE APPLICATIONS

Francesco dell'Isola

*Università degli Studi di Roma La Sapienza,
Dipartimento di Ingegneria Strutturale e Geotecnica*

The theory of generalized continua - which was started by E. and F. Cosserat - was greatly developed in the period between 1960 and 1974 by creative scientists as Mindlin, Rivlin, Green, Sedov, Toupin, Casal, Germain and many others.

More recently this topic started again to attract the interest of many scientist interested in the application of the generalized continua theories to model phenomena where different kinds of boundary layers may develop and grow as for instance in plasticity, damage and fracture, phase transition, flow in porous media, capillarity. Also the possibility of designing "exotic" materials exhibiting "non standard" material behavior seems to become technologically possible with the development of nano-sciences.

The advancement of the theory of generalized continua has been blocked by the crystallization of mechanical theories in the format due to Cauchy and Navier and considered by Truesdell and his epigones the only one which is acceptable. Only when the original D'Alembertian and Lagrangian spirit has been fully recovered then the theory of generalized continua can be consistently formulated.

In this presentation it is described the conceptual frame leading to the representation formula for contact interactions in terms of internal state of stress valid for generalized n-th gradient continua.

The mathematical tools needed are from differential geometry and theory of distributions, the postulation framework is based on the principle of virtual works, the mechanical phenomenology is described by means of suitable tensor sets describing the generalized stress and deformation states.

Finally some possible applications of generalized continua models are discussed: indeed these models seem suitable to describe many multi-scale mechanical systems presenting strong microscopic heterogeneities.

EFFECT OF INERTIA ON MULTIPLE NECKING AND ON DYNAMIC FAILURE OF DUCTILE MATERIALS

S. Mercier¹, N. Jacques² and A. Molinari¹

¹ LEM3, UMR CNRS 7239, University of Lorraine, Ile du Saulcy 57045 Metz, France

² LBMS, ENSTA Bretagne, 2 rue Francois Verny, 29806 Brest, France

1. Introduction

When subjected to high loading rates, materials and structures may fail via fragmentation process, shear banding, dynamic failure.... Such softening mechanisms which lead to a loss of stress carrying capacity of structures or of materials occur in numerous situations and concerns a wide range of domain. One may cite the security of structures, the crash of cars as well as high speed processing.

In the present talk, we will focus first on the occurrence of multiple necking patterns during dynamic extension. In a second step, we propose new insights in the development of damage and fracture by micro-voiding under dynamic loading. In both cases, inertia will be shown to be a key factor that controls damage growth, localization and failure in dynamic conditions.

2. Multiple necking

In rapid stretching, structures develop a multiple necking pattern which leads to the fracture in several fragments as observed on different experimental configurations by Niordson [1], Zhang and Ravi-Chandar [2] for example.

We propose to concentrate on the onset of the multiple necking via linear stability analyses. In Fressengeas and Molinari [3], it was shown that the interplay between multidimensional effects and inertia lead to a wavelength selection mechanism. The former approach has been revisited recently by Mercier and Molinari [4], adopting the formalism of Shenoy and Freund [5]. Different configurations were analysed: dynamic extension of plates [4], of rings and of tubes [6].

An illustration of the adopted methodology is proposed by considering a plate subjected to rapid extension. The material is assumed to be thermo-viscoplastic with strain hardening. Different flow laws have been used to describe the material response (powerlaw, Zerilli Amstrong, Preston Tonks and Wallace). As an important result, an effective strain rate sensitivity which links the effect of strain hardening, of thermal softening and of strain rate sensitivity appears naturally in the modelling and is thought to control the development of the necking instabilities [7]. To validate our theoretical approach, rapid expansions of hemispheres have been performed by the CEA Valduc (France). The deformation of the hemisphere was recorded by high-speed camera. The onset of necking was determined with a good accuracy. A comparison between theoretical results and rapid expansions of hemisphere demonstrates the pertinence of our approach with regards to the number of necks and the strain at the onset of instability.

3. Dynamic damage

The fracture of ductile materials is often the result of the nucleation, growth and coalescence of microscopic voids. In dynamic fracture, micro-voids sustain an extremely rapid expansion which generates strong acceleration of particles in the vicinity of cavities. These micro-inertial effects are thought to play an important role in the development of dynamic damage in plate impact tests (spall fracture). Due to the interplay between reflected waves, a large tensile stress develops in the target plate, and can lead to the complete fracture of the material in a few microseconds. To analyse ductile failure under dynamic conditions, a multiscale approach has been proposed recently [8]. The material

is initially free of void, but contains potential nucleation sites for microvoids. Each nucleation site is characterized by its own nucleation pressure. The evolution of the void radii is governed by a hollow sphere model that account for micro-inertia (local radial inertia around the expanding voids). The proposed model has been implemented in the finite element code ABAQUS/Explicit. Simulations of plate impact tests have been carried out. Simulated free-surface velocity profiles were found to be in agreement with experimental data available in the literature. The present approach is also able to reproduce the porosity map and void size distribution inside the target plate [9].

More recently, the multiscale approach has been extended for the analysis of dynamic crack propagation. The fracture of an axisymmetric notched bar and of a double edge cracked specimen were investigated. In both cases, the influence of microscale inertia is found to be significant. Because micro-inertia prevents damage to develop too rapidly, a regularizing effect is observed. As an important result, simulations based on our physically based model are less sensitive. Microscale inertia reduces the mesh sensitivity of the simulations. Micro-inertia is also found to lead to lower crack speed and higher fracture toughness, compared to situation where this contribution is neglected [10].

4. References

- [1] FL. Niordson (1965), A unit for testing materials at high strain rates, *Exp. Mech.* **5**:23-32
- [2] H. Zhang and K. Ravi-Chandar (2006), On the dynamic of necking and fragmentation – I. Real time and post mortem observations in AL 6061-O, *Int J. Fract.* **142**:183-217
- [3] C. Fressengeas and A. Molinari (1994), Fragmentation of rapidly stretching sheets, *Eur J. Mech A-Solid* **13**:251-268
- [4] S. Mercier and A. Molinari (2003), Predictions of bifurcation and instabilities during dynamic extension, *Int. J. Solids Struct* **40**:1995-2016
- [5] VB. Shenoy and LB. Freund (1999), Necking bifurcations during high strain rate extension, *J. Mech. Phys. Solids* **47**:2209-2233
- [6] S. Mercier and A. Molinari (2004), Analysis of multiple necking in rings under rapid radial expansion, *Int. Impact Engng.* **30**:403-419.
- [7] S. Mercier and N. Granier and A. Molinari and F. Llorca and F. Buy (2010) Multiple necking during the dynamic expansion of hemispherical metallic shells, from experiments to modelling, *J. Mech Phys Solids* **58**:955-982
- [8] C. Czarnota , N. Jacques, S. Mercier, A. Molinari , (2008). Modelling of dynamic ductile fracture and application to the simulation of plate impact tests on tantalum, *J. Mech. Phys. Solids* **56**(4):1624-1650.
- [9] N. Jacques, C. Czarnota, S. Mercier, A. Molinari, (2010). A micromechanical constitutive model for dynamic damage and fracture of ductile materials. *Int. J. Fract.* **162**:159-175
- [10] N. Jacques, S. Mercier, A. Molinari, (2012). Effects of microscale inertia on dynamic ductile crack growth. *J. Mech. Phys. Solids* **60**(4):665–690.

INTERDISCIPLINARY METHODS FOR DAMAGE ASSESSMENT OF MATERIALS SUBJECTED TO CREEP AND FATIGUE

Z.L. Kowalewski

Institute of Fundamental Technological Research, Warsaw, Poland

1. Introduction

Many testing techniques commonly used for damage assessments have been developed up to now. Among them we can generally distinguish destructive and non-destructive methods [1, 2]. Having the parameters of destructive and non-destructive methods for damage development evaluation it is instructive to analyze their variation in order to find possible correlations. This is because of the fact that typical destructive investigations, like creep or fatigue tests, give the macroscopic parameters characterizing the lifetime, strain rate, yield point, ultimate tensile stress, ductility, etc. without any information concerning microstructural damage development and material microstructure variation. On the other hand, non-destructive methods provide information about damage at a particular time of the entire working period of an element, however, without sufficient information about the microstructure and how it varies with time. Therefore, it seems reasonable to plan damage development investigations in the form of interdisciplinary tests connecting results achieved using destructive and non-destructive methods with microscopic observations in order to find mutual correlations between their parameters. This is the main issue considered in this paper.

2. Experimental procedure and results

Damage development during creep and fatigue was investigated using destructive and non-destructive methods in steels commonly applied in power plants (40HNMA, 13HMF and P91). In order to assess damage during such type processes the tests for each kind of steel were interrupted for a range of the selected time periods (creep) and number of cycles (fatigue). The standard tension tests of specimens prestrained due to creep or fatigue were carried out as destructive method of damage assessment. Subsequently, an evolution of the selected tensile parameters was taken into account for damage identification. Taking into account the results for the pre-fatigued 13HMF steel, Fig.1, it is easy to note that this material in terms of typical stress parameters is almost insensitive to fatigue prestraining, i.e. the yield point and ultimate tensile stress variations are rather small. An opposite effect can be observed for the same material prestrained under creep conditions. In this case the prior deformation leads to the hardening effect. Details of investigations on the 40HNMA and P91 steels were described earlier [1, 2]. The results for creep prestrained 40HNMA steel exhibited significant effect of softening. For all steels in question the same effect was achieved in the case of prestraining induced by means of plastic deformation at room temperature, i.e. hardening.

The ultrasonic and magnetic techniques were used as the non-destructive methods for damage evaluation. The results indicate that the acoustic birefringence, $U_{b_{pp}}$ - measure of the MBE (magnetic Barkhausen emission) and $U_{a_{pp}}$ - measure of the MAE (magnetoacoustic emission) are sensitive to the amount of prior deformation. Having parameters of destructive and non-destructive methods of damage assessments their mutual relationships were considered in order to find their character. The results exhibited that magnetic techniques can be very sensitive to degradation development for the small strain levels (up to 2%), and almost insensitive above that value. The ultrasonic techniques gave a completely opposite assessment: very poor sensitivity for small deformations and good for deformations greater than 2%.

In the case of material prestrained due to fatigue the destructive tests gave no clear assessment of material degradation, because the basic mechanical parameters (i.e. yield point and ultimate tensile stress) underwent to increase. Therefore, in order to assess a degree of fatigue damage the alternative techniques were proposed. The Wöhler diagram was determined as the first step of fatigue tests on the 13HMF and P91 steels. It represents the number of cycles necessary to failure under given stress amplitude. In the case of 13HMF steel this diagram was determined for the material in the as-received state and after exploitation (80 000h). Both Wöhler diagrams differ significantly, identifying a fatigue strength reduction due to the loading history applied. In the second step of fatigue investigations the tests were performed in order to assess variations of the hysteresis loop width under constant stress amplitude.

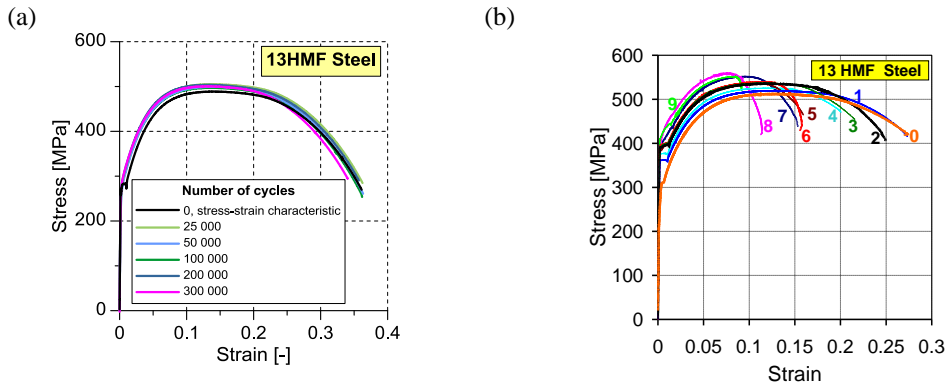


Fig. 1. Tensile characteristics after fatigue (a) and creep (b) prestraining for the 13HMF steel (numbers in the right diagram identify time to stop of creep test: 1 - 149h, 2 - 300h, 3 - 360h, 4 - 407h, 5 - 441h, 6 - 587h, 7 - 664h, 8 - 796h and 9 - 1720h; 0 – as-received material).

The results of these tests enabled damage identification under fatigue conditions. Two basic types of mechanisms in terms of the damage development can be distinguished. The first group is described by the ratcheting, whereas the second one by cyclic plasticity. In both cases, the strain changes measured for the entire sample volume are the sum of local deformations developing around defects in the form of non-metallic inclusions and voids (first group) or developing slips within individual grains (second group).

3. Conclusion

The results of parallel destructive and non-destructive tests on the prestrained power engineering steels enabled determination of damage sensitive parameters which were afterwards correlated, thus giving new tools for better predictions of damage development in materials subjected to creep or fatigue.

Acknowledgement: The support from the National Centre for Research and Development (Poland) under grant NR 15-0049-04/2008 is greatly appreciated.

4. References

- [1] Z.L. Kowalewski J. Szelażek S. Mackiewicz K. Pietrzak B. Augustyniak (2008). Evaluation of Damage in Steels Subjected to Exploitation Loading - Destructive and Non-Destructive Methods, *Int. J. Mod. Phys. Letter B* **22**, No 31/32, 5533.
- [2] B. Augustyniak M. Chmielewski L. Piotrowski Z.L. Kowalewski (2008). Comparison of properties of magnetoacoustic emission and mechanical Barkhausen effects for P91 steel after plastic flow and creep, *IEEE Tran. Mag.*, **4**, No 11, 3273.

Biomechanics

BONE REMODELING BASED ON SURFACE GROWTH. THEORY AND NUMERICS

J.F. Ganghoffer, G. Maurice
LEMTA. Université de Lorraine

The surface growth of biological tissues is presently analyzed at the continuum scale of tissue elements, adopting the framework of the thermodynamics of surfaces. Growth is assumed to occur in a moving referential configuration (called the natural configuration), considered as an open evolving domain exchanging mass, work, and nutrients with its environment. The growing surface is endowed with a superficial excess concentration of moles, which is ruled by an appropriate kinetic equation. From a thermodynamic framework of surface growth, the equilibrium equations are derived in material format from a suitable thermodynamic potential, highlighting the material surface forces for growth based on a surface Eshelby stress. Those forces depend upon a surface Eshelby stress, the curvature tensor of the growing surface, the gradient of the chemical potential of nutrients, and a surface force field. Application of the developed formalism to bone external remodeling highlights the interplay between transport phenomena and generation of surface mechanical forces. The model is able to describe both bone growth and resorption, according to the respective magnitude of the chemical and mechanical contributions to the material surface driving force for growth. Finite element simulations of the evolution of the shape of human femur under external stress due to external remodeling illustrate the model.

References

- [1] J.F. Ganghoffer (2012). A contribution to the mechanics and thermodynamics of surface growth. Application to bone external remodeling. *Int. J. Engng Sci.* **50**, Issue 1, 166–191.
- [2] J.F. Ganghoffer (2011). Mechanical modeling of growth considering domain variation. Part II: volumetric and surface growth involving Eshelby tensors. *J. Mech. Phys. Solids*. doi: 10.1016/j.jmps.2010.05.003.

ASSESSING ARTERIAL FLOW PARAMETERS TO MEASURE THE INFLUENCE OF BLOOD FLOW ON THE ARTERIAL WALLS

Krzysztof Czechowicz^{1,2}, Janusz Badur¹, Krzysztof Narkiweicz²

¹*Institute of Fluid-Flow Machinery PAN, Gdańsk, Poland*

²*Medical University of Gdansk, Gdańsk, Poland*

1. Introduction

Some flow parameters influence pathological changes in the arteries. Some of those parameters are very difficult to measure due to technical problems. The most renowned parameter is the Wall Shear Stress τ , which generates a reaction in the structure of the vessel walls and also has a major influence on the thickness of the wall.

One of the methods to assess most of the parameters is by creating computer models. We have proposed a method to create a computer model of the flow in the common carotid artery based on 2D ultrasound images.

2. Measurements

Input data has been acquired using an automatic ultrasound wall tracking system (ART.LAB, Esaote, Maastricht, Netherlands). The system automatically identifies walls of the vessel and calculates the diameter and arterial wall thickness, defined as the Intima Media Thickness (IMT). Data is gathered with a frequency of around 600Hz, and the spatial resolution is 23 μ m. This data has been used to generate a 3D geometry of the artery. For the purpose of the computer model the artery has been assumed to be a straight tube with the length of 75mm and the diameter that is assessed for every patient. Thanks to high time and spatial resolution this data can be used to model the pulsate flow condition.

3. Measurement analysis

To recreate blood flow conditions, vessel walls were assumed to have linear mechanical properties. It has been shown that such an assumption to the stress-strain relationship for the Common Carotid Artery (CCA) does not generate a significant error [1]. Local arterial blood pressure was assessed with the assumption that the diastolic (P_d) and mean blood pressure (MAP) is constant throughout the entire arterial system. The pressure waveform was calculated by rescaling the distention waveform to pressure values:

$$(1) \quad P(t) = \Delta d(t) \cdot \frac{MAP - P_d}{\Delta d} + P_d$$

Blood flow was next calculated using a 2-parameter Windkessel model:

$$(2) \quad \dot{m}(t) = \frac{P(t)}{R} + C \frac{dP(t)}{dt}$$

The parameters C and R model have been calculated by solving the above equation under the assumption that the average cardiac output is 100ml per cycle and 17% of the blood goes to the brain. It also has been assumed that in the end of the cardiac cycle, there is no blood flow.

The Young's Modulus for the arterial walls was calculated using the pulse pressure Δp , diastolic (minimal) diameter D and wall thickness IMT . Vessel wall tissues are incompressible thus the Poissons coefficient was assumed $\nu = 0.495$ [2].

$$(3) \quad E = 0,75 \cdot \frac{\Delta p \cdot D^2}{2 \cdot \text{IMT} \cdot \Delta D}$$

Also local pulse wave velocity was calculated using the Moens-Korteweg equation [3]. The blood itself is has been assumed to be non-Newtonian with viscosity obeying the Power Law:

$$(4) \quad \mu = K \cdot (\dot{\gamma})^n$$

where according to [4] best coefficient values are $K = 14.67 \text{ mPas}^n$ and $n = 0.7755$. The densities of the blood and vessel walls are very close and were assumed be constant. The density of blood was assumed $\rho_b = 1050 \frac{\text{kg}}{\text{m}^3}$, and similarly the density of the vessel wall was $\rho_w = 1040 \frac{\text{kg}}{\text{m}^3}$

4. Model

The computational model was generated and calculated using ANSYS Workbench. The fluid domain was solved using CFX and the solid domain was calculated using ANSYS. The coupling between two domains was set at the level of momentum exchange with no heat transfer. Thus the governing equations are reduced to the momentum and continuity equations [5]. Additionally the model allows change in the geometry, and according to two-way fluid structure interaction coupling, change in the shape of the walls also cause mesh displacement in the fluid. The coupling method required the use of Arbitrary Lagrangian-Euler (ALE) formulation to solve the Navier-Stokes equations in a moving domain. This coupling method allows to take into account changes of the blood flow and its influence on artery walls throughout the entire heart cycle.

The nodes of the vessel wall have been fixed on both inlet and outlet end. This has forced the increase of the model length. Patient data has been collected by a 2,5 cm long probe and the remaining 5cm have been added to compensate for the boundary conditions at the ends. It was necessary for the flow to stabilize to avoid the influence of the nozzle created at the inlet by the distention of the artery. The remaining nodes were taken to be free.

Due to a pulsate characteristic of the flow with a possibility of returning flow, opening conditions have been placed at the inlet and outlet of the fluid domain. Relative total pressure has been placed at the inlet and mass flow normal to the boundary has been placed at the outlet. The start of the increase in pressure at the outflow has been shifted in the time by the amount of time necessary for the pulse wave to reach the end of the model vessel.

5. Results

The calculations of the model showed that the distention of the walls in the model is not significantly different from the measured distention. This shows that the proposed method can be used to analyze flow parameters in the model instead of carrying out expensive and patient time consuming measurements.

6. References

- [1] Kips J., Vanmolkot F., Mahieu D., Vermeersch S., Fabry I., Hoon J., Bortell L., Segers P.. (2010) The use of diameter distension waveforms as an alternative for tonometric pressure to assess carotid blood pressure. *Physiological Measurement* **33**(4), 543-554.
- [2] Bębenek B. (1999) *Przepływy w układzie krwionośnym* Wydawnictwo politechniki krakowskiej.
- [3] Korteweg, D., J., (1878) *Über die Fortpflanzungsgeschwindigkeit des Schalles in elastischen Röhren*, *Annalen der Physik und Chemie* (NS) **5**, 525-542
- [4] Neofytou P., Tsangaris S., (2006) Flow effects of blood constitutive equations in 3D models of vascular tree, *Int. J. Numer. Meth. Fluid* (**51**), 323-338
- [5] Badur J.. (2005) *Pięć wykładów ze współczesnej termomechaniki płynów*.

MODELING OF FRACTURE IN COROTICAL BONE USING THE GURSON-TVERGAARD MODEL

S. Hernik, P. J. Sulich

Cracow University of Technology, Cracow, Poland

1. Introduction

This paper deals with study of modeling fracture in corotical bone using the Gurson-Tvergaard damage model [1, 2]. Bone tissue is very complicated and interesting structure. From mechanical point of view bone could be described as a composite material, because it is composed by hydroxyapatite, collagen, small amounts of proteoglycans, noncollagenous proteins and water. In general it is a heterogeneous, porous and anisotropic material. Although porosity can vary continuously from 5 to 95%, most bone tissues have either very low or very high porosity [3].

In this paper, the main idea is focused on long bones (for example tibial bone), usually named corotical or compact bone with 5-10% porosity. There are few types of pores. Vascular porosity is the largest (50 μm diameter), formed by the Haversian canals (aligned with the long axis of the bone) and Volkmann's canals (transverse canals connecting Haversian canals) with capillaries and nerves. Other porosities are associated with lacunae (cavities connected through small canals known as canaliculi) and with the space between collagen and hydroxyapatite (very small, around 10 nm). Cortical bone consists of cylindrical structures known as osteons or Haversian systems, with a diameter of about 200 μm formed by cylindrical lamellae surrounding the Haversian canal. The boundary between the osteon and the surrounding bone is know as the cement line [4].

Poroelasticity is theory about the interactions between solid with porous and fluid or gas flow saturated porous medium. The theory was proposed by Biot in 1935. It was a extension of classical soil consolidation models. The theory has been widely applied to geotechnical problems beyond soil consolidation, most notably problems in rock mechanics [5]. From the macroscopic point of view, especially focused on the structure of material like bone and soil, there are lots of similarities. Both of them, contains some solid material, fluids and gas. In soil fluid phase is a water, in bones fluid is a blood or another fluid in human body. All facts considered, the theory of poroelasticity is possible to used for modeling bones and in this paper it is used too.

2. Formulation of the problem

Poroelasticity is described by two equations. The first of them is the consolidation equation (1), as follows:

$$(1) \quad c\nabla^2 p = -\gamma_w \dot{p}, \quad c = k \frac{E}{3(1-2\nu)}$$

where: p – pressure, γ_w – specific gravity of fluid, E – Young modulus, ν – Poisson ratio and k is a coefficient of filtration. The mechanical part of the formulation is described by classical elasticity equations with Terzghagi law (2) as a coupled between porous and elasticity theories [6].

$$(2) \quad \sigma'_{ij} = \sigma_{ij}^e - p\delta_{ij}$$

Following the clinical literature, there are two main causes of fractures in bones: an external impact produced or, quite common, in elderly people with osteoporosis. Another important cause of pathologic fractures are bone tumors, which modify bone mechanical properties and produce stress concentrators. Removing the tumor usually increases the risk of fracture [3].

In this paper the fracture is modeling by the Gurson-Tvergaard formulation, where yield potential is as follows:

$$(3) \quad F(\sigma_{ij}, \sigma_s, f) = \frac{\sigma_{eq}^2}{\sigma_s^2} + 2q_1 f_v^* \cosh\left(\frac{3}{2}q_2 \frac{\sigma_H}{\sigma_s}\right) - (1 + q_3 f_v^*)^2 = 0$$

where f_v^* is a void fraction defined as:

$$(4) \quad f_v^* = \begin{cases} f_v & \text{if } f_v \leq f_{cr} \\ f_{cr} + \kappa (f_v - f_{cr}) & \text{if } f_v > f_{cr} \end{cases}$$

Symbols $\sigma_{eq} = \left(\frac{3}{2}s_{ij}^e s_{ij}^e\right)^{\frac{1}{2}}$ means equivalent stress tensor of elastic part, $\sigma_H = \frac{1}{3}\sigma_{kk}^e$ is a mean stress of elastic part, $f = \frac{V_p - V_s}{V_s}$, where V_p and V_s is a volume of porous and solid and $\sigma_s = \sigma_y + R$ is actual yield stress.

The void fraction could be growth, because the porous can be connected or the new void can be created. Previous process is described by equation (5):

$$(5) \quad \dot{f}_v = \dot{f}_{nucl} + \dot{f}_{growth}$$

where:

$$(6) \quad \begin{aligned} \dot{f}_{nucl} &= A_n \dot{p} \\ \dot{f}_{growth} &= (1 - f_v) \dot{\varepsilon}_{kk}^p \end{aligned}$$

Nucleation and growth of voids is related to the plastic process, where \dot{p} is a cumulative plastic strain and $\dot{\varepsilon}_{kk}^p$ is a mean plastic strain [7, 1, 2].

3. References

- [1] A. L. Gurson (1997). Continuum Theory of Ductile Rupture by Void Nucleation and Growth: Part I Yield Criteria and Flow Rules for Porous Ductile Media, *Journal of Engineering Materials and Technology*, **99**, 2-15.
- [2] V. Tvergaard, A. Needleman (1984). Analysis of cup-cone fracture in a round tensile bar, *Acta metall.* **32**, 157-169.
- [3] M. Doblaré, J. M. García and M. J. Gómez (2004). Modelling bone tissue fracture and healing: a review, *Engineering Fracture Mechanics*, **71**, 1809-1840.
- [4] J. D. Currey (2002). *Bones. Structure and mechanics*, NJ: Princeton University Press, Princeton.
- [5] S. C. Cowin (1999), Bone poroelasticity, *Journal of Biomechanics*, **32**, 217-238.
- [6] W. T. Lambe, R. V. Whitman (1978). *Mechanika gruntów*, Arkady, Warszawa, t. 2, 317-319.
- [7] J. J. Skrzypek (2006). *Podstawy Mechaniki Uszkodzeń*, Wydawnictwo Politechniki Krakowskiej, Kraków, 61-63.

DEFORMATION OF RED BLOOD CELLS

A. Jakubowicz, M. Pietrzyk

Department of Applied Computer Science and Modelling, AGH Kraków, Poland

1. Introduction

The blood flow in cardiovascular systems can be fully described as uniform fluid on macroscopic level by Navier–Stokes equations [1]. However, in the case of small veins or medical devices this approach it is not accurate. It is needed to take into account a non-homogeneous structure and thixotropic properties of blood. The deformation of red blood cells (RBC) influence blood ability to transport oxygen and carbon, as well as can cause even the erythrocytes destruction. The concentrated suspension of deformable RBC in a macromolecule environment is a viscoelastic material that experiences a loading history. Thixotropic behavior is explained by changes in blood internal structure, which is experimentally sheared, thereby by the kinetics of both reversible RBC aggregation and deformation, with their time scales. The aim of this paper is to provide a mathematical model of deformable membrane of RBC, as well as present simulation results.

2. Membrane model

The RBC shape represents an equilibrium configuration that minimizes the curvature energy of a closed surface for given surface area and volume with a geometrical asymmetry. The erythrocyte experiences large reversible deformations during its life span due to changes of fluids velocity. A dimensionless parameter, the capillary number, is influencing an erythrocytes deformability:

$$(1) \quad Ca_G \equiv \frac{\mu \dot{\gamma} r}{G}$$

where μ is the viscosity, $\dot{\gamma}$ is the fluid shear rate, r is the particle radius and G is membrane shear modulus. The motion of RBC depends on the shear rate, the viscosity ratio between the inner and outer fluids of RBCs, the material properties of the elastic membrane and other physical constants. The most popular neo-Hookean, Skalak, and Mooney–Rivlin laws for membrane deformation are presented as well as main differences between these models. A three-dimensional spectrin-link membrane method [2,3] (SL) is used in this paper to describe the deformable behavior of the RBCs. Based on this estimation, the RBC membrane can be described as triangulated surface. The total energy of the erythrocyte membrane is the sum of the total energy for stretch, compression, change of surface area and the total energy for the bending. Each particle in membrane movement is described by Newton equations which minimalize forces existing in the system. Those forces determine external forces of fluid–structure and structure–structure interaction and Helmholtz free energy of membrane. Due to need of providing coarse grids the procedure developed by Pivkin and Karniadakis [5] was applied.

3. Numerical model

The formation of RBC clusters cannot be handle by classical computational fluid dynamics methods. The following simplifications were made: RBCs are considered as phase with specific elastic properties, the plasma and rest of the blood are represented by a uniform suspension. The lattice-Boltzmann method (LBM) is used to solve a discretized Boltzmann equation which converges to the Navier–Stokes equation. Parameters of each kind of energy in SL depend on

Boltzmann constant and temperature, however, in this paper they are set constant. Simulation was conducted due to Ca_G change based on change of the effective suspension viscosity. The RBC shape is initially set to biconcave with a transmural pressure and different natural states of the membrane with the same initial shape are examined in numerical simulations of RBC motion.

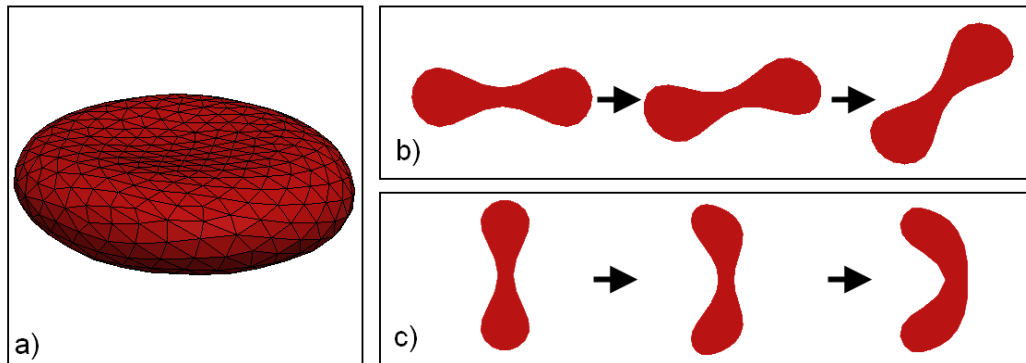


Figure 1. On left side (a) the representation of RBC membrane in SL, on right side (b,c): cross sections results of deformation due to different velocities distribution at 0, 200 and 400 time steps.

The preliminary results for single RBC deformation are presented at Fig.1a. The initial mesh was obtained by minimization of the Helmholtz free energy based on 500 nodes structure. The boundary conditions are treated as periodic so that the RBC can reach a steady-state configuration without need of big computational space. At Fig.1b the RBC tumbling at low ($0.5s^{-1}$) shear rates are considered. The RBC dynamics in Poiseuille flow in tube with a diameter comparable with the RBC diameter was show at Fig.1c. The transmission from biconcave shape to parachute shape is observed.

4. Summary

Presented studies are applicable to various conditions of blood flow such as hematocrit change, flow velocity and vessel geometry. The macroscopic multiple blood cells flow is affected by the motions of a single erythrocyte. That indicates needs of providing detailed model, which makes able to understanding multiscale mechanics of blood flow in a micro-vessel network system.

5. Acknowledgements

Financial assistance of the National Science Centre, project no. 2011/01/N/ST6/05976.

6. References

- [1] D. Szeliga, M. Kopernik, M. Pietrzyk (2009). Critical evaluation and sensitivity analysis of rheological models of human blood. *Computer Methods in Materials Science*, **9**, 435-450.
- [2] M. Dao, J. Li, S. Suresh (2006). Molecularly based analysis of deformation of spectrin network and human erythrocyte, *Materials Science and Engineering*, **26**, 1232-1244.
- [3] J. Li, M. Dao, CT. Lim, S. Suresh (2005). Spectrin-level modeling of the cytoskeleton and optical tweezers stretching of the erythrocyte, *Biophysical Journal*, **88**, 3707-3719.
- [4] I.V. Pivkin, G.E. Karniadakis (2008). Accurate coarse-grained modeling of red blood cells, *Physical Review Letters*, **101**, 1-4.
- [5] D. Hartmann (2010). A multiscale model for red blood cell mechanics, *Biomechanics and Modeling in Mechanobiology*, **9**, 1-17.

MODELING OF A COLLECTION OF TENSEGRITY PARTICLES WITH A NON SMOOTH DISCRETE ELEMENT METHOD

E. Postek¹, F. Dubois² and R. Mozul²

¹*Institute of Fundamental Technological Research, Warsaw, Poland*

²*Université de Montpellier 2, Montpellier, France*

1. Introduction

It is believed that the mechanical environment that cells experience is very important to their behaviour. A change of stresses in a cancer cell can cause that it starts to behave more like a healthy one [1].

A biological tissue made of a collection of cells can be modeled as a discrete system similar to a granular media. Since each cell is deformable and prestressed, we propose a dedicated DEM- FEM model of granular medium in which each particle is modeled through a tensegrity structure.

2. Tensegrity model of a cell

Since we aim to model a piece of tissue of a range of one million cells, we employ the simplest possible model for the cell. This is the icosahedron based tensegrity structure consisting of tendons (fair) and struts (dark) at first instance, Fig. 1 (a). The model enriched with membranes is shown in the Fig. 1 (b). The example of group of cells is shown in Fig. 1 (c).

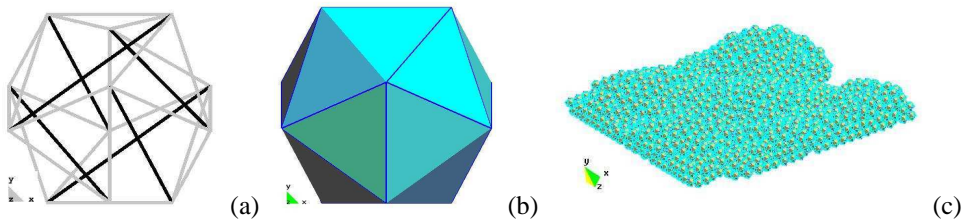


Fig. 1. Single cell (a), cell with mebranes (b), group of cells (c)

3. Multibody approach

The vehicle for the model is the LMGC90 software [2], [3] in which we use the tensegrity model of the cell which, in fact, is a deformable viscoelastic particles model. In this approach, we simultaneously have to compute the contact between the particles and the stresses in the particles at each time instance.

Dynamics is written using the framework proposed by Moreau and Jean (see [3] for details). The set of equations of motion including the initial and the boundary conditions is of the form :

$$(1) \quad \mathbf{M}(\dot{\mathbf{q}}_{i+1} - \dot{\mathbf{q}}_i) = \int_{t_i}^{t_{i+1}} (\mathbf{F}(\mathbf{q}, \dot{\mathbf{q}}, s) + \mathbf{P}(s)) ds + \mathbf{p}_{i+1}$$

$$(2) \quad \mathbf{q}_{i+1} = \mathbf{q}_i + \int_{t_i}^{t_{i+1}} \dot{\mathbf{q}} ds$$

where \mathbf{M} is the mass matrix, \mathbf{q} is the vector of generalized displacements, $\mathbf{P}(t)$ is the vector of external forces, $\mathbf{F}(\mathbf{q}, \dot{\mathbf{q}}, t)$ is the vector of internal forces including the inertia terms and \mathbf{p}_{i+1} is the vector of impulse resulting from contacts over the time step.

While applying a Newton-Raphson procedure to the previous nonlinear system, which was integrated through a θ scheme, leads to the following equation which will be used in the NSCD method:

$$(3) \quad \tilde{\mathbf{M}}^k \Delta \dot{\mathbf{q}}_i^{k+1} = \mathbf{p}_{free}^k + \mathbf{p}_{i+1}^{k+1}$$

The effective mass matrix $\tilde{\mathbf{M}}^k$ writes as follows

$$(4) \quad \tilde{\mathbf{M}}^k = \mathbf{M} + h^2 \theta^2 \mathbf{K}^k$$

where h is the time increment, θ is the integration coefficient [0.5, 1] and \mathbf{K} is the tangent stiffness. The θ coefficient is usually taken as 0.5 yielding the Crank-Nicholson integration rule. The effective impulse vector of forces free of contact is of the form

$$(5) \quad \mathbf{p}_{free}^k = \tilde{\mathbf{M}}^k \dot{\mathbf{q}}_{i+1}^k + \mathbf{M}(\dot{\mathbf{q}}_i - \dot{\mathbf{q}}_{i+1}^k) + h[(1 - \theta)(\mathbf{F}_i + \mathbf{P}_i) + \theta(\mathbf{F}_{i+1}^k + \mathbf{P}_{i+1})]$$

Contact impulses are computed using the NSCD method implemented in the LMGC90 software. First it will perform contacts detection between cells. Then the previous dynamics equations will be expressed in term of contacts unknowns (gap or relative velocity and contact impulse). Afterward a Non Linear Gauss-Seidel method computes the contacts impulses. Finally, the resulting impulse on cells nodes due to contacts impulses are added to the dynamics equation to compute the new velocities and positions.

Eventually a parallel version of the NSCD method can be used [2].

4. Concluding remarks

The presented scheme, based on a coupling of LMGC90 software and a dedicated modeling of cells, has been joined to an agent model able to take into account the effect of the stress evolution in the growing tissue [4]. The agent modeling is based on the FLAME framework (Flexible Large-scale Agent Modelling Environment) [5].

5. References

- [1] C. Ainsworth (2008), Stretching the imagination, *Nature*, **456**, 696-699.
- [2] M. Renouf, F. Dubois and P. Alart (2004). A parallel version of the Non Smooth Contact Dynamics Algorithm applied to the simulation of granular media *J. Comput. Appl. Math.*, **168**, 375-382.
- [3] F. Radjai, F. Dubois (2011), Discrete-element Modelling of Granular Materials, *Wiley & Sons, New York*.
- [4] E. Postek (2012), Concept of an Agent-stress Model of a Tissue, *accepted in Techn. Mechanik*.
- [5] S. Adra, T. Sun, S. McNeil, M. Holcombe, R. Smallwood (2010), Development of a three dimensional multiscale computational model of the human epidermis, *PLoS ONE*, **5**, 1-13.

MULTIOBJECTIVE OPTIMIZATION OF TWO-COMPONENT IMPLANTOLOGY SYSTEM

K. Szajek, M. Wierszycki and T. Łodygowski

*Institute of Structural Engineering, Poznań University of Technology
Centre of Mechatronics, Biomechanics and Nanotechnology of PUT*

1. Introduction

Restorations with the application of implants are effective and commonly used in dental treatment. However, despite the high rate of long term success many problems are still reported. The paper presents the optimization procedure of commonly used two-component implantology system in terms of problems observed in its utilization and implantation, namely: fatigue and static failure [2], screw loosening, tightening inaccuracy and tightness. The simplified, axisymmetric FE model, yet capable to simulate asymmetric deformation, is utilized in order to calculate stress/strain field. The procedures for estimation of crucial design features based on the simplified model are also provided. The formulated multiobjective optimization task is solved using weighted sum approach where the weights estimation is done with Analytic Hierarchy Process (AHP) [3] on the basis of survey carried out among the group of medical engineers, producers and practitioners. The weighted objective function is minimized with the use of genetic algorithm hybridized with Hooke-Jeeves procedures.

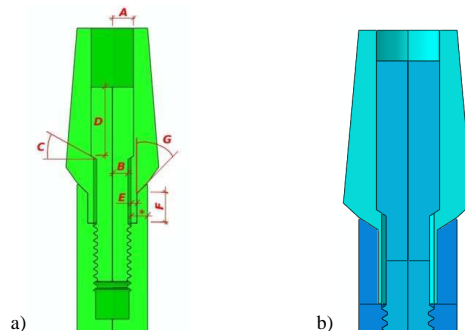


Figure 1. Dental implant geometry: a) the initial model with assumed geometric design parameters, b) the best solution obtained.

2. Model

The two-component implantological system is considered (OSTEOPLANT). It consists of root and abutment which are connected with a non-rotational hexagonal slot and assembled by a screw (Fig. 1a). The geometry of implant is simplified to axisymmetric, however the loads and response are asymmetric. It is done with the use of cylindrical finite elements, which utilize standard isoparametric interpolation in the radial – symmetry axis plane and the trigonometric interpolation function with respect to the angle of revolution. The formulation enables to describe a nonlinear asymmetric deformation of axisymmetric geometry due to asymmetric loads. It simultaneously significantly reduces the size of the problem (ca. 94 000 dof) in comparison with a full three dimensional model (ca. 600 000 dof). All components of the implant are made of medical titanium alloys. In the FE model the isotropic, non-linear elastic-plastic characteristics of material models are taken into account. The contact conditions are defined between all the components using penalty method as the contact constraint enforcement. Tangential surface behavior follows classical isotropic Coulomb friction model. The friction coefficient is the same for

all contact pairs and amounts to 0.19.

The loads are applied in two steps. The first step is simulation of tightening. The pre-tension force is defined in the middle part of the screw and its value is calculated based on the analytical equation [1]. The second step is bending, which is caused by the worst component of service load, perpendicular to axisymmetric axis. The bending force (30N, 60N) is applied to the tip of abutment by means of a surface-based coupling constrains.

Seven geometrical parameters and screw preload are defined as variables (Fig. 1a). For each design parameter range and, due to GA requirements, number of bit for encoding are defined. The ranges come from both, the geometry limitations and manufacture requirements.

3. Optimization procedure

The optimization bases on complex, nonlinear FE model, which reliability does not ensure the result for all configurations of design parameters. Therefore, genetic algorithm (GA) which is resistant to non-continuous design space is proposed. Unlike conventional optimization techniques, GAs explore simultaneously the entire design space and therefore are likely to reach the global optimum. Unfortunately, the algorithm is computationally expensive in the same time, especially if a precise solution is expected. As a result, the hybrid method is used in order to provide both global search of the design space and a precise solution. The presented approach starts with the genetic processing and after a few iterations the best solution is assumed to be the starting point of Hooke-Jeeves procedure. The procedure stops when sufficient accuracy of the solution is achieved. The static, exterior penalty approach is used in order to control the constraints.

4. Results

The optimization process was carried out three times. All obtained solutions fulfill assumed constraints and differ from each other. The differences consider either the geometry or the screw preload and influence the objective function values. Therefore, it can be concluded that all the solutions represent local minima. Fig. 1b presents the geometry of the best solution. The effective stresses amplitude increased by 91%, static resistance is higher by 63%, screw loosening moment by 2% while tightening inaccuracy worsen by 9%. None of the constraints applied is violated (tightness, tightening moment).

5. Conclusions

The complex dental implant model was optimized based on FE analyses successfully incorporated into the hybrid optimization procedure (genetic and Hooke-Jeeves algorithms). The study and the final results give evidence that presented method is efficient and can be used for dental implant improvement. The obtained proposition of new design improves fatigue life, static resistance and screw loosening worsening tightening inaccuracy at the same time.

Acknowledgment: The support of Polish Ministry of Higher Education and Science under the grant R13 0020 06 “Development and preparation of dental implant prototypes” is kindly acknowledged.

References

- [1] D. Bozkaya, S., Muftu (2004). Mechanics of the taper integrated screwed in (TIS) abutments used in dental implants. *J Prosthet Dent*, 91, 326-334.
- [2] T. Łodygowski, M. Wierszycki, K. Szajek, W. Hędzielek, R. Zagalak (2010). Tooth-Implant Life Cycle Design, *Computer Methods in Mechanics, Lectures of the CMM 2009, ASM 1*, 391-422, Springer-Verlag Berlin Heidelberg 2010.
- [3] T.L. Saaty (1977). A scaling method for priorities in hierarchical structures. *J Math Psychol*, 15, 234-81.

MODELING OF THE LATERAL TRAUMAS OF THE HUMAN SKULL

G. Wróblewski

Warsaw University of Technology, Department of Engineering Production, Warsaw, Poland

1. Introduction

Many articles about modelling of stress state in the human skull appear in journals [1], [2]. Most of the articles are about stress state as a result of complex external loads occurring after e.g. communication accidents. The range of bone fractures are depend on many factors, e.g. on size the body which contact with head during an accident. The direction of external force applied on human head is very important too. There are many classifications of human skull (*calvarium*) traumas. Generally we are talk about central and lateral traumas. In this article are presented some results of numerical simulation stress state occurring during lateral traumas.

2. Geometrical model

To perform numerical calculation the geometrical model of the human cranium was done. This model was created on basis of data acquired during computer tomography (CT). A patient (43 years, without bone pathology) was examined in Warsaw Medical University. As a result, 85 DICOM images were obtained (3 mm distance between slices, thickness of single layer – 5 mm).

Then, the set of data was transferred into MIMICS 10.1 system to perform the geometrical model. All surfaces of the virtual model (outer and internal) were described by triangular surfaces in STL format. A preliminary model was optimized to reduce of triangles number and its shape was modified.

3. Numerical model

The final geometrical model was transferred into ABAQUS system in order to perform numerical simulations. In these investigations two different external loadings were assumed. These loadings were applied onto the model as is shown on Fig. 1. The first so-called “high” (Fig. 1a, b) – the external force is applied on frontal bone (*os frontale*) on the region shown on Fig. 1b. The second one is so-called “low” is shown of the Fig. 1c and d – the force is applied on the zygoma (*os zygomaticum*). Calculations were performed for two different values of static resultant external loadings (9500N and 15000N). Values of external loads were assumed from literature [3].

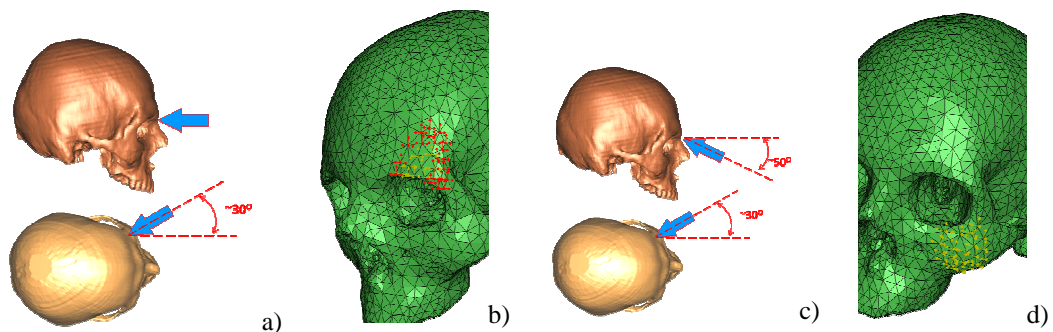


Figure 1. Models of external loads: a) directions of applied loads, b) “narrow” model, c) “wide” model

The mesh of finite element method model consists of 50274 tetrahedral elements. In a whole model cortical bone material was assumed, material data were taken from [4]. It is a simplification, because the CT data not allowed to exact separation between cortical and sponge bone. In an additional simplification the orthotropic material model was assumed. Then the boundary conditions were assumed and simulations were performed.

4. Results

As a result of numerical simulations stress and strain distributions were obtained. Some stress distributions after external loading value 9500N applied on “high” and “low” models are shown on Fig. 2.

The Fig. 2 show stress distribution from inside view of the skull. It is shown that high stresses are concentrated mainly in the nasal bone (*os nasale*). It may be an effect of small thickness of these bones.

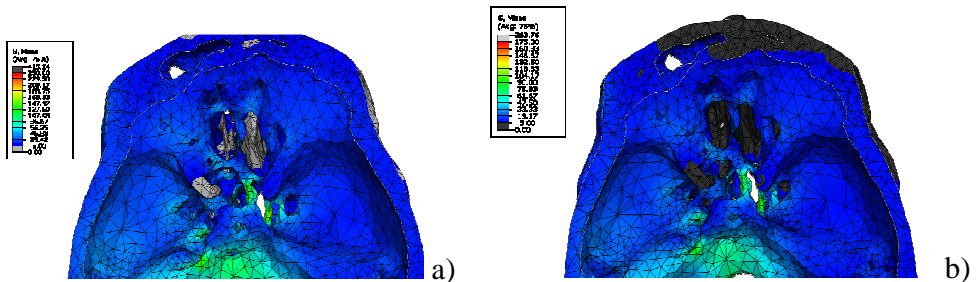


Fig. 2. Examples of the results stresses in: the “high” (a) and “low” (b) models respectively

5. Discussion

In this work are presented some results of the first stage of researches. Some conclusions after these calculations:

- it is necessary to prepare a new geometrical model of human skull on the basis of computer tomography to obtain more exact results,
- a new model may reflect different materials of the cranium. The division on cortical, spongy bone as well as tooth material may be assumed in this model.

The next calculation may assume that the forces applied on the model are depending on time.

6. References

- [1] D. Samolczyk-Wanyura, G. Wróblewski (2007). Numerical study of the upper part of the face displacements using finite element method, *J. Stoma.*, **60**, 503-518.
- [2] H. Wanyura, P. Kowalczyk, M. Bossak, D. Samolczyk-Wanyura, Z. Stopa (2011). Finite element analysis of external loads resulting in orbito-nasal dislocations, *J. Stoma.*, **64**, 411-424.
- [3] D.C. Vian, I.R. Casso, E.J. Pellma, C.A. Bi, L Zhan., D.C. Sherma, M.A. Boitan (2005). Concussion in Professional Football: Comparison with Boxing Head Impacts - Part 10, *Neurosurgery*, **57**, 1154-1172.
- [4] J.Y. Rho, R.B. Ashma, C.H. Turne (1993). Young’s modulus of trabecular and cortical bone material: ultrasonic and microtensile measurements, *Journal of Biomech.*, **26**, 111-119.

Computational Aspects of Solid Mechanics

FORMULATION AND FEM IMPLEMENTATION OF NONLINEAR THERMO-MECHANICAL COUPLING

*J. Jaśkowiec, P. Pluciński, R. Putanowicz, A. Stankiewicz, A. Wosatko and J. Pamin
Department of Civil Engineering, Cracow University of Technology, Poland*

1. General

Thermo-plasticity is a well-established theory, rooted in thermodynamics. However, there is still need for formulation of fully coupled nonlinear thermo-plastic models and their robust implementation. The paper presents such a fairly general formulation, composed of the plastic flow theory with any yield function and hardening, fully coupled to non-stationary heat flow equations via the dependence of mechanical variables on temperature and through plastic dissipation. Linear kinematic relations are assumed.

The model is implemented in the software environment FEMDK, developed by the authors for the analysis of nonlinear and time-dependent coupled problems of physics [1]. The application domain are engineering materials, see for instance [2, 3]. In the context of thermo-plasticity the applications extend to the analysis of thermal softening of solids [4].

2. Summary of computational thermo-plasticity

The aim is to incorporate arbitrary nonlinearity (within small-strain kinematics) and coupling in the analysis. This means that, in addition to the elastic-plastic response, the mechanical and thermal properties (e.g. Young's modulus and/or conductivity) are considered as temperature-dependent.

We start the analysis by writing in Voigt's notation the standard equation of equilibrium (momentum balance), valid at each point of the considered isotropic solid:

$$(1) \quad \mathbf{L}^T \boldsymbol{\sigma} + \rho \mathbf{b} = \mathbf{0}$$

where \mathbf{L} is a suitable matrix of differential operators, $\boldsymbol{\sigma}$ is the stress tensor, ρ is the material density, \mathbf{b} is the gravity vector. The equation should be complemented by proper boundary conditions. It can be written in terms of displacement vector \mathbf{u} and relative temperature θ , which are usually the discretized fundamental unknowns in thermo-mechanical problems.

The stress $\boldsymbol{\sigma}$ is derived from a certain free energy functional and is related to the displacement vector and temperature according to:

$$(2) \quad \boldsymbol{\sigma} = \mathbf{E}(\mathbf{L}\mathbf{u} - \boldsymbol{\epsilon}^p - \alpha\theta\boldsymbol{\Pi}), \quad \mathbf{E} = \mathbf{E}(\theta)$$

where $\boldsymbol{\epsilon}^p$ are plastic strains, \mathbf{E} is the elasticity matrix which depends on θ , α is the expansion coefficient, $\boldsymbol{\Pi}$ represents the unit tensor. The classical plastic flow theory with work hardening is assumed. Additionally, thermal softening can be admitted.

Next, the balance equation for non-stationary heat flow is written:

$$(3) \quad \rho c \dot{\theta} + \nabla^T \mathbf{q} = r$$

where c the specific heat capacity, \mathbf{q} the heat flux density, r the heat source density. Again, proper boundary conditions have to be specified, and moreover an initial condition for the θ field is needed. The heat flux density is usually expressed in terms of temperature gradient (Fourier's law):

$$(4) \quad \mathbf{q} = -\boldsymbol{\Lambda} \nabla \theta, \quad \boldsymbol{\Lambda} = \boldsymbol{\Lambda}(\theta)$$

where Λ is the conductivity matrix which can depend on θ . Moreover, the heat source density is related to plastic dissipation, cf. [7, 4].

A generalization of the mathematical formulation of multi-field problems can be found for instance in [3], while the extension of the theory to multicomponent materials (together with its thermodynamic background) is presented for instance in [6]. The local mathematical model can be reworked into a global weak formulation using the weighted residual approach, see e.g. [5].

The full coupling of momentum balance to heat conduction leads to a monolithic incremental-iterative scheme. The backward Euler algorithm is employed to integrate over time and the generalized return mapping algorithm is applied to solve the plasticity equations. The weak-forms of equations 1 and 3 are linearized at the current time step $t + \Delta t$. The fundamental unknown fields of displacement and temperature are discretized using a suitable finite element interpolation between nodal values $\check{\mathbf{u}}$ and $\check{\theta}$, leading to the set of incremental equations:

$$(5) \quad \begin{bmatrix} \mathbf{K}_{uu} & \mathbf{K}_{u\theta} \\ \mathbf{K}_{\theta u} & \mathbf{K}_{\theta\theta} \end{bmatrix} \begin{bmatrix} \delta\check{\mathbf{u}} \\ \delta\check{\theta} \end{bmatrix} = \begin{bmatrix} \mathbf{R}_u \\ \mathbf{R}_\theta \end{bmatrix}$$

where δ denotes the corrective increment of a quantity, \mathbf{R}_u and \mathbf{R}_θ are respective residual terms.

3. Simulation environment FEMDK

In order to manage the complexity and the development costs of a simulation system, it has been decided to use ready components, in particular Open Source Software. Such component programming is enabled by the appearance of many comprehensive, high quality software packages and improvement of standard interfaces between components. The purpose of the developed package FEMDK is to solve multi-field problems that occur during the analysis of degradation phenomena of engineering materials. The task is to build an environment which would facilitate fast creation of tools for solving coupled problems. The software should satisfy various requirements regarding data formats, geometric models, interpolation, solvers, etc. The components of the constructed package FEMDK are briefly presented in [1]. The useful features of FEMDK are: arbitrary number of coupled fields, in other words arbitrary number of degrees of freedom per node (which also allows for XFEM extension); possibility of using different finite elements available in GetFEM++ library and different meshes for different discretized fields; possibility of selecting particular algorithms, for instance for time or space integration.

4. References

- [1] R. Putanowicz. Grounds for the selection of software components for building fem simulation systems for coupled problems. *Mechanics and Control*, 30(4):234–244, 2011.
- [2] D. Gawin. *Degradation processes in microstructure of cement composites at high temperature (in Polish)*. Polish Academy of Sciences, Warsaw, 2010. Engineering studies no 69.
- [3] D. Kuhl. *Modellierung und Simulation von Mehrfeldproblemen der Strukturmechanik*. Ph.D. dissertation, Ruhr University of Bochum, Bochum, 2005.
- [4] J.J.L. Cela and I.M. Diaz. Numerical study of strain localisation in plane strain thermo-viscoplastic solids under dynamic conditions. *Comput. & Struct.*, 83:1824–1833, 2005.
- [5] D.W. Nicholson. *Finite element analysis. Thermomechanics of solids*. CRC Press, Boca Raton, 2008.
- [6] J. Kubik. *Elements of the thermomechanics (in Polish)*. Politechnika Opolska, Opole, 2004.
- [7] G. A. Maugin. *The Thermomechanics of Plasticity and Fracture*. Cambridge University Press, Cambridge, 1992.

Acknowledgement: scientific research has been carried out as a part of the project "Innovative recourses and effective methods of safety improvement and durability of buildings and transport infrastructure in the sustainable development" financed by the European Union from the European Fund of Regional Development based on the Operational Program of the Innovative Economy.

ELASTOPLASTIC ANALYSIS BY AN AUTOMATIC AND ADAPTIVE BEM-FEM COUPLING STRATEGY

A. Pereira

Department of Civil Engineering of Fluminense Federal University, Niterói, Brazil

1. Introduction

The purpose of this work is to introduce a novel approach to treat two-dimensional elastoplastic problems by means of an adaptive and automatic coupling strategy using the main advantages of the Boundary Element Method (BEM) and the Finite Element Method (FEM).

The correct and more realistic modeling (accurate results) combined to a simple geometry representation (easy mesh generation) is indispensable for efficient design of complex structures. Moreover, non-linear behavior should be considered for a better description of the material properties. The choice of the numerical tool to model these structures depends on many variants and there are no absolute advantages of one method over another. The main advantage of the BEM over the other methods is the reduction of the model dimension by one, leading to a much simpler mesh generation. However, the most common approach for elastoplasticity with the BEM makes use of pre-defined internal cells, which is not as efficient as the FEM in dealing with non-linear material.

Overcoming the drawbacks and to benefit of the advantages of each numerical method, the general idea proposed in this work concerns in the initial modeling of the structure using only the BEM, i.e. the proposed technique deals with such non-linear effects in a straightforward manner, without requiring a priori information on the plastic domain, requiring just the boundary discretization of the model.

2. Proposed Procedure

In the following, the regions where non-linear behavior is expected are detected direct and automatically based on a post-processing technique. Finally, these regions are filled with finite elements, using an automatic mesh generator, and then the coupled non-linear problem is solved taking the advantages of both BEM and FEM, where they are more useful, as shown in Figure 1.

The starting point of the proposed technique is a boundary element modeling of the problem, with the purpose of performing a simple linear elastic analysis, since the BEM is a user friendly and efficient method for a continuum. In addition, the method has the advantage that the results inside the domain are functions (over this domain) which exactly satisfy the differential equation of the problem (in elasticity). Another advantage is that it is possible to derivates these functions without deteriorating the quality (which is not the case in the FEM). Indeed, this is a great benefit when computing the interface between different regions, which corresponds to the next step of the proposed technique.

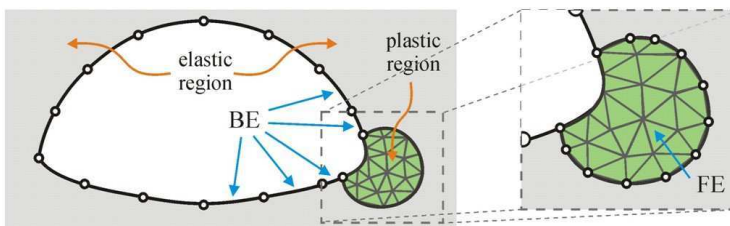


Figure 1: Boundary and finite element discretization for the elastic and plastic regions, respectively.

Therefore, regions inside the domain, which should contain nonlinearities, are first estimated by means of a post-processing algorithm based on the direct and automatic identification of isocurves and isobands [1]. In the case of elastoplasticity, the contours of the plastic zones are defined by isocurve plotted for the yield functions (the limit where the failure condition has been violated), as illustrated in Figure 2. For more details on the post-processing technique the reader is encouraged to consult [1].

Once these regions have been determined, the plastic zones are automatically modeled with the FEM, which is a powerful method in dealing with nonlinear problems, and thus, the problem is finally solved by means of a BEM/FEM coupling procedure.

3. Results

In order to validate the accuracy, efficiency and usability of the proposed technique, a tunneling problem is solved and compared to results from another numerical model, as shown in Figure 2.

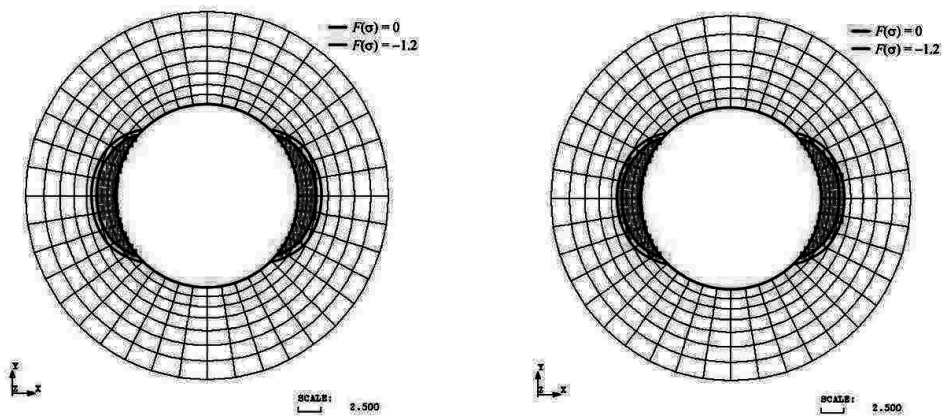


Figure 2: FEM model comparing the yield functions obtained with BEM: 1st iteration and converged solution.

4. References

- [1] A.M.B. Pereira and M. Noronha (2010). Post-processing and visualization techniques in 2D boundary element analysis, *Engineering with Computers*, **26**, 35–47.

CONSTITUTIVE RUBBER MATERIAL MODELS COMPARISON STUDIES IN QUASI-STATIC LOADING

P. Baranowski, J. Małachowski, Ł. Mazurkiewicz and K. Damaziak

*Department of Mechanics and Applied Computer Science, Military University of Technology,
S. Kaliskiego 2 Street, 00-908 Warsaw, Poland*

1. Abstract

Presented paper shows subsequent stages of vehicle tire coupons mechanical characteristics numerical assessment, with experimental data taking into consideration. Experimental uniaxial tension tests were carried out on the fatigue machine with the assistance of high-speed camera and special software for strain measurements. Obtained stress-strain curves were applied into the chosen constitutive rubber material models which are available in the LS-Dyna code. In the next stages numerical quasi-static analyses of tension tests were performed, which allowed to compare implemented material laws and validate obtained results with experimental ones.

2. Introduction

Rubber and rubber-like materials are very popular in many areas of economy and for sure within it there is the automotive industry, where materials and rubber-based composites are often used to produce tires with high strength and durability. There is no doubt that such popularity is caused by its mechanical characteristics, including ability to reversible deformation under the loading of mechanical forces. Because of their low modulus and excellent damping characteristics rubbery materials are often used in energy absorption structures like shock absorbers or isolations. Therefore, their mechanical properties in various operational conditions have much importance in engineering applications. After material development it is advisable to conduct both numerical and experimental material characteristics assessment and validation of the specific rubber (rubber-like) material.

Mechanical properties of rubber in static experimental tests were effectively determined and understood [1,2] with both compression and tension characteristics taking into consideration. Numerical simulations of elastomeric structures and also its constitutive material modelling are subjects of many engineering problems. It can be seen that major commercial FEA software offer a large number of materials constitutive laws for rubbery materials. Generally, in quasi-static area elastomers can be considered as incompressible (or nearly-incompressible) materials. Rubber constitutive relations, which are essential in modelling tires, i.e. the relationship between stress and strain, are formulated within the nonlinear elasticity theory, called hyperelasticity. For this kind of strongly non-linear material a large number of constitutive models are available in most of programs with LS-Dyna code among them. Authors of the papers [3,4] investigated the Blatz-Ko material law, in [5,6] the Mooney-Rivlin constitutive equation was implemented, Arruda and Boyce model was applied in [7,8], whereas Ogden rubber material was effectively modelled in [9,10].

The authors of this paper present subsequent stages of vehicle tire coupons mechanical characteristics numerical assessment, with experimental data taking into consideration. Experimental uniaxial tension tests were carried out on the fatigue machine with the assistance of high-speed camera and special software for strain measurements. Obtained stress-strain curves were applied into the chosen constitutive rubber material models which are available in the LS-Dyna code. In the next stages numerical quasi-static analyses of tension tests were performed with particular emphasis put on the differences outline between chosen constitutive rubber material models. Moreover, comparison studies of implemented material laws were carried out with subsequent validation of obtained results with experimental data.

3. Numerical modelling and results

At this stage of investigations there was necessary to develop numerical models of tire rubber coupons for tension tests with the same geometric dimensions as in the experimental tests. FE coupons were modelled using Belytschko-Tsay shell elements [11]. Mesh density was selected through analyses in order to guarantee high accuracy of computations and also the most optimum simulation time. Simulation conditions directly corresponded to the experiment. Rubber coupon with applied initial-boundary conditions is presented in Figure 1. In Figure 2 exemplary force-displacement curves for Mooney-Rivlin model simulation and experimental tests are presented.

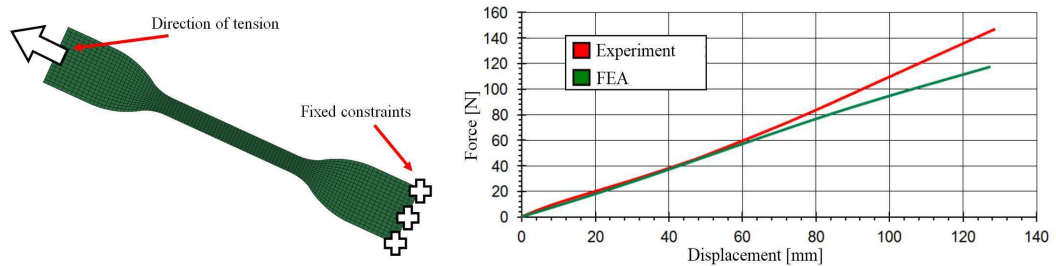


Fig. 1 Rubber coupon with applied initial-boundary conditions and exemplary force-displacement curves comparison for Mooney-Rivlin model and experimental tests

4. Conclusions

From the carried out analyses the material characteristics include force versus displacement were obtained for all constitutive material models. Consequently, results were compared with each other and validated with experimental data. It was shown that with accurate material characteristics and proper material model it is possible to assess mechanical behaviour of rubber (rubber-like) materials with good efficiency and accuracy with different material laws taking into consideration.

5. References

- [1] S. Ochelski and others, Influence of hardness on mechanical properties of elastomers, *Journal of KONES*, **17**, 317-325.
- [2] A. Krawczyk and others (1985), Mechanics of polymer and composite materials, *Science*.
- [3] P.A. Du Bois (2004), Crashworthiness Engineering Course Notes, *Livermore Software Technology Corporation*.
- [4] P.A. Du Bois, WL Ko (1962), Application of finite elastic theory to the deformation of rubber materials, *Trans Soc Rheol*, **6**, 223-251.
- [5] P. Baranowski, J. Małachowski (2011), Blast wave and suspension system interaction-numerical approach, *Journal of KONES*, **18**, 17-24.
- [6] B. Pondel, J. Małachowski (2006), Numeryczna analiza pracy opony samochodowej, WAT, Warszawa.
- [7] E.M. Arruda, M.C. Boyce (1993), A three-dimensional constitutive model for the large stretch behavior of rubber elastic materials, *J Mech. Phys. Solids*, **41**, 389-412.
- [8] T. Ignacio and others (2008), Efficient and robust explicit and implicit integration schemes for the arruda-boyce viscoplastic model, **27**, 1003-1042.
- [9] R.W. Ogden (1982), Elastic deformations of rubberlike solids, *Mechanics of solids*, Pergamon Press, Oxford.
- [10] R.W Ogden (1972), Large deformation isotropic elasticity: on the correlation of theory and experiment for compressible rubberlike solids. *Proc. R. Soc. Lond.*, **328**, 567-583.
- [11] J.O. Hallquist (2006), LS-Dyna Theory manual, *California Livermore Software Technology Corporation*.

ADAPTIVE ESTIMATION OF PENALTY FACTORS IN CONTACT MODELLING

T. Bednarek^{1,2} and P. Kowalczyk¹

¹*Institute of Fundamental Technological Research, Warsaw, Poland*

²*Kazimierz Wielki University, Bydgoszcz, Poland*

1. Introduction

The main objective of this paper is to improve stability conditions, uniqueness and convergence of numerical analysis of metal forming processes with contact constraints enforced by the penalty method. A commonly known drawback of this approach is the choice of penalty factor values. When assumed too low, they result in inaccurate fulfillment of the constraints while when assumed too high, they lead to bad conditioning of the equations system which affects stability and uniqueness of the solution. The proposed modification of the penalty algorithm consists in adaptive estimation of the penalty factor values for the particular system of finite element equations and for the assumed allowed inaccuracy in fulfillment of the contact constraints. The algorithm is tested on realistic examples of sheet metal forming. The finite element code based on flow approach formulation [1, 2] (for rigid-plastic and rigid-viscoplastic material model) has been used.

2. Main idea of penalty algorithm modification

The main idea is to estimate the penalty factors, adjusting their values to current stiffness and load conditions of the model and to an assumed accuracy of contact modelling. It is assumed that the penalty factors ϵ_k differ at different locations (for different discrete node-to-surface contact constraints $k = 1, \dots, M$) and at different time steps or even equilibrium iterations.

The idea is first explained on a 1D example. The model shown in figure 1 is considered; k denotes stiffness of the spring, q is the exciting force, \hat{u} is the assumed value of displacement (restriction resulting from the contact constraint), ϵ is the penalty factor and δ is the allowed inaccuracy of contact modelling (limit penetration depth). It is clear that, in order to preserve the desired accuracy of the solution, the penalty ϵ must at least equal $[k(\hat{u} - \delta) - q] / \delta$.

Let us now pass to the general 3D case, i.e. consider a FE-discretized structure, with a non-linear system of equations solved by the Newton–Raphson scheme for the unknown displacement vector \mathbf{u} . Our goal is now to estimate the penalty factor values ϵ_k as large enough to preserve the desired accuracy of contact constraints but not larger so that the conditioning of the system matrix is not significantly worsened.

The allowed inaccuracy of contact modeling (penetration) is now a vector $\boldsymbol{\delta} = \{\delta_k\}$. Thus, in the worst case we allow $\mathbf{D}\mathbf{u} - \hat{\mathbf{u}} = \boldsymbol{\delta}$, where \mathbf{D} is a geometric matrix of directional cosines of rigid surfaces at the contact points. Substituting this to the general contact-penalized system of equations [4]

$$(1) \quad (\mathbf{K} + \mathbf{D}^T \boldsymbol{\epsilon} \mathbf{D}) \mathbf{u}' = \mathbf{q}' + \mathbf{D}^T \boldsymbol{\epsilon} \hat{\mathbf{u}}', \quad \boldsymbol{\epsilon} = \text{diag}(\epsilon_k),$$

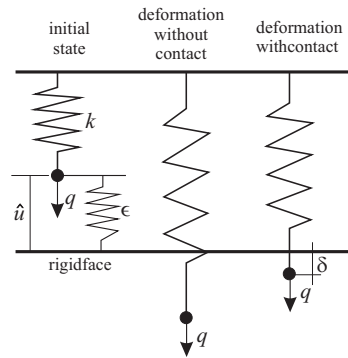


Figure 1. Elastic spring with contact constraint

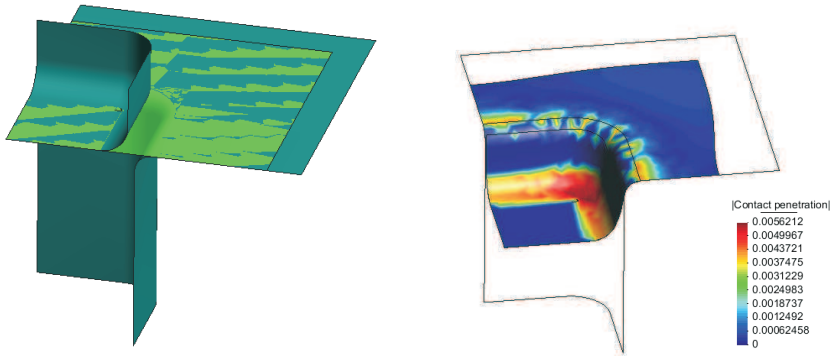


Figure 2. Benchmark test of deep drawing: initial geometry and deformed shape with contact penetration map.

(where \mathbf{u}' is the solution corrector at the current iteration and \mathbf{q}' the vector of residual forces), one can derive after a series of transformations the formula $\epsilon \delta = \mathbf{D}(\mathbf{q}' - \mathbf{K}\mathbf{u}')$. Recalling that ϵ is a diagonal matrix, we rewrite it the index notation as

$$(2) \quad \epsilon_k = \frac{D_{ki}(q'_i - K_{ij}u'_j)}{\delta_k} \quad (\text{no summation over } k).$$

Equation (2) is the recipe for the adaptive penalty factor values. Unfortunately, the displacement correctors u'_j on the right hand side are not known the moment and we need to replace them by their available approximate. Since in the convergent iteration scheme the subsequent corrections tend to zero, it is proposed to set $u'_j = 0$, except for the nodes where active contact constraints apply – there u'_j are set to simple orthogonal projection vectors of the current node position onto the contact surface. Thus, the formula (2) does actually yield approximate rather than exact values of desired penalty factors, which does not guarantee fulfillment of the imposed accuracy condition of contact modelling, but appears to be sufficient to keep the inaccuracy at least at the order of magnitude of the allowed limits, $\mathbf{D}\mathbf{u} - \hat{\mathbf{u}} \sim \delta$.

3. Numerical example: Deep drawing of a plastic sheet

The numerical example is a deep drawing of a sheet. The drawing parameters and geometry of tools are taken from the benchmark proposed by Woo in [3]. The geometry of the sheet and tools are presented in figure 2. The assumed inaccuracy of contact modelling at all nodes is $\delta = 0.001$ mm.

Figure 2 (right) presents the contact modeling inaccuracy, i.e. the penetration depth of sheet nodes into rigid tools. The picture presents the results for the step for which the worst inaccuracy was detected. As it can be seen, its magnitude is kept at the level of 10^{-3} mm.

Acknowledgement. This research was partially supported by European Regional Development Fund within the framework of the Innovative Economy Programme, project no. POIG.01.03.01-14-209/09.

- [1] E. Oñate and C. Agelet de Saracibar. Numerical modelling of sheet metal forming problems. In P. Hartley, I. Pillinger and C.E.N. Sturgess, eds, *Numerical Modelling of Material Deformation Processes: Research, Development and Applications*. Springer-Verlag, 1992.
- [2] P. Perzyna. Fundamental problems in viscoplasticity. *Advances in Applied Mechanics*, (9):243–377, 1966.
- [3] D.M. Woo. On the complete solution of the deep drawing problem. *Int. J. Mech. Sci.*, 10:83–94, 1968.
- [4] P. Wriggers. *Computational Contact Mechanics*. Wiley, Chichester, 2002.

A FLOW OF THE NONWETTING LIQUID THROUGH UNSATURATED POROUS LAYER

M. Cieszko, T. Bednarek and A. Słuszniaik

Institute of Mechanics and Applied Computer Science, Bydgoszcz, Poland

Institute of Fundamental Technological Research PAN

1. Introduction

The paper deals with stationary flow of nonwetting liquid (mercury) through a unsaturated porous layer. This type of one-dimensional flows, due to its geometric simplicity, are often the subject of experimental studies, devoted to determination of the flow characteristics of porous material. Theoretical considerations are based on the new macroscopic description of capillary transport of liquid and gas in porous materials formulated by the first author of this paper within concepts of multiphase continuum mechanics. In this theory it is assumed that gas and liquid filling rigid porous material form macroscopic continuum composed of three constituents: gas, mobile liquid and capillary liquid. The division of liquid into two continua is justified both from kinematical and energetic point of view. The capillary liquid is contained in the thin layer covering the internal surface of pores. This liquid gather the whole capillary energy of the liquid and is immovable. It can, however, exchange the mass with the mobile liquid in the vicinity of meniscus surfaces. The mass exchange appears only during their motion in the pore space and is described by the separate velocity field. This makes it possible to model the mechanism of meniscus motion in the pore space. The mobile liquid is located in the internal area of liquid surrounded by its internal contact surface with the skeleton and surfaces of meniscus. Each constituent is characterized by the mass densities and their distributions are defined by parameters of saturation.

Description of the flow of nonwetting liquid through unsaturated porous material is a special case of this theory and is given by the system of three nonlinear coupled equations for spatial distribution of liquid saturation and pressure and for velocity of liquid flow through porous layer.

2. The formulation of the problem

Basic assumptions

We consider a system composed of porous layer of thickness L surrounded by nonwetting incompressible liquid (figure 1). Due to strong influence of liquid distribution in the layer on its flow, the analysis is performed in two steps. First, we consider quasistatic process of liquid intrusion into ini-

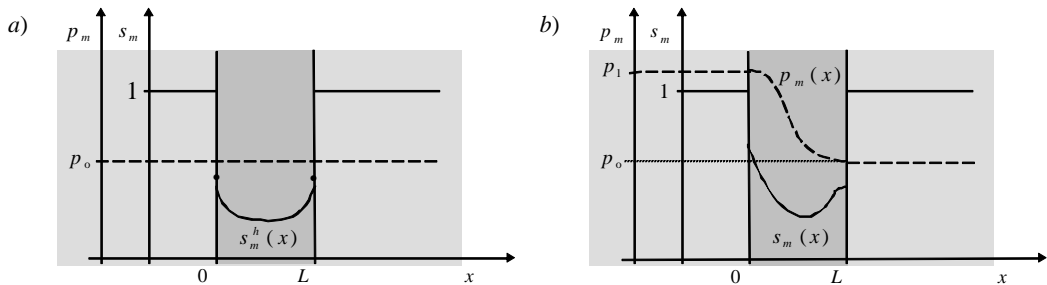


Figure 1. Distribution of pressure and liquid saturation in the layer during its intrusion (a) and flow through the layer (b).

tially empty layer by uniform increasing of liquid pressure on both side of the layer. This produce initial distribution of liquid (figure 1a). Next, the pressure is increased only on the left hand side of the layer resulting in non-uniform pressure distribution inside the layer and stationary flow of liquid. As a consequence, liquid distribution in the layer is also modified (figure 1b).

Basic equations

One dimensional problem of nonwetting liquid flow through porous layer is described by the following system of coupled nonlinear differential equations

$$(1) \quad \frac{\partial \hat{s}}{\partial \bar{p}} - 2 \frac{\bar{C}_o \bar{C}_1}{\hat{s}} \frac{\partial^2 \hat{s}}{\partial \bar{x} \partial \bar{p}} - \bar{C}_o \frac{\partial^2 \hat{s}}{\partial \bar{x}^2} = 0$$

$$(2) \quad \hat{s}(\bar{x}, \bar{p}(\bar{x})) \frac{d\bar{p}}{d\bar{x}} = -\bar{C}_1$$

$$(3) \quad \frac{v_m^f}{v_{m0}^f} = \frac{k_m^{re}}{\hat{s}(\bar{x}, \bar{p}(\bar{x}))}$$

where $\bar{x} = x/L$ is dimensionless spatial coordinate, $\bar{p} = p/p_0$ is dimensionless pressure, $\hat{s}(\bar{x}, \bar{p}(\bar{x}))$ and v_m^f stand for liquid saturation and velocity of mobile liquid, respectively. Whereas, v_{m0}^f is the velocity of mobile liquid flow through saturated porous layer and \bar{C}_0 is the dimensionless coefficient of diffusive transport of meniscus in unsaturated porous material. The constant coefficient \bar{C}_1 is given by relation

$$(4) \quad \bar{C}_1 = k_m^{re}(\bar{p}(0) - \bar{p}(1))$$

where k_m^{re} is the relative permeability coefficient. Its value is determined by liquid saturation

$$(5) \quad \frac{1}{k_m^{re}} = \int_0^1 \frac{d\bar{x}}{\hat{s}(\bar{x}, \bar{p}(\bar{x}))}$$

Equation (1) for \bar{C}_1 ($\bar{p}(0) = \bar{p}(1)$) describes quasistatic process of nonwetting liquid intrusion into porous layer.

Boundary conditions

Boundary conditions for stationary flow of nonwetting fluid through porous layer are as follows

$$(6) \quad \bar{p}(0) = p_1/p_0, \quad \bar{p}(1) = 1, \quad \hat{s}(0) = s(\bar{p}(0)), \quad \hat{s}(1) = s(\bar{p}(1)).$$

where $s(\bar{p})$ is known function of pressure directly related with the pore diameter distribution on the surface of the layer.

3. Numerical implementation

The system of equations (1)-(3) has been solved by Newton method. Due to their strong nonlinearity the solution is very sensitive to assumed perturbations in differential scheme, especially in the pressure domain. In spite of the geometrical simplicity of the problem its solution requires quite large computational effort.

Numerical solution of equations (1)-(3) allows analysis of influence of pressure on distribution of liquid saturation in the quasistatic process as well as analysis of dependence of liquid saturation, pressure, velocity of liquid flow through the layer and relative permeability parameter on pressures at both sides of the layer in the stationery processes.

ON DETERMINATION OF THE ELASTIC PROPERTIES OF HETEROGENEOUS RODS

O.V. Denina

Southern Scientific Center of RAS, Rostov-on-Don, Russian Federation

1. Introduction

Materials with complex mechanical properties (composites, functionally gradient materials) are widely distributed in the industry (measurement technology, precision machinery industry, aircraft industry). Therefore, when producing the structural elements made of these materials and during the quality control of their manufacturing, the determination of the laws of variation in their properties is very important and urgent problem. Traditional experimental methods for evaluating the properties of such materials in the framework of the homogeneity hypothesis are rather crude, and, therefore, the development of alternative non-destructive methods is necessary for the identification of heterogeneous characteristics, which allows to clarify the structure of the heterogeneity.

The proposed method of investigation is based on the apparatus of inverse coefficient problems in mechanics of deformable solids, and allows to reconstruct the unknown functions using the data of acoustic sensing, measured at some points of the object under study [1]. In this paper the problem is considered for determining three heterogeneous characteristics of the rod: the Young modulus $E(x)$, shear modulus $G(x)$ and density $\rho(x)$, in the combined analysis of longitudinal, bending and torsional oscillations.

2. Statement of the problem and construction of the solving operator equations

Lets consider the problem for reconstruction of three mechanical characteristics $E(x)$, $G(x)$, $\rho(x)$ for an inhomogeneous isotropic elastic rod of length l , for which $F(x)$, $J(x)$, $J_p(x)$ are the cross-section area, axial and polar moments, respectively.

To solve this problem, we implement the various modes of oscillation: longitudinal, bending and torsional. It is assumed that the information about the amplitude-frequency characteristics at the end of a cantilever clamped rod is known: $u(l, \omega) = f_1(\omega)$, $\omega \in [\omega_1, \omega_2]$, for the longitudinal oscillation; $w(l, \omega) = f_2(\omega)$, $\omega \in [\omega_3, \omega_4]$, for the bending oscillation; $v(l, \omega) = f_3(\omega)$, $\omega \in [\omega_5, \omega_6]$, for the torsional oscillation.

In the present paper, the following scheme is proposed to determine the unknown functions: at the first stage, on the basis of combined analysis of longitudinal and bending oscillations, we determined the functions that characterize the laws of variation for the Young modulus $E(x)$ and density $\rho(x)$; at the second stage, from analysis of torsional oscillations for a known density function we determined the function characterizing the law of variation for the shear modulus $G(x)$.

On the basis of generalized reciprocity relation [2] the operator equations are obtained, which relate the unknown functions and functions measured in the analysis of wave processes.

In the case of longitudinal oscillations, the operator equation has the form (1):

$$(1) \quad \int_0^l \left(\frac{du^{(n-1)}(x, \omega)}{dx} \right)^2 F(x) E^{(n)}(x) dx - \omega^2 \int_0^l (u^{(n-1)}(x, \omega))^2 F(x) \rho^{(n)}(x) dx = P(f_1(\omega) - u^{(n-1)}(l, \omega)), \omega \in [\omega_1, \omega_2]$$

In the case of bending and torsional oscillations, the operator equations have the form (2), (3) respectively:

$$\int_0^l \left(\frac{d^2 w^{(n-1)}(x, \omega)}{dx^2} \right)^2 J(x) E^{(n)}(x) dx - \omega^2 \int_0^l (w^{(n-1)}(x, \omega))^2 F(x) \rho^{(n)}(x) dx =$$

$$(2) \quad = -P(f_2(\omega) - w^{(n-1)}(l, \omega)), \quad \omega \in [\omega_3, \omega_4]$$

$$(3) \quad \int_0^l \left(\frac{dv^{(n-1)}(x, \omega)}{dx} \right)^2 J_p(x) G^{(n)}(x) dx = M(f_3(\omega) - v^{(n-1)}(l, \omega)), \quad \omega \in [\omega_5, \omega_6]$$

3. The numerical realization

Note that each step of the iterative process requires the solution of the direct problem with the revised properties. Direct problems were solved by reduction to Fredholm integral equations of the second kind as in [3]. Thus, on the basis of the apparatus of Fredholm integral equations of the first and second kind have been constructed iterative processes for the identification of unknown functions that are allowed to carry out the cleavage of the initial inverse problem into a sequence of problems of two types - solution of the direct problem with variable coefficients and the definition of the amendments on the basis of a standard solution of ill-posed problem - treatment of Fredholm integral equation of the first kind with smooth kernel.

Several computational experiments in the problems of identifying the mechanical characteristics of the rod for different types of inhomogeneities were carried out. The experimental results showed that the proposed method can effectively restore smooth inhomogeneity laws: polynomial, trigonometric, functions with a large gradient (for the reconstruction with an accuracy of 8% is sufficient 5 - 7 iterations). Piecewise-constant heterogeneities restored much worse. The result of the restoration of these functions on the basis of the proposed method are smooth functions, similar to the original in the mean-square.

This work was supported by the President of Russian Federation (grant MK-6213.2012.1)

4. References

- [1] A. O. Vatulyan (2007). *Inverse problems in mechanics of deformed solids* (in Russian), Fizmatlit, Moscow, 223.
- [2] A. O. Vatulyan (2005). Integral equations in inverse problems of determining the coefficients of differential operators in the theory of elasticity (in Russian), *Dokl. Ros. akad. nauk*, **405**, № 3, 333–345.
- [3] Bocharova O. V., Vatul'yan A. O (2009). The Reconstruction of Density and Young's Modulus of an Inhomogeneous Rod // *Acoustical Physics*, **55**, №3, 281–288.

EVOLUTIONARY MULTIOBJECTIVE OPTIMIZATION OF MICROACTUATORS

A. Długosz¹ and T. Burczyński^{1,2}

*¹ Department of Strength of Materials and Computational Mechanics
Silesian University of Technology, Konarskiego 18a, 44-100 Gliwice*

*² Institute of Computer Modelling, Cracow University of Technology,
Warszawska 24, 31-455 Cracow*

1. Introduction

MEMS actuators (microactuators) produce movement and force, transforming (in most cases) electrical energy into mechanical energy. There are different types of microactuators, like: thermal, electrostatic, magnetic, piezoelectric and SMA (Shape Memory Alloys) ones. They use different types of physical phenomena to produce mechanical energy. In the thermal actuators movement is generated by means of high electrical resistivity of material and specific geometry. Electrostatic or electromagnetic actuators use electrostatic or electromagnetic force between movable and stationary parts (comb drive actuators). Piezoelectric microactuators use piezoelectric phenomenon and can be fabricated as a bimorph or expansion types. Shape optimization is an important phase in MEMS actuators designing. Majority of papers dedicated to the shape optimization of the microactuators consider only one criterion. If more than one criterion is considered, the optimization is performed by choosing one optimization criterion with other treated as restrictions. Another common approach is scalarization of the criteria by using weighting method. Such attitudes can be treated as multiobjective optimization but they are rather inadequate and inefficient. In multiobjective optimization based on Pareto concept several objectives (or cost functions) are minimized or maximized simultaneously. Obviously, in these problems there is no single solution that is the best with respect to all objectives. The designer has to choose one solution from a set of solutions, which are called optimal in the sense of Pareto.

Different models of electrostatic and thermal microactuators are optimized in the paper. The objectives can be created on the basis of different quantities derived from particular coupled-field analyses. Finite Element Method (FEM) [3] is used to solve electrostatic-structural and electrothermo-mechanical boundary-value problems. Objective function value calculated on the basis of numerical models of microactuators are usually multimodal. Analytical optimization methods are widely applied and they have good mathematical foundations, but for multimodal functions they usually stuck in local optima. Application of evolutionary algorithms (EAs) allows to avoid these difficulties. Moreover, EAs are ideal candidates for finding the Pareto optimal solutions because they work on the population of potential solutions in each generation.

2. Multiobjective optimization problem

Among many different types of multiobjective evolutionary algorithms, Strength Pareto Evolutionary Algorithm and Non-Dominated Sorting Genetic Algorithm are the most popular multiobjective optimization tools. Consecutive versions of such algorithms: SPEA2 and NSGAII [1] have many practical applications in different engineering disciplines. An own implementation of evolutionary multiobjective algorithm is used in the paper. Some specific methods implemented in NSGAII are applied in proposed method. Proposed algorithm has been tested on several benchmark and engineering problems. The results obtained by means of our method in most cases are better in comparison with the results obtained using NSGAII [2]. Finite element method is used to simulate direct problems numerically. MSC.Mentat/Marc and Ansys Multiphysics software packages are adapted to create the optimization system. Suitable interfaces between optimization algorithm and the FEM software are created.

3. Example of multiobjective shape optimization

The model of microelectrothermal actuator is considered (Fig. 1a). The microactuator is fabricated from polycrystalline silicon. The deflection of the microactuator occurs if the electrical potential difference is applied across two electrical pads (EP1, EP2). Caused by material properties - high electrical resistivity and different thermal expansion coefficient between thin and wide arms. The device is subjected to the electrical, thermal and mechanical boundary conditions. The length of the actuator is equal to 260 microns, while electrical pads are 20x20 microns wide. The multiobjective problem concerns determining the specified dimensions of the actuator shape, which minimize: (i) volume of the microactuator, (ii) maximal value of equivalent stress and maximize (iii) vertical deflection of the microactuator. Six design variables ($Z1-Z6$) are assumed (Fig.1a). Fig.1b presents a set of Pareto optimal solutions. The design variables for extreme solutions are as follows: Point A ($Z1=1.0$ $Z2=1.048$ $Z3=1.0$ $Z4=12.0$ $Z5=100.0$ $Z6=2.0$), Point B ($Z1=1.24$ $Z2=1.91$ $Z3=1.01$ $Z4=14.3$ $Z5=98.46$ $Z6=5.14$), Point C ($Z1=1.0$ $Z2=1.0$ $Z3=1.081$ $Z4=18.0$ $Z5=30.0$ $Z6=2.0$).

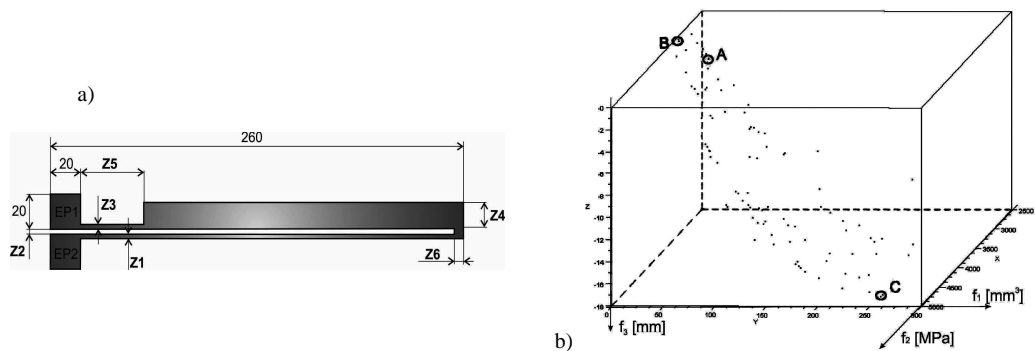


Fig.1. a) Geometry and parametrization of the thermal microactuator, b) Set of Pareto-optimal solutions

4. Final remarks

An effective intelligent technique based on the multiobjective evolutionary algorithm is used for shape optimization of microactuators. Positive results of multiobjective optimization are obtained for different type of microactuators. Coupled electrostatic-structural and electro-thermo-mechanical FEM analysis are performed to calculate objective functions for each individual in each generation. Numerical computations for such multiphysics problems using FEM is usually time consuming, especially for more complicated models.

Acknowledgements

The financial support of the National Centre for Research and Development (NCBiR) project no. R07 0006 10 is acknowledged.

6. References

- [1] Deb K., Pratap A., Agarwal S., Meyarivan T., A fast and elitist multi-objective genetic algorithm: NSGA-II, IEEE Transaction on Evolutionary Computation, 6(2), pp. 181-197, 2002.
- [2] Długosz A., Multiobjective Evolutionary Optimization of MEMS Structures, Computer Assisted Mechanics and Engineering Sciences, vol. 17, no.1, pp.41-50, 2010.
- [3] O.C. Zienkiewicz, R. Taylor, The Finite Element Method, Vol.1-3, Butterworth, Oxford 2000.

PARALLEL SPARSE INCOMPLETE CHOLESKY CONJUGATE GRADIENT SOLVER FOR MULTI-CORE COMPUTERS

S. Fialko

Cracow University of Technology, Kraków, Poland

1. Introduction

More and more high-dimensionality problems of mechanics of solids and structures become solvable on personal desktop computers without involving expensive workstations, clusters, networking etc. This type of computers requires a specific development of FEA software because of a restricted capacity of the core memory and a narrow bandwidth of the memory system.

The finite element method which has become most popular among numerical methods for the solution of problems of the structural and solid mechanics, leads to the linear algebraic equation sets with the sparse symmetric matrices. There are classes of problems that are preferable to solve by iterative methods instead of direct ones, because the duration of solution for iterative methods depends on dimension of problem almost linearly. Usually it is the design models of structures having rather short and wide structure of levels of an nodal adjacency graph.

The algorithm of matrix multiplication is possible to be essentially accelerated on the base of multithreading parallelization for shared memory multicore computers due to efficient usage of a cache-memory and registers of processors. It allows us to unload the system of memory possessing narrow bandwidth; therefore this algorithm demonstrates a good speedup while the processors number increases. The factoring of the sparse matrix is reduced to repeated application of algorithm of matrix multiplication for dense submatrices. Therefore it is possible to achieve a good speedup for direct methods at a stage of numerical factoring [1].

For problems of structural mechanics the preconditioned conjugate gradient method has appeared the most effective. In this work we apply the sparse incomplete Cholesky factorization method – a combination of incomplete Cholesky factorization by value approach with technique of sparse matrix. The main stages of this method are the sparse incomplete Cholesky factoring and iteration process. We will discuss the both: the parallelization of sparse incomplete factorization procedure and the stage of iterative one.

2. Sparse incomplete Cholesky factorization procedure

The sparse technique allows us essentially improve the property of preconditioning to accelerate of convergence. The multiple minimum degrees algorithm is applied to reduce the fill-ins, arising during incomplete factoring. In average, such a technique reduces the number of rejections comparing with conventional (non-sparse) method and allows us to approach the property of incomplete factor H to complete L without essentially increasing the size of incomplete factor H.

The looking-left column-by-column algorithm is applied:

1. **do** $j = 1, N$
2. Copy nonzero elements of column j of source matrix in dense vector \mathbf{s}_j .
3. Parallel update column j by columns, are located at left: $\mathbf{s}_j = \mathbf{s}_j - \sum_{k \in \text{List}[j]} a_{j,k} \mathbf{s}_k$
4. Factoring of column j .
5. Analyze of elements \mathbf{s}_j : *if* $(a_{ij}^2 < \psi a_{ii} a_{jj})$ – reject a_{ij} and correct the diagonal entries

$$a_{ii} = \sqrt{\frac{a_{ii}}{a_{jj}} |a_{ij}|}, \quad a_{jj} = \sqrt{\frac{a_{jj}}{a_{ii}} |a_{ij}|}, \quad \text{otherwise – put } a_{ij} \text{ to nonzero structure of column } j.$$

6. end do

Here $k \in List[j]$ means that the subscript k accepts only those values, for which $a_{jk} \neq 0$. Vectors s_j, s_k contains the matrix elements, located below row $i = j$. Threshold value ψ is taken so small how much it the amount of RAM and performance of the computer allow. The stage 3 requires almost 95% – 97% of computing time during factoring; therefore this part of algorithm should be parallelized first of all. We avoid splitting of a matrix into blocks as such procedure inevitably leads to increase in the size of incomplete factor H. It in turn increases requirements to amount of RAM and slows down the forward-back substitutions repeatedly applied in the course of iterations.

3. Iterative procedure

We can't produce the parallel computing on different steps of iterations because for obtaining of solution on a step $k+1$ it is necessary to know the solution on a step k . The parallelization only within each iterative step does not lead to considerable acceleration on multi-core computers. The matrix - vector multiplication and forward-back substitutions respectively incomplete factor H are the main time consuming operations. Unlike matrix multiplication these procedures are not to be accelerated considerably due to parallelization on computers of the specified architecture having a weak bandwidth of memory system [2]. Therefore we use parallel execution of iterations for different right parts, considering the fact that in practical problems of structural mechanics the structures are subjected by package of loads – dead load, exploitation loads, wind load, snow loads and so on. The number of load cases usually is about 6 – 60.

4. Numerical results

The design model of a real multistory building from collection of SCAD Soft (www.scadsoft.com) is considered. Model comprises 2 002 848 equations and 7 right-hand sides. The computer with four-core AMD Phenom™ II x4 995 3.2 GHz processor, RAM DDR3 1066 MT/s, 16 GB core memory is taken. The resignation parameter $\psi = 10^{-13}$.

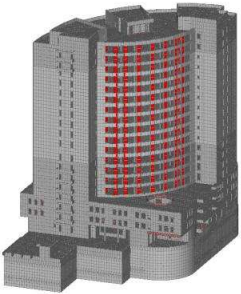
	Nos of threads	Incomplete factoring	Stage of iterations	Total time
	1	1 000	345	1 345
	2	578	213	791
	3	465	172	637
	4	421	144	565

Table 1. Duration of several stages of iterative solution, s.

6. References

- [1] S. Fialko. PARFES: A method for solving finite element linear equations on multi-core computers. *Advances in Engineering software*, v 40, 12, 2010, 1256 – 1265.
- [2] S. Fialko. *The direct methods for solution of linear equation sets in modern FEA software*. Moscow, SCAD SOFT, 2009 (In Russian).

MATHEMATICAL MODELING OF THIN-WALLED BEAMS AND FEM APPLICATIONS

*Alessandra Genoese, Andrea Genoese, Antonio Bilotta and Giovanni Garcea
Department of Engineering Modeling, University of Calabria, Rende (CS), Italy*

1. Introduction

3D beams with thin walled or compact section are widely used in engineering practice and the improvement of both linear and nonlinear models suitable to perform FEM analyses still represents an important task for researchers.

Although in the past notable contributions have appeared [1, 2], in recent literature interesting works [3, 4, 5, 6, 7] have presented beam theories with non-uniform warping and shear deformations for non-symmetric open/closed cross-sections.

This work deals with the theoretical generalization of the Saint-Venant linear solution (SV) to the case of nonuniform warping and its FEM formulation for the numerical analysis. The model is based on independent descriptions of both the 3D kinematical and stress parts. The kinematical description is based on standard assumptions that consider a rigid section motion plus an out-of-plane warping, derived by the SV solution, now generalized to allow the three warping functions corresponding to shear and torsion to vary along the axis with three independent descriptors, while the cross-sections maintain their shape. The warping functions are calculated numerically, as FEM solution of three Neumann boundary-value problems as in classical SV solution (see [8]). The 3D stresses are independently described by summing to the SV stress shape some further terms due to the variable warping.

The field so obtained are entered in the Hellinger-Reissner variational principle to obtain the model in terms of sections resultants.

Two different approaches will be developed and compared: the first one uses a Benscoter-like [9] expression for the secondary shear stresses derived from the generalized kinematic; the second one evaluates the shear stresses by the equilibrium equation in the axial direction. The second approach requires the solution of a new set of PDEs problems on the cross section domain, whose boundary conditions are obtained by imposing the zeroing of the traction vector on the free cylindrical surface, as no body forces or loads on the lateral boundary are considered. The numerical solution of the involved functions makes the formulation particularly general and easy to be used in the case of generic cross-section where the centroid and the shear center are not necessarily coincident. Once all the involved warping function are known, an automatic evaluation of the compliance matrixes is in fact possible.

The model could be exploited also as the starting point for geometrically nonlinear formulations, due to the possibility to filter the rigid body motion by means of standard Corotational descriptions (see [10] for example) or at the continuum level. A first important attempt in this direction is represented by the Implicit Cotational Method proposed in [11]. The resulting nonlinear models maintain all the information of their linear counterpart and can be accurate up to the order required. This aspect is very significant when performing Koiter-like asymptotic analyses, as a second order kinematical accuracy is inadequate.

A series of numerical tests will show the accuracy and the effectiveness of the proposed model and its discrete implementation.

2. References

- [1] V. Z. Vlasov, (1961). *Thin-Walled Elastic Beams*, Israel Program for Scientific Translations, Jerusalem, Israel.
- [2] A. Tralli, (1986). A simple hybrid model for torsion and flexure of thin-walled beams, *Computer and Structures*, **22**, 649-658.
- [3] S. Y. Back and K. M. Will, (1998). A shear-flexible element with warping for thin-walled open beams, *International Journal for Numerical Methods in Engineering*, **43**, 1173-1191.
- [4] N.-I. Kim, M.-Y. Kim (2005). Exact dynamic/static stiffness matrices of non-symmetric thin-walled beams considering coupled shear deformation effects, *Thin-Walled Structures*, **43**, 701-734.
- [5] R. Emre Erkmen, Magdi Mohareb (2006). Torsion analysis of thin-walled beams including shear deformation effects, *Thin-Walled Structures*, **44**, 1096-1108.
- [6] R. Fatmi (2007). Non-uniform warping including the effects of torsion and shear forces. Part I: A general beam theory, *International Journal of Solids and Structures*, **44**, 5912-5929.
- [7] V. G. Mokos, E. J. Sapountzakis (2011). Secondary torsional moment deformation effect by BEM, *International Journal of Mechanical Sciences*, **53**, 897-909.
- [8] W. Lacarbonara, A. Paolone (2007). On solution strategies to Saint-Venant problem, *Journal of Applied Mechanics*, **206**, 473-497.
- [9] S. Benscoter (1954). A theory of torsion bending for multicell beams, *Journal Computational and Applied Mathematics*, **53**, 25-34.
- [10] G. Garcea A. Madeo G. Zagari R. Casciaro, (2009). Asymptotic postbuckling FEM analysis using corotational formulation, *Journal of Solid and Structures*, **146**, 377-397.
- [11] G. Garcea, A. Madeo, R. Casciaro, *The Implicit Corotational Method: a tool for obtaining geometrically nonlinear models for fibred continua*, Report Labmec number 56.

MODELLING OF CORROSION INTERFACE IN RC CROSS-SECTION

M. German, J. Pamin

Institute for Computational Civil Engineering, Cracow University of Technology, Poland

1. Introduction

The chloride corrosion is one of the most important destructive factors of durability of concrete structures. During the process, chlorides penetrate the concrete cover and gather around passive reinforcement bars. As time passes by, the chloride concentration in concrete increases until it reaches a chloride threshold value, estimated as 0.4% of the cement mass. At this moment the passive layer on the steel bar surface becomes decomposed and the rebar starts corroding. The rust has a smaller density than steel, which means that the volume occupied by rust is much larger than the volume of steel consumed in the process, thus a volumetric expansion occurs [1]. This generates an internal pressure acting on the concrete surrounding the reinforcement. As a result tensile stresses occur in the concrete cover, which leads to cracking, splitting, spalling and general failure of the element.

2. Corrosion interface model

The proposed model of corrosion interface in RC cross-section is focused on the analysis of cracking of the concrete. The constitutive model for concrete behavior is the plasticity-based damage model proposed in [2]. The model uses concepts of isotropic damaged elasticity in combination with multi-surface plasticity to represent the inelastic behavior of concrete. It assumes that the two main failure mechanisms are tensile cracking and compressive crushing of the material. The evolution of failure is controlled by tensile and compressive equivalent plastic strains. Under uniaxial tension, the stress-strain response follows a linear elastic relationship until a failure stress is reached. Beyond the failure stress the formation of micro-cracks is represented macroscopically with a softening stress-strain response. Under uniaxial compression the response is linear until the value of initial yield strength is reached. In the plastic regime the response is typically characterized by stress hardening followed by strain softening beyond the ultimate stress. Steel is modelled as an elastic-plastic material without hardening. Rust is introduced as a layer of elastic material.

These three material models are used to build a numerical representation of corrosion interface. The two-dimensional model is created using FE package Abaqus. Concrete and steel are modelled as a solid using 8-node continuum elements (CPS8R). Rust is modelled as an interface, using 4-node cohesive elements (COH2D4). The constitutive response of the cohesive layer can be defined using a traction-separation description or a continuum approach. Both types are considered in the model. For comparison, rust can also be modelled as another continuous material. The three materials are connected using tie constraint.

3. Tests and application

Firstly, numerical tests are performed on a sample with dimensions 200mm x 300mm. The model is a composition of three materials tied and loaded by unit uniaxial tension. The interface response is described in terms of traction-separation or using continuum approach. In the third model rust is treated as a solid material. On the basis of the results, achieved from the test, for further calculations only cohesive elements with traction-separation response are implemented.

Damage due to corrosion product expansion is simulated for an RC cross-section with the dimensions of 350mm x 600mm. The cross-section is reinforced with four 25mm-diameter bars. The bars spacing is 75mm. The C25/30 concrete is assumed, the concrete cover is 50mm, and the rust

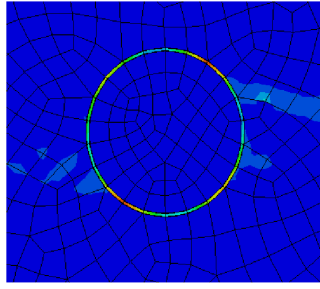


Figure 1. Model of corrosion interface in RC cross-section

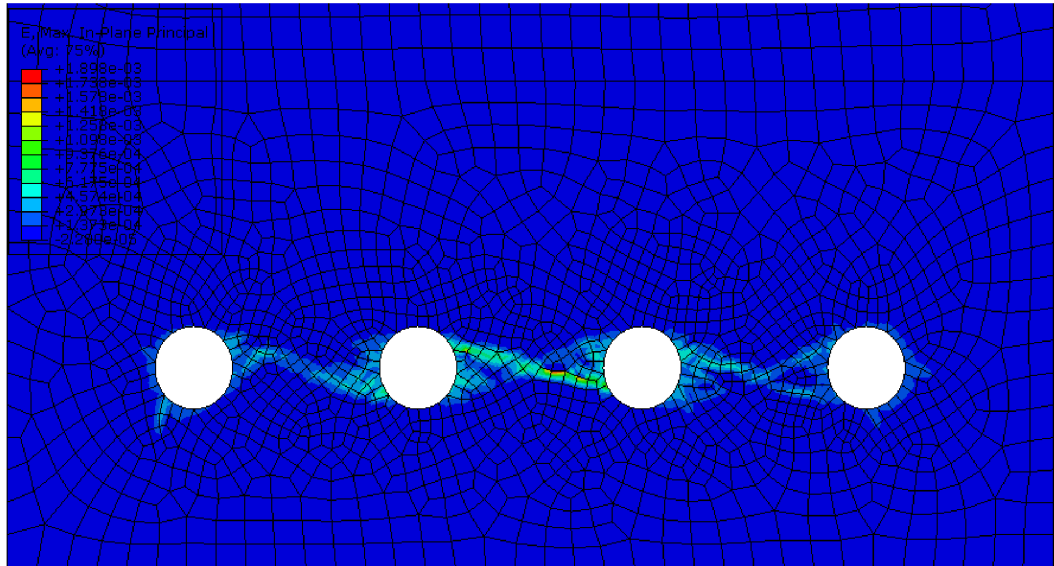


Figure 2. Localized strains appearing in concrete due to corrosion

layer is 0.5mm thick. The representation of the corrosion interface is presented in Figure 1. The internal pressure, generated by the volumetric expansion of corrosion products, is calculated according to chloride corrosion model presented in [3], assuming uniformly distributed corrosion. In the Abaqus model the expansion is represented by substitute internal pressure, acting at the reinforcement-rust and rust-concrete contact surfaces. The paper presents the results of these simulations and their sensitivity to selected model parameters. Example tensile cracking of concrete is presented in Figure 2.

4. References

- [1] A. Zybura, M. Jaśniok and T. Jaśniok (2011). *Diagnostyka Konstrukcji Żelbetowych*, Wydawnictwo Naukowe PWN, Warszawa.
- [2] J. Lee and G.L. Fenves (1998). Plastic-damage model for cyclic loading of concrete structures, *Journal of Engineering Mechanics*, **124**, 892-900.
- [3] M. German and A. Zaborski (2011). Numerical analysis of chloride corrosion of reinforced concrete, *Technical Transactions*, **3**, 47-60.

TREATMENT OF AN INHOMOGENEOUS INCLUSION WITH THE AUGMENTED CORRECTED COLLOCATION METHOD

A. Hashemian and H. M. Shodja

Center of Excellence in Structures and Earthquake Engineering, Department of Civil Engineering, Sharif University of Technology, Tehran, Iran

1. Problem definition

Inhomogeneity is a subdomain of a body whose material is different from those of its surrounding matrix. If the inhomogeneity is under an eigenstrain field, it is referred to as inhomogeneous inclusion, Figure 1. Assuming both phases are isotropic and the eigenstrain is uniform through the field, the exact solution can be found in [1].

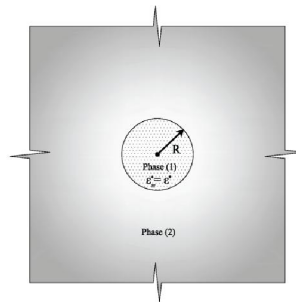


Figure 1. Circular inhomogeneous inclusion in an infinite body.

Many numerical investigations utilize the circular inhomogeneous inclusion with uniform eigenstrain field as a benchmark to demonstrate the efficacy of their solutions. Among these studies [1–3] can be mentioned.

2. Methodology

In the present work, the problem of circular inhomogeneous inclusion with uniform eigenstrain field is employed to examine the robustness of the augmented corrected collocation method (ACCM) proposed by Shodja, Khezri, Hashemian and Behzadan [4].

ACCM is a method in the context of meshless methods, particularly reproducing kernel particle method (RKPM). ACCM is applied to enforce exactly not only the continuity of displacements at the interface particles but also the essential boundary conditions at the boundary particles. This leads to analyze the material discontinuity problems with much more accuracy [4].

3. Solution

Suppose $R = 1$ and Young's modulus and Poisson's ratio for phase one and two should be $E_1 = 1000, \nu_1 = 0.28$ and $E_2 = 900, \nu_2 = 0.33$, respectively. Due to the axisymmetry, only one quarter of the domain ($0 \leq \theta \leq \frac{\pi}{2}$) with the size of 5×5 has been selected to be modeled. Each phase is discretized separately with the RKPM shape functions. 302 and 503 particles have been used for discretizations within the first and the second phase, respectively. The area associated with each particle is calculated employing the proposed algorithm in [4]. At the interface, 41 pairs of particles are located, Figure 2. In each pair, one particle belongs to phase one and the other is of phase two with the same coordinate.

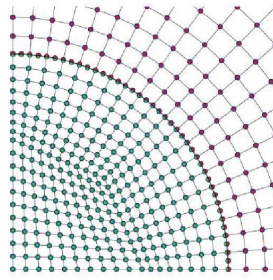


Figure 2. The arrangement of particles in the first phase and in the interface boundary.

Since the selected domain is finite, the displacements in the right and upper edges of the plate have been calculated using the theoretical solution [1] and have been considered as EBCs. Also symmetry boundary conditions are applied at the left and lower edges of the plate. Note that at the interface, the continuity of displacements should be met.

4. Results

The radial strain along $\theta = \frac{\pi}{4}$ has been plotted in Figure 3. It is seen that, the discontinuity at the interface has been captured accurately without any undesired oscillation and there is a considerable accordance between the numerical and exact solutions. This verifies the efficacy of the ACCM. Figure 4 shows the radial variation of hoop stress along $\theta = \frac{\pi}{4}$ which exhibits a jump discontinuity across the interface. The conformity of numerical results and exact solution, once again emphasizes the accuracy and the efficacy of the ACCM

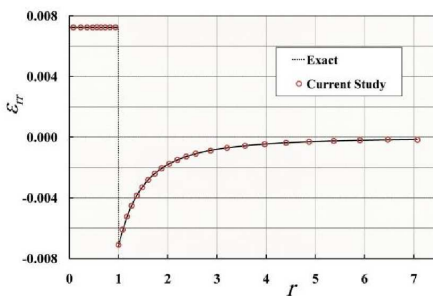


Figure 3. Distribution of radial strain.

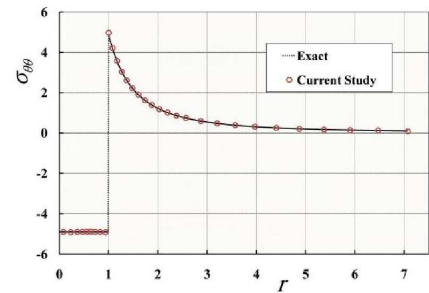


Figure 4. Distribution of hoop stress.

5. References

- [1] L.W. Cordes and B. Moran (1996). Treatment of material discontinuity in the Element-Free Galerkin method, *Comput. Methods Appl. Mech. Engrg.*, **139**, 75–89.
- [2] B. Krongauz and T. Belytschko, (1998). EFG approximation with discontinuous derivatives. *Int. J. Numer. Meth. Engrg.*, **41**, 1215–1233.
- [3] Q. Li, S. Shen, Z.D. Han, and S.N. Atluri (2003). Application of Meshless Local Petrov-Galerkin (MLPG) to problems with singularities, and material discontinuities, in 3-D elasticity, *CMES: Computer Modeling in Engineering & Sciences*, **4**, 571–585.
- [4] H.M. Shodja, M. khezri, A. Hashemian, and A. Behzadan (2010). RKPM with augmented corrected collocation method for treatment of material discontinuities, *CMES: Computer Modeling in Engineering & Sciences*, **62**, 171–204.

FRACTURE MECHANICS ANALYSIS OF A CYLINDRICAL SAMPLE LOADED BY TIME-DEPENDENT HEATING

M. Leindl, E. R. Oberaigner

Institute of Mechanics, University of Leoben, Leoben, Austria

1. Abstract

In this work the thermomechanical loading through dielectric heating of a cylindrical sample made of a brittle material is investigated. Such heating occurs due to irradiation by microwaves in a cavity or by a beam [1]. The suitable modelling of the dielectric heating is of crucial importance in the analysis. In literature there can be found two approaches to model microwave heating in dielectric media. The first one utilise Maxwell's equations in dielectric media [2], the second one is known as Lambert-Beer's law [3]. In contrast to the Maxwell's equations approach, with Lambert-Beer's law it is not necessary to solve the propagation of electromagnetic waves inside the medium and the heating is modelled via a volumetric heat source. The expression for this source or body flux can be derived from Maxwell's equation [4, 5]. In this work the time-dependent temperature field is obtained via the Green's function approach and compared with numerical results from finite element calculations. The following analysis for the time-dependent stress-strain field is performed in the same manner, and again analytical results are compared with numerical calculations. With the information how the stress-field varies with time, it is possible to perform a fracture-mechanics analysis for several crack configurations. Due to the fact that the material shows a brittle behaviour it is admissible to use linear-elastic fracture mechanics and the K-factor concept [6]. As a result stress intensity factors are obtained and can be compared with critical values from literature. Additionally a possible procedure for a crack propagation and life-time calculation will be given in the outlook.

2. References

- [1] P. Hartlieb, M. Leindl, F. Kuchar, T. Antretter and P. Moser (2012). Damage of basalt induced by microwave irradiation, *Miner. Eng.*, **In Press**, Available online 15 February 2012.
- [2] D. D. Dincov, K. A. Parrott and K. A. Pericleous (2004). Heat and mass transfer in two-phase porous materials under intensive microwave heating, *J. Food Eng.*, **65**, 403-412.
- [3] H. Ni and A. K. Datta and K. E. Torrance (1999). Moisture transport in intensive microwave heating of biomaterials: a multiphase porous media model, *Int. J. Heat Mass Tran.*, **42**, 1501-1512.
- [4] K. G. Ayappa, H. T. Davis, G. Crapiste, E. A. Davis and J. Gordon (1991). Microwave Heating: An Evaluation of Power Formulations, *Chem. Eng. Sci.*, **46**, 10051016.
- [5] A. C. Metaxas (1986). *Foundations of Electroheat*, John Wiley & Sons, Inc., New York.
- [6] D. Gross and T. Seelig (2011). *Fracture Mechanics: With an Introduction to Micromechanics*, 2nd ed. Springer, Heidelberg.

THE GENERAL BOUNDARY ELEMENT METHOD FOR DUAL PHASE LAG MODEL OF MICROSCALE HEAT TRANSFER

E. Majchrzak^{1,2}

¹ *Silesian University of Technology, Gliwice, Poland*

² *Czestochowa University of Technology, Czestochowa, Poland*

1. Introduction

Micro-domain subjected to the external heating is considered. Mathematical description of the process discussed bases on the dual phase lag equation in which the relaxation time and the thermalization one appear. The DPL equation contains a second order time derivative and higher order mixed derivative in both time and space. This equation is supplemented by the adequate boundary and initial conditions. To solve the problem the general boundary element method is adapted

2. Mathematical model

Heat transfer processes proceeding in a rapidly heated micro-domains can be described, among others, by the dual phase lag equation [1, 2] (2D problem is considered)

$$(1) \quad C \left[\frac{\partial T(x, y, t)}{\partial t} + \tau_q \frac{\partial^2 T(x, y, t)}{\partial t^2} \right] = \lambda \nabla^2 T(x, y, t) + \tau_T \lambda \frac{\partial \nabla^2 T(x, y, t)}{\partial t}$$

where C is the volumetric specific heat, λ is the thermal conductivity, τ_q is the relaxation time, τ_T is the thermalization time, T is the temperature, (x, y) are the spatial co-ordinates and t is the time.

This equation is supplemented by the boundary conditions

$$(x, y) \in \Gamma_1 : \quad T(x, y, t) = T_b(x, y, t)$$

$$(2) \quad (x, y) \in \Gamma_2 : \quad q_b(x, y, t) + \tau_q \frac{\partial q_b(x, y, t)}{\partial t} = -\lambda \left[\frac{\partial T(x, y, t)}{\partial n} + \tau_T \frac{\partial}{\partial t} \left(\frac{\partial T(x, y, t)}{\partial n} \right) \right]$$

and initial ones

$$(3) \quad t = 0 : \quad T(x, y, t) = T_p, \quad \left. \frac{\partial T(x, y, t)}{\partial t} \right|_{t=0} = 0$$

where $T_b(x, y, t)$ is a known boundary temperature, $q_b(x, y, t)$ is a known boundary heat flux, n is the normal outward vector, $\partial(\cdot)/\partial n$ is the normal derivative and T_p is an initial temperature.

3. General boundary element method

It should be pointed out that for $\tau_q = \tau_T = 0$ the equation (1) reduces to the well known Fourier one. To solve the Fourier equation by means of the boundary element method the several variants basing on a time marching technique have been applied, for example the 1st scheme of the BEM, the BEM using discretization in time and the dual reciprocity BEM. In this work, the general boundary element method (GBEM) for hyperbolic heat conduction equation proposed by Liao [3] is adapted in order to solve the dual-phase lag equation.

Let $\beta = 1/\Delta t$ and $T^f = T(x, y, f\Delta t)$, where Δt is the time step. Then, for time $t^f = f\Delta t$ ($f \geq 2$) the following approximate form of equation (1) can be taken into account

$$(4) \quad \beta(T^f - T^{f-1}) + \tau_q \beta^2 (T^f - 2T^{f-1} + T^{f-2}) = a \nabla^2 T^f + a \tau_T \beta (\nabla^2 T^f - \nabla^2 T^{f-1})$$

where $a = \lambda/C$. From initial conditions (3) results that $T^0 = T(x, y, 0) = T_p$ and $T^1 = T(x, y, \Delta t) = T_p$. It should be pointed out that when the equation (4) is solved at the f -th time step $t^f = f \Delta t$ then the temperature distributions T^{f-1} at time t^{f-1} and T^{f-2} at time t^{f-2} are known.

At first, a family of partial differential equations for $\Phi(x, y; p)$ is constructed [3]

$$(5) \quad (1-p)L[\Phi(x, y; p) - U(x, y)] = -pA[\Phi(x, y; p)]$$

where $p \in [0, 1]$ is a parameter, $U(x, y)$ is an initial approximation of temperature distribution T^f (for example $U(x, y) = T^{f-1}$), L is a 2D linear operator whose fundamental solution is known and A is a non-linear operator. The form of operators L and A results from the equation (4) [3]. The equation (5) should be supplemented by adequate boundary conditions resulting from conditions (2).

If $p = 0$ then $\Phi(x, y; p)$ corresponds to the initial approximation $U(x, y)$, while if $p = 1$ then $\Phi(x, y; p)$ corresponds to the unknown temperature $T^f = T(x, y, t^f)$. So, the equations (5) form a family of equations in parameter $p \in [0, 1]$ and the process of continuous change of the parameter p from 0 to 1 is the process of continuous variation of solution $\Phi(x, y; p)$ from $U(x, y)$ to $T^f = T(x, y, t^f)$.

Function $\Phi(x, y; p)$ is expanded into a Taylor series about value $p = 0$ taking into account the first derivative and under the assumption that $U(x, y) = T^{f-1}$ one has

$$(6) \quad T^f = T^{f-1} + U^{(1)}(x, y)$$

where $U^{(1)}(x, y) = (\partial \Phi(x, y; p) / \partial p)|_{p=0}$.

Taking into account the form of operators L and A the equation $\nabla^2 U^{(1)} - BU^{(1)} + R(U) = 0$ should be solved using the traditional BEM for steady-state problem.

As an example, the domain of dimensions $100\text{nm} \times 100\text{nm}$ made of gold is considered. At the upper surface the heat flux described by Gaussian function is assumed, at all other boundaries the zero heat flux is accepted. Initial temperature equals to 300K. Figure 1 shows the temperature history at the two internal points close to the central part of upper surface.

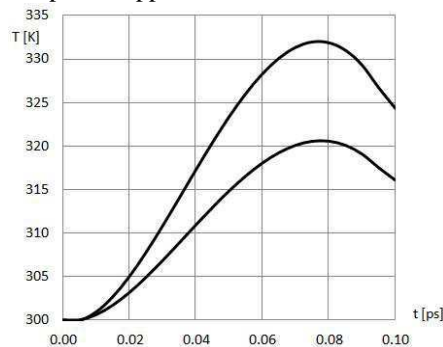


Figure 1. Temperature history at the two internal points.

4. References

- [1] A.N.Smith, P.M.Norris (2003). *Microscale heat transfer*, Chapter 18 in: *Heat Transfer Handbook*, John Wiley & Sons.
- [2] E.Majchrzak (2010), Numerical solution of dual phase lag model of bioheat transfer using the general boundary element method, *CMES: Computer Modeling in Engineering and Sciences*, **69**, 1, 43–60.
- [3] S.Liao (1997) General boundary element method for non-linear heat transfer problems governed by hyperbolic heat conduction equation, *Computational Mechanics*, **20**, 397–406.

The paper is a part of Grant N N501 2167 37.

METAL FOAM STRUCTURE FINITE ELEMENT MODELLING BASED ON COMPUTED TOMOGRAPHY

A.D. Miedzińska and T. Niezgoda

*Military University of Technology, Department of Mechanics and Applied Computer Science,
Warsaw, Poland*

1. Introduction

Metal foams (Fig. 1) are a new, as yet imperfectly characterized, class of materials with low densities and novel physical, mechanical, thermal, electrical and acoustic properties. They offer potential for lightweight structures, for energy absorption, and for thermal management; and some of them, at least, are cheap.

The paper deals with the experimental and numerical studies of the open-cell aluminum foam microstructural behavior. The aim of the research was to describe the main mechanisms that appear in the foam structure during the compression. The first step of the research was the compression test of the samples in the tomography testing stage that was coupled with sample X-ray scanning to describe the deformations in the researched material for the FE model verification. The next step of the study was the development and the analyses of the numerical model of tested undeformed sample in accordance to computed tomography results. Both results were compared. On the base of good correspondence the main mechanisms in the foam structure were described.

2. Computed tomography description and research results

SkyScan 1174 (Fig. 2) compact micro-CT was utilized to carry out the compression tests for samples made of an open cell ERG Aerospace aluminum foam of 10 PPI¹. The foam relative density was 9%. The conducted test was performed to compress the sample by 40% of its height. The compression was done in the following stages of 1 mm and after each stage the compressed sample tomography was carried out. The load velocity was 2,5 mm/min. The examples of deformations and strain – stress curves are presented in Fig. 3.

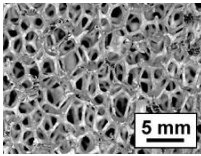


Fig. 1. Open cell aluminum foam



Fig. 2. SkyScan 1174 compact micro-CT

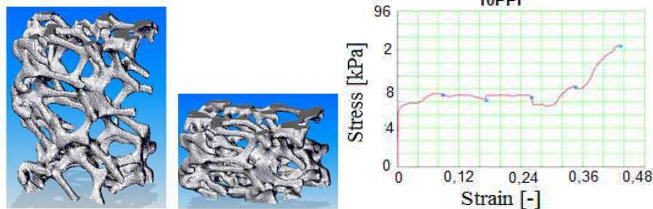


Fig. 3. CT compression test results – deformations (undeformed and compressed samples) and stress-strain curve

¹ PPI – *pores per inch* – the number of open pores linearly arranged along the distance of one inch

3. Finite element model, analysis and results

Foamed materials numerical models are often developed on the base of the real structure image (2D photograph or 3D scan) [1,2]. Idealized models suitable for investigations to determine the influence of particular geometrical or material parameters onto global properties of a foam are also used (i.e. Kelvin's polyhedron [3], Weaire-Phelan structure [3] or Voronoi 3D tessellation [4]).

The model was built with the use of a unique computer code created to transform the scan point cloud into FE raster model based on solid 8-node elements (Fig. 4). The numerical compression test was carried out with the use of LS Dyna computer code. The boundary conditions were applied as in the experiment. The elastic-plastic material model with isotropic hardening was applied to describe the material properties for aluminium (Young modulus $E=71\text{GPa}$, Poisson ratio $\nu=0,33$, yield stress $R_e=318\text{MPa}$). The comparison of numerical and experimental tests was carried out for deformations and stress-strain curve (Fig. 5) and showed good accordance. The differences result from material model and properties approximations.

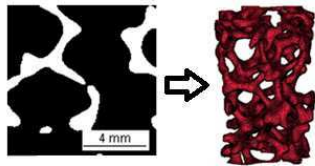


Fig. 4. Numerical model development

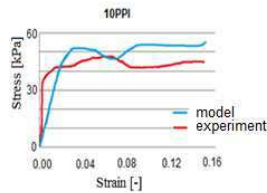


Fig. 5. Comparison of experimental and FE results

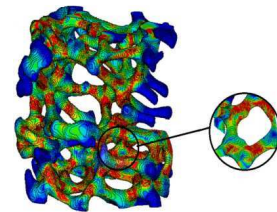


Fig. 6. Stress distribution in compressed FE model

Due to the high correspondence between numerical and experimental tests, the main mechanisms appearing in the foam microstructure were assessed on the base of the von Mises stress distributions (Fig. 6). The main mechanism of the foam damage is the plastic joints development in the connection areas between foam beams as well as in the beams.

4. Discussion and conclusions

The development process of the real foam structure numerical model on the base of the computed tomography was presented. The experimental and numerical study of the 10PPI foam samples was presented. The results of strain – stress behavior and deformations were compared and showed good compatibility. The stress distributions were studied in order to characterize the main mechanisms in the structure. The most important conclusion is that the foam structures can be considered as the complex beams constructions where the local instabilities determine energy absorbing capabilities.

5. References

- [1] T. Niezgoda, W. Szymczyk, J. Małachowski (2005). *Modelowanie numeryczne mikrostruktury ceramiki*, WNT, Warsaw.
- [2] K. Lee, S. Ghosh (1999). A microstructure based numerical method for constitutive modeling of composite and porous materials, *Materials Science and Engineering*, **272**, 120-133.
- [3] R. Kutner, J.M. Sullivan (1996). Comparing the Weaire-Phelan Equal-Volume Foam to Kelvin's Foam, *Forma*, **11**, 164-330.
- [4] Y. Shoshany, D. Prialnik, M. Podolak (2002). Monte Carlo Modeling of the Thermal Conductivity of Porous Cometary Ice, *Icarus*, **157**, 219.

MICROSCALE HEAT TRANSFER. COMPARISON OF NUMERICAL SOLUTIONS USING TWO-TEMPERATURE MODEL AND DUAL PHASE LAG MODEL

B.Mochnacki¹, J. Dziaekiewicz²

¹ *Czestochowa University of Technology, Czestochowa, Poland*

² *Silesian University of Technology, Gliwice, Poland*

1. Introduction

The problems connected with the numerical modeling of microscale heat transfer are here discussed. Generally speaking, the differences between the macroscopic heat conduction equation basing on the Fourier law and the models describing the same process in microdomains appear, first of all, in the case of extremely short duration, extreme temperature gradients and very small dimensions of domain considered [1].

From the mathematical point of view, nowadays there exist different models describing the mechanism of process discussed. In this place the microscopic two-step parabolic model can be mentioned [2]. The two-temperature parabolic model involves two energy equations determining the thermal processes in the electron gas and the metal lattice. The other governing equation can be obtained on the basis of classical Fourier-Kirchhoff equation in which the vector of heat flux \mathbf{q} is defined in a special way (both the relaxation and thermalization times are taken into account). The relaxation time is the mean time for electrons to change their energy states, while the thermalization time is the mean time required for electrons and lattice to reach equilibrium. This approach is called the dual phase lag model (DPLM).

In the paper the thermal processes proceeding in domain of thin metal film subjected to a laser pulse are considered. The numerical algorithms simulating the course of the process are constructed using the FDM in version being the generalization of variant discussed in [3]. Both two-temperature model and DPLM one are taken into account and the comparison of solutions obtained constitutes the main goal of research.

2. Two-temperature parabolic and DPL models

At first, the microscopic two-step model presented among others in [2] will be discussed. The two-step model involves two energy equations determining the heat exchange in the electron gas and the metal lattice. The equations creating the model discussed can be written in the form

$$(1) \quad C_e(T_e) \frac{\partial T_e}{\partial t} = \nabla[\lambda_e(T_e, T_l) \nabla T_e] - G(T_e - T_l) + Q$$

$$(2) \quad C_l(T_l) \frac{\partial T_l}{\partial t} = \nabla[\lambda_l(T_l) \nabla T_l] + G(T_e - T_l)$$

where $T_e = T_e(x, t)$, $T_l = T_l(x, t)$ are the temperatures of electrons and lattice, respectively, $C_e(T_e)$, $C_l(T_l)$ are the volumetric specific heats, $\lambda_e(T_e, T_l)$, $\lambda_l(T_l)$ are the thermal conductivities, G is the coupling factor which characterizes the energy exchange between phonon and electrons, Q is the capacity of internal heat sources resulting from the laser action [4]. Taking into account the geometrical properties of domain considered, the 1D task constitutes sufficiently good approximation of the real heat transfer processes proceeding in the system. Introduction of internal heat source Q allows one to assume the no-flux boundary conditions on the upper and lower surfaces of the metal film. The initial conditions of the task discussed are also known.

The other approach resulting from the generalized Fourier law leads to the following equation

corresponding to DPL model [4]

$$(3) \quad C \left[\frac{\partial T}{\partial t} + \tau_q \frac{\partial^2 T}{\partial t^2} \right] = \nabla [\lambda \nabla T] + \tau_r \nabla \left[\lambda \frac{\partial \nabla T}{\partial t} \right] + Q + \tau_q \frac{\partial Q}{\partial t}$$

where $T(x, t) = T_l(x, t)$ is the macroscopic lattice temperature, $C = C_l + C_e$ is the effective volumetric specific heat resulting from the serial assembly of electrons and phonons and $\lambda = \lambda_e$. The boundary conditions are the same as previously, the initial one determined the initial temperature and initial heating rate.

3. Example of computations

The thin gold film of thickness $L = 100$ nm subjected to a short-pulse laser irradiation [4] is considered. Thermophysical parameters are taken from [4]. In Figure 1 the solution of two-temperature parabolic model is shown, while Figure 2 presents the solution of dual phase lag model. It is visible that electron temperature is much higher than lattice temperature. Solution of DPL model is between temperature of electrons and lattice in two-temperature model.

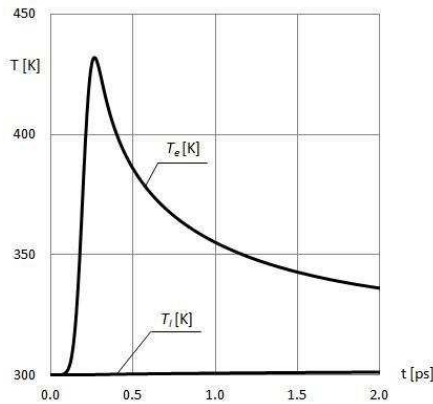


Figure 1: Electrons and lattice temperature at the irradiated surface

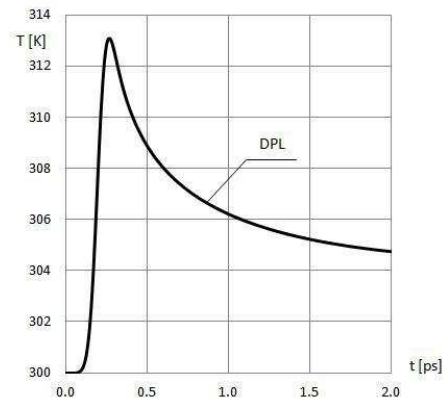


Figure 2: Macroscopic temperature at the irradiated surface

4. References

- [1] K.K.Tamma, X. Zhou (1998): Macroscale and microscale thermal transport and thermo-mechanical interactions: some noteworthy perspectives. *Journal of Thermal Stresses*, vol. 21, pp. 405-449.
- [2] I.K. Kaba, W. Dai W. (2005): A stable three-level finite difference scheme for solving the parabolic two-step model in a 3D micro-sphere heated by ultrashort-pulsed lasers. *Journal of Computational and Applied Mathematics*, vol. 181, pp. 125-147
- [3] B.Mochnacki, J.S.Suchy (1996), *Numerical methods in computations of foundry processes*, PFTA, Cracow, 1996.
- [4] E.Majchrzak, B.Mochnacki, A.I.Greer, J.S.Suchy (2009), Numerical modeling of short pulse laser interactions with multi-layered metal film, *CMES*, vol.41, No.2, pp. 131-146.

The paper is a part of Grant N N501 2167 37.

AUTOMATIC GENERATION OF BENCHMARK PROBLEMS FOR STRESS ANALYSIS FEM PROGRAMS USING MANUFACTURED SOLUTIONS METHOD

A. Perduta and R. Putanowicz

*Institute for Computational Civil Engineering,
Faculty of Civil Engineering, Cracow University of Technology, Cracow Poland*

1. Motivation

Verification of computer programs is one of the key issues in ensuring quality of numerical simulations. Verification usually means comparison of the results obtained from computer simulations with a reference solution. In case of problems governed by a PDE or a set of PDE's one can obtain exact reference solution only in the most simple cases. What is more, such solution might be not enough to fully cover all aspects of the code that is to be verified. A possible remedy to this problem is to perform code verification using method of manufactured solutions [1]. In this approach one assumes a solution having the desired properties, and then, by filtering the solution through the problem equations, recovers source terms and boundary conditions that lead to this solution. Automation of this recovery can make the verification of numerical codes much easier.

2. Program structure

Figure 1 shows the structure and the data flow of our application aimed at providing help in the construction manufactured solutions for verification of the structural analysis codes. The application

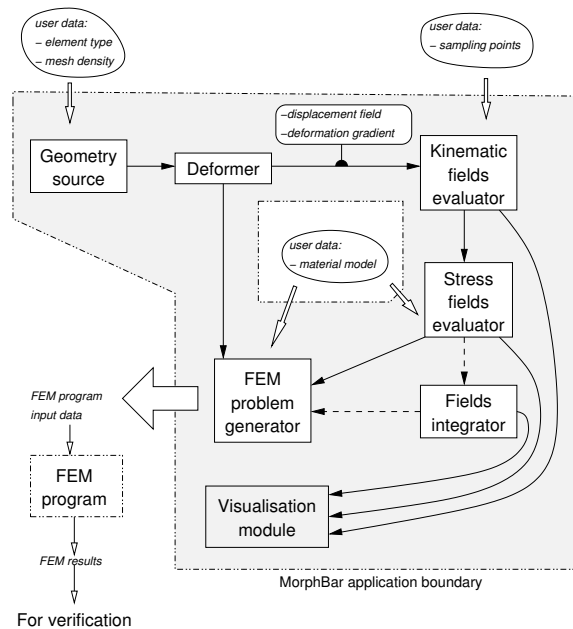


Figure 1. Structure and data flow for MorphBar application.

can be used in two modes. In the first mode, the application takes on input a specification of equation of motion, data for body discretisation in terms of a mesh, and data for material model. On output it produces a set of files containing input data for a finite element method application. Running the FEM application on these input files should produce a solution that approximates the assumed equation of motion. In the second mode, the application takes on input a specification of sampling points and calculates values of various fields (strains, stresses) that are derived from the assumed equation of motion and material model. By automating generation of FEM program input files and subsequent sampling of the fields of interest, the application can substantially help in rigorous, systematic and, what is more, automated verification of computational codes.

Sampling the displacement field involves direct evaluation of the equations of motion. Calculation of the deformation gradient tensor field is more difficult as it involves differentiation of the equations of motion. For some cases the deformation gradient can be calculated from closed analytic formulas as in the case of "Axis Deformer" described below. The application makes also provision for calculating the approximation to the deformation gradient using finite element method techniques (FEM Deformer), symbolic calculations via external package (Analytic Deformer), and calculation of the deformation gradient using automatic differentiation (AD Deformer). The hierarchy of deformer classes is shown in Figure 2.

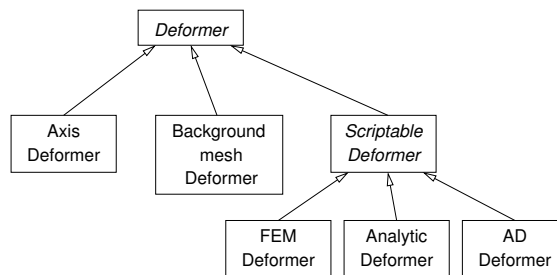


Figure 2. Class hierarchy for Deformers.

3. AxisDeformer module

The "MorphBar" application was conceived by considering a particular case of deforming a rectangular cross-section bar. The bar is mapped (morphed) from an undeformed to a deformed configuration by providing the description of the deformed axis via NURBS curve [2] and assuming that plane cross-sections orthogonal to the undeformed axis remain plane and orthogonal to the deformed one. In other words we assume the kinematics of the classical Euler–Bernoulli beam theory but without restriction of small deflections. This particular form of the deformation allows us to express the deformation gradient by the versors of Frenet–Serret frame, torsion and curvature of the axis curve. The NURBS form of the deformed axis is assumed to facilitate exact analysis of the axis geometry with the help of the openNURBS C++ library [3].

[1] K. Salari and P. Knupp (2000). Code Verification by the Method of Manufactured Solutions, SAND2000 - 1444, Sandia National Laboratories.

[2] Les A. Piegl and Wayne Tiller (1997). *The NURBS book*, Springer.

[3] The openNURBS Toolkit, <http://www.opennurbs.org/>.

MODIFIED CONTACT SEARCH ALGORITHM FOR SHEET METAL FORMING

K. Wawrzyk, P. Kowalczyk

Institute of Fundamental Technological Research, Warsaw, Poland

1. Introduction

The presented contribution concerns algorithm for detecting contact in numerical simulations of sheet metal forming. An amendment to a standard contact searching algorithm is proposed that allows to eliminate errors leading to wrong solution results. The considered algorithm is designated for the cases of triangular discretization of contact surfaces. Furthermore, numerical cost of the presented algorithm is discussed.

2. The concept of the proposed algorithm

The standard algorithm for detection of contact between a point and a surface (discretized by finite elements) [1,2] assumes that the contact element (also called contact segment) is one of the elements sharing the node that is the closest to the point considered. For some finite element meshes this assumption may prove false. An example of such a case is shown in figure 1. Here, one can see the surface S discretized by triangular elements and the point P located above or below the surface. Since the closest node of the surface element mesh to the given point P is the node K , the standard procedure will search for the projection point in one of the elements containing this node, although the correct solution is the element N_{min} which is none of them though it actually contains the projection point of P onto S .

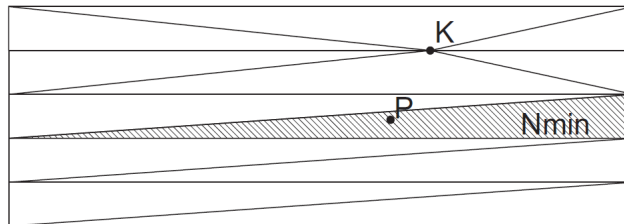


Figure 1. Example discretization of surface.

In order to determine the contact element correctly, an alternative way is proposed. Unlike the standard algorithm, the proposed one consists in finding the closest element for the given point. The procedure is as follows. The point is projected orthogonally onto surfaces of subsequent triangles constituting the finite element mesh of the surface. By solving a 3×3 linear system of equations, the projection distance D and the barycentric coordinates $T_1, T_2, T_3 = 1 - T_1 - T_2$ of the projection point are computed. If $T_1 \geq 0 \wedge T_2 \geq 0 \wedge T_3 \geq 0$ then the projection belongs to this element and the distance between the point and the element is D (figure 2a). Otherwise, the point is projected onto the triangle edges, and, depending on the results, D is assigned the value of distance from the point to one of the edges or vertices of the triangle (figure 2b). Repeating this procedure for all the surface elements and saving the one with the lowest value of D_{min} , the algorithm comes up with the correct contact element (or possibly a set of elements if the projection point is located on an edge or vertex).

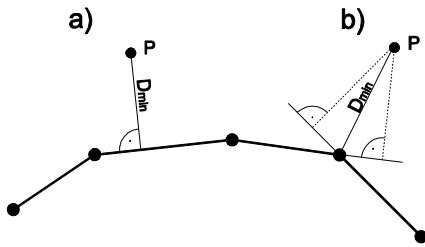


Figure 2. The orthogonal projection.

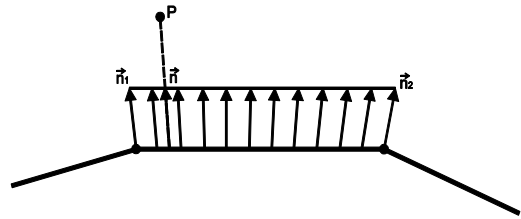


Figure 3. The interpolated projection

The next stage, similarly as in the standard algorithm, is to perform the so-called “interpolated projection”, i.e. the projection of a point onto a triangle along an “interpolated normal” vector. This interpolated vector is obtained on the basis of averaged normal vectors computed in each node of the considered element, being the normalized arithmetic average of normal vectors in elements sharing the considered vertex. The idea of interpolated projection is shown in figure 3. The purpose of this action is smoothing the results of the projection procedure as a function of location of the considered point. The interpolated projection of point is done onto the closest contact element (or a number of neighboring elements) indicated in the previous stage of the algorithm.

3. Numerical cost of the algorithm

The numerical cost is defined as the total number of dominating operations that must be performed to obtain the result of analysis. Here, these are operations of multiplication and division, as their execution time is much longer than that of addition and subtraction [3]. Having estimated numerical cost for both the proposed and the standard algorithm, we have found that (1) in both the cases the numerical cost of algorithm is a linear function of the number of rigid surface elements and (2) the numerical cost of the proposed algorithm is significantly higher than that of the standard algorithm. On the other hand, however, the proposed algorithm appears in many cases the only reliable.

4. References

- [1] Benson D.J., Hallquist J.O., A single surface contact algorithm for the post-buckling analysis of shell structures. *Computer Methods in Applied Mechanics and Engineering*, 78:141-163 (1990).
- [2] Peter Wriggers, *Computational Contact Mechanics*, John Wiley & Sons Ltd (2002).
- [3] David Kincaid, Ward Cheney; *Analiza numeryczna*, Wydawnictwa Naukowo-Techniczne Warszawa, 168-169.

GRADIENT-ENHANCED DAMAGE MODEL FOR LARGE DEFORMATIONS OF ELASTIC-PLASTIC MATERIALS

B. Wcisto and J. Pamin

Cracow University of Technology, Poland

1. Introduction

The paper describes the formulation of a hyperelastic-plastic model coupled with gradient damage for materials subjected to large strains. The work addresses also aspects of its finite element implementation within AceGen/AceFEM environment. The analyzed theory and algorithm are appropriate for simulations of composite and metallic materials failure.

2. Material description

The kinematical framework of the presented model is based on a multiplicative decomposition of the deformation gradient \mathbf{F} in the form: $\mathbf{F} = \mathbf{F}^e \mathbf{F}^p$. Free energy function is assumed to be an isotropic function of the elastic left Cauchy-Green tensor $\mathbf{b}^e = \mathbf{F}^e \mathbf{F}^{eT}$, scalar measure quantifying the amount of plastic flow γ and scalar damage parameter ω :

$$(1) \quad \psi = (1 - \omega)\psi^e(\mathbf{b}^e) + \psi^p(\gamma)$$

The parameter ω grows from zero for the intact material to one for a complete material destruction and is computed from the damage growth function $\omega = f^d(\kappa)$, where $\kappa = \max(\bar{\epsilon}, \kappa_0)$, $\bar{\epsilon}$ is an equivalent strain or energy measure and κ_0 is the threshold.

Elastic constitutive relations between Kirchhoff stress tensor $\boldsymbol{\tau}$ and left Cauchy-Green tensor \mathbf{b}^e are described through an elastic strain potential ψ^e :

$$(2) \quad \boldsymbol{\tau} = 2 \frac{\partial \psi^e}{\partial \mathbf{b}^e} \mathbf{b}^e$$

The yield criterion F_p is an isotropic function of the effective Kirchhoff stress tensor $\hat{\boldsymbol{\tau}} = \boldsymbol{\tau}/(1 - \omega)$ and plastic strain measure γ :

$$(3) \quad F_p(\boldsymbol{\tau}, \gamma) = \hat{\tau}(\hat{\boldsymbol{\tau}}) - q(\gamma) \leq 0$$

Function q represents the yield strength with isotropic hardening. Associative flow rule is assumed.

Whether damage grows is decided on the basis of a nonlocal loading function:

$$(4) \quad F_d(\bar{\epsilon}, \kappa) = \bar{\epsilon} - \kappa \leq 0$$

where $\bar{\epsilon}$ is nonlocal equivalent strain or energy measure and κ is the damage history parameter. For $F_d < 0$ there is no growth of damage.

The nonlocal averaging is performed through the solution of an additional second order partial differential equation as first proposed in quasi-brittle damage mechanics [1]:

$$(5) \quad \bar{\epsilon} - l^2 \nabla^2 \bar{\epsilon} = \tilde{\epsilon}$$

l is a material dependent length parameter commonly called the internal or intrinsic length scale. The Laplacian and the parameter l can be referred to either the deformed or the undeformed configuration [2].

The gradient enhancement applied to the considered model preserves it from pathological sensitivity to the finite element discretization (Figure 1).

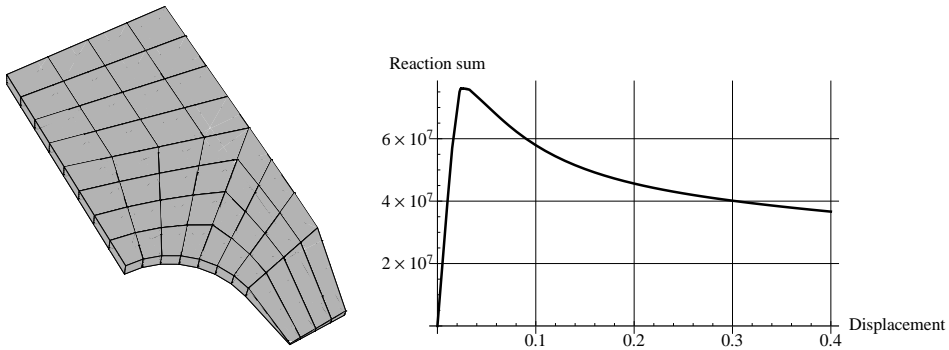


Figure 1. Deformed mesh and relations between displacement and sum of reactions for perforated plate in tension for damage-elastic material model

3. Implementation

The focus of this paper is the three-dimensional numerical simulation based on the presented model. The simulation is performed with the Mathematica-based package AceGen [3]. The programme is a novel code generator that consists of the symbolic and the automatic capabilities of Mathematica, automatic differentiation technique and simultaneous optimization of expressions. FEM implementation within AceGen consists of symbolic description of a residual vector and tangent matrix for one element and automatic generation of a code for a chosen FE environment (e.g. AceFEM, FEAP, ANSYS). Due to this approach the cumbersome derivation of the consistent tangent for the Newton-Raphson method is avoided.

Numerical verification tests of the described model are performed with the Mathematica-based package AceFEM. Particularly, uniaxial tension test (c.f. Figure 2) and perforated plate in tension (c.f. Figure 1) are examined.

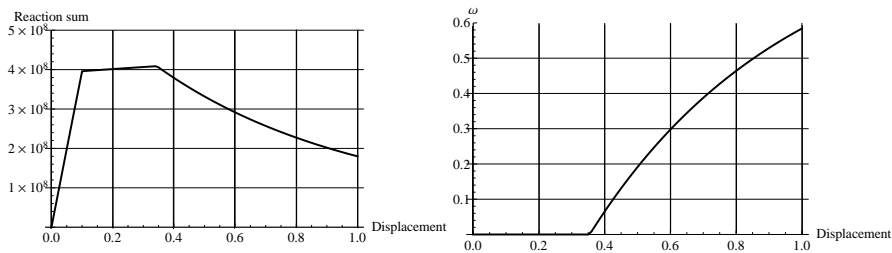


Figure 2. Uniaxial tension test for elastic-plastic model coupled with damage: displacement vs reaction sum and damage growth

4. References

- [1] R.H.J. Peerlings, R. de Borst, W.A.M. Brekelmans and J.H.P. de Vree (1996). Gradient-enhanced damage for quasi-brittle materials, *Int. J. Numer. Methods Engrg.*, **39**, 3391-3403.
- [2] P. Steinmann (1999). Formulation and computation of the geometrically non-linear gradient damage, *Int. J. Numer. Methods Engrg.*, **46**, 757-779.
- [3] J. Korelc (2009). Automation of primal and sensitivity analysis of transient coupled problems, *Computational Mechanics*, **44**, 631-649.

**Continuum Mechanics, Elasticity and Plasticity
(Special Session in Memory of Jan Rychlewski)**

SPECIFICATION OF INTERATOMIC POTENTIALS BY SYMMETRY

Kinga Nalepka

Department of Strength and Fatigue of Materials and Structures, Faculty of Mechanical Engineering and Robotics, AGH University of Science and Technology, Al. Mickiewicza 30, 30-059 Cracow, Poland

1. Object of the paper

A new method of the parametrization of models describing interatomic interactions in metal crystals has been developed. The proposed approach enables us to obtain parametrization conditions which have a coherent physical interpretation and additionally, they are simpler and more efficient than those applied classically. The reason is the double use of symmetry: at the continuum level and the atomistic one.

2. Motivation

At present, there are created more and more complex materials both with structural and functional applications: metal-ceramic composites as well as micro- and spin-electronic devices can be representative examples. Advanced microscope techniques enable a detailed characterization of the microstructures of these materials. Information obtained in this way constitutes the basis for building models at the atomistic level. The models allow us to describe and understand a number of processes in the materials such as the nucleation and propagation of cracks or dislocation evolution. Additionally, the atomistic models enable identification of key properties necessary for building reliable models at the continuum level.

Interatomic interaction in metals are described mostly by means of potentials whose form is defined by the Embedded Atom Method (EAM) [1]. According to the EAM approach, the energy of the metal crystal per atom E^{at} consists of the energy of pair interactions between a central atom and its neighbors Φ and the embedding energy F of the central atom in an electron density ρ coming from neighboring atoms:

$$(1) \quad E^{at} = \frac{1}{2} \sum_{m=1}^K \phi(r_m) + F(\rho)$$

where $\frac{1}{2}\phi(r_m)$ is the contribution to Φ from an atom m th while ρ is a sum of densities f introduced by successive neighbors:

$$(2) \quad \rho = \sum_{m=1}^K f(r_m).$$

In the above equations, r_m is the distance between the central atom and its m th neighbor.

The EAM functions ϕ and f contain parameters which enable the application of a given model to various metals. In literature, the parameters are specified at the assumption that the considered model correctly predicts the crystal properties at the equilibrium state, that is, that the lattice constants, the cohesive energy and the elastic constants are equal to the experimental values. The relationships obtained in this way constitute the key parametrization conditions used classically [1]. These conditions have not a coherent physical interpretation, are not unique and take complex forms. As a result, the parametrization is not efficient.

3. Solution

According to the newly formulated conditions [2], the considered EAM model should correctly reproduce elementary strain processes resulting from the spectral decomposition of the elasticity tensor [3]. The fulfillment of these conditions means that an arbitrary process of small strains will be proceed in accordance with the experiment. The elementary processes are determined by the crystal symmetry. Therefore, the obtained parametrization conditions can be further simplified, this time, by the application of the orthogonal relationships in the point group of the considered crystal. Thanks to the double use of symmetry, at the continuum level and the atomistic one, the finally formulated relationships enable more efficient parametrization than the classically used ones.

The developed approach to the parametrization of the EAM-type models is applied to cubic metals. According to the obtained conditions, the crystal energy per atom E^{at} as well as the Kelvin moduli λ_i , $i = I, II, III$ predicted by the potential should be consistent with the experimental data. Additionally, the pressure p in the system should be equal to zero:

$$(3) \quad E^{at}(\varepsilon = 0) = E_{coh}^{exp}$$

$$(4) \quad p = -\frac{1}{3} \sum_{s=1}^S l_s R_s \left(\frac{1}{2} \phi_s' + F' f_s' \right) = 0$$

$$(5) \quad \lambda_I = \frac{1}{3\Omega_{at}} \left[\frac{1}{2} \sum_{s=1}^S l_s \phi_s^{norm} + F' \sum_{s=1}^S l_s f_s^{norm} + F'' \left(\sum_{s=1}^S l_s R_s f_s' \right)^2 \right] = \lambda_I^{exp}$$

$$(6) \quad \lambda_{II} = \frac{1}{3\Omega_{at}} \left[\frac{1}{2} \sum_{s=1}^S l_s (1 - 3b_s) \phi_s^{norm} + F' \sum_{s=1}^S l_s (1 - 3b_s) f_s^{norm} \right] = \lambda_{II}^{exp}$$

$$(7) \quad \lambda_{III} = \frac{2}{3\Omega_{at}} \left[\frac{1}{2} \sum_{s=1}^S l_s b_s \phi_s^{norm} + F' \sum_{s=1}^S l_s b_s f_s^{norm} \right] = \lambda_{III}^{exp}$$

In the formulated conditions, ϕ_s^{norm} and f_s^{norm} are the normalized contribution to the shear moduli coming from the pair interaction and from the electron densities, respectively. These contributions as well as the structural parameters R_s , l_s and b_s are determined in [2]. The proposed conditions are used for the parametrization of the Rosato-Guillopo-Legrand potential applied to copper. The obtained model not only better describes the equilibrium state but also the defect formation. To illustrate the performance of the formulated model, the shearing process in the plane (1 1 1) is examined. The simulations are carried out with the use of the buffer layers introduced in [4]

Acknowledgments

The research was done within the framework of the Project N501 156638 founded by the Polish Ministry of Science and Higher Education.

4. References

- [1] M.S. Daw and M.I. Baskes (1984). Embedded-atom-method function for the fcc metals: Cu, Ag, Au, Ni, Pd, Pt, *Phys. Rev. B*, **29**, 6443-6453
- [2] K. Nalepka (2012). Symmetry-based approach to parametrization of Embedded-Atom-Method interatomic potential, *Comp. Mater. Sci.*, **56**, 100-107
- [3] J. Rychlewski (1984). *J. Applied Mathematics and Mechanics* **48**, 303-314;
- [4] K. Nalepka (2012). Efficient approach to metal/metal oxide interfaces within variable charge model, *Eur. Phys. J. B*, **85**, 45

ON A BACKWARD IN TIME THERMO-MICROSTRETCH PROBLEM

E. Bulgariu

Al. I. Cuza University of Iași, Department of Mathematics, Blvd. Carol I, no. 11, 700506, Iași, Romania and

The University of Agricultural Sciences and Veterinary Medicine, Aleea M. Sadoveanu, no. 3, 700490, Iași, Romania

1. Introduction

In this article we consider the boundary-final value problem for the linear theory of thermo-microstretch elastic solids introduced by Eringen [1]. It is well known that this type of problem is ill-posed, but imposing some mild conditions, we will prove some uniqueness and the continuous dependence results. The data are given for the final time $t = 0$ and we want to study the solution at the previous moments. By an appropriate change of variable, we transform this problem into a boundary-initial value problem. Using the Lagrange-Brun identities, we deduce some preliminary results that combined with a method based on Gronwall's inequality will be the principal ingredients in obtaining the uniqueness and the continuous dependence results. This paper continues the study started by Bulgariu [2].

A study of uniqueness and continuous dependence upon mild requirements concerning the thermoelastic coefficients for the solution of the boundary-value problems associated with the linear theory of thermoelasticity have been made by Ciarletta [3].

Passarella and Tibullo [4] have demonstrated the uniqueness of solutions for the backward in time problem of the linear theory of thermo-microstretch elastic materials and the impossibility of the localization in time of the solution of the corresponding forward in time problem. Our results concerning the uniqueness of solution extend in a particular case the uniqueness theorem of Passarella and Tibullo [4] and we also discuss a different class of problems than the one considered by them. Some estimates that prove the continuous dependence of solution with respect to the final data are obtained.

2. The boundary-final value problem and the transformed problem

The fundamental system of field equations for the the boundary-final value problem is the one considered by Bulgariu [1] on the time interval $(-T, 0]$, $T > 0$ and T may be infinite. Using the change of variables: $t \rightsquigarrow -t$, we transform the considered boundary-final value problem (\mathcal{P}) into a boundary-initial value problem ($\overline{\mathcal{P}}$) on the time interval $[0, T)$. We observe that only the energy equation has a different form in the two considered problems because only in this equation occurs the first order derivative with respect to time.

3. Uniqueness results

We consider the hypotheses:

- (H_1) the relation symmetry relations for the constitutive coefficients considered holds true and the conductivity tensor k_{ij} and microinertia I_{ij} tensor are positive definite tensors;
- (H_2) the internal energy density W per unit of volume is a positive semidefinite quadratic form;
- (H_3) the specific heat is nonpositive, that is $a(\mathbf{x}) \leq a_0 < 0$, where a_0 is a constant.

Theorem 1. Assume that (H_1) and (H_2) hold true. Then the boundary-initial value problem $(\overline{\mathcal{P}})$ has at most one solution.

Theorem 2. Assume that (H_1) and (H_3) hold true. Then the boundary-initial value problem $(\overline{\mathcal{P}})$ has at most one solution.

Remark 1. If we assume that (H_1) , (H_2) and (H_3) hold true, we obtain the uniqueness of the solution of the boundary-initial value problem $(\overline{\mathcal{P}})$ in $\Omega \times [0, T)$, without any procedure of extension.

4. Continuous dependence with respect to the final data

Theorem 3. If $\varpi = [u_i, \varphi_i, \psi, e_{ij}, \kappa_{ij}, \gamma_i, t_{ij}, m_{ij}, \pi_i, \sigma, \theta, \theta_{,i}, q_i]$ is a solution of the boundary-initial value problem $(\overline{\mathcal{P}})$ corresponding to the external given data $\mathcal{D}_0 = [0, 0, 0, 0, u_i^0, \dot{u}_i^0, \varphi_i^0, \dot{\varphi}_i^0, \psi^0, \dot{\psi}^0, \theta^0, 0, 0, 0, 0, 0, 0]$, assuming that the hypotheses (H_1) , (H_2) and (H_3) hold true, we have the estimate

$$(1) \quad \mathcal{E}(t) + \int_0^t \int_{\Omega} \frac{1}{T_0} k_{ij} \theta_{,i}(s) \theta_{,j}(s) dv ds \leq \mathcal{E}(0) \exp(Mt), \quad \forall t \in [0, T)$$

where $M > 0$ is a constant which depends on some constants defined in the previous sections and

$$(2) \quad \mathcal{E}(t) = \int_{\Omega} \left[\rho \dot{u}_i(t) \dot{u}_i(t) + I_{ij} \dot{\varphi}_i(t) \dot{\varphi}_j(t) + 3J \dot{\psi}^2(t) + 2W(t) - a\theta^2(t) \right] dv.$$

5. References

- [1] A.C. Eringen (1990). *Theory of thermo-microstretch elastic solids*, Int. J. Eng. Sci., **28**, 1291–1301.
- [2] E. Bulgariu (2012). *On the uniqueness and continuous dependence in the linear theory of thermo-microstretch elasticity backward in time*, An. Ştiinţ. Univ. Al. I. Cuza Iaşi, S.N. Matematică: accepted.
- [3] M. Ciarletta (2002). *On the uniqueness and continuous dependence of solutions in dynamical thermoelasticity backward in time*, J. Thermal Stresses **25**, 969–984.
- [4] F. Passarella and V. Tibullo (2010). *Some Results in Linear Theory of Thermoelasticity Backward in Time for Microstretch Materials*, J. Therm. Stresses, **33**: 6 , 559-576.

MODELLING OF THERMO-VISCOPLASTIC COUPLING IN AISI L6 STEEL

H. Egner and W. Egner

Institute of Applied Mechanics, Cracow University of Technology, Cracow, Poland

1. Introduction

In the present analysis the 2 mechanisms – 1 yield criterion (2M1C) model identified in [1] to describe the elasto-viscoplastic behaviour of AISI L6 steel at different (but constant) temperatures, is extended to account for the effect of temperature change (nonisothermal conditions).

2. Equations of thermo-elastic-viscoplastic material

The model is based on the assumption of small strains. Total strain is partitioned into an elastic, inelastic and thermal components, $\varepsilon_{ij} = \varepsilon_{ij}^E + \varepsilon_{ij}^I + \varepsilon_{ij}^\theta$, while the inelastic strain in 2M1C model can be partitioned itself in two different strain mechanisms, $\varepsilon_{ij}^I = A_1(\theta)\varepsilon_{ij}^{(1)} + A_2(\theta)\varepsilon_{ij}^{(2)}$. The complete set of state variables for the thermo-elastic-viscoplastic material consists of elastic strain ε_{ij}^E and absolute temperature θ ; internal variables: kinematic and isotropic plastic hardening variables $\alpha_{ij}^{(1)}$, $\alpha_{ij}^{(2)}$ and $r^{(1)}$, $r^{(2)}$, respectively.

The state equations result from the assumed form of the state potential, which is here the Helmholtz free energy, decomposed into thermo-elastic ($\rho\psi^{te}$) and thermo-plastic ($\rho\psi^{tp}$) terms, after [1]:

$$\sigma_{ij} = \rho \frac{\partial \psi^{te}}{\partial \varepsilon_{ij}^E} = E_{ijkl}(\theta)(\varepsilon_{kl} - \varepsilon_{kl}^I) - \beta_{ij}(\theta)(\theta - \theta_0), \quad \beta_{ij}(\theta) = E_{ijkl}(\theta)\alpha_{kl}^\theta(\theta)$$

$$X_{ij}^{(1)} = \rho \frac{\partial \psi^{tp}}{\partial \alpha_{ij}^{(1)}} = \frac{2}{3}(C_{11}(\theta)\alpha_{ij}^{(1)} + C_{12}(\theta)\alpha_{ij}^{(2)}), \quad X_{ij}^{(2)} = \rho \frac{\partial \psi^{tp}}{\partial \alpha_{ij}^{(2)}} = \frac{2}{3}(C_{22}(\theta)\alpha_{ij}^{(2)} + C_{12}(\theta)\alpha_{ij}^{(1)})$$

$$R^{(1)} = \rho \frac{\partial \psi^{tp}}{\partial r^{(1)}} = b_1(\theta)Q_1(\theta)r^{(1)}, \quad R^{(2)} = \rho \frac{\partial \psi^{tp}}{\partial r^{(2)}} = b_2(\theta)Q_2(\theta)r^{(2)}$$

In the above expressions $\alpha_{ij}^\theta(\theta)$ is the thermal expansion tensor, $C_{11}(\theta)$, $C_{22}(\theta)$, $C_{12}(\theta)$, $Q^{(1)}(\theta)$, $Q^{(2)}(\theta)$, $b_1(\theta)$, $b_2(\theta)$ are material parameters, which are temperature dependent (cf [1]).

Potential of dissipation is assumed (after [1]) not equal to plastic yield surface (non-associated thermo-viscoplasticity), which allows to obtain non-linear plastic hardening rules, which give more realistic description of the material response.

The rates of state variables are obtained by the use of the classical normality rule, while the evolution equations for thermodynamic conjugate forces are derived taking the time rate of state equations, see Table 1.

By taking into account the temperature dependence of material characteristics the additional terms appear in the above evolution equations, which may play a significant role when solving high temperature problems, such as fire conditions or thermal shock problems.

In the case of thermo-elastic-viscoplastic material, the general coupled heat equation takes the following form:

$$\rho c_\varepsilon^\theta \dot{\theta} = -q_{i,i} + r - \theta P_{ij} (\dot{\varepsilon}_{ij} - \dot{\varepsilon}_{ij}^I) + \sigma_{ij} \dot{\varepsilon}_{ij}^I - (R^{(1)} - \theta \frac{\partial R^{(1)}}{\partial \theta}) \dot{r}^{(1)} - (X_{ij}^{(1)} - \theta \frac{\partial X_{ij}^{(1)}}{\partial \theta}) \dot{\alpha}_{ij}^{(1)} +$$

$$- (R^{(2)} - \theta \frac{\partial R^{(2)}}{\partial \theta}) \dot{r}^{(2)} - (X_{ij}^{(2)} - \theta \frac{\partial X_{ij}^{(2)}}{\partial \theta}) \dot{\alpha}_{ij}^{(2)}$$

which is nonlinear and fully coupled to mechanical problem. Heat flux is given by the Fourier’s law: $q_i = -k_{ij} \theta_{,j}$.

A more general case of thermo-plastic-damage coupling is described in [2].

	No coupling	Coupling with temperature
$\dot{\sigma}_{ij} =$	$E_{ijkl} \dot{\varepsilon}_{kl}^E$	$-[\frac{\partial E_{ijkl}}{\partial \theta} (\varepsilon_{kl} - \varepsilon_{kl}^I) + \frac{\partial \beta_{ij}}{\partial \theta} (\theta - \theta_0) + \beta_{ij}] \dot{\theta}$
$\dot{X}_{kl}^{(i)} =$	$\frac{2}{3} (C_{ii} \dot{\alpha}_{kl}^{(i)} + C_{ij} \dot{\alpha}_{kl}^{(j)})$	$+\frac{2}{3} (\frac{\partial C_{ii}}{\partial \theta} \alpha_{kl}^{(i)} + \frac{\partial C_{ij}}{\partial \theta} \alpha_{kl}^{(j)}) \dot{\theta}; i, j = 1,2; i \neq j, \text{ no sum}$
$\dot{R}^{(i)} =$	$b_i (Q_i \dot{r}^{(i)} + \dot{Q}_i r^{(i)})$	$+(\frac{\partial b_i}{\partial \theta} Q_i + b_i \frac{\partial Q_i}{\partial \theta}) r^{(i)} \dot{\theta}; i = 1,2, \text{ no sum}$

Table 1. Kinetic equations for thermodynamic conjugate forces

2. Numerical implementation

The mathematic model is implemented into ABAQUS UMAT procedure and numerical simulations are performed to investigate the influence of thermo-viscoplastic coupling on the material response. The fully implicit backward Euler scheme is chosen, which is always stable and very accurate. Adopting the Newton-Raphson method, the iterative solution procedure is defined as $\Delta \mathbf{S}^{(k+1)} = \Delta \mathbf{S}^{(k)} - [\mathbf{J}^{(k)}]^{-1} \mathbf{R}^{(k)}$, where $\Delta \mathbf{S}$ is the vector containing the increments of the unknowns, $[\mathbf{J}] = \frac{\partial \mathbf{R}}{\partial \Delta \mathbf{S}}$ is the Jacobian matrix and \mathbf{R} is a residual vector, containing the components $\mathbf{R}_{S_i} = \Delta S_i - \Delta \hat{S}_i$, where ΔS_i is a variable while $\Delta \hat{S}_i$ denotes the function resulting from the evolution rule for i-th variable S_i . The iteration procedure is stopped when the norm of \mathbf{R} is sufficiently small. The state variables \mathbf{S}_{n+1}^k in the current k-th iteration are expressed at the end of the step as the values at the beginning of the step \mathbf{S}_n corrected by the current iterate increments $\Delta \mathbf{S}^k$: $\mathbf{S}_{n+1}^k = \mathbf{S}_n + \Delta \mathbf{S}^k$.

Acknowledgements

The financial support under grant number 2285/B/T02/2011/40 from the Polish Ministry of Science and Higher Education is gratefully acknowledged.

3. References

- [1] Velay V., Bernhart G., Penazzi L.: Cyclic behavior modeling of a tempered martensitic hot work tool steel, *International Journal of Plasticity*, **22**, 459-496, 2006.
- [2] Egner H.: On the full coupling between thermo-plasticity and thermo-damage in thermodynamic modeling of dissipative materials. *International Journal of Solids and Structures*, **49**, 279-288, 2010.

CALIBRATION AND VALIDATION OF A CONSTITUTIVE MODEL FOR SINGLE CRYSTAL NICKEL BASED SUPERALLOYS

F. Fournier Dît Chabert¹, A. Gaubert¹, A. Longuet² and S. Quilici³

¹ ONERA, The French Aerospace Lab, Paris, France

² SNECMA Villaroche, Moissy-Cramayel, France

³ Centre des Matériaux, Ecole des Mines de Paris, Evry, France

1. Introduction

Life time prediction of turbine blades is of great interest for engine manufacturers in order to enhance the engine performances or to optimize the overhaul intervals. To perform accurate life time predictions, the first step of the approach is to develop a model able to simulate properly the mechanical behaviour of the representative volume element. In particular, the choice of the constitutive equations and the calibration of the parameters of the model are really essential.

The originality of this work lies on the richness of the experimental database available which brings out the high capability of the proposed model to reproduce a very large set of experimental data in both isothermal or anisothermal conditions and, thus, to show the sturdiness of the model to be included into a life time prediction approach.

2. Constitutive equations for single crystal plasticity

As a single crystal nickel based superalloy, AM1 exhibits quite strong elastic and viscoplastic anisotropy which must be taken into account in the modelling. A crystal plasticity approach has been chosen. Plastic flow $\underline{\dot{\epsilon}}_p$ is the result of glide processes according to a certain number of slip systems “s”. Such an approach has already been widely described by Méric and Cailletaud [1]. However, in that study some improvements have been added to the initial crystallographic model. The viscoplastic flow rule, linking the resolved shear stress τ^s to the increment of plastic slip $\dot{\gamma}^s$ on a given slip system “s”, is using a sinus hyperbolic form to take into account the saturation of viscosity experimentally observed at high strain rates (above 10^{-1}s^{-1}):

$$(1) \quad \dot{\gamma}^s = \varepsilon_0^s \sinh \left(\left\langle \frac{|\tau^s - x^s| - r^s}{K^s} \right\rangle^{n^s} \right) \text{sign}(\tau^s - x^s), \quad \dot{x}^s = C^s \dot{\gamma}^s - D^s x^s |\dot{\gamma}^s| - \left(\frac{|x^s|}{M^s} \right)^{m^s} \text{sign}(x^s)$$

The threshold r^s is called isotropic hardening variable. The internal stress x^s is associated to the kinematic hardening. The evolution equation for the kinematic hardening contains dynamic and static recovery terms to enable the simulation of relaxation and creep tests.

3. Results

The experimental database consists of hundreds of mechanical tests performed from 20°C up to 1150°C. Many different types of tests, either isothermal or anisothermal, are available: tension, cyclic loading, hysteresis loop, creep, relaxation, thermomechanical tests... Four different crystallographic directions were tested: [001], [111], [011] and [123]. First of all, for some specific crystallographic directions and temperatures, a relevant limited number of isothermal experimental tests is defined to carry out the complete calibration of the model. The way to achieve properly such a calibration will be discussed more in details in the presentation. Then, the entire database is simulated for validation. Some results are shown on Figure 1.

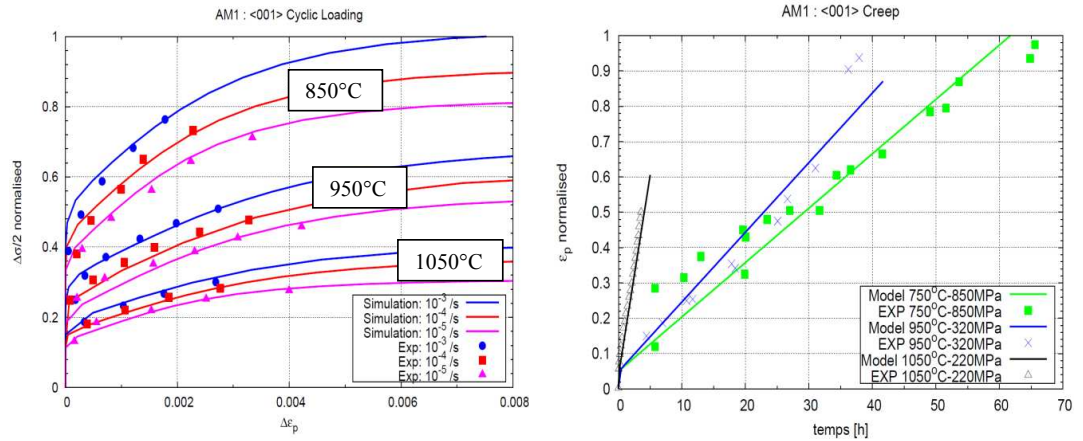


Figure 1. Comparison simulation-experiment for some isothermal experimental tests.

Once the model is fully calibrated, it becomes possible to predict the mechanical behaviour of the representative volume element for more complex anisothermal tests, over the whole temperature range [20°C-1200°C], and, this, whatever the crystallographic direction considered. For instance, the evolution of the 0,2% yield stress with temperature for three strain rates, in the <001> direction, is shown on Figure 2, together with the simulation of a complex thermomechanical test performed between 600°C and 1100°C, along <123> crystallographic direction.

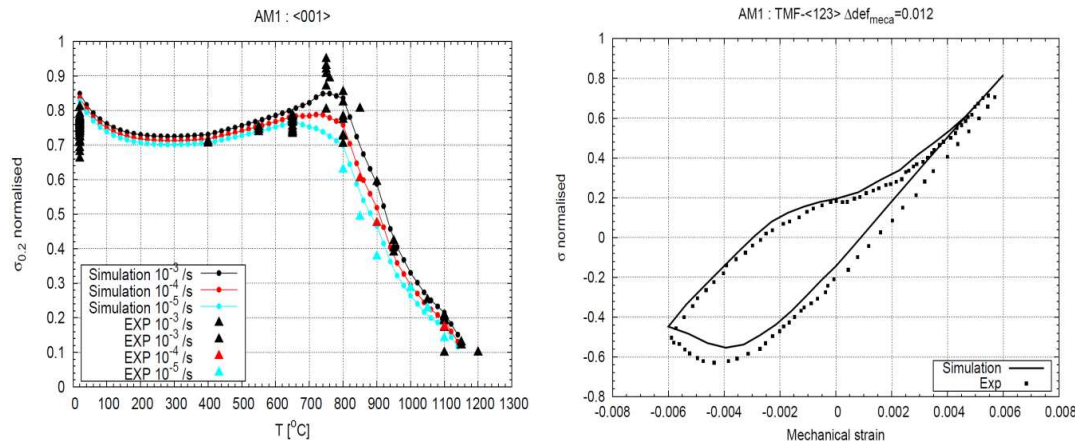


Figure 2. Comparison simulation-experiment for some anisothermal experimental tests.

To conclude, a constitutive model has been proposed, calibrated and validated on a very large database. Many types of experiments are well described and, in particular, complex thermomechanical loadings which are more representative of turbine blade service conditions. The sturdiness of such a model with quite little number of parameters to be calibrated is shown. Finally, it is ready to be included into an industrial life time prediction approach.

4. References

[1] L. Meric, P. Poubanne and G. Cailletaud (1991). Single crystal modeling for structure calculations : Part 1 - Model presentation, *J. of Eng. Mat. and Tech.*, **113**, 162–170.

EXACT ANALYTICAL SOLUTIONS TO PROBLEMS ON EQUILIBRIUM STATE OF ELASTIC ANISOTROPIC HEAVY BODIES WITH CENTRAL AND AXIAL SYMMETRY AND THEIR APPLICATIONS TO GEOMECHANICAL PROBLEMS

A. Fukalov, A. Kutergin and A. Zaitsev

Perm National Research Polytechnic University, Perm, Russian Federation

1. Introduction

The need to solve problems for anisotropic heavy spherical and cylindrical bodies is due to a wide range of applications in various industries, construction, and geology. For instance, the problems of geomechanics of storing and mining (i.e. monolithic mine working supports) and road construction (i.e. tunnel lining) must be solved taking into account central and axial symmetry, uniform and/or nonuniform distribution of external and/or internal pressure. Obtaining of new analytical solutions is important and urgent for development of engineering methods of amended strength analysis, for testing computational algorithms of solving complex problems in which individual elements of designs and constructions are similar in geometry and boundary conditions and for working out methods for the experimental research of heavy bodies with simple geometry.

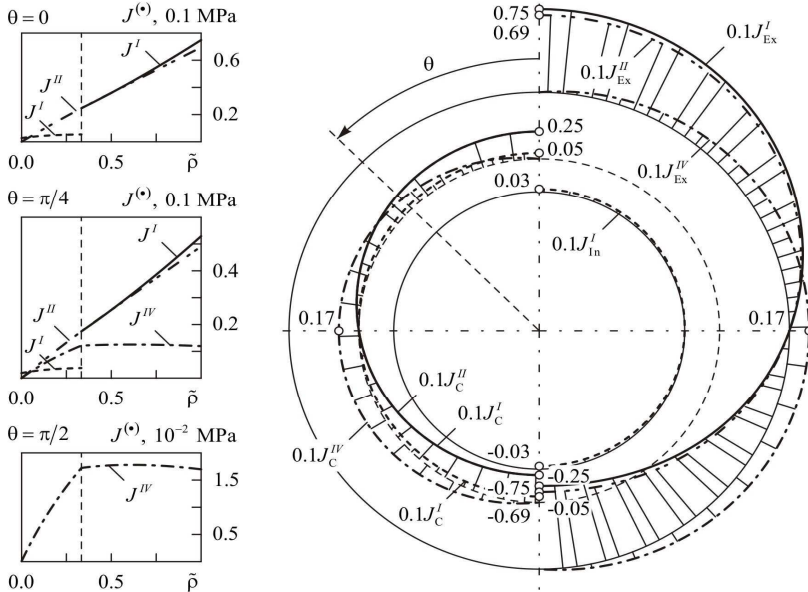


Fig. 1. Distribution of the independent invariant of stress tensor (MPa) on the fixed external ($J_{Ex}^{(\bullet)}$), free from pressures internal ($J_{In}^{(\bullet)}$) and contact ($J_C^{(\bullet)}$) surfaces, with radiuses $\rho_{In} = 2,5$ m,

$$\rho_C = 3,1 \text{ m and } \rho_{Ex} = 4,3 \text{ m; } J^I = \sigma_{\phi\phi} = \sigma_{\theta\theta}, J^{II} = \sigma_{\rho\rho}, J^{IV} = \sqrt{\sigma_{\phi\phi}^2 + \sigma_{\theta\theta}^2}$$

2. Method for solving

New exact analytical solutions to problems on equilibrium state of hollow and combined thick-walled heavy transversally-isotropic spheres [1] and orthotropic cylinders [2], which are fixed on the interior or exterior surfaces and are subject to the action of uniform and/or nonuniform external or internal lateral pressure, are obtained. When integrated heterogeneous system of Lamé differential equations in cylindrical and spherical orthogonal coordinates, the variable separation method led us to reduce the dimension of the problem, and the usage of generalized power series enabled us

to write a general solution. The obtained solutions can set a pattern for exact solutions in particular cases of the relations for displacements, stresses and strains at the points inside hollow and combined heavy isotropic spheres and cylinders with the similar boundary conditions [3, 4].

3. Applications to geomechanical problems

The reinforced concrete monolithic roof supports of spherical mining and the surrounding array of sedimentary rocks are considered as a single mechanical system. The influence of construction geometries and material properties on the distribution of the independent invariants of stress tensor for spherically transversally-isotropic bodies in cross-sections (Fig. 1) is analyzed in the directions of meridian θ and dimensionless radial $\tilde{\rho}$ coordinates. The estimation of an initial strength is carried out on the basis of a multicriteria approach taking into account various fracture mechanisms and areas where the fracture may be initiated and defined.

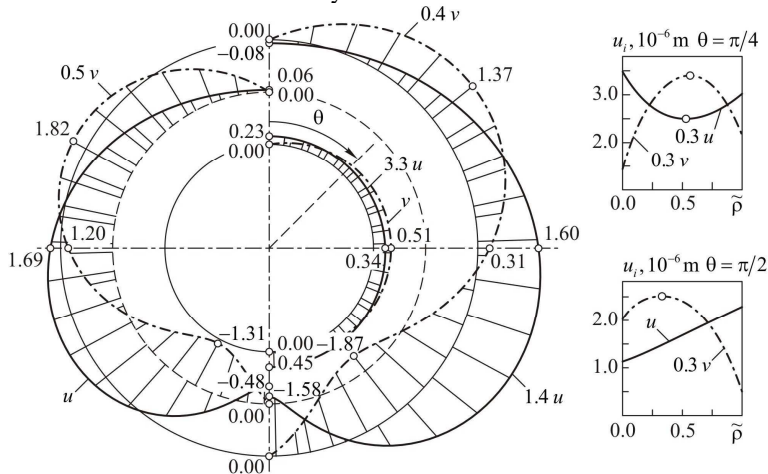


Fig. 2. Distribution of radial ($u, 10^{-6}$ m) and hoop ($v, 10^{-6}$ m) displacement in reinforced concrete cylinder on external, internal and median surfaces, with radiuses $\rho_{In} = 3,0$ m, $\rho_{Ex} = 5,5$ m

The problem on equilibrium state of heavy reinforced concrete cylinder located on foundation soil is considered. Contact surface area was assumed to be known and unchanged. The reaction of soil is given in the form of a quadratic function which meets the condition that its integral sum equals weight of the constructions. The assumption allows us to write the boundary conditions for the determination of the integration constants of partial solution. On the basis of this the distribution of displacements (Fig. 2) and stresses in transversal cross-sections of horizontal monolithic reinforced concrete cylinders are shown, the lower half of which are dug into the soil.

4. References

- [1] Zaitsev A. V. and Fukalov A. A. (2010). Elastic equilibrium state of thick-walled heavy transversally-isotropic spheres fixed on the interior surface, *Samara State Techn. Univ. Mech. Bulletin*, **5(21)**, 85–95. (in Russian)
- [2] Fukalov A. A. and Kutergin A. V. (2011). Exact analytical solutions to problems of the equilibrium state of elastic anisotropic heavy central and axial-symmetric bodies and their applications, *Vestnik of Lobachevsky State Univ. of N. Novgorod*, **4**, Is. **3**, 1831–1833. (in Russian)
- [3] Kozhevnikova L. L., Kuznetsov G. B., Matveenko V. P. and Shardakov I. N. (1974). Analytical investigation of the elastic equilibrium of a hollow sphere rigidly fixed along the outer contour, *Strength of Materials*, **9**, 20–23.
- [4] Kuznetsov G. B. (1979). *Elastic, viscoelastic and long-term strength of cylindrical and spherical bodies*, Nauka, Moscow. (in Russian)

MECHANICAL STATE SIMULATION RESEARCH OF HYDROMECHANICAL FORMING PROCESSES OF NICKEL SUPERALLOYS

M. Hycza-Michalska

Silesian University of Technology, Gliwice, Poland

1. General

The paper introduced the results of research on drawability of nickel superalloys continuation, mainly on formability INCONEL alloys using advanced drawing processes as hydromechanical forming – forming using liquid pressure. The using of INCONEL sheets in cold working processing is a faintly recognized question, because of applying this type technological solutions only at short-waves manufacturing in aircraft industries, for example civil and military aircraft engines casings. Moreover, the consequence of heat-resistance and creep-resistance of nickel superalloys is high susceptibility of these alloys to plastic strength during deformation. The hydromechanical forming of nickel sheet metals is realized only in support from the technologists' practically experience, which is taken on road of trials and errors. Additionally, the short-waves production of airplanes in comparison to long-waves production of cars, it generates the higher costs of designing and manufacturing elements in aircraft industry.

It in support about many years' experience of team of Department of Materials Technology of the Silesian University [1, 2], the use of chosen methods of physic and numeric modelling for improvement of design process and the recognition of production results of nickel superalloys were proposed.

2. Research and simulations results analysis

The results of simulation and computer aided designing of jet engine body panels drawpieces – cone showed in *Fig.1* made of INCONEL 625 sheet metals were contained in this paper. To numerical modelling the environment of the commercial software ETA/Dynaform 5.7 version and its advanced options were applied.

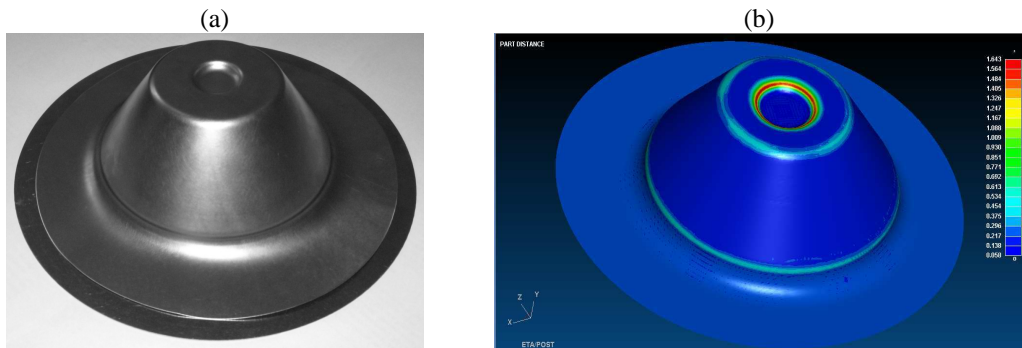


Fig.1. Cone drawpiece made of Inconel 625: (a) charge and industrial drawpiece photography, (b) results of cone hydromechanical forming simulations – comparison between die and processing drawpiece geometry.

In simulating questions of mechanical state of hydromechanical forming process were used the complete data characteristics of INCONEL 625 sheet metals, which were worked out: using

basic and technological tests, pointing out the forming limit diagram and conducting industrial tests. The practical possibilities of using of presented methodology have been presented in the paper.

3. Conclusions

The so far obtained research results reveal that there are potential plasticity properties of nickel super alloys like Inconel 625, which make it possible to produce the cone drawpiece in the process of hydromechanical forming. Simulation using ETA/Dynaform 5.7 software allowed recognizing mechanical state of this forming process. Comparison between industrial tests and simulation results are good corresponding in range of geometry representation. Simulation tests are being carried out at present in order to recommend a modified technology for cones made of Inconel 625 alloy processing.

Acknowledgements

These research works were carried out within the framework of Developmental Investigative Project number N R15 0042 06 financially supported by The National Centre for Research and Development (NCBiR).

References

- [1] M. Hycza-Michalska and F. Grosman (2008). *The research of laser welded blanks characteristic in basic and technological drawability tests*, Metal Forming Conference 2008, *Steel Research International*, **79** special Edition Metal Forming Conf., Vol. 1, 780-787.
- [2] M. Hycza-Michalska (2010). *Drawability of advanced high strength steel and creep-resisting nickel superalloys*, *Steel Research International*, **81**, No. 9, Special Edition 2010 Including computer files, 817÷820.

ON THE PRINCIPLE OF STATIONARY ACTION FOR DISSIPATIVE SOLIDS WITH THERMO-MECHANICAL COUPLINGS

W. Kosiński¹ and P. Perzyna²

¹*Polish-Japanese Institute of Information Technology*

ul. Koszykowa 86, 02-008 Warsaw, Poland

Kazimierz Wielki University of Bydgoszcz

ul. Chodkiewicza 30, 85-064 Bydgoszcz, Poland

²*Institute of Fundamental Technological Research, Warsaw, Poland*

1. Introduction

In the literature one can find always an interest in describing the governing equations of a physical process as a variational principle. The interest comes not only from the purely theoretical view-point but also from the practical one: a variational principle can help to form a general and systematic approximative procedure for establishing the solution from a direct study of the variational integral, and then to use it in formulation numerical methods and calculations. In most cases (e.g. FEM and BVM) of them solutions are searched by minimization techniques in which weak formulation of governing equations appear with arbitrary variations.

2. Stationary action principle

Historically, at the beginning the classical Lagrange and Hamilton's formalisms were formulated for the point mechanics problems. Accordingly, if a dynamical system is described by the vector-valued coordinate \mathbf{q} and the Lagrangian $L = T - V$, where T and V are, respectively, the kinetic and potential energy, then one formulates the principle of stationary action (a variational principle of the dynamical system) by requiring that between all curves $\mathbf{q} = \mathbf{q}(t)$ in a configuration space \mathcal{V} the actual path (i.e. the solution of the system) is that which makes the action integral

$$(1) \quad I = \int_{t_0}^{t_1} L(\mathbf{q}, \dot{\mathbf{q}}, t) dt$$

stationary. Taking the first variation $\delta\mathbf{q}$ subject to the conditions $\delta\mathbf{q}(t_0) = \delta\mathbf{q}(t_1) = 0$ the stationarity of the action requires $\delta I = 0$, which is equivalent to the Euler-Lagrange's equation

$$(2) \quad \frac{d}{dt} \frac{\partial L}{\partial \dot{\mathbf{q}}} - \frac{\partial L}{\partial \mathbf{q}} = 0, \text{ provided the commutative rule } \delta \frac{d}{dt} \mathbf{q} = \frac{d}{dt} \delta \mathbf{q} \text{ holds.}$$

It is well known that the general equations of continuum mechanics and dissipative phenomena employed at the present time cannot be derived from Hamilton's variational principle. The case of bodies described by hyper-elastic material structure is exceptional [2].

For many years it was a known fact that the equations of heat transfer could not be derived from exact variational principle. In 1974-1975 B. Vujanović, from Novi Sad, proposed in [3, 4] that in the case of the *irreversibility* in time when the energy of the system is not conserved, to describe the irreversible phenomena by a Hamilton's stationary principle one faces with neglecting the commutative rule between the operation of variation and time differentiation.

3. Dissipative bodies with thermomechanical coupling

Recently the present authors with a coworker [1, 5] while basing on the Vujanović's observation, proposed new method for deriving the class of equations appearing in some physical irreversible processes based on the variational principle which has a Hamiltonian structure. The crucial assumption of the proposed method is in *non-commutative rule* between operations of taking variations of the field and their partial time and/or spatial derivatives.

In the paper [1] the principle of stationary action was applied to long-line (telegraph) equation and to two models of heat conduction: parabolic and hyperbolic ones. In the recent paper [5] consequences of the principle of stationary action formulated for a dissipative body modelled with the help the material structure with internal state variables was considered. Then the density of the Lagrangian of the body was proposed in which additionally to the terms responsible for the potential and kinetic energies a dissipation term has appeared. Possible variations of fields of dependent state variables: namely the motion function and a vector of internal state variables (ISV), were introduced together with a non-commutative rule between operations of taking variations of the ISV - field and their partial time derivatives. Assuming vanishing first variation of the functional the balance of linear momentum in differential form is received together with evolution equations for internal state variables and stress boundary condition.

In the present paper we will generalize the recent derivations to the case of thermo-mechanical coupling. We consider two cases: hyperbolic and parabolic model of heat conduction. In the first case additional to the absolute temperature a thermal state variable appears, responsible for the history of the temperature dependence. This dependence has been already broadly discussed by the first author and his coworkers in a number of publications [6, 7, 8]. In that model the heat conduction vector is proportional to the gradient of this new thermal variable. The parabolic model discussed in the paper, however, is the classical one in which the heat conduction vector is proportional to the temperature gradient. Then some thermal initial boundary–value problems of technical interest will be analyzed to reduce them to ordinary differential equations whose solutions are often capable of being expressed in analytic closed form.

4. References

- [1] B. Grochowicz and W. Kosiński (2011). Lagrange's method for derivation of long line equations, *Acta Technica*, **56** (3), 331–341.
- [2] Hughes and Marsden J. E., Hughes T. J. R. (1983). *Mathematical Theory of Elasticity*, Prentice-Hall, Englewood Cliffs, New York,
- [3] B. Vujanovic (1974). On one variational principle for irreversible phenomena. *Acta Mechanica*, **19**, 259–275.
- [4] B. Vujanovic (1975). A variational principle for non-conservative dynamical systems. *ZAMM – Zeitschrift für Angewandte Mathematik und Mechanik*, **55**(6), 321–331.
- [5] W. Kosinski and P.Perzyna (2012). On consequences of the principle of stationary action for dissipative bodies, *Arch. Mech.*, **64** (1), 95–106.
- [6] W. Kosiński (1989). Elastic waves in the presence of a new temperature scale. In: *Elastic Wave Propagation* (M.F. McCarthy, M. Hayes, eds.), Elsevier Science (North Holland), New York 1989, pp.629–634.
- [7] V. Cimmelli and W. Kosiński (1991). Nonequilibrium semi-empirical temperature in materials with thermal relaxation. *Arch. Mech.*, **43** , 753–767.
- [8] W. Kosiński and K. Frischmuth (2001). Thermomechanical coupled waves in nonlinear medium, *Wave Motion*, **34** 131–141.

INFLUENCE OF GRAIN SHAPE ON THE OVERALL BEHAVIOUR OF INCOMPRESSIBLE POLYCRYSTALS

K. Kowalczyk-Gajewska

Institute of Fundamental Technological Research, Warsaw, Poland

1. General

The self-consistent estimates [1] of linear overall properties of polycrystals are considered. A method employing the invariant decompositions of Hooke's tensors [3, 4] developed in [2] is applied. The analysis is extended to take into account a non-spherical shape of grains. The attention is focused on crystals with locally constrained deformation. Steady creep of metals with insufficient number of easy slip systems can be indicated as an example falling into the class of problems under consideration.

2. Basic assumptions

One-phase polycrystal is analyzed composed of incompressible anisotropic grains (the local bulk modulus is infinite). All grains have the same ellipsoidal shape with lengths of ellipsoid axes $a = b \neq c$, so that the shape can be described by single parameter $\alpha = a/c$. Moreover ellipsoid axes are co-axial with the anisotropy axes of the local properties and the distribution of grain orientation within the representative volume is random (Fig 1). As a result the overall behaviour of polycrystal is isotropic.

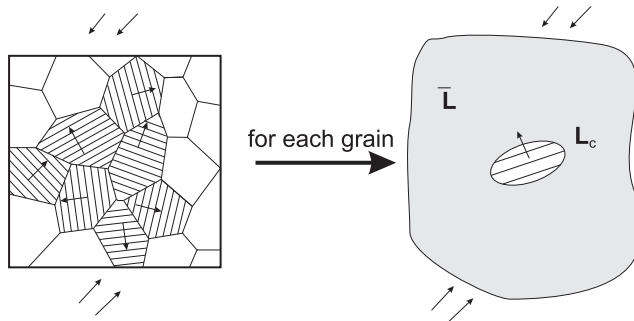


Figure 1. Idea of the self-consistent model of polycrystal.

3. Results

Due to the above assumptions the overall bulk modulus of polycrystal is infinite. The self-consistent estimate of the overall shear modulus \bar{h}_D is obtained from the following fourth order tensorial equation [1]

$$(1) \quad \langle (\bar{\mathbf{L}} - \mathbf{L}_c) \mathbf{A}_c \rangle = \mathbf{0}, \quad \mathbf{A}_c = (\mathbf{I} + \mathbf{P}_c(\mathbf{L}_c - \bar{\mathbf{L}}))^{-1},$$

where $\langle \cdot \rangle$ denotes averaging over the orientation space, $\bar{\mathbf{L}}$ and \mathbf{L}_c are the isotropic overall stiffness and anisotropic local stiffness, respectively, \mathbf{A}_c is the concentration tensor, \mathbf{I} is the symmetrized identity tensor and \mathbf{P}_c is the polarisation tensor. This tensor depends on the overall properties as well as on the ellipsoid shape and orientation. It can be derived with use of the Eshelby tensor for which specific

formulae can be found in [5]. It is important for the performed analysis that the polarisation tensor is a Hooke's tensor. For the considered case it exhibits transverse isotropy and its representation in crystal axes is the same for all grains. It is specified in terms of the shape parameter α and \bar{h}_D .

Using the procedure proposed in [2] it can be demonstrated that for the wide class of local anisotropy the tensorial relation (1)₁ reduces to the single polynomial equation of 5th degree in \bar{h}_D , which has a single positive root. Using this relation one can study the existence of the finite overall flow stress for the steady creep of the considered class of polycrystals composed of grains with an insufficient number of easy slip systems. The results of the analysis are summarized in Fig. 2. The answer to the posed question depends on the number of independent easy slip systems as well as on the relative orientation of these systems and the spheroid axis.

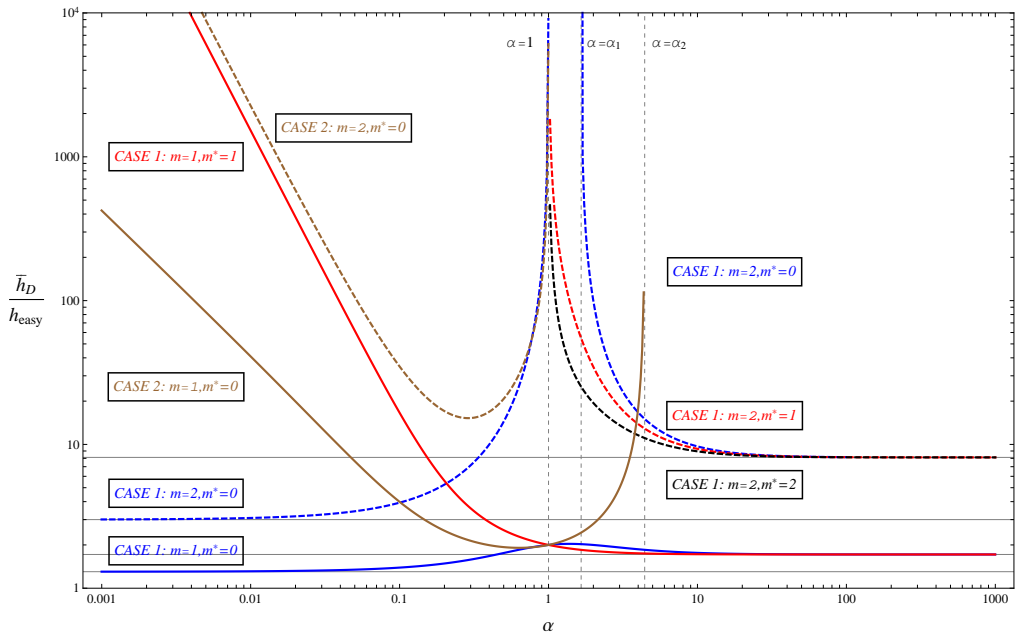


Figure 2. Dependence of an overall shear modulus on the shape parameter for random polycrystals with insufficient number of easy slip systems (m - dimension of space of constraint deformation; m^* , Case 1 and 2 depend on relation between eigen-subspaces of polarisation tensor \mathbf{P}_c and the local anisotropic tensor \mathbf{L}_c - details will be given later).

4. References

- [1] R. Hill (1965). Continuum Micro-Mechanics of Elastoplastic Polycrystals. *J. Mech. Phys. Solids*, **13**, 89–101.
- [2] K. Kowalczyk-Gajewska (2009). Bounds and self-consistent estimates of overall properties for random polycrystals described by linear constitutive laws. *Arch. Mech.*, **61**, 475–503.
- [3] J. Rychlewski (1995). Unconventional approach to linear elasticity. *Arch. Mech.*, **47**, 149–171.
- [4] J. Rychlewski (2000,2001). A qualitative approach to Hooke's tensors. Part I and Part II. *Arch. Mech.*, **52**, 737–759, **53**, 45–63.
- [5] S. Torquato (2002). *Random Heterogeneous Materials*, Springer.

SENSITIVITY ANALYSIS OF MICRO - SCALE MODEL OF TiN / SUBSTRATE IN NANOINDENTATION TEST

A. Milenin¹, M. Kopernik¹ and I. Tsukrov²

¹ AGH University of Science and Technology, Cracow, Poland

² University of New Hampshire, New Hampshire, Poland

1. Introduction

The Polish ventricular assist device (POLVAD_EXT) is made of polymer and is covered with a nanocoating of TiN by laser ablation. The results of experimental nanoindentation test, inverse analysis and a mathematical model of a nanoindentation test developed in the Authors' FE code were applied in [1] to identify the material model of TiN. The sensitivities of the Authors' FE model of nanoindentation test to mechanical properties of the soft (polymer) and hard (steel) substrates, and the nanocoating of TiN deposited on the substrates are examined in the present work.

2. Materials and Methods

The model of nanoindentation test is composed of thick polymer or steel, and a TiN nanocoating (350 nm). The bilinear material models are used for: a) polymer: $\varepsilon_1 = 0.01$, $\sigma_1 = 4.7$ MPa, $\varepsilon_2 = 0.03$ and $\sigma_2 = 10$ MPa, b) steel: $\varepsilon_1 = 0.0015$, $\sigma_1 = 220$ MPa, $\varepsilon_2 = 0.5$ and $\sigma_2 = 650$ MPa and c) TiN: $\varepsilon_1 = 0.009$, $\sigma_1 = 2\ 614$ MPa, $\varepsilon_2 = 0.166$ and $\sigma_2 = 9\ 107$ MPa. For each substrate seven models were developed: model 1 – reference model, and models 2-7 with disturbed parameters of material model of TiN. The disturbed parameters of TiN are: a) σ_1 (models 2 and 3), b) σ_2 (models 4 and 5), and c) ε_1 (models 6 and 7). Each of disturbed parameters was changed by 5% up in the first version of model and down in the second version of model.

3. Results and Discussion

The distributions of an effective strain in loading and unloading phases for the two substrates and TiN are presented in Fig.1 for the model 1. The difference between Figs.1a-1b and Figs.1c-1d is observed in the behavior of the substrate, especially in the unloading phase. The polymer exhibits hyperplastic behavior, while the steel is a typical elastic-plastic material.

The force versus displacement for the two substrates and TiN is shown in Figure 2a for model 1. The difference between substrates is similar to the observation made on the basis of Fig.1. The results of sensitivity analysis are presented in Fig.2b, as values of a normalized maximum force versus version of the material model of TiN deposited on the two substrates. Comparing to the reference model (model 1), the biggest sensitivity of a maximum force is computed with respect to the parameter σ_1 (models 2 and 3). The variation of σ_1 results in variation of an elastic modulus. The small sensitivities considered as values of the normalized force relative to the reference model are observed with respect to the parameters σ_2 (models 4 and 5) and ε_1 (models 6 and 7). It means that the model is not sensitive to the variation of a plastic modulus. The variation of ε_1 also results in the variation of Young' modulus, but the model is not sensitive to such variation. The differences of sensitivities for the two substrates are visible in the models 5 and 7. The variations of σ_2 and ε_1 by 5% down for polymer result in smaller values of the normalized force than it is for steel.

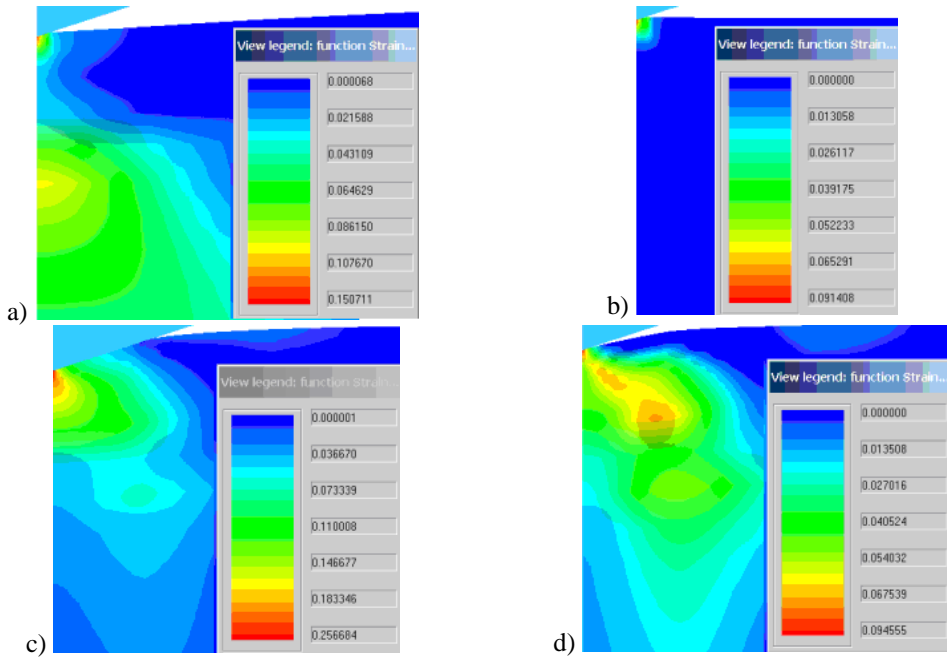


Fig.1. Distributions of an effective strain in the model 1 of TiN / polymer in the phases of: a) loading, b) unloading, and in the model 1 of TiN / steel in the phases of: c) loading, d) unloading.

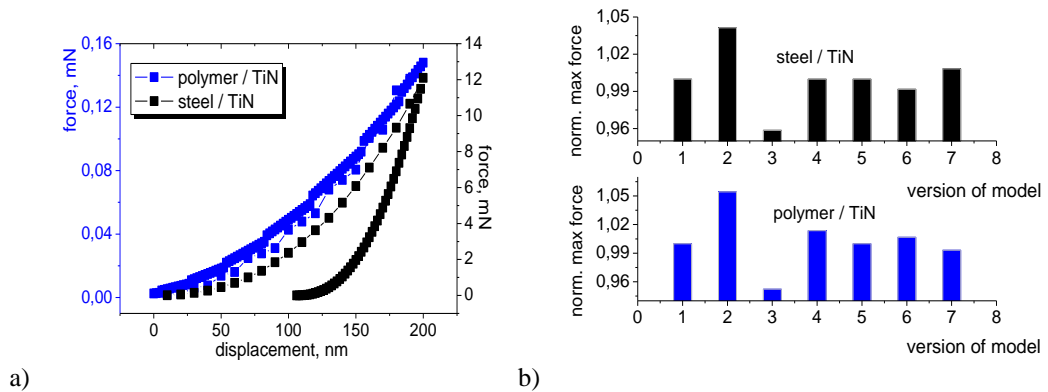


Fig.2. a) The force versus displacement for the model 1: TiN / polymer and TiN / steel, b) The normalized maximum force for the models 1-7: TiN / polymer and TiN / steel.

4. Acknowledgements

Financial assistance of the MNiSzW, project no. 2011/01/D/ST8/04087, is acknowledged.

5. References

[1] M. Kopernik, A. Milenin, R. Major and J.M. Lackner (2011). Identification of material model of TiN using numerical simulation of nanoindentation test, *Mater. Sci. Tech.*, **27**, 604-616.

ANALYSIS OF THE FORMING PROCESSES ACCOUNTING FOR ASYMMETRY OF ELASTIC RANGE

Zdzisław Nowak, Teresa Frąs, Marcin Nowak and Ryszard Pęcherski
Institute of Fundamental Technological Research, Warsaw, Poland

The aim of the paper is to propose a new approach to the material description using the concept of Burzyński paraboloid yield surface with correction for initial anisotropy [1]. The correction takes into account the deviation of the determined experimentally yield surface from classical Huber-Mises yield condition for isotropic material. Finite element method is used for the simulation of sheet metal forming processes including cup drawing and stamping. Proper description of material properties is crucial for accurate analysis. In particular, the initial anisotropy and asymmetry of elastic range of considered materials play an important role in the adequate finite element simulation. For metal forming analysis many experimental tests are needed to obtain the proper description of metal sheets behaviour. There are some attempts to account for the elastic range asymmetry, e.g. [2], [3], [5]. However, according to our opinion, there is still lack of workable description of initial anisotropy, which could allow analysing effectively practical problems.

In the case of plane stress the yield surface is assumed in the following form [1], [4]:

$$(1) \quad f = \sigma_1^2 + \sigma_3^2 - 2\lambda\sigma_1\sigma_3 + (k_c - k_r)(\sigma_1 + \sigma_3) - k_c k_r$$

where k_c , k_r are initial yield stress for compression and tension and λ is the correction coefficient introduced by Burzyński [1]. The return mapping algorithm was applied by numerical scheme formulation of the integration of elasto-plasticity equations. The problem of the cup drawing of the DP600 steel sheet is studied. The comparison with the results obtained from the simulation of similar forming process with application of Hill conditions for anisotropy sheet material was made.

Numerical simulation was performed with application of ABAQUS finite element program. The own UMAT was implemented for calculations.

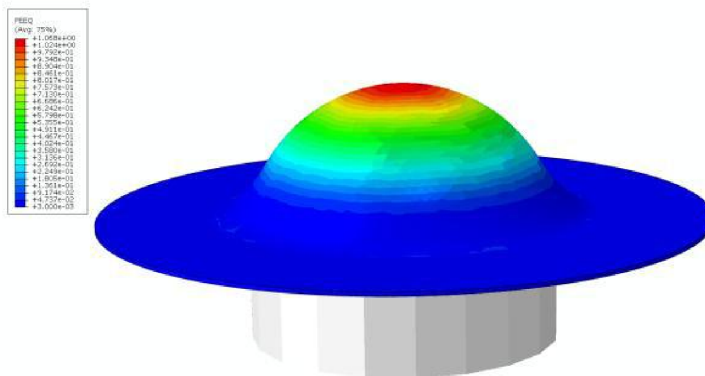


Fig. 1: The geometry and finite element mesh of sheet metal forming processes.



Fig. 2: The experimentally deformed shape of sheet metal

Acknowledgments

The research reported in the paper was partly obtained in the framework of the research project NUMPRESS carried out in IPPT PAN (Poland), co-funded by European Regional Development Fund grant nr: POIG.01.03.01-14-209/09.

References

- [1] W. Burzyński (2009). Study on Material Effort Hypotheses (selected passages form doctoral dissertation "Study on material effort hypotheses" Lwów 1928, 1-192), *Engineering Transactions*, **57** (3-4), 185-215.
- [2] B. Plunkett, O. Cazacu, F. Barlat (2006). Orthotropic yield criteria for description of the anisotropy in tension and compression of sheet metals, *International Journal of Plasticity*, **22**, 1171–1194.
- [3] O. Cazacu, B. Plunkett, F. Barlat (2008). Orthotropic yield criterion for hexagonal closed packed metals, *International Journal of Plasticity*, **24**, 847–866.
- [4] Dietrich L., Grzywna P., Fraś T., Rusinek A., Pęcherski R.B. (2012). Application of the Burzyński's correction in determining the yield condition for the OFHC copper with initial anisotropy, in preparation.
- [5] G. Vadillo, J. Fernandez-Saez, R.B. Pęcherski (2010). Some applications of Burzynski yield condition in metal plasticity, *Materials and Design*, **32**, 628–635.

THE IDENTIFICATION PROCEDURE FOR THE CONSTITUTIVE MODEL OF ELASTO-VISCOPLASTICITY DESCRIBING THE BEHAVIOUR OF NANOCRYSTALLINE TITANIUM

Zdzisław Nowak and Piotr Perzyna

Institute of Fundamental Technological Research, Warsaw, Poland

The main objective of the present paper is the development of identification procedure of the constitutive model of elasto-viscoplasticity describing the behaviour of nanocrystalline titanium. We intend to utilize the constitutive model presented by Perzyna (2010). The procedure is based on experimental observation data obtained by Jia et al. (2001) for ultrafine-grained titanium and by Wang et al. (2007) for nanostructured titanium. Hexagonal close-packed (hcp) ultrafine-grained (UFG) titanium processed by severe plastic deformation (SPD) has gained wide interest due to its excellent mechanical properties and potential applications as biomedical implants.

1. The constitutive model

We propose to introduce some simplification of the constitutive model developed by Perzyna (2010) by assuming that the internal state variable vector $\boldsymbol{\mu} = (\epsilon^p, d, \boldsymbol{\xi})$ consists of two scalars and one tensor, i.e. ϵ^p denotes the equivalent viscoplastic deformation, d defines the mean grain diameter and $\boldsymbol{\xi}$ is the microdamage second order tensor, with the physical interpretation that $(\boldsymbol{\xi} : \boldsymbol{\xi})^{1/2} = \xi$ defines the volume fraction porosity. The equivalent inelastic deformation ϵ^p describes the dissipation effects generated by viscoplastic flow phenomena, the microdamage tensor $\boldsymbol{\xi}$ takes into account the anisotropic intrinsic microdamage mechanisms on internal dissipation and d describes the dynamic grain growth during intensive deformation process. We postulate the plastic potential function in the form $f = f(J_1, J_2, \vartheta, \boldsymbol{\mu})$, where J_1, J_2 denote the first two invariants of the Kirchhoff stress tensor $\boldsymbol{\tau}$ and ϑ is absolute temperature. The evolution equations are assumed as follows

$$(1) \quad \mathbf{d}^p = \Lambda \mathbf{P}, \quad L_{\mathbf{v}} \boldsymbol{\xi} = \boldsymbol{\Xi}, \quad \dot{d} = D$$

where

$$(2) \quad \Lambda = \frac{1}{T_m} \left\langle \Phi \left(\frac{f}{\kappa} - 1 \right) \right\rangle, \quad \mathbf{P} = \frac{\partial f}{\partial \boldsymbol{\tau}} \Big|_{\boldsymbol{\xi} = \text{const}} \left(\left\| \frac{\partial f}{\partial \boldsymbol{\tau}} \right\| \right)^{-1},$$

\mathbf{d}^p denotes the rate of inelastic deformation tensor, T_m denotes the relaxation time for mechanical disturbances, the isotropic work-hardening-softening function $\kappa = \hat{\kappa}(\epsilon^p, \vartheta, \boldsymbol{\xi}, d)$, Φ is the empirical overstress function, the bracket $\langle \cdot \rangle$ defines the ramp function, $L_{\mathbf{v}}$ denotes the Lie derivative and $\boldsymbol{\Xi}$ and D denote the evolution functions which have to be determined.

Let us assume that the intrinsic microdamage process is generated by growth mechanism only. Based on the heuristic suggestions and taking into account the influence of the stress triaxiality and anisotropic effects on the growth mechanism we assume the evolution equation for the microdamage tensor $\boldsymbol{\xi}$ as follows

$$(3) \quad L_{\mathbf{v}} \boldsymbol{\xi} = \frac{\partial g^*}{\partial \boldsymbol{\tau}} \frac{1}{T_m} \left\langle \Phi \left[\frac{I_g}{\tau_{eq}(\vartheta, \boldsymbol{\mu})} - 1 \right] \right\rangle.$$

The tensorial function $\frac{\partial g^*}{\partial \boldsymbol{\tau}}$ represents the mutual micro(nano)crack interaction for growth process, $\tau_{eq} = \hat{\tau}(\vartheta, \boldsymbol{\mu})$ denotes the threshold stress function for growth mechanism, $I_g = b_1 J_1 + b_2 \sqrt{J_2}$ defines the stress intensity invariant, b_i ($i = 1, 2$) are the material coefficients which can depend on d . In the

evolution equation (3) the function $g = \hat{g}(\boldsymbol{\tau}, \vartheta, \boldsymbol{\mu})$ plays the fundamental role, and we introduce the denotation $\frac{\partial g^*}{\partial \boldsymbol{\tau}} = \frac{\partial \hat{g}}{\partial \boldsymbol{\tau}} \left(\left\| \frac{\partial \hat{g}}{\partial \boldsymbol{\tau}} \right\| \right)^{-1}$. Assuming that the dynamic grain growth is the rate dependent mechanism (cf. Perzyna (2010)) we postulate

$$(4) \quad \dot{d} = \frac{\hat{\mathcal{G}}(\vartheta, \boldsymbol{\mu})}{T_m} \left\langle \Phi \left[\frac{I_d}{\tau_d(\vartheta, \boldsymbol{\mu})} - 1 \right] \right\rangle,$$

where $\mathcal{G} = \hat{\mathcal{G}}(\vartheta, \boldsymbol{\mu})$ is the material function, $I_d = c_1 J_1 + c_2 \sqrt{J_2'}$ represents the stress intensity invariant for grain growth, c_i ($i = 1, 2$) are the material coefficients which may depend on d , and $\tau_d = \hat{\tau}_d(\vartheta, \boldsymbol{\mu})$ denotes the threshold stress for dynamic grain growth mechanism.

2. The identification procedure

Let us introduce the particular form for the plastic potential function as follows $f = [J_2' + n(\vartheta, d)(\boldsymbol{\xi} : \boldsymbol{\xi})^{1/2} (J_1^2)]^{\frac{1}{2}}$, where J_2' denotes the second invariant of the stress deviator of the Kirchhoff stress $\boldsymbol{\tau}$ and $n = n(\vartheta, d)$ is the material function. From (1)₁, (2)₁ and (2) we have the dynamical yield criterion in the form

$$(5) \quad [J_2' + n(\vartheta, d)(\boldsymbol{\xi} : \boldsymbol{\xi})^{1/2} (J_1^2)]^{\frac{1}{2}} = \kappa \left[1 + \Phi^{-1} \left(\frac{\sqrt{3}}{2} T_m \dot{\epsilon}^P \right) \right].$$

Taking advantage of the description of the microshear banding effects for nanocrystalline titanium we can propose the relation for the relaxation time (cf. Perzyna (2010))

$$(6) \quad T_m = T_m^0 \left[1 - f_{ms}^0 \frac{1}{1 + \exp(a - b\epsilon^P)} \right] \left(\frac{\dot{\epsilon}^P}{\dot{\epsilon}_s^P} - 1 \right)^{\frac{1}{p}},$$

where T_m^0 , f_{ms}^0 , a , b , p and $\dot{\epsilon}_s^P$ are material function of d . We propose that the identification procedure consists of two parts. In the first part the determination of the material functions and the material constants involved in the description of the dynamic yield criterion (5) is presented. As an experimental base the results concerning experimental observation for ultrafine-grained titanium obtained by Jia et al. (2001) and for nanostructured titanium obtained from the compression tests at high strain rates ($10^3 - 10^4 \text{ s}^{-1}$) by Wang et al. (2007). The second part is focused on the determination of the material functions and the material constants appeared in the evolution equations (3) and (4). To do that we consider a dynamic process of compression test (cf. Wang et al. (2007)).

3. Final comments

There is our hope that proposed identification procedure for the thermodynamical theory of elasto-viscoplasticity of nanocrystalline metals may be used as a base for the description of the behaviour of hexagonal close-packed ultrafine-grained titanium processed by sever plastic deformation and may allow to do the investigation of plastic strain localization and fracture phenomena in nano-mechanical processes. These coming results and excellent mechanical properties of this kind of titanium make potential applications possible as biomedical implants.

4. References

- [1] P. Perzyna, Thermodynamical theory of elasto-viscoplasticity for description of nanocrystalline metals, *Engng. Trans.*, **58** (1–2), 15–74, 2010.
- [2] D. Jia, Y. M. Wang, K. T. Ramesh, E. Ma, Y. T. Zhu, R. Z. Valiev, Deformation behavior and plastic instabilities of ultrafine-grain titanium, *Applied Physics Letters*, **79**, 611–613, 2001.
- [3] Y. M. Wang, J. Y. Huang, T. Jiao, Y. T. Zhu, A. V. Hamza, Abnormal strain hardening in nanostructured titanium at high strain rates and large strains, *J. Mater. Sci.*, **42**, 1751–1756, 2007.

THIRD ORDER TENSORS: THEIR PROPERTIES AND APPLICATION TO COUPLED THEORIES

J. Ostrowska-Maciejewska and K. Kowalczyk-Gajewska

Institute of Fundamental Technological Research, Warsaw, Poland

1. General

Coupled behaviour is a long-standing domain of interest in physics. These effects are due to the interaction between mechanics, magnetism, electricity, thermics, etc [1, 2]. For example, the piezoelectricity phenomena is observed when the permittivity of a material depends on the level of stress or when the strain depends on the level of the electric induction.

The constitutive laws are usually written separately for each uncoupled behaviour. For an elastic problem Hooke's law is given

$$\boldsymbol{\sigma} = \mathbf{C} \cdot \boldsymbol{\varepsilon},$$

where $\boldsymbol{\sigma}, \boldsymbol{\varepsilon} \in T^2$ and the stiffness tensor $\mathbf{C} \in T^4$. For uncoupled electric behaviour the dual state variables are the electric field $\mathbf{E} = -\nabla\varphi$ and the electric induction \mathbf{D}

$$\mathbf{D} = \boldsymbol{\varepsilon} \cdot \mathbf{E},$$

where \mathbf{E}, \mathbf{D} are vectors and $\boldsymbol{\varepsilon}$ is the second order tensor of permittivity.

For the material exhibiting coupling piezoelectric phenomena the global constitutive law includes coupling tensorial parameters

$$\boldsymbol{\sigma} = \mathbf{C} \cdot \boldsymbol{\varepsilon} + \boldsymbol{\alpha} \cdot \mathbf{E} \quad \text{or} \quad \mathbf{D} = \boldsymbol{\beta} \cdot \boldsymbol{\varepsilon} + \boldsymbol{\varepsilon} \cdot \mathbf{E},$$

where $\boldsymbol{\alpha}$ and $\boldsymbol{\beta}$ are tensors of the third order which have some internal symmetries due to the symmetry of the strain and stress tensor, that is

$$(1) \quad \alpha_{ijk} = \alpha_{jik}, \quad \beta_{ijk} = \beta_{ikj}.$$

In classical continuum mechanics the main role is played by the second and fourth order tensors. The theory for such tensors is well developed. The properties of the third order tensors which appear in the coupled theories are not sufficiently described. In our paper the basic properties, the symmetry groups and the harmonic decomposition for such tensors will be discussed in the spirit of [3].

2. Properties of the third order tensors

The theory of linear operators implies that the third order tensor can be treated as a linear operator in the following linear mappings

$$l : T^2 \rightarrow T^1, \quad \text{or} \quad l : T^1 \rightarrow T^2.$$

Therefore for the third order tensors the spectral theorem has no meaning. However, the harmonic decomposition [4, 3] and the symmetry groups can be discussed for these tensors.

In the paper the attention will be mainly focused on the tensors which exhibit the symmetries (1). In general the space of the third order tensors is $3^3 = 27$ dimensional but when we take into account this symmetry the space is reduced to 18-dimensional. In the paper [1] the representation of such tensors has been presented using the modified Voigt notation in the form of 6×3 or 3×6 matrices. Such representation will be used in our presentation as well.

Symmetry group of the third order tensor α is defined as a set of the orthogonal second order tensors such that

$$\mathbf{Q} \star \alpha = \alpha_{ijk} (\mathbf{Q}e_i) \otimes (\mathbf{Q}e_j) \otimes (\mathbf{Q}e_k) = \alpha .$$

On the basis of the above definition one can show that isotropic third order tensors do not exist and the hemitropic third order tensor has a representation

$$\alpha_{ijk} = \alpha e_{ijk} ,$$

where e_{ijk} is the so-called permutation symbol which is completely skewsymmetric. Consequently, the space of skewsymmetric tensors is one-dimensional. Other symmetry groups will be also analyzed.

3. Harmonic decomposition of third order tensor

It will be shown that the harmonic (invariant) decomposition of the space of third order tensors has the form

$$T^3 = A \oplus D \oplus J \oplus W ,$$

where A is the one-dimensional space of fully skewsymmetric tensors, D is the 7-dimensional space of fully symmetric and traceless tensors, J is the 9-dimensional space generated by tensors

$$\mathbf{1} \otimes \mathbf{u} , \quad \mathbf{1} \otimes \mathbf{v} , \quad \mathbf{1} \otimes \mathbf{w} ,$$

where $\mathbf{u}, \mathbf{v}, \mathbf{w}$ arbitrary non-coaxial vectors and $\mathbf{1}$ is the second order identity tensors and W is the 10-dimensional space orthogonal to A, D and J .

The symmetry groups and the harmonic decomposition will be also discussed for the two-dimensional third order tensors.

4. References

- [1] R. Corcolle, L. Daniel and F. Bouillaut (2008). Generic formalism for homogenization of coupled behavior: Application to magnetoelectroelastic behaviour. *Physical Review B*, **78**, 210110(1-12).
- [2] R. Kotowski and C. Rymarz (2004). *Modelowanie ośrodków mikrostrukturalnych*. Instytut Naukowo-Badawczy. Monografie - Zastosowania Elektromagnetyzmu Nr 5, Warszawa (In Polish).
- [3] J. Rychlewski (2000,2001). A qualitative approach to Hooke's tensors. Part I and Part II. *Arch. Mech.*, **52**, 737-759, **53**, 45-63.
- [4] Q.-S.Zheng (2000). Irreducible decompositions of physical tensors of high orders. *Journal of Engineering Materials*, **37**, 273-288.

REFORMULATION OF 3D ELASTICITY EQUATIONS BASED ON ORTHOGONAL TENSOR SPHERICAL HARMONICS

H.M. Shodja^{1,2} and A. Khorshidi¹

¹*Department of Civil Engineering, Sharif University of Technology, P. O. Box 11155-9313, Tehran, Iran*

²*Institute for Nanoscience and Nanotechnology, Sharif University of Technology, P. O. Box 11155-9161, Tehran, Iran*

In this work, the elastic fields are considered as tensor fields defined on spherical surfaces. Subsequently, the complete three-dimensional equations of elasticity for functionally graded (FG) spherically isotropic materials are reformulated using vector and tensor spherical harmonics (VSHs and TSHs), which are defined on the surface of the unit sphere. In the literature, TSHs have been mainly employed to describe the angular momentum in quantum mechanical studies. This alternative formulation not only provides a rigorous approach for finding solutions of the relevant problems in the literature, but also leads to the solutions of the more involved boundary value problems with less effort [1, 2]. The exact determination of the elastic fields associated with spherical multi-inclusions/-inhomogeneities/-inhomogeneous inclusions with FG spherically isotropic constituents and isotropic surrounding matrix is of particular interest. In the absence of the matrix, the problem reduces to a multi-phase spherical elastic solid. In addition to a prescribed piecewise nonuniform misfit strains or eigenstrains distribution within the spherical regions, a nonuniform external applied loading may be prescribed as well. A schematic of the problem of interest is shown in Fig. 1.

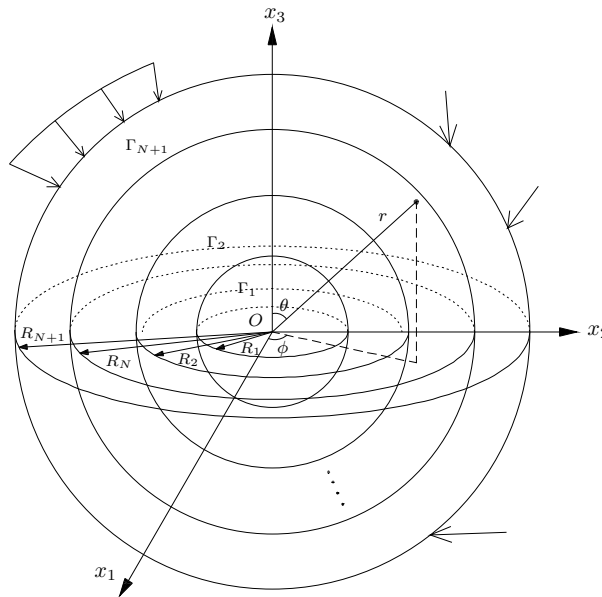


Figure 1. The nomenclature of a spherical core-multi-shell ensemble.

-
- [1] A. Khorshidi, A. and H.M. Shodja (2012). Spectral Theory of Elasticity: Spherical Multi-Phase Ensemble/Multi-Inhomogeneous Inclusion with Spherically Isotropic and Functionally Graded Phases under Nonuniform Loading, Manuscript submitted to *J. Elast.*
- [2] H.M. Shodja, and A. Khorshidi (2012). Tensor Spherical Harmonic Theories on the Exact Nature of the Elastic Fields of a Spherically Isotropic Multi-Inhomogeneous Inclusion, Manuscript submitted to *J. Mech. Phys. Solids*.

ACCELERATED SHAKEDOWN IN TWO-PHASE STRUCTURES CAUSED BY THE PLASTIC STRAIN INDUCED PHASE TRANSFORMATION

B. Skoczeń

Cracow University of Technology, Cracow, Poland

1. Introduction

Influence of plastic strain induced $\gamma \rightarrow \alpha'$ phase transformation, that occurs in metastable materials strained at very low temperatures, on acceleration of the shakedown process is investigated. The main mechanism that leads to the accelerated shakedown consists in the microstructural evolution associated with phase transformation, which results in substantial increase of the volume fraction of secondary phase (elastic) in the matrix composed of primary phase (elastic-plastic). Thus, the classical shakedown conditions are substantially altered by significant reduction of dissipative nature of two-phase continuum due to the lattice transition from fcc to bcc structure. In this context, special class of two-phase materials with functionally graded microstructure, obtained at cryogenic temperatures [3] as a result of controlled plastic strain induced phase transformation, is studied. Among other materials, the austenitic stainless steels are known to behave in a metastable way when strained at very low temperatures and are extensively used to construct components of the superconducting magnets.

2. The constitutive model

A linearised law describing kinetics of the $\gamma \rightarrow \alpha'$ phase transformation in metastable austenitic stainless steels, specially adapted to extremely low temperatures, was postulated by Garion and Skoczeń [1]:

$$\dot{\xi} = A(T, \underline{\dot{\epsilon}}^p, \underline{\sigma}) \dot{p} H((p - p_\xi)(\xi_L - \xi))$$

The constitutive model used to describe mathematically the plastic strain induced $\gamma \rightarrow \alpha'$ phase transformation at very low temperatures [2] involves mixed kinematic/isotropic strain hardening where two fundamental effects play important role: interaction of dislocations with the martensite inclusions and increase in transient material tangent stiffness due to the evolution of harder martensite content within the softer austenitic matrix.

$$d\underline{\underline{X}} = d\underline{\underline{X}}_a + d\underline{\underline{X}}_{a+m} = \frac{2}{3} C_x(\xi) d\underline{\underline{\epsilon}}^p \quad ; \quad dR = C_R(\xi) dp$$

It is assumed that the back stress increment is composed of the classical term which corresponds to the behaviour of the austenitic phase (dX_a) in the presence of localized small inclusions, uniformly distributed and randomly oriented in the RVE, and a term related to the combination of austenite and martensite via the homogenization algorithm (dX_{a+m}). The interaction of dislocations with the martensite inclusions is reflected by the hardening modulus that depends on the evolution of the volume fraction of martensite. Here, an approximation based on the micro-mechanical analysis has been used:

$$d\underline{\underline{X}}_a = d\underline{\underline{X}}_{a0} + d\underline{\underline{X}}_{a\xi} = \frac{2}{3} C_0 d\underline{\underline{\epsilon}}^p + \frac{2}{3} C_0 h \xi d\underline{\underline{\epsilon}}^p = \frac{2}{3} C(\xi) d\underline{\underline{\epsilon}}^p$$

On the other hand, evaluation of the transient tangent stiffness of two-phase continuum (for updated proportion between the phases) is based on the classical homogenization scheme and takes into account the local tangent stiffness moduli of the constituents, as postulated by Hill, 1965. Mori-Tanaka homogenization algorithm has been used in order to obtain instantaneous tangent stiffness operator of two-phase continuum:

$$d\underline{X}_{a+m} = 2(\mu_{MT} - \mu_{\alpha})d\underline{\varepsilon}^p = (2C_{a+m}/3)d\underline{\varepsilon}^p$$

where C_{a+m} denotes surplus tangent stiffness modulus. Finally, the mixed hardening is described by the following model:

$$d\underline{X} = \frac{2}{3}C_X(\xi)d\underline{\varepsilon}^p = \frac{2}{3}[C(\xi) + \beta C_{a+m}(\xi)]d\underline{\varepsilon}^p \quad ; \quad dR = C_R(\xi)dp = (1 - \beta)C_{a+m}(\xi)dp$$

It is worth pointing out that the model is attractive in view of its simplicity and relatively small number of parameters to be identified at cryogenic temperatures.

3. Shakedown of functionally graded structural members (FGSM)

When analyzing the phase transformation process in the basic structures, the concept of functionally graded structural members (FGSM) has been developed. The rods of circular cross-section subjected to torsion (Fig.1) [5] and the beams of rectangular cross-section subjected to bending [3] at very low temperatures are characterized by functional distribution of mechanical properties in the direction orthogonal with respect to their axis. The response of FGSMs to quasistatic and to cyclic loads has been investigated [4]. In the case of quasistatic torsion and bending, closed form analytical solutions were obtained. For cyclic loads, accelerated shakedown due to the evolution of microstructure has been observed in the course of numerical simulations.

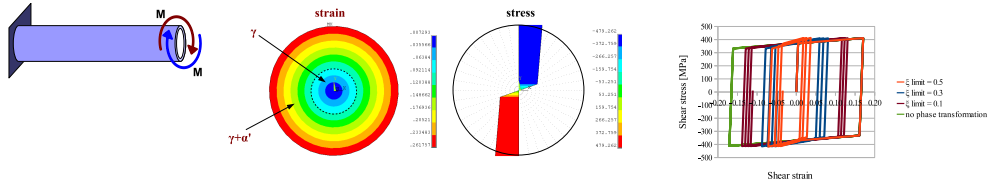


Fig. 1 Shakedown of functionally graded structural members subjected to cyclic torsion.

Evolution of two-phase continuum, where the elastic-plastic matrix is gradually replaced by the elastic inclusions, clearly indicates that in the limit case where 100% of primary phase is replaced by the secondary phase the shakedown occurs by definition. This important and new conclusion has very practical meaning. As soon as the $\gamma \rightarrow \alpha'$ phase transformation begins, the evolution of material structure accelerates the process of adaptation of structural members to cyclic loads and, therefore, enhances their fatigue life when compared to the classical elastic-plastic structures. Finally, this particular feature of structures made of metastable materials is explained in the framework of Melan and Koiter adaptation/inadaptation theorems.

Acknowledgement. Grant of Polish National Science Centre: PB N N501 228440 is gratefully acknowledged.

4. References

- [1] C. Garion and B. Skocz n (2002). Modeling of plastic strain-induced martensitic transformation for cryogenic applications, *Journal of Applied Mechanics*, **69**, 755–762.
- [2] C. Garion, B. Skocz n and S. Sgobba (2006). Constitutive modelling and identification of parameters of the plastic strain-induced martensitic transformation in 316L stainless steel at cryogenic temperatures, *International Journal of Plasticity*, **22**, 1234–1264.
- [3] M. Sitko, B. Skocz n and A. Wr blewski (2010). FCC-BCC phase transformation in rectangular beams subjected to plastic straining at cryogenic temperatures, *International Journal of Mechanical Sciences*, **52**, 7, 993-1007.
- [4] M. Sitko and B. Skocz n (2012). Effect of $\gamma \rightarrow \alpha'$ phase transformation on plastic adaptation to cyclic loads at cryogenic temperatures, *Int. Journal of Solids and Structures*, **49**, 3-4, 613-634.
- [5] B. Skocz n (2007). Functionally graded structural members obtained via the low temperature strain induced phase transformation, *Int. Journal of Solids and Structures*, **44**, 5182–5207.

FRACTIONAL VISCOPLASTICITY

W. Sumelka

Poznan University of Technology, Institute of Structural Engineering, Poznan, Poland

1. Introduction

In the presented paper the idea is to replace the classical gradient operator in viscoplastic flow rule by the fractional one to define the specific case of what we call **fractional viscoplasticity** (the case with fractional rate of viscoplastic strains was discussed in [6]).

2. Fractional viscoplasticity

Classical viscoplastic flow we define as [3, 4]

$$(1) \quad \mathbf{d}^p = \Lambda^{vp} \mathbf{p},$$

where \mathbf{d}^p denotes the rate of viscoplastic strains, Λ^{vp} and \mathbf{p} denote flow magnitude and direction, respectively. The explicit definition for Λ^{vp} and \mathbf{p} can be given as

$$(2) \quad \Lambda^{vp} = \frac{1}{T_m} \langle \Phi^{vp} \left(\frac{f}{\kappa} - 1 \right) \rangle = \frac{1}{T_m} \langle \left(\frac{f}{\kappa} - 1 \right)^{m_{pl}} \rangle, \quad \text{and} \quad \mathbf{p} = \frac{\partial f}{\partial \boldsymbol{\tau}} \Big|_{\boldsymbol{\xi}=\text{const}} \left(\left\| \frac{\partial f}{\partial \boldsymbol{\tau}} \right\| \right)^{-1},$$

where f denotes the potential function, κ is the isotropic work-hardening-softening function, T_m is relaxation time, $\boldsymbol{\xi}$ denotes the intrinsic anisotropic microdamage and $\boldsymbol{\tau}$ is Kirchhoff stress tensor.

So we can rewrite classical formulation using fractional gradient operator as

$$(3) \quad \mathbf{p} = {}^{RLC}D_{\Theta a+, b-}^{\alpha} f(\boldsymbol{\tau}) \left(\left\| {}^{RLC}D_{\Theta a+, b-}^{\alpha} f(\boldsymbol{\tau}) \right\| \right)^{-1},$$

where ${}^{RLC}D_{\Theta a+, b-}^{\alpha}$ denotes Right-Left-Caputo (RLC) partial fractional derivative operator [5] for $\tau_{ij} \in (a, b)$ and Θ denotes the skewness parameter [2]. Let us emphasise that terminals a and b are not constant, they depend on current thermomechanical state, hence we utilise so called "short-memory" principle [1].

Formal definition of the RLC fractional derivative is

$$(4) \quad {}^{RLC}D_{\Theta a+, b-}^{\alpha} f(\boldsymbol{\tau}) = - \left[c_L(\alpha, \Theta) {}^C D_{a+}^{\alpha} f(\boldsymbol{\tau}) + c_R(\alpha, \Theta) {}^C D_{b-}^{\alpha} f(\boldsymbol{\tau}) \right].$$

In Eq. (4) we have:

$$(5) \quad c_L = \frac{\sin\left(\frac{(\alpha-\Theta)\pi}{2}\right)}{\sin(\pi\alpha)},$$

$$(6) \quad {}^C D_{a+}^{\alpha} f(\boldsymbol{\tau}) = \frac{1}{\Gamma(n-\alpha)} \int_a^{\tau_{ij}} \frac{d^n f(u)}{du^n} (\tau_{ij} - u)^{\alpha-n+1} du,$$

$$(7) \quad c_R = \frac{\sin\left(\frac{(\alpha+\Theta)\pi}{2}\right)}{\sin(\pi\alpha)},$$

$$(8) \quad {}^C D_{b-}^{\alpha} f(\boldsymbol{\tau}) = \frac{(-1)^n}{\Gamma(n-\alpha)} \int_{\tau_{ij}}^b \frac{d^n f(u)}{du^n} (u - \tau_{ij})^{\alpha-n+1} du,$$

where Θ denotes the skewness parameter, Γ is gamma function and $n = [\alpha] + 1$ where symbol $[\cdot]$ denotes integer part of a real number.

3. Example

Let us consider a yield surface of the HMH type written in a stress principal directions (we assume that $\tau_3 = 0$ for simplest calculations)

$$(9) \quad \tau_1^2 - \tau_1\tau_2 + \tau_2^2 - \kappa^2 = 0.$$

It can be shown that for a such case the unnormalized flow directions are:

- through direction 1

$$(10) \quad {}^{RLC}_{\Theta}D_{a+,b-}^{\alpha}f(\boldsymbol{\tau}) = -[c_L(\alpha, \Theta) {}^C D_{a+}^{\alpha}f(\boldsymbol{\tau}) + c_R(\alpha, \Theta) {}^C D_{b-}^{\alpha}f(\boldsymbol{\tau})],$$

- through direction 2

$$(11) \quad {}^{RLC}_{\Theta}D_{a+,b-}^{\alpha}f(\boldsymbol{\tau}) = -[c_L(\alpha, \Theta) {}^C D_{a+}^{\alpha}f(\boldsymbol{\tau}) + c_R(\alpha, \Theta) {}^C D_{b-}^{\alpha}f(\boldsymbol{\tau})],$$

where

$$(12) \quad {}^C D_{a+}^{\alpha}f(\boldsymbol{\tau}) = \frac{\Gamma(3)}{\Gamma(3-\alpha)}(\tau_i - a)^{2-\alpha} + (2a - \tau_j) \frac{\Gamma(2)}{\Gamma(2-\alpha)}(\tau_i - a)^{1-\alpha},$$

$$(13) \quad {}^C D_{b-}^{\alpha}f(\boldsymbol{\tau}) = \frac{\Gamma(3)}{\Gamma(3-\alpha)}(b - \tau_i)^{2-\alpha} + (\tau_j - 2b) \frac{\Gamma(2)}{\Gamma(2-\alpha)}(b - \tau_i)^{1-\alpha},$$

for $i, j \in \{1, 2\}$ but $i \neq j$ and $0 < \alpha < 1$.

Some illustrative examples will be presented.

Acknowledgments

I would like to thank Prof. Jacek Leszczyński and Dr Tomasz Błaszczyk for private communication concerning fractional derivatives calculations.

- [1] Podlubny I. *Fractional Differential Equations*, volume 198 of *Mathematics in Science and Engineering*. Academic Press, 1999.
- [2] Leszczyński J.S. *An introduction to fractional mechanics*. Monographs No 198. The Publishing Office of Czestochowa University of Technology, 2011.
- [3] P. Perzyna. The thermodynamical theory of elasto-viscoplasticity. *Engineering Transactions*, **53**:235–316, 2005.
- [4] W. Sumelka. *The Constitutive Model of the Anisotropy Evolution for Metals with Microstructural Defects*. Publishing House of Poznan University of Technology, Poznań, Poland, 2009.
- [5] Tarasov V.E. Fractional vector calculus and fractional Maxwell's equations. *Annals of Physics*, **323**:2756—2778, 2008.
- [6] Sumelka W. Fractional viscoplasticity - an introduction. In *Workshop 2012 - Dynamic Behavior of Materials and Safety of Structures*, pages 1–2, Poznań, Poland, 2-4 May 2012.

MATHEMATICAL PROBLEMS IN THE FULL COUPLED THEORY OF DOUBLE-POROSITY MATERIALS

M. Svanadze

*Institute for Fundamental and Interdisciplinary Mathematics Research,
Ilia State University, Tbilisi, Georgia*

1. Introduction

The materials with double porosity play an important role in many branches of engineering, e.g., the petroleum industry, chemical engineering, geomechanics, and, in recent years, biomechanics. The quasi-static theory of elasticity for materials with double porosity in the framework of mixture theory to model the flow and deformation behavior of porous media characterized by two coexisting degree of porosity was presented by Aifantis and his co-workers [1], [2]. The Aifantis' theory unifies the earlier proposed models of Barenblatt's [3] for porous media with double porosity and Biot's [4] for porous media with single porosity.

However, Aifantis' quasi-static theory was incomplete, in the sense that it ignored the cross-coupling effects between the volume change of the pores and fissures in the system. This deficiency was eliminated and cross-coupled terms were included in the equations of conservation of mass for the pore and fissure fluid and in the Darcy's law for solid with double porosity (see [5]). The significance of the cross-coupling effects on the pore and fracture fluid pressure response of double porosity media was highlighted by Khalili [6].

In the governing equations of the above mentioned theories of poroelasticity the inertial term was neglected and the quasi-static problems were investigated. On the other hand, inertial effect play a pivotal role in investigation of various problems of vibrations and wave propagation through double porosity media. Therefore, it is important to study a full dynamic model for materials with double porosity. The fully dynamic system to describe deformation in single porosity media was developed by Biot [7].

In the present paper, we shall consider flow and deformation processes of the double porosity media in the case for with the inertia effect is included (full dynamic case). Some basic results of the classical mathematical theories of elasticity are generalized and the following results are obtained: the properties of plane harmonic waves are established, the fundamental solutions of equations of steady vibrations are constructed, the Green's formulae in the considered theory are obtained, the uniqueness theorem of the external boundary value problems (BVPs) is proved, the representation of Galerkin type solution is obtained, the basic properties of the surface and volume potentials and singular integral operators are established, and finally, the existence theorems for the external BVPs are proved by means of the boundary integral method and the theory of singular integral equations.

2. Basic Equations

Let $\mathbf{x} = (x_1, x_2, x_3)$ be a point of the Euclidean three-dimensional space R^3 , $\mathbf{u}(\mathbf{x})$ is the displacement vector in solid, $\mathbf{u} = (u_1, u_2, u_3)$; $p_1(\mathbf{x})$ and $p_2(\mathbf{x})$ are the pore and fissure fluid pressures, respectively. The system of homogeneous equations of steady vibrations in the full coupled linear theory of elasticity for solid with double porosity has the following form

$$\begin{aligned} & \mu \Delta \mathbf{u} + (\lambda + \mu) \text{grad div } \mathbf{u} - \beta_1 \text{grad } p_1 - \beta_2 \text{grad } p_2 + \rho \omega^2 \mathbf{u} = \mathbf{0}, \\ (1) \quad & (k_1 \Delta + a_1) p_1 + (k_{12} \Delta + a_{12}) p_2 + i\omega \beta_1 \text{div } \mathbf{u} = 0, \\ & (k_{21} \Delta + a_{21}) p_1 + (k_2 \Delta + a_2) p_2 + i\omega \beta_2 \text{div } \mathbf{u} = 0. \end{aligned}$$

where Δ is the Laplacian, $\lambda, \mu, \beta_j, k_j, k_{12}, k_{21}, \alpha_j, \alpha_{12}, \alpha_{21}$ and γ are the constitutive coefficients, $a_j = i\omega \alpha_j - \gamma$, $a_{lj} = i\omega \alpha_{lj} + \gamma$ ($l, j = 1, 2$), ω is the oscillation frequency, $\omega > 0$, ρ is the reference mass density, $\rho > 0$.

Let S be a closed smooth surface surrounding the finite domain Ω^+ in E^3 , $\bar{\Omega}^+ = \Omega^+ \cup S$, $\Omega^- = E^3 \setminus \bar{\Omega}^+$, $\mathbf{n}(\mathbf{z})$ is the external unit normal vector to S at $\mathbf{z} \in S$. The basic external BVPs of steady vibrations in the full coupled linear theory of elasticity for solid with double porosity are formulated as follows: find a regular solution $\mathbf{U} = (\mathbf{u}, p_1, p_2)$ to system (1) in Ω^- satisfying the boundary condition $\lim_{\Omega^- \ni \mathbf{x} \rightarrow \mathbf{z} \in S} \mathbf{U}(\mathbf{x}) \equiv \{\mathbf{U}(\mathbf{z})\}^- = \mathbf{f}(\mathbf{z})$ in the problem $(I)_{\mathbf{f}}^-$ and $\lim_{\Omega^- \ni \mathbf{x} \rightarrow \mathbf{z} \in S} \mathbf{R}(\mathbf{D}_{\mathbf{x}}, \mathbf{n}(\mathbf{z}))\mathbf{U}(\mathbf{x}) \equiv \{\mathbf{R}(\mathbf{D}_{\mathbf{z}}, \mathbf{n}(\mathbf{z}))\mathbf{U}(\mathbf{z})\}^- = \mathbf{f}(\mathbf{z})$ in the problem $(II)_{\mathbf{f}}^-$, where \mathbf{f} is the known five-component vector functions, \mathbf{R} is the stress operator.

3. Basic results

Theorem 1. Through a solid with double porosity propagates three longitudinal and two transverse plane waves; the longitudinal plane waves are damped and the transverse plane waves have the constant amplitude.

Theorem 2. The external BVPs $(I)_{\mathbf{f}}^-$ and $(II)_{\mathbf{f}}^-$ have one regular solution.

Theorem 3. If $S \in C^{2,\nu}$, $\mathbf{f} \in C^{1,\tau}(S)$, $0 < \tau < \nu \leq 1$, then a regular solution of the BVP $(I)_{\mathbf{f}}^-$ exists, is unique and is represented by sum $\mathbf{U}(\mathbf{x}) = \mathbf{Z}^{(2)}(\mathbf{x}, \mathbf{g}) - i\mathbf{Z}^{(1)}(\mathbf{x}, \mathbf{g})$ for $\mathbf{x} \in \Omega^-$, where $\mathbf{Z}^{(1)}(\mathbf{x}, \mathbf{g})$ and $\mathbf{Z}^{(2)}(\mathbf{x}, \mathbf{g})$ are the single-layer and double-layer potentials, respectively, and \mathbf{g} is a solution of the singular integral equation $\frac{1}{2}\mathbf{g}(\mathbf{z}) + \mathbf{Z}^{(2)}(\mathbf{z}, \mathbf{g}) - i\mathbf{Z}^{(1)}(\mathbf{z}, \mathbf{g}) = \mathbf{f}(\mathbf{z})$ for $\mathbf{z} \in S$ which is always solvable for an arbitrary vector \mathbf{f} .

Theorem 4. If $S \in C^{2,\nu}$, $\mathbf{f} \in C^{1,\tau}(S)$, $0 < \tau < \nu \leq 1$, then a regular solution of the BVP $(II)_{\mathbf{f}}^-$ exists, is unique and is represented by sum $\mathbf{U}(\mathbf{x}) = -i\mathbf{Z}^{(2)}(\mathbf{x}, \mathbf{g}) + \mathbf{Z}^{(1)}(\mathbf{x}, \mathbf{g})$ for $\mathbf{x} \in \Omega^-$, where \mathbf{g} is a solution of the singular integral equation $-\frac{1}{2}\mathbf{g}(\mathbf{z}) - i\mathbf{R}\mathbf{Z}^{(2)}(\mathbf{z}, \mathbf{g}) + \mathbf{R}\mathbf{Z}^{(1)}(\mathbf{z}, \mathbf{g}) = \mathbf{f}(\mathbf{z})$ for $\mathbf{z} \in S$ which is always solvable for an arbitrary vector \mathbf{f} .

Theorems 3 and 4 are proved by means of the boundary integral method and the theory of singular integral equations (for details, see [8]).

4. References

- [1] R.K. Wilson and E.C. Aifantis (1982). On the theory of consolidation with double porosity -I, *Int. J. Engng. Sci.* **20**, 1009-1035.
- [2] M.Y. Khaled, D.E. Beskos and E.C. Aifantis (1984). On the theory of consolidation with double porosity III, *Int. J. Numer. Anal. Methods Geomech.* **8**, 101-123.
- [3] G.I. Barenblatt, I.P. Zheltov and I.N. Kochina (1960). Basic concept in the theory of seepage of homogeneous liquids in fissured rocks (strata), *J. Appl. Math. Mech.*, **24**, 1286-1303.
- [4] M.A. Biot (1941). General theory of three-dimensional consolidation, *J. Appl. Phys.*, **12**, 155-164.
- [5] N. Khalili and S. Valliappan (1996). Unified theory of flow and deformation in double porous media, *Eur. J. Mech./A Solids* **15**, 321-336.
- [6] N. Khalili (2003). Coupling effects in double porosity media with deformable matrix. *Geophys. Res. Letters*, **30** (22), 2153.
- [7] M.A. Biot (1956). Theory of propagation of elastic waves in a fluid-saturated porous solid, I. Low frequency range, II. Higher frequency range, *J. Acoust. Soc. Amer.*, **28**, 168-178, 179-191.
- [8] V.D. Kupradze, T.G. Gegelia, M.O. Bacheleishvili and T.V. Burchuladze (1979). *Three-Dimensional Problems of the Mathematical Theory of Elasticity and Thermoelasticity*, North-Holland, Amsterdam, New York, Oxford.

EXTENSION OF THE RYCHLEWSKI LIMIT STATE CRITERION ACCOUNTING FOR THE ASYMMETRY OF ELASTIC RANGE

P. Szeptyński¹, J. Ostrowska-Maciejewska² and R.B. Peçherski^{1,2}

¹ AGH University of Science and Technology, Faculty of Mechanical Engineering and Robotics,
Department of the Strength and Fatigue of Materials and Structures, Krakow, Poland

² Institute of Fundamental Technological Research, Warsaw, Poland

1. The subject of research

Recently the application of modern materials exhibiting some unconventional features becomes still more common. Among those new materials one should distinguish various composites, materials with internal micro- or nanostructure, modern alloys, heavily rolled metal sheets etc. It is clearly visible those materials distinguish themselves with certain uncommon mechanical properties which for a long time were considered unnecessary or negligible in the analysis of the problem of reaching a limit state. Among those features one should mention: low elastic symmetry, pressure dependence, Lode angle dependence, strength-differential effect etc. Many of the classical propositions of the limit state criteria cannot involve all or at least majority of those effects. The aim of authors is to provide possibly general yet precise limit state condition of simple mathematical form derived from physical energy-based considerations.

2. The Rychlewski limit state criterion

J. Rychlewski performed in 1984 the spectral analysis of elasticity tensors [1] describing precisely the mathematical form of constitutive relations of anisotropic linear elasticity in terms of eigenvalues (Kelvin moduli) and eigenstates of stiffness and compliance tensors. He introduced also the concept of energetically orthogonal decompositions of elastic energy density [2] and suggested that a linear combination of the terms of such a decomposition might be considered as a measure of material effort. The limit state criterion derived from the hypothesis of Rychlewski is of the following form:

$$(1) \quad \frac{\Phi_1}{h_1} + \frac{\Phi_2}{h_2} + \dots + \frac{\Phi_\mu}{h_\mu} = 1, \quad \mu \leq 6$$

3. Extension of the Rychlewski criterion using the concept of influence functions

Due to strictly energetic formulation of the limit state criterion of Rychlewski, which is expressed as a quadratic form in space of stress states, it cannot account for the strength differential effect. The authors suggest to extend the original proposition of Rychlewski in the same manner as Burzyński [3] developed the classical hypothesis of Huber so that it involved asymmetry of the elastic range, namely by multiplying the terms of the energy decomposition by certain stress state dependent functions. Depending on their character they should be termed *influence functions* or *stress mode indicators*. The modified limit state criterion takes the form

$$(2) \quad \eta_1 \cdot \Phi_1 + \eta_2 \cdot \Phi_2 + \dots + \eta_\mu \cdot \Phi_\mu = 1, \quad \mu \leq 6$$

There are certain assumptions made on the properties of the parameters η :

- It is assumed that the parameters η depend only on the stress state corresponding with the term of energy decomposition which is respective for that parameter.

- Parameters η are assumed to be isotropic in their domain – i.e. they can be expressed as a scalar functions of the invariants of their argument.
- Parameters η respective for the deviatoric (shear) stress states are assumed to be an even (symmetric) functions – in particular they will be often assumed to be independent of the norm of their arguments. They will be termed then the *shear mode indicators*.
- Parameter η is called the influence function if it depends on the norm of its argument (it changes its value as the magnitude of the corresponding stress state changes) – otherwise it is called the stress mode indicator.

Further properties of the influence functions and stress mode indicators can be derived basing on those basic assumptions and additional analysis taking into account the dimension of the corresponding stress state subspace

4. Specification of the new limit state criterion for chosen elastic symmetries

The new limit state criterion was specified for all plane elastic symmetries and most of spatial elastic symmetries after assuming that the considered energetically orthogonal decomposition of the elastic energy density was the – so called by Rychlewski – main energy decomposition, namely the decomposition into the terms corresponding with different eigensubspaces of the elasticity tensors. The criterion for each symmetry involves in general different number of influence functions and stress mode indicators depending on the stress states uniquely determined by the elastic properties of the considered material. For certain cases a direct formula was given which enables finding the value of the unknown influence functions for certain values of their arguments basing on simple strength tests.

5. Summary

A new proposition of an energy-based limit state criterion for anisotropic materials exhibiting asymmetry of the elastic range is presented. Certain assumption on the criterion parameters are made. Specification of the limit state criterion for a large number of elastic symmetries is given as well as the general methodology of determination of the form of unknown parameters of the criterion. Detailed discussion on the introduced criterion was already published in [4] [5] [6].

6. References

- [1] J. Rychlewski (1984). On Hooke's Law, *J. Appl. Mech. Math.*, **48**, 303–314.
- [2] J. Rychlewski (1984). Elastic energy decomposition and limit criteria (in Russian). *Uspekhi Mekhaniki*, **7**, 51-80; English translation in *Engng. Trans.*, **59**, 1, 31–63.
- [3] W. Burzyński (1928). *Study on material effort hypotheses* (in Polish), Akademia Nauk Technicznych, Lwów; English translation in *Engng. Trans.*, **57**, 3-4, 185–215.
- [4] M. Nowak, et. al (2011). Yield criterion accounting for the influence of the third invariant of stress tensor deviator. Part I: Proposition of the yield criterion based on the concept of influence functions, *Engng. Trans.*, **59**, 4, 273–281.
- [5] J. Ostrowska-Maciejewska, R.B. Pęcherski, P. Szeptyński (2012). Limit condition for anisotropic materials with asymmetric elastic range, *Engng. Trans.*, **60**, 2.
- [6] P. Szeptyński, R.B. Pęcherski (2012). Proposition of a new yield criterion for orthotropic metal sheets accounting for asymmetry of elastic range. *Rudy i metale nieżelazne*, **57**, 4, 243–250.

FLOW STRESS IN UNCONVENTIONAL METAL FORMING PROCESSES

M. Tkocz, J. Pawlicki and F. Grosman

Silesian University of Technology, Department of Materials Technology, Katowice, Poland

There are two fundamental characteristics of materials formability: the flow stress and the limit deformation. Determining the flow stress function is necessary for mathematical modeling and designing of metal forming processes. It is frequent that the strain path during unconventional forming changes in an oscillatory manner [1]. In these conditions the flow stress curves differ substantially from the commonly known, classic strain-hardening curves (Fig.1) [2].

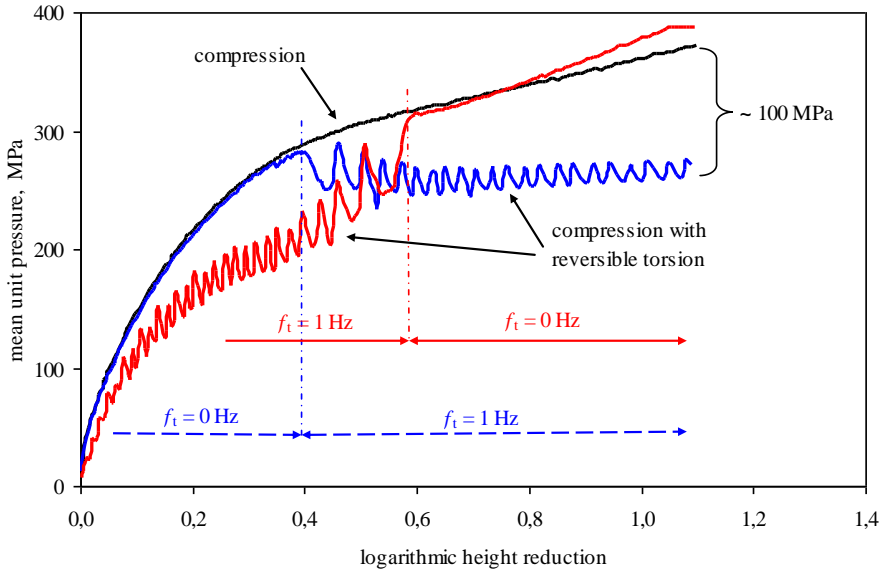


Figure 1. The effect of cyclic change of the strain path on the flow stress for copper; parameters of reversible torsion: frequency 1 Hz, amplitude 10°

In order to perform the unconventional cold forming tests with cyclic change of the strain path, the unique research stands were developed in the Department of Materials Technology at the Silesian University of Technology [3,4]. Specimens were made of electrolytic copper and austenitic steel. Analysis of the tests results allowed to determine functional relationships between the flow stress σ_p , strain ε and the deformation history h_ε for each tested material:

$$(1) \quad \sigma_p = \sigma_p(\varepsilon, h_\varepsilon)$$

The deformation history is described by: the strain ε_{sin} in the single deformation phase, the change of principal axis direction α_s and the principal strain components $\varepsilon_1, \varepsilon_2, \varepsilon_3$ in subsequent deformation phases, the number of deformation phases n_{def} and the total strain ε_{tot} .

A series of experiments were performed for various loading schemes. The most favourable effects were achieved when deformation was realized by reversible torsion or by complex loading that combines simultaneous tension or compression with reversible torsion. Advantages of such deformation techniques include decreasing the maximum flow stress values and increasing the limit deformation values.

An extensive experience has been gained during research, both concerned with the technique for performing the deformation tests under complex loading conditions as well as the measurement and data acquisition. On this basis, an original method has been developed for material testing under cyclically varying, complex loading within large plastic strain range. Moreover, two other laboratory research stands have been developed which enable rolling [5,6] and forging [3] aided by shear stresses.

Acknowledgements

Financial support of Structural Funds in the Operational Programme - Innovative Economy (IE OP) financed from the European Regional Development Fund - Project "Modern material technologies in aerospace industry", Nr POIG.01.01.02-00-015/08-00 is gratefully acknowledged.

References

- [1] F. Grosman and J. Pawlicki (2004). Processes with forced deformation path. *1st Int. Conf. on New Forming Technology, Harbin, China*, 361-366.
- [2] F. Grosman and J. Pawlicki (2005). Wpływ parametrów ściskania z oscylacyjnym skręcaniem na technologiczną plastyczność metali. *Rudy i Metale Nieżelazne*, **10-11**, 590-594.
- [3] J. Pawlicki and F. Grosman (2003). Analiza efektów siłowo-energetycznych dla procesów z wymuszoną drogą odkształcenia. *Rudy i Metale Nieżelazne*, **10-11**, 479- 483.
- [4] J. Pawlicki and F. Grosman (2007). Naprężenie uplastyczniające materiałów metalicznych w warunkach cyklicznie zmiennych złożonych stanów obciążeń. *Hutnik - Wiadomości Hutnicze*, **5**, 239-243.
- [5] A. Milenin F. Grosman, L. Madej and J. Pawlicki (2010). Development and validation of the numerical model of rolling process with cyclic horizontal movement of rolls, *Steel Research Int.*, **81**, 204-209.
- [6] F. Grosman and Z. Cyganek (2008). The research of rolling process with cyclic change of the strain path, *Steel Research Int., Special Edition*, **79**, 453-458.

ENERGY-BASED MODEL OF NONLINEAR ELASTIC ORTHOTROPIC MATERIAL ON THE EXAMPLE OF CAR'S TARPAULIN

T. Wegner and D. Kurpisz
Institute of Applied Mechanics, Poznań, Poland

1. General

The modeling of mechanical properties of material is very important due to its engineering applications, and useful because correctly constructed and employed model allows precise estimate the behavior of material under complex load state. In majority known from literature papers anisotropic linear elastic material [1] or isotropic nonlinear elastic material [2] is taken into investigations. Hardest and still open problem is description of mechanical properties by simultaneous pronouncement of material anisotropy and nonlinear elasticity. An example of such material can be car's tarpaulin. The main aim of this work is construction an energy-based model of mechanical properties of nonlinear elastic orthotropic material on the example of cars tarpaulin under plane state of stress.

2. The constitutive relations of the model

Basing on approximations of the experimental characteristics and using a phenomenological conception of description (see Fig. 1), the main constitutive relations of energy-based model were introduced.

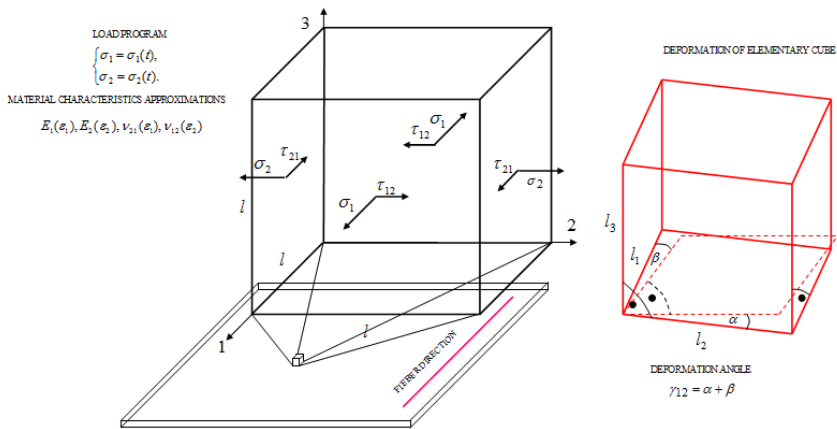


Fig. 1. Geometrical interpretation of stress state

Relations between normal stresses and strains in plane state of stress can be written as:

$$(1) \quad \begin{cases} \varepsilon_1 = \frac{\sigma_1}{E_1(\varepsilon_1)} - \nu_{12}(\varepsilon_2) \frac{\sigma_2}{E_2(\varepsilon_2)}, \\ \varepsilon_2 = -\nu_{21}(\varepsilon_1) \frac{\sigma_1}{E_1(\varepsilon_1)} + \frac{\sigma_2}{E_2(\varepsilon_2)}, \\ \varepsilon_3 = -\nu_{31}(\varepsilon_1) \frac{\sigma_1}{E_1(\varepsilon_1)} - \nu_{32}(\varepsilon_2) \frac{\sigma_2}{E_2(\varepsilon_2)}, \end{cases}$$

and after series of transformations:

$$(2) \quad \begin{cases} \varepsilon_1 = f_1(\sigma_1, \sigma_2), \\ \varepsilon_2 = f_2(\sigma_1, \sigma_2), \\ \varepsilon_3 = f_3(\sigma_1, \sigma_2). \end{cases}$$

The introduction of theoretical relation between shear stress and deformation angle is possible in the way of extraction the pure volumetric deformations in the uniaxial tension test. The residual part of energy represents the energy of deformation comes from shear stresses in plains sloped to tensile directions at an angle of 45° .

Let's take a plane state of stress in 1-2 plane and 1 as the fiber direction. Then basing on energy conservation principle, the analytical form of the strain energy density function can be expressed as:

$$(3) \quad W = \int (\sigma_1 d\varepsilon_1 + \sigma_2 d\varepsilon_2 + \tau_{12} d\gamma_{12}).$$

3. Stability assumptions

According to mathematical definition of stability given in [3] for material deformation state, we can write that:

$$(4) \quad \delta^2 W = \frac{\partial^2 W}{\partial \sigma_1^2} (\delta \sigma_1)^2 + \frac{\partial^2 W}{\partial \sigma_2^2} (\delta \sigma_2)^2 + 2 \frac{\partial^2 W}{\partial \sigma_1 \partial \sigma_2} \delta \sigma_1 \delta \sigma_2 + \frac{\partial^2 W}{\partial \tau_{12}^2} (\delta \tau_{12})^2 \geq 0$$

The regions of stability in space $\sigma_1, \sigma_2, \tau_{12}$ can be selected by applying Sylvester's theorem to (4) presented as quadratic form.

4. Conclusions

The main conclusions are the following:

- the mechanical properties of nonlinear-elastic orthotropic material can be modeled with using an energy-based model,
- nonlinear elasticity and orthotropic properties of material have a significant influence on shape of stability region,
- the classic form of Hook's law can not be applied to stress-strain relations description in case of nonlinear elasticity.

5. References

- [1] R. Mucke and O. Bernhardt (2003). A constitutive model for anisotropic materials based on Neuber's rule, *Computer methods in applied mechanics and engineering* 2003, vol. 192, n°37-38, 4237-4255 .
- [2] R.W. Ogden (1997). Non-linear elastic deformations, *Dover Publications, Mineola, New York*.
- [3] T. Wegner (2005). Matematyczne modelowanie mechanicznych właściwości materiałów, *Biuletyn WAT*, vol. LIV, nr 12, 5-51.

MODELING THE STRAIN INDUCED MARTENSITIC TRANSFORMATION UNDER IMPACT AND ITS INFLUENCE ON THE TAYLOR-QUINNEY COEFFICIENT

R. Zaera¹, J.A. Rodríguez-Martínez¹ and D. Rittel²

¹*Department of Continuum Mechanics and Structural Analysis. University Carlos III of Madrid. Avda. de la Universidad, 30. 28911 Leganés, Madrid*

²*Faculty of Mechanical Engineering, Technion, 32000 Haifa, Israel*

1. Abstract

The main source for temperature increase in the absence of external heat usually comes from plastic dissipation. In practice, a correct evaluation of this dissipation is needed for a proper evaluation of material softening in high strain rate applications. Following Tresca [1], Taylor and coworkers [2, 3] were the first who observed that plastic work is not entirely converted into heat in the deformation of metals, so that part of it is stored in cold work. Following these seminal contributions, the Taylor-Quinney coefficient β has been defined as the ratio of dissipated to plastic works (in its integral form β_{int}), or dissipated to plastic powers (in its differential form β_{diff}). These coefficients are used to calculate the temperature increase in the simulation of dynamic processes.

Different authors have measured those coefficients in polymers and metals by using a variety of experimental techniques such as thermography, embedded thermocouples or high speed infrared detectors. For the sake of simplicity it is often assumed that both β factors are constant, usually taking a value lower than 1, or equal to 1 when all the plastic work is used to heat the material [4]. Once determined, they can be used in a model to calculate thermal output work as a fraction of the dissipated input plastic power. However, different authors reported a functional dependence of β_{int} upon strain and/or strain rate [5, 6, 7], a fact that may significantly complicate the solution of the coupled heat equation.

When plastic deformation is governed by dislocation slip, this dependence has been explained through the effect of strain hardening in the dislocation density increase and work converted into heat. However additional processes may take place during plastic deformation, of which twinning is quite commonly observed, as a mechanism that stores little energy of cold work while contributing significantly to the strain hardening. Additional phenomena may be induced by high rate straining of crystalline solids, among which dynamic recrystallization [8], or even phase transformations, such as the conversion of austenite to martensite, well known to occur in a reversible way in pure iron [6] or to develop in many ferrous alloys such as metastable austenitic steel of the 3XX series [9]. In such cases, the measured temperature rise comprises the effects of exothermal phase transformations during which latent heat is released. When this is the case, a simple ratio of the thermal to mechanical work, into which this extraneous heat source is included, may yield effective values of β_{int} which exceed 1, as reported e.g. by Rittel et al. [6] for pure iron, by Rusinek and Klepaczko [7] for TRIP steels or by Jovic et al. [10] for austenitic steels.

Considering specifically strain-induced phase transformations, the Strain Induced Martensitic Transformation (SIMT), is found in multiphase TRIP steels and metastable austenitic grades. This type of martensitic transformation occurs in a given range of temperatures M_s^σ to M_d covering the in-service conditions of TRIP and austenitic steels in many industrial applications. Above M_s^σ the stress needed for martensite nucleation exceeds the flow stress of the austenitic phase, which should thus strain-harden to sustain martensite formation. As the temperature rises, austenite stability increases thereby limiting the transformation. Above M_d , martensite is not produced anymore.

Therefore a strong coupling is expected to exist between SIMT and heat generation in these

alloys: SIMT contributes to heat through a latent heat term, and heat, in turn, hinders SIMT. Thus the latent heat released during martensitic transformation should modify the ratio of dissipated to plastic power. And the weight of dislocation mediated (slip) plasticity in the inelastic deformation of the alloy should progressively decrease as austenite transforms into martensite, analogous to a twinned phase, thus leading to additional changes in the value of the stored energy of cold work. All these factors will most likely affect the value of the Taylor-Quinney coefficient upon deformation.

This contribution presents a theoretical approach to evaluate the variability of the Taylor-Quinney coefficient in steels exhibiting SIMT. A constitutive model, previously proposed by Zaera et al. [11], and now modified to account for the different heat rates, has been used. This model includes temperature effects in the phase transformation kinetics, and in the softening of each solid phase through the use of a homogenization technique. The model also allows considering the influence of triaxiality in the SIMT. The new model sheds light on previous experimental results reporting unusual (> 1) values for β_{int} , [6, 7, 10], apparently related to an exothermal phase transformation, through a differential treatment of the dissipative terms, namely latent heat, and heat due to austenite and martensite deformation. Likewise the model accounts for the strong coupling existing between strain rate, stress state, heat and martensitic transformation, thus allowing to perform a thorough analysis of their influence in the evolution of the ratio of dissipated to plastic work. The variability observed in the integral Taylor-Quinney coefficient shows the inherent limitations of assuming a constant value of β_{int} when modeling high strain rate problems in alloys showing SIMT. On the contrary, taking into account the functional dependence of β_{int} avoids considering an averaged value which may either under- or over-estimate the heat dissipated during the deformation process.

- [1] H. Tresca (1879). Sur la fluidité et l'écoulement des corps solides, *Annales du Conservatoire des Arts et Mtiers*, **4**.
- [2] W. S. Farren and G. I. Taylor (1925). The heat developed during plastic extension of metals, *Proceedings of the Royal Society. London*, **A107**, 422-451.
- [3] G. I. Taylor and H. Quinney (1934). The latent energy remaining in a metal after cold working, *Proceedings of the Royal Society. London*, **143**, 307-326.
- [4] R. Kapoor and S. Nemat-Nasser (1998). Determination of temperature rise during high strain rate deformation, *Mechanics of Materials*, **27**, 1-12.
- [5] D. Macdougall (2000). Determination of the plastic work converted to heat using radiometry, *Experimental Mechanics*, **40**, 298306.
- [6] D. Rittel and G. Ravichandran and A. Venkert (2006). The mechanical response of pure iron at high strain rates under dominant shear, *Materials Science and Engineering A*, **432**, 191201.
- [7] A. Rusinek and J. R. Klepaczko (2009). Experiments on heat generated during plastic deformation and stored energy for TRIP steels, *Materials and Design*, **30**, 35-48.
- [8] D. Rittel and P. Landau and A. Venkert (2008). Dynamic recrystallization as a potential cause for adiabatic shear failure, *Physical Review Letters*, **101**, 165501.
- [9] J. A. Rodríguez-Martínez and R. Pesci and A. Rusinek (2011). Experimental study on the martensitic transformation in AISI 304 steel sheets subjected to tension under wide ranges of strain rate at room temperature, *Materials Science and Engineering A*, **528**, 5974-5982.
- [10] C. Jovic and D. Wagner and P. Herve and G. Gary and L. Lazzarotto (2006). Mechanical behaviour and temperature measurement during dynamic deformation on split Hopkinson bar of 304L stainless steel and 5754 aluminium alloy, *Journal Physique IV*, **134**, 1279-1285.
- [11] R. Zaera and J. A. Rodríguez-Martínez and A. Casado and J. Fernandez-Saez and A. Rusinek and R. Pesci (2012). A constitutive model for analyzing martensite formation in austenitic steels deforming at high strain rates, *International Journal of Plasticity*, **29**, 77-101.

THERMOMECHANICAL MODEL FOR AUSTENITIC STEEL WITH MARTENSITIC TRANSFORMATION INDUCED BY TEMPERATURE AND STRESS VARIATION

G.Ziętek¹, Z.Mróz²

¹ Wrocław University of Technology, Wrocław, Poland

² Institute of Fundamental Technological Research, Warsaw, Poland

1. Introduction

The martensitic phase transformation in austenitic steels may be induced by changes of temperature, stress or plastic deformation. The growth of the second phase affects strength properties of material, particularly the hardening rate occurring during monotonic or cyclic deformation. This phenomenon should be taken into account in formulation of the constitutive equations. The materials subjected to martensitic transformation have been extensively investigated by applying the framework of thermodynamic of irreversible processes with account for internal state parameters [1, 2, 3]. The internal variables represent phenomenologically the internal structure of material and its effect on the macroscopic response during plastic deformation accompanied by martensitic transformation. The selection of proper internal variables, formulation of the Helmholtz free energy and the dissipation potential, provide a framework for formulation of constitutive relation specifying flow rule, hardening rate and phase evolution.

The present work is aimed at description of the inelastic material response during coupled plastic deformation and martensitic transformation occurring during varying stress and temperature states. The main attention is focused on the identification of the thermomechanical internal variables and the conjugate driving force associated with progressive or reverse plastic flow and martensitic transformation. The assumed free energy and dissipation functions provide specification of driving and dissipative forces. The model is applied to simulate uniaxial and biaxial cyclic deformation curves and related temperature variations.

2. Material model – main assumptions

There are two modes of martensitic transformation: mechanically induced [1] (*stress-assisted* and *strain-induced martensite*) or thermally induced [2]. These two modes correspond to different generation of the nucleation sites and to different morphologies of martensite in a form of plate or lathlike structures. In the literature, two kinds of martensite are distinguished, namely the martensite induced by proper temperature variation and the martensite induced by stress or plastic strain variations [1, 2]. The most popular macroscopic parameter ξ representing the volume fraction of martensite can now be decomposed into two portions, $\xi = \xi_T + \xi_\sigma$, where ξ_T represents the fraction of martensite induced by temperature variation and ξ_σ is the martensite fraction transformed by stress or plastic strain variation (oriented martensite).

The two-phase material is treated as a thermodynamic system with three coupled irreversible processes namely, plastic deformation and two kinds of phase transformation. Thus, three conditions of process occurrence must be formulated.

- the yield condition

$$(1) \quad F_p = \sqrt{J_2(\sigma_{ij} - f_{ij}(X_{ij}, T, \xi))} - R_p(T, \xi) \leq 0,$$

- the condition of transformation induced by stress variation

$$(2) \quad F_1^r = -\Sigma_\sigma + \beta \sqrt{\frac{3}{2}(s_{ij} - Z_{ij}^d)(s_{ij} - Z_{ij}^d)} - R_1(T, \xi_T, \xi_\sigma) \leq 0,$$

- the condition of transformation induced by temperature variation (progressive transformation austenite→martensite and reverse transformation martensite→austenite)

$$(3) \quad F_2^{tr} = [-\Sigma_T - R_2(T, \xi_T, \xi_\sigma)] [-\Sigma_T - R_3(T, \sigma_m, \xi_T, \xi_\sigma)] \leq 0,$$

where s_{ij} is the stress deviator, $\sigma_m = \frac{1}{3}\sigma_{ii}$ is the mean stress and T denotes the temperature. Σ_T and Σ_σ are the driving forces conjugate to volume fraction of martensite. The yield condition (1) takes a familiar Huber-Mises form, but the kinematic hardening represented by the translation of yield surface is specified the deviatoric tensor f_{ij} related to the back stress X_{ij} . Equation (2) represents the transformation condition connected with the stress loading but it can be activated by temperature variation and equation (3) determines the condition of transformation induced by the temperature variation. Next, the set of internal parameters is chosen, two parameters connected with plastic straining: microstrain $\boldsymbol{\eta}$ conjugate to the backstress \mathbf{X} , \mathbf{z} conjugate to the backstress \mathbf{Z} and two parameters representing volume fraction of martensite: ξ_T, ξ_σ conjugated to driving force Σ_T and Σ_σ . The specific free energy is assumed in the form:

$$(4) \quad \rho\Psi = \frac{1}{2}\Lambda_{ijkl}\varepsilon_{ij}^e\varepsilon_{kl}^e - \gamma\varepsilon_m^e T + \rho c_\varepsilon \left((T - T_o) - \ln\left(\frac{T}{T_o}\right) \right) + \frac{1}{2}C_1(\xi_\sigma, \xi_T)\eta_{ij}\eta_{ij} + \frac{1}{2}C_2 z_{ij}z_{ij} + \rho(\varphi_{ch,m} - \Delta\varphi_{ch}(1 - \xi_\sigma - \xi_T) + \psi_{ir})$$

where $\Delta\varphi_{ch} = \varphi_{ch,m} - \varphi_{ch,a}$ is the difference between chemical energy of austenite and martensite. In turn, $\psi_{ir} = \varphi_1(1 - \xi)\xi + \varphi_2\xi_\sigma\xi_T$ is interaction energy between austenite and martensite. Assumption of the associated flow rule (except microstrain $\boldsymbol{\eta}$ and metallurgical strain) allow to deduce a set of constitutive and evolutions equations.

3. Simulation of cyclic uniaxial loading and cyclic changing of temperature

The proposed model has been applied to simulate cyclic hardening response for cyclic tension-compression tests and for varying temperature test. The model parameters for austenitic steel AISI 304 were specified from the identification on the basis of experimental data for the steady state of cyclic tension and compression and from the literature. Examples are presented in Fig. 1.

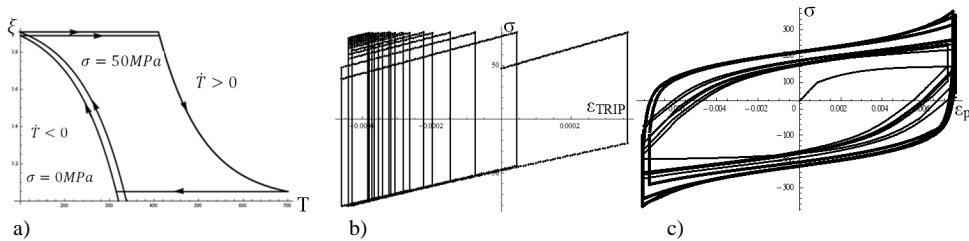


Fig. 1. a) Dependence of the volume fraction of martensite on temperature, b) the hysteresis loop for stress below yield stress, c) the hysteresis loop for the stress above yield stress.

4. References

- [1] M. Panico and L. Brinson (2007). A three-dimensional phenomenological model for martensite reorientation in shape memory alloys, *J. Mech. and Phys. of Solids*, **55**, 2491-2511.
- [2] F.D. Fischer, E.R. Oberaigner and K. Tanaka (1996). A micromechanical approach to constitutive equations for phase changing materials, *Comp. Materials Science*, **9**, 56-63,
- [3] G. Ziętek and Z. Mróz (2011). On the hardening rule for austenitic steels accounting for the strain induced martensitic transformation, *Int. J. of Structural Changes in Solids*, **3**, 21-34.

Experimental Mechanics

EVALUATION OF DYNAMIC PROPERTIES OF PLA/PBAT POLYMER ALLOYS USING TENSILE SPLIT HOPKINSON BAR

M. Nishida¹, H. Watanabe¹, N. Fukuda² and H. Ito³

¹ *Nagoya Institute of Technology, Nagoya, Aichi, Japan*

² *Headquarters, Aichi Center for Industry and Science Technology, Toyota, Aichi, Japan*

³ *Industrial Research Center, Aichi Center for Industry and Science Technology, Kariya, Aichi, Japan*

1. Introduction

The increasing use of plastic products worldwide is causing considerable damage to the environment; therefore, biodegradable plastics (plastics that can decompose in the natural environment) and bio-based plastics (plant-derived or recyclable resource-based plastics) are being extensively investigated, and new biodegradable and bio-based plastics are continuously being developed. Poly(lactic acid) (PLA) is a typical biodegradable bio-based polymer (plant-derived polymer). Polymer blends/alloys or natural fiber reinforcing have been required to overcome the low impact resistance and the brittleness of PLA. Because poly(butylene adipate/terephthalate) (PBAT) is a ductile and biodegradable polymer, polymer alloys of PLA and PBAT have great potential for high impact strength.

In the present study, the stress–strain curves of PLA and PBAT polymer alloys were measured at high strain rates using a tensile split Hopkinson pressure bar (Kolsky bar). The effects of the addition of dialkyl peroxide (compatibilizing agent) and the mixing ratio of PLA and PBAT on the maximum stress, the elongation at break, and fracture morphology were also discussed.

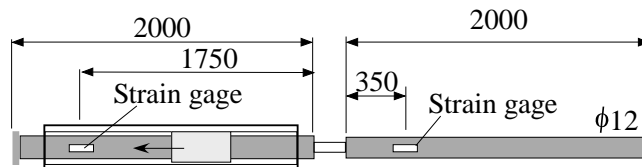


Figure 1 Experimental setup for dynamic tensile tests.

2. Specimens and experimental methods

PLA and PBAT alloys of differing ratios were prepared using PLA from Toyota Motor Corporation (Toyota Eco-Plastic S-17) and PBAT from BASF (Ecoflex). In order to examine the effect of a compatibilizing agent, dialkyl peroxide (NOF Corporation, PERHEXA 25B) was used. The mixing ratios of PLA and PBAT were 60/40, 50/50, and 30/70. The mixing ratios of PLA/PBAT/dialkyl peroxide were 60/40/1, 50/50/1, and 30/70/1. We prepared the polymer alloys using a twin-screw extruder (Technovel Co., Osaka Japan) at 180°C. The screw speed was 400 rpm, and the feed rate was 100 g/min. After melt mixing, the strands prepared by the twin-screw extruder were cooled rapidly, pelletized, and then dried. Next, 10-mm-thick plates were prepared using a conventional hot press at 190°C and 5 MPa for 30 min.

Dynamic tensile test specimens with a gage mark area of approximately 2 mm × 2 mm and a gage length of 4 mm were used. Specimens for dynamic tensile tests were produced from plates of 5 mm thickness using a milling machine. At high strain rates of 500 to 1000 s⁻¹, the tensile properties of the specimens were examined by the tensile split Hopkinson (Kolsky) bar test, as shown in Fig. 1. The input and output bars were made of stainless steel (SUU304), and their diameter and length were 12 mm and 2000 mm, respectively. Strain gages were applied to both the input and output bars at

distances of 1750 mm and 350 mm from the specimen, respectively. Because the stress histories were almost the same on both ends of the specimens, the strain and stress on the specimens were calculated from the strain on the bars, as measured by the strain gages, using the following equations [1-2]:

$$(1) \quad \sigma_{av}(t) = \frac{AE}{A_s} \varepsilon_T(t)$$

$$(2) \quad \varepsilon_{av}(t) = \frac{2c_3}{L} \int_0^t [\varepsilon_I(t) - \varepsilon_T(t)] dt .$$

Here ε_I and ε_T are the axial strains induced in the input bar by the incident wave and in the output bar by the transmitted wave, respectively. E and c_3 are Young's modulus and elastic wave velocity, respectively, of both the input and the output bars. L is the gage length. A and A_s are the cross-sectional areas of the input/output bars and specimens, respectively.

3. Results and discussion

Figure 2(a) shows the stress–strain curves without dialkyl peroxide and Fig. 2(b) shows the stress–strain curves of dialkyl peroxide addition. The 50/50/1 and 30/70/1 specimens of PLA/PBAT/dialkyl peroxide did not break at a strain of 0.34 under this experimental condition. Regardless of dialkyl peroxide addition, the maximum stress decreased and the elongation at break increased with increasing PBAT content. Comparing Fig. 1(a) to (b), it was concluded that the dialkyl peroxide addition clearly increased the elongation at break. In particular, for the PLA/PBAT ratios of 60/40, 50/50, and 30/70, the dialkyl peroxide addition dramatically increased the elongation at break. When the PLA/PBAT ratio was 80/20, the dialkyl peroxide addition only slightly increased the elongation at break. Compared to the elongation at break, the dialkyl peroxide addition had less or no effect on the maximum stress.

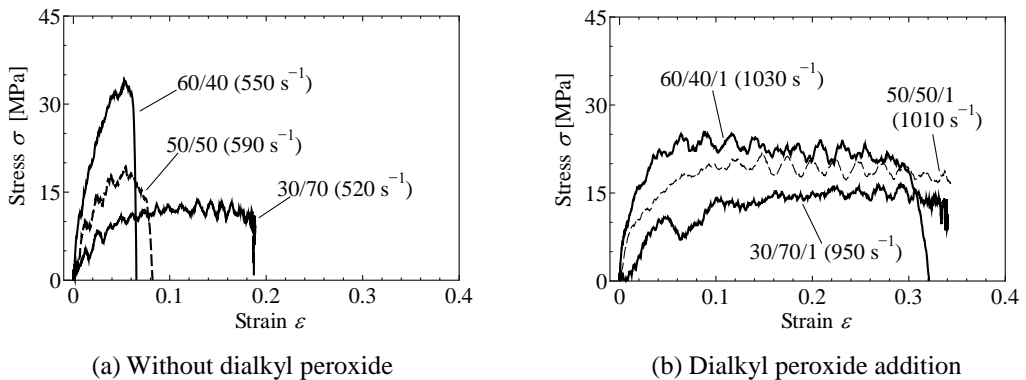


Figure 2 Effect of PBAT content on stress–strain curve.

4. Conclusion

The stress–strain curves of PLA/PBAT and PLA/PBAT/dialkyl peroxide specimens were measured using the tensile split Hopkinson pressure bar. When dialkyl peroxide was added, the elongation at break clearly increased with increasing PBAT content. The dialkyl peroxide addition increased the elongation at break and the areas under the stress–strain curve before the breaking point.

5. References

- [1] G.T. Gray III (2000). Classic split Hopkinson pressure bar testing, *ASM Handbook Vol. 8, Mechanical Testing and Evaluation*, 462-476.
- [2] W. Chen and B. Song (2010), *Split Hopkinson (Kolsky) Bar: Design, Testing and Applications*, Springer.

INVESTIGATION OF MICROSTRUCTURAL INFLUENCES ON THE MECHANICAL PROPERTIES OF CU-AG EUTECTIC ALLOY

Srihari Dodla and Albrecht Bertram

*Institute of Mechanics, Otto von Guericke University
39106 Magdeburg, Germany*

Copper-Silver compositions are used to produce high strength, high conductor wires and sheets for the pulsed and resistive magnets. The specimen of 20 mm diameter is obtained from the continuous casting of Cu-60at%Ag eutectic alloy. The material was cold formed to a diameter 12.5 mm and it was drawn to a diameter of 6.7 mm. In this study, Cu-Ag samples of diameter 12.5 mm and 6.7 mm have been taken for the microstructure evolution and finding its mechanical behavior. The samples were prepared in both drawing and transverse directions. The aim of this study is to analyze the microstructure and modeling the nonlinear behavior of the material and its verification by experiment. The inspection of microstructure was done using optical microscope and scanning electron microscope. The lamella spacing, the thickness of Cu and Ag was investigated. The lamella thickness and spacing were measured to quantify the changes in microstructure for both drawing and transverse directions. The microscopy results shown that eutectic Cu-60at%Ag composite has a homogenous distribution of alternating Cu and Ag lamella layers. The mechanical properties of a eutectic Cu-Ag alloy were investigated at room temperature by compression tests. The material has high anisotropy level and its effective properties depend on lamella orientation. From experimental compression tests, an attempt is made to model the material behavior using classical elasto-plastic nonlinear hardening law. At the end, material properties required for the assumed model are approximated. The results are in good agreement.

Assumptions involved

- The deformations are small.
- The hardening is isotropic and can be modeled by Voce-law.
- The plastic and hardening behavior are rate independent.

Experimental method

In order to analyze the microstructure of two samples having diameter 12.5 mm and 6.7 mm, transverse and longitudinal sections were cut perpendicular and parallel to the rolling direction for microstructural observation. To prepare for metallographic analysis, all samples were cold mounted, hand ground using 180-, 320-, 600-, 800-, 1200-grit SiC paper, hand polished with 3- μ m diamond paste and given a finer polish with 1- μ m in diameter, to produce a smooth surface. Specimens were chemically etched for 45 seconds in Nital (20-40% nitric acid in 80-60% ethanol) depending on the strain level. The microstructure was observed with a scanning electron microscope (SEM) and an optical microscope.

Results

Figs. 1 and 2 are SEM and optical microscope images showing the microstructure of the Cu-72 mass% Ag alloy. The porosity of Cu-72mass% Ag alloy can be appreciated in Fig. 1(a). The transverse section, shown in Fig.1, displays typical Cu-Ag alloy microstructural features for both the specimens. The darker phase is the Cu-rich solid solution, while the lighter regions are Ag-rich solid solutions.

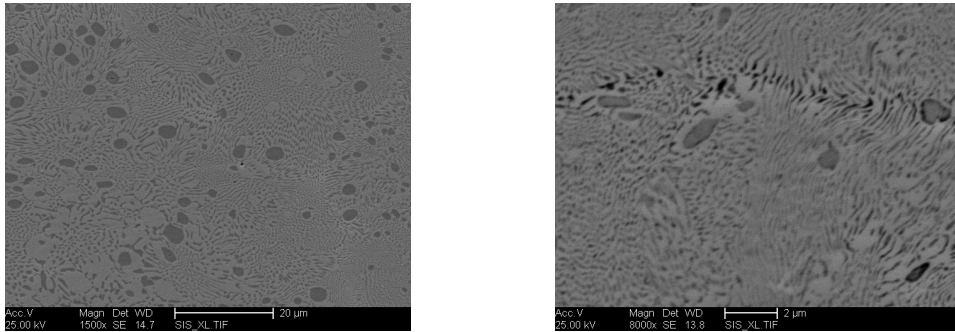


Fig.1. SEM transverse images of the eutectic Cu-72mass% Ag alloy (a) undeformed specimen (Ø 12.5 mm) and (b) deformed specimen (Ø 6.7 mm)

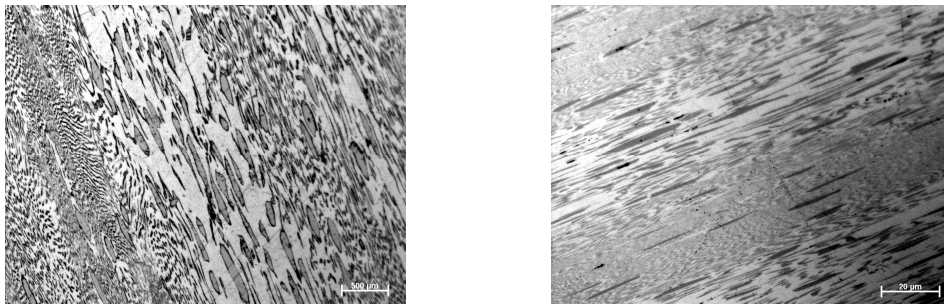


Fig.2. Optical microscope longitudinal images of the eutectic Cu-72mass% Ag alloy (a) undeformed specimen (Ø 12.5 mm) and (b) deformed specimen (Ø 6.7 mm)

Fig.2 (a) represents the curvy lamella pattern due to shearing, the pattern continues with some level of alignment. For a deformed specimen shown in Fig.2 (b), the lamellae are aligned in the drawing direction with continuous refinement.

References

- [1] C. A. Davy, Ke Han, P. N. Kalu and S. T. Bole (2008). Examinations of Cu-Ag Composite Conductors in Sheet Forms, *IEEE Trans. Magn.*, vol. 18, pp.560-563.

EXPERIMENTAL INVESTIGATIONS OF THE INFLUENCE OF MODERATE STRAINS AND STRAIN RATES ON THE YIELD SURFACE OF OFHC COPPER

T. Frąs^{1,2}, R. Pęcherski¹ and A. Rusinek²

¹ *Institute of Fundamental Technological Research, Polish Academy of Sciences (IPPT PAN), Pawińskiego 5B, 02-106 Warsaw, Poland*

² *National Engineering School of Metz (ENIM), Laboratory of Mechanics, Biomechanics, Polymers and Structures, Route d'Arts Laquenexy, 57000 Metz, France*

The aim of the work is to investigate the influence of moderate strains and strain rates of the range of $10^{-4} \leq \dot{\epsilon} \leq 10^{-2} \text{ s}^{-1}$ on the evolution of the yield limit surface. The experimental investigations were performed on the as received oxygen free high conductivity (OFHC) Copper. The specimens were machined from the commercially available round bars of the diameter 12mm. Four kinds of experimental tests were performed: tensile test for smooth round specimens and compression test of smooth cylinders as well as biaxial compression test using cube specimens and double shear tests of cuboid specimens with machined narrow shear zones. The elaborated experimental data show that the investigated material reveals a slight pressure sensitivity showing small strength differential effect of the order of $\kappa = k_c / k_T \approx 1,1$ and certain influence of initial anisotropy, which is confirmed by the investigation of texture pole figures. The effect of initial anisotropy manifests itself in the observed deviation from the Huber-Mises yield condition. The deviation was observed in the confrontation of experimental data using limit values in shear test and biaxial compression test.

To find more adequate description of experimental results the Burzyński yield criterion was applied, [1]. The criterion is assumed for isotropic solids and the effects of initial anisotropy are captured by means of certain correction factor λ . The meaning of this factor can be explained by means of the relation between the yield limits obtained in the tensile k_T , compression k_C and shear k_S tests, respectively [1]:

$$(1) \quad \sqrt{3} k_s^2 = \frac{k_T k_C}{2(1 + \lambda)} .$$

Observe that for ideal isotropy with symmetry of elastic range, $k_T = k_C = k$ the factor λ is equal 0,5 and the above relation takes form $\sqrt{3} k_s = k$ known from the Huber-Mises condition. In general, the Burzyński factor λ takes values in the range $0 < \lambda < 1$. The yield condition for isotropic solids accounting for Burzyński's correction can be expressed in the principal stress axes in the following form [1], and $\sigma_1 \geq \sigma_2 \geq \sigma_3$:

$$(2) \quad (1 - \lambda)(\sigma_2 - \sigma_3)^2 + \lambda(\sigma_3 - \sigma_1)^2 + (1 - \lambda)(\sigma_1 - \sigma_2)^2 + (k_C - k_T)(\sigma_1 + \sigma_2 + \sigma_3) = k_C k_T ,$$

The following states of stress were considered with use of the performed experimental tests:

1. Uniaxial tension: $\sigma_1 = k_T$, $\sigma_2 = 0$, $\sigma_3 = 0$.
2. Uniaxial compression: $\sigma_1 = 0$, $\sigma_2 = 0$, $\sigma_3 = -k_C$.
3. Pure shear: $\sigma_1 = k_S$, $\sigma_2 = 0$, $\sigma_3 = -k_S$.
4. Biaxial compression: $\sigma_1 = 0$, $\sigma_2 = -\nu k_{CC}$, $\sigma_3 = -k_{CC}$

A representation of experimental points in the plane (σ_{eq}, σ_m) together with yield curves of corrected Burzyński (1) and Huber-Mises (2) is displayed below

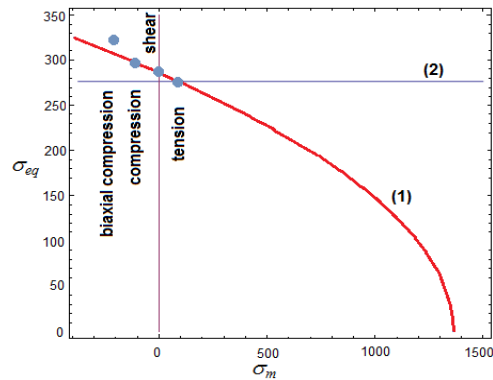


Fig 1. Results of experiments and yield curves in the (σ_{eq}, σ_m) plane.

Another example of yield limit curves for OHFC Cu in the plane state of stress (σ_1, σ_3) and (σ_2, σ_3) for strain rate 0.001 s^{-1} and strain level 0.002 is presented below.

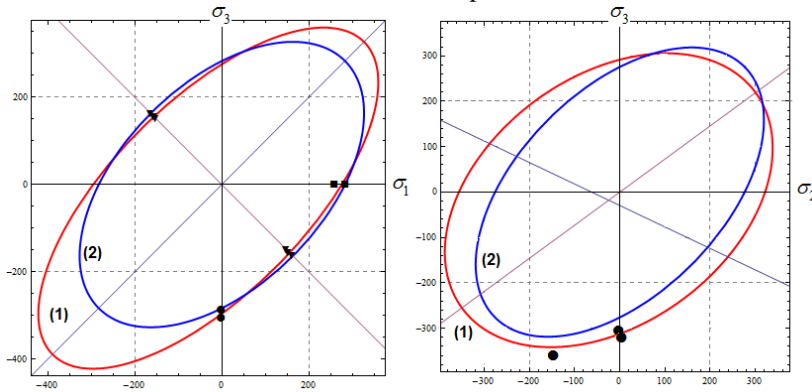


Fig 2. Results of experiments and yield curves in the planes (σ_1, σ_3) and (σ_2, σ_3) .

It is visible that the corrected Burzyński criterion appears more adequate in comparison with the classical Huber-Mises condition.

The study of strain-rate sensitivity shows also that the yield surface increases uniformly with increase of strain-rate. In conclusions, the relation with the studied in the literature effect of the third invariant of the stress deviator (Lode angle), [3-6] is also discussed.

References:

- [1] W. Burzyński: *Studjum nad Hipotezami Wyteżenia*, Akademia Nauk Technicznych, Lwów 1928; cf. also English translation: *Selected passages from Włodzimierz Burzyński's doctoral dissertation: "Study on Material Effort Hypotheses"*, Engng. Trans., **57**, 185-215, 2009.
- [2] Bai, T. Wierzbicki: *A new model of metal plasticity and fracture with pressure and Lode dependence*, International Journal of Plasticity **24**, 1071–1096, 2008.
- [3] N.J. Huffington: *A re-examination of the plastic flow criterion for Copper*, Technical report BRL-TR-3368, 1992.

A STUDY ON STRAIN RATE SENSITIVITY OF TRANSFORMATION BEHAVIOR OF ON TRIP STEEL BY CAPTURING CHANGE IN IMPEDANCE

Daiki Inoshita¹, Shiro Yamanaka² and Takeshi Iwamoto³

¹*Graduate School of Engineering, Hiroshima University, 1-4-1 Kagamiyama, Higashi-Hiroshima, Hiroshima, 739-8527 JAPAN, b086560@hiroshima-u.ac.jp*

²*Kawasaki Heavy Industries, 1-1-3 Kawasaki, Kobe, Hyogo,*

³*Faculty of Engineering, Hiroshima University, 1-4-1 Kagamiyama, Higashi-Hiroshima, Hiroshima, 739-8527 JAPAN, iwamoto@mec.hiroshima-u.ac.jp*

Key words: TRIP Steel, Strain-induced Martensitic Transformation, Impedance, Alternating Current Potential Difference, Maxwell Bridge

When steels which have a metastable austenitic phase are deformed plastically, the phase partially transforms to a stable martensitic phase. This phenomenon is called strain-induced martensitic transformation (SIMT). The steel with SIMT can be expected to increase not only its strength but also ductility and toughness because of a transition to the martensitic phase. The steel with these excellent mechanical properties by SIMT is called TRIP (TRansformation Induced Plasticity) steel [1].

For automotive industries, a thickness of members can be decreased easier because of its excellent ductility if TRIP steel can be applied for shock absorption members. This advantage is connected to weight reduction of automobiles. However, transformation behavior of TRIP steel is not clarified. Therefore, in order to improve a reliability of TRIP steel, it is essential to clarify the amount of transformed martensite which may determine such excellent characteristics of TRIP steel.

In previous studies [2][3], the amount of transformed martensite has been measured quasi-statically during deformation by capturing impedance. Since martensite indicates a ferromagnetic characteristic, it can be measured continuously by impedance including inductance during plastic deformation. However, this experimental study have been conducted at only single strain rate even though a deformation behavior of TRIP steel shows strain rate sensitivity [4]. The above mentioned members is crashed at high strain rate. Therefore, it is important to discuss about the strain rate sensitivity of SIMT. In addition, the amount of martensite at various strain rates have been evaluated by measuring the volume resistivity [5]. Unfortunately, it can be said that this method is likely to be affected by a noise and change in resistance caused by internal defects such as dislocations and thermal effect concerning with deformation. Thus, it is difficult to extract the effect of martensite from the signals obtained by change in volume resistivity.

In this study, it is attempted to capture the amount of transformed martensite experimentally by measuring continuous change in impedance during plastic deformation. A specimen made of AISI 304, which is a kind of TRIP steel, is used for a core of a prototype solenoid coil and compressed quasi-statically inside the coil at the various strain rates. During the compressive test, two kind of circuits based on both alternating current potential difference method and Maxwell bridge are manufactured by authors to measure continuous change in impedance. Then, comparing measurement value obtained by a commercial LCR meter and prototype circuits manufactured, validity and characteristics of both circuits manufactured will be shown. Finally, it will be challenged

that the strain rate sensitivity of the change in impedance of TRIP steel will be discussed by comparing the rate of the change in impedance at each strain rate.

References

- [1] Imao TAMURA, Tetsu-to-Hagane, Vol.56(1970), pp.429-445.
- [2] B.D.Westermo and L.D.Thompson, SPIE, Vol.2446(1995), pp.37-46.
- [3] Masanori OHORI et al., Production Research, Vol.52, No.5(2000), pp.39-42.(in Japanese)
- [4] Yoshinori TAKAGI et al., Vol.97, No.8(2011), pp.44-50. (in Japanese)
- [5] Hidefumi Date et al., Proc. Jpn. Soc. Mech. Eng., (2001), pp.363-364.(in Japanese)

INFLUENCE OF ALUMINUM ALLOY SURFACE TREATMENTS AND CURING TEMPERATURE FOR BONDING STRENGTH AND STRAIN CONCENTRATION

M. Kneć¹ and T. Sadowski²

*¹Civil Engineering Laboratory ²Department of Solid Mechanics
Faculty of Civil Engineering and Architecture, Lublin University of Technology
Nadbystrzycka 40, 20 618 Lublin*

Keywords: bonding, DIC, strain concentrations, alodining, Aramis, SLJ

1. Abstract

Aluminum bonding is widely used in many aviation applications. In this article we investigate technological aspects the quality of bonding adherends by different surface treatment for bonding purposes including abrasive paper, degreasing and alodining. Moreover, each of the surface treatment methods are compared according to three cure temperatures and vacuum adhesive melting. The finding of optimal solution for surface of adherends and adhesive preparation lead to significant increase of the joints strength and durability.

Helicopter factories commonly use aluminum alloys with high strength - i.e. 2024 (Pa7 - old Polish Standards). The investigated material is mainly used in inner helicopter parts, transitions, gears, pistons, couplings etc. However, structural helicopter elements require the application of joining techniques, and one of each is the bonding technique.

Collecting bonding strength results for different surface preparations, different cure temperature and bond preparation together gives clear base to choice adequate method for application. All of the specimens has been prepared using the same condition - load during curing, the same bond and curing time.

A special surface treatment method, called alodinasation, was used [1]. Alodining is a process in which a metal is coated with a chemical called alodine. This coating hardens the surface and increases bonding contact area.

The paper presents experimental investigation of the mechanical response of Single Lap Joints (SLJ) taking into account the above specified technological aspects. The SJL samples, made of aluminum alloy 2024 T45 with tensile strength 400 - 410 MPa, were subjected to quasistatic uniaxial loading. The thickness of the joint parts was 2mm, whereas the bonding area was 15x15 mm. Fracture toughness parameters G_I and G_{II} were estimated by double cantilever beam test and 4-point bending test, in order to estimate bonding layer properties necessary to numerical SLJ modeling. The whole deformation process was observed by the Digital Image Correlation (DIC) method (ARAMIS system).

The obtained results lead to the conclusion that the best choice is the alodinasation technique both for surface preparation and for adhesive preparation by vacuum melting. All characteristic parameters, like fracture toughness parameters, strength of the joints and the energy absorption to the final failure of the samples, are significantly higher in comparison to the classical technique of the joints production.

2. References

- [1] A. Posmyk (2010). Warstwy powierzchniowe aluminiowych tworzyw konstrukcyjnych, WPS.
- [2] L. Marsavina, T. Sadowski, M. Kneć (2009), Crack propagation paths near bi-material interfaces. Int. Conf. Fracture, Montreal (Canada).

DIRECT IMPACT COMPRESSION TEST OF TANTALUM - EXPERIMENTAL INVESTIGATION AND MODEL IDENTIFICATION

Zbigniew Kowalewski, Zdzisław Nowak and Wojciech Moćko
Institute of Fundamental Technological Research, Warsaw, Poland

1. Introduction

The examples of high strain rate of loading, high speed impact, high speed machining, and high dissipation of energy at forming processes take place in many engineering applications. In order to predict and control behaviour of materials used under such extreme loading conditions, the mechanical parameters of materials should be precisely identified. It is well known that the mechanical behaviour of metal depends on the strain rate level. The Split Hopkinson Pressure Bar (SHPB) or Kolsky apparatus are widely used for the investigations of mechanical properties of materials at high strain rates up to $1.0 \times 10^3 \text{ s}^{-1}$. In order to reach strain rates higher than $1.0 \times 10^3 \text{ s}^{-1}$, Dharan and Hauser (1970) [1] introduced a modification of the SHPB concept by eliminating the incident bar. Thus, application of the direct impact of a striker onto a small disk or prismatic specimen supported by the transmitter bar enabled to reach strain rates up to $0.5 \times 10^6 \text{ s}^{-1}$. Such modification can be defined as the Direct Impact Compression Test (DICT), cf. Jia and Ramesh (2004) [2] or Malinowski, Klepaczko and Kowalewski (2007) [3].

2. Problem formulation

Experimental and numerical investigations of the effect of strain rate on mechanical properties of pure tantalum are presented. Experimental studies were carried out on Direct Impact Compression Testing stand. Miniaturization of the experimental setup with specimen dimensions: diameter $d_s=1.5 \text{ mm}$ and thickness $l_s=0.50 \text{ mm}$, Hopkinson transmitter bar diameter $d_H=3.0 \text{ mm}$ and striker $d_I=11.5 \text{ mm}$ and $l_I=12 \text{ mm}$, with application of a novel optical arrangement in measurement of striker velocity, enabled compression tests to be carried out at strain rates within the range from $1.0 \times 10^3 \text{ s}^{-1}$ to $0.5 \times 10^6 \text{ s}^{-1}$. Perzyna constitutive model for the elasto-viscoplastic material, cf. Perzyna (2011) [4], was applied to predict the dynamic compression yield strength of the tantalum tested at different strain rates. The formulation of the Perzyna model with Voce hardening law can be expressed in the following way:

$$\bar{\sigma}(\bar{\epsilon}^p, \dot{\bar{\epsilon}}^p, T) = [(A + B(1 - \exp(-C\bar{\epsilon})))] \left[1 + (T_{rel}(\dot{\bar{\epsilon}}^p) \cdot \bar{\epsilon}^p)^D \right] (1 - \Theta^m) \quad (1)$$

where T_{ref} is relaxation time, and A, B, C, D, and m are material parameters, Θ denotes the modified temperature given by:

$$\Theta = \frac{T - T_0}{T_m - T_0} \quad (2)$$

where T_0 is the temperature of reference and T_m is the melting temperature.

The main objective of the paper was to investigate either experimentally or numerically a behaviour of tantalum using DICT technique. The special emphasis was taken on the description of the strain rate influence on the basic mechanical properties of pure tantalum. In order to extend the range of the analysed strain rates the experimental programme was supplemented by tests carried out on the SHPB testing stand and quasi-static hydraulic servo-controlled testing machine.

3. Experimental identification of the material model

The identification of the constitutive model parameters was obtained by an inverse method. Numerical simulation was performed with application of ABAQUS finite element program. The own VUMAT was implemented for calculations. The identification of constants was carried out using the true stress-strain diagrams. These curves were generated from the experimental tests performed at various strain rates. The elasto-viscoplastic model parameters were determined for each kind of specimen. Firstly, the computations were started assuming a broad range of the feasible parameters. Starting values of the model parameters were assumed and calculations carried out. In the next stage the final material constants were determined, and then the model was applied to execute numerical simulation in order to obtain final reaction force and displacement.

Generally, there was a good match between the experimental data and the Perzyna overstress model predictions for strain rates up to 0.5×10^6 1/s, Fig.1.

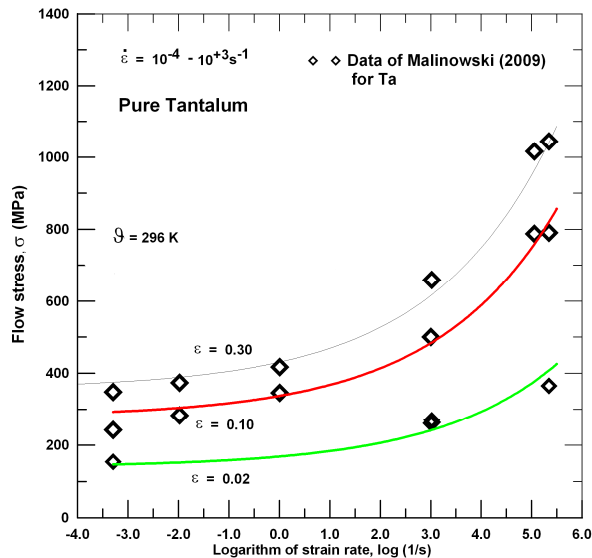


Fig. 1. Comparison of the current Perzyna model (solid lines) and the experimental flow stress data (symbols \diamond) of pure tantalum with respect to logarithmic strain rate at 296 K (results for three strain levels were considered, i.e. $\epsilon=0.02, 0.1$ and 0.3).

Acknowledgement: The research reported in this paper was partly supported by the National Centre for Research and Development, project No O R00 0056 07.

4. References

- [1] Dharan C.K.H. and Hauser F.E., Determination of stress-strain characteristics at very high strain rates, *Exp. Mech.*, **10**, 370, 1970.
- [2] Jia D., Ramesh K.T., A rigorous assessment of the benefits of miniaturization in the Kolsky bar system, *Exp. Mech.*, **44**, 445, 2004
- [3] Malinowski J.Z, Klepaczko J.R., Kowalewski Z.L, Miniaturized compression test at very high strain rates by direct impact, *Exp. Mech.*, **47**, 451, 2007.
- [4] Perzyna P., Micromechanics of localized fracture phenomena in inelastic solids generated by impact-loaded adiabatic processes, *Eng. Trans.*, **59** (4), 299, 2011.

VARIATIONS OF STRESS STATE COMPONENTS DURING STEP CYCLIC LOADING OF POWER PLANT STEEL

Z.L. Kowalewski¹, T. Szymczak²

¹ Institute of Fundamental Technological Research, Warsaw, Poland

² Motor Transport Institute, Warsaw, Poland

1. Introduction

The essential attempt for reduction of forces acting in the selected metal forming processes has been done by Korbel and Bochniak [1] who modified procedures of forging and extrusion by an application of cyclic torsion. Nowadays, this subject is still widely investigated by other research groups i.e. [2-4] since it seems to be very promising for many other possible applications. Better knowledge of this subject is important for both industrial and research groups, since it may improve selected manufacturing processes and the numerical simulation by taking into account new effects observed in materials. Therefore, it was decided in this paper to investigate how the amplitude and frequency of torsion cycles influence the axial stress–axial strain characteristic of power engineering steel. A significant difference of this research in comparison to previous papers is related to the levels of magnitude of the cyclic strain amplitude. In all our experiments it was less than 1%.

2. Experimental procedure and results

All tests were carried out at room temperature using thin-walled tubular mini-specimens (Fig. 1) made of the 10H2M steel subjected to biaxial stress state controlled by strain signals. Monotonic tension was combined with cyclic torsion, Fig. 2. Four blocks of cyclic torsion of amplitude equal to: $\pm 0.1\%$, $\pm 0.2\%$, $\pm 0.4\%$, $\pm 0.8\%$ were considered.

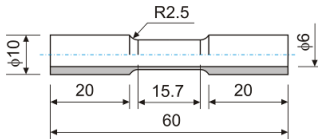


Fig. 1. Geometry and dimensions of mini-specimen.

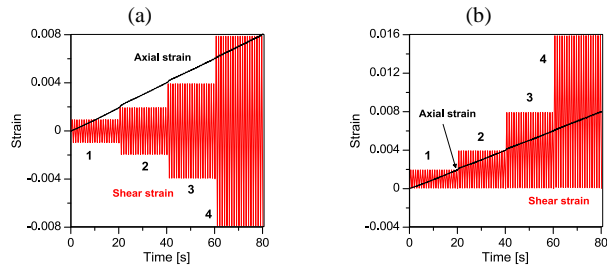


Fig. 2. Two types of loading programme comprised monotonic tension and: (a) symmetric torsion cycles; (b) asymmetric torsion cycles.

The stress responses into the strain controlled programme shown in Fig. 2 are presented in Fig. 3. A comparison of the conventional tensile characteristic with similar curve determined while the torsion cycles were applied shows a gradual decrease of the axial stress when the shear strain amplitude increases. It attained the level of 400 MPa what was almost equivalent to the unloaded state in the tensile direction for the highest strain amplitude considered, Fig. 3. Such behaviour was observed independently on the type of cyclic loading (symmetric and asymmetric).

Besides of an influence of the cyclic strain amplitude on the monotonic tension, effects of cyclic loading frequency were also investigated at wide range of magnitudes, i.e. from 0.005Hz to 15Hz. Investigations were carried out for the 10H2M steel and their results are illustrated in Fig. 4.

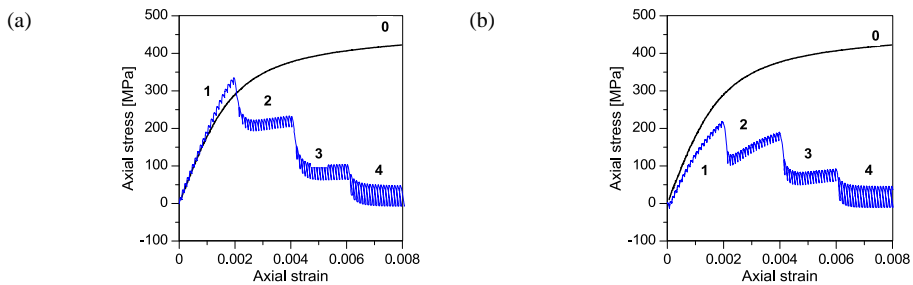


Fig. 3. Comparison of partial tensile characteristics determined without (0) and with assistance of torsion cycles for loading paths shown in: (a) Fig. 2a and (b) Fig. 2b. Numbers 1, 2, 3, 4 correspond to strain amplitudes: $\pm 0.1\%$, $\pm 0.2\%$, $\pm 0.4\%$, $\pm 0.8\%$, respectively.

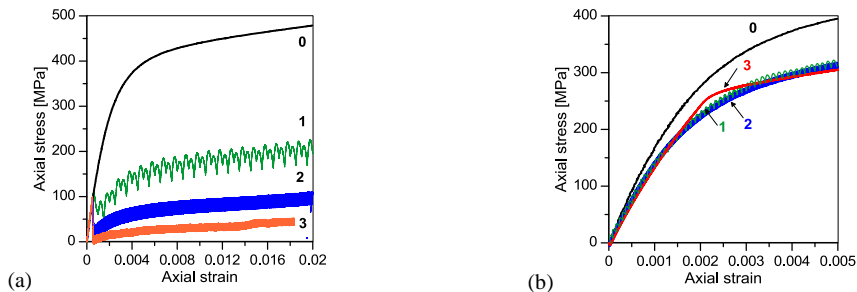


Fig. 4. An influence of frequency of torsion cycles on tensile curve of the 10H2M steel for: (a) strain amplitude of $\pm 0.4\%$ and frequency equal to: (1) - 0.005Hz, (2) - 0.05Hz, (3) - 0.5Hz; (b) strain amplitude of $\pm 0.1\%$ and frequency equal to: (1) - 1Hz, (2) - 5Hz, (3) - 15Hz.

3. Conclusions

- An increase of the amplitude of cyclic loading leads to gradual lowering of the axial stress.
- Asymmetrical step-increased torsion cycles caused similar effect as that observed under symmetrical torsion cycles.
- An influence of the frequency of torsion cycles on the tensile curve was discovered; it played important role especially for the magnitudes within the range from 0.005Hz to 0.5Hz.

Acknowledgements

The support from the Ministry of Science and Higher Education (Poland) under grant No N N501 121 036 is greatly appreciated.

4. References

- W. Bochniak, A. Korbel, R. Szyndler, R. Hanarz, F. Stalony-Dobrzański, L. Błaż, P. Snarski (2006). New forging method of bevel gears from structural steel, *J. Mater. Proc. Tech.*, **173**, 75–83.
- L.X. Kong, P.D. Hodgson (2000). Constitutive modelling of extrusion of lead with cyclic torsion, *Mater. Sci. Eng.*, **A 276**, 32-38.
- E.C.S. Correa, M.T.P. Aguilar, E.M.P. Silva, P.R. Cetlin (2003). The effect of sequential tensile and cyclic torsion straining on work hardening of steel and brass, *J. Mater. Proc. Tech.* **142**, 282–288.
- Z.L. Kowalewski, T. Szymczak (2011). Modification of simple deformation processes of metallic materials by means of cyclic loading, *Materials Research Innovations*, **15**, 1, 73-76(4).

FRACTURE PROPERTIES DETERMINATION ON PMMA BEAMS IN THREE-POINT BENDING TESTS

J. Loya, J. Fernández-Sáez

*Department of Continuum Mechanics and Structural Analysis,
University Carlos III of Madrid, Spain.*

1. General

The knowledge of fracture behaviour of materials in service conditions like is required to design structural elements and components. In mode I, this behaviour is described by fracture parameters such as the fracture-initiation toughness, which represents the critical value of the Stress Intensity Factor, SIF, at which a crack begins to propagate, and the dynamic fracture energy of the material, which depends on the crack velocity.

For dynamic three-point bending (TPB) tests, special arrangements of the Split Hopkinson Pressure Bar (SHPB) [1- 4] have been proposed, were the SIF can be evaluated experimentally throughout different optical [5, 6] and photoelastic [7] techniques, but in general this require complex equipment. Alternatively, by means of the use of high speed cameras and image-processing techniques [4], a sequence of the Crack Mouth Opening Displacement (CMOD) evolution during the test (see figure 1(a)) was obtained. Assuming that the same relationships between SIF and CMOD used in the static cases apply to the dynamic ones, as is demonstrated in [3], the SIF was evaluated in specimens with different initial crack-length and thickness.

Related to the dynamic crack tip evolution, in particular in polymer specimens, it has been investigated using different experimental methods, such as photoelasticity [8, 9], the method of caustics [10, 11], or by bands [12]. In a previous work [13], authors measured the crack-propagation velocity in PMMA specimens with different initial notch-lengths in quasi-static conditions in TPB tests. For this purpose, using a high-speed photographic equipment, a new methodology able to analyze the crack-propagation process in different planes of the specimen thickness was developed. During the tests, due to the optical properties of the PMMA, the crack-front propagation was recorded using a high-speed camera focussing the crack-propagation plane at oblique angle, as shows the figure 1. By means of an selfmade image-processing code, the crack front and its evolution is clearly distinguished, and the SIF history from the CMOD(t), crack-front evolution, and crack-length and crack-velocity at different planes through the thickness at any time were provided.

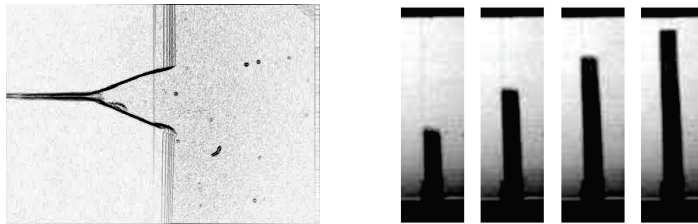


Figure 1. a) Sequence of the CMOD evolution in a dynamic TPB test, b) Sequence of a crack-front propagation in a quasi-static TPB test

From the tests performed on PMMA specimens with different thickness and initial crack-to-width ratios in TPB test in quasi-static and dynamic conditions, following conclusions can be drawn:

- Fracture properties in PMMA cracked beams with different initial crack lengths and thicknesses was measured in quasi-static and dynamic three-point-bending tests.
- The optical methodology used, provided information of the crack-initiation and propagation process at different points through the thickness of the specimen during the test.
- The results obtained were correlated with the stored elastic energy, and compared with those reported in case of notched-specimens [13], and by other authors for different test conditions.
- The information gained from these tests, enabled the relationship between the softening function of the material with the crack propagation speed to be determined, knowledge which is key when using cohesive zone models to analyse these kind of materials.

Acknowledgments: Authors thank the Comisión Interministerial de Ciencia y Tecnología of the Spanish Government and to the Comunidad Autónoma de Madrid for partial support of this work through the research projects DPI2011-23191 and CCG10-UC3M-DPI-5596, respectively.

2. References

- [1] C. Ruiz, R.A.W. Mines, *The Hopkinson Pressure Bar: An alternative to the instrumented pendulum for Charpy test*. International Journal of Fracture, 29, 101-109, (1985)
- [2] T. Yokoyama, *Determination of dynamic fracture-initiation toughness using a novel impact bend test procedure*. Journal of Pressure Vessel Technology, 115, 389-397, (1993)
- [3] L. Rubio, J. Fernández-Sáez, C. Navarro, *Determination of dynamic fracture-initiation toughness using three-point bending tests in a modified Hopkinson Pressure Bar*, Experimental Mechanics, 43, 379 - 386, (2003)
- [4] J.A. Loya, J. Fernandez-Saez, *Three-dimensional effects on the dynamic fracture determination of Al 7075-T651 using TPB specimens*, International Journal of Solids and Structures, 45, 2203-2219, (2008)
- [5] J. Beinert, J.F. Kalthoff, *Experimental determination of Dynamic Stress Intensity factors by shadow patterns*. Mechanics of Fracture, (1981), 7, 281-330, Ed. G.C. Sih, La Hague
- [6] K. Ravi-Chandar, W.G. Knauss, *An experimental investigation into dynamic fracture: I. Crack Initiation and arrest*. International Journal of Fracture, 25, 247-262, (1984)
- [7] J.W. Dally, D.B. Barker, *Dynamic measurements of initiation toughness at high loading rates*. Experimental Mechanics, 28, 298-303 (1988)
- [8] J.W. Dally, W.L. Fourney, G.R Irwin, *On the uniqueness of the stress intensity factor-crack velocity relationship*. International Journal of Fracture, 27, 159-168, (1985)
- [9] A.S. Kobayashi, M. Ramulu, M. S. Dadkhah, K. H. Yang, B. S. J. Kang, *Dynamic fracture toughness*. International Journal of Fracture 30, 275-285, (1986)
- [10] A.J. Rosakis, *Two optical techniques sensitive to gradients of optical path difference: the method of caustics and the coherent gradient sensor (CGS)*. In J.S. Epstein (ed.), Experimental Techniques in Fracture, VCH Publishers, 327-425, (1993)
- [11] W.G. Knauss, K. Ravi-Chandar, *Some basic problems in stress wave dominated fracture*. International Journal of Fracture 27, 127-143, (1985)
- [12] F. Zhou, J. F. Molinari, T. Shioya, *A rate-dependent cohesive model for simulating dynamic crack propagation in brittle materials*. Engineering Fracture Mechanics, 72, 1383-1410, (2005)
- [13] J.A. Loya, E. I. Villa, J. Fernandez-Saez, *Crack-front propagation during three-point-bending tests of polymethyl-methacrylate beams*. Polymer Testing, 29, 113-118, (2010)

STRUCTURAL AND MECHANICAL PROPERTIES ESTIMATED BY MEANS OF ULTRASONIC TECHNIQUE

*K. Makowska*¹, *Z.L. Kowalewski*^{1,2}, *J. Szelązek*²

¹ *Motor Transport Institute, Warsaw, Poland*

² *Institute of Fundamental Technological Research, Warsaw, Poland*

1. Introduction

Evaluation of structural degradation and mechanical properties still seems to be an attractive direction of investigations due to unsolved problems related to safety of different construction elements, installations or machine devices. Among many non-destructive techniques of damage assessments the ultrasonic method is used at different branches of industry. However, it has to be mentioned, that the conventional ultrasonic parameters (e.g. attenuation coefficient, wave velocity) suffer on some limits in application. The attenuation coefficient allows to detect material damage in a late creep stage when voids are created [1] and its application in industrial conditions is difficult due to surface roughness and local material heterogeneity. In the case of wave velocity, in addition to the above mentioned factors also the non-uniform thickness of elements tested may disturb its measurements. Taking into account these facts, the acoustic birefringence was proposed [2] as the alternative ultrasonic parameter enabling assessments of structural degradation. Its measurement is based on the wave velocity difference between two shear waves polarized in the mutually perpendicular directions [1]. Variations of the acoustic birefringence coefficient are attributed to the material texture (preferred grain orientation) and even small, oriented voids resulted from creep [3]. According to previous investigations [2, 3] the acoustic birefringence seems to be more sensitive to damage development than the attenuation coefficient and wave velocity. Among advantages in measurements of this parameter one can indicate a high speed, low price and simplicity in use at the industrial conditions. It can be measured on unknown thickness elements, its value is temperature independent, and measurements can be made with a single shear SH wave transducer.

2. Experimental procedure

The specimens manufactured from power engineering steels were subjected to creep under tensile conditions. The creep tests were interrupted for a range of the selected time periods in order to achieve specimens with an increasing level of strain. After each loading process the specimens were tested using ultrasonic technique and then the qualitative observations and quantitative metallographic assessment of specimens were carried out by means of light microscope (Olympus PMG3) coupled on-line with image analyser (CLEMEX), (Fig. 1a,b). The quantitative image analysis was carried out at the same areas (6,11 mm²) of each specimen; close to the fracture (about 0-1mm) and far away from it up to several millimetres using systematic area scanning. The measurements were interrupted when the differences between successive quantitative results were not observed. The observations of fractures by means of scanning electron microscopy (SEM - JEOL 6360 LA) were also carried out.

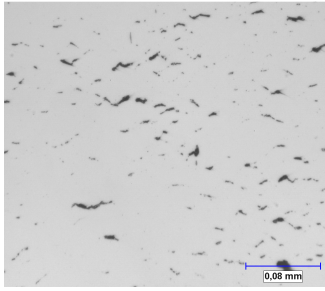


Fig. 1a. Specimen prestrained up to $\varepsilon = 6.51\%$, non-etched state, conventional light, magn. 200 \times .

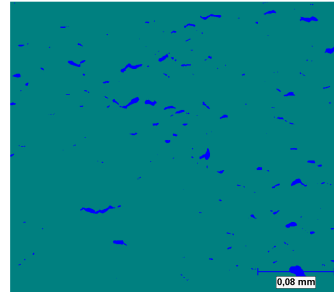


Fig. 1b. The same image, prepared to quantitative analysis.

3. Results

The representative results for the 40HNMA are presented in Figs. 2-3.

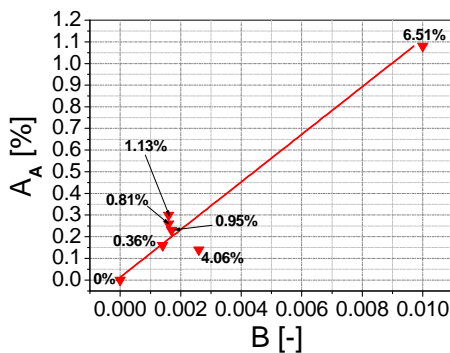


Fig. 2. Relationships between volume fraction of voids from area about 1mm from the fracture and acoustic birefringence.

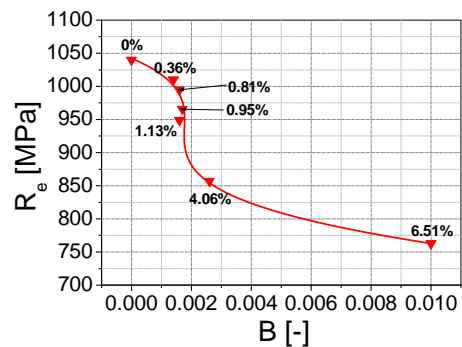


Fig. 3. Relationships between yield point and acoustic birefringence of the 40HNMA steel.

4. Conclusions

It is shown that the relationships between acoustic birefringence and selected destructive parameters (stereological and mechanical) can be determined for the 40HNMA steel. They seem to be applicable for elaboration of a new promising method for early stage detection of material degradation.

5. References

- [1] S. Mackiewicz (2005). *Possibilities of ultrasonic evaluation of energetic steels as a result long-term exploitation (in Polish)*, Conference Book, VII Information and Training Seminar "Diagnostic and Renovations Energetic Devices. New Diagnostic Problems on the Old Power Units", Ustroń, Poland.
- [2] Z.L. Kowalewski, J. Szelażek, S. Mackiewicz and B. Augustyniak (2009): *A role of interdisciplinarity in a damage degree investigations of power plant steels (in Polish)* Conference Book, XV Seminar on Nondestructive Material Testing, Zakopane, Poland.
- [3] S. Mackiewicz, Z. L. Kowalewski, J. Szelażek and J. Deputat (2005). Mechanical and ultrasonic research of materials failure condition due to creep process (in Polish), *Przegląd Mechaniczny*, 7-8, 15-24.

MECHANICAL PROPERTIES OF SELECTED ALUMINIUM ALLOYS AT WIDE RANGE OF STRAIN RATES

W. Moćko^{1,2} *Z.L. Kowalewski*^{1,2}

¹ *Institute of Fundamental Technological Research, Warsaw, Poland*

² *Motor Transport Institute, Warsaw, Poland*

1. Introduction

Aluminium alloys (AA) are characterized by a very good ratio of strength to weight which enforces their application in structures where weight reduction is a key factor for operational parameters. Typical examples are lightweight construction alloys used for the purposes of automotive and aircraft industry, what in consequence leads to the overall vehicle weight lowering and finally to reduction of the fuel consumption. The vehicle structure must fulfill requirements of the occupants protection during vehicle crash. Therefore, mechanical behaviour of materials under dynamic loading conditions must be taken into account during designing stage. Moreover an intensive research has been done to improve ballistic protection by application of AA. In the case of armor also an influence of strain rate on the mechanical characteristic of a material must be considered.

The reliable constitutive model for the applied material should be developed and calibrated in order to provide an efficient finite element method (FEM) giving an opportunity to design process and simulate the results captured as close as possible. For this purpose the stress-strain curves should be determined for various strain rates and temperatures. The usual way of material characterization at higher strain rates is the Hopkinson bar method, which enables strain rate sensitivity evaluation of materials in the range up to $5 \times 10^3 \text{ s}^{-1}$. However, this is insufficient in many cases, because local strain rates in the structure during extreme loading may overcome this value. An essential increase of the flow stress, which occurs in material at strain rates higher than $5 \times 10^3 \text{ s}^{-1}$ is caused by appearance of the drag stress component. The discrepancy between predictions of constitutive model developed and the experimentally observed properties of the material may lead to significant errors in design procedure of the whole structure. Hence it is of great importance to provide the adequate testing methodology and reliable data of mechanical properties of materials tested at strain rates higher than 10^4 s^{-1} .

2. Experimental method

Quasi-static compression tests were performed on the standard servo-hydraulic testing machine (Instron), at room temperature. The dynamic compression experiments were carried out on both, the modified Hopkinson bar apparatus [1] at strain rate below $5 \times 10^3 \text{ s}^{-1}$ and the miniaturized direct impact compression testing stand (MDICT) [2] at strain rates within a range from $3 \times 10^4 \text{ s}^{-1}$ to $1,1 \times 10^5 \text{ s}^{-1}$. As a result a wide picture of AA mechanical behaviour at strain rates ranging from 10^4 s^{-1} to 10^5 s^{-1} was determined. The cylindrical specimens of 10 mm diameter and 5 mm length were fabricated from extruded bars of 15 mm diameter using electro-discharging machine. The size of specimen for the purposes of miniaturized compression test was reduced to 1,5 mm of diameter and 0,5 mm of length.

3. Results

The stress-strain curves of tested materials are presented in Fig. 1(a) for 6082-T6 alloy and Fig. 1(b) for 7075-T6 alloy. Both materials show very narrow strain hardening effects which

occurs only at strain values lower than 0,05. Moreover, plastic strain hardening exponent doesn't change significantly with deformation rate.

Summarized results for all measurement techniques applied are show in Fig. 2 in the form of strain rate sensitivity chart. In could be seen that 6082-T6 AA doesn't shows any strain rate hardening effects below $5 \times 10^3 \text{ s}^{-1}$, whilst 7075-T6 AA exhibits negative strain rate sensitivity value (dynamic strain ageing effect). At deformation rates higher than $5 \times 10^3 \text{ s}^{-1}$ a significant increase of plastic flow rate, may be observed. The reason of such effect may be attributed to appearance of the viscous drag component of high magnitude [3] related to high velocity motion of dislocations.

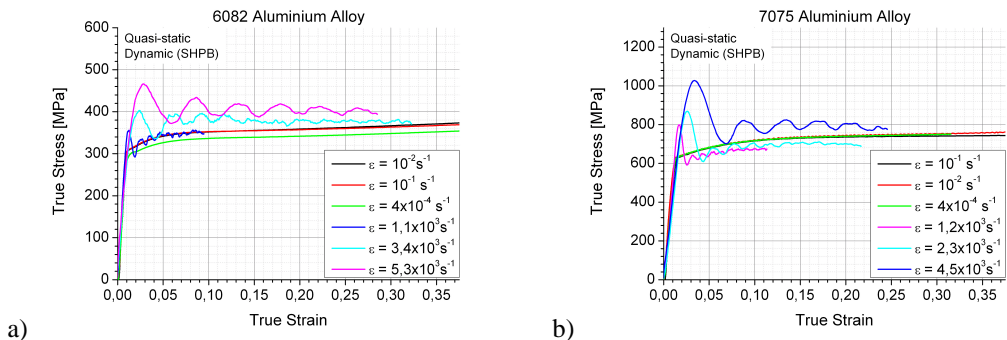


Fig.1 Stress-strain curves of AA obtained under quasi-static and dynamic loading conditions; a) – AA 6082-T6; b) – AA7076-T6

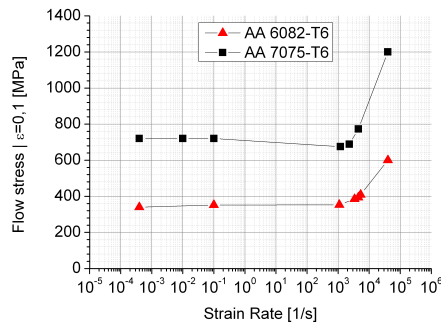


Fig.2 Strain rate sensitivity of tested AA

6. References

- [1] H. Kolsky (1949) An investigation of the mechanical properties of materials at very high rates of loading, *Proc Phys Soc (London)*, 63, p.676–700.
- [2] J. Z. Malinowski, J. R. Klepaczko i Z. L. Kowalewski. Miniaturized Compression Test at Very High Strain Rates by Direct Impact. *Exp. Mech.* (2007) 47. pp 451-463.
- [3] A. Rusinek, J. A. Rodriguez-Martinez, J. R. Klepaczko i R. B. Pęcherski. Analysis of thermo-visco-plastic behaviour of six high strength steels. *Materials & Design* (2009) 30. pp.1748–1761.

DETERMINATION OF THERMAL DIFFUSIVITY OF AUSTENITIC STEEL USING PULSED INFRARED THERMOGRAPHY.

W. Oliferuk^{1,2}, K. Kochanowski¹, Z. Płochocki², A. Adamowicz¹

¹ *Mechanical Engineering and Applied Informatics, Technical University of Białystok*

² *Institute of Fundamental Technological Research, Polish Academy of Sciences, Warsaw, Poland*

1. Introduction

Thermal diffusivity is a material parameter describing the movement of the isothermal surface during the heat flow through the material.

Thermal diffusivity characterizes a material in a complex way, because it includes the heat conductivity λ , specific heat c_w and the mass density ρ of the material:

$$(1) \quad \alpha = \frac{\lambda}{c_w \rho}$$

The range of thermal diffusivity values of solids is quite wide. The value depends on the chemical composition of the material and its internal structure.

Pulsed infrared thermography is one of the active methods based on stimulation of the material surface by a heat pulse (pulse duration is equal to few milliseconds) and recording the material response, as a time evolution of the surface temperature distribution, by means of an IR camera. Such evolution contains information about thermal diffusivity of the tested material. The objective of the presented work is to extract this information.

2. Theoretical foundations of the method

The theoretical basis of determining thermal diffusivity of materials is based on solutions of heat conduction equation formulated for a plate of a finite thickness g when one of its surfaces is heated by a very short heat pulse. If the surface of the plate is sufficiently large in comparison with the region of interest, it may be considered as infinite and then the one-dimensional model of heat conduction can be presumed. The differential equation of heat conduction for the one-dimensional model has the following form:

$$(2) \quad \frac{\partial T}{\partial t} = \alpha \frac{\partial^2 T}{\partial z^2} + \frac{1}{\rho c} \cdot q,$$

where: α is the thermal diffusivity, ρ is the mass density, c is the specific heat of the measured material and q is the function of heat sources associated with the surface density of energy Q_s delivered to the specimen during its heat pulse stimulation.

The solution of such problem determines the temperature as a function of time at any point $z \in [0, g]$. The time evolution of temperature of the opposite surface with respect to the stimulated one is described by the solution for $z = g$. This solution includes the thermal diffusivity of the material of the plate. Therefore, if the temperature of this surface can be measured in time, it is possible to determine the thermal diffusivity of the tested material.

Assuming relatively simple, initial and boundary conditions:

$$(3) \quad T(t=0) = T_o, \quad \frac{\partial T}{\partial z}(z=0) = 0 \quad \text{and} \quad \frac{\partial T}{\partial z}(z=1) = 0$$

and considering a character of the heat source, we obtain an expression for the temperature on the

opposite specimen surface to the stimulated one:

$$(4) \quad T(t) = T_{\infty} - 2(T_{\infty} - T_0) \exp\left(-\frac{\pi^2 \alpha}{g^2} t\right),$$

where T_0 is initial temperature, T_{∞} is maximum temperature.

The logarithm of Eq. (4) has a linear character:

$$(5) \quad \ln(T_{\infty} - T) = \left(-\frac{\pi^2}{g^2} \cdot \alpha\right)t + \ln 2(T_{\infty} - T_0)$$

and the tangent of the slope straight line to the time line:

$$(6) \quad A = \frac{\pi^2 \alpha}{g^2}.$$

Then, if one of the specimen surfaces will be heated by a short impulse of heat and the temperature of the opposite surface will be measured as a function of time, we can determine the thermal diffusivity α from Eq. (6).

3. Experimental procedure and results

The measuring system for determining the thermal diffusivity of the tested material is presented in Fig. 1.

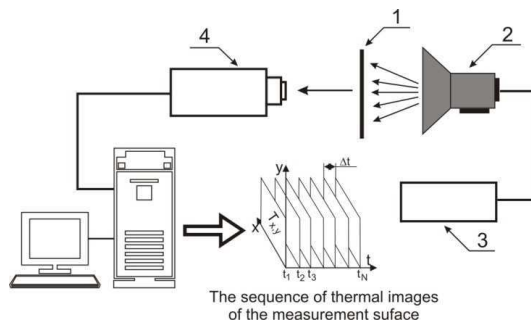


Fig. 1. The scheme of the measuring systems for determining the diffusivity of solids. 1 - specimen, 2 - flash lamp, 3- power supply, 4 - IR camera, 5 - computer with appropriate software to enable recording thermal images of the specimen surface, as functions of time.

After some simple transformations from the obtained relation, we can draw a straight line and obtain its tangent of the slope straight line to the time line.

Substituting to (6) the value of the tangent and thickness of the specimen, we obtain the thermal diffusivity of the sample.

The experiments were performed on austenitic steel 316L. The determined value of the thermal diffusivity of this material is $3.65 \cdot 10^{-6} \text{ m}^2/\text{s}$, whereas the value given in the literature [1] is $3.71 \cdot 10^{-6} \text{ m}^2/\text{s}$.

4. References

- [1] Goodfellow. Metals, Alloys, Compounds, Ceramics, Polymers, Composites. Catalogue 1993/94.

DISTRIBUTION OF ENERGY STORAGE RATE IN AREA OF STRAIN LOCALIZATION DURING TENSION OF AUSTENITIC STEEL

W. Oliferuk^{1,2}, M. Maj¹ and K. Zembrzycki¹

¹ *Institute of Fundamental Technological Research, Warsaw, Poland*

² *Bialystok University of Technology, Bialystok, Poland*

1. Introduction

When a material deforms plastically, a part of the mechanical energy w_p expended on plastic deformation is converted into heat q_d while the remainder e_s is stored within the material.

$$(1) \quad e_s = w_p - q_d.$$

The measure of energy conversion at each instant of plastic deformation process is the rate of energy storage Z defined as the ratio of the stored energy increment to the plastic work increment; $Z = \Delta e_s / \Delta w_p$. The stored energy increment is equal to difference between Δw_p and the increment of energy dissipated as a heat Δq_d (see Eq (1)), $\Delta e_s = \Delta w_p - \Delta q_d$. Then:

$$(2) \quad Z = \Delta e_s / \Delta w_p = 1 - \Delta q_d / \Delta w_p.$$

In the previous works by Oliferuk and co-workers it has been shown that during non-uniform deformation (localization of plastic strain) of polycrystalline material, the energy storage rate rapidly decreases reaching the 0 value and then becomes negative [1,2]. The 0 value of the energy storage rate means that the deformed material losing the ability to store the energy. But the energy storage rate was determined as the average value for the total gauge part (25 mm) of specimen. The estimation of $\Delta e_s / \Delta w_p$ was based on the comparison of the temperature increment of deformed specimen related to the given increment of the expended energy during uniform deformation with the average temperature increment during non-uniform one. The question appears: What is the energy storage rate distribution along the gauge length of the strained specimen during development of plastic strain localization? The purpose of the presented work is to answer this question.

2. Experiments

A new method of determination the distribution of energy storage rate is proposed. The method is based on the experimental procedure for the simultaneous measurements of temperature and displacement distributions on the surface of tested specimen during tensile deformation. This procedure involves two complementary imaging techniques: CCD technique in visible range and infrared thermography (IRT). In order to determine the strain distribution, markers in form of graphite dots were plotted on one surface of the specimen. In this way, the surface was divided into sections, whose sizes are determined by the distance between centers of dots (Fig. 1).

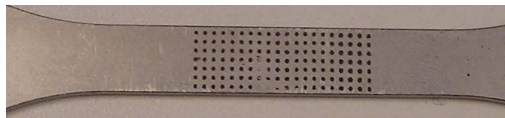


Fig. 1. The graphite dots on the gauge part of specimen.

Displacements of the dots were recorded by means of CCD camera during deformation process. The local true strain was obtained by taking the logarithm of the ratio of the current distance

between graphite dots to initial one. The true stress was calculated by dividing the load by the current cross-sectional area of the specimen corresponding to given section. The strain and stress distributions were used to calculate surface distribution of plastic work.

Temperature distribution on the opposite surface of the specimen was measured by means of IR Thermographic System. The surface was covered by soot, to ensure its high and homogeneous emissivity. From the surface temperature distribution, the distribution of energy dissipated as a heat was determined using local form of heat equation. Dependences of this energy on plastic work for local sections of deformed specimen allow to calculate $\Delta q_d / \Delta w_p$ and then to obtain from Eq. (2) the energy storage rate.

The experiments were performed on specimens cut out from a sheet of austenitic steel.

3. Results

The local values of the energy storage rate as a function of plastic work was determined. Such dependences for selected sections lying on the axis of deformed specimen are presented in Fig. 2.

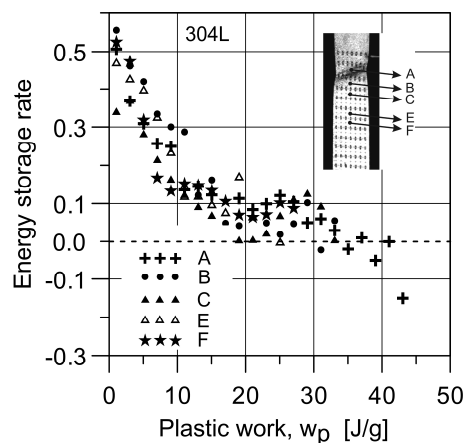


Fig. 2. The energy storage rate as a function of plastic work for selected sections lying on the axis of the specimen.

The obtained results shown that the energy storage rate for all tested sections decreases with strain. During evolution of plastic strain localization some sections cease to deform, while the energy storage rate in the others drops to zero and even to negative values. To identify micro-mechanisms corresponding to appearance and evolution of plastic strain localization microstructural characterization was performed by electron backscattered diffraction (EBSD) and transmission electron microscopy (TEM).

4. References

- [1] W. Oliferuk, A. Korbel and W. Bochniak (2001). Energy balance and macroscopic strain localization during plastic deformation of polycrystalline metals, *Mater. Sci. Eng.*, (A319-321), 1-2, 250–253.
- [2] W. Oliferuk and M. Maj (2007). Plastic instability criterion based on energy conversion, *Mater. Sci. Eng.*, A462, 363-366.

RESEARCH ON DURABILITY OF ADHESIVE COMPOSITES WITH REGARD TO EXPEDIENT REPAIR OF TECHNICAL OBJECTS

M. Roškowicz¹ and T. Smał²

¹ *Institute of Air Technology, Military University of Technology, Warsaw, Poland*

² *Institute of Command, The Gen. T. Kosciuszko Military Academy of Land Forces, Wrocław, Poland*

1. Introduction

Technical objects repairs are more and more often taking advantage of structural bonding [1] [2], as well as, quick chemically setting materials; so-called, adhesive composites, which create new possibilities in the scope of expedient or permanent removal of different types of damages [3]. However, the adhesive materials are characterised with relatively low durability. These materials are very sensitive to repair's conditions, as well as, they have got limited shear and long-term strength; that is, an ability to transfer constant loads in time, and limited fatigue life – an ability to transfer changing loads [7]. Without familiarity with these properties, the application of adhesive materials in repairs is burdened with the risk of damage to a repaired element in a relatively short time after the performed repair.

2. Methodology and results of research

Currently, a wide range of specialist adhesive composites of different purposes is produced. However, the best groups for military purposes seems to be “super metals”, designed mainly for reconstructing losses of metal parts and „rapid” group characterized by a short time of setting. Therefore, the main object of research are well-known and available in the Polish market adhesive composites of Belzona, Unirep and Chester Metal.

Application of adhesive materials to repairs requires; among others, determining their durability, which is broadly understood as a material ability to transfer long-lasting static load (static long-lasting strength) and their durability to changing load (fatigue life). Since that information are not provided by manufacturers, the main aim of the work is to determine the mentioned features of selected adhesive composites.

Firstly, creep curves for the selected adhesive composites were determined (Fig. 1). In order to define an influence of curing conditions of adhesive composites on their long term strength, the curing was carried out by single-stage (in room temperature) and by double-stage (in increased temperature).

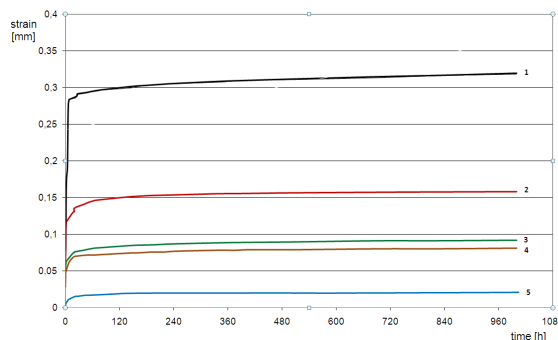


Fig. 1. Creep curves of the adhesive composites

In order to determine durability of lap joints made with adhesive composites, experimental research was conducted, which was preceded by defining their immediate strength on which basis the loads for long-term research were selected. The measure of durability of lap joints was a lapse of time between the commencement of research and specimen destruction (Fig. 2).

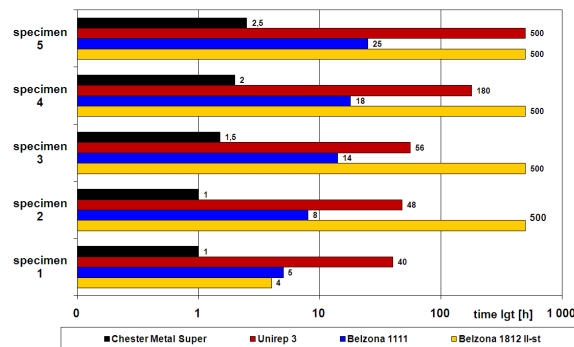


Fig. 2. Static long-term strength of lap joints made of the adhesive composites

Furthermore, the discussed materials were subject to a fatigue life test in cylinder and lap joints (Fig. 3).

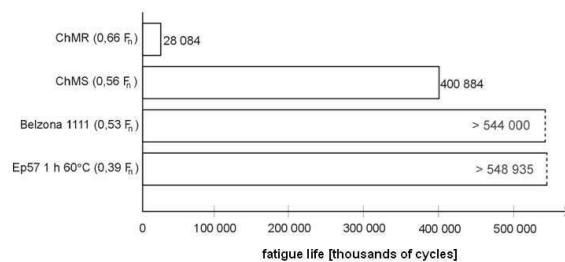


Fig. 3. Comparison of absolute shear fatigue life of researched adhesive composites

4. Conclusion

With regard to requirements of expedient repairs executed in field conditions, the long term strength of adhesive joints higher than 50 hours and fatigue strength of adhesive joints higher than 100 000 cycles can be accepted as sufficient in most of the cases. Therefore, safe value of maximum long-lasting and fatigue loads of researched adhesive composites that ensures the required durability of joints made of these composites, should be of 0,5 of breaking load in a static test of short term strength.

6. References

- [1] A.A. Baker (1999). Bonded composite repair of fatigue-cracked primary aircraft structure. *Comp. Struct.*, **47**, 431-443. ISSN 0263-8223.
- [2] R.J. Chester and K.F. Walker and P.D. Chalkey (1999). Adhesively bonded repairs to primary aircraft structure. *Int. J. of Adhesion and Adhesives*, **19**. ISSN 0143-7496.
- [3] M.J. Davis (1996). *The role of materials and processes in defective bonded structural repairs*. In Proceedings of 41st. International Conference SAMPE, Anaheim, 936-50.
- [4] J. Godzimirski (Eds.) (2010). *Epoxy adhesives. An application in repairs of machines and equipment* (In Polish). Ed. WNT, Warsaw, ISBN 978-83-204-3605-1.

ELECTRO-OPTICAL MEASURING SYSTEM MODEL 200XY

H.-D. Rudolph

H.-D. Rudolph GmbH, Reinheim, Germany

Model 200XY serves the purpose of measuring the necking on material samples (specimens) during high-speed tension tests. Over a sample height of **Y** the instrument contactlessly measures 20000 times per second the width of the specimen.

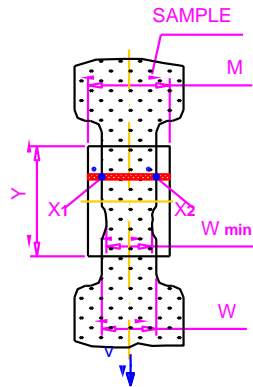
For recording, the following calibrated measuring signals are available at the outputs of the instrument:

Edge positions: **X₁** and **X₂**

Width of specimen: **W = X₁ - X₂**

Minimal width of specimen: **W_{min}**

Sample height to be scanned: **Y**



Width **W** of the specimen is measured with a resolution 2 – 25 μm (adjustment of low-pass filter). Per scan the smallest sample width (**W_{min}**) is calculated, stored, and delivered as measuring value/scan).

The measuring range (**M**) of the instrument depends on the lens unit used. The lens unit can be exchanged. In case the standard version of Model 200XY is used, an LED illuminator has to be placed behind the specimen.

Through a window in a test chamber there is the possibility of measuring necking on samples in it; these samples can be hot up to 2500°C.

For our website please contact: www.rudolph-optics.com

AlMg/SiC METAL MATRIX COMPOSITE UNDER FATIGUE AND CREEP CONDITIONS

A. Rutecka¹, Z. L. Kowalewski^{1,2}, K. Pietrzak², L. Dietrich¹, K. Makowska², J. Woźniak³,
M. Kostecki³, W. Bochniak⁴ and A. Olszyna³

¹ Institute of Fundamental Technological Research, Warsaw, Poland

² Motor Transport Institute, Warsaw, Poland

³ Warsaw University of Technology, Faculty of Materials Science and Engineering, Warsaw, Poland

⁴ AGH University of Science and Technology, Faculty of Non-Ferrous Metals, Cracow, Poland

1. Introduction

Metal matrix composites (MMCs) belong to ceramic reinforced materials that mechanical properties should be enhanced in comparison to the matrix [1, 2]. Moreover, the composites are to be used in aerospace and automotive industries where light and simultaneously durable materials are required. One of the advantages of MMCs is that they can be produced using methods similar to those used for the monolithic materials. Hence, the KoBo method was used to manufacture AlMg/SiC MMCs [3]. Mechanical tests and microstructural observations were carried out to investigate damage process under fatigue and creep conditions [4].

2. Materials

The Al7,9Mg powder of 99,7% purity and the SiC powder of 99,8% purity were used during MMCs production; an average particle size were equal to 14,6 μm and 0,42 μm , respectively. Powders were blended, pressed and extruded in the form of rods using the KoBo 100T horizontal hydraulic press. The SiC content was equal to 0; 2,5; 5; 7,5 and 10%.

3. Details of experimental procedure

Fatigue tension-compression tests were performed under stress control at ambient temperature. Stress amplitudes were equal to 220 and 240 MPa. Sine shape cycles ($R=-1$) were applied with the frequency of 20 Hz. Hysteresis loops during subsequent cycles were captured.

Step increasing tensile creep tests were carried out at 200°C. Three levels of stress equal to 40, 60 and 70 MPa were applied. Creep curves were elaborated.

Microstructural observations using optical light microscopy and scanning electron microscopy were performed before and after fatigue and creep tests. An influence of reinforcement content as well as an influence of fatigue and creep processes on material degradation were analyzed.

4. Synthesis of experimental results obtained

Representative fatigue and creep results in a form of the hysteresis loops and creep curves, respectively, are presented in Figs 1 and 2. Microscopic patterns of fracture surfaces are also shown in these figures. Cyclic softening followed by decreasing of inelastic strain amplitude were observed during subsequent cycles. The effect was indentified for higher stress amplitude (240 MPa). Moreover, it was stronger for lower content of SiC particles. In most cases, higher SiC content resulted in lower cyclic softening. Unfortunately, shorter lifetimes with increasing SiC content were obtained. Creep parameters become more favorable if the SiC content did not exceed 5%. Above this value they decreased. It is worth to notice that creep resistance was higher for reinforced materials in comparison to the matrix.

Microstructural observations showed existence of discontinuities before and after mechanical tests. The volumetric fraction of defects increased with an increase of reinforcement content.

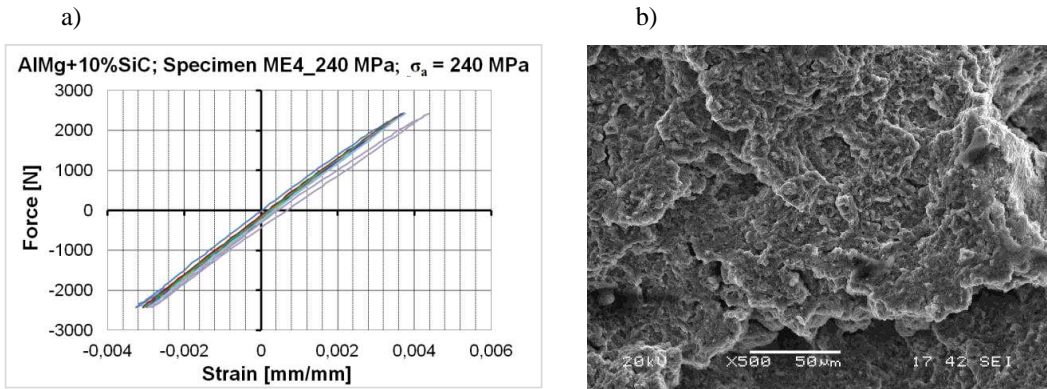


Fig. 1. AlMg+10%SiC: (a) fatigue test results in the form of hysteresis loops after 100 cycles; (b) fracture surface (SEM, magn. x500)

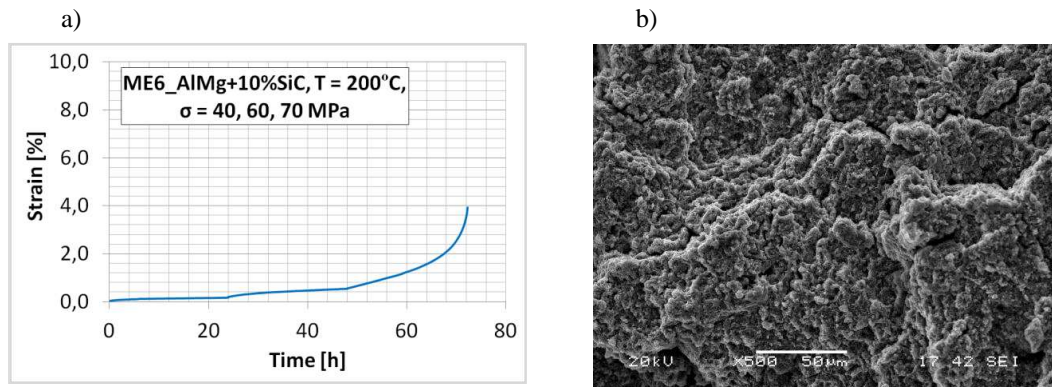


Fig. 2. AlMg+10%SiC: (a) creep test results in the form of creep curve; (b) fracture surface (SEM, magn. x500)

5. Acknowledgements

The results presented in this paper have been obtained within the project “KomCerMet” (project no. POIG.01.03.01-00-013/08 with the Polish Ministry of Science and Higher Education) in the framework of the Operational Programme Innovative Economy 2007-2013.

6. References

- [1] T.W. Clyne and P.J. Withers (2003). *An introduction to Metal Matrix Composites*. Cambridge University Press.
- [2] N. Chawla and Y.L. Shen (2001). Mechanical Behaviour of Particle Reinforced Metal Matrix Composites. *Advanced Engineering Materials*, **3**, No. 6; 357-370.
- [3] W. Bochniak and A. Korbel (2003). KOBO – type forming: forging of metals under complex conditions of the process, *J. Mat. Process. Techn.*, **134**, 120-134.
- [4] A. Rutecka, Z.L. Kowalewski, K. Pietrzak, L. Dietrich, K. Makowska, J. Woźniak, M. Kostecki, W. Bochniak, A. Olszyna (2011). Damage development of Al/SiC metal matrix composite under fatigue, creep and monotonic loading conditions, *Procedia Engineering*, **10**, 1420-1425.

YIELD CRITERIA AND THEIR VERIFICATION FOR METAL FOAMS

A.M. Stręk

*Faculty of Mechanical Engineering and Robotics, AGH-University of Science and Technology,
Krakow, Poland*

1. General

The presentation covers an important question of yield criteria for cellulars. It is crucial to be able to foresee material's failure behaviour before its use in practical applications. A variety of failure criteria is available, though not all of them are verified experimentally, which may have consequences in terms of their potential use.

Because of diversity of structure of foams as well as materials of which they are made of it is very difficult to construct a unified approach of assessment of material effort in those cellulars. Another problem might be to include all foam characteristics at once, like: open vs closed cells or all different failure component mechanisms in cells.

Historically first yield criteria were based on idealised cell failure behaviour, that is on uniaxial tensile/compressive response of ribs in a cubic cell. Naturally, such approach had to be developed in order to cover at least orthotropy, not to mention lower symmetries. Moreover, other mechanisms in cells, which lead to collapse, had to be taken into account: first bending of ribs, then plastic hinges, which arise in vertices leading to rotation, also buckling in compressive situations. Plastic and brittle response of foam skeleton had to be identified and included in criteria.

The most well-known criterion based on theoretical assumptions of cell structure and collapse mechanisms is the classic yield criterion for ideal foams proposed by Gibson's et al. There are also couple of phenomenological criteria that can be simplified under special assumptions to that of Gibson, including Millers' yield criterion for foams with plastic compressibility and Desphande and Fleck's phenomenological criterion for metal foams. There are many other ideas published in the subject literature over recent years on how to assess material effort in foams. Most interesting theories include statistical approach or purely empirical criteria. On the other hand, factors like different yield strength in tension and compression (SDE effect) and its consideration within the theory behind a given criterion is also crucial.

The presentation covers a range of existing criteria for foams, including giving their origin and interconnections, if any. For those criteria which have been studied in terms of experimental validation the results are cited. Some criteria meet experimental results with good agreement; however, there are always some factors which need to be accounted for. These include mostly testing techniques, which are very specific as for cellular materials. Conclusions summing convergence between theoretical provisions and tests are given. Suggestions in terms of calibration of both test methods and criteria are also presented.

Moreover, not all criteria use the same quantitative material strength results - some use values determined in different tests; this of course makes it an ambitious aim to compare between the criteria. It is worth mentioning that though difficult such comparison leads to choosing the best criterion for a given application. One of the objectives of this presentation is to chose potentially best criterion to assess material effort of a new class of materials: auxetic foams.

2. References

- [1] A-F. Bastawros et al. (2000). Experimental analysis of deformation mechanisms in a closed-cell aluminum alloy foam, *J. of the Mechanics and Physics of Solids*, **48**, 301-322.

- [2] J-S. Blazy et al. (2004). Deformation and fracture of aluminium foams under proportional and non proportional multi-axial loading: statistical analysis and size effect, *Int. J. Mech. Sci.*, **46**, 217-244.
- [3] C.P. Chen, R.S. Lakes (1991). Holographic study of conventional and negative Poisson's ratio metallic foams: elasticity, yield and micro-deformation, *J Materials Science*, **26**, pp. 5397-5402
- [4] C.P. Chen, R.S. Lakes (1993). Holographic study of non-affine deformation in copper foam with a negative Poisson's ratio -0.8, *Scripta Metall et Mater.*, **29**, 395-399.
- [5] J.B. Choi, R.S. Lakes (1996). Fracture toughness of re-entrant foam materials with a negative Poisson's ratio: experiment and analysis, *Int. J. Fracture*, **80**, 73-83.
- [6] J.B. Choi, R.S. Lakes (1992). Nonlinear properties of metallic cellular materials with a negative Poisson's ratio, *J Materials Science*, **27**, 5373-5381.
- [7] L.J. Gibson et al. (1989). Failure surfaces for cellular materials under multiaxial loads: I modelling, *Int. J. Mech. Sci*, **31**, 635-663.
- [8] G. Gioux et al. (2000). Failure of aluminum foams under multiaxial loads, *Int. J. Mech. Sci.*, **42**, 1097-1117.
- [9] R. Lakes (1987). Foam structures with a negative Poisson's ratio, *Science*, **235**, 1038-1040.
- [10] L-P. Lefebvre et al. (2008). Porous Metals and Metallic Foams: Current Status and Recent Developments, *Advanced Engineering Materials*, **10**, 775-787.
- [11] D. Ruan et al. (2007). Triaxial compression of aluminium foams, *Composites Science and Technology*, **67**, 1118-1234.
- [12] J. Schwerdtfeger et al. (2010). Auxetic cellular structures through selective electron-beam melting, *Phys. Status Solidi B*, **247**, 269-272.
- [13] T.C. Triantafillou et al. (1989). Failure surfaces for cellular materials under multiaxial loads—II. Comparison of models with experiment, *Int. J. Mech. Sci.*, **31**, 665-678.
- [14] M. Janus-Michalska, R.B. Pecherski (2003). Macroscopic Properties of Open-Cell Foams Based on Micromechanical Modelling, *Tech. Mech.*, **23**, 234-244.

QUALITY OPTIMIZATION OF STRAIN MEASUREMENT PATH INCLUDED IN THE EXPERIMENTAL CRYOGENIC STAND FOR TENSILE TESTING AT ULTRA-LOW TEMPERATURES

J. Tabin

Institute of Applied Mechanics, Cracow University of Technology, Cracow, Poland

1. Introduction

Cryogenic stand for uniaxial tensile testing of ductile materials at ultra-low temperatures is located in Faculty of Mechanical Engineering at the Cracow University of Technology (Fig.1). The main tensile test aim is to identify constitutive model parameters of materials (e.g., 304L, 316L, 316LN, 316Ti stainless steel, Cu-OFe, etc.) which are used at ultra-low temperature. During tensile test DAQ systems record: force applied to a specimen, temperature of a specimen surface and elongation of a specimen.

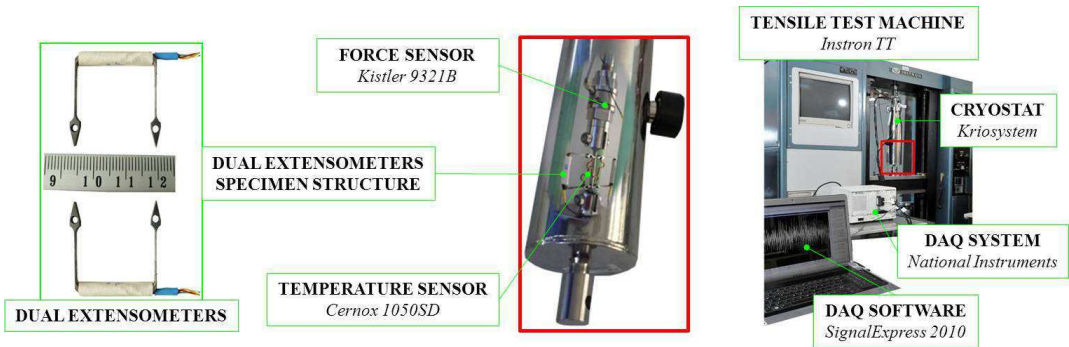


Figure 1. University experimental cryogenic stand for uniaxial tensile test at ultra-low temperature

For ductile materials applied at very low temperatures (in particular at liquid helium temperature–4,2 K) and for sufficiently high strain rate discontinuous plastic flow (serrated yielding) is observed. The main feature of serrated yielding consists in frequent abrupt drops of stress as a function of strain during monotonic loading. Reasons and constitutive model of discontinuous plastic flow phenomenon are described by Skoczeń [1], [2].

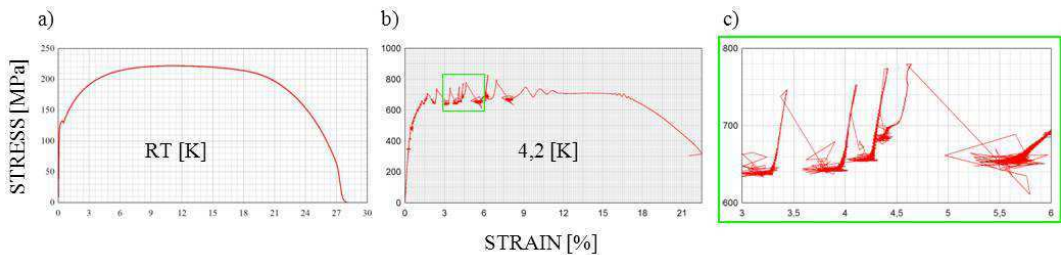


Figure 2. Stress-strain curve for Niobium - Ti6Al4V specimen. a) tensile test at room temperature, b) tensile test at liquid helium temperature, c) extensometers vibrations effect

In order to perform correct data logging of discontinuous plastic flow should be prepare quality optimization process of strain measurement path.

2. Experimental results

Dynamic character of discontinues plastic flow phenomenon generates vibrations of dual extensometers-specimen structure, influencing appropriate plotting of strain–stress curve (Figure 2c.).

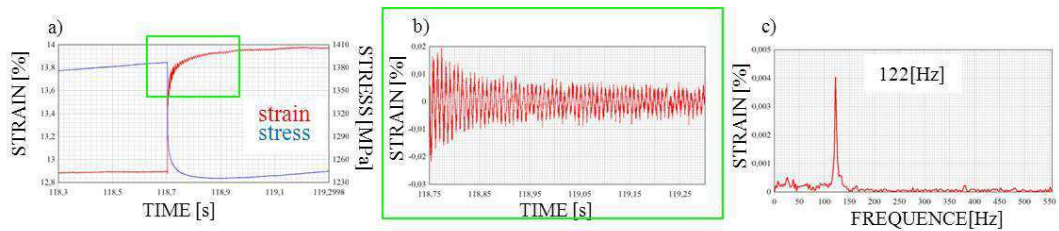


Figure 3. Determination of "dual extensometers-specimen structure" natural frequency, forces during cryogenic tensile test of JK2LB specimen. a) strain and stress in time domain, b) strain without trend, c) frequency spectrum of dual extensometers

In order to verify, if strain oscillations on stress-strain curve are generated by vibrations of dual extensometers-specimen structure, in the Dynamic of Material System Laboratory at Cracow University of Technology was created special measurement path (Figure 4.)

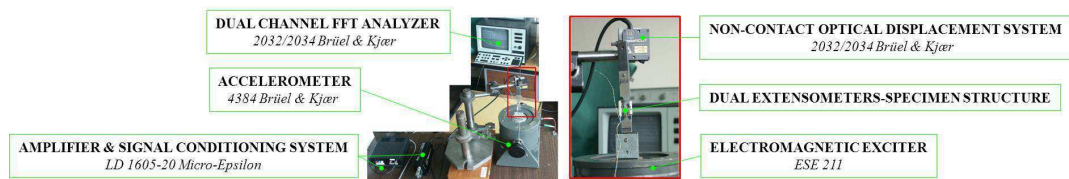


Figure 4. Special measurement path to verify of extensometer-specimen structure natural frequency

Tests on special measurement path shown that natural frequency of structure is 126 Hz.

Currently, is created model of all phenomena occurring on test facilities and measurement system during tensile test at ultra-low temperature. Preparation of advanced model will be crucial for optimization process.

3. Acknowledgment

The research work is created in cooperation with the CERN.

4. Remarks

Presented paper describes only small part of strain measurement path optimization process.

5. References

- [1] B. Skoczeń, J. Bielski, S. Sgobba and D. Marcinek, (2009). Constitutive Model of Discontinuous Plastic Flow at Cryogenic Temperatures. International Journal of Plasticity.
- [2] B. Skoczeń, (2008). Constitutive description of plastic strain induced phenomena at cryogenic temperature, XXII ICTAM Adelaide, Australia.

Fracture, Damage and Fatigue of Materials

SOME RESULTS ON THREE-DIMENSIONAL EFFECTS IN MODE I FRACTURE PROBLEMS

J. Fernández-Sáez¹, E. Giner², D. Fernández-Zúñiga³, J.A. Loya¹, A. Fernández-Canteli³

¹*Department of Continuum Mechanics and Structural Analysis, University Carlos III of Madrid, Spain.*

²*Centro de Investigación de Tecnología de Vehículos-CITV, Departamento de Ingeniería Mecánica y de Materiales, Universitat Politècnica de València, Spain.*

³*Department of Construction and Manufacturing Engineering, University of Oviedo, Spain.*

1. General

Despite the number of works devoted to the three-dimensional analysis of the static and dynamic behaviour of cracked solids ([1, 2], among others), showing the important difference existing between the 3D and 2D cases and the consequences arising from the proper consideration of the through-thickness stress and strain fields in a finite thickness cracked plate, engineering applications, in general, obviate these facts, and accept the simplicity of the 2D analysis.

In previous works ([3, 4]) a tensor description has been introduced to characterize the singular stress field in the vicinity of the crack front in accordance to the Williams' series expansion. In these studies, it is concluded that the existence of second order terms cannot be, in general, neglected. In addition to the in-plane T -stress often considered in 2D problems, the out-of-plane component of the so-called constraint tensor t_{ij} plays an important role in the constraint due to the thickness effect.

From the numerical analysis, performed by FEM, of cracked plates with different thickness B and crack depth ratios a/W , subjected to a uniform stress σ applied on the top side of the plate (see Fig. 1) [5, 6], the following conclusions on the three-dimensional effects can be drawn [4, 5]:

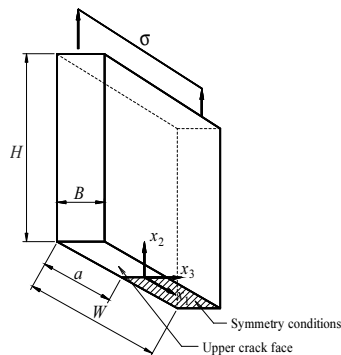


Figure 1. Geometric model of the cracked plates.

1. The presence of singular in-plane stress fields together with the requirement of bounded out-of-plane strain along the crack front promotes the existence of a singular out-of-plane normal stress at the crack front, irrespective of the specimen thickness. It proves the impossibility of existence of a plane stress state at the crack front, within the LEFM scope, for any specimen type under mode I loading when the specimen thickness tends to zero.
2. In three-dimensional situations, as those present in real cracked specimens of finite thickness, the classical 2D J -integral is not strictly applicable because the actual out-of-

plane stress and strain fields are ignored. The usual consideration of an equivalent Young's modulus E' (depending on constraint conditions) to find a simple relation between the J_{3D} -integral and K_I for different constraint levels (see [7]; for instance) is misleading. The only valid relationship between J_{3D} -integral and K_I is $J_{3D} = (1-\nu^2) K_I^2 / E$, independently of the specimen thickness.

3. While in the calculation of K_I in 2D problems the geometric factors used only depend on the in-plane dimensions, a proper three-dimensional geometrical factor related also on the specimen thickness, B should be included.
4. From the analysis of the second order term (constant) of the Williams expansion, (i.e. constraint tensor t_{ij}), it can be concluded that the out-of-plane component t_{33} plays an important role (similarly to the in-plane component t_{11} , the so-called T -stress in biparametric approaches for plane problems), explaining the loss of constraint phenomena. Since the apparent fracture toughness increases for decreasing thicknesses B , for a given crack length a , due to the loss of constraint as compared to the constraint existing in a thick plate, it follows the necessity of considering the whole constraint tensor (in particular t_{11} and t_{33} together) in order to explain this experimental fact.

The above findings correspond to static conditions, though numerical results of three-dimensional simulations of dynamic three-point-bending fracture tests performed on a modified Hopkinson Split Pressure Bar [8] are also presented. The 3D model proposed includes the whole experimental device. In the dynamic simulation, specimens with different thickness and crack lengths tested with two impact velocities (5 m/s and 10 m/s) were considered. These results also point out the importance of three-dimensional effects on the determination of the dynamic fracture toughness of materials.

Acknowledgements: The authors gratefully acknowledge the financial support given by the DGICYT of the Spanish Ministry of Science and Innovation (Projects DPI2010-20990, DPI2011-23191, BIA 2012-19920) and by FICYT (Project IB08-171).

2. References

- [1] R.J. Hartranft and G.C. Sih (1969). The use of eigenfunction expansions in the general solution of three-dimensional crack problems, *J. Math. Mech.*, **19**, 123–138.
- [2] J. P. Benthem (1977). State of stress at the vertex of a quarter-infinite crack in a halfspace, *Int. J. Solids Struct.*, **13**, 479–492.
- [3] A. Fernández-Canteli, E. Castillo and D. Fernández-Zúñiga (2006). Lateral constraint index to assess the influence of specimen thickness. In: *Proceedings of the 16th European Conference of Fracture*, Gdoutos, E. (Ed.), Alexandropoulis.
- [4] D. Fernández-Zúñiga (2011). Modelo tensorial tridimensional para la consideración en fractura de la constricción en el frente de grieta, PhD Thesis, Universidad de Oviedo. Spain.
- [5] E. Giner, D. Fernández-Zúñiga, J. Fernández-Sáez and A. Fernández-Canteli (2010). On the J_{x1} -integral and the out-of-plane constraint in a 3D elastic cracked plate loaded in tension, *Int. J. Solids Struct.*, **47**, 934-946.
- [6] V.F. González-Albuixech, E. Giner, J. Fernández-Sáez and A. Fernández-Canteli, (2011). Influence of the t_{33} -stress on the 3-D stress state around corner cracks in an elastic plate, *Eng. Fract. Mech.*, **78**, 412–427.
- [7] G.P. Nikishkov, S.N. Atluri (1987). Calculation of fracture mechanics parameters for an arbitrary three-dimensional crack by the 'equivalent domain integral' method, *Int. J. Numer. Methods Eng.*, **24**, 1801–1821.
- [8] J.A. Loya and J. Fernández-Sáez (2008). Three-dimensional effects on the dynamic fracture determination of Al 7075-T651 using TPB specimens, *Int. J. Solids Struct.*, **45**, 2203-2219.

MULTISCALE CONSTITUTIVE MODELLING OF THE INFLUENCE OF ANISOTROPY EFFECTS ON FRACTURE PHENOMENA IN INELASTIC SOLIDS

Piotr Perzyna

*Institute of Fundamental Technological Research, Polish Academy of Sciences
Pawińskiego 5B, 02-106 Warszawa, Poland*

A main objective of the present paper is the development of the thermodynamical theory of elasto-viscoplasticity as a unique material constitutive structure within the framework of a general covariant deterministic theory. The focus of attention on the description of the influence of anisotropy effects on fracture phenomena as well as on multiscale considerations in the analysis of the physical foundations and experimental motivations is proposed. Experiment precisely suggests that for proper description of the thermomechanical couplings we have to base our considerations on thermodynamics.

1. Kinematics of finite deformation and fundamental definitions

The description of kinematics of finite deformation and the stress tensor of the continuum medium is presented. The fundamental measures of total deformation are introduced. The description is based on notions of the Riemannian space on manifolds and the tangent space. A multiplicative decomposition of the deformation gradient is adopted. The decomposition of the strain tensor into the elastic and viscoplastic parts is presented. The Lie derivative is used to define all objective rates for the introduced vectors and tensors. The rates of the deformation tensor and the stress tensor are precisely defined.

2. General principle of determinism. A unique constitutive material structure

The original conception of the intrinsic state of a particle X during motion of a body B has been assumed. A notion of the method of preparation of the deformation-temperature configuration of a particle X has been proposed as simple way of the gathering information for the description of the internal dissipation. A general principle of determinism for thermodynamical processes has been formulated. The topology for the intrinsic state space and some smoothness assumptions for processes and response functions (functionals) are postulated. As the basis of the thermodynamic requirements the dissipation principle in the form of the Clausius-Duhem, inequality is assumed. The dissipation principle implies two fundamental criteria, namely the criterion of the selection of the response functions (functionals) and the criterion of the accessibility of the intrinsic states. The principle of the increase of entropy has also been deduced. These results have a great importance to the thermodynamical theory of inelastic materials.

3. Internal state variable material structure

Assuming that the method of preparation space for a unique constitutive material structure is a finite dimensional vector space and postulating that the initial value problem for the element of the method of preparation space has unique solutions we construct the material structure with internal state variables. The rate of internal dissipation function for the internal state variable material structure is obtained. From this results we can directly observed that full information given in the method of preparation at the actual intrinsic state essentially determines the rate of internal dissipation for this intrinsic state. This conclusion is of fundamental importance for the physical interpretation of the internal state variables.

4. Thermodynamical theory of elasto-viscoplasticity

The main purpose is to develop the thermodynamical theory of elasto-viscoplasticity within the internal state variable material structure and to take into account the influence of anisotropy effects on fracture phenomena as well as the observed contribution to strain rate effects generated by microshear banding. Thus the problem is to deduce and interpret a finite set of the internal state variables basing on multiscale considerations in analysis of the physical foundations of inelastic solids and experimental observation results.

Experimental observation concerning investigation of dynamic loading processes have shown that formation of microshear bands influences the evolution of microstructure of material. We can conclude that microshear banding contributes to viscoplastic strain rate effects. For the elastic-viscoplastic model of polycrystalline solids the relaxation time T_m governs the viscoplastic flow in the entire range of strain rate changes and has to be a function of the rate of equivalent inelastic deformation $\dot{\epsilon}^P$ and the active microshear bands fraction f_{ms} . On the other hand analysis of recent experimental observation concerning investigations of fracture phenomena under dynamic loading processes suggests that there are two kinds of induced anisotropy: (i) the first caused by the residual type stress produced by the heterogeneous nature of the finite plastic deformation in polycrystalline solids; (ii) the second the fracture induced anisotropy generated by the microdamage mechanism. It is noteworthy to stress that both these induced anisotropy effects are coupled. Multiscale considerations in the analysis of the physical foundations of inelastic solids and experimental observation results suggest that a material of an investigated body B is a dispersive and dissipative medium. In a dispersive medium any initial disturbance is broken up into a system of wave groups. Then the energy is propagated to the particular nucleated microcrack with the appropriate group velocity. Thus, each of nucleated microcracks will receive different portion of energy distributed by various group velocities. This important fact observed leads to the fundamental conclusion that the evolution of microdamage has anisotropic nature. As the result of this multiscale analysis we have very crucial suggestions concerning the constitutive description:

- (i) Since a material of a body B (for various metals like nickel, copper, aluminium, lead and mild steel) is a dispersive and dissipative medium, then it can be modelled as an elastic-viscoplastic.
- (ii) Since the dispersive effects for propagation of wave phenomena play so important role, then we have very heterogeneous deformation processes which lead to the residual type stresses and generate the strain induced anisotropy. Experimental evidence indicates that yield surface exhibit anisotropic hardening. Subsequent yield surfaces are both translated and deformed in stress space.
- (iii) The anisotropy of intrinsic microdamage mechanisms observed experimentally and discussed on the basis of multiscale considerations is very fundamental for the proper description of fracture phenomena.

We have good foundations to suggest a finite set of the internal state variables. We propose to assume as the internal state variables: the equivalent viscoplastic deformation ϵ^P , which will describe inelastic flow phenomena, the microdamage second order tensor ξ with the physical interpretation that $(\xi : \xi)^{1/2} = \xi$ defines the volume fraction porosity, to take account for the anisotropic microdamage mechanisms, and the back stress (residual stress) α , which will model the

kinematic hardening intrinsic mechanisms as an approximate description of the strain induced anisotropy.

Particular attention is focused on the determination of the evolution laws for the internal state variables introduced. The fundamental viscoplastic law for the rate of spatial deformation tensor is assumed to be proportional to the empirical overstress function. To describe suitably the influence of the both induced anisotropy effects and the stress triaxiality observed experimentally the new evolution equations for the microdamage tensor ξ and for the back stress tensor α are proposed.

The fundamental rate type constitutive equations for the Kirchhoff stress τ and for temperature ϑ are formulated. Thermomechanical couplings are investigated. Fracture criterion based on the evolution of the anisotropic intrinsic microdamage is proposed. The fundamental features of the proposed constitutive theory have been carefully discussed.

The propose of the development of this theory is in future applications for the description of important problems in modern manufacturing processes, and particularly for meso-, micro-, and nano-mechanical issues.

References

- [1] Perzyna P., Kosiński W. (1973), *A mathematical theory of materials*, Bull. Acad. Polon. Sci., Ser. Sci. Tech., **21**, 647–654.
- [2] Kosiński W., Perzyna P. (1973), *The unique material structure*, Bull. Acad. Polon. Sci., Ser. Sci. Tech., **21**, 655–662.
- [3] Perzyna P. (1975a), *Thermodynamics of a unique material structure*, Arch. Mechanics, **27**, 791–806.
- [4] Perzyna P. (1975b), *On material isomorphism in description of dynamic plasticity*, Arch. Mech., **27**, 473–484.
- [5] Perzyna P. (2005), *The thermodynamical theory of elasto-viscoplasticity*, Engineering Transactions, **53**, 235–316.
- [6] Perzyna P. (2008), *The thermodynamical theory of elasto-viscoplasticity accounting for microshear and induced anisotropy effects*, Mechanics, **27**, 25–42.

PREDICTION OF MATERIAL INSTABILITY BY LINEAR STABILITY METHOD. APPLICATION TO ELASTO-VISCOPLASTIC MEDIA

G. Altmeyer

*Laboratoire d'Etude des Microstructures et de Mécanique des Matériaux, UMR CNRS 7239,
Metz, France*

1. Context

Environmental constraints lead major mechanical industries to reduce the weight of the structures. This objective can be achieved by using new materials, such as high strength steels or advanced alloys, but new unexpected diffuse and localized necking modes may then occur, leading to defective products during sheet metal forming. Prediction of material instability become again a major industrial challenge and an academic subject of interest to understand the physical phenomena leading to necking and to determine the most appropriate dimensioning methods. A review of four theoretical principle commonly used to predict the occurrence of necking lighten their ability to take into account the physics of necking or their limits to be coupled with advanced material modeling.

2. Prediction of formability

A first approach to determine the formability limits is based on the existence of multiple heterogeneous areas in the sheet. According to Marciniak-Kuczynski [1], a band of reduced thickness in which necking is expected is arbitrarily introduced in a safe media. The comparison of the evolution of the mechanical properties inside and outside the defect area allows the prediction of localization. M-K model is applicable to a wide range of materials. A limitation of this criterion comes from the requirement of user defined parameters, as for example the initial defect size or the threshold value. An other analytical method, the Maximum Force Principle (MFP), is based on an empirical observation according to which diffuse necking occurs when the load reaches its maximum during a uniaxiale tensile test. Extensions to this criterion have been proposed to predict diffuse necking [2] and latter localized necking [3] of metal sheets submitted to biaxial loadings. Although some interesting trends are found by comparing experimental and numerical results obtained with these criteria, their theoretical bases still have to be reinforced to take into account advanced material modeling. To overcome these limitations some relations with the bifurcation analysis criteria can be investigated [4]. According to the bifurcation approach, a necessary condition for diffuse necking is given by the loss of positivity of the second order work [5]. For localized modes, the loss of ellipticity criterion was established to predict necking or shear banding [6]. This criterion is however restricted to both rate independent materials and softening behavior for associative plasticity. This first restriction can lead to unrealistic and too restrictive formability predictions for rate dependant materials. In such case, stability analysis by a linear perturbation method may be used to improve the forming limit diagram predictions. Necking and localization are seen as instability of the global or local mechanical equilibrium [7].

3. Linear stability method

Recent methods based on the material stability analysis allow the prediction of multiple necking of plates and hemispherical shells subjected to dynamic expansion for viscoplastic

materials at high strain rates [8] or the prediction of localization in elasto-plastic soil media [9]. In this work, an original method is developed to take into account a large class of phenomenological elasto-viscoplastic modeling.

A general modeling framework is considered here to introduce various classical isotropic and kinematic hardening models and to take into account the effects of anisotropy and damage. As softening effects are shown necessary to predict localized modes with Rice criterion, this effect is introduced here by taking into account damage. After introduction of a small perturbation in the equilibrium equations and linearization of the system, stress perturbation and strain perturbation are then related by an elasto-viscoplastic operator. Stability of linear system is investigated by the evaluation of the evolution of the growth rate of the introduced perturbation. In accordance with previous theoretical observations [10], formability predictions proposed with this instability criterion tend to those obtained with bifurcation analysis when elasto-viscoplastic material behavior tends to the elasto-plastic case.

4. Conclusions

To overcome limitations observed on different categories of necking and localization criteria, as for example the impossibility to take into account the effects of strain rate and their influence on formability, a method based on linear stability analysis is proposed. The original criterion obtained for elasto-viscoplastic materials is compared with the criterion based on the bifurcation analysis. The originality of the approach used here is to present stability conditions of metallic materials modeled by general phenomenological laws.

5. References

- [1] Z. Marciniak and K. Kuczyński (1967). Limit Strains in the Processes of Stretch-Forming Sheet Metal. *International Journal of Mechanical Sciences*, 9(9), 613-620.
- [2] H. W. Swift (1952). Plastic instability under plane stress. *Journal of the Mechanics and Physics of Solids*, 1(1), 1-18.
- [3] P. Hora, T. Longchang and J. Reissner (1994). Prediction methods for ductile sheet metal failure using FE-simulation. Proceedings of *IDDRG'94*.
- [4] G. Altmeyer (2011). Theoretical and numerical modeling of material instability criteria. PhD thesis. Arts et Métiers ParisTech, Metz, France.
- [5] D.C. Drucker (1956). On uniqueness in the theory of plasticity. *Quart. Appl. Math.*, 14, 35-42.
- [6] J.W. Rudnicki and J.R. Rice (1975). Conditions for the localization of deformation in pressure-sensitive dilatant materials. *Journal of the Mechanics and Physics of Solids*, 23(6), 371-394.
- [7] A. Molinari (1985). Instabilité thermoviscoplastique en cisaillement simple. *Journal de Mécanique Théorique et Appliquée*, 4(5).
- [8] S. Mercier, N. Granier, A. Molinari, F. Llorca and F. Buy (2010). Multiple necking during the dynamic expansion of hemispherical metallic shells from experiments to modeling. *Journal of the Mechanics and Physics of Solids*, 58, 955-982.
- [9] N. G. Diouta and I. Shahrour (2006). A full 3-D material stability analysis of a classical elasto-plastic medium through a linear perturbation approach. *European Physical Journal of Applied Physics*, 34, 85-96.
- [10] G. Barbier, A. Benallal and V. Cano (1998). Relation théorique entre la méthode de perturbation linéaire et l'analyse de bifurcation pour la prédiction de la localisation des déformations. *Comptes Rendus de l'Académie des Sciences - Series IIB*, 326(3), 153-158.

PROGRESSIVE FRICTIONAL DELAMINATION OF AN INFINITE ELASTIC FILM ON A RIGID SUBSTRATE DUE TO IN-PLANE POINT LOADING

M. Białas

Institute of Fundamental Technological Research, Warsaw, Poland

1. Introduction

The contribution presents a solution to a 2D delamination problem of an infinite elastic film resting on a rigid substrate and loaded by a monotonically increasing in-plane point force. The problem can be encountered in many practical applications, for example fiber reinforced polymer sheets used in structural strengthening techniques [1] or in laminated glass, where two or more glass plies are bonded together by a polymeric interlayer through treatment at high temperature and pressure in autoclave [2].

2. Problem formulation

Let us consider an infinite elastic film of thickness h resting on an infinite rigid foundation. The film is subjected to a monotonically increasing point load \mathbf{P} acting in the plane xy on its upper surface, as presented in Fig. 1(a). By assuming rigid-slip interaction between the film and the substrate we have two zones developed at the interface, namely Ω , where the film is displaced due to the external loading \mathbf{P} , and Σ where the structure remains fully bonded with vanishing film displacements. Let $\partial\Omega$ denote the delamination front between the regions Ω and Σ , as schematically presented in Fig. 1(b). Assuming the film thickness h to be small as compared to $2l$, being the characteristic length of the delaminated zone Ω , the problem can be treated as two dimensional with the film in plane stress conditions. The interaction between the film and the substrate is reduced to shear traction τ^f treated as in-plane body forces acting on the film. Magnitude of traction τ^f reaches the critical value $|\tau^f| = \tau^f = \text{const}$ within the delaminated zone Ω . Due to their continuity, there are neither traction nor displacements on the boundary $\partial\Omega$.

3. Superposition of solution

Due to the fact that the film is assumed to remain elastic during the delamination process, the displacements and the stresses within the film are the superposition of respectively displacements and stresses induced by both the point load \mathbf{P} and the forces at the interface. There are zero tractions and

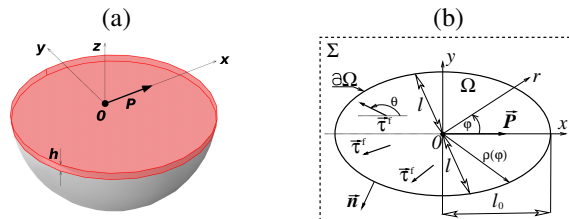


Figure 1. (a) Infinite elastic film resting on a rigid substrate. In-plane point loading. (b) Two dimensional model: plane stress conditions with interfacial traction τ^f treated as in-plane body forces.

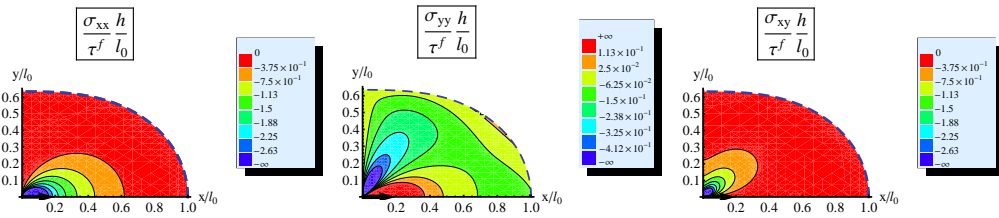


Figure 2. Distribution of stresses in the plate within one quadrant of the delaminated zone Ω ($x \geq 0, y \geq 0$) obtained for $\nu = 0.3$. Dashed line indicates the moving boundary.

displacements at the moving boundary $\partial\Omega$ and we can write

$$(1) \quad u_i(\mathbf{x}) = u_i^P(\mathbf{x}) + u_i^{\tau^f}(\mathbf{x}), \quad \sigma_{ij}(\mathbf{x}) = \sigma_{ij}^P(\mathbf{x}) + \sigma_{ij}^{\tau^f}(\mathbf{x}),$$

where

$$(2) \quad \begin{aligned} u_i^P(\mathbf{x}) &= P \tilde{u}_i^x(\mathbf{x}; \mathbf{0}), \quad \sigma_{ij}^P(\mathbf{x}) = P \tilde{\sigma}_{ij}^x(\mathbf{x}; \mathbf{0}), \\ u_i^{\tau^f}(\mathbf{x}) &= \iint_{\Omega} \left[\tau_x^f(\mathbf{X}) \tilde{u}_i^x(\mathbf{x}; \mathbf{X}) + \tau_y^f(\mathbf{X}) \tilde{u}_i^y(\mathbf{x}; \mathbf{X}) \right] d\Omega, \\ \sigma_{ij}^{\tau^f}(\mathbf{x}) &= \iint_{\Omega} \left[\tau_x^f(\mathbf{X}) \tilde{\sigma}_{ij}^x(\mathbf{x}; \mathbf{X}) + \tau_y^f(\mathbf{X}) \tilde{\sigma}_{ij}^y(\mathbf{x}; \mathbf{X}) \right] d\Omega. \end{aligned}$$

With j being either x or y , the functions $\tilde{u}^j(\mathbf{x}; \mathbf{X})$ and $\tilde{\sigma}^j(\mathbf{x}; \mathbf{X})$ in equations (2) are respectively plane stress displacements and stresses at point \mathbf{x} resulting from a unit force imposed at point \mathbf{X} of an infinite plate of given thickness h and acting in the j direction.

To effectively make use of Eqs. (2) we have to determine two unknowns, namely the distribution of the shear forces at the interface, that is the angle θ in Fig. 1(b), and the shape of the delaminated zone Ω . Making use of problem's self-similarity, an approximate procedure providing these two functions will be presented.

4. Results

Due to the complexity of the integrands the integration in (1) can be done only numerically. For $\nu = -1$ the integrals in (1) simplify and one obtains an exact analytical solution. For this special case the stresses within the delaminated zone have the simple form

$$\sigma_{xx} = -\sigma_{yy} = \frac{\tau^f (r^2 - l_0^2) \cos \varphi}{2hr}, \quad \sigma_{xy} = \frac{\tau^f (r^2 - l_0^2) \sin \varphi}{2hr}.$$

It will be argued that this is a particular situation of a rigid film delaminating from a rigid substrate.

Figure 2 presents one quadrant of the slip zone and contour stress fields obtained for Poisson's ratio $\nu = 0.3$. The components σ_{ij}^P in Eqs. (1) introduce the singular behaviour of the stress field in the point O , where the concentrated force is imposed. Due to the approximate character of the solution the boundary condition $\boldsymbol{\sigma} = \mathbf{0}$ is not exactly satisfied, which is clearly seen for stress component σ_{yy} .

References

- [1] A. Cottone and G. Giambanco (2009). Minimum bond length and size effects in FRP-substrate bonded joints. *Eng. Fract. Mech.*, **76**, 1957-1976.
- [2] I.V. Ivanov (2006). Analysis, modelling and optimization of laminated glasses as plane beam. *Int. J. Solids Struct.* **43**, 6887-6907.

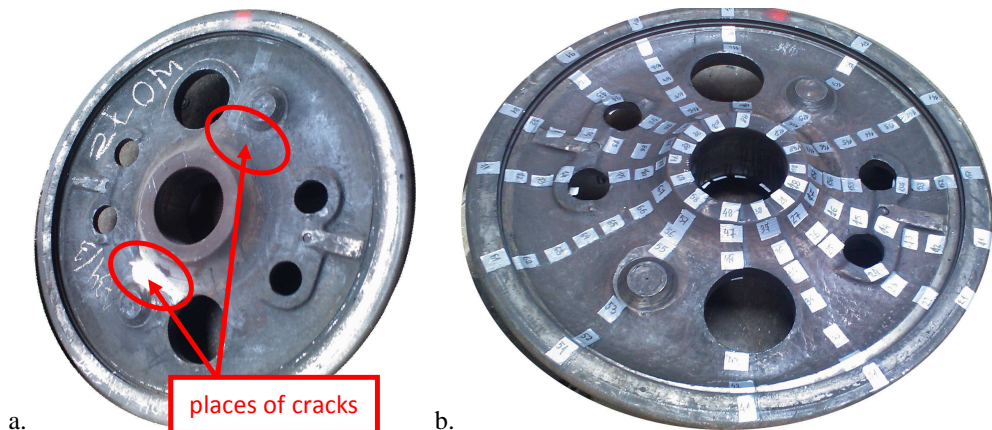
THE USE OF MAGNETIC METHODS FOR THE EVALUATION OF THE DEGREE OF FATIGUE DEGRADATION OF CAST STEEL LII500 EXEMPLIFIED BY DRIVE WHEELS OF LOCOMOTIVE EU07

K. Bizoń

Silesian University of Technology, Katowice, Poland

1. Aim, scope and object of research

The aim of the research was to demonstrate possibilities of using measurements of value of magnetic properties characteristic for cast steel LII500 material to evaluate the degree of its fatigue degradation, as exemplified by drive wheel of EU07 locomotive [1, 2]. The scope of the research has covered both magnetic properties of real object i.e. locomotive drive wheel and laboratory research of magnetic properties of samples of wheel material. The object of the research has been the drive wheel which has been taken out of operation due to cracks on its disc (Fig.1a). The occurrence of the cracks has been noticed during the general overhaul of the locomotive drive system which was carried at the Zakłady Naprawcze Lokomotyw Elektrycznych in Gliwice. They have been detected by a dye penetration method (Fig.1a). Samples of wheel material taken from the areas of lesser and greater degree of fatigue degradation have also been laboratory tested as far as their magnetic properties were concerned.



Rys.1. a. Drive wheel of EU07 locomotive with a marked location of a crack
b. net of measurement points on the inner surface of the wheel

2. Measurements of magnetic properties value of a real object

Measurements of dynamic loop of magnetic hysteresis in selected measuring points have been made on both inner and outer surface of the wheel disc. The method of measurement has been based on the value of magnetic induction in an air fissure of magnetic system, where the yoke with winding magnetize the material under research. Hall sensor has been used for the measurement of magnetic induction (expressed as value of electric voltage). The studied material served as a keeper in magnetic set, which has been limited to the area of the rail wheel disc. The recorded lines of input and output voltage of a probe allowed determination of dynamic loops of magnetic hysteresis

in coordinating set of input voltage- output voltage of a probe. The value of input voltage of the probe was proportional to the value of coercion intensity, whereas the value of output voltage was proportional to the maximum value of the vector of magnetic induction. Colorful maps of the distribution of the voltages on the inner surface of the wheel disc have been selected (i.e. the surface where by means of dye penetration the cracks have been identified) [3].

There have been also made measurements by means of Foerster's probe and as a result a colorful map with the distribution of parameter (expressed in voltage units), describing the change in inductivity of the probe depending on the location on the inner surface of the wheel disc, has been produced (Fig.2a) [4].

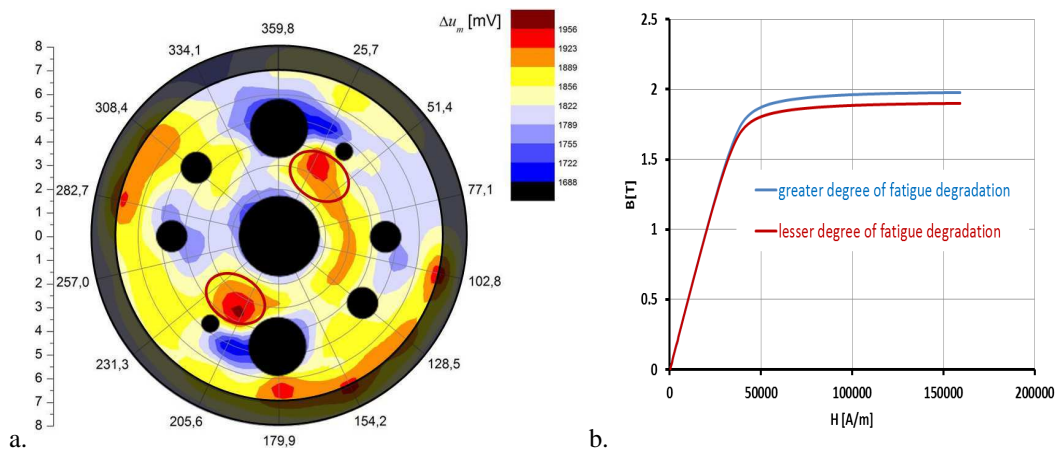


Fig.2. a. Colorful map of parameter distribution describing the change in inductivity of measuring probe, depending on the location of the measurement on the inner surface of the wheel disc
b. curves of the primary magnetizing of material samples.

3. Laboratory research on magnetic and mechanical properties of material samples

Laboratory research has been carried on material samples of a wheel from the areas of greater and lesser degree of fatigue degradation. The measurements on magnetic properties allowed determination of inductivity (both active and passive), tangent of loss angle and curves of primary magnetizing (Fig.2b). These curves have been used for the simulation of computer magnetic phenomena carried with the aid of the finite elements method.

4. References

1. Bizoń K.: Symulacyjna ocean obciążeń zmęczeniowych w tarczy koła napędnego zestawu kołowego, I Congress of Polish Mechanics, 28-31 August 2007, Warsaw, published on CD.
2. Żurek Z. H.: Opracowanie metody magnetycznej do wczesnej detekcji procesów zmęczeniowych w stalach niskostopowych i niskowęglowych. Government's Research Project N N507 0807 33, ended 15.11.2009, (K. Bizon - the main contractor).
3. Bizoń K., Żurek Z. H.: Badania wytrzymałości zmęczeniowej stali stosowanej na zestawy kołowe w oparciu o jej parametry magnetyczne, XIX Conference on Rail Vehicles, Targanice near Andrychów, 15-17 September 2010, Proceedings, Volume I, pages 29-36.
4. Bizoń K.: Wykrywanie stref wpływu procesów zmęczeniowych w tarczy koła napędnego lokomotywy eu07 metodami magneto-indukcyjnymi, 40. National Conference on Non-Destructive Testing, Warsaw 2011, electronic publishing.

MODELING OF INTERACTION BETWEEN DAMAGE AND PHASE TRANSFORMATION IN TWO-PHASE MATERIALS AT CRYOGENIC TEMPERATURES

H. Egner, M. Ryś and B. Skoczzeń

Institute of Applied Mechanics, Cracow University of Technology, Cracow, Poland

1. Introduction

FCC metals and alloys are frequently used in cryogenic applications because of their excellent physical and mechanical properties including ductility. These materials undergo at low temperatures three distinct phenomena: dynamic strain ageing, plastic strain induced transformation from the parent phase (γ) to the secondary phase (α') and evolution of micro-damage.

The phase transformation process leads to creation of two-phase continuum where the parent phase coexists with the inclusions of secondary phase. Experimental results indicate the correlation between decreasing damage rate and increasing martensite content.

2. Basic equations

The model is based on the following assumptions: (1) two-phase continuum is composed of the austenitic matrix and martensite platelets represented by small type Eshelby ellipsoidal inclusions, randomly distributed and randomly oriented in the matrix; (2) the austenitic matrix is elasto-plastic-damage, whereas the inclusions show purely brittle response; (3) current damage state is described by the use of second-order classical damage tensor; (4) rate independent plasticity is applied: it is assumed that the influence of the strain rate is small for the range of temperatures 2-77 K; (5) small strains are assumed: the accumulated plastic strain does not exceed 0.2; (6) mixed isotropic/kinematic hardening affected by the presence of martensite fraction is included; (7) the two-phase material obeys the associated flow rule.

The general constitutive law includes plastic, thermal and transformation strains: $\sigma_{ij} = E_{ijkl}(\mathbf{D})(\epsilon_{kl} - \epsilon_{kl}^p - \epsilon_{kl}^{th} - \xi \epsilon_{kl}^{bs})$ where ϵ^p is the plastic strain tensor, ξ denotes the volume fraction of martensite, ϵ^{bs} denotes the free deformation called bain strain, and ϵ^{th} stands for the thermal strain tensor. As the model is based on the rate independent plasticity, the plastic yield surface takes the form: $f_p(\tilde{\sigma}, \tilde{\mathbf{X}}, \tilde{R}) = J_2(\tilde{\sigma} - \tilde{\mathbf{X}}) - \sigma_y - \tilde{R} = 0$, where $\tilde{\sigma}$, $\tilde{\mathbf{X}}$ and \tilde{R} are the effective stress, kinematic and isotropic hardening variables, respectively. The hardening model is represented by equations: $dX_{ij} = \frac{2}{3} g(\xi) d\epsilon_{ij}^p$, $dR = f(\xi) dp$ where $g(\xi)$ and $f(\xi)$ are derived in [2].

The kinetic law of ductile damage evolution in austenite $D_{ij}^{(\gamma)}$ is proposed in the form (cf. [1]): $\dot{D}_{ij}^{(\gamma)} = C_{ik} Y_{kl} C_{ij} \dot{p} H(p - p_D)$ where p_D denotes damage threshold, Y_{ij} is thermodynamic force and $C_{ij}(\epsilon^p)$ represents texture induced anisotropy of damage, which is also subjected to evolution.

Martensite inclusions are subject to brittle damage described by the second order damage tensor $D_{ij}^{(\alpha')}$. According to [3] the deterioration of the brittle material structure due to applied load can be described by the damage evolution equation expressed in the form of the tensorial function: $D_{ij}^{(\alpha')} = f_1(\boldsymbol{\sigma}) \delta_{ij} + f_2(\boldsymbol{\sigma}) \sigma_{ij}$ where the damage tensor depends directly on the stresses applied.

The total amount of damage in a representative volume element is obtained via the linear rule of mixture, $D_{ij} = (1 - \xi) D_{ij}^{(\gamma)} + \xi D_{ij}^{(\alpha')}$, where ξ denotes the volume fraction of martensite. A

simplified evolution law for the volume fraction of martensite has been introduced after [3]: $\dot{\xi} = A(T, \boldsymbol{\varepsilon}^p, \boldsymbol{\sigma}) \dot{p} H((p - p_\xi)(\xi_L - \xi))$. A is a function of temperature, stress state and strain rate; p_ξ denotes the accumulated plastic strain threshold (to trigger the formation of martensite), ξ_L stands for the martensite content limit and H represents the Heaviside function. Consistency multiplier $\dot{\lambda}$ is obtained from the consistency condition (cf [4]):

$$\dot{f}_p = \frac{\partial f_p}{\partial \sigma_{ij}} (\dot{\sigma}_{ij} - \dot{X}_{ij}) + \frac{\partial f_p}{\partial R} \dot{R} + \frac{\partial f_p}{\partial D_{ij}} \dot{D}_{ij} + \frac{\partial f_p}{\partial \xi} \dot{\xi} = \frac{\partial f_p}{\partial \sigma_{ij}} E_{ijkl}(\mathbf{D}) \dot{\varepsilon}_{kl} - h(\boldsymbol{\varepsilon}, \mathbf{D}, \xi) \dot{\lambda} + S(\boldsymbol{\varepsilon}, \mathbf{D}) \dot{\xi} = 0$$

where h is the generalized hardening modulus and S is the sensitivity parameter describing the influence of phase transformation on the yield surface.

3. Numerical simulation

The derived constitutive model is implemented into ABAQUS/Explicit by the use of VUMAT procedure and used to numerically simulate the behaviour of steel structural elements at cryogenic temperatures. The numerical algorithm consists of three steps: elastic predictor, plastic corrector and damage update. For plastic corrector, performed for the frozen state of damage, a residual vector is built, $\mathbf{R} = [R_\sigma, R_x, R_R, R_f]^T$, and the corresponding vector of unknowns, $\mathbf{U} = [\boldsymbol{\sigma}, \mathbf{X}, R, \Delta\lambda]^T$. The condition $\mathbf{R}(\mathbf{U}) = \mathbf{0}$ defines the solution. The expansion into a Taylor series results in the following solution for \mathbf{U} :

$$\mathbf{U}^{n+1} = \mathbf{U}^n - \left[\left(\frac{\partial \mathbf{R}}{\partial \mathbf{U}} \right)^n \right]^{-1} \mathbf{R}^n.$$

The iteration procedure is stopped when the norm of $\mathbf{R}(\mathbf{U})$ is sufficiently small.

Acknowledgements

The Grant No. 2284/B/T02/2011/40 from the Polish Ministry of Science and Higher Education is gratefully acknowledged.

4. References

- [1] Egner H., Skoczeń B.: Ductile damage development in two-phase metallic materials applied at cryogenic temperatures. *International Journal of Plasticity* **26**:488-506, 2010.
- [2] Garion C., Skoczeń B., Sgobba S.: Constitutive modelling and identification of parameters of the plastic strain-induced martensitic transformation in 316L stainless steel at cryogenic temperatures, *International Journal of Plasticity* **22**:1234-1264, 2003.
- [3] Litewka A., Debinski J.: Load-induced oriented damage and anisotropy of rock-like materials, *International Journal of Plasticity* **19**: 2171-2191, 2003.
- [4] Egner H.: On the full coupling between thermo-plasticity and thermo-damage in thermodynamic modeling of dissipative materials, *International Journal of Solids and Structures* **49**:279-288, 2012.

ON THE 3D THERMOELASTIC PROBLEM FOR AN ANTICRACK SUBJECTED TO A UNIFORM HEAT FLOW IN THE INCLUSION PLANE

A. Kaczyński¹, B. Monastyrskyy²

¹ *Warsaw University of Technology, Warsaw, Poland*

² *Pidstryhach Institute for Applied Problems of Mechanics and Mathematics, Lviv, Ukraine*

Problems dealing with stress concentrations in deformable solids containing different kinds of defects attract the attention of specialists from many areas, such as geomechanics, metallurgy, materials science. Rigid inclusions (called anticracks) are the counterpart of cracks. From the standpoint of inhomogeneities in solids, these defects are the two extreme cases, namely, for a rigid inclusion $\mu \rightarrow \infty$, and for a crack $\mu \rightarrow 0$, where μ is the shear modulus of the inhomogeneity phase. These are the two most dangerous extremes. Many elements of constructions are operated in high-temperature environments. Hence, the study of thermoelastic field disturbed by an anticrack is important from the point of view of fracture mechanics.

This paper examines the three-dimensional problem of finding thermal stresses due to an insulated rigid sheet-like inclusion under a uniform heat flow directed parallel to the inclusion plane (Fig. 1). The corresponding problem with a uniform thermal flux perpendicular to the plane of the inclusion was considered in [1] and [2].

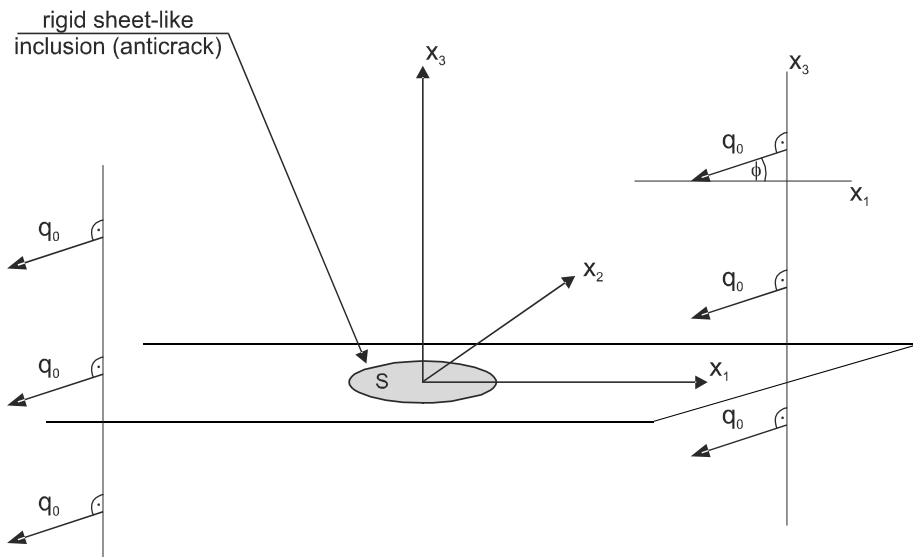


Fig. 1. An anticrack in an elastic space under a uniform heat flow parallel to the inclusion plane

It is assumed that a uniform heat flow with far field constant intensity q_0 and directed at an angle ϕ to the Ox_1 -axis is incident parallel to the surface of the heat-insulated rigid inclusion. Moreover, external loads are absent. It turns out that the inclusion does not disturb the linear temperature field, so it remains to solve the thermal stress problem with the boundary conditions involving an arbitrary shaped anticrack. A general method of solving this problem is presented.

With the use of appropriate harmonic potentials and the Fourier transform technique, the problem is reduced to the solution of two-dimensional singular equations for the shear stress jumps across the inclusion. For the purpose of illustration, exact results are given for the penny-shaped rigid inclusion. It is observed that the thermal stress fields near the inclusion front have the typical inverse square root singularities. Two mechanisms of material failure are found to be possible: opening Mode I deformation and exfoliation of the material from the inclusion.

References

- [1] A. Kaczyński and W. Kozłowski (2009). Thermal stresses in an elastic space with a perfectly rigid flat inclusion under perpendicular heat flow, *Int. J. Solids Structures*, **46**, 1772–1777.
- [2] A. Kaczyński and B. Monastyrskyy (2009). On the thermoelastic problem of uniform heat flow disturbed by a circular rigid lamellate inclusion, *Arch. Mech.*, **61**, 3-4, 309–324.

CREEP-FATIGUE RELIABILITY OF HIGH TEMPERATURE MATERIALS APPLIED IN TURBINE HOUSINGS OF TURBOCHARGERS

F. Laengler¹, T. Mao² and A. Scholz²

¹BorgWarner Turbo Systems Engineering GmbH, Kirchheimbolanden, Germany

²Institute for Materials Science, Technical University of Darmstadt, Germany

1. Introduction

The turbine housing (T/H) of an exhaust turbocharger as the most cost-intensive key component is exposed to extensive multiaxial thermo-mechanical fatigue (TMF). This leads to a major design challenge with the T/H to ensure the guaranteed lifetime in relation to the high-temperature behavior of the materials.

The first step was to develop and validate a phenomenological lifetime approach together with a constitutive material model of Chaboche-type applied in a preceding Finite-Element analysis (FEA) for application on the casting materials of type Ni-resist D5S and vermicular cast iron GJV [1], [2]. Both TMF tests on specimens subject to characteristic load conditions and thermal shock tests on T/H have been conducted for identification and verification purposes. The scatter band of the estimated number of cycles until crack initiation compared to experimental results on various critical T/H positions has clarified the requirement for more experimental and analytical work during approach adaption for T/H design.

The present study deals with the more detailed analysis of application-specific phenomena and microstructural phenomena to improve the description of both the deformation behavior and the damage behavior with respect to the mechanism acting on the microstructure. Furthermore, out-of-phase (OoP) TMF tests have been used to validate the material-specific creep-fatigue damage sum compared to previous in-phase (IP) TMF tests.

2. Results and conclusion

Isothermal strain controlled low-cycle fatigue (LCF) tests at varying temperatures have been conducted on smooth specimens by applying triangular shaped cycles without a dwell period to investigate the influence of strain rate, mean strain and aging as representative phenomena, which could occur due to arbitrary operation conditions. The cyclic deformation behavior at mid-life affects the calibration of the material model applied in the FEA, and the LCF life curves are important for the fatigue damage calculation.

For example, in Fig. 1, the effect of the strain rate $d\varepsilon=10^{-3}s^{-1}$ compared to a power of ten lower strain rate of $10^{-4}s^{-1}$ for D5S is shown. At a moderate temperature of around 200°C, the influence is insignificant. Beginning at approximately 500°C, the lower strain rate has more relevance. The LCF life curves in Fig. 1 (a) illustrate two effects. At a higher strain width range, the cycle number decreases together with a lower strain rate. Due to the higher strain load and the lower strain rate, the superimposed creep damage should be the main damage mechanism. In contrast to lower strain width ranges, the cycle number increases. It seems that in the latter case, the ductility of the material dominates the failure mechanism and creep, especially at lower loads may become of subordinate relevance. Fig. 1 (b) demonstrates a significant drop in strength at 700°C caused by lower strain rate.

Compared to the in [1] proposed geometric equivalent fatigue damage calculation of an anisothermal stress-strain hysteresis loop, further damage calculation procedures considering mean stress/strain effects have been developed. Several critical plane approaches and energy criteria have been applied to handle multiaxial stress states.

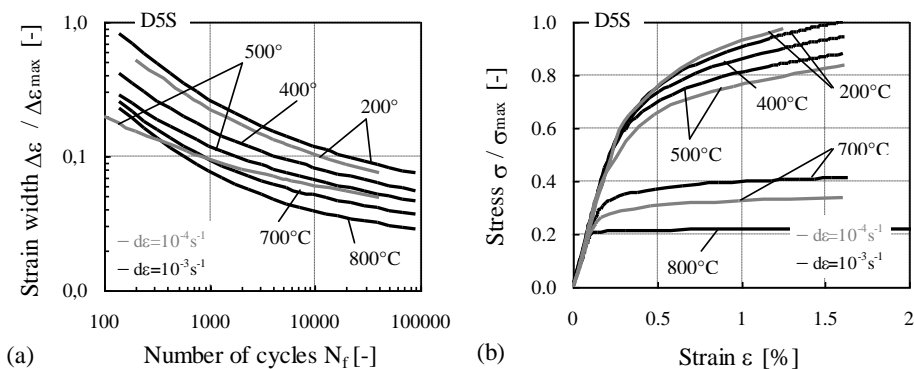


Figure 1. (a) LCF life curves and (b) cyclic stress-strain curves of D5S at strain rate of 10^{-3}s^{-1} (black shaded line) and 10^{-4}s^{-1} (gray shaded line), respectively.

By applying the underlying numerical calculation method of the lifetime approach, creep damage fraction and fatigue damage fraction until crack initiation have been determined by use of a representative cycle at mid-life on basis of the TMF tests conducted; the results for D5S, consisting of an austenitic matrix with spherical graphite inclusions and pearlite fractions, are shown in Fig. 2. Both damage fractions are approximately of the same amount. Moreover, equal TMF lifetime behavior results from OoP and IP testing conditions, respectively. The assumption of using only the mid-life cycle is justified due to minor hardening and softening effects during TMF loading.

Based on the results of advanced LCF testing under application-specific conditions and applying the validated creep-fatigue damage sums a more accurate estimation of the cycle number until crack initiation was demonstrated on specimens subject to characteristic TMF load conditions as well as on critical positions of the T/H design. Alternative fatigue damage methods, e.g. based on micro crack growth, are also being focused on. In addition, the analysis of microstructural phenomena should help to enhance the creep-fatigue interaction together with a more detailed failure description. It is assumed that tensile and compressive stress both have an equal effect on creep, and no distinction is made when calculating the creep damage. In a further step, it is proposed to describe crack propagation following crack initiation as part of the approach. This enables expansion of the lifetime assessment up until leakage and design failure.

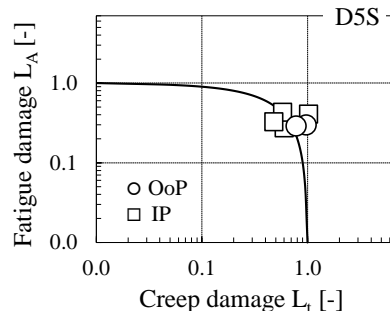


Figure 2. Fatigue and creep damage fractions of D5S specimens under characteristic TMF OoP and IP load conditions.

3. References

- [1] F. Laengler, T. Mao and A. Scholz (2010). Validation of a phenomenological lifetime estimation approach for application on turbine housings of turbochargers. *9th Int. Conf. on Turbochargers and Turbocharging*, May 19-20, London, p. 193-205.
- [2] F. Laengler, T. Mao and A. Scholz (2010). Phenomenological lifetime assessment for turbine housings of turbochargers. *9th Int. Conf. on Multiaxial Fatigue & Fracture*, June 7-9, Parma.

NUMERICAL STUDIES OF FORMABILITY OF PRE-STRETCHED STEEL SHEET

*D. Lumelskyy*¹, *J. Rojek*¹, *R. Pecherski*¹, *F. Grosman*², *M. Tkocz*²

¹*Institute of Fundamental Technological Research, Warsaw, Poland*

²*Silesian University of Technology, Faculty of Materials Engineering and Metallurgy, Katowice, Poland*

This paper presents results of numerical simulation of formability tests carried out for a pre-stretched steel sheet. Numerical modelling has been verified using experimental results. The tests consisted in stretching of the specimens of different widths over the hemispherical punch. The specimens were cut from the 1 mm thick DC04 steel blank in the as-received state and after pre-stretching by 13% along the rolling direction. The specimens were orientated parallel and perpendicularly to the rolling and pre-strain direction.

The experimental forming limit curves (FLC) were determined for the as-received and pre-deformed blank. FLCs provide a failure criterion in the forming limit diagrams (FLD) used for the estimation of the metal sheet formability. The known drawback of the strain based forming limit curves (FLC) is their dependence on strain paths [1], [2].

The aim of this study is to develop a numerical model allowing us to simulate complex deformation paths of the material subjected to a preliminary stretching, and then bulging tests performed to determine the FLC. Numerical analyses have been performed using the authors own computer explicit dynamic finite element program [3].

Numerical simulation consisted of the following subsequent stages: uniaxial stretching of the sheet, unloading and stress relaxation, cutting a specimen out of the pre-stretched sheet and bulging a specimen with a hemispherical punch. The onset of strain localization in the specimen was determined by post-processing time histories of major and minor strains and their first and second derivatives in accordance with the methodology presented in [4]. This procedure allows us to locate the inflection point in the major strain rate curve associated with the localization. The final shape of the specimens with thickness distribution are shown in Figure 1 together with fractured specimens. A good agreement between simulation and experiment in the failure location can be seen.

The experimental FLC for the as-received and pre-stretched steel blanks are shown in Figure 2. The FLD is built taking the rolling direction as the y axis and the transverse direction as the x axis. The effect of pre-stretching is visible in Figure 2 in the changed form and shift of the forming limit curve for the pre-stretched blanks in comparison to the as received FLC. The major and minor principal strains near the failure zone obtained for the two specimens analysed were compared in Figure 2 with the experimental FLC for the pre-stretched blank and experimental principal strains measured at fractured zones in the respective specimens. We can notice that the strains in the failure zone predicted

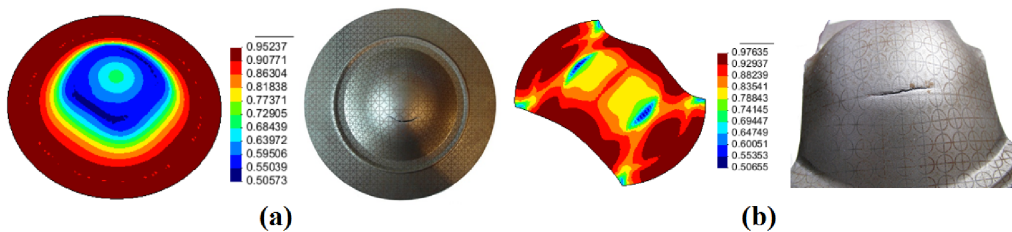


Figure 1. Comparison of numerical and experimental results – deformed specimens with thickness distribution and fractured specimens after test: (a) circular specimen, (b) 77 mm wide specimen

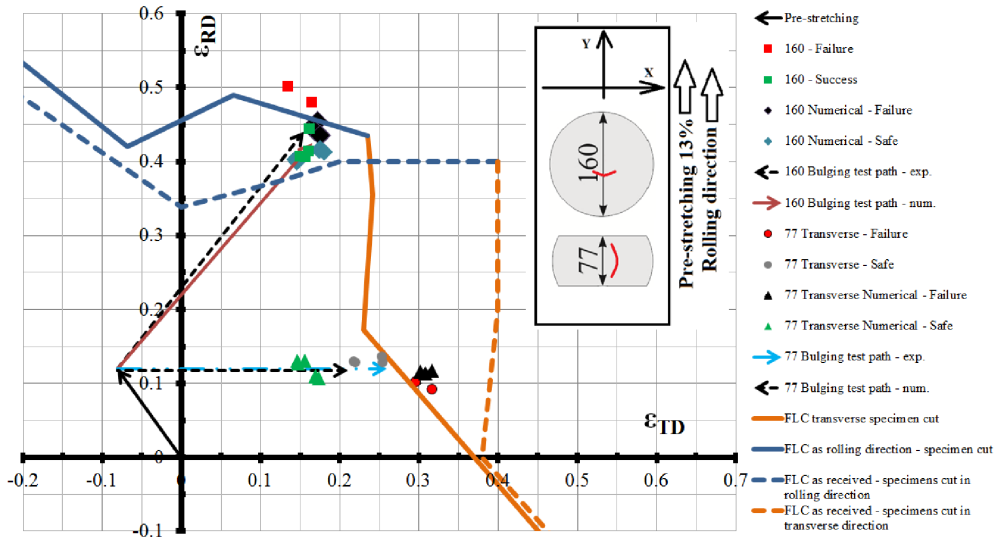


Figure 2. Strain paths and principal strains in the failure zones –numerical and experimental results.

by numerical simulation are in a good agreement with experimental data. Some discrepancies can be attributed to size dependency of strain localization in the finite element models as well as inaccuracy of strain measurements in experimental tests. Figure 2 also shows schematically complete strain paths for the material in failure zones in both specimens.

Comparison of numerical and experimental results obtained in formability tests performed for the pre-stretched blanks confirms validity of the developed numerical model. The model can be used in further theoretical studies. It can be applied to study the effect of different strain paths on the FLC. Different strain paths can be obtained easily in the model.

Acknowledgements

The authors acknowledge funding from: (1) European Regional Development Fund within the framework of the Innovative Economy Program, project number POIG.01.03.01-14-209/09, acronym – NUMPRESS, (2) Ministry of Science and Higher Education through research project N N501 1215 36, (3) National Science Centre through research project No. 2311/B/T02/2011/40

References

- [1] A. Graf and W.F. Hosford (1993). Effect of changing strain paths on forming limit diagrams of Al 2008-T4, *Metallurgical and Materials Transactions*, **24**, No. 11, 2503.
- [2] M. Nurcheshmeh and D. E. Green (2011). Investigation on the strain-path dependency of stress-based forming limit curves, *Int. Journal of Material Forming*, 4, No. 1, 25-37.
- [3] J. Rojek, O.C. Zienkiewicz, E. Onate E. and Postek E. (2001). Advances in FE Explicit Formulation for Simulation of Metalforming Processes, *Journal of Materials Processing Technology*, 119/1-3, pp. 41-47.
- [4] Q. Situ, M.K. Jain and D.R. Metzger, (2011). Determination of forming limit diagrams of sheet materials with a hybrid experimental-numerical approach, *Int. Journal of Mechanical Sciences*, 53, Issue 9, pp. 707—719.

ON THE GEOMETRY AND COMPRESSIVE STRENGTH OF CERAMIC FOAMS

M. Nowak¹, Z. Nowak¹, R. Pęcherski¹, M. Potoczek², R. Śliwa²
¹ Institute of Fundamental Technological Research, Warsaw, Poland
² Rzeszów University of Technology

1. General

Metal/ceramics interpenetrating composites are new materials obtained by liquid metal infiltration into a ceramic foam, called a preform. Ceramic preforms are produced by a new method of manufacturing of porous ceramics known as gelcasting of foams. Porous ceramics fabricated by this method is characterized by a continuous network of spherical cells interconnected by circular windows. The open porosity due to the presence of windows creates good hydro-dynamical properties for liquid metals infiltration. For better understanding mechanical properties of such composites a numerical model of ceramic foam is needed.

2. Geometry of ceramic foams

Geometry of ceramic foams can be generated in two steps. First, the coordinates of the center point of the spherical bubbles and its diameter are produced by PYTHON scripts. The diameters of spherical bubbles were estimated from micro-tomography and scanning electron microscopy images. On the other hand, the coordinates of the center points are determined in such a way that the bubbles have to intersect with each other. Finally, the intersecting bubbles are subtracted from the bulk block of any shape.

3. Numerical simulations

Several numerical simulations of uni-axial compression test have been performed. The bottom surface of the sample was full constrained and the top surface of this sample was moved parallel to the z- axis. The force was resulted from the final step of displacement in simulation. As a result the effective Young modulus of the investigated foam was determined.

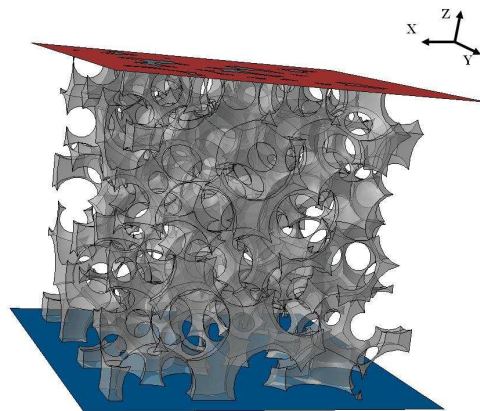


Fig 1. Numerical model of the foam with porosity 90% subjected to compression.

4. References

- [1] M. Kirca, A. Gul, E. Ekinici, F. Yadim, A. Mugan, Computational modeling of micro-cellular carbon foams, *Finite Elements in Analysis and Design*, 44, 2007, 45-52.
- [2] F.V. Antunes, J.A.M Ferreira, C. Capela, Numerical modeling of the Young's modulus of syntactic foams, *Finite Elements in Analysis and Design*, 47, 2011, 78-84.
- [3] S. Sihn, A.K. Roy, Modeling and prediction of bulk properties of open-cell carbon foam, *Journal of the Mechanics and Physics of Solids*, 52 2004, 167-191.
- [4] L. James, S. Austin, C. A. Moore, D. Sephens, K. K. Walsh, G. D. Wesson, Modeling the principle physical parameters of graphite carbon foam, *Carbon*, 48 2010 2418-2424.
- [5] Y.X. Gan, C. Chen, Y.P. Shen, Three-dimensional modeling of the mechanical property of linearly elastic open cell foams, *International Journal of Solids and Structures*, 42, 2005, 6628-6642.
- [6] A. P. Roberts, E. J. Garboczi, Elastic properties of model random three-dimensional open-cell solids, *Journal of the Mechanics and Physics of Solids*, 50, 2002, 33-55.
- [7] W. Jang, S. Kyriakides, A. M. Kraynik, On the compressive strength of open-cell metal foams with Kelvin and random cell structures, *International Journal of Solids and Structures*, 47, 2010, 2872-2883.
- [8] R. M. Sullivan, L. J. Bradley, A. Lerch, A general tetrakaidecahedron model for open-celled foams, *International Journal of Solids and Structures*, 45, 2008, 1754-1765.
- [9] A. P. Roberts, E. J. Garboczi, Elastic moduli of model random three-dimensional closed-cell cellular solids, *Acta Materialia*, 49, 2001, 189-197.
- [10] Y. Takahashi, D. Okumura, N. Ohno, Yield and buckling behavior of Kelvin open-cell foams subjected to uniaxial compression, *International Journal of Mechanical Sciences*, 52, 2010, 377-385.

Geomechanics

ASSESSMENT OF SLOPE STABILITY IN COHESIVE SOILS DUE TO A RAINFALL

S. Pietruszczak, E. Haghghat

McMaster University, Hamilton, Canada

Introduction

It is well known that a heavy rainfall can trigger a loss of stability of slopes. This is particularly the case for slopes constructed in cohesive soils, such as clay or a cemented soil. The problem of stability of natural and engineered slopes has been a subject of research for a number of decades.

The primary difficulty in modelling the loss of stability due to a rainfall lies in assessing the in-situ conditions and in describing the coupling between the time-dependent process of water infiltration and the evolution of stress field. The problem is typically analysed by integrated software in which the transient seepage analysis is coupled with traditional limit equilibrium slope stability analysis. Alternatively, the frameworks for unsaturated soil are implemented in which the suction pressure is considered as a state parameter and an optimization technique is used to search for a critical slip surface. In general, the conventional methods for assessing the stability of unsaturated soils, based on limit equilibrium approach, significantly underestimate the safety factors. Therefore, more accurate techniques are required.

In clays, the bond strength increases rapidly with decreasing water content. It is rather apparent that free water in clays has low compressibility and virtually no viscosity. The water in the vicinity of minerals, however, has quite different properties which cannot, in fact, be quantified due to complex chemical interactions. Therefore, the measurement and/or control of suction pressures are difficult, which is the main reason why the developments in the area of mechanics of unsaturated clays have not advanced that significantly.

Recognizing the above limitations, the approach implemented here is based on a phenomenological framework of chemo-plasticity. This is believed to be a pragmatic alternative to both the micro-mechanical approach (which in view of complexity of chemical interactions represents an overwhelming task) and the classical notions of unsaturated soil mechanics. Within the proposed framework, the injection of water is said to trigger a volume change (swelling/collapse) that is coupled with reduction in suction pressures that, in turn, results in degradation of strength and deformation properties.

The scope of the work

The first part of this paper deals with the formulation of the problem. This includes the derivation of the constitutive relation, specification of a criterion for the onset of global instability and a brief review of the coupled transient formulation.

Within the framework of chemo-plasticity, the progress in the chemo-mechanical interaction is monitored by a scalar parameter that reflects the evolution of the matrix suction pressure. This parameter is embedded in the classical plasticity framework. Since the kinetic of the chemical reactions at the micro-level depends explicitly on time, the macroscopic response is also time-dependent. The progress in the chemo-mechanical interaction is coupled with a continuing degradation of strength and deformation properties. The specific mathematical framework employed is that of deviatoric hardening, which incorporates a non-associated flow rule and attributes the hardening effects to accumulated plastic distortions. Here, the constitutive relation is derived first, followed by the formulation of an explicit (backward Euler) and implicit (forward

Euler) integration schemes. An illustrative example is provided involving a typical creep test in which the chemo-mechanical interaction results in either stationary conditions or a spontaneous failure of the sample.

The governing equations describing the transient hydro-mechanical coupling are analogous to those employed in Biot's theory. The problem is formulated by considering the overall linear momentum balance for the soil-fluid mixture, the momentum balance for the fluid and the mass conservation for the fluid. Assuming that the fluid flow is governed by Darcy's law and neglecting the connective terms, the original formulation, in terms of displacement - fluid velocity - pore pressure, can be simplified to that in which the primary nodal variables are the displacements of the soil skeleton and the pore pressures. In this case, the boundary conditions are expressed in terms of traction/displacements and pore pressures/influx. Since the primary application here involves the case of unconfined flow, the material is considered as partially saturated under the constraint of no excess of air pressure. This assumption is perceived purely as a numerical strategy that enables to trace the history of evolution of phreatic surface.

The numerical analysis, discussed in the second part of this paper, involves a slope in a cohesive soil (clay) subjected to a period of an intense rainfall. The slope examined in this study has dimensions typical of engineered slopes in Singapore; it is also representative of shallow slopes in the province of Manitoba (Canada) that underwent a translational failure in the late 1990's. A major rainfall event of a prescribed intensity is considered. Note that the actual amount of rainfall that can infiltrate the ground at a given time ranges from zero to infiltration capacity, which depends on moisture content and porosity of the specific soil. Apparently, if the precipitation rate exceeds the infiltration rate, the runoff will usually occur. In the simulations presented here, no antecedent rainfall is applied prior to the major event.

The finite element analysis incorporates the transient hydro-mechanical coupling, as described earlier. The evolution of the wetting front is monitored and the framework of chemo-plasticity is employed to model the mechanical characteristics of clay. The overall stability of the slope is assessed by introducing a criterion that is expressed in terms of second order work normalized with respect to that of an elastic continuum.

Keywords: chemo-plasticity, rainfall infiltration, hydro-mechanical coupling, transient phreatic surface, stability criterion

MODELING OF THE COMBINED SLIP AND FINITE SLIDING IN A FRICTIONAL CONTACT INTERACTION OF SPHERICAL PARTICLES: STATIC AND DYNAMIC RESPONSE

R. Balevičius¹ and Z. Mróz²

¹ *Vilnius Gediminas Technical University, Vilnius, Lithuania*

² *Institute of Fundamental Technological Research, Warsaw, Poland*

1. Introduction

The contact interaction of two elastic spheres under normal or oblique loading and torsional couple has been studied by Mindlin and Deresiewicz [1], Lubkin [2], Walton [3], Segalman et al. [4]. For oblique loading only the contact slip regime was studied with the sticking zone in the central part and the slip zone in the outer part of contact area. The sliding regime then occurs when the slip zone develops within the whole contact area. The discrete memory of contact response with consecutive creation and erasure of loading events has been presented by consecutive loading surfaces in the \mathbf{T} – N space, where \mathbf{T} is the tangential load vector and N is the normal load to the contact plane; cf., Dobry et al. [5], Jarzębowski and Mróz [6].

When a *sliding regime* develops under the finite normal load N and the increasing tangential load T , the central sticking zone is erased and sliding occurs along the whole area of contact. For a specified trajectory of the sphere centre, both N and T vary and the contact force evolution, length of sliding path, time-period of contact interaction and frictional energy dissipation become of primary importance in the deformation and flow analyses of granular matter.

In particular, the static and dynamic contact response is considered for the linear and circular sphere motion trajectories, analyzing the contact force traction evolution and dissipated energy due to frictional interaction. For the periodic sliding motion, the hysteretic response is analysed and combined slip and sliding regimes are considered. The modeling is performed analytically and numerically as well for the displacement and force controlled processes.

2. Analysis of the contact response

The sliding regime between to identical sphere of radii R , elastic moduli E and Poisson ratios ν can be easily specified requiring $\varphi > \varphi_u$, where φ is the angle between the line normal to the contact zone radius a_i and the linear path of the sliding sphere. An ultimate angle φ_u was specified by formula $\tan(\varphi) \geq \frac{(2-\nu)\mu}{4(1-\nu)} \approx \frac{\mu}{4}(2+\nu) = \tan(\varphi_u)$ (μ is the friction coefficient between the sphere surfaces) and plotted in Figure 1(a). The circle of radius $R_s = 2R \sin(\varphi_u)$ plotted at point O indicates that the sliding regime occurs for all linear paths emanating from the point O_1 and not intersecting the circle. On the other hand, the slip regime develops for all linear paths intersecting the circle. In other words, there is the sphere of radius R_s and conical domain with its vertex at O_1 and tangential to the sphere specifying the slip regime and the external domain specifying the sliding regime bounded by the plane normal to OO_1 . The contact separation occurs for the paths emanating from O_1 in the exterior of slip and sliding domains.

During sliding the contact zone moves with respect to both spheres, changing its orientation and size. In particular, at the contact engagement the overlap is zero, while with progress of sliding path s_r , the overlap h_t starts to grow up reaching the maximal value at the symmetry line, and, subsequently, it diminishes tending to zero again at the contact separation Figure 1(b). The analytical solution within the continuum mechanics formulation is not available and only the

numerical incremental procedure can be applied. Therefore, a simplified model was developed by assuming the normal contact traction N to be specified by the Hertz solution in terms of the contacting spheres overlap geometry and material characteristics, while the tangential traction is defined by the sliding friction rule, $T = \mu N$. In Figure 1(b), the tangential force (b) traction during the hysteretic behaviour under the imposed linear trajectory of the contacting sphere is demonstrated. Here, the unloading curve may be accounted for neglecting the slip displacement δ_u (i.e., an instant unloading) or with account that. The tangential force vs. slip curve was described in terms of a power law function accounting for the ultimate slip displacement, at which the sliding regime starts, and varying contact zone radius.

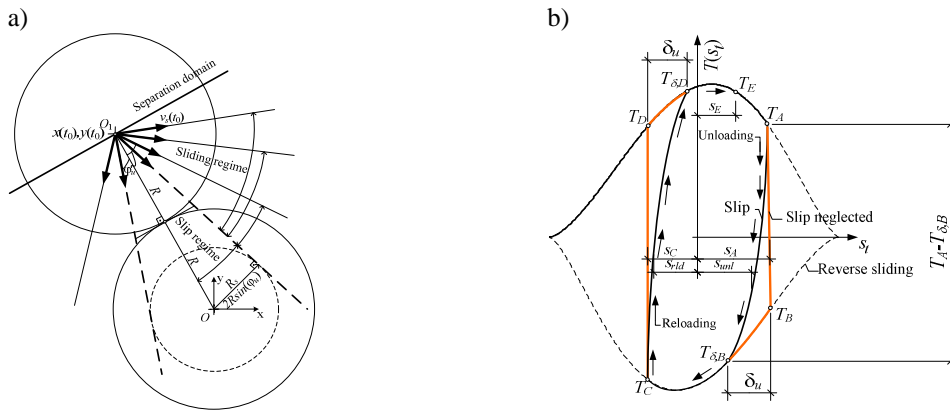


Figure 1 Slip, sliding and separation domains for the linear sliding paths (a); tangential force traction during the hysteretic behaviour (b)

3. Concluding remarks

The evaluation of driving force during contact sliding motion was determined for both monotonic and reciprocal sliding motion. The analytical formulae and diagrams of driving force versus sliding path have been specified for linear and circular paths. The sliding trajectories are also determined for the load controlled programs. The results presented can be applied in the experimental testing of frictional response of contacting bodies, in a wear study of rough surfaces or in the contact interaction analysis of granular material during flow. The results can also be relevant for the ongoing development of the discrete element method.

4. References

- [1] R.D. Mindlin and H. Deresiewicz, (1953). Elastic spheres in contact under varying oblique forces, *Journal of Applied Mechanics*, **20**, 327-344.
- [2] J.L. Lubkin (1951). The torsion of elastic spheres in contact, *Journal of Applied Mechanics*, **18**, 183-187.
- [3] K. Walton (1978). The oblique compression of two elastic spheres, *Journal of the Mechanics and Physics of Solids*, **35**, 213-226.
- [4] J.D. Segalman, J.M. Starr and H.V. Heinstein (2005). New approximations for elastic spheres under an oscillating torsional couple, *Journal of Applied Mechanics*, **72**, 705-710.
- [5] R. Dobry, T.-T. Ng, E. Petrakis and A. Seridi (1991). General model for contact law between two rough spheres, *Journal of Engineering Mechanics*, **117**, 1365-1381.
- [6] A. Jarzembowski and Z. Mróz (1994). On slip and memory rules in elastic, friction contact problems, *Acta Mechanica*, **102**, 199-216.

DISCRETE SIMULATIONS OF QUASI-STATIC TRIAXIAL AND BIAXIAL COMPRESSION FOR SAND USING DEM

J. Kozicki and J. Tejchman

Gdańsk University of Technology, Gdańsk, Poland

1. General

Granular materials consist of grains in contact and of surrounding voids, which change their arrangement depending on environmental factors and initial density. Their micromechanical and fabric behaviour is inherently discontinuous, heterogeneous and non-linear. To describe their behaviour, two main approaches are used: continuum and discrete ones. The first ones perform simulations at the global scale using the finite element method on the basis of e.g. elasto-plastic and hypoplastic constitutive models enhanced by a characteristic length of micro-structure to describe strain localization. In turn, the latter ones perform simulations at the grain scale, i.e. each grain is modelled individually. Their advantages are that they directly model micro-structure and can be used to comprehensively study the mechanism of the initiation, growth and formation of shear zones at the micro-level which strongly affect macro-properties of granular matter. The disadvantages are: high computational cost, inability to model grain shape accurately, difficulty to validate it experimentally as the inertial and damping effects lose their meaning in quasi-static problems. However, they become more and more popular nowadays for modelling granular materials due to an increasing speed of computers and a connection possibility to the finite element method. A large number of tests and simulations reveal that irregularly shaped grains strongly affect the quasi-static mechanical behaviour of granular materials. To resemble the real grain shape (roughness), two main approaches are usually used: 1) contact moments between rigid spheres or disks are assumed or 2) clusters of combined discrete elements that form irregularly-shaped grains are introduced.

2. Discrete results

The objective of this paper is to present numerical analyses of quasi-static triaxial and biaxial compression tests carried out to determine the macroscopic behaviour of a sand specimen composed of discrete elements in the form of: a) spheres with contact moments and b) symmetric and non-symmetric clusters of spheres. A three-dimensional discrete model YADE developed at University of Grenoble was used [1], [2] which takes advantage of the so-called soft-particle approach (i.e. the model allows for particle deformation, modeled as an overlap of particles). Two contact models were considered (linear and non-linear according to Hertz [3] and Mindlin and Deresiewicz [4]). The particle breakage has not been considered yet. The main intention of our studies was to calculate the effect of the grain roughness (shape) on the shear strength, dilatancy, elastic and dissipated energies of real sand (so-called Karlsruhe sand), which had the same initial void ratio, mean grain diameter and grain distribution. Attention was paid to the energy transformation in sand and its elastic and dissipative characteristics, playing a fundamental role in the granular matter behaviour [5]. In addition, the effect of the grain distribution curve, initial void ratio, pressure level, mean grain diameter and specimen size was numerically analyzed. Discrete simulation results for triaxial and biaxial compression were compared with corresponding experimental data from drained axisymmetric triaxial compression tests performed by Wu [6] and drained biaxial compression tests carried out by Vardoulakis [7] at Karlsruhe University with real sand.

The discrete results were compared with the corresponding FE results carried out with a micro-polar hypoplastic constitutive model which is capable to realistically capture the macroscopic

behaviour of granular materials by taking into account shear localization [8], [9]. The micro-polar constitutive law takes into account the effect of density, pressure, direction of deformation rate, mean grain size, grain roughness and grain crushing on the material behaviour. Due to the presence of a characteristic length in the form of a mean grain diameter, the constitutive model can describe the formation of shear zones: their thickness and spacing, and the related size effect. A micro-polar model makes use of rotations and couple stresses, which have clear physical meaning for granular materials. First, the rotations and couple stresses can be observed during shearing and remain negligible during homogeneous deformation. Second, the additional rotational degree of freedom of a micro-polar continuum arises naturally by mathematical homogenization of an originally discrete system of spherical grains with contact forces and contact moments. Thanks to a direct comparison between FEM and DEM [2], it is possible to calibrate more precisely both approaches to simulate shear localization in granular materials.

Finally, the evolution of micro-structure within a shear zone (during their initiation, formation and propagation) and to relationship between the self-organization of force chain networks and loaded grain contacts was studied during a biaxial compression test. Several characteristic and remarkable events occurring within a shear zone such as: vortices, buckled granular columns, shear micro-bands, alternating periodic dilatant and contractant regions were numerically investigated in order to determine their effect on the width of a shear zone.

3. References

- [1] J. Kozicki and F.V. Donze (2008). A new open-source software developed for numerical simulations using discrete modelling methods, *Computer Methods in Applied Mechanics and Engineering*, **197**, 4429-4443.
- [2] L. Widulinski, J. Tejchman, J. Kozicki and D. Leśniewska (2011). Discrete simulations of shear zone patterning in sand in earth pressure problems of a retaining wall, *Int. J. Solids and Structures*, **48**, 7-8, 1191-1209.
- [3] H. Hertz (1882). On the contact of elastic solids, *J. Reine u. Angewandte Mathematik*, **92**, 156-171.
- [4] R. D. Mindlin and H. Deresiewicz (1953). Elastic spheres in contact under varying oblique forces, *J. Appl. Mech. Trans. A.S.M.E.* **75**, 327-344.
- [5] J. Kozicki, J. Tejchman and Z. Mróz (2011). Effect of grain roughness on strength, volume changes, elastic and dissipated energies during quasi-static homogeneous triaxial compression using DEM, *Granular Matter* (under review).
- [6] W. Wu (1992). *Hypoplastizität als mathematisches Modell zum mechanischen Verhalten granularer Stoffe*. Heft 129, Institute for Soil- and Rock-Mechanics, University of Karlsruhe.
- [7] I. Vardoulakis (1980). Shear band inclination and shear modulus in biaxial tests, *Int. J. Num. Anal. Meth. Geomech.* **4**, 103-119.
- [8] J. Tejchman and W. Wu (2010). Boundary effects on behaviour of granular material during plane strain compression, *European Journal of Mechanics / A Solids* **29**, 18-27.
- [9] J. Tejchman and J. Górski (2010). FE study of patterns of shear zones in granular bodies during plane strain compression, *Acta Geotechnica* **5**, 2, 95-112.

EXPERIMENTAL STUDY ON SHEAR LOCALIZATION IN GRANULAR MATERIALS WITHIN COMBINED STRAIN AND STRESS FIELD

D. Leśniewska^{1,2}, M. Niedostatkiewicz³ and J. Tejchman³

¹ Koszalin University of Technology, Koszalin, Poland

² Institute of Hydro-Engineering Polish Academy of Sciences, Gdansk, Poland

³ Gdańsk University of Technology, Gdańsk, Poland

1. General

The practical knowledge of the mechanical behaviour of granular materials is largely based on element tests assumed to represent uniform stress and homogeneous strain. Some important parameters such as the angle of internal friction and dilatancy angle usually come from element tests. These parameters are determined from global measurements of forces and displacements at a specimen's boundaries and vary from their local quantities, which cannot be easily measured. The difference between local and global (averaged over the whole volume of the sample) measurements are mainly due to localised deformation, concentrated within narrow shear zones, but also due to imperfect boundaries of the test equipment. The effect of localised deformation and imperfect boundary conditions have to be separated to distinguish the material behaviour from the structural one. And, as it is broadly accepted that localised deformation controls a global post-peak response of granular material, it is necessary to understand its behaviour within shear zones. It became recently much easier due to some full field measurement methods based on digital image correlation.

Validation of soil constitutive models has been usually performed by numerical simulations of element tests – there is less possibility to do it for the entire geotechnical system, even at a small scale. This paper delivers the experimental material to enable a validation of some theoretical soil models – especially hypotheses including soil micro-structure, which can only be verified with the local knowledge of stresses and strains. Small scale plane strain tests were performed, which modelled a simple soil mechanics boundary value problem – granular material retained by a rigid wall. The wall could translate horizontally into and out of granular material. This kind of test arrangement was chosen, since it produces a relatively simple and easy to analyse localisation pattern. The characteristic features of the shear zones formation in deforming granular materials were investigated using Particle Image Velocimetry (PIV), which was combined with a photo-elastic study of the stress field. PIV is an optical technique for measuring displacement fields from successive digital images and was employed to analyse experiments on two different granular materials, composed of (1) sand grains and (2) glass granules. The tests on glass granules were supplemented by taking photo-elastic images in circularly polarised light to gather information on changes in the average stress field, accompanying the specimen deformation. Attention was focused on the effect of the initial density, grain coarseness and magnitude of wall displacement on shear localisation within a strain field and its geometrical relation to some structures found in the stress field.

We need the simultaneous knowledge of both stress and strain fields to recognise internal conditions in granular materials. It was shown by Leśniewska and Muir Wood [1], that one can successfully combine stress and strain measurements in case of glass ballotini – a good substitute material for quartz sand. The question then arises to which extent the observations performed on glass ballotini can be considered as relevant also for real sands. Any comparison between sand and glass ballotini can be made through the strain fields only, as sand grains cannot be made transparent, so do not show the photo-elastic effect. As a result, any direct conclusions regarding the

relation between stress and strain fields can be made solely on the base of glass ballotini tests. We believe, however, that if both granular materials show similar deformation patterns, their stress fields have to be also similar and equally related to the strain field. So the knowledge on the stress field in the case of a sand sample can be obtained in an indirect way, if only the quality of representing real granular material by glass ballotini is sufficient.

The specific objective of this paper was therefore to verify the quality of glass ballotini as a surrogate granular material, in terms of a full field analysis, by pointing out any significant similarities or differences within strain fields produced in the same type of tests on both granular materials, using the same test box, same loading system and same sample preparation method [2]. The paper belongs to the longer series, which general goal is to increase our still insufficient knowledge on the geometrical relation between strain and stress fields in granular materials and we believe that the data presented here add to this knowledge some crucial information, especially important for the future work.

The comparison between glass granules and sand grains was done for initially dense materials, as it is known that in such a case, a localisation pattern is usually simpler, better developed and easier for observations than in the case of granular material in an initially loose state. The other reason was that due to the high uniformity of glass granules it was difficult to produce initially loose sample – the almost mono-disperse granulate tended to organise at approximately one density with the evidence of a local cristallisation (order). Due to that the photo-elastic tests on the initially loose glass granulate were postponed for the future (use of at least bi-disperse glass granulate is planned).

We performed also tests on initially loose sand and some results are presented to show that our experimental procedure can properly capture the difference between a loose and dense state of granular material.

2. Conclusions

Strain localisation and changes in the stress field are closely correlated. The nature of this correlation has to be further studied. Our hypothesis from the present analysis is that the shear band is adjacent to the elevated stress region and coincides with some lowered stress area.

The procedure to compare photo-elastic stress fields and strain fields obtained by digital image correlation may contribute to the development of rational constitutive models including shear localisation and can be used to provide a qualitative support for advanced hypotheses of the behaviour of granular materials in shear zones.

The tests performed on spherical glass granules provide the information helpful in verifying discrete element analysis models of granular materials. Discrete elements can have different geometries, but to keep a low calculation cost, usually the simplest spherical geometry is chosen (dealing with realistic shapes would lead to a prohibitive calculation cost). In spite of objections to the spherical geometry being too idealised to accurately model the real granular material behaviour, our tests show they can represent the real soil behaviour with respect to the width and mode of shear localisation (the shear resistance may be however strongly underestimated [3]).

3. References

- [1] D. Leśniewska and D. Muir Wood (2009). Observations of stresses and strains in a granular material, *Journal of Engineering Mechanics* **135**, 9, 1038-1054.
- [2] D. Leśniewska, M., Niedostatkiewicz and J. Tejchman (2012). Experimental study on shear localization in granular materials within combined strain and stress field, *Strain* (in print).
- [3] L. Widulinski, J. Tejchman, J. Kozicki and D. Leśniewska (2011). Discrete simulations of shear zone patterning in sand in earth pressure problems of a retaining wall, *Int. J. Solids and Structures*, **48**, 7-8, 1191-1209.

STEADY AXIALLY- SYMMETRIC POLAR ICE SHEET FLOW WITH EVOLVING AND RECRYSTALLIZING FABRIC

Ryszard Staroszczyk

Institute of Hydro-Engineering, Polish Academy of Sciences, Gdańsk, Poland

1. Introduction

Ice cores drilled in large polar ice caps in Antarctica and Greenland show strong anisotropic micro-structures (fabrics), in which individual ice crystal c -axes (axes of crystal hexagonal symmetry) are aligned along some preferential directions (Gow *et al.* [1], Thorsteinsson *et al.* [2]). Such spatially oriented micro-structures form, and subsequently evolve, in the crystalline material in response to changing stress and deformation states which ice particles experience during their descent from the free surface to depth in an ice sheet. As a result, the microscopic structure of the material significantly varies with ice depth, and this is reflected by considerable changes in the macroscopic properties (viscosities) of the medium.

Two major microscopic mechanisms are involved in the development, and subsequent evolution, of anisotropic fabrics in polar ice masses. The first is the process of crystal lattice rotation, which operates throughout the entire domain of an ice sheet, and progressively leads to the formation of strong single-maximum fabrics, with the majority of the crystal c -axes clustered along the vertical. Such strong fabrics are usually found in bottom layers in central parts of a typical glacier. The other major micro-mechanism affecting the anisotropic properties of ice is the phenomenon of migration (or dynamic) recrystallization, which usually occurs in highly sheared near-bed regions of ice sheets. This process modifies the anisotropic micro-structures that have been created earlier by the crystal lattice rotation, and gives rise to so-called girdle or multi-maxima fabrics (Budd and Jacka [3], Alley [4]), with very coarse and interlocking grains (Duval and Castelnau [5]). Such changes in the micro-structure of ice result in significant changes in macroscopic viscosities of ice; therefore they must be accounted for in ice sheet flow models to properly simulate the real behaviour of polar glaciers.

2. Polar ice sheet flow model

In large-scale numerical models that have been developed so far, and are used to reconstruct the past, or predict the future, climatic scenarios and their effects on the behaviour of polar ice caps, the evolution of ice anisotropy caused by the migration recrystallization mechanism is commonly ignored. It is possible that still the only exception is the paper by Staroszczyk [6]. In that work, however, a simplified case of an ice sheet flow with an a priori prescribed free surface profile is analysed, so that it cannot serve as the solution of a real flow problem in which the free surface is a result of the flow; that is, the determination of an unknown free surface shape is part of the solution procedure.

The proposed ice sheet flow model is an attempt to fill this gap; that is, to solve a problem with an unknown free surface geometry and incorporating the migration recrystallization effects. Hence, a steady flow of an axially-symmetric ice sheet which slides on a rigid bedrock is considered, in which the glacier motion is driven by gravity forces under the action of prescribed climatic conditions (i.e., average accumulation and melt rates on the glacier boundaries). Temperature field in an ice sheet is also prescribed in order to uncouple the mass and momentum balance equations from the energy balance relations. For the above input conditions, the free surface profile (including the maximum glacier thickness and the lateral span) is determined. The main objective of the analysis is to examine how the migration recrystallization of ice influences the overall flow of a glacier, and, in particular,

to investigate its effect on the free surface shape and the velocity field within the glacier. For this purpose, a method developed by Gillet-Chaulet *et al.* [7] is adopted. The idea of the method is to relate the micro-mechanical properties of ice to a small set of geometric parameters (invariants of so-called orientation tensors) which characterize the micro-structure. Then, the six macroscopic viscosities in the orthotropic law are also calculated as functions of the above geometric parameters, linking thus the macroscopic properties to microscopic fabric. The microscopic behaviour of recrystallizing ice is described by two versions of a micro-mechanical model formulated earlier by Staroszczyk: a uniform strain-rate model [8], and a uniform stress model [9]. A new feature, compared to the original forms of the laws, is an inclusion of strongly non-linear effects of temperature and deviatoric stress magnitudes on the viscosities of ice.

The solution of the flow problem is constructed by a method of asymptotic expansions, known in glaciology as the shallow ice approximation (Hutter [10], Patterson [11]). Hence, a small parameter ϵ is introduced in the analysis, reflecting the small ratio of stress and velocity gradients in the lateral direction of an ice sheet compared to those in the thickness direction. This parameter is used to scale the flow equations and the associated boundary conditions. In the ensuing equations, all terms of order ϵ and smaller relative to unity are then neglected, with the aim to derive simpler, leading-order, forms. The reduced equations are subsequently integrated through the ice thickness to eliminate one spatial coordinate, which leads to a two-point boundary-value problem for a second order parabolic differential equation. The latter is solved numerically to calculate a function describing the free surface profile. Numerical simulations have been carried out for different accumulation, ablation and basal melt rates, in order to examine their effects on the glacier geometry (thickness and lateral span), and the depth profiles of the ice velocities. For illustrations, the results for isotropic ice flows are compared with those for anisotropic ice flows, with and without migration recrystallization involved.

3. References

- [1] A. J. Gow, D. A. Meese, R. B. Alley, J. J. Fitzpatrick, S. Anandakrishnan, G. A. Woods, and B. C. Elder. Physical and structural properties of the Greenland Ice Sheet Project 2 ice core: A review. *J. Geophys. Res.*, **102** (C12), 26 559–26 575, 1997.
- [2] T. Thorsteinsson, J. Kipfstuhl, and H. Miller. Textures and fabrics in the GRIP ice core. *J. Geophys. Res.*, **102** (C12), 26 583–26 599, 1997.
- [3] W. F. Budd and T. H. Jacka. A review of ice rheology for ice sheet modelling. *Cold Reg. Sci. Technol.*, **16** (2), 107–144, 1989.
- [4] R. B. Alley. Flow-law hypotheses for ice-sheet modelling. *J. Glaciol.*, **38** (129), 245–256, 1992.
- [5] P. Duval and O. Castelnau. Dynamic recrystallization of ice in polar ice sheets. *J. Phys. IV*, **5** (C3), 197–205, 1995.
- [6] R. Staroszczyk. Plane ice sheet flow with evolving and recrystallising fabric. *Ann. Glaciol.*, **37** (1), 247–251, 2003.
- [7] F. Gillet-Chaulet, O. Gagliardini, J. Meyssonier, M. Montagnat, and O. Castelnau. A user-friendly anisotropic flow law for ice-sheet modelling. *J. Glaciol.*, **51** (172), 3–14, 2005.
- [8] R. Staroszczyk. A multi-grain model for migration recrystallization in polar ice. *Arch. Mech.*, **61** (3-4), 259–282, 2009.
- [9] R. Staroszczyk. A uniform stress, multi-grain model for migration recrystallization in polar ice. *Acta Geophys.*, **59** (5), 833–857, 2011.
- [10] K. Hutter. *Theoretical Glaciology. Material Science of Ice and the Mechanics of Glaciers and Ice Sheets*. Reidel, Dordrecht, 1983.
- [11] W. S. B. Paterson. *The Physics of Glaciers*. Butterworth-Heinemann, Oxford, 3rd edition, 1994.

Micromechanics, Interfaces and Multi-Scale Modelling

FUNCTIONALLY GRADED COMPOSITES: NUMERICAL MODELING WITH FINITE ELEMENT METHOD AND ARTIFICIAL NEURAL NETWORK

M. Wojciechowski¹, M. Lefik¹ and D.P. Boso²

¹ *Technical University of Lodz, Lodz, Poland*

² *University of Padua, Padua, Italy*

1. Introduction

In this paper we present our numerical model of static, possibly physically non-linear effective behaviour of a body made of Functionally Graded Material (FGM). As it is known, geometry and materials composition of a “representative volume” (“RV”) (“RV” means: representative volume RV suitably defined for the case of FGM) is a function of a global variable \mathbf{x} , thus effective material coefficients defined for some small neighborhood surrounding \mathbf{x} are also functions of the global variable. In a solution of the boundary value problem (BVP) found for FGM the spatial variation of its macro properties must be taken into consideration. In a case when variation of mechanical properties of components can be expressed by elementary functions, a tolerance averaging technique (see [3]) is used to develop a symbolic formulae for effective material properties as a function of the microstructure. In our approach, in a case when the geometry of the microstructure is complex, Finite Element Method (FEM) and Artificial Neural Network (ANN) are jointly applied to describe dependence of effective material parameters on physical characteristics of micro components. We use ANN for approximation of the functional dependence of the composite properties on its microstructure. For each different “RV” we compute effective material properties using classical algorithm of a “virtual testing” of periodic composites. Elements of these procedures are described in [1] and [2].

2. Algorithm of the hybrid solution

The overall algorithm we follow consists of ix main steps and is defined below:

- i. Definition of FE scheme for global BVP for the composite. Parametrisation of “RV” should be passed to the global FEM description.
- ii. Definition of FE schemes for local BVPs for a family of local representative volumes.
- iii. Solution of selected local BVPs for averaged constitutive relations, parametrised with parameters of local representative volumes using “a virtual testing”.
- iv. Initial learning of the ANN with the results of the above step.
- v. Use and a random verification of the approximated by ANN, effective constitutive data while assembling global stiffness matrix. Possible additional trainings of ANN.
- vi. Solution of the global BVP for FGM composite

3. Modified soil as a FGM material

Various modifications of mechanical properties of soils are widely used in engineering. In the presented paper we limit our consideration to cohesivless soils. We focus our attention on the most common mechanism of such the modification that assumes an introduction of a reinforcing medium as a liquid phase that fills the pores. The hydro-mechanical properties of the soil change after some time, needed for solidification of the filling medium. In this way, the resulting medium is treated as a composite with solidified matrix and inclusions that reflect a granular composition of the initial granular material. All kind of injections can thus be modeled with the method of the analysis proposed in the paper. We exclude the techniques that result with composition of two different types of soils (“deep soil mixing”). Both hydrofobisation and reinforcing with cementitious materials can be considered as a possible fields of practical applications of the proposed numerical

approach. The purpose of our work is to predict the resulting hydro-mechanical properties of the soils in function of distance measured from the source of injection. This is very important since the existing estimation of the injection-pails diameter or the size of the hydrofobized area are mostly phenomenological. The estimated hydro-mechanical properties of the modified soil will be expressed in terms of the known properties of the initial materials used.

4. Non-fully reacted alloy as functionally (but not intentionally) graded material

This example is taken directly from a numerical modelling of a thermo-mechanical behaviour of a super-conducting cable for a nuclear fusion device (see [2]). These cables are widely used to create high electromagnetic fields and are produced as a very complex, hierarchical composite with many levels of hierarchy. Here, we limit ourselves to study the structure at a micro level. At the reaction temperature (about 920K-950K, depending on the manufacturer) the Sn included in the bronze diffuses into Nb and forms Nb_3Sn – a super-conducting alloy. Usually the filaments are not completely reacted. In modeling, we must take into consideration the presence of the non reacted kernel, its diameter, its position in the section of the strand. Since the diameter of the not reacted kernel is depending on the position of strand in the cable (due to the process of manufacturing), this composite is clearly, functionally (but not intentionally) graded. The similar gradation of properties is superposed with yielding which is non homogeneous in the cable, because of bending due to Lorentz forces. We have trained the ANN with several results of virtual tests, performed on various geometries of the “RV”. Relatively simple scripts allow to execute the computations and to redefine mesh for all virtual tests for different inner diameter, various eccentricity and, possibly, various yielded zones. The effective properties, resulting from these computations, are used then for ANN training and global FEM computations.

5. Conclusions

Numerical analyses show that the functional dependence of material parameters on the global position \mathbf{x} is very easy to be approximated and then – interpolated using ANN trained with small number of learning patterns. It was tested numerically that the use of various “RV” (means – representative volume suitably defined for the case of FGM) in the virtual testing procedure seems to be sufficient to take into account the variation of the FGMs geometry within given, finite tolerance.

Acknowledgment

The scientific research reported here has been carried out as a part of the Project „Innovative recourses and effective methods of safety improvement and durability of buildings and transport infrastructure in the sustainable development” at the Technical University of Łódź, Poland, financed by the European Union from the European Fund of Regional Development based on the Operational Program of the Innovative Economy.

6. References

- [1] M. Lefik, M. Wojciechowski (2005), Artificial Neural Network as a numerical form of effective constitutive law for composites with parametrized and hierarchical microstructure, *Computer Assisted Mechanics and Engineering Sciences*, Vol. 12, 183-194
- [2] M. Lefik, D.P. Boso, B.A. Schrefler (2009), Artificial Neural Networks in Numerical Modelling of Composites, *Computer Methods in Applied Mechanics and Engineering*, vol. 198, p. 1785–1804.
- [3] Woźniak, Cz., Wierzbicki, E. (2000), Averaging techniques in thermomechanics of composite solids. Tolerance averaging versus homogenization. *Wyd. Pol. Częst., Częstochowa*.

DEVELOPMENT OF A PASSIVE HEAT DISSIPATION SYSTEM USING PHASE CHANGE MATERIALS ASSOCIATED WITH OPEN CELL METAL FOAMS

J. Bajolet^{1,2}, S. Philippon¹, K. Huynen¹, J. Salat² and P. Lipinski¹

¹*Laboratoire de mécanique, Biomécanique, Polymère, Structures, ENIM, UPVM*

²*Hispano-Suiza, groupe SAFRAN, Réau, Rond Point René Ravaud 77551 Moissy-Cramayel*

To avoid damage of electronic devices the heat generated has to be dissipated by adequate cooling systems. In aeronautics for instance, some electronic parts work during short periods of flight (take-off, landing, breaking ...). But they have to be cooled in order to protect the electronic devices from themselves. The major part of cooling methods is based on the forced convection of a cooling liquid. This solution has good performances but requires a lot of equipment like pumps, filters, networks... So, this is not the best opportunity for aeronautical field where weight, price and reliability are critical. The aim of this study is to develop a passive system which works without any energy supply. The basic solution to create a passive heat dissipation system is to fix on the electronic device a bloc made of aluminium or copper to dissipate heat. But such a system can become heavy prohibiting its use for aircrafts because of the additional weight. Another technical solution consists in using the latent heat of phase change materials (PCMs). The controlled mass of PCM can dissipate the quantity of heat generated by the electronic device during a short period. The major disadvantage of the chosen PCM, a polymer material is its low thermal conductivity. This is why it is necessary to improve the global heat flux between the heat source and the PCM by the use of open cell aluminium or copper foams. This association allows obtaining a homogeneous temperature inside the PCM [2]. Experimental tests have been performed in this study to evaluate and compare the performances of such heat dissipation systems with respect to a PCM system.

Numerical analyses by finite element and finite volume methods have been performed to simulate the phase change of the PCM and the thermal evolution of the system. The complex geometry of the aluminium foam is a problem for the simulation: a huge number of elements is necessary to mesh the PCM embedded in open cell foams, (over 6 million of 3D elements). To circumvent this difficulty, it has been decided to replace the PCM and the open cell foam by a homogeneous material having the equivalent thermal properties of the composite. Several thermo-physical properties are needed for thermal transient analyses, namely: the density, the thermal conductivity, the specific heat and the latent heat of the PCM. Scalar quantities such as density, specific heat and the latent heat of PCM/foam equivalent material are determined in function of the mass fraction or concentration of each component. For the tensors quantities such as thermal conductivity, it is necessary to take into account the specific geometry of the open cell metal foam. A model using the geometry of open cell metal foam has been proposed by Boomsma et al. [1]. This model is based on an ideal geometry of the foam: the tetrakaidecahedron. This polyhedron has been chosen as a result of statistical observations on the open cell foams and because the tetrakaidecahedron is the space filling arrangement of cells of equal size with the minimal surface energy [1].

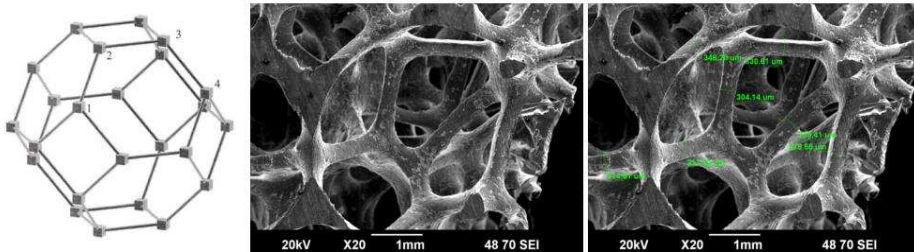


Figure 1: Tetrakaidecahedron and measurement of the foam pore size

In order to calculate the effective thermal conductivity according to Boomsma et al.'s model [1] various geometric characteristics of the foam pores are necessary as well as the thermal conductivities of the composite components. To validate the obtained thermal conductivity of the meso-homogeneous material, a heat transfer problem analyses has been compared for the homogeneous material and a volume of PCM containing open cell foam. The geometry of the foam has been obtained by X tomography, in order to reproduce the realistic 3D object. A representative part of the foam has been selected to limit the number of elements for the meshing of foam and PCM.

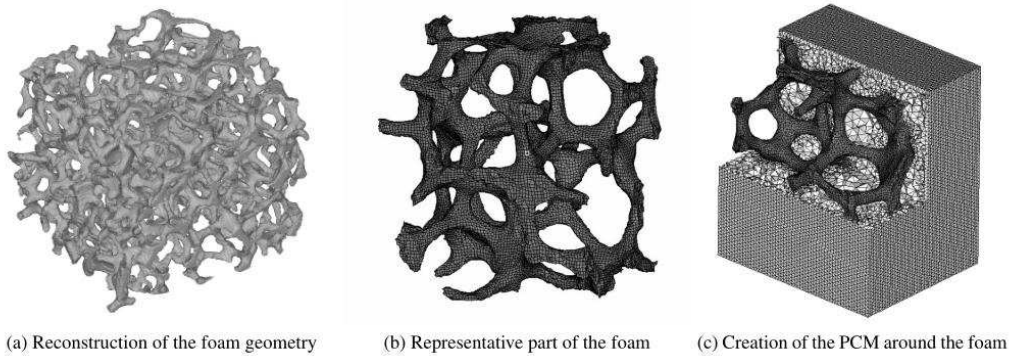


Figure 2: Meshing of the PCM embedded inside open cell foam

After validation of the homogenization model, the thermal properties have been applied to the numerical model representing the experimental tests. Then, the results were compared concerning the temperature evolution at the heater contact and the top PCM surface. This comparison is illustrated in figure 3. Good qualitative and quantitative agreement between these experimental and numerical results can be observed.

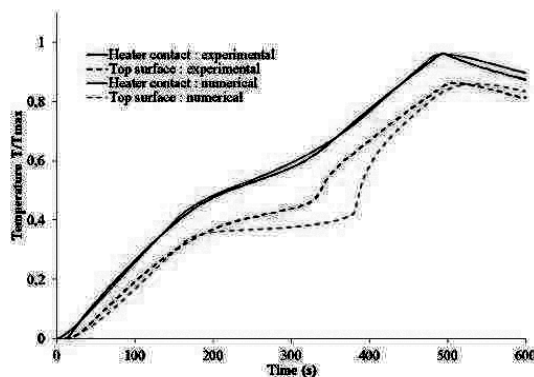


Figure 3: Comparison of experimental and numerical results for PCM embedded into open cell metal foam

- [1] Boomsma, K., Poulikakos, D., Feb. 2001. On the effective thermal conductivity of a three-dimensionally structured fluid-saturated metal foam. *International Journal of Heat and Mass Transfer* 44 (4), 827–836. 1, 2
- [2] Zhao, C., Lu, W., Tian, Y., 2010. Heat transfer enhancement for thermal energy storage using metal foams embedded within phase change materials (pcms). *Solar Energy* 84 (8), 1402 – 1412. 1

CONTINUUM DESCRIPTION OF QUASISTATIC CAPILLARY TRANSPORT OF LIQUID IN UNSATURATED POROUS MATERIALS

M. Cieszko

*Institute of Mechanics and Applied Computer Science,
Kazimierz Wielki University, Bydgoszcz, Poland*

1. Introduction

In the paper a new macroscopic description of quasistatic capillary transport of liquid and gas in unsaturated porous materials is presented. Theoretical considerations are based on the concepts of multiphase continuum mechanics. The three component model of the medium is proposed, for which the balance equations of mass, linear momentum and internal mechanical energy are formulated. The new approach has been proposed for derivation of the constitutive relations, similar to that used in the rational thermodynamics. The constitutive relations are derived basing on the balance inequality of the internal mechanical energy formulated for the whole system and on the Lagrange multipliers method.

A new definition of the quasistatic processes is introduced allowing derivation of their description as a special case of the general model given by balance equations and constitutive relations. The obtained equations have been applied for description of no wetting liquid intrusion into porous sphere. Macroscopic description of such process is very useful, e.g. for interpretation of experimental data of mercury porosimetry and has been obtained first time.

2. Kinematics. Basic assumptions

It was assumed that gas and liquid filling rigid porous material form macroscopic continuum composed of three constituents: gas, mobile liquid and capillary liquid. The division of liquid into two continua is justified both from kinematical and energetic point of view. The capillary liquid is contained in the thin layer covering the internal surface of pores. This liquid gathers the whole capillary energy of the liquid and is immovable. It can, however, exchange the mass with the mobile liquid in the vicinity of meniscus surfaces. The mass exchange occurs only during the meniscus motion in the pore space and is described by the separate velocity field. This makes it possible to model the mechanism of meniscus motion in the pore space. The mobile liquid is located in the internal area of liquid surrounded by its internal contact surface with the skeleton and surfaces of meniscus. Each constituent is characterized by the mass densities and their distributions are defined by parameters of saturations.

3. Mass balance equations

The local balance equations of mass for gas, mobile and capillary liquids take the form, respectively:

$$(1) \quad \frac{\partial \bar{\rho}_g}{\partial t} + \operatorname{div} \left(\bar{\rho}_g \left(\mathbf{v}_r \frac{\partial r}{\partial t} + \mathbf{v}_g \right) \right) = 0, \quad \frac{\partial \bar{\rho}_m}{\partial t} + \operatorname{div} \left(\bar{\rho}_m \left(\mathbf{v}_r \frac{\partial r}{\partial t} + \mathbf{v}_m \right) \right) = 0, \quad \frac{\partial \bar{\rho}_c}{\partial t} = \bar{s}_r \frac{\partial r}{\partial t}$$

where

$$\bar{\rho}_g = f_v s_g \rho_g, \quad \bar{\rho}_m = f_v s_m \rho_m, \quad \bar{\rho}_c = f_v s_c \rho_c$$

and f_v is the volume porosity, whereas s_g , s_m , s_c ($s_g + s_m + s_c = 1$) stand for volume saturations of gas, mobile and capillary liquid in the pore space, respectively. Vectors \mathbf{v}_g and \mathbf{v}_m denote velocities of mobile liquid and gas, and \mathbf{v}_r represents velocity field of the meniscus in the r -space. Parameter r defines equilibrium state of the meniscus and for the quasistatic processes can be interpreted as the capillary pressure. Motion of the meniscus take place only when the parameter r changes.

For the quasistatic processes of capillary liquid transport in unsaturated porous material mass balance equations take form

$$(2) \quad \rho_m \left(\frac{\partial \theta_m}{\partial r} + \text{div}(\theta_m \mathbf{v}_r) \right) + \frac{\partial(\theta_c \rho_c)}{\partial r} = 0, \quad \frac{\partial \theta_g}{\partial r} + \text{div}(\theta_g \mathbf{v}_r) = 0.$$

They represent balance equations of the mobile liquid and gas in the r -space and describe their saturations during the quasistatic processes.

4. Constitutive relations

The constitutive relations for quantities describing mechanical processes in unsaturated porous materials are derived basing on the balance inequality for the mechanical internal energy of the three-component system. The new approach is proposed similar to that used in the rational thermodynamics based on the entropy inequality analysis and the Lagrange multipliers method. In this approach balance equations of the system are used as constraints imposed on independent constitutive quantities. It was assumed that internal energy of gas, mobile and capillary liquids are unique functions of their mass densities and that saturation of capillary liquid is a unique function of mobile liquid saturation.

The obtained constitutive relations for the energy exchanged between mobile and capillary liquids take the form:

$$(3) \quad \frac{p_m}{\rho_m} + u_m - \frac{p_c}{\rho_c} - u_c = 0, \quad p_m - p_g + \frac{ds_c}{ds_m}(p_c - p_g) = 0;$$

The pressures of gas, mobile and capillary liquids are defined by relations:

$$(4) \quad p_g = (\rho_g)^2 \frac{\partial u_g}{\partial \rho_g}, \quad p_m = (\rho_m)^2 \frac{\partial u_m}{\partial \rho_m}, \quad p_c = (\rho_c)^2 \frac{\partial u_c}{\partial \rho_c}$$

where u_g, u_m, u_c are mass densities of their mechanical internal energies.

For the velocity \mathbf{v}_r modeling mechanism of meniscus motion it is assumed that is proportional to the gradient of capillary liquid saturation,

$$(5) \quad \mathbf{v}_r = -C(s_c, p_c) \mathbf{grad}(s_c).$$

DETERMINATION OF PORE SPACE STRUCTURE OF AUTOCLAVED AERATED CONCRETE BASED ON 3D μ CT IMAGES AND MERCURY POROSIMETRY

*M. Cieszko, P. Gadzała, Z. Szczepański and M. Kempinski
Institute of Mechanics and Applied Computer Science,
Kazimierz Wielki University, Bydgoszcz, Poland*

1. Introduction

Identification of microscopic pore geometry and macroscopic parameters of the pore space structure of autoclaved aerated concretes (AAC) is a very important issue in the study of their physical properties. The internal pore structure defines mechanical properties of AAC and plays important role in many physical and chemical processes occurring in such materials, e.g. in transport of moisture, heat and chemicals, in wave propagation and chemical reactions.

The ACC belong to the group of porous materials with two porosities. It means that their pore space is formed by pores of two classes of sizes: micropores the characteristic sizes of which ranges from several microns to millimeter, and nanopores of size from several nanometers to micron. The volumes of both types of pores are comparable. This causes that investigations of such materials are very difficult.

The aim of the paper is to present two complementary methods of investigation of ACC pore space structure based on micro-computed tomography (μ CT) and mercury porosimetry (MP). They have been used to determine micropore and nanopore porosities of ACC samples and their pore size distributions. Due to resolution of μ CT limited to 1 micrometer this method can be used only for investigation of micropore space. The investigation of this space by MP method is doubtful because of its bubble structure that causes bottle ink effect. The MP method is useful however for investigation of nanopore space. It can be performed measuring disintegrated samples of ACC.

2. Investigation of the micropore space structure.

It is assumed that 3D scan of ACC sample form a set of voxels with various relative densities ρ the frequency of occurrence of which in that set is described by normed histogram $\psi(\rho)$. This set is composed of two type voxels: pore and skeleton one with various densities. Their frequency of occurrence are described by the probability distributions $\psi_p(\rho)$ and $\psi_s(\rho)$, respectively. Both functions are defined on the whole range of voxels density values (i.e. for eight bit scan $\rho \in \langle 0, 255 \rangle$). This means that attachment of voxel with a given density to the subset of pore or skeleton type has a stochastic character, determined by the value of probability.

For the normed histogram the following model is proposed

$$(1) \quad \psi(\rho) = f_v^\mu \psi_p(\rho) + (1 - f_v^\mu) \psi_s(\rho)$$

where f_v^μ denotes volume porosity of the micropore space. This parameter, as well as parameters of probability distributions $\psi_p(\rho)$ and $\psi_s(\rho)$, are determined using standard optimization methods implemented in Matlab. Then, the porosity f_v^n of the nanopore space is calculated from relation

$$(2) \quad f_v^n = f_v - f_v^\mu$$

where f_v stand for the total porosity of ACC sample measured by the pycnometry method.

Next, the obtained porosity f_v^μ is used for determination of the binarization threshold that allows reconstruction of the micropore space. After reconstruction we are able to determine pore size distribution. Each voxel of micropore space has assigned the diameter of the largest sphere which contains this voxel and is completely included in this space.

3. Investigation of the nanopore space structure

To determine directly the porosity f_v^n of the nanopore space, the following relation between porosities in double porous materials was applied

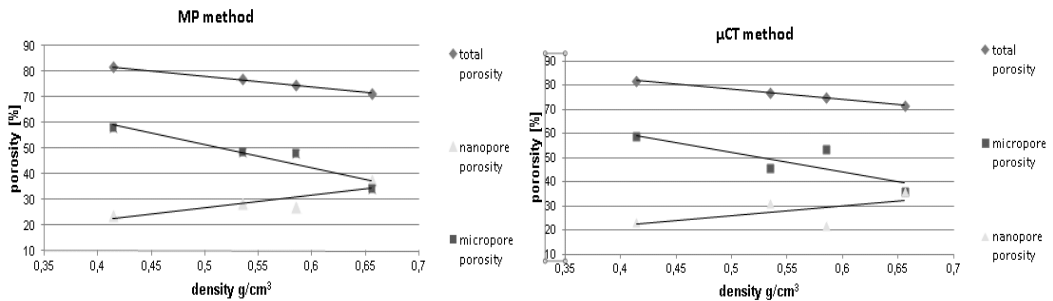
$$(3) \quad f_v^n = f_v^s \frac{1 - f_v^\mu}{1 - f_v^s}$$

where f_v^s denotes the volume porosity of the skeleton in ACC sample. This porosity is measured by MP method on disintegrated ACC samples. It is possible, because two parts of the intrusion curve related to intrusion into intergranular pores and into nanopore space are distinctly separated. This allows additionally determination of pore size distribution of nanopores. Again, relation (2) can be used to calculate the porosity f_v^μ of the micropore space.

4. Results

Both complementary methods have been applied to investigation of the pore space structure of four classes of AAC samples produced by SOLBET Capital Group. Part of the obtained results are presented in table and illustrated graphically in figure.

class of ACC samples	volume density ρ [g/cm ³]	pycnometry method	μ CT method		MP method		
		total porosity f_v	micropore porosity f_v^μ	nanopore porosity f_v^n	skeleton porosity f_v^s	nanopore porosity f_v^n	micropore porosity f_v^μ
400	0,414	0.818	0.588	0.231	0.568	0.239	0.579
500	0,535	0.769	0.458	0.312	0.552	0.284	0.485
600	0,585	0.749	0.534	0.215	0.518	0.270	0.479
700	0,656	0.717	0.358	0.358	0.570	0.376	0.340



THERMOMECHANICAL SOLIDS WITH ENERGETIC MATERIAL INTERFACES

A. Javili, A. McBride and P. Steinmann

*Chair of Applied Mechanics, University of Erlangen–Nuremberg,
Egerlandstr. 5, 91058-Erlangen, Germany*

This presentation is concerned with the description of interfaces of thermomechanical solid bodies. The description includes both the derivation of the governing equations and their approximation using the finite element method, see [1, 2, ?].

The surface of a solid body typically exhibits properties that differ from those of the enclosed bulk. These differences, caused by processes such as surface oxidation, ageing, coating, atomic rearrangement and the termination of atomic bonds, are present in comparatively thin boundary layers. Similarly, interfaces within the bulk can be viewed as two-sided internal surfaces. The mechanical and thermal properties of the interface can also differ significantly from the surrounding bulk. Surface and interface effects are especially significant for nanomaterials due to their large surface-to-volume ratio. These effects could be modelled phenomenologically by surfaces equipped with their own energies or, alternatively, in terms of tensorial surface stresses according to surface elasticity theory of Gurtin & Murdoch [4].

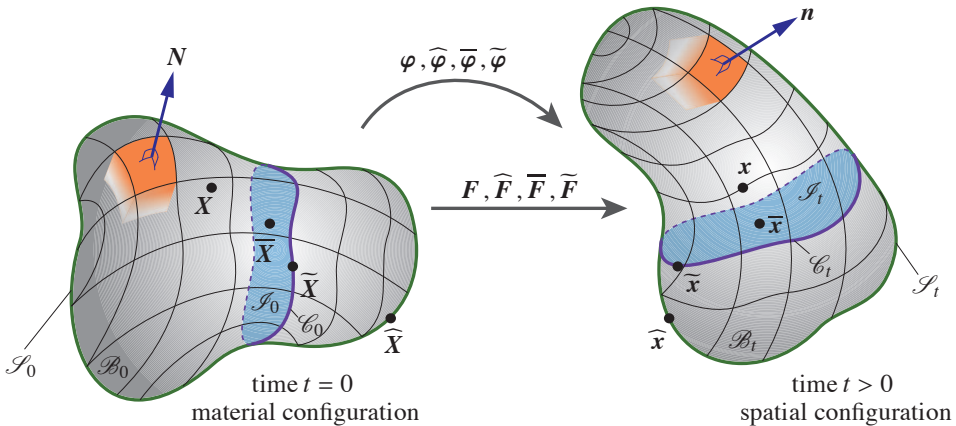


Figure 1. The material and spatial configurations of a continuum body, and the associated motions and deformation gradients in the various parts of the body.

Consider a continuum body that takes the material configuration \mathcal{B}_0 at the time $t = 0$. The boundary of the body is denoted by the surface $\mathcal{S}_0 := \partial\mathcal{B}_0$. The body is partitioned into two disjoint subdomains by a two-sided interface \mathcal{I}_0 . The boundary of the interface, a two-sided curve, is denoted as $\mathcal{C}_0 := \partial\mathcal{I}_0$. In a similar fashion to the interface, the curve \mathcal{C}_0 partitions the surface \mathcal{S}_0 into two open sets.

Let $\mathbb{T} = [0, T] \subset \mathbb{R}_+$ denote the time domain. A motion of the reference placement for a time $t \in \mathbb{T}$ is denoted by the orientation-preserving map $\varphi : \mathcal{B}_0 \times \mathbb{T} \rightarrow \mathbb{E}^3$. The current placement of the bulk associated with the motion φ is denoted $\mathcal{B}_t = \varphi(\mathcal{B}_0, t)$. The restriction of the motion φ to the surface \mathcal{S}_0 , interface \mathcal{I}_0 and curve \mathcal{C}_0 , is denoted $\widehat{\varphi}$, $\overline{\varphi}$ and $\widetilde{\varphi}$, respectively. The deformation gradients, i.e. linear tangent maps between the line elements, in the bulk, on the surface, interface and curve are denoted \mathbf{F} , $\widehat{\mathbf{F}}$, $\overline{\mathbf{F}}$ and $\widetilde{\mathbf{F}}$, respectively. Throughout the presentation, quantities or

operators corresponding to the bulk, surface, interface and curve are denoted as $\{\bullet\}$, $\{\hat{\bullet}\}$, $\{\bar{\bullet}\}$ and $\{\tilde{\bullet}\}$, respectively.

In this work we first derive the thermodynamically consistent balance equations for coherent solid interfaces. The interface is equipped with its own thermomechanical ingredients, such as free energy, entropy, etc. Next, the impact of the energetic interfaces on the overall response of the body is explored by means of a series of numerical examples.

- [1] A. Javili and P. Steinmann, On thermomechanical solids with boundary structures, *International Journal of Solids and Structures*, 47, 3245 – 3253, 2010.
- [2] A. Javili and P. Steinmann, A finite element framework for continua with boundary energies. Part III: The thermomechanical case, *Computer Methods in Applied Mechanics and Engineering*, 200, 1963–1977, 2011.
- [3] A. Javili, A. McBride and P. Steinmann, Numerical modelling of thermomechanical solids with highly-conductive energetic interfaces, In review, 2012.
- [4] M. E. Gurtin and A. Ian Murdoch, A continuum theory of elastic material surfaces, *Archive for Rational Mechanics and Analysis*, 57 291 – 323, 1975.

ADHESIVE JOINTS IN COMPOSITE BEAMS OF STEEL AND CONCRETE – MODELLING, EXPERIMENT AND COMPUTER SIMULATION

B. Kuczma and M. Kuczma

Institute of Building Engineering, University of Zielona Góra, Zielona Góra, Poland

1. Introduction

Composite construction in steel and concrete makes it possible to use with advantage the very intrinsic mechanical properties of the constituent materials – steel in tension and concrete in compression [2], [5]. Composite beams are the most common form of composite structural element widely used in steel frame building construction and in bridge engineering for mid-range steel bridges.

In this paper we shall present results of our theoretical studies and those of many experimental tests we have carried out in the laboratory of our home Institute of Building Engineering [3]. The objectives of these investigations were composite beams of steel and concrete subject to static loading, in which the connection of steel and concrete was realized in the form of adhesively bonded joints by both flexible and stiff structural adhesives. In the cross-section of tested composite beams we can distinguish three components: 1 – steel girder, 2 – concrete plate (slab), 3 – adhesive joint, see fig. 1.

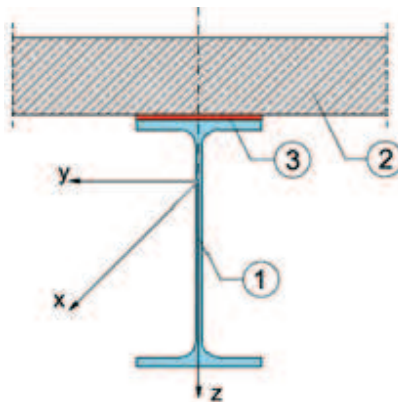


Figure 1. Cross-section of composite beam: 1 – steel girder, 2 – concrete plate, 3 – adhesive joint

Our aim was to take into account deformability and strength of the connection. To account for a mutual displacement (slip and separation) between the concrete plate and the steel girder, a four displacement field formulation was applied: w_1, w_2 - transverse displacement (deflection) of the girder and plate, and u_1, u_2 - longitudinal displacement of the centroid of the cross-section of girder and plate, respectively. In addition, fields of multipliers λ_i are used to control the irreversible (unilateral) properties of nonlinear behaviour of steel and concrete and progressive interface failure [1].

The evolutionary boundary value problem for the composite beam under consideration is formulated as a sequence of incremental problems in time that take the form of a variational inequality

$$(1) \quad \mathbf{u} \in \mathcal{K} : \quad a(\mathbf{u}, \mathbf{v} - \mathbf{u}) \geq \langle \mathbf{f}, \mathbf{v} - \mathbf{u} \rangle \quad \forall \mathbf{v} \in \mathcal{K}$$

in which $a(\cdot, \cdot)$ is a bilinear form, $\mathbf{u} = (w_1, w_2, u_1, u_2, \lambda_i)$, \mathbf{f} represents loading, and \mathcal{K} is a convex cone in the Cartesian product of function spaces involved [4].

2. Experiments

In the experiments we used the modern equipment: a strength testing machine Instron 8804 with two actuators, each of capacity ± 500 kN, a non-contact optical measuring system Aramis/Pontos, a high-performance digital data acquisition system ESAM Traveller. Tested were the component materials, fragments corresponding to the composite beams, and six composite beams B1 – B6 of length 3700 mm (span 3600 mm) made from a steel IPE 240 girder and a prefabricated concrete plate, which were bonded by different connectors including a layer of stiff or elastic adhesive. The simply supported composite beams were subjected to a three-point bending test.

How decisive is the role of the bond of concrete and steel in the composite beam, can be best appreciated by comparing the results of the final test for each tested beam as shown in fig. 2.

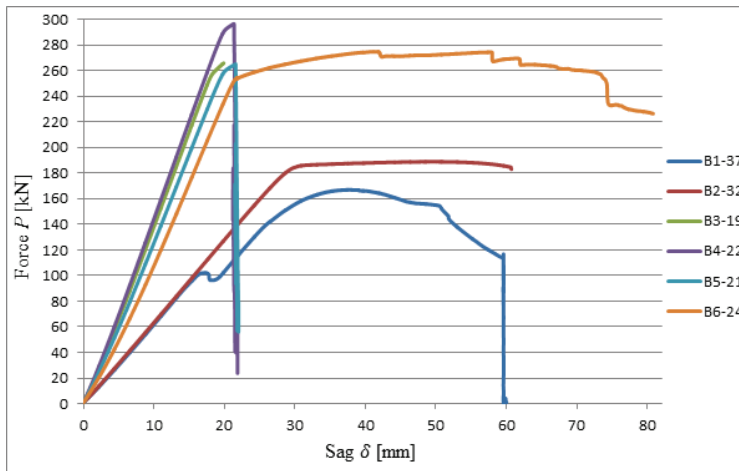


Figure 2. Force vs. sag for composite beams with different joints by the testing machine Instron 8804

3. Computational model

The computational model is based on the proposed variational inequality formulation (1), which has been discretized by the finite element method and solved as a complementarity problem [4].

Good agreement of theory and experiment was obtained.

4. References

- [1] M. Białaś and Z. Mróz (2005). Modelling of progressive interface failure under combined normal compression and shear stress, *Int. J. Solids and Structures*, **42**, 4436-4467.
- [2] R.P. Johnson (2004). *Composite Structures of Steel and Concrete: Beams, Slabs, Columns, and Frames for Buildings*, Blackwell Publishing, Oxford.
- [3] B. Kuczma (2011). *Static-strength analysis of steel-concrete composite beams with deformable connectors* (in Polish). PhD thesis, supervisor Prof. T. Biliński, University of Zielona Góra, Zielona Góra.
- [4] M. Kuczma (2010). *Foundations of the mechanics of shape memory structures. Modelling and numerics* (in Polish). University of Zielona Góra Press, Zielona Góra.
- [5] D.J. Oehlers and M.A. Bradford (1999). *Composite steel and concrete structural members*, Butterworth-Heinemann, Oxford.

MICROMECHANICAL STUDY OF FRICTIONAL ANISOTROPY IN ROUGH ELASTIC CONTACTS

J. Lengiewicz and S. Stupkiewicz

Institute of Fundamental Technological Research (IPPT), Warsaw, Poland

1. Introduction

Anisotropic topography of surface roughness at the micro-scale may result in frictional anisotropy at the macro-scale, i.e. in the dependence of friction coefficient on the direction of sliding, cf. [1–3]. So far, macroscopic modelling of anisotropic friction is mostly restricted to the case of orthotropic friction, e.g., [4–8]. On the other hand, micromechanical approaches to study the phenomenon are limited to simplified models [4, 7]. Therefore, deeper investigation is necessary to assess still-unresolved problems, including the analysis of the influence of surface roughness on anisotropy of friction and on the nature of sliding rules in anisotropic friction.

Micromechanical modelling seems to be a suitable tool to analyze such multi-scale structure-property relationships, and this approach is pursued in this work: a computational contact homogenization methodology is developed, and anisotropic friction in rough elastic contacts is analyzed. At the micro-scale, the finite element method is used to solve the problem of contact interaction of elastic rough surface layers. Subsequently, appropriate averaging rules are applied to derive macroscopic contact properties.

2. Micromechanical modelling approach

In the present work, the micromechanical modelling approach presented in [9] is extended to analyze a more general case of two rough and deformable bodies in contact. Two scales are considered. At the micro-scale, due to the interaction and deformation of surface asperities, the contact is concentrated at small spots, so-called real contacts. Therefore, the distribution of contact traction is highly inhomogeneous, cf. Fig. 1. At the macro-scale, the overall deformation of the contacting bodies is more homogeneous, as it is determined by the slowly-varying average (macroscopic) contact traction.

In order to determine macroscopic contact properties, finite element analysis of contact interaction is carried out at the scale of surface asperities. Three-dimensional finite element models of representative samples of surface layers of the contacting bodies are constructed and their interaction under relative sliding is simulated. Subsequent application of spatial and temporal averaging schemes yields macroscopic response expressed in terms of the limit friction condition and sliding potential.

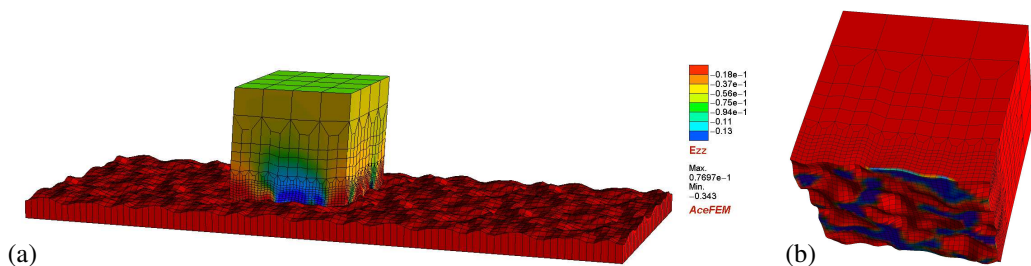


Figure 1. FE analysis of rough surfaces in contact. A periodic unit cell of an elastic surface layer is slid against a periodic rough rigid surface (a). Due to roughness, contact tractions are concentrated at real contacts (b).

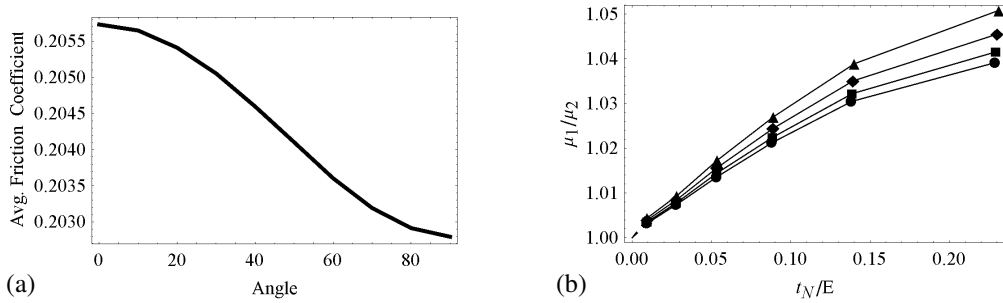


Figure 2. Contact of a flat elastic sample with sinusoidal rigid surface. Macroscopic friction coefficient varies with moving direction (a), and macroscopic anisotropy indicator grows with increasing normal load (b).

The analysis is performed for artificially generated rough surface topographies, and the effect of roughness properties on the macroscopic (anisotropic) friction response is studied, cf. Fig. 2. The influence of other problem parameters, such as the contact pressure, elastic constants of the contacting bodies, and the size of the representative surface element, is also investigated.

3. References

- [1] E. Rabinowicz. Direction of the friction forces. *Nature*, 179:1703, 1957.
- [2] M. Halaunbrenner. Directional effects in friction. *Wear*, 3:421–425, 1960.
- [3] A. Konyukhov, P. Vielsack, and K. Schweizerhof. On coupled models of anisotropic contact surfaces and their experimental validation. *Wear*, 264:579–588, 2008.
- [4] R. Michałowski and Z. Mróz. Associated and non-associated sliding rules in contact friction problems. *Arch. Mech.*, 30:259–276, 1978.
- [5] A. Zmitrowicz. Mathematical descriptions of anisotropic friction. *Int. J. Sol. Struct.*, 25:837–862, 1989.
- [6] Q. C. He and A. Curnier. Anisotropic dry friction between 2 orthotropic surfaces undergoing large displacements. *Eur. J. Mech. A/Solids*, 12:631–666, 1993.
- [7] Z. Mróz and S. Stupkiewicz. An anisotropic friction and wear model. *Int. J. Solids Struct.*, 31: 1113–1131, 1994.
- [8] M. Hjiiaj, Z. Q. Feng, G. de Saxcé, and Z. Mróz. On the modelling of complex anisotropic frictional contact laws. *Int. J. Eng. Sci.*, 42:1013–1034, 2004.
- [9] S. Stupkiewicz. *Micromechanics of Contact and Interphase Layers*. Springer, Berlin Heidelberg New York, 2007.

ATOMISTIC MODEL OF DECOHESION OF COPPER-CORUNDUM INTERFACE

Marcin Maździarz¹, Kinga Nalepka^{1,4}, Zygmunt Szymański¹, Jacek Hoffman¹, Sławomir Kret², Stanisław Kucharski¹ and Paweł Nalepka³

¹*Department of Computational Science, Institute of Fundamental Technological Research Polish Academy of Sciences, Pawińskiego 5B, 02-106 Warsaw, Poland*

²*Institute of Physics Polish Academy of Sciences, Al. Lotników 32/46, 02-668 Warsaw, Poland*

³*Department of Engineering and Machinery for Food Industry, Agriculture University of Cracow, ul. Balicka 122, 131-149 Cracow, Poland*

⁴*Department of Strength and Fatigue of Materials and Structures, Faculty of Mechanical Engineering and Robotics, AGH University of Science and Technology, Al. Mickiewicza 30, 30-059 Cracow, Poland*

1. Aim of the paper

The object of the paper is an atomistic, molecular statics (MS) reconstruction of the Cu- α -Al₂O₃ heterostructure formed by means of a pulsed laser deposition technique (PLD). The molecularly reconstructed copper on sapphire substrate is then used for the examination of decohesion in the region of the interface. For this purpose, a molecular statics nanoindentation simulation is performed.

2. Introduction

The strength of metal-ceramic interfaces is the key properties for the performance of many devices and structural elements: microelectronic devices, thermal barrier coatings used to protect the metallic components and metal-ceramic composites are just a few examples. Therefore, a detailed research of the decohesion in the phase boundary is an important issue.

Applying the PLD technique, an epitaxial Cu layer has been formed on a sapphire substrate. The obtained heterostructure has been examined by means of the High Resolution Transmission Electron Microscopy (HRTEM) (see Figure 1). As a result, the misorientation of Cu layer relative to the α -Al₂O₃ substrate is determined and subsequently, the system of defects due to the mismatch between the copper and sapphire is identified. Describing the interatomic interaction by the Tight Binding Second Moment Approximation (TB-SMA) potential [2] in the formed proposed in [5], the experimentally observed microstructure in the region of the interface is reconstructed. The obtained, atomistic model of the copper layer is subjected to nanoindentation [1, 3, 4]. During the carried out simulation, the displacement vs. applied force curve is registered, which enable us to identify the decohesion in the interface region [6].

3. Problem description

In this research, copper with purity 99.999% (Kurt J. Lesker Company Ltd.) was deposited on the (0001) α -Al₂O₃ surface (CrysTec GmbH) by PLD. For this purpose, a Nd:YAG laser beam with the wavelength 355 nm, pulse duration 10 ns and the frequency repetition 10 Hz was focused on the copper target (focal spot area 2.5 mm², fluence 2 J/cm²). The sapphire substrate was heated at 800 °C and pressure in the chamber was set to 5x10⁻⁶Pa.

During the deposition, Cu islands are formed (Volmer-Weber growth mode), (see Figure 1). The reason is that, copper has the higher surface energy than sapphire. The dominant orientation of Cu islands with respect to the α -Al₂O₃ substrate is (111) [01 $\bar{1}$]Cu|| (0001) [1 $\bar{1}$ 00]Al₂O₃, that is, the closed packed planes and directions of the both crystals are parallel to each other. Additionally, the HRTEM images enable the identification of the Cu lattice deformation resulting from the mismatch between

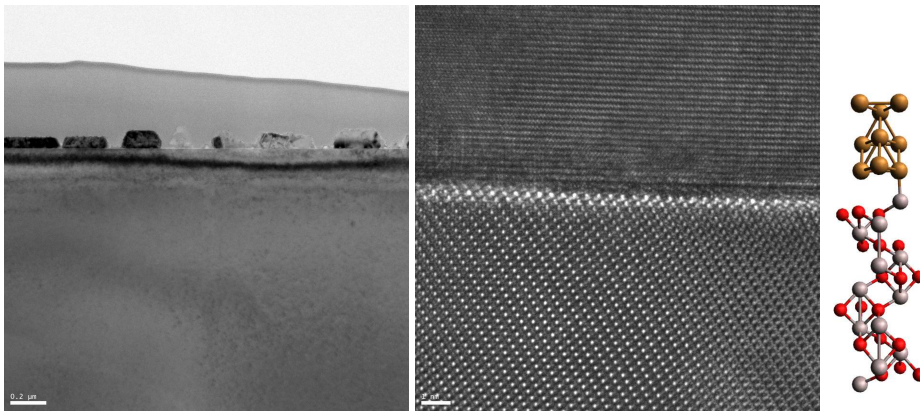


Figure 1. Islands of Cu on Al_2O_3 substrate, HRTEM images of the Cu(top layer) Al_2O_3 (down layer) interface and periodic cell of Cu- Al_2O_3 .

the copper and sapphire. The obtained data are used for the reconstruction of the microstructure in the interface region. For this purpose, the interatomic interaction in the Cu layer are described by the TB-SMA potential [2] in the form determined in [5]. Performing the relaxation of the Cu layer (Molecular Static Simulation), the final microstructure in the interface region is obtained.

The reconstructed Cu layer on the $\alpha\text{-Al}_2\text{O}_3$ substrate is used in the molecular statics simulation of nanoindentation in which the behaviour of the defected structure in a nonequilibrium configuration is investigated [4]. Analyzing the obtained displacement vs. applied force curve we try to explain the observed decohesion [6].

Acknowledgments

The research was done within the framework of the Project N501 156638 founded by the Polish Ministry of Science and Higher Education.

4. References

- [1] M. Mazdziarz, T.D. Young, P. Dłużewski, T. Wejrzanowski, and K.J. Kurzydłowski(2010). Computer modelling of nanoindentation in the limits of a coupled molecular–statics and elastic scheme. *Journal of Computational and Theoretical Nanoscience*, **7**.
- [2] F. Cleri V. Rosato(1993). Tight–binding potentials for transition metals and alloys. *Phys. Rev. B*, **48**.
- [3] P. Dłużewski, M. Maździarz, G. Jurczak, P. Traczykowski (2008). A hybrid atomistic-continuum finite element modelling of nanondentation and experimental verification for copper crystal. *CAMES*, **15**.
- [4] M. Maździarz, T.D. Young and G. Jurczak (2011). A study of the effect of prerelaxation on the nanoindentation process of crystalline copper . *Archives of Mechanics*, **63**.
- [5] Kinga Nalepka (2012). Symmetry-based approach to parametrization of embedded-atom-method interatomic potentials. *Computational Materials Science*, **56**.
- [6] G. Dehm, M. Rühle, H.D. Conway and R. Raj (1997). A microindentation method for estimating interfacial shear strength and its use in studying the influence of titanium transition layers on the interface strength of epitaxial copper films on sapphire . *Acta Materialia* , **45**.

DISCRETE ELEMENT MODELLING OF SOLID STATE SINTERING PROCESS OF METAL-CERAMIC COMPOSITE

S. Nosewicz¹, J. Rojek¹, K. Pietrzak², M. Chmielewski², D. Kaliński², R. Kačianauskas³

¹*Institute of Fundamental Technological Research Polish Academy of Science, Warsaw, Poland*

²*Institute of Electronic Materials Technology, Warsaw, Poland*

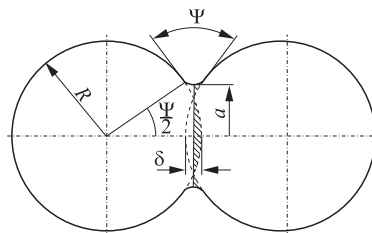
³*Vilnius Gediminas Technical University, Vilnius, Lithuania*

The paper presents discrete element modelling of two-phase powder sintering process. Sintering is the main stage of powder metallurgy process, which is the most common technique of fabricate metal matrix composites with ceramic reinforcement, advanced materials with several applications. As a technological process powder metallurgy consists of several stages including metal and ceramic powder manufacturing, preparation of metal-ceramic powder mixture, powder pressing and sintering. Sintering consists in consolidation of loose or weakly bonded powders at elevated temperatures, close to the melting temperature with or without additional pressure. This is a complex process affected by many factors. Modelling can be used to optimize and to understand better the sintering process and improve the quality of sintered components.

Modelling of sintering process is still a challenging research task. There are different approaches in modelling of sintering processes, ranging from continuum phenomenological models to micromechanical and atomistic ones. In this work, the micromechanical model of sintering was implemented in the discrete element method framework. In the discrete element method, material is represented as a large collection of particles interacting with one another by contact forces. It is a suitable tool to model granular and rock materials [1]. Modelling of sintering requires introduction of the cohesive interaction among particles representing inter-particle sintering forces. Following [2] the discrete element model adopted in this work employs the following equation for the sintering interaction between powder grains:

$$(1) \quad F = \pi\gamma_S \left[4R \left(1 - \cos \frac{\Psi}{2} \right) + a \sin \frac{\Psi}{2} \right] + \frac{\pi a^4}{8D_b} V$$

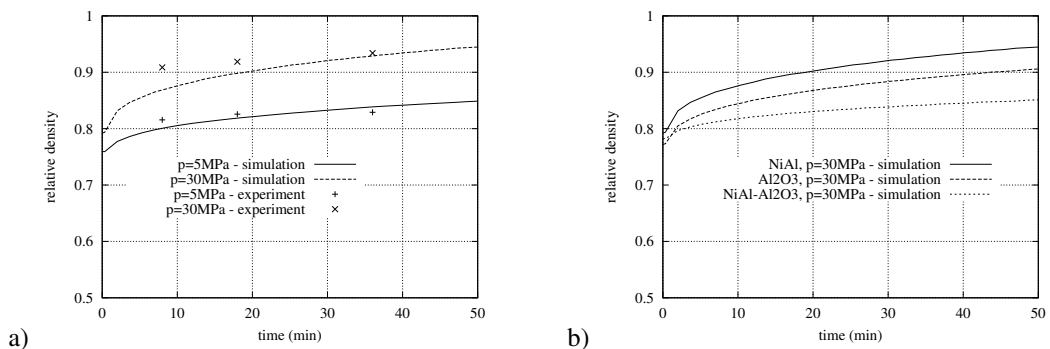
where V is the normal relative velocity, R – the particle radius, a – the radius of the interparticle grain boundary, Ψ – the dihedral angle, γ_S – the surface energy and D_b – the effective grain boundary diffusion coefficient. The first term on the right hand side of Eq. (1) represents the sintering driving force and the second one – the viscous resistance of the material. The geometrical parameters of the model are defined in Fig. 1.



Rysunek 1. Two-particle model of sintering.

The model has been extended to include elastic and thermal effects. It enables modelling of a powder metallurgy process consisting of powder compaction, sintering and cooling of the sintered component. It allows us to study the grains during sintering and rearrangement of grains during sintering, material shrinkage and internal stresses.

The numerical model has been applied to analyze sintering behaviour of different mixtures NiAl/Al₂O₃. Numerical simulations are combined with experimental studies of sintering. First, sintering of each phase, NiAl and Al₂O₃, is studied separately at different parameters: temperature, time and pressure. Finally, sintering of mixtures NiAl/Al₂O₃ will be performed at similar conditions. The kinetics of sintering is evaluated by investigation of the bulk density change in time. The evolution of the bulk density obtained in experimental studies is used in calibration and validation of the numerical model. Comparison of experimental and numerical results for sintering of NiAl powder at temperature 1300°C under pressure of 30 MPa is shown in Fig. 2a. Since experimental tests for mixtures NiAl/Al₂O₃ have not been finished yet, numerical results are shown only in Fig. 2b.



Rysunek 2. Evolution of relative density during sintering: a) numerical vs. numerical results for NiAl, b) numerical results for NiAl, Al₂O₃ and mixture NiAl/Al₂O₃.

Acknowledgements

The results presented in this paper have been obtained within the project “KomCerMet” (contract no. POIG.01.03.01-14-013/08-00 with the Polish Ministry of Science and Higher Education) in the framework of the Operational Programme Innovative Economy 2007-2013.

References

- [1] J. Rojek, E. Oñate, C. Labra, H. Kargl: Discrete element simulation of rock cutting. *International Journal of Rock Mechanics and Mining Sciences*, 48 (2011), 996–1010.
- [2] C.L. Martin, L.C.R. Schneider, L. Olmos, D. Bouvard: Discrete element modeling of metallic powder sintering. *Scripta Materialia*, 55 (2006), 425–428.

THERMOMECHANICAL ANALYSIS OF STEADY STATE WEAR PROBLEMS FOR MONOTONIC AND PERIODIC CONTACT SLIDING MOTION.

I. Páczelt¹ and Z. Mróz²

¹ *University of Miskolc, Miskolc, Hungary*

² *Institute of Fundamental Technological Research, Warsaw, Poland*

1. Introduction

The wear process on the frictional interface of two bodies in a relative sliding motion induces contact shape evolution. A most typical case occurs when one body plays the role of punch executing a relative sliding motion on a substrate body. The transient process usually tends to a steady or quasi-steady state occurring at fixed contact stress and strain distribution.

In many practical industrial applications it is very important to predict the form of wear shape and contact stresses distribution. Usually, the simulation is performed by calculating incremental contact shape and pressure evolution by numerically integrating the modified Archard wear rate rule expressed in terms of relative sliding velocity and contact pressure. However, much more effective procedure can be developed by postulating minimization of the contact response functional [1-5]. The stationary condition of the functional then provides the contact stress distribution compatible with the wear rate, assuring equilibrium and support constraint conditions.

Usually the wear process of punch or combined wear of two bodies is accompanied by the rigid body motion of punch with normal and tangential velocity components. A fundamental assumption is now introduced, namely, *in the steady state the wear rate vector is collinear with the rigid body wear velocity of punch*. When there is no wear of punch and only the wear of substrate, the contact surface shape in the steady state satisfies the compatibility condition requiring coaxiality of the wear rate vector and the elastic displacement rate difference at the contact point.

For two bodies in the relative sliding motion 5 classes of wear problems can be distinguished for the fixed (in time) loading conditions:

Class 1. The rigid body wear displacements are constrained by the boundary conditions assuring structure support reactions equilibrating applied loading. The wear profile follows the elastic or thermal displacements and the steady state corresponds to vanishing contact pressure.

Class 2. The contact surface S_c evolves in time due to progressing wear process, for instance, in the case of spherical indenter sliding on a substrate with varying radius $a = a(t)$ of the contact zone. The quasi-steady wear state is then reached with stress distribution dependent on $a(t)$. In fact, first the steady state distribution of contact pressure and the surface shape can then be specified for constant value of a . The evolution of steady states in the wear process can next be specified for varying contact radius.

Class 3. The contact surface S_c does not evolve in time and is specified. The rigid body wear velocity does not vanish and is compatible with the specified boundary conditions. The steady state is reached at which the contact stress is fixed with respect to the moving contact domain. Assuming the body B_1 to play the role of an indenter and the body B_2 executing sliding motion, the contact surface will be fixed on B_1 and translating on B_2 .

Class 4. The class of problems is the same as for *Class 2* but body B_2 is assumed to execute a periodic sliding motion of the contact surface.

Class 5. The class of problems is the same as for *Class 3* but body B_2 is assumed to execute a periodic slipping motion.

The present paper is aimed to extend the previous analyses [1-5] of steady state conditions to cases

of periodic sliding of contacting bodies, assuming cyclic steady state conditions for the heat generation. In our analysis it is supposed that the gross slip (or sliding) regime occurs between the bodies. In this case the sticking zone no longer exists and the whole contact zone undergoes slip. The tangential stress can then be directly calculated from the contact pressure and the coefficient of friction.

2. Wear rule and wear rate vector

The modified Archard wear rule [1] specifies the wear rate $\dot{w}_{i,n}$ of the i -th body in the normal contact direction. Following the previous work [1, 2] it is assumed that

$$(1) \quad \dot{w}_{i,n} = \beta_i (\tau_n)^{b_i} \|\dot{\mathbf{u}}_\tau\|^{a_i} = \beta_i (\mu p_n)^{b_i} \|\dot{\mathbf{u}}_\tau\|^{a_i} = \beta_i (\mu p_n)^{b_i} v_r^{a_i} = \tilde{\beta}_i p_n^{b_i} v_r^{a_i}, \quad i = 1, 2$$

where μ is the friction coefficient, β_i, a_i, b_i are the wear parameters, $\tilde{\beta}_i = \beta_i \mu^{b_i}$, $v_r = \|\dot{\mathbf{u}}_\tau\|$ is the relative velocity which is specified from rigid body movement of the bodies, constrained by the boundary conditions. The shear stress at the contact surface is denoted by τ_n and calculated in terms of the contact pressure p_n by using the Coulomb friction law $\tau_n = \mu p_n$.

2. Numerical experiments

The specific case is related to wear analysis induced by a punch periodically translating on an elastic strip. Referring to the steady state contact pressure distributions for arbitrarily constrained punch and noting that the pressure at one contact edge vanishes, then the maximal pressure at the other edge is twice the mean pressure [5] when heat generation is absent.

We analyse the wear process induced by the reciprocal punch translation and the heat generation. Our goal is to specify the contact pressure distribution and the corresponding shape of contact surface in the steady wear state. The stress and temperature fields are calculated in the iterative numerical process and the weak forms of equilibrium and heat conduction equations are applied [3,4]. The coupled thermo-mechanical problem will be solved by operator split technique. The mechanical and thermal fields discretized by the p -version finite element approximation will be specified separately in the consecutive time steps. The wear effect is calculated incrementally by applying the wear rule (1). The investigated examples demonstrate that the thermal distortion affects essentially the contact shape associated with the steady state and also the contact pressure distribution during periodic sliding. The p -version of finite elements is used, thus assuring fast convergence of the numerical process and accurate specification of geometry for shape optimization.

3. References

- [1] I. Páczelt and Z. Mróz (2009). On the analysis of steady sliding wear process, *Tribology International*, **42**, 275-283
- [2] I. Páczelt, Z. Mróz (2010), Variational approach to the analysis of steady state thermo-elastic wear regimes, *Int. J. Num. Meth. Eng.*, **81**, 728-760.
- [3] Z. Mróz, I. Páczelt (2011), Analysis of thermo-elastic wear problems, *J. Thermal Stresses*, **34-35**, 569-606.
- [4] I. Páczelt, Z. Mróz (2011), Numerical analysis of steady thermo-elastic wear regimes induced by translating and rotating punches, *Computers and Structures*, **89**, 2495-2521.
- [5] I. Páczelt, Z. Mróz (2012), "Solution of wear problems for monotonic and periodic sliding with p -version of the finite element method", *Comp. Meth. Appl. Mech. Eng.*, (2012) (in print)

INVESTIGATION OF THE NORMAL CONTACT BETWEEN TWO SPHERICAL PARTICLES WITH INTERFACE MATERIAL

V. Rimša¹, S. Pilkavičius¹, R. Kačianauskas¹, J. Rojek²

¹*Vilnius Gediminas Technical University, Saulėtekio al. 11, 10223 Vilnius, Lithuania*

²*Polish Academy of Sciences, Pawińskiego ul. 5B, 02-106 Warszawa, Poland*

Abstract

The evaluation of mechanical properties of heterogeneous materials presents multidisciplinary task where the contribution of microstructural effects is of major important. Direct simulating of the material structures as heterogeneous continuum is inappropriate for several reasons, because it requires a large CPU time and did not improve the understanding of the role of microstructure. Recently, multi-scale approach became useful simulating technique, where macroscopic mechanical properties of the heterogeneous solids are defined in terms of grain properties and their interactions.

Among the numerical simulation methods, the Discrete Element Method (DEM), introduced by Cundall and Strack [1] has become the most useful tool. Evaluation of the contact behaviour between particles is decisive in the DEM. Originally, most of the DEM applications are aimed to simulate non-cohesive granular materials with unilateral repulsive normal contact.

Presented report addresses the normal contact between two elastic relatively stiff spherical particles interacting via weaker interface material (Fig. 1a). The problem is considered analytically and by applying the Finite Element Method (FEM). The 3D FE comprises two spheres bonded by the three dimensional cylinder. The above approach is aimed for development of the DEM. Two types of the interface material models were considered. The purely elastic material was examined in the first series of samples and comprising wide range of various parameters. The analytical model comprising combination of three sequential and parallel bonding springs (Fig. 1b) was developed.

The viscoelastic interface material between two contacting particles was examined in the second series of samples. Viscoelastic properties of the solid obey of the Maxwell model (Fig. 1c), while relaxation was described via Prony series [2].

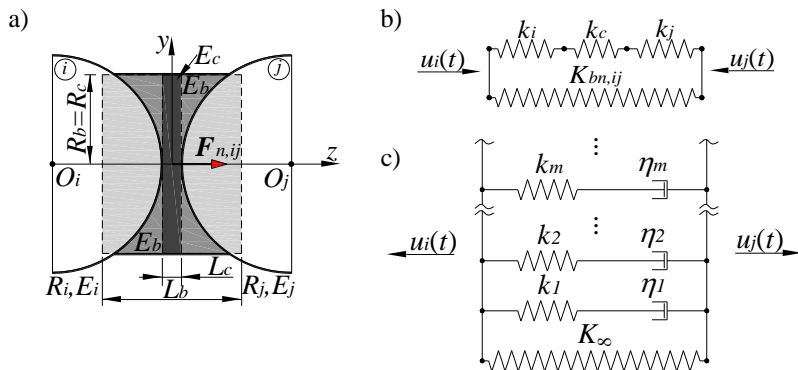


Fig. 1. Modified normal contact model: a) geometry; b) bond model for elastic interface – springs system; c) bond model for viscoelastic interface – springs-dashpots system

Variation of the linear bond stiffness parameters against relative elasticity modulus $E^* = E_{ij}/E_b$ illustrating the weakening of the interface is given in Fig. 2a in logarithmic scale. Here, full interface with the data value $E^* = 5$ corresponds to the heterogeneous case of granite grains

embedded into cement paste, while the data value E^* approximately equal to 10000 corresponds to the heterogeneous case of granite grains embedded into asphalt. Dashed horizontal line shows contribution of the stiffness of particles k_i and k_j which are independent on interface. The contribution of interface material expressed in terms of stiffness of the interface layer k_c and the parallel bond $K_{bn,ij}$ exponentially decay with decay of the interface properties. The main observation is that resultant stiffness of the sequentially connected springs K_{ijc} (thin line) and total stiffness $K_{n,ij}$ (bold line) converges to the stiffness of the interface layer k_c . This model as the FEM shows, that deformability of particles is negligibly small and could be neglected in the computational models with the relatively weak interface bonds. Consequently, particles could be presented by rigid surface, thereby, simplifying computational model and reducing the size of the model.

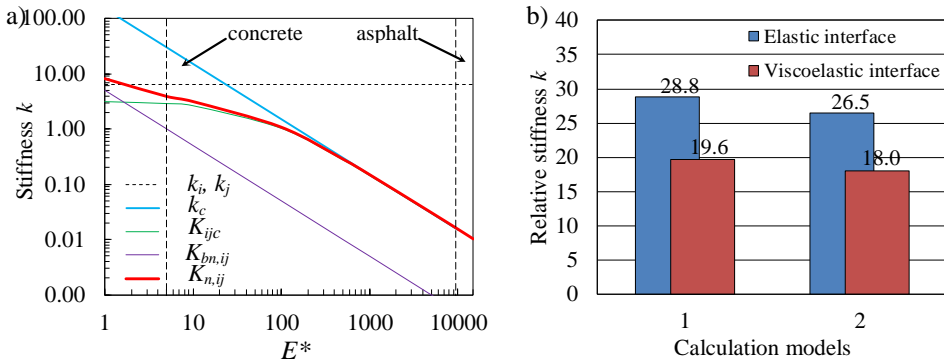


Fig. 2. Illustration of simulation results: a) variation of separate bond stiffness parameters with weakening of the interface; b) comparison calculation models for weaker interface: 1 – FE linear model, 2 – FE geometrically nonlinear model

Comparison of employed elastic and visco-elastic models for the case of weak interface relevant to asphalt in terms of relative stiffness k is illustrated by column-diagram given in Fig. 2b. Here columns 1 and 2 illustrate FE results. Results show that this proposed model fails however for the case relatively weaker interface bonds. The above model of contacting particles with the parallel bond is suitable for the evaluation of contact with thick interface, for the relatively strong bonds. Therefore will be offered corrected normal contact model for weaker interface bonds.

It was found that for weaker interface the FE nonlinear model with large deflection should be applied, because it gives higher accuracy of contact relative stiffness compared with the modified analytical calculation contact model.

Obtained results by FE model clearly demonstrate influence of the viscosity of interface solid. For normal displacement of particles equal to 6.6% of particle radius R , yields reduction of the interaction force up to 56.7% when compared to purely elastic properties.

References

- [1] Cundall P. A. and Struck O. D. L (1979). A discrete numerical model for granular asseblies. *Geotechnique* 29(1): 45-75.
- [2] Masad E., Huang C., W., Airey G., Muliana A. (2008). Nonlinear viscoelastic analysis of unaged and aged asphalt binders. *Construction and Building Materials* 22(11): 2170-2179.

CONSTRUCTION OF STATISTICALLY SIMILAR RVEs FOR 3D MICROSTRUCTURES

L. Scheunemann, J. Schröder, D. Balzani and D. Brands
Institute of Mechanics, University Duisburg-Essen, Essen, Germany

1. Motivation

For many materials used in advanced engineering applications, the macroscopic mechanical response is governed by the characteristic microstructure of the material, which should therefore be incorporated in numerical computations. A suitable tool for the simulation of such micro-heterogeneous materials is the FE² method, see e.g. [3] and [5]. In this context a microscopic boundary value problem is solved at each integration point of the macroscopic boundary value problem based on the discretization of a representative volume element (RVE). A drawback of this approach is the high computation time and high amount of memory required when applying it to complex microstructures. The definition of statistically similar RVEs (SSRVEs), which are characterized by a reduced complexity compared with real microstructures lead to more efficient calculations. In 2D the construction of SSRVEs proves to be successful in a series of numerical examples, cf. [1], [4].

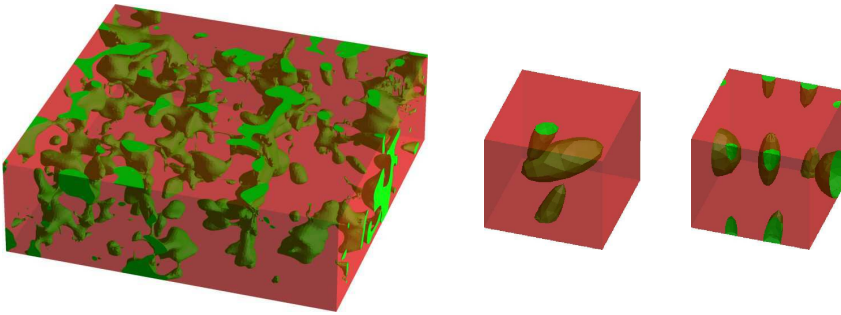


Figure 1. Real DP-steel microstructure (in cooperation with D. Raabe, Max-Planck-Institut für Eisenforschung, Düsseldorf) and two SSRVEs with two and five ellipsoidal inclusions.

2. Construction of SSRVEs

We propose a method to construct 3D SSRVEs based on the minimization of a least-square functional taking into account the differences of suitable statistical measures characterizing the inclusion morphology of a given real microstructure. As statistical measures we use the volume fraction (\mathcal{P}_V), spectral density (\mathcal{P}_{SD}) and lineal path function (\mathcal{P}_{LP}), which e.g. is given by

$$(1) \quad \mathcal{P}_{LP}^I(m, k, l) = \frac{1}{N_x N_y N_z} \sum_{p=1}^{N_x} \sum_{q=1}^{N_y} \sum_{o=1}^{N_z} \chi^I(\overrightarrow{x_1 x_2})$$

describing the probability of a line segment $\overrightarrow{x_1 x_2}$ to be located completely in the inclusion phase I , see [2]. Therein the indicator function χ^I is equal to one if the line segment $\overrightarrow{x_1 x_2}$ is in phase I and zero else. N_x , N_y and N_z denote the number of voxels considered in the three coordinate axis directions. The least-square functional

$$(2) \quad \mathcal{L}(\gamma) = \sum_i \omega_i (\mathcal{P}_i^{real} - \mathcal{P}_i^{SSRVE}(\gamma))^2 \rightarrow \min_{\gamma}$$

is minimized by an optimization procedure, cf. [1], where γ represents a suitable parametrization of the inclusion phase morphology. Several types of SSRVEs are considered, which differ in the number of ellipsoidal inclusions representing the inclusion phase of the microstructure. We focus on the construction of SSRVEs for a real microstructure of a DP-steel obtained from measurements by Electron Backscatter Diffraction (EBSD) combined with a Focused Ion Beam (FIB), cf. [6]. A DP-steel microstructure and two corresponding SSRVEs are depicted in Fig. 1.

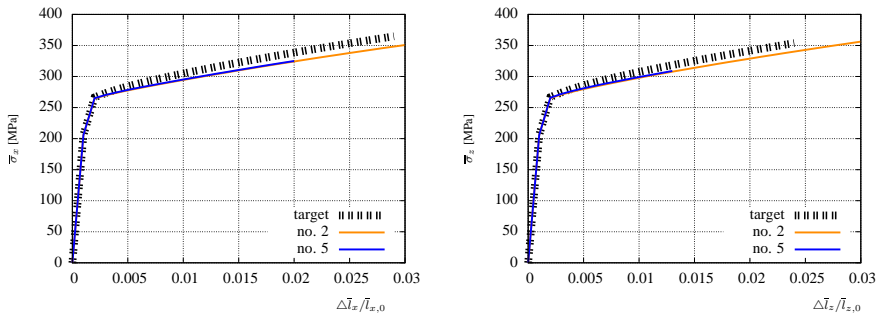


Figure 2. Comparison of mechanical response in uniaxial tension tests based on the target structure and on two different SSRVEs.

A first check of the quality of the method is performed by comparing the mechanical response of the real EBSD microstructure with the ones of the SSRVEs in virtual experiments. For uniaxial tension in x- and z-direction it turns out that the mechanical behavior is comparable, see Fig. 2. Further numerical examples are discussed to demonstrate the performance of the method.

3. References

- [1] D. Balzani, D. Brands, J. Schröder and C. Carstensen (2010), Sensitivity Analysis of statistical measures for the reconstruction of microstructures based in the minimization of generalized least-square functionals *Technische Mechanik*, **30**:297-315.
- [2] B.L. Lu, S. Torquato (1992). Lineal-path function of random heterogeneous materials *Physical Reviews A*, **45**:922-929.
- [3] C. Miehe, J. Schröder and J. Schotte (1999). Computational homogenization analysis in finite plasticity. Simulation of texture development in polycrystalline materials, *Computer Methods in Applied Mechanics and Engineering* **171**:387-418
- [4] J. Schröder, D. Balzani, D. Brands (2011). Approximation of random microstructures by periodic statistically similar representative volume element based on lineal-path functions, *Archive of Mechanics*, **81**:975-997
- [5] R.J.M. Smits, W.A.M. Brekelmans, H.E.H. Meyer (1998). Prediction of the mechanical behavior of nonlinear heterogeneous systems by multi-level finite element modeling, *Computer Methods in Applied Mechanics and Engineering*, **155**:181-192
- [6] R. N. Singh, N. Zaafarani, D. Raabe, F. Roters and S. Zaefferer (2006). Three-Dimensional investigation of the texture and microstructure below a nanoindent in a Cu single crystal using 3D EBSD and crystal plasticity finite element simulations, *Acta Materialia* **54**:1863-1876

TWO-STEP HOMOGENIZATION SIMULATION OF POLYCRYSTALLINE PIEZOELECTRIC MATERIALS

Y. Uetsuji¹, H. Kuramae¹ and K. Tsuchiya²

¹ *Osaka Institute of Technology, Osaka, Japan*

² *Tokai University, Hiratsuka, Japan*

1. Introduction

Piezoelectric materials generally consist of many grains at a mesoscale and domains at a microscale. Each domain shows strong anisotropy according to the asymmetric crystal structure. The macroscopic material properties of polycrystalline piezoelectric materials have a large dependence on these microscopic crystal morphology. Therefore, it is important to understand the effect of multidomain and multigrain structures on macroscopic material properties. In this paper, a multiscale modeling of multigrain and multidomain structures was presented for piezoelectric materials.

2. Computational scheme

Figure 1 shows a multiscale modeling of multigrain and multidomain structures in piezoelectric materials. The microstructure consists of intragranular domains and the mesostructure is an aggregate of random-orientating grains. The asymptotic homogenization theory was employed for bridging three scales among micro, meso and macro structures. Then multiscale formulations of a coupled problem which involves mechanical displacement and electric potential were discretized and solved by finite element method [1]. In addition EBSD-measured crystal orientations [2] were introduced into multigrain mesostructure.

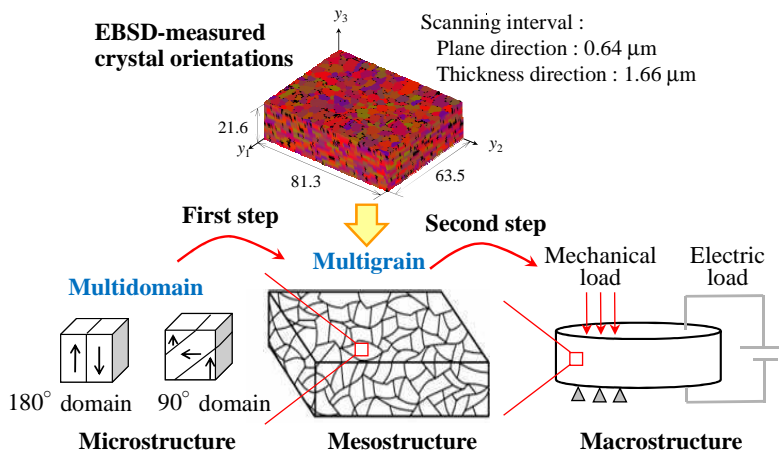


Figure 1 Multiscale modeling of multigrain and multidomain structures in piezoelectric materials.

3. Results and discussions

The first step is the homogenization of multidomain microstructure. A typical microstructure, a dual-domain structure consisting of 0 and 180 degree domains, was modeled. The material properties of a BaTiO₃ single crystal was inputted into each domain. The homogenized material properties were estimated as changing the volume fraction of 0 degree domain from 50% to 100%. In case of

piezoelectric strain constants, the computation indicated their homogenized properties increase linearly from zero at unpoled state to the maximum at full-poled state. On the other hand, it was recognized that the some specific components of dielectric constants and elastic compliance constants don't satisfy the law of mixture and the piezoelectric effect makes their components change nonlinearly according to volume fraction of 0 degree domains.

The next step is the homogenization of multigrain mesostructure. A realistic three-dimensional model of a BaTiO₃ polycrystal, which was constructed by repeating EBSD measurement, was applied to mesostructure. The mean diameter of a grain was approximately 6.71 μm. Then the above homogenized material properties of multidomain structures were inputted into every grain of the mesostructure. Figure 2-4 shows the relation between the macrostructural homogenized material property and the volume fraction. Piezoelectric strain constants increase linearly, but all other components of dielectric and elastic compliance constants vary nonlinearly according to volume fraction of domains.

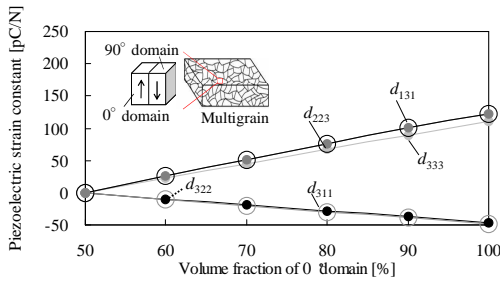
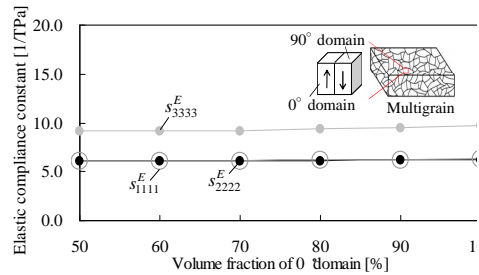


Figure 2 Relation between homogenized piezoelectric strain constant of multigrain structure and volume fraction of 0 degree domain.



(a) Normal components

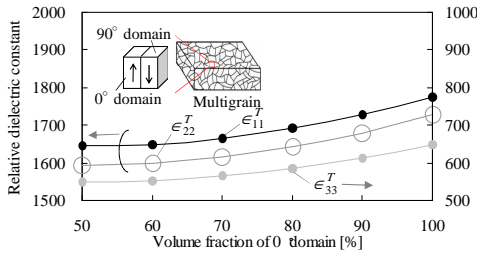
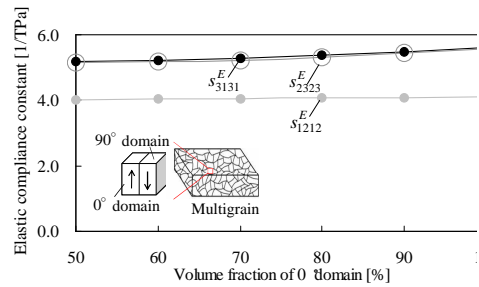


Figure 3 Relation between homogenized dielectric constant of multigrain structure and volume fraction of 0 degree domain.



(b) Shearing components

Figure 4 Relation between homogenized elastic compliance constant of multigrain structure and volume fraction of 0 degree domain.

Acknowledgment

One of the authors (Y. Uetsuji) was financially supported by a Grant-in-Aid for Young Scientists (B) (No. 22760087) from the Ministry of Education, Culture, Sports, Science and Technology of Japan.

References

[1] Y. Uetsuji, Y. Nakamura, S. Ueda and E. Nakamachi (2004). Numerical investigation on ferroelectric properties of piezoelectric materials, *Modelling and Simulation in Materials Science and Engineering*, **12**, S303-S317.

[2] Y. Uetsuji, H. Kuramae, K. Tsuchiya and M. Kamlah (2011). A multiscale finite element simulation of piezoelectric materials using realistic crystal morphology, *WIT Transactions on Modelling and Simulation*, **51**, 601-611.

CONCURRENCE OF THE MICRO-SCALE CALCULATION AND INVERSE IDENTIFICATION OF PARAMETERS USED FOR MODELLING ACOUSTICS OF POROUS MEDIA

T. G. Zieliński

Institute of Fundamental Technological Research, Warsaw, Poland

1. Introduction

There are several widely-used acoustic models of porous media, starting from that simple, purely phenomenological, model proposed by Delany and Bazely, and finishing with semi-phenomenological propositions of Johnson et al., combined with the ones of Champoux and Allard, with some important variations proposed by Pride, Lafarge, and others [1]. All these models use some average macroscopic parameters, namely: the total porosity and flow resistivity (or permeability) – for the Delany-Bazely model – which are supplemented by the average tortuosity of pores and their characteristic dimensions – in the case of more advanced semi-phenomenological models. These models allow to describe the acoustic wave propagation in porous media in a wide frequency range, provided that the skeleton is rigid. However, using some formulas derived for these models with the Biot's theory of poroelasticity permits to describe correctly sound propagation in soft porous materials. Thus, the determination of the above-mentioned parameters is very important. For direct, experimental measurements specialistic equipment is required, different for various parameters. Therefore, an inverse identification based on curves of, for example, acoustic impedance or absorption (measured for samples of known thickness) can be used to estimate the model parameters. In this work, it will be shown that knowledge of micro-structural geometry of porous medium is very helpful to validate correct estimation. Moreover, a periodic microscopic cell consisting of a few pores representing an average morphology of porous ceramics is proposed to serve for numerical analyses to estimate permeability parameters. The concurrence of such micro-scale derivation and inverse identification is discussed.

2. Inverse identification and microstructural analysis

Samples of porous ceramics Al_2O_3 , with the known total porosity of 90%, are examined in the impedance tube using the transfer function method, in the frequency range from 500 Hz to 6.4 kHz. Experimentally-determined curves of acoustic impedance and absorption are then used for an inverse identification of the remaining model parameters, namely: tortuosity α , viscous and thermal permeabilities, k_0 and k'_0 , and two characteristic lengths – for viscous and thermal effects, Λ and Λ' . To this end, five dimensionless parameters, p_1, \dots, p_5 , are defined in some relation with the model parameters and then, an optimization procedure with appropriate constraints is carried out, in order to match the curves measured experimentally with the ones calculated from the equations of the Johnson-Allard model [1]. As a matter of fact, some experimental data are used for the determination of parameters while the other data – obtained for another sample of the same porous ceramics, yet having different height – serve for the validation purposes. The absorption curves, obtained for two samples of different height, namely, $h = 18$ mm and $h = 24$ mm, are shown in Figure 1(a). Figure 1(b) presents the identified values of the five dimensionless parameters, whereas the corresponding initial and identified values of model parameters are given in Table 1. It is observed that the identified characteristic length for thermal effects corresponds very well to the average radius of pores, whereas the characteristic length for viscous forces is similar with the average radius of “windows” linking the pores (cf. also $2\Lambda = 127 \mu\text{m}$ and $2\Lambda' = 581 \mu\text{m}$ from Table 1 with, respectively: $113 \mu\text{m}$ and $529 \mu\text{m}$ found in Table 1 in [2]). This is a very important agreement which validates the results of identification.

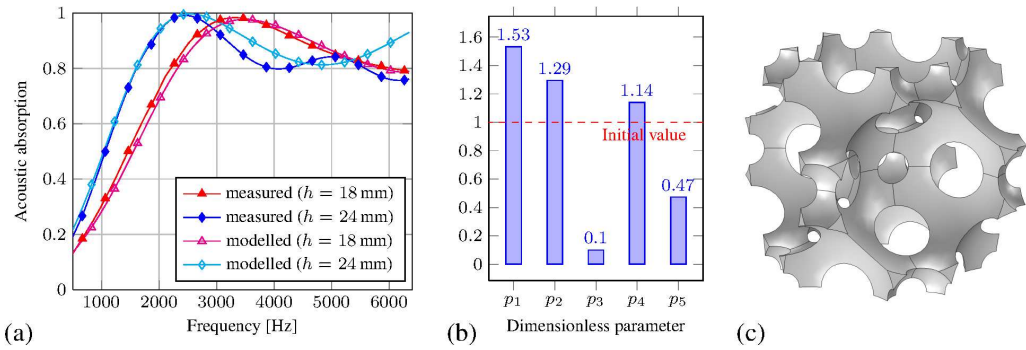


Figure 1. (a) Absorption curves (measured and modelled after parameter identification) for samples of porous ceramics of height h , (b) identified values of dimensionless parameters, (c) periodic cell with porosity of 90%.

	α	Λ [m]	Λ' [m]	k_0 [m ²]	k'_0 [m ²]
(a)	1.0000e+000	2.0000e-005	2.0000e-005	9.0000e-010	9.0000e-010
(b)	1.5318e+000	6.3439e-005	2.9044e-004	6.9538e-010	8.9897e-009

Table 1. Initial (a) and identified (b) values of model parameters.

Moreover, using these average radii of pores and windows, a periodic cell with porosity of 90% is constructed, see Figure 1(c). It is used for three-dimensional numerical analysis of the micro-macro transition approach for sound absorbing porous media [3, 4]. To this end, the multi-scale asymptotic method is applied [5], which permits to determine the macroscopic material description from knowledge of the physics and geometry at the microscopic level. The viscous permeability, obtained in that way, corresponds to the value identified from the experimental curves.

Acknowledgments

The author wishes to express his sincere gratitude to Dr. Marek Potoczek from Rzeszow University of Technology for providing samples of porous ceramics. Financial support of the Foundation for Polish Science Team Programme co-financed by the EU European Regional Development Fund Operational Programme “Innovative Economy 2007-626 2013”: Project “Smart Technologies for Safety Engineering SMART and SAFE”, No. TEAM/2008-1/4, and Project “Modern Material Technologies in Aerospace Industry”, No. 629 POIG.01.01.02-00-015/08, is gratefully acknowledged.

References

[1] J.F. Allard, N. Atalla (2009). *Propagation of Sound in Porous Media: Modelling Sound Absorbing Materials*, 2nd ed., Wiley.

[2] M. Potoczek (2008). Gelcasting of alumina foams using agarose solutions, *Ceram. Int.*, **34**, 661667, **24**, 334-357.

[3] C. Perrot, F. Chevillotte, R. Panneton (2008). Dynamic viscous permeability of an open-cell aluminum foam: Computations versus experiments. *J. Appl. Phys.*, **103**, 024909-1-8.

[4] C. Perrot, F. Chevillotte, R. Panneton (2008). Bottom-up approach for microstructure optimization of sound absorbing materials, *J. Acoust. Soc. Am.*, **124**(2), 940-948.

[5] C.-Y. Lee, M.J. Leamy, J.H. Nadler (2009). Acoustic absorption calculation in irreducible porous media: A unified computational approach. *J. Acoust. Soc. Am.*, **126**(4), 1862-1870.

Nonlinear and Stochastic Dynamics

ROTATIONAL MOTION OF A STOCHASTIC NON LINEAR MATHIEU EQUATION UNDER WHITE NOISE AND NARROWBAND EXCITATION

D. Yurchenko¹, A. Naess² and P. Alevras¹

¹*Department of Mechanical Engineering, Heriot-Watt University, Edinburgh, UK*

²*Department of Mathematical Sciences, NTNU, Trondheim, Norway*

1. Introduction

This paper considers the stochastic dynamics of a non-linear Mathieu equation which describes the motion of a linearly damped mathematical pendulum with a vertically excited suspension point also known as parametric excitation. The previous system is governed by the following equation:

$$(1) \quad \ddot{\theta} + 2\alpha\dot{\theta} + \left[\frac{g}{l} + \frac{f(\ddot{t})}{l} \right] \sin \theta = 0$$

where θ is the angle of inclination, α - the damping coefficient, l - the length of the pendulum and most studies consider the excitation force to be perfectly harmonic, $f(t) = A \cos(\omega t)$.

It has been proved by numerous studies [1, 2, 3] that system (1) is capable of establishing different types of motion from small oscillations to pure rotations and chaos. Different numerical techniques, such as bifurcation analysis, Lyapunov exponent, etc., have been used to identify the instability domains of (1) corresponding to rotational and chaotic motion and especially the rotational subdomains. Such an interest has been motivated by the idea of using the parametrically excited system for designing of a Wave Energy Converter (WEC) [2, 3] which can extract energy out of the rotating pendulum, while ocean waves provide a vertical excitation of the pendulum suspension point. Despite the interesting idea, it should be noted that ocean waves are not perfectly periodic and should be modeled as a narrowband process [4]. Here, two types of modeling options are considered. First, random phase modulation proposed by Wedig [5] reading:

$$(2) \quad f(t) = A \cos q(t), \quad \dot{q} = \frac{\omega}{\Omega} + \sigma \zeta(t), \quad E[\zeta(t)] = 0, \quad E[\zeta(t)\zeta(t + \tau)] = D\delta(\tau)$$

where $\zeta(t)$ denotes the stationary Gaussian white noise with a constant intensity $D = \sigma^2$ and $E[\cdot]$ is the operation of expectation. Thus, in view of the potential application for energy harvesting, first approach leads to understanding the behavior of the system (1) after a proper non-dimensionless time is introduced:

$$(3) \quad \theta'' + \gamma\theta' + [1 + \lambda \cos q(t)] \sin \theta = 0, \quad \gamma = \frac{2\alpha}{\Omega}, \lambda = \frac{A}{l}$$

with $q(t)$ defined in (2). The second one is described simply as $f(\ddot{t}) = \zeta(t)$ resulting in:

$$(4) \quad \ddot{\theta} + 2\alpha\dot{\theta} + \left[\frac{g}{l} + \frac{\zeta(t)}{l} \right] \sin \theta = 0$$

2. Path integration technique

For the analysis of the aforementioned systems, a numerical approach was adapted based on the path integration (PI) technique [6]. The PI method constructs the joint response probability density function (PDF) taking advantage of and requiring the stochastic process to be Markovian. Particularly

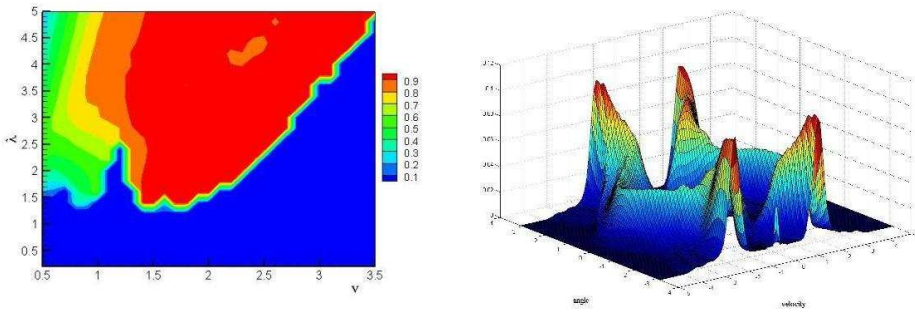


Figure 1. (a) Parameter space plot for random phase modulation and values of $\gamma=0.3$, $D = 0.005$, $x(0) = 0.01\pi$; (b) PDF for $\nu = 1.8$, $\lambda=4.0$;

for the three dimensional case, the joint PDF at time t is calculated based on the one at time $t' = t - \Delta t$ as from the Chapman-Kolmogorov equation:

$$(5) \quad p(x, y, q, t) = \int_{-\infty}^{\infty} \int_{-\infty}^{\infty} \int_{-\pi}^{\pi} p(x, y, q, t | x', y', q', t') p(x', y', q', t') dq' dx' dy'.$$

where $p(x, y, q, t | x', y', q', t')$ will be referred to as the transition probability density function (TPD). The evaluation of the TPD stems from noticing its Gaussian nature since $\zeta(t)$ is Gaussian white noise [6].

3. Results and conclusions

In this paper, identification of the rotational instability subdomains was conducted by building parameter space plots (fig. 1(a)) characterising the probability of rotational motion through the response PDF (fig. 1(b)). Different initial conditions, damping coefficients and noise intensities were studied regarding their affect on rotational motion. Numerical results showed that the initial conditions selection had no influence on the resulting motion of the system (1), unlike the behaviour of the deterministic one. As for the damping term, bigger values would help maintain the rotational motion robustness while increasing noise intensity tends to eliminate rotational subdomains.

4. References

- [1] Xu X., Wiercigroch M., Cartmell M.P. *Rotating orbits of a parametrically-excited pendulum* Chaos, Solitons & Fractals. 23. 1537-1548. 2005.
- [2] Xu X., et.al. *Dynamic Interactions between parametric pendulum and electro-dynamical shaker.* ZAMM, 87, 172-186, 2007.
- [3] Lenci S., et.al. *Experimental rotations of a pendulum on water waves.* J. of Computational and Nonlinear Dynamics, 7, 2012.
- [4] Cruz J., (2008). *Ocean Wave Energy. Current status and future perspectives.* Springer.
- [5] Wedig W.V. *Invariant measures and Lyapunov exponents for generalized parameter fluctuations.* Structural Safety, 8, 13-25, 1990.
- [6] Naess A., Moe V. *Efficient path integration methods for nonlinear dynamic systems,* Probabilistic Engineering Mechanics 15, p. 221-231, 2000.

**GENERALIZED MOMENT EQUATIONS TECHNIQUE FOR DYNAMIC SYSTEMS
UNDER NON-POISSON IMPULSES: APPROACH BASED ON
INTEGRO-DIFFERENTIAL CHAPMAN-KOLMOGOROV EQUATIONS**

R. Iwankiewicz

*Institute of Mechanics and Ocean Engineering, Hamburg University of Technology, Hamburg,
Germany*

1. Introduction

If the excitation is a non-Poisson (e.g. renewal) impulse process, the state vector of the dynamic system is not a Markov process. The conversion of the original non-Markov pulse problem into a Markov one is in some cases possible owing to the introduction of auxiliary state variables in form of pure-jump stochastic processes. If auxiliary state variables are governed by stochastic differential equations driven by a single Poisson process or by independent Poisson processes, the original state vector augmented by those auxiliary variables becomes a non-diffusive, Poisson-driven Markov process. Then the differential equations for moments may be derived. These pure-jump stochastic processes have to be explicitly formulated either as some transformations of a Poisson counting process [1, 2], or directly with the aid of the stochastic differential equation [3, 4]. The explicitly introduced, Poisson-driven, pure-jump stochastic processes are characterized by a chain of Markov states. Consequently the original state variables and the states of the auxiliary pure-jump stochastic process are jointly Markovian and the problem is characterized by a mixed-type joint probability density - discrete distribution function. Such a function is governed by the forward integro-differential Chapman-Kolmogorov equation. The moments are defined as integrals with respect to the mixed-type, probability density - discrete distribution function. Based on the forward integro-differential Chapman-Kolmogorov equation the generating differential equation for moments is obtained. An illustrating example is also given.

2. Statement of the problem

A general case of a non-linear oscillator under an external or parametric impulse process excitation is considered. A random impulse process excitation is defined as

$$(1) \quad F(t) = \sum_{i=1}^{\mathcal{N}(t)} P_i \delta(t - t_i),$$

where the occurrence times t_i of impulses are driven by a non-Poisson counting process $\mathcal{N}(t)$, giving the number of counts in the time interval $[0, t)$, i.e. excluding the one that possibly occurs at the time t . The impulses magnitudes P_i are assumed to be identically distributed, independent random variables.

An auxiliary, pure-jump stochastic process is introduced, characterized by a number of Markov states [5]. The jumps are defined in such a way that the actual impulse (i.e. the jump in the velocity response $Z_2(t)$) only occurs if there is a jump between some particular Markov states. Then the problem described by the original state variables of the dynamic system and by the Markov states of the auxiliary jump process is jointly Markovian. Accordingly, the response probability distribution is characterized by a joint probability density - discrete distribution function $q_j(z_1, z_2, t)$ of the response state variables - the displacement $Z_1(t)$ and the velocity $Z_2(t)$ and of m states $S(t)$ of a pertinent Markov chain, defined as [5]

$$(2) \quad q_j(z_1, z_2, t) dz_1 dz_2 = \Pr\{Z_1(t) \in (z_1, z_1 + dz_1) \wedge Z_2(t) \in (z_2, z_2 + dz_2) \wedge S(t) = j\},$$

where $j = 1, 2, \dots, m$. The fundamental equation for such a continuous-jump Markov process is the general forward integro-differential Chapman-Kolmogorov equation [5, 6]

$$(3) \quad \frac{\partial}{\partial t} q_j(\mathbf{z}, t) = - \sum_{r=1}^2 \frac{\partial}{\partial z_r} [c_r(\mathbf{z}, t) q_j(\mathbf{z}, t)] + \sum_{i=1}^m \int_{-\infty}^{\infty} [J_{\{\mathbf{z}\}}(\mathbf{z}, j | \mathbf{x}, i, t) q_i(\mathbf{x}, t) - J_{\{\mathbf{z}\}}(\mathbf{x}, i | \mathbf{z}, j, t) q_j(\mathbf{z}, t)] d\mathbf{x}$$

where $c_r(\mathbf{z}, t)$ are the drift terms of the equation of motion written down in the state space form and $J_{\{\mathbf{z}\}}(\mathbf{z}, j | \mathbf{x}, i, t)$ is the jump probability intensity function [5, 6] which must be determined for the pertinent chain of Markov states.

The moments are defined as

$$(4) \quad E_j [V(\mathbf{Z}(t), t)] = \int_{-\infty}^{\infty} V(\mathbf{z}(t), t) q_j(\mathbf{z}, t) d\mathbf{z}, \quad j = 1, 2, \dots, m.$$

The generating equation for moments is obtained, with the aid of the forward integro-differential Chapman-Kolmogorov equation, as

$$(5) \quad \frac{d}{dt} E_j [V(\mathbf{Z}(t), t)] = \frac{\partial}{\partial t} \int_{-\infty}^{\infty} V(\mathbf{z}(t), t) q_j(\mathbf{z}, t) d\mathbf{z} = E_j \left[\frac{\partial}{\partial t} V(\mathbf{Z}(t), t) \right] + \sum_{r=1}^2 E_j \left[\frac{\partial V(\mathbf{Z}(t), t)}{\partial Z_r} c_r(\mathbf{Z}(t), t) \right] + \sum_{i=1}^m \int_{-\infty}^{\infty} \int_{-\infty}^{\infty} [V(\mathbf{y}(t), t) J_{\{\mathbf{z}\}}(\mathbf{y}, j | \mathbf{z}, i, t) q_i(\mathbf{z}, t) - V(\mathbf{z}(t), t) J_{\{\mathbf{z}\}}(\mathbf{y}, i | \mathbf{z}, j, t) q_j(\mathbf{z}, t)] d\mathbf{y} d\mathbf{z}.$$

3. References

- [1] Nielsen S.R.K., Iwankiewicz R. and Skjaerbaek P.S. (1995) Moment equations for non-linear systems under renewal-driven random impulses with gamma-distributed interarrival times. In: *Proc. IUTAM Symposium on Advances in Nonlinear Mechanics, Trondheim, Norway, July 1995*, Eds.A. Naess and S. Krenk. Kluwer, 331-340.
- [2] Iwankiewicz R. and Nielsen S.R.K. (2000) Solution techniques for pulse problems in non-linear stochastic dynamics. *Probabilistic Engineering Mechanics*, **15**, 25-36.
- [3] Iwankiewicz R. (2003) Dynamic systems under random impulses driven by a generalized Erlang renewal process. In: *Proc. 10th IFIP WG 7.5 Working Conference on Reliability and Optimization of Structural Systems, 25-27 March 2002, Kansai University, Osaka, Japan*. Eds. H.Furuta, M.Dogaki and M.Sakano, Balkema, 103-110.
- [4] Tellier M. and Iwankiewicz R. (2005) Response of linear dynamic systems to non-Erlang renewal impulses: stochastic equations approach. *Probabilistic Engineering Mechanics*, **20**, 281-295.
- [5] Iwankiewicz R. (2008) Equations for probability density of response of dynamic systems to a class of non-Poisson random impulse process excitations. *Probabilistic Engineering Mechanics*, **23**:198-207.
- [6] Gardiner C.W. (1985) *Handbook of stochastic methods for physics, chemistry and the natural sciences*, Springer-Verlag.

WAVELET ANALYSIS OF A DYNAMIC RESPONSE OF A BEAM RESTING ON A NONLINEAR FOUNDATION

P. Koziół and T. Krzyżyński

Koszalin University of Technology, Koszalin, Poland

1. Introduction

Due to the recent intensive development of transportation, new construction possibilities and better methods for prediction of vibrations impact on an environment are needed. Experimental studies show that nonlinear approaches are better for modelling of real behaviour of existing structures subject to dynamic excitations, compared to linear models. One can recognize a lack of analytical methods for analysis of nonlinear systems. For moving load problems, one finds a number of published results involving numerical computations. Few analytical solutions are obtained for a dynamic response of a beam resting on a nonlinear foundation [1-3]. These solutions are usually based on perturbation methods and can give results insufficiently exact for parametric analysis. A method using wavelet expansion of functions combined with the Adomian's decomposition [4] is applied in this paper to the model consisting of the Timoshenko beam resting on a nonlinear viscoelastic foundation and subjected to a moving load representing a train movement.

2. Model formulation and semi-analytical solution

The following equations for a homogeneous infinite Timoshenko beam resting on a nonlinear viscoelastic foundation are considered:

$$(1) \quad m_b \frac{\partial^2 W}{\partial t^2} + C_d \frac{\partial W}{\partial t} - S \frac{\partial^2 W}{\partial x^2} + S \frac{\partial \Psi}{\partial x} + f(W) = P(x, t), \quad J \frac{\partial^2 \Psi}{\partial t^2} - EI \frac{\partial^2 \Psi}{\partial x^2} + S \Psi - S \frac{\partial W}{\partial x} = 0$$

where W is the transverse displacement, Ψ is the angular rotation of the cross-section, x is the space coordinate in a direction along the beam, t represents the time and the parameters are: the mass per unit length $m_b = \rho A$, the viscous damping of foundation C_d , the shear stiffness $S = \kappa AG$, the mass moment of inertia $J = \rho I$, the beam flexural rigidity EI , the Young's modulus E , the moment of inertia I , the shear modulus G , the mass density ρ , the cross-section area A and the shear correction factor κ . The boundary conditions should reflect the fact that the displacement, the bending moment, the shear force and the slope of the beam curvature tend to zero.

The term $f(W)$ represents the nonlinear restoration [3]:

$$(2) \quad f(W) = k_L W + k_N N(W)$$

where k_L is the linear coefficient of foundation stiffness and k_N is a nonlinear part of foundation stiffness. The function $N(W)$ describes the form of the nonlinear factor, usually taken as $N(W) = W^3$ [1,2]. A more general form of function $N(W)$ is considered in present paper. It is assumed that the function f is analytic and therefore it can be expanded by the Taylor series [3].

The moving force is modelled as a finite sum of loads harmonically varying in time and distributed on separated intervals:

$$(3) \quad P(x, t) = \sum_{l=0}^{L-1} \frac{P_0}{2a} \cos^2\left(\frac{\pi(x - Vt - (2a + s)l)}{2a}\right) H(a^2 - (x - Vt - (2a + s)l)^2) \exp(i\Omega t)$$

where $H(\cdot)$, $2a$, $P_0/2a$, V , $\Omega = 2\pi f_\Omega$, L and s are the Heaviside function, the span of load, the amplitude of the load, the velocity and the frequency of the moving load, a number of separated impulses and the distance between them, respectively.

A special method using a wavelet expansion of functions combined with the Adomian's decomposition is adopted for solving the investigated model [4]. The usefulness of the wavelet-based approximation for the analysis of various linear and stochastic problems was proved before [4,5]. An expansion of functions using the wavelet filter of coiflet type (p_j) is applied for solution:

$$(4) \quad f(x) = \lim_{n \rightarrow \infty} f_n(x) = \lim_{n \rightarrow \infty} \frac{1}{2^{n+1}\pi} \prod_{k=1}^{k_p} \left(\sum_{j=0}^{N_p} p_j e^{ijx/2^{n+k}} \right) \sum_{k=k_{\min}}^{k_{\max}} \tilde{f} \left((k + \sum_{j=0}^{N_p} jp_j) 2^{-n} \right) e^{ixk2^{-n}}$$

where k_p and N_p are the parameters associated with a specific set of coiflets (p_j) and \tilde{f} denotes the Fourier transform of function f . A generalized coiflet filter of length 8 is used for the improvement of the efficiency of the method, instead of the classical filter of length 18 applied in past papers [4,5]. The Adomian's decomposition assumes a form of solution represented by a series with one linear term and an infinite number of unknown functions related to the nonlinear part, which must be determined in order to solve the problem:

$$(5) \quad W(x) = \sum_{j=0}^{\infty} W_j(x), \quad \Psi(x) = \sum_{j=0}^{\infty} \Psi_j(x).$$

The nonlinear term $N(W)$ is represented by a sum of Adomian polynomials Q_j [3]:

$$(6) \quad f(N(x,t)) = \sum_{j=0}^{\infty} Q_j(x-Vt).$$

For a derivation of terms W_j and Ψ_j (Eqs. 5) the coiflet-based approximation (Eq. 4) is used.

3. Conclusions

The developed method allows to alleviate difficulties associated with numerical computations and gives possibility of effective parametric studies. The obtained semi-analytical solution enables discussion regarding the influence of the considered nonlinearity on the beam response. Numerical examples showing the system behaviour for various parameters are presented.

4. References

- [1] M.H. Kargarnovin, D. Younesian, D.J. Thompson, C.J. Jones (2005). Response of beams on nonlinear viscoelastic foundations to harmonic moving loads, *Computers and Structures*, **83**, 1865-1877.
- [2] E.J. Sapountzakis, A.E. Kampitsis (2011). Nonlinear response of shear deformable beams on tensionless nonlinear viscoelastic foundation under moving loads, *Journal of Sound and Vibration*, **330**, 5410-5426.
- [3] T.S. Jang, H.S. Baek, J.K. Paik (2011). A new method for the non-linear deflection of an infinite beam resting on a non-linear elastic foundation, *International Journal of Non-Linear Mechanics*, **46**, 339-346.
- [4] P. Koziol (2010). *Wavelet approach for the vibratory analysis of beam-soil structures: dynamically loaded systems*, VDM Verlag Dr. Müller, Saarbrücken.
- [5] P. Koziol, C. Mares (2010). Wavelet approach for vibration analysis of fast moving load on a viscoelastic medium, *Shock and Vibration*, **17** (4-5), 461-472.

Shells and Plates

ON SHELL ELEMENTS DERIVED FROM HU-WASHIZU FUNCTIONAL

K. Wiśniewski¹ and E. Turska²

¹*Institute of Fundamental Technological Research, Warsaw, Poland*

²*Polish Japanese Institute of Information Technology, Warsaw, Poland*

1. Introduction

The purpose of the presentation is to summarize our recent results regarding the formulation of shell elements based on the Hu-Washizu (HW) functional with rotational degrees of freedom, [1, 2, 3, 4]. Several numerical examples will illustrate such aspects of their performance as: accuracy, radius of convergence, required number of iterations of the Newton method or the arc-length method and time of computations. Some examples enabling comparisons with the 'solid-shell' element based on the HW functional will be provided.

2. HW shell element with rotational degrees of freedom

The formulation of our four-node shell element with rotational degrees of freedom based on the Hu-Washizu (HW) functional is described in detail in [1]. It is an enhanced element with six dofs/node, enabling finite (unrestricted) rotations, and developed for Green strain. The drilling rotation is included through the drilling Rotation Constraint equation. The key features of the approach are as follows.

1. The shell HW functional is derived from the shell potential energy functional, which is an alternative to the derivation from the three-dimensional HW functional. This method is more versatile as it enables the derivation of the so-called partial HW functionals, with different treatment of the bending/twisting part and the transverse shear part of strain energy.
2. For the membrane part of HW shell elements, a 7-parameter stress, a 9-parameter strain and a 2-parameter EADG enhancement are selected as optimal. The assumed representations of stress and strain are defined in skew coordinates in the natural basis at the element's center. This improves accuracy and has positive theoretical consequences.
3. The drilling Rotation Constraint equation is treated by the Perturbed Lagrange method. The faulty term resulting from the equal-order approximations of displacements and the drilling rotation is eliminated and one spurious mode is stabilized using the gamma method. The proposed formulation is insensitive to the element's distortions and yields a large radius of convergence in the examples involving in-plane bending.

The performance of 4 four-node shell HW elements, differing in formulation of the bending/twisting and the transverse shear parts, is analyzed on several numerical examples. The element with 29 parameters (HW29) is selected as the best performer.

3. Example: quarter of orthotropic hemisphere

A quarter of the hemispherical shell with an 18° hole is loaded by two external forces, see Fig.1a. The same boundary conditions are used as for an isotropic material, which for an orthotropic material do not preserve symmetry of deformation. The mesh consists of 16 × 16 elements, and the 4-node element HW29 with rotational dofs and the 8-node 'solid-shell' element SS HW47 are used.

The material is the carbon T300/epoxy composite, and the orthotropic material constants are as follows: $E_{11} = 58.9$, $E_{22} = 52.1$, $E_{33} = 11.2$, $\nu_{12} = 0.048$, $\nu_{13} = 0.442$, $\nu_{23} = 0.46$, $G_{12} = 4.01$,

$G_{13} = 3.87, G_{23} = 3.71$. The material orientation is defined using the spherical coordinate system and the material direction vector 1 is tangent to the parallels of latitude.

The nonlinear analyzes are performed using the arc-length method for $P = 1/10^5$ and the results are shown in Fig.1b. The element HW29 crashes at the inward displacement equal to 13.5, while the 'solid-shell' elements SS HW47 performs up to 15, for which a very distorted shape of is obtained. Up to the inward displacement equal to 10, both these classes of elements yield an almost identical deflection, despite the fact that they use different types of orthotropy; the first one uses full orthotropy (9 constants) while the other uses the orthotropy modified by the Zero-Normal-Stress condition (6 constants).

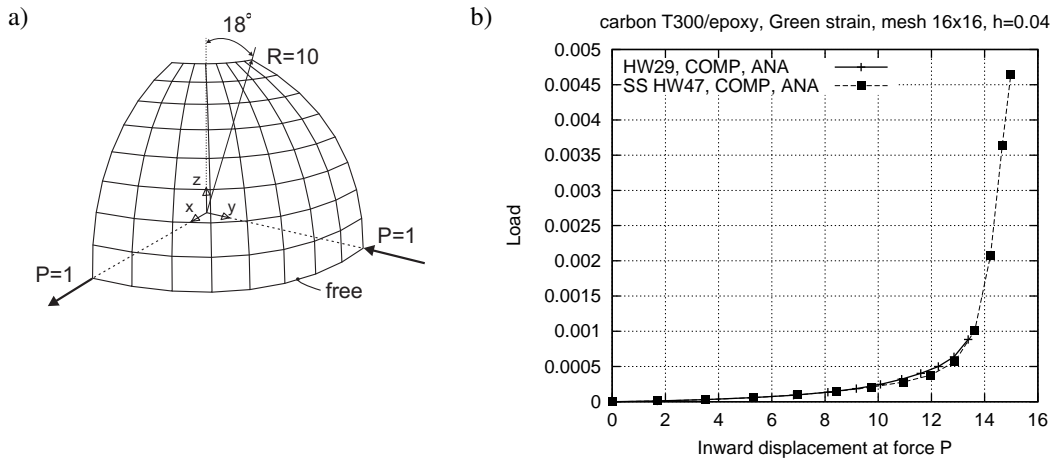


Figure 1. Quarter of hemispherical shell. a) Geometry, b) Nonlinear displacements for various HW elements.

4. References

- [1] K. Wisniewski, E. Turska (2012). Four-node mixed Hu-Washizu shell element with drilling rotation, *Int. J. Num. Meth. Engng*, Wiley Online Library DOI: 10.1002/nme.3335
- [2] K. Wisniewski (2010). *Finite Rotation Shells. Basic Equations and Finite Elements for Reissner Kinematics*, CIMNE-Springer.
- [3] K. Wisniewski, W. Wagner, E. Turska, F. Gruttmann (2010). Four-node Hu-Washizu elements based on skew coordinates and contravariant assumed strain, *Computers & Structures*, **88**, 1278-1284
- [4] K. Wisniewski, E. Turska (2009). Improved four-node Hu-Washizu elements based on skew coordinates, *Computers & Structures*, **87**, 407-424

ON TWO-DIMENSIONAL MODELS OF THERMOELASTIC SHELLS IN THE FRAMEWORK OF LORD-SHULMAN NONCLASSICAL THEORY OF THERMOELASTICITY

G. Avalishvili¹ and M. Avalishvili²

¹ *I. Javakhishvili Tbilisi State University, Tbilisi, Georgia*

² *University of Georgia, Tbilisi, Georgia*

The present paper is devoted to investigation of initial-boundary value problem corresponding to Lord-Shulman dynamical linear three-dimensional model of thermoelastic bodies, and to construction and justification of hierarchical two-dimensional models for thermoelastic shells in corresponding Sobolev spaces. We consider Lord-Shulman linear three-dimensional model for anisotropic homogeneous thermoelastic bodies, which was obtained by H. Lord and Y. Shulman [1] to eliminate shortcomings of the classical thermoelasticity, such as infinite velocity of thermoelastic disturbances that is inconsistent with the real physical properties of elastic bodies. In Lord-Shulman model instead of the classical Fourier law of heat conduction Maxwell-Cattaneo law was used, which is a generalization of Fourier law and depend on one relaxation time parameter. Hence, the equation corresponding to the temperature field involve second order derivatives of temperature and divergence of displacement vector-function with respect to the time variable. The problem of propagation of a thermoelastic wave was studied and domain of influence result for Lord-Shulman model in spaces of classical smooth enough functions was obtained in [2], and problems of steady oscillations and pseudo-oscillations were investigated in [3] applying methods of the theory of integral equations.

We consider variation formulation of initial-boundary value problem in differential form corresponding to Lord-Shulman dynamical nonclassical three-dimensional model and show their equivalence in the spaces of smooth enough functions. On basis of variation formulation we define spaces of vector-valued distributions in which the initial-boundary value problem corresponding to Lord-Shulman model is well-posed, and applying suitable a priori estimates we prove the existence and uniqueness of solution of the three-dimensional initial-boundary value problem. In addition, we obtain energetic identity, which permits one to prove continuous dependence of solution on initial and boundary conditions and densities of body forces and heat sources.

Since numerical solution of initial-boundary value problem corresponding to Lord-Shulman three-dimensional model requires complicated algorithms, it is important to construct approximate two-dimensional models for three-dimensional problem taking into account geometric shape of thermoelastic body. In the framework of Lord-Shulman nonclassical theory of elasticity we consider general thermoelastic shell with variable thickness in curvilinear coordinates, which may vanish on a part of the lateral surface, and construct its two-dimensional hierarchical models applying spectral method, which is a generalization of the dimensional reduction method suggested by I. Vekua [4, 5] in the theory of elasticity for plates with variable thickness and shells. To construct two-dimensional models of plate I. Vekua considered differential formulation of the three-dimensional initial-boundary value problem and approximating components of the displacement vector-function by partial sums of orthogonal Fourier-Legendre series with respect to the variable of plate thickness a hierarchy of initial-boundary value problems defined on two-dimensional space domain was obtained. Note that the classical Kirchhoff-Love and Reissner-Mindlin models can be incorporated into the hierarchy obtained by I. Vekua so that it can be considered as an extension of the frequently used engineering plate models. Static two-dimensional models constructed by I. Vekua for thin shallow shells first were investigated in Sobolev spaces in [6] and for homogenous isotropic plate the rate of approximation of the exact solution of the three-dimensional problem by the vector-functions of three space variables restored from the solutions of the reduced two-

dimensional problems in the spaces of classical smooth functions was estimated in [7]. Later on, various two-dimensional and one-dimensional models were constructed and investigated for problems of the theory of elasticity and mathematical physics applying I. Vekua's reduction method and its generalizations (see [8-10] and references given therein).

To obtain a hierarchy of two-dimensional models of thermoelastic shell we construct sequences of subspaces of the spaces corresponding to the original three-dimensional initial-boundary value problem, which consist of vector-functions whose components are polynomials with respect to the variable of shell thickness. Note that the constructed subspaces are weighted Sobolev spaces of function defined in two-dimensional Lipschitz domain, when the thickness of the shell vanishes on a part of the boundary. Projecting the original three-dimensional problem on these subspaces we construct a hierarchy of dynamical two-dimensional models, when surface force and heat flux densities are given along the face surfaces and along a part of the lateral surface, and the shell is clamped and the temperature vanishes along the remaining part of the boundary. We prove the existence and uniqueness of solution of two-dimensional initial-boundary value problem in suitable spaces of vector-valued distributions. We also obtain energetic identity, which permits one to show continuous dependence of solution on given functions. We investigate relationship between the hierarchy of dynamical two-dimensional models of anisotropic homogeneous thermoelastic shells obtained from Lord-Shulman model and original three-dimensional initial-boundary value problem and prove that the sequence of vector-functions of three space variables reconstructed from solutions of the reduced problems converges in corresponding Sobolev spaces pointwise with respect to the time variable to the solution of the three-dimensional initial-boundary value problem and under additional regularity conditions we estimate the rate of convergence.

References

- [1] H.W. Lord and Y. Shulman (1967). A generalized dynamical theory of thermoelasticity, *J. Mech. Phys. Solids*, **15**, 229-309.
- [2] J. Ignaczak, B. Carbonaro, and R. Russo (1986). Domain of influence theorem in thermoelasticity with one relaxation time, *J. Thermal Stresses*, **9**, 79-91.
- [3] T.V. Burchuladze and T.G. Gegelia (1985). *Development of the method of potential in the theory of elasticity*, Mecniereba, Tbilisi (Russian).
- [4] I.N. Vekua (1955). On one method of calculating of prismatic shells, *Tr. Tbil. Mat. Inst. im. A. Razmadze*, **21**, 191-259 (Russian).
- [5] I.N. Vekua (1985). *Shell theory: General methods of construction*, Pitman Adv. Publ. Program, Boston.
- [6] D.G. Gordeziani (1974). On the solvability of some boundary value problems for a variant of the theory of thin shells, *Dokl. Akad. Nauk SSSR*, **215**, 6, 1289-1292 (Russian).
- [7] D.G. Gordeziani (1974). To the exactness of one variant of the theory of thin shells, *Dokl. Akad. Nauk SSSR*, **216**, 4, 751-754 (Russian).
- [8] M. Avalishvili (2002). Investigation of a mathematical model of elastic bar with variable cross-sections, *Bull. Georgian Acad. Sci.*, **166**, 37-40.
- [9] M. Dauge, E. Faou, and Z. Yosibash (2004). Plates and shells: Asymptotic expansions and hierarchical models, *Encyclopedia of Computational Mechanics*, **1**, 199-236.
- [10] G. Avalishvili, M. Avalishvili, D. Gordeziani, and B. Miara (2010). Hierarchical modeling of thermoelastic plates with variable thickness, *Analysis and Applications*, **8**, 125-159.

BUCKLING OF THE COMPOSITE PLATES WITH HOLES SUBJECTED TO UNIAXIAL AND BIAXIAL COMPRESSION

M. Barski, A. Muc

Institute of Machine Design, Cracow University of Technology, Kraków, Poland

1. Introduction

The presence of a hole in an otherwise uniformly compressed composite plane sheet generally causes a stress concentration and a reduction of the resistance to the loss of a global stability. However, cut - outs of a different shapes have to be made into laminates for practical reasons. This problem is extensively researched and discussed in the literature [2] - [6].

In this work the influence of a holes of an arbitrary shape on the global stability of a laminate plates is investigated. In the Fig. 1. there is shown a multilayered composite structure in the Cartesian co - ordinate system. The structure is made of two parts: the host plate Ω that occupies the volume $\Omega = \Omega_p - \Omega_h$, where Ω_p is the volume of the composite plate and Ω_h denotes the volume of the arbitrary shape hole. The considered plates consists of $N = 30$ layers and the feasible configurations are as follows: $[0^\circ]_{30}$, $[\pm 45^\circ]_{15}$ and $[90^\circ]_{30}$. Material of fiber are highly anisotropic mechanics properties. It means that the young modulus E_1 (fiber direction) is greater than E_2 (direction perpendicular to the fiber). The compressive loading of the plate is assumed to be in the form of uniform stress boundary condition on each edges. Moreover, the plate is simply supported.

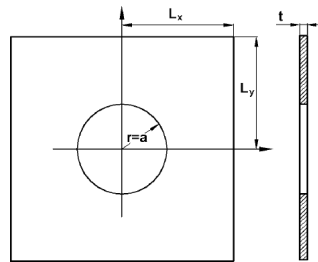


Fig. 1. Laminated composite rectangular plate with a circular hole.

2. Arbitrary shape of openings

The geometrical representation of a different shape cutouts in the XY-plane is presented by Abuefoutouh [1] as simple equations:

$$(1) \quad x = \lambda(\cos(\varphi) + w\cos(n\varphi)), \quad y = \lambda(c\sin(\varphi) - w\sin(n\varphi)).$$

The parameter λ , which is a positive and real number, controls the size of the cutout. The integer n and the parameter c determines the shape of cutout. The parameter w is the bluntness factor which changes the radius of curvature at the corner of the cutout. For example, for $w = 0$, $n = 1$, $c = 1$ the circular shape can be obtained, $w = 0.1$, $n = 3$, $c = 1$ - the square shape and $w = 0.25$, $n = 2$, $c = 1$ - the triangular shape.

3. Method of the analysis and results

In order to obtain the buckling mode and corresponding value of the critical load multiplier for the different shape and size of the cut - outs the numerical analysis was performed. The

calculations were made with use of commercial finite element system ANSYS12. We use the shell elements, namely multilayered shell element SHELL181. The maximal size of the cut - outs is limited by the stress concentration, which can cause the composite damage in first ply failure (FPF) sense. Below in the Fig. 2 shown the results of calculation for arbitrary chosen shape and load case are shown.

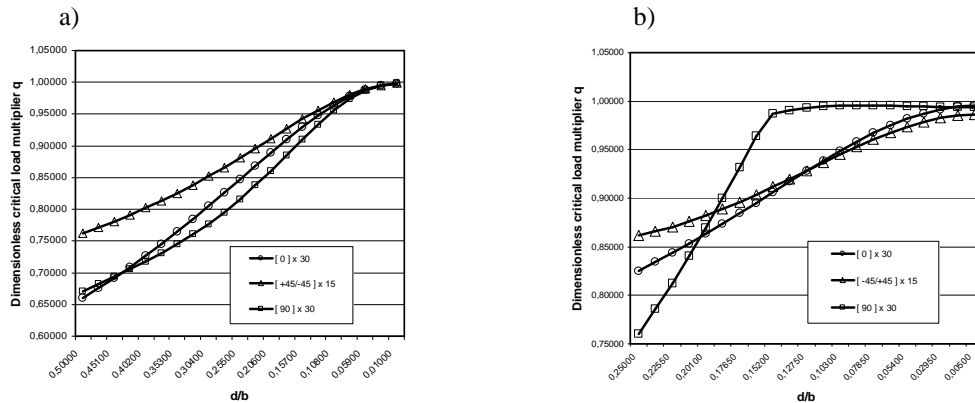


Fig. 2. Critical load multiplier for a) rectangular plate with circular hole $k = 1$, b) square plate with ellipsoidal hole $k = 0.5$, where $k = \sigma_x / \sigma_y$ is the ratio of external load stress

As it can be observed, the significant influence on the value of critical load multiplier has the configuration of the laminate. The highest absolute values are obtained for the configuration $[\pm 45^\circ]_{15}$ and the lowest for the configuration $[90^\circ]_{30}$. Moreover, in the Fig. 2b for $[90^\circ]_{30}$ the number of half-waves changes with respect to the size of elliptical cut-outs.

Generally, the presence of a openings cause the loss of buckling resistance. For a very small cut - outs the value of critical load multiplier is comparable with values obtained for structure without any holes. For a large openings, where the ratio d/b (d diameter of an hole, b is a shorter edge of a plate) is about 0.25 the reduction of the value of critical load multiplier is over 40 %. Detailed results varies significantly depending on the adopted configuration of the laminate as well as the shape of the hole and the applied load.

4. References

- [1] N.M. Abulfoutouh (1993). Preliminary design of unstiffened composite shells, Proceedings of symposium of seventh technical conference of ASC, 693-786.
- [2] S. A. M. Ghannadpour, A. Najafi and B. Mohammadi (2006). On the buckling behavior of cross - ply laminated composite plates due to circular/elliptical cutouts, *Comp. Struct.*, **75**, 3 - 6.
- [3] Mehmet Fatih Altan and Murat Emre Kartal (2009). Investigation of buckling behavior of laminated reinforced concrete plates with central rectangular hole using finite element method, *Materials & Design*, **30**, 2243 - 2249.
- [4] M.P. Nemeth (1995), *Buckling and postbuckling of laminated composite plates with a cut-out, Buckling and postbuckling of composite plates*, (G.J. Turvey, I.H. Marshall, eds), Chapman & Hall, London, 260 – 298.
- [5] Ömer Sinan Şahin (2005). Thermal buckling of hybrid angle - ply laminated composite plates with a hole, *Comp. Sci. & Technology*, **65**, 1780 - 1790.
- [6] Wann Jane Chen, Psang Dain Lin and Lien Wen Chen (1991). Thermal buckling behavior of composite laminated plates with a circular hole, *Comp. Struct.*, **18**, 379 - 397.

THE STRESS-STRAIN STATE OF A THREE-LAYERED SPHERICAL SHELL UNDER NORMAL PRESSURE

S. Bauer, E. Voronkova and L. Karamshina

St. Petersburg State University, St. Petersburg, Russia

1. Introduction

The current paper is concerned with the mechanical behavior of multilayered orthotropic spherical shells loaded by normal pressure.

Laminated plates and shells appear in a number of engineering or biomechanical applications. Namely, three-layered spherical shell can be used as a basic model for the human eye. The layers represent the main layers of the outer coat of the eye (the sclera, the choroid and the retina), respectively.

2. Material and methods

We consider a multilayered spherical shell deformed by inner normal pressure. Transversal isotropy is assumed for each layer. The mechanical and geometrical characteristics of the layers differ from each other.

Two refined theories for orthotropic plates of moderate thicknesses worked out by Paliy-Spiro (PS) [1] and by Rodinova-Titaev-Chernykh (RTC) [2] are employed to study the stress-strain state of the shell. Results found with the RTC and PS theories are compared with those obtained with the exact 3D theory of elasticity.

We also compare results for obtained the three-layered shell with those for one-layer shell with average elastic properties.

3. Results

For transversally isotropic spherical shell of one layer, we obtain the displacement of the middle surface by means of the 2D PS theory (u^{PS}) and the RTC theory (u^{RTC}) as

$$(1) \quad u^{PS}/u^{KL} = 1 - \alpha(1 - \nu^*),$$

$$(2) \quad u^{RTC}/u^{KL} = 1 - \alpha(1 - \nu^*) - \alpha^2 \left(\frac{1}{4} - \frac{6\nu^*}{5\nu'} - \frac{\nu^*}{12} - \frac{(\nu^*)^2}{6} \right),$$

where u^{KL} is the Kirchhoff-Love approximation of the mid-surface deflection ($u^{KL} = \frac{p(1-\nu)R^2}{2E_1h}$), p — the load parameter, $\alpha = h/R$ — the relative shell thickness, (here h is the shell thickness and R is the typical radius of the curvature), E_1, E_3, ν, ν' — the independent elastic parameters, $\nu^* = E_1\nu'/(E_3(1-\nu))$.

Considering $\alpha \ll 1$, the exact 3D-theory (u^{3D}) gives [3]

$$(3) \quad u^{3D}/u^{KL} = 1 - \alpha(1 - \nu^*) - \alpha^2 \left(\frac{1}{4} - \frac{\nu^*}{12\nu'} - \frac{11}{12}\nu^* \right) + O(\alpha^3).$$

One can find the exact 3D solution for isotropic spherical shell, for example, in [4].

The comparison of relations (1), (2) and (3) shows that both 2D-theories give two first terms of the 3D solution (3). The RTC theory gives one of three terms of the third order in (3). For multilayered shells the similar, but much lengthy formulas are also obtained.

In the multilayer shell, the salient points were revealed for radial stresses and displacements. Circumferential stresses possessed jump discontinuities (gaps) near layer-to-layer contact lines. The

more material properties differ from each other, the larger were the gaps. For the eyeball such effects may lead to internal detachments of the inner layers of the eye shell under increased intraocular pressure, e.g. a detachment of the choroid and the sclera.

4. Conclusions

The presented 2D shell theories give acceptable fit to the 3D exact solution for spherical shells with a transversal isotropy. For orthotropic spherical shells or/and ellipsoidal shells adequate results can be obtained by means of these theories.

5. References

- [1] O.M. Paliy, V.E. Spiro (1977). *Anisotropic Shells in Shipbuildings. Theory and Analysis. Sudostroenie (in Russian)*, Leningrad, 386 p.
- [2] V.A. Rodionova, V.F. Titaev, K.F. Chernykh (1996). *Applied Theory of Anisotropic Plates and Shells*, St. Petersburg University Press, St.Petersburg, 280 p.
- [3] K.E. Kotliar, M. Maier, S.M. Bauer, N. Feucht, C. Lohmann, I. Lanzl (2007). Effect of Intravitreal Injections and volume changes on Intraocular Pressure: clinical results and biomechanical model, *Acta Ophthalmologica Scandinavica*, **85**, 777-781.
- [4] T.M. Atanackovic, A. Guran (2002). *Theory of Elasticity for Scientists and Engineers*, Birkhauser, Berlin, 374 p.
- [5] S.M. Bauer, E.B. Voronkova (2011). Nonclassical shells theories for the analysis of transversally isotropic spherical and cylindrical layers under normal pressure (in Russian), *Vestnik SPbGU*, **3**, 86–93

HARMONIC VIBRATION OF A CUSPED PLATE IN THE ZERO APPROXIMATION OF VEKUA'S HIERARCHICAL MODELS

N. Chinchaladze

*Iv. Javakhishvili Tbilisi State University, I. Vekua Institute of Applied Mathematics,
2 University Str., 0186 Tbilisi, Georgia*

In the case of harmonic vibration we study the well-posedness of boundary value problems for elastic cusped *symmetric prismatic shells* in the zeroth approximation of I. Vekua's hierarchical model. A survey of results concerning cusped prismatic shells one can find [4]. To the investigation of cusped plates within the framework of classical Kirchhoff-Love model are devoted works of E. Makhover [6], G. Jaiani [5], N. Chinchaladze [1], etc. In 2000 by G. Devdariani, G. V. Jaiani, S. S. Kharibegashvili and D. Natroshvili (see [3]) the first boundary value problem for the system of cusped prismatic shells in the first approximation was investigated. In [2] bending of the cusped plate in case of Vekua's hierarchical models was studied.

We consider symmetric cusped prismatic shells, i.e., plates of variable thickness with cusped edges. We assume that the cusped plate projection ω has a Lipschitz boundary $\partial\omega = \bar{\gamma}_0 \cup \bar{\gamma}_1$, where $\bar{\gamma}_0$ is a segment of the x_1 -axis and $\bar{\gamma}_1$ lies in the upper half-plane $x_2 > 0$; moreover, in some neighborhood of an edge of the plate which may be cusped, the plate thickness have the following form

$$2h(x_1, x_2) = \overset{(+)}{h}(x_1, x_2) - \overset{(-)}{h}(x_1, x_2) = h_0 x_2^\kappa, \quad h_0 = \text{const} > 0, \quad \kappa = \text{const} \geq 0, \quad x_2 \geq 0.$$

Then γ_0 will be a cusped edge for $\kappa > 0$.

In what follows X_{ij} and e_{ij} are the stress and strain tensors, respectively, u_i are the displacements, Φ_i are the volume force components, ρ is the density, λ and μ are the Lamé constants, δ_{ij} is the Kronecker delta. Moreover, repeated indices imply summation, bar under one of the repeated indices means that we do not sum.

By u_{ir} , X_{ijr} , e_{ijr} , Φ_{jr} we denote the r -th order moments of the corresponding quantities u_i , X_{ij} , e_{ij} , Φ_j as defined below:

$$\left(u_{ir}, X_{ijr}, e_{ijr}, \Phi_{jr} \right) (x_1, x_2, t) := \int_{\overset{(-)}{h}(x_1, x_2)}^{\overset{(+)}{h}(x_1, x_2)} \left(u_i, X_{ij}, e_{ij}, \Phi_j \right) (x_1, x_2, x_3, t) P_r(ax_3 - b) dx_3, \quad j = \overline{1, 3}.$$

I. Vekua's hierarchical models for elastic prismatic shells are the mathematical models (see, e.g., [7], [8], and [4]). Their constructing is based on the multiplication of the basic equations of linear elasticity by Legendre polynomials $P_r(ax_3 - b)$, where

$$a(x_1, x_2) := \frac{1}{h(x_1, x_2)}, \quad b(x_1, x_2) := \frac{\overset{(+)}{h}(x_1, x_2) + \overset{(-)}{h}(x_1, x_2)}{\overset{(+)}{h}(x_1, x_2) - \overset{(-)}{h}(x_1, x_2)},$$

and then integration with respect to x_3 within the limits $\overset{(-)}{h}(x_1, x_2)$ and $\overset{(+)}{h}(x_1, x_2)$. By constructing Vekua's hierarchical models in Vekua's first version on upper and lower face surfaces stress vectors are assumed to be known.

The mathematical model of elastic cusped plates with variable thickness, in the zeroth approximation is described by the following degenerating hyperbolic system [4]

$$(1) \quad \begin{aligned} \rho h v_{\beta 0, tt} - \mu \left[(h v_{\alpha 0, \beta})_{, \alpha} + (h v_{\beta 0, \alpha})_{, \alpha} \right] - \lambda (h v_{\alpha 0, \alpha})_{, 1} &= \Phi_{\beta}^{(0)}, \quad \alpha \neq \beta, \quad \alpha, \beta = 1, 2, \\ \rho h v_{30, tt} - \mu (h v_{30, \alpha})_{, \alpha} &= \Phi_3^{(0)}. \end{aligned}$$

where $\Phi_j^{(0)} := \sqrt{1 + \left(\frac{(+)}{h_{,1}}\right)^2 + \left(\frac{(+)}{h_{,2}}\right)^2} Q_j^+ + \sqrt{1 + \left(\frac{(-)}{h_{,1}}\right)^2 + \left(\frac{(-)}{h_{,2}}\right)^2} Q_j^- + \Phi_{j0}$, are the zeroth moments of the volume forces Φ_j , v_{j0} are the components of the zeroth moment of the displacement vector. Q_j^+ and Q_j^- are projections on the axis x_j , $j = 1, 2, 3$, of the surface forces Q^+ and Q^- acting on the upper and lower faces of the prismatic shell; the ranges of Latin and Greek indices are $\{1, 2, 3\}$ and $\{1, 2\}$ correspondingly.

Let us consider the case of harmonic vibration, i.e., $v_{i0}(x, t) := e^{-\nu t} v_{i0}^0(x)$, $\Phi_i^{(0)}(x, t) := e^{-\nu t} \Phi_i^{(0)}(x)$, $\nu = \text{const} > 0$, $i = 1, 2, 3$. For $v_{i0}^0(x)$ taking into account (1) we get the following system (in what follows we omit the overscript index 0 if it will not lead to a misunderstanding)

$$\begin{aligned} -\rho \nu^2 h v_{\beta 0} - \mu \left[(h v_{\alpha 0, \beta})_{, \alpha} + (h v_{\beta 0, \alpha})_{, \alpha} \right] - \lambda (h v_{\alpha 0, \alpha})_{, \beta} &= \Phi_{\beta}^{(0)}, \quad \alpha \neq \beta, \quad \alpha, \beta = 1, 2, \\ -\rho \nu^2 h v_{30} - \mu (h v_{30, \alpha})_{, \alpha} &= \Phi_3^{(0)}. \end{aligned}$$

For arbitrary $\kappa \geq 0$ we introduce appropriate function spaces $X_{0, \nu}^{\kappa}$ which are crucial in our analysis. We show coerciveness of the corresponding bilinear form and prove uniqueness and existence results for the variational problem. We describe in detail the structure of the spaces $X_{0, \nu}^{\kappa}$ and establish their connection with weighted Sobolev spaces. Moreover, we give some sufficient conditions for a linear functional arising in the right hand side of the variational equation to be bounded.

References

- [1] N. Chinchaladze (2008). *On Some Nonclassical Problems for Differential Equations and Their Applications to the Theory of Cusped Prismatic Shells*, Lecture Notes of TICMI, **9**, 1-92.
- [2] N. Chinchaladze, G. Jaiani, R. Gilbert, S. Kharibegashvili, D. Natroshvili (2008). Existence and uniqueness Theorems for cusped prismatic shells in the N-th hierarchical model, *Mathematical Methods in Applied Sciences*, **31** (11), 1345-1367.
- [3] G. Devdariani, G. V. Jaiani, S. S. Kharibegashvili, D. Natroshvili (2000). The first boundary value problem for the system of cusped prismatic shells in the first approximation, *Appl. Math. Inform.*, **5**(2), 26-46.
- [4] G. Jaiani (2011). *Cusped Shell-like Structures*, SpringerBriefs in Applied Science and Technology, Springer-Heidelberg-Dordrecht-London-New York.
- [5] G. Jaiani (1992). On some applications of variational methods in the bending theory of prismatic sharp edged shells. *Proceedings of I.Vekua Institute of Applied Mathematics of Tbilisi University*, **47**, 36-43.
- [6] E. Makhover (1957). Bending of a plate of variable thickness with a cusped edge. *Scientific Notes of Leningrad State Ped. Institute*, **17** (2), 28-39 (Russian).
- [7] I.N. Vekua (1955). On a way of calculating of prismatic shells, *Proceedings of A. Razmadze Institute of Mathematics of Georgian Academy of Sciences*, **21**, 191-259 (Russian).
- [8] I.N. Vekua (1985). *Shell Theory: General Methods of Construction*, Pitman Advanced Publishing Program, Boston-London-Melbourne.

RELAXATION OF RESIDUAL STRESSES IN A NONLINEARLY ELASTIC PLATE

S.V. Derezin, L.M. Zubov

*Faculty of Mathematics, Mechanics and Computer Science,
Southern Federal University, Rostov on Don, Russia*

1. Introduction

In the framework of general nonlinear plate theory we consider a buckling problem for an elastic plate containing residual or eigen-(internal) stresses. In contrast to the Föppl-von Kármán model [1, 2] the tangential strains are not supposed to be small. We obtain a system of nonlinear partial differential equations with respect to the transverse deflection and the coefficients of the first fundamental form. The system describes in particular the bending of the plate due to relaxation of internal stresses with no external forces applied. In the case of very thin plate (membrane) that doesn't resist bending we show that there exists along with the plane stress state solution also the bent form which corresponds to the relaxed state of the membrane.

2. Residual stresses

Residual stresses in the plate occur via the general incompatibility equation [3] of the plane nonlinear elasticity theory

$$(1) \quad \nabla \cdot [(\det \mathbf{U})^{-1} \mathbf{e} \cdot \mathbf{U} \cdot (\nabla \cdot \mathbf{e} \cdot \mathbf{U})] = \nabla \cdot [(\det \mathbf{U})^{-1} \mathbf{e} \cdot \mathbf{G} \cdot \boldsymbol{\alpha}] + \beta.$$

Here $\mathbf{G} = \mathbf{U}^2$ is the Cauchy-Green strain measure, $\mathbf{e} = -\mathbf{E} \times \mathbf{i}_3$ is the 2D permutation tensor, \mathbf{E} is the identity tensor, $\boldsymbol{\alpha}$ is the density of edge dislocations, β is the density of wedge disclinations. Please note, that other sources of residual stresses like distributed heat or growth parameters for biological tissues [4] could be placed in the right hand side of the equation (1).

3. Relaxation process

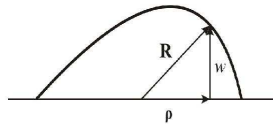


Figure 1. Buckling of the plate due to the relaxation process

The particular advantage of slender bodies makes it possible to consider relaxation of stresses by the escape in the third dimension. Here w is used to denote the transverse deflection of the plate. Then

$$(2) \quad \mathbf{G} = \nabla \mathbf{R} \cdot \nabla \mathbf{R}^T = \nabla \boldsymbol{\rho} \cdot \nabla \boldsymbol{\rho}^T + \nabla w \nabla w = \mathbf{G}^* + \nabla w \nabla w.$$

Substituting (2) into (1) we have in the membrane limit ($\mathbf{G} = \mathbf{E}$)

$$(3) \quad [w, w] = \left[1 - (\nabla w)^2\right]^{\frac{3}{2}} \beta, \quad [w, w] = \frac{\partial^2 w}{\partial x_1^2} \frac{\partial^2 w}{\partial x_2^2} - \left(\frac{\partial^2 w}{\partial x_1 \partial x_2}\right)^2,$$

where $[w, w]$ is the Monge-Ampere operator. In the case of the Föppl-von Kármán theory [1, 2] instead of (3) one should use $[w, w] = \beta$. This type of equation according to the general theory [5] gives no direct way of taking into account negative β .

4. Some results

Let the domain occupied by the plate, the distribution of incompatibilities β and the transverse deflection w be axially-symmetric. Then equation (3) admits exact integration. Moreover we assume the usual zero-slope condition [6] in the center of the membrane: $w'(r)|_{r=0} = 0$.

Under such conditions for constant positive β we obtain

$$(4) \quad w(r) = \frac{1}{\beta} \sqrt{\beta^2 r^2 + 4\beta} - \frac{1}{\sqrt{2\beta}} \log \left| \frac{\sqrt{2\beta} + \sqrt{\beta^2 r^2 + 4\beta}}{\sqrt{2\beta} - \sqrt{\beta^2 r^2 + 4\beta}} \right| - C,$$

whereas for constant negative β

$$(5) \quad w(r) = \frac{1}{\beta} \sqrt{\beta^2 r^2 + 4\beta} + \frac{1}{\sqrt{-2\beta}} \arctan \frac{\sqrt{\beta^2 r^2 + 4\beta}}{\sqrt{-2\beta}} - C,$$

the constant C in both cases is furnished by vanishing $w(r)$ on the outer radius $r = r_0$ of the plate.

For negative β the solution exists only in some part of the unit disk, where $r \geq \sqrt{-4/\beta}$.

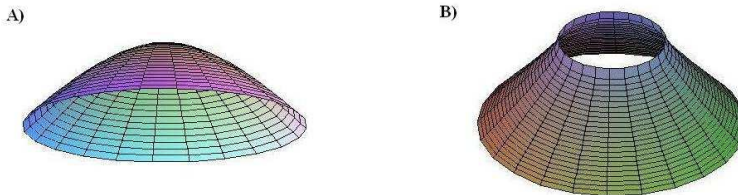


Figure 2. A) Positive disclinations; B) Negative disclinations

Acknowledgement. This work was supported financially by the Russian Foundation for Basic Research (grant N 09-01-00459) and the Federal target programme "Research and Pedagogical Cadre for Innovative Russia" for 2009-2013 years (government contract N P596).

- [1] L.M. Zubov (2007). Von Kármán equations for an elastic plate with dislocations and disclinations, *Doklady Physics*, **52**, 67-70.
- [2] H.S. Seung and D.R. Nelson (1988). Defects in flexible membranes with crystalline order, *Phys. Rev. A*, **38**, 1005-1018.
- [3] S.V. Derezin and L.M. Zubov (2011). Disclinations in nonlinear elasticity, *Z. Angew. Math. Mech.*, **91**, 433-442.
- [4] J. Dervaux, P. Ciarletta and M. Ben Amar (2009). Morphogenesis of thin hyperelastic plates: A constitutive theory of biological growth in the Föppl-von Kármán limit, *Journ. Mech. Phys. Sol.*, **57**, 458-471.
- [5] A.V. Pogorelov (2008). *Multidimensional Monge-Ampere Equation*, Cambridge Scientific Publishers, Cambridge.
- [6] S.P. Timoshenko and S. Woinowsky-Krieger (1991). *Theory of Plates and Shells*, 2nd ed. McGraw Hill, New York.

THE MODELS OF NONCLASSICAL ANISOTROPIC SPHERICAL SHELLS

A. Ermakov

St. Petersburg State University, St. Petersburg, Russia

1. Introduction

The problem of stress-strain state of conjugated orthotropic spherical shells under internal pressure by means of new nonclassical shell theories and three-dimensional theory [1] is studied. The comparison of solutions obtained with the use of improved nonclassical shell theories of Rodionova-Titaev-Chernykh (RTCH) [2] and Paliy-Spiro (PS) [3] is done.

The improved iterative RTCH theory is based on the following hypotheses:

1. transverse tangential and normal stresses are distributed on shell's thickness according to quadratic and cubic laws respectively;
2. tangential and normal components of the displacement vector are distributed on the shell thickness according to quadratic and cubic laws respectively. This theory allows taking into account turns of fibers, their deviation and change of their length.

The Paliy-Spiro shells theory is a theory of shells of moderate thickness which assumes the following hypotheses:

1. straight fibers of the shell which are perpendicular to its middle surface before deformation remain also straight after deformation;
2. cosine of the slope angle of these fibers to the middle surface of the deformed shell is equal to the averaged angle of transverse shear.

The influence of relative thickness for the PS, RTCH shells theory and 3D theory were compared. Also the influence of modulus of elasticity ratio on the deformation form is investigated.

2. Differential equation and Numerical methods

Taking into account the objects symmetry we assume, that all sizes depend only on two coordinates: first defines a parallel line, second the shell thickness. Due to the symmetry of section along the rotation axis, we consider only 2 conjugated arches.

We solve the problem in displacements. As a result of transformation of the basic relationship of the shell theory the 2 system of 3 differential equations of 6th order with 6 boundary conditions of symmetry and 6 boundary conditions of conjugated is obtained.

For the three-dimensional theory the 2 systems of the 2 differential equations in private derivatives of the 8 order with 4 boundary conditions of symmetry, 4 boundary conditions of conjugated and 8 conditions on layers surface have been received.

We solve this systems with the use of the program written in package Matematica 8.0 which realizes the finite-difference method. Using a this method the overall picture of deformation of shells for various ratios of modules of elasticity was obtained.

Such problem can model behaviour of a corneoscleral shell of an eye with increasing of intraocular pressure. An outer shell of the eye, the cornea-scleral (fibrous) tunic consists of the cornea and the sclera. The sclera shell forms about 4/5 of the total fibrous tunic of the human eye and is a spatially reinforced constructers where it is possible to allocate four shells in course of collagen fibres [4]. The

structure of the sclera shell explains its anisotropy and heterogeneity. For normal human eyesight it is necessary that the rays received by an eye after reflection focus strictly on retina). Myopia (near-sightedness) can be caused by the fact that an eye-ball has a shape of an oblong ellipsoid (fig. 1, a). Due to it the image of distant objects focuses in front of the retina. Hypermetropia (farsightedness) can be caused by the fact that an eye has a shape of a flattened ellipsoid (fig. 1, b). Due to it the focus point is behind the retina.

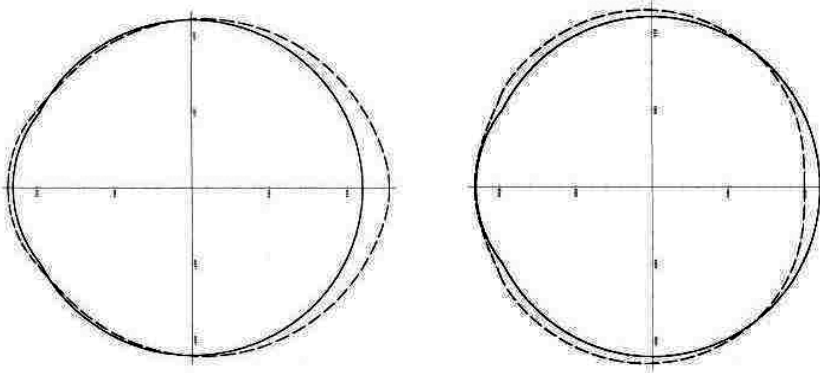


Figure 1. A deformation overall pictures (a,b)

3. Conclusions

On the basis of the performed research we can conclude the following. If we consider the sclera of the eye as a transversally-isotropic material, the internal pressure influences the change of anteroposterior axis of an eye insignificantly. As regards the orthotropic material we can note that in the case when the elasticity module operating in a direction of a line of latitude is more than the elasticity module operating in a direction of a line of a longitude then the overall picture of deformation corresponds to a condition of myopia. In the opposite case, the deformation corresponds to a hypermetropia condition.

4. References

- [1] T.M. Atanackovic and A. Guran (2000). *Theory of Elasticity for Scientists and Engineers*. Birkhauser, Boston.
- [2] V.A. Rodionova, B.F. Titaev and K.F. Chernykh (1996). *Applied Theory of Anisotropic Plates and Shells*. St. Peterburg University Press, St. Petersburg, (in Russian).
- [3] O.M. Paliy and V.E. Spiro (1977). *Anisotropic Shells in Shipbuilding. Theory and Analysis*. Sudostroenie, Leningrad, (in Russian).
- [4] G.K. Lang (2000). *Ophthalmology*. Stugart, New York, Thieme, 566 p.

EXACT LEVINSON-TYPE SOLUTIONS FOR MULTILAYERED PLATES

*G. Formica*¹, *M. Lembo*¹ and *P. Podio-Guidugli*²

¹*University of Rome Tre, Rome, Italy*

²*University of Rome TorVergata, Rome, Italy*

1. Literature survey

In 1985, M. Levinson presented an exact solution for the equilibrium of a three-dimensional plate-like body with rectangular cross section, simply supported at the edge, made of an isotropic linearly elastic material, and subject to transversal loads on its end sections [1]. Levinson's approach, which was based on a simple parametric representation of the candidate solution in terms of displacements, has been found expedient to solve a number of similar problems, where one or another of the original data were changed or generalized. Specifically, a Levinson-type solution has been given: (i) for plate-like bodies with rectangular cross section and simply-supported at the edge, when they are formed by several layers of transversely isotropic materials [2] and when they are piezoelectric, both in statics [3] and dynamics [7]; (ii) for plate-like bodies of general cross section, when they are transversely isotropic [4] and when any one of the boundary conditions from an exhaustive list, including transverse sliding and elastic support, prevails on the lateral boundary [6]. Moreover, explicit solutions have been found for the equilibrium of plate-like bodies with circular cross section, simply supported at the edge, and made of isotropic [5] and transversely isotropic materials [8].

2. Method and results

In the present paper, we derive Levinson-type solutions for the equilibrium problem of plate-like bodies composed of several layers of transversely isotropic materials and simply supported at the edge. We treat both rectangular and circular cross sections. In the former instance, arbitrary transverse loads are applied at the end faces, while the lateral surface is load-free; in the latter, the end-face loads are axisymmetric and suitable radial tractions are applied on the lateral surface. Our derivation begins by requiring that

- in each layer, a displacement field of the type proposed by Levinson for a single-layered plate-like body satisfy that layer's equilibrium equations.

Next, we impose

- continuity of displacements and traction vectors across the interfaces between layers, so as to exclude sliding or, worse, detachment of adjacent layers and to guarantee equilibrium of body parts containing interlayer surfaces, that is to say, possibly singular surfaces for the overall stress field.

The first requirement implies that: (i) in each layer, the function describing the dependence of the displacement components on the in-plane coordinates is an eigenfunction of the laplacian, and as such is written as a double trigonometric series when the cross section is rectangular, as a Bessel series for a circular cross section; (ii) the function describing the dependence of the displacement components on the transverse coordinate are the integrals of ordinary differential equations with constant coefficients, whose integration constants are expressible in terms of the loads acting on the layer's end sections.

As a consequence of (i), to find the dependence on the in-plane coordinates of the displacement field in the whole plate is the matter of determining as many constants as the layers for each coefficient of the relevante series; in fact, to satisfy the second requirement, each of these constants has to

be proportional by a calculable coefficient to one of them, which can be chosen at will. Furthermore, by an elimination process justified by (ii) and the second requirement, we obtain a system of four equations that determine in terms of the loads applied on the two end faces of the plate the four integration constants needed to specify the dependence on the transverse coordinate of the displacement field in one of the layers, which again can be chosen at will; the corresponding integration constants for all other layers are then found sequentially.

3. References

- [1] M. Levinson (1985). The simply supported rectangular plate: An exact, three dimensional, linear elasticity solution, *J. Elasticity*, **15**, 283-291.
- [2] E. Pan (1991). An exact solution for transversely isotropic, simply supported and layered rectangular plates, *J. Elasticity*, **25**, 101-116.
- [3] P. Bisegna and F. Maceri (1996). An exact three-dimensional solution for piezoelectric plates, *J. Appl. Mech.*, **63**, 628-638.
- [4] V. Nicotra, P. Podio-Guidugli and A. Tiero (1999). Exact equilibrium solutions for linearly elastic plate-like bodies, *J. Elasticity*, **56**, 231-245.
- [5] V. Nicotra (2000). Soluzioni di benchmark per piastre appoggiate di forma arbitraria. Il caso della piastra circolare. *Quaderno IAC*, Vol. 4.
- [6] P. Nardinocchi and P. Podio-Guidugli (2003). Levinson-type benchmarks for slide-clamped and elastically supported plates, *J. Elasticity*, **73**, 211-220.
- [7] V. Nicotra and A. Tiero (2004). Exact solutions for linearly electro-elastic plate-like bodies, *J. Elasticity*, **74**, 249-263.
- [8] M. Lembo and P. Podio-Guidugli (2007). How to use reactive stresses to improve plate-theory approximations of the stress field in a linearly elastic plate-like body, *Int. J. Solids and Structures*, **44**, 231-245.

INSTABILITY OF A PIEZOELECTRIC HELICAL SHELL UNDER ELECTRICAL FIELD

A. Girchenko¹, H. Altenbach¹ and V. A. Eremeyev^{1,2}

¹ *Otto-von-Guericke University, Magdeburg, Germany*

² *South Scientific Center of RASci and South Federal University, Rostov on Don, Russia*

In recent years a significant progress in manufacturing and applications of metamaterials is observed [1, 2]. Metamaterials are a special type of materials which physical and mechanical properties are determined almost by their geometrical structure. A special type of metamaterials is the helical or chiral metamaterial which microstructure is based on helical elements, see e.g. [3]. Applications of such materials are in micro- and nanoelectromechanical systems (MEMS/NEMS).

For such flexible structures as a helical shell the buckling analysis plays an important role. Since many chiral metamaterials demonstrate coupling between electro-magnetic and mechanical fields the buckling analysis should be performed with taking into account the electro-mechanical interaction.

In this paper we discuss the buckling of a helical shell made of GaAs under applied electric field. The geometry of the shell is presented in Fig. 1. This material is a semiconductor with piezoelectric properties. It is used in optoelectronic devices as a light-emitting diodes, semiconductor lasers, etc., see e.g. [4, 5]. The helical shell elements can be also used in manufacturing of chiral piezoelectric composites.

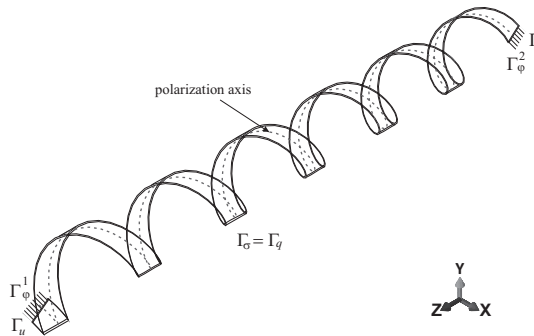


Figure 1. Helical shell: geometry and boundary conditions.

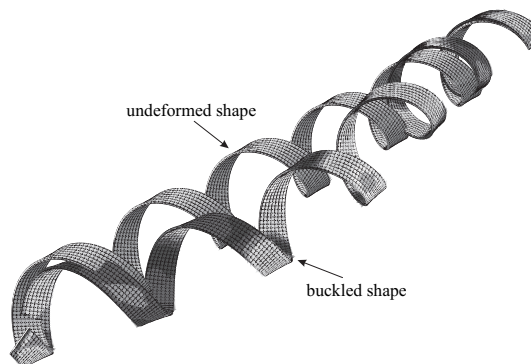


Figure 2. Initial and buckled shapes of the shell.

The basic Lagrangian equations of an electroelastic bodies in the case of quasielectrostatics and absence of external loads take the form [10]

$$(1) \quad \nabla \cdot [\boldsymbol{\sigma} \cdot \mathbf{F}] = \mathbf{0}, \quad \nabla \cdot \mathbf{D} = 0, \quad \boldsymbol{\sigma} = \mathbf{C} : \boldsymbol{\varepsilon} - \mathbf{e} \cdot \mathbf{E}, \quad \mathbf{D} = \mathbf{e} \cdot \boldsymbol{\varepsilon} + \mathbf{d} \cdot \mathbf{E},$$

$$(2) \quad \boldsymbol{\varepsilon} = \frac{1}{2}(\nabla \mathbf{u} + \nabla \mathbf{u}^T + \nabla \mathbf{u} \cdot \nabla \mathbf{u}^T), \quad \mathbf{E} = \nabla \varphi,$$

$$(3) \quad \varphi|_{\Gamma_\varphi^1} = \varphi_0, \quad \varphi|_{\Gamma_\varphi^2} = 0, \quad \mathbf{n} \cdot \mathbf{D}|_{\Gamma_q} = 0, \quad \mathbf{u}|_{\Gamma_u} = \mathbf{0}, \quad \mathbf{n} \cdot \boldsymbol{\sigma}|_{\Gamma_\sigma} = \mathbf{0},$$

where \mathbf{n} is the normal vector to the shell boundary $\Gamma = \Gamma_u \cup \Gamma_\sigma = \Gamma_\varphi^1 \cup \Gamma_\varphi^2 \cup \Gamma_q$, $\mathbf{F} = \mathbf{I} + \nabla \mathbf{u}$ is the deformation gradient, \mathbf{u} is the vector of displacement, \mathbf{E} is the vector of the electric field, expressed by the electric potential φ , $\boldsymbol{\sigma}$ is the 2nd Piola-Kirchhoff stress tensor, \mathbf{D} is the vector of electric induction, $\boldsymbol{\varepsilon}$ is the strain tensor, \mathbf{C} , \mathbf{e} , \mathbf{d} are the elasticity tensor, the tensors of the piezoelectric and dielectric parameters, respectively. Here $\Gamma_q = \Gamma_\sigma$, $\Gamma_u = \Gamma_\varphi^1 \cup \Gamma_\varphi^2$. Let us note that we take into account the geometric nonlinearity in the strain tensor. The shell is deformed by the difference of the electric potential applied along Γ_φ^1 and Γ_φ^2 .

The buckling analysis of the shell is performed by the finite element packages Simulia ABAQUS and COMSOL Multiphysics. Since we take into account electric degrees of freedom, the problem is solved with finite elements, which have both displacement and electrical potential as nodal variables. In particular, the ABAQUS C3D20RE elements (20-node quadratic piezoelectric brick, reduced integration) are used. GaAs is an anisotropic material. We assume that the polarization axis of a piezoelectric material is directed along the helix, see the dashed line in Fig. 1. Hence, the matrix of piezoelectric coefficients rotates in every finite element as in [7]. For the determination of critical states and buckling modes we use the energy criterion of the stability, see e.g. [8, 9]. As an example the first buckling mode is shown in Fig. 2.

The peculiarities of the shell buckling under electric field are analyzed. Let us note that there exist specific buckling modes which are not observed in classical elastic analysis. We also compare the results with ones based on the theory of naturally twisted rods. Finally, we discuss the possible applications of the chiral shells buckling in the control of chiral piezoelectric composites.

- [1] N. Engheta and R.W. Ziolkowski (Eds) (2006). *Metamaterials: Physics and Engineering Explorations*. Wiley, Hoboken.
- [2] F. Capolino (Ed.) (2009). *Theory and Phenomena of Metamaterials*. CRC Press, Boca Raton.
- [3] B. Wang, J. Zhou, T. Koschny, M. Kafesaki, and C. Soukoulis (2009) Chiral metamaterials: simulations and experiments. *J. Opt. A: Pure Appl. Opt.*, **11**, 1-10.
- [4] K. Fricke (1991). Piezoelectric properties of GaAs for application in stress transducers, *J. Appl. Phys.*, **70**, 914-918.
- [5] J. Söderkvist and K. Hjort (1994). The piezoelectric effect of GaAs used for resonators and resonant sensors, *J. Micromech. Microeng.*, **4**, 28-34.
- [6] A. Ghosh and P. Fischer (2009). Controlled propulsion of artificial magnetic nanostructured propellers. *Nano Letters*, **9**, 2243-2245.
- [7] A.A. Girchenko, V.A. Eremeyev and N.F. Morozov (2011). Modelling of spiral nanofilms with piezoelectric properties. *Physical Mesomechanics*, **14**, 10-15.
- [8] P.E. Tovstik, A.L. Smirnov (2001). *Asymptotic Methods in the Buckling Theory of Elastic Shells*. World Scientific, Singapore.
- [9] G.J. Simitses and D.H. Hodges (2006). *Fundamentals of Structural Stability*. Butterworth-Heinemann, Oxford.
- [10] G.A. Maugin (1988). *Continuum Mechanics of Electromagnetic Solids*. Elsevier, Oxford.

AN ASYMPTOTIC MODEL FOR THE KONENKOV WAVE

J. Kaplunov¹, D.A. Prikazchikov²

¹*Brunel University, London, UK*

²*The Bauman Moscow State Technical University, Moscow, Russia*

1. Introduction

This study is concerned with the asymptotic model for the Konenkov wave propagating along the edge of a semi-infinite elastic plate [1], see also [2] for history and review on the subject. The approach of this note is extending the methodology for the surface Rayleigh wave [3] relying on representation in terms of harmonic functions [4]. A recent contribution [5] illustrating the possibility of similar formulation in case of the flexural edge wave, provides the foundation for the asymptotic process. A multi-scale slow time perturbation scheme leads to an asymptotic model containing elliptic equation, governing the decay away from the edge, and a parabolic equation describing the edge wave propagation. The described model is oriented for the extraction of the flexural edge wave contribution into the overall dynamic response. The model also reveals an elliptic-parabolic nature of the wave. It is remarkable that within the derived asymptotic model the edge behaviour is governed by a parabolic beam-type equation, while in the case of the Rayleigh wave surface dynamics was described through a hyperbolic string equation [3].

2. Statement of the problem

We consider an elastic, isotropic, semi-infinite Kirchhoff plate $-\infty < x < \infty$, $0 \leq y < \infty$, $-h \leq z \leq h$. The governing plate bending equation is taken in its classical form, see e.g. [6], with the flexural rigidity $D = 2Eh^3 / (3 - 3\nu^2)$, where E is the Young's modulus and ν is the Poisson ratio. The boundary conditions at the edge $y = 0$ are taken in the form of prescribed edge loading moment $M(x, t)$ and shear force $N(x, t)$, respectively. Due to the linearity of the problem these may be split into two cases, namely $N(x, t) \equiv 0$ and $M(x, t) \neq 0$, and $M(x, t) \equiv 0$ and $N(x, t) \neq 0$.

3. Asymptotic model for the Konenkov wave

Introduction of the multi-scale dimensionless parameters

$$(1) \quad \xi = \frac{x}{h}, \quad \eta = \frac{y}{h}, \quad \tau = \frac{c_2 t}{h}, \quad \tau_{sl} = \varepsilon \tau,$$

where c_2 is the shear wave speed, ε is a small parameter and τ_{sl} is slow time variable, serves as a basis for the perturbation scheme. The physical interpretation of the small parameter is essentially the deviation of phase velocity of the propagating wave in the near-edge vicinity from the Konenkov wave speed.

A key assumption of beam-type behaviour

$$(2) \quad \frac{\partial^4 W}{\partial \xi^4} + c \frac{\partial^2 W}{\partial \tau^2} = 0,$$

where W is the deflection of the plate and c is a parameter, transforms the classical plate bending equation to an elliptic equation, which may be expressed in terms of the original variables as

$$(3) \quad \left[\partial_{yy} + \sqrt{1 - c_K^2} \partial_{xx} \right] \left[\partial_{yy} + \sqrt{1 + c_K^2} \partial_{xx} \right] W = 0,$$

implying the solution in terms of harmonic functions. Here c_K is the well-known Kononkov root

$$(4) \quad c_K = \left[(1 - \nu) \left(3\nu - 1 + 2\sqrt{\nu^2 + (\nu - 1)^2} \right) \right]^{1/4}.$$

Let us focus first on the first type of edge boundary conditions, when $M(x, t) \neq 0$. A treatment analogous to that presented in [3] is then performed, giving at the leading order the dispersion relation of the Kononkov wave, and resulting at the next order in the parabolic equation at the edge $y = 0$

$$(5) \quad c_K^4 \frac{\partial^4 W}{\partial x^4} + \frac{2\rho h}{D} \frac{\partial^2 W}{\partial t^2} = A \frac{\partial^2 M}{\partial x^2},$$

where A is a material constant, combined with the part of leading order boundary conditions, namely

$$(6) \quad \frac{\partial^2 W}{\partial y^2} + \nu \frac{\partial^2 W}{\partial x^2} = 0, \quad \text{at } y = 0.$$

The last relation may be used for representation of solution in terms of a single harmonic function. The resulting asymptotic model for the Kononkov wave contains the Laplace equation together with the boundary condition (5). It is worth noting, that the dynamic factor is present only in the boundary condition.

For the second type of the boundary conditions when $M(x, t) \equiv 0$ and $N(x, t) \neq 0$ the asymptotic model is formulated in respect of the rotation angle around the Ox -axis

$$(7) \quad V = \frac{\partial W}{\partial y}.$$

The results are similar to that obtained in the first case, also containing an elliptic equation over the interior and a parabolic equation at the edge.

It should be emphasized that the representation in terms of a single plane harmonic function, see [5], simplifies the formulation of the problem, since the initial fourth order problem is reduced to a Dirichlet problem for the Laplace equation, where the solution at the boundary is given by the parabolic equation (5). We also remark that the obtained model highlights the dual elliptic-parabolic nature of the flexural edge wave, therefore improving the physical understanding.

The possible extension of the approach could be performed for anisotropic or pre-stressed plates, and also for interfacial flexural waves. The cases of curved plates and shells may also be considered but are of seemingly less interest due to the growing length of algebraic expressions.

4. Acknowledgements

The work of DAP has been carried out under partial support of the Russian President Award for Support of Young Scientists MK-3150.2012.8, which is gratefully acknowledged.

5. References

- [1] Yu.K. Kononkov (1960). A Rayleigh-type flexural wave, *Sov. Phys. Acoust.*, **6**, 122-123.
- [2] J.B. Lawrie, J.D. Kaplunov (2012). Edge waves and resonance on elastic structures: an overview, *Math. Mech. Sol.*, **17**(1), 4-16.
- [3] J. Kaplunov, A. Zakharov and D.A. Prikazchikov (2006). Explicit models for elastic and piezoelectric surface waves, *IMA J. Appl. Math.*, **71**, 768-782.
- [4] P. Chadwick (1976). Surface and interfacial waves of arbitrary form in isotropic media, *J. Elasticity*, **6**, 73-80.
- [5] J. Kaplunov and D.A. Prikazchikov (2011). Flexural edge waves with general time dependence, *Vestnik MGTU im. Baumana, Ser. Nat. Sci., special issue Math. Modelling*, 164-170 (in Russian).
- [6] K. F. Graff (1991). *Wave motion in elastic solids*, Dover, New York, 229-235.

LOCAL MODEL OF FREE VIBRATION OF A MULTILAYERED SANDWICH STRIP WITH SOME SPECIFIC FASTENING OF TWO PARALLEL EDGES

S. Karczmarzyk

Institute of Machine Design Fundamentals, Warsaw University of Technology, Warsaw, Poland

1. Introduction

Sandwich panels are widely used in engineering constructions, see e.g. [1]. Therefore, the classical sandwich three-layer plates and shells, composed of thin, stiff, outer layers (faces) and a thick, compliant, middle layer (core), were investigated by many researches. The classical sandwich members are still investigated in many aspects, mainly because of their specific cross-sectional structure and resulting properties, but it is well justified to investigate multilayered (i.e., five-layer, seven-layer, etc.) sandwich panels since they are more realistic and useful than the three-layer counterparts.

Irrespective of number of layers all the sandwich structures are more or less sensitive on the local loadings. The problem appears in particular in vicinity of the edges. Therefore, the edges of sandwich panels are usually stiffened with C profiles or with some local inserts. Obviously, both including of the stiffeners or inserts into the structures and some attempts to remove them imply necessity of looking for better, more refined mechanical models for the structures, see e.g. [2,3].

The present contribution is devoted to modeling of free vibration of a multilayered plane rectangular sandwich panel fastened with a frame along its two parallel edges by means of bolts. Such solution enables one quick mounting of the panel. The plane strain problem is solved within the local theory of linear elastodynamics which enables us to create accurate models for the multilayered structures with realistic edge solutions. The model (solution) outlined here is obtained following the way presented in [4]. All through-the-thickness local boundary and compatibility equations, for the displacements and stresses, have been satisfied and some new edge boundary conditions have been included in the model. In each layer, irrespective of its thickness, the cross-sectional warping is assumed. Any simplifications or limitations concerning the structure have not been introduced.

The model is also applicable to the sandwich beam and therefore its predictions, seven eigenfrequencies, for a three-layer beam are compared with the corresponding results obtained by a commercial FEM program. The results are very well convergent.

2. Some mathematical details of the model

The final, numerical form of the problem consists of three coupled transcendental equations,

$$(1) \quad F_1(\alpha, \omega) = 0, \quad F_2(\gamma, \omega) = 0, \quad F_3(\alpha, \gamma, \omega) = 0.$$

The first and second equations result from through-the-thickness boundary and compatibility conditions while the third one is obtained after satisfying the following edge boundary conditions for the in-plane and out-of-plane displacements,

$$(2) \quad \begin{aligned} u_x(x = -L/2, z = \pm h_1) = u_x(x = +L/2, z = \pm h_1) = 0, \\ u_z(x = -L/2, z = \pm h_1) = u_z(x = +L/2, z = \pm h_1) = 0. \end{aligned}$$

Symbols h_1 , L and x, z in (2) denote co-ordinates of the bolts fastening the panel to a frame and the space variables, respectively.

3. Numerical results

To test the model a few eigenfrequencies of a three-layer sandwich beam were calculated and compared with eigenfrequencies predicted by the FEM model. The computations were made for the following data: thicknesses of layers of the structure (mm): 1, 20, 1, Young's mod. of the layers (GPa): 68.9, 0.1833, 68.9, Poisson's ratios of the layers: 0.33, 0.33, 0.33, densities of the layers (kg/m³): 2687, 119.7, 2687. Length of the structure $L=0.55$ m. Part of results of the computations are given in Table 1.

m=1	m=2	m=3	m=4
1984.77	4185.98	6728.92	9344.72
2015.33	4241.27	6797.78	9420.38
1.52%	1.30%	1.01%	0.80%

Table 1. Eigenfrequencies (rad/s) for vibration modes 1-4.

The values in the first row of the Table are predicted by the new model, outlined in the above sections, while the results in the second row are predicted by the FEM model. It is seen that the results are very well convergent. The percentage differences given in the third row are lower than 1.6%, for the first mode of vibration it is 1,52 %, and decrease for the next vibration modes.

4. Conclusion

The model can be used for computing accurate eigenfrequencies for both multilayered panels, including the sandwich strips and beams, and for homogeneous structures. Comparing eigenfrequencies for a particular structure with different edge boundary conditions one can observe significant influence of the way of fastening of the structure on its eigenvalues.

5. References

- [1] S. Karczmarzyk (2011). Local model of plane acoustic waves propagation in multilayered infinite sandwich structures, *Archives of Mechanics*, **63**, 573–598.
- [2] S. Karczmarzyk (2010). A new 2D single series model of transverse vibration of a multilayered sandwich beam with perfectly clamped edges, *Journal of Theoretical and Applied Mechanics*, **48**, 789–812.
- [3] S. Karczmarzyk (2009). A new 2D local model for unidirectional clamped-clamped sandwich structure with edge stiffeners, *Journal of Sandwich Structures & Materials*, **11**, 519–538.
- [4] S. Karczmarzyk (1992). A new linear elastodynamic solution to boundary eigenvalue problem of flexural vibration of viscoelastic layered and homogeneous bands, *Journal of Theoretical and Applied Mechanics*, **30**, 663–682.

hp FINITE ELEMENT MODEL FOR CYLINDRICAL SHELLS USING FIRST-ORDER STRESS FUNCTIONS

L. G. Kocsán

Department of Mechanics, University of Miskolc, Hungary

1. Introduction

The dual-mixed variational principle in terms of rotations and *a priori* non-symmetric stresses was introduced by Fraeijns de Veubeke [4], where the translational equilibrium equations is satisfied by the first-order stress function tensor. This method was applied to plane elasticity, membrane and plate problems by Bertóti [1, 2, 3]. In the work [3] a dimensional reduction procedure for plates and shells is described, which is admissible for dual variational principles with *a priori* non-symmetric stresses. This dimensional reduction concept was applied in [6] to cylindrical shell problems based on the three-field dual-mixed Hellinger-Reissner variational principle. The numerical results obtained for axisymmetrically loaded cylindrical shell problems based on the first-order stress functions [5] prove that this concept is worth investigated for two-dimensional shell problems.

2. Fraeijns de Veubeke variational principle

The functional of the three-dimensional two-field dual-mixed variational principle can be obtained by adding a Lagrange multiplier term enforcing the symmetry of the stress tensor to the complementary energy functional [4]:

$$(1) \quad \mathcal{F}(\sigma^{pq}, \phi_{pq}) = \int_V [W_c(\sigma^{pq}) + \epsilon_{pqc} \varphi^c \sigma^{pq}] dV - \int_{S_u} \tilde{u}_p \sigma^{pq} n_q dS,$$

where σ^{pq} is the stress tensor, φ^c is the rotation vector and the permutation tensor is denoted by ϵ_{pqc} . Here the V denotes the volume of the body bounded with surface $S = S_u \cup S_p$. The complementary strain energy is given by

$$(2) \quad W_c(\sigma^{pq}) = \frac{1}{2} \sigma^{k\ell} \varepsilon_{k\ell}(\sigma^{pq}) = \frac{1}{2} \sigma^{k\ell} D_{k\ell pq} \sigma^{pq} \quad \text{in } V,$$

where the symmetric strain tensor $\varepsilon_{k\ell}$ can be expressed with the aid of the fourth-order elastic compliance tensor $D_{k\ell pq}$. Applicability of (1) requires that the stress tensor satisfy *a priori* the translation equilibrium equation

$$(3) \quad \sigma^{k\ell}_{\dots;\ell} + q^k = 0 \quad \text{in } V$$

and the stress boundary condition

$$(4) \quad \sigma^{k\ell} n_\ell = \tilde{p}^k \quad \text{on } S_p,$$

where q^k is the density of the body forces and \tilde{p}^k is the prescribed surface traction on the surface S_p with outward unit normal n_ℓ . It should be mentioned that the displacement boundary condition $u_p = \tilde{u}_p$ on surface S_u is imposed weakly.

A stress field that fulfills (3) can be obtained by introducing the first-order stress function tensor $\Psi^k_{.q}$, as

$$(5) \quad \sigma^{k\ell} = \epsilon^{\ell pq} \Psi^k_{.q;p} + \hat{\sigma}^{k\ell} \quad \text{in } V.$$

where $\hat{\sigma}^{k\ell}$ is a particular solution to (3).

3. Cylindrical shell model

Our main goal is to derive a dimensionally reduced cylindrical shell model based on the three-dimensional dual-mixed variational principle of Fraeijns de Veubeke. All the variables have been expanded into power series with respect to the thickness coordinate. Assuming a thin cylindrical shell the translational equilibrium equation in terms of expanded stresses is obtained. The structure of the translational equilibrium equations in terms of expanded stresses tempting us to prescribe one degree higher approximations for the transverse shear and transverse normal stresses, this opportunity is the favorable property of the application of non *a priori* symmetric stress tensor. In this way several shell models can be derived by using different approximations. In the derived model the stresses are linear or parabolic with respect to the thickness. Further, the approximation of the stresses determines the approximation of the other variables.

A shell model derived in this way makes the application of the classical kinematical hypotheses regarding the deformation of the normal to the shell middle surface unnecessary. As the classical kinematical hypotheses are not incorporated into the formulation, unmodified three-dimensional constitutive equations can be employed.

4. Acknowledgements

The published work was carried out as part of the TMOP-4.2.2/B-10/1-2010-0008 project in the framework of the New Hungarian Development Plan. The realization of this project is supported by the European Union, co-financed by the European Social Fund.

5. References

- [1] E. Bertóti (2000). Dual-mixed *hp* finite element methods using first-order stress functions and rotations, *Comput. Mech.* **26**, 39–51.
- [2] E. Bertóti (2002). Dual-mixed *p* and *hp* finite elements for elastic membrane problems, *Int. J. Num. Meth. Eng.* **53** 3–29.
- [3] E. Bertóti (2005). Derivation of plate and shell models using the Fraeijns de Veubeke variational principle, in: E. Ramm, W. A. Wall, K.-U. Bletzinger, M. Bischoff (Eds.), *Proceedings of the Fifth International Conference on Computation of Shell and Spatial Structures*, Austria, pp. 1–4.
- [4] B. M. Fraeijns de Veubeke (1975). Stress function approach, in: *Proceedings of the World Congress on Finite Element Methods in Structural Mechanics*, Bournemouth, UK, J.1–J.51.
- [5] L. G. Kocsán (2011). Derivation of a dual-mixed *hp*-finite element model for axisymmetrically loaded cylindrical shells, *Arch. Appl. Mech.*, **81**, 1953-1971.
- [6] B. Tóth (2011). Dual-mixed *hp* finite element model for elastic cylindrical shells, *Z. Angew. Math. Mech.*, Available online: <http://dx.doi.org/10.1002/zamm.201100044>

THE FINITE INFLATION OF AN ELASTIC CURVED TUBE WITH NONCIRCULAR CROSS SECTION

A. M. Kolesnikov

Southern Federal University, Rostov-on-Don, Russian Federation

1. Introduction

Consider the shell which is a sector of torus with a closed cross section. We call this shell the curved tube. It is known, that the curved tube with a circular cross section under internal pressure do not changes its curvature in linear theory [1]. This is confirmed experimentally for small strains and isotropic materials. The tube with an elliptic cross section changes its curvature under internal pressure. If $r_2 < r_1$ (Fig. 1c) then the curvature of a pressurized curved tube decreases. If $r_2 > r_1$ (Fig. 1d) then the curvature increases. This phenomenon is widely used in manometric tubes.

The behavior of curved tube under internal pressure is more complex for large strains. It is shown in [2], that the curvature of thin-walled nonlinear elastic curved tube with a circular cross section changes during inflation. Under internal pressure the curved tube made of neo-Hookean material unbends, i.e. its curvature decreases.

In this work the thin-walled nonlinear elastic curved tubes with an elliptic cross section are considered.

2. Formulation

The problem describing the equilibrium of a curved tube under internal pressure is the special case of a pure bending [2]. The approach to the solution of pure bending problem is given in the book by A. Libai and J. S. Simmonds [3] and the paper by L. M. Zubov [4]. This approach allows us to decompose the deformation into two parts: an in-plane deformation of meridional cross section, plus a rigid rotation of each of these meridional planes about some axis by linearly varying angles. In this case the equilibrium equations are reduced to the ordinary differential equations.

Consider the thin-walled shell with a constant thickness h made of hyperelastic material. We will use the incompressible neo-Hookean model of the material with the constant μ . The problem will be considered within the framework of the nonlinear theory of membrane [5]. Let in the undeformed state the median surface of the tube is given by the equations

$$\mathbf{r} = x_1(s)\mathbf{i}_1 + x_2(s)\mathbf{e}_2, \quad \mathbf{e}_2 = \mathbf{i}_2 \sin \beta t + \mathbf{i}_3 \cos \beta t, \quad s \in [0; 2\pi], \quad t \in [0; l]$$

$$x_1(s) = r_1 \sin s, \quad x_2(s) = \beta^{-1} - r_2 \cos s.$$

Here $\{\mathbf{i}_1, \mathbf{i}_2, \mathbf{i}_3\}$ is the standart orthonormal basis in a fixed Cartesian frame, s and t are the Gaussian surface coordinates.

Let the external load will only be the uniformly distributed pressure p in the tube. Suppose that in the deformed state the median surface is given by the following equations [4]

$$\mathbf{R} = X_1(s)\mathbf{i}_1 + X_2(s)\mathbf{E}_2, \quad \mathbf{E}_2 = \mathbf{i}_2 \sin Bt + \mathbf{i}_3 \cos Bt.$$

Then the equilibrium equations reduce to the system of ordinary differential equations [2]. The obtained boundry value problem is solved numerically using a shooting method.

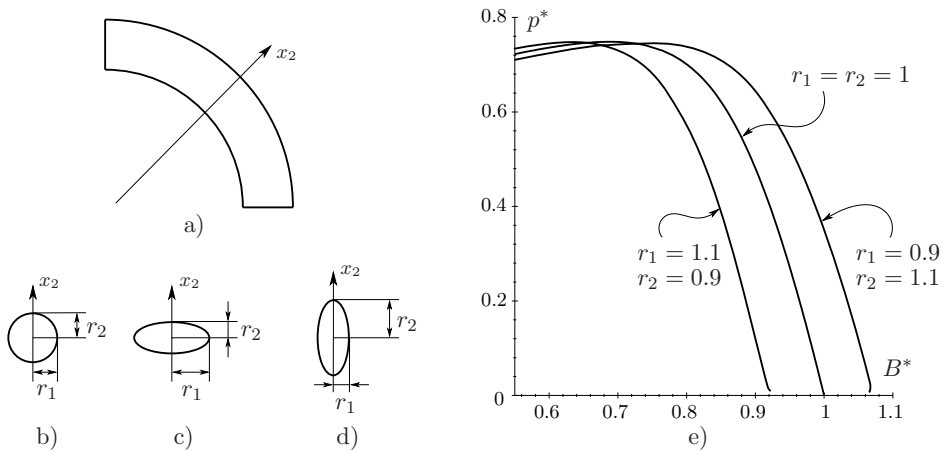


Figure 1. a) Longitudinal section; b), c), d) cross sections; e) pressure vs curvature parameter.

3. Results

Introduce the dimensionless pressure p^* and curvature parameter B^*

$$p^* = \frac{(r_1 + r_2)p}{2\mu h}, \quad B^* = \frac{B}{\beta}.$$

In Fig. 1e the dependence between the pressure and the curvature parameter is shown for three cross sections: one circular ($r_1 = r_2 = 1$) and two elliptical ($r_1 = 1.1, r_2 = 0.9$ and $r_1 = 0.9, r_2 = 1.1$). Under small strains the behavior of the curved tubes could be described by linear theory. Under small internal pressure the curvature of the tube with $r_2 < r_1$ decreases and the curvature of the tube with $r_2 > r_1$ increases. During the inflation the elliptic cross section tends to a circular shape. After that the behavior of tubes is changed radically. The curvature decreases to all tubes under large strains.

Acknowledgements

This research was supported by the President of the Russian Federation (grant MK-439.2011.1), by the Ministry of Education and Science of the Russian Federation (the state contract No. P596) and by the Russian Foundation for Basic Research (grant 1-08-01152-a).

4. References

- [1] V. I. Feodos'ev (1949). *Elastic Elements in Precision Instrument Making*, (In Russian), Oborongiz, Moscow.
- [2] A. M. Kolesnikov (2011). Large bending deformations of pressurized curved tubes, *Arch. Mech.*, **63** (5-6), 507-516.
- [3] A. Libai and J. S. Simmonds (1998). *The Nonlinear Theory of Elastic and Shells*, 2nd ed. Cambridge Univ. Press., Cambridge.
- [4] L. M. Zubov (2001). Semi-inverse solution in non-linear theory of elastic shells Large bending deformations of a cylindrical membrane with internal pressure, *Arch. Mech.*, **53** (4-5), 599-610.
- [5] A. M. Kolesnikov and L. M. Zubov (2009). Large bending deformations of a cylindrical membrane with internal pressure, *ZAMM*, **89**, 288-305.

GOVERNING EQUATIONS FOR MULTI-WALLED CARBON NANOTUBE DERIVED FROM ORTHOTROPIC FLÜGGE SHELL THEORY AND NONLOCAL ELASTICITY

G. Mikhasev and A. Sheiko

Belarusian State University, Minsk, Belarus

1. Model

We consider a multi-walled carbon nanotube (MWCNT) consisting of N layers. The tube is assumed to be in a nonhomogeneous elastic medium and pre-stressed. The MWCNT is modeled as the system of concentrically nested cylindrical shells characterized by length $L = Rl$, mass density per unit volume ρ_n , radius $R_n = Rr_n$ and effective thickness h_n of the n th layer, where R is the tube characteristic size and $n = 1, \dots, N$. At the middle surface of the n th cylinder, the curvilinear co-ordinate system $\alpha = Rx, \beta_n = Rr_n\varphi$ is introduced, where x is the dimensionless longitudinal co-ordinate, and φ is an angle. Following to paper [1], every layer composing the tube is assumed to be orthotropic cylindrical shell with Young's moduli $E_{n,i}$, Poisson's ratios $\nu_{n,i}$ and shear modulus G_n , where indexes $i = 1, 2$ correspond to longitudinal and circumferential directions respectively.

2. Microscopic and macroscopic stresses. Constitutive equations

Let $T_{n,i}^0, S_{n,i}^0$ be the initial membrane stresses in the n th layer. We introduce also the additional microscopic stresses $T_{n,i}, S_{n,i}, Q_{n,i}, H_{n,i}, M_{n,i}$ acting in these layers, where $T_{n,i}, S_{n,i}, Q_{n,i}$ are the membrane and transverse stress resultants respectively, and $H_{n,i}, M_{n,i}$ are the resultant microscopic moments. Let us also introduce the macroscopic (classic) stresses $T_{n,i}^{(m)}, S_{n,i}^{(m)}, Q_{n,i}^{(m)}$ and moments $H_{n,i}^{(m)}, M_{n,i}^{(m)}$ corresponding to the microscopic ones. According to the nonlocal elasticity theory [2], these stresses are linked as follows

$$(1) \quad \mathcal{L}_n(T_{n,i}, S_{n,i}, Q_{n,i}, H_{n,i}, M_{n,i}) = (T_{n,i}^{(m)}, S_{n,i}^{(m)}, Q_{n,i}^{(m)}, H_{n,i}^{(m)}, M_{n,i}^{(m)}), \quad i = 1, 2,$$

where the appropriate two-dimensional linear operator \mathcal{L}_n is written as [3]

$$(2) \quad \mathcal{L}_n = (1 - \varepsilon^2 \Delta_n), \quad \Delta = \left(\frac{\partial^2}{\partial x^2} + \frac{1}{r_n^2} \frac{\partial^2}{\partial \varphi^2} \right), \quad \varepsilon = \frac{e_0 a}{R}.$$

In equation (2), a is the internal characteristic length of the tube material (for carbon $a \approx 0.142\text{nm}$), and e_0 is the material constant of non-locality (e.g, Eringen [2] gives $e_0 = 0.39$).

The constitutive equations for orthotropic layers are assumed to be of the form

$$(3) \quad \begin{aligned} T_{n,i}^{(m)} &= C_{n,ii}\varepsilon_{n,i} + C_{n,ij}\varepsilon_{n,j}, \\ S_{n,i}^{(m)} &= C_{n,66}\omega_n, \quad H_{n,i}^{(m)} = D_{n,66}\tau_n, \\ M_{n,i}^{(m)} &= D_{n,ii}\kappa_{n,i} + D_{n,ij}\kappa_{n,j}, \quad i, j = 1, 2, \quad i \neq j, \end{aligned}$$

where the strains $\varepsilon_{n,i}, \omega_n, \tau_n, \kappa_{n,i}$ are found through the displacements $u_{n,i}$ in the n th layer according to the kinematic hypothesis accepted here (e.g., see in [4]), and the magnitudes $C_{n,ij}, D_{n,ij}$ are expressed through the elastic constants $E_{n,i}, G_n, \nu_{n,i}$ of the orthotropic material which depend on the tube chirality [1].

3. Governing equations

The governing equations for the MWCNT may be derived from the Flügge type shell theory [5]. Taking into account the initial membrane stresses as well as the van der Waals (vdW) forces, they are easily written in terms of the microscopic stresses like that was made in [3], [4]. After multiplying the operator (2) from the left to both sides of these equations, if equations (1), (3) and the strains-displacements relations are taken into consideration, the following governing equations written in the dimensionless form are obtained:

$$(4) \quad \sum_{j=1}^3 \left(\mu^4 \zeta_n \mathbf{M}_{n,ij} + \mathbf{L}_{n,ij} + \mathbf{T}_{n,ij} \right) u_{n,j} - \delta_n \mathcal{L}_n \frac{\partial^2 u_{n,i}}{\partial t^2} - \mathcal{L}_n \left[\hat{c}_{n+1,i} (u_{n+1,i} - u_{n,i}) - \hat{c}_{n,i} (u_{n,i} - u_{n-1,i}) + \hat{q}_{n,i} \right] = 0,$$

where

$$(5) \quad i = 1, 2, 3, \quad n = 1, 2, \dots, N, \quad \mu^4 = \frac{h_N^2}{12R^2}, \quad \zeta_n = \left(\frac{h_n}{h_N} \right), \quad \delta_n = \left(\frac{\omega_N}{\omega_n} \right), \\ \omega_n^2 = \frac{E_n^*}{\rho_n R^2}, \quad E_n^* = \frac{2E_{n,1}\nu_{n,2}}{\nu_{n,1} + \nu_{n,2}}, \quad \hat{c}_{n,i} = \frac{R^2 c_{n,i}^{(vdW)}}{h_n E_n^*}, \quad \hat{q}_{n,i}(x, \varphi, t) = \frac{R^2 q_{n,i}}{h_n E_n^*}.$$

Here $\mathbf{M}_{n,ij}$, $\mathbf{L}_{n,ij}$ and $\mathbf{T}_{n,ij}$ are the (3×3) matrix with elements being differential operators, t/ω_N is time, $c_{n,i}^{(vdW)}$ are the vdW interaction spring constants [3], and $q_{n,i}$ are the distributed surface forces. In equations (4), the operators $\mathbf{M}_{n,ij}$, $\mathbf{L}_{n,ij}$ correspond to the moment and membrane theories respectively [4] of elastic orthotropic shells, and the operator $\mathbf{T}_{n,ij}$ takes into account the initial membrane stresses $T_{n,i}^0, S_{n,i}^0$. It should be noted that $c_{1,i} = u_{N+1,i} = 0$ for any $i = 1, 2, 3$, and $c_{N+1,i}(x, \varphi)$ are the variable dimensionless spring constants of the surrounding nonuniform elastic medium.

Equations (4) may be applied for studying vibrations of the MWCNT taking into account the tube chirality, non-locality, the initial membrane and vdW forces, and the elastic properties of the surrounding nonhomogeneous matrix as well. As an example, free vibrations of the medium length tube lying in the uniform elastic medium have been studied. Performed calculations have shown that introducing the parameter of non-locality e_0 into our model results in decreasing the natural frequencies of the MWCNT. In addition, using the asymptotic approach developed in book [4], the localized axisymmetric free vibrations of the MWCNT have been examined. It has been found that inhomogeneity of the surrounding elastic medium may lead to strong localization of the natural modes of the pre-stressed tube in a neighborhood of some parallel where the coefficient of soil reaction is minimum.

4. References

- [1] T. Chang (2010). A molecular based anisotropic shell model for single-walled carbon nanotubes, *J. Mech. Phys. Solids*, **58**, 1422-1433.
- [2] A.C. Eringen (1983). On differential equations of nonlocal elasticity and solutions of screw dislocation and surface waves, *J.Apple Phys* **54**, 4703-4710.
- [3] T. Usuki, K. Yogo (2009). Beam equations for multi-walled carbon nanotubes derived from Flügge shell theory, *Proc. R. Soc. A.*, **465**, 1199-1226.
- [4] G.I. Mikhasev, P.E. Tovstik (2009). *Localized Vibrations and Waves in Thin Shells. Asymptotic Methods*. FIZMATLIT, Moscow, 292 p.
- [5] W. Flügge (1934). *Statik und Dynamik der Schalen*. Springer, Berlin.

RECENT DEVELOPMENTS IN COMPUTATIONAL METHODS FOR MASONRY SHELLS

G. Milani¹, A. Tralli²

¹ *Technical University in Milan, Italy*

² *University of Ferrara, Italy*

1. Summary

Masonry curved elements – as for instance arches, domes and vaults – represent one of the most diffuse structural typologies of historical buildings both of Eastern and Western architecture. Moreover, the growing interest in the preservation and rehabilitation of historical constructions has created a need for the development of new efficient tools for the analysis and the evaluation of the load-bearing capacity of these structures. Finally, the study of masonry vaults should take into account the essential of the “masonry” material- i.e. heterogeneity, almost no resistance to traction combined with a good compressive strength and a high friction coefficient, as well as the overall importance of the geometry for achieving the equilibrium.

However, at present only a limited number of available FE codes (e.g. Diana –TNO Delft) contains specific modules for analyzing masonry structures and, as concerns large masonry vaults, such a codes use, in the framework of an incremental procedure, continuous elastic-plastic-damaging constitutive models, so producing very heavy and often not completely reliable computational models.

As it is well known, the history of the theory of curved masonry structures as exposed for instance in the classical treatise by Benvenuto [1], is not based on the developments of the theory of elasticity. As a matter of fact, the first “scientific” graphical attempts for the study of the equilibrium of masonry domes go back to the early 18th century and are due to, e.g., Bouguer (1734), Bossut (1778) and Mascheroni (1785) who stated simple 1D equilibrium equations, neglecting the role of circumferential forces. Anyway, what appeared clear from the beginning was that cracking occurs on curved masonry elements in presence of self-weight and at very low level of tensile stresses. In this context, a considerable improvement in the analysis of spherical domes was achieved when Levy (1888) proposed a graphical analysis aimed at finding the circle on which circumferential forces vanish. Nowadays it can be affirmed (Huerta [2]) that “the modern theory of limit analysis of masonry structures, which has been developed mainly by Heyman [3] is the tool to understand and analyze masonry structures”.

For these reasons, to evaluate the load-bearing capacity of masonry shells, in a series of papers [4–6], the Authors have dealt with the limit analysis of such kind structures. They have developed a two steps approach:

- In the first step, in order to take into account the actual mechanical properties and the heterogeneity of unreinforced masonry, macroscopic strength domains have been obtained either by a suitable application of the homogenization theory [4] or by means of a compatible approach [5], in which each brick was supposed interacting with its six neighbors by means of rigid-plastic interfaces with frictional behavior representing mortar joints. In this latter case, a sub-class of possible elementary deformations was a-priori chosen to describe joints cracking under in- and out-of-plane loads. Suitable internal macroscopic actions were finally applied on the boundary of the Representative Element of Volume (REV). Several examples consisting of single and double curvature elementary cells were analyzed, obtaining, for each REV inspected, in- and out-of-plane homogenized failure surfaces to be used at a structural level.

- In the second step, the 3D structural limit analysis problem was solved assuming masonry as an orthotropic homogeneous material and adopting an upper bound approach, discretizing homogenized masonry by means of six-noded rigid infinitely resistant wedge elements interacting with rigid-plastic interfaces. In this way, internal power dissipation was possible only at the interfaces between wedge adjoining elements. Entire vaults either in absence or in presence of FRP reinforcements were analyzed in detail, comparing results with existing literature and alternative FE approaches [6].

One of the most popular advantages of limit analysis is that the collapse multiplier does not depend on load history. However, limit analysis is incapable to provide any information about deformations and displacements near failure. To circumvent this critical drawback, in [7], a 3D model for the evaluation of the non-linear behavior of masonry double curvature structures was presented. In such approach, the heterogeneous assemblage of blocks was substituted with a macroscopically equivalent homogeneous non-linear material. At the meso-scale, similarly to the limit analysis case, a curved running bond REV constituted by a central block interconnected with its six neighbors was discretized through a few six-noded rigid wedge elements and rectangular interfaces. Non linearity was again concentrated exclusively on joints reduced to interfaces, exhibiting a frictional behavior with limited tensile and compressive strength with softening. The macroscopic homogenous masonry behavior was then evaluated on the REV imposing separately increasing internal actions (in-plane membrane actions, meridian and parallel bending, torsion and out-of-plane shear). This simplified approach allows estimating heuristically the macroscopic stress-strain behavior of masonry at the meso-scale. The non-linear behavior so obtained was subsequently implemented at a structural level in a novel FE non-linear code, relying on an assemblage of rigid infinitely resistant six-noded wedge elements and non-linear interfaces, exhibiting deterioration of the mechanical properties. Several numerical examples were analyzed, consisting of different typologies of curved masonry structures, comparing results with existing data and additional non-linear FE analyses conducted with commercial codes. In addition, a simplified model to be used in common design practice was proposed, relying in performing at a structural level a preliminary limit analysis – which allows to identify the failure mechanism – and subsequently in modeling masonry through elastic elements and non-linear interfaces placed only in correspondence or near the failure mechanism provided by limit analysis.

The aim of the present contribution is to review the proposed methods and critically assess their computational efficiency and reliability by a systematic comparison with existing experimental tests and with the results provided by available FE programs.

2. References

- [1] E. Benvenuto (1991). An introduction to the history of structural mechanics. Volume II: Vaulted Structures and Elastic Systems. Springer-Verlag, Berlin, New York.
- [2] S. Huerta (2001). Mechanics of masonry vaults: the equilibrium approach. In: P.B. Lourenço & P. Roca (Eds.), Proc. Historical Constructions, Guimarães PT
- [3] J. Heyman (1977). Equilibrium of Shell Structures. Oxford University Press, Oxford.
- [4] E. Milani, G. Milani and A. Tralli (2008). Limit analysis of masonry vaults by means of curved finite elements and homogenization, *Int. J. Solids & Structures* 45, pp.5258-5288.
- [5] G. Milani, E. Milani and A. Tralli (2009). Upper bound homogenized limit analysis of FRP-reinforced masonry curved structures. Part I: unreinforced masonry failure surfaces, *Computers & Structures*, 87, 23-24, pp. 1516-1533.
- [6] G. Milani, E. Milani and A. Tralli (2009). Upper bound homogenized limit analysis of FRP-reinforced masonry curved structures. Part II: structural analysis, *Computers & Structures*, 87, 23-24, pp. 1534-1558.
- [7] G. Milani and A. Tralli (2012). A simple meso-macro model based on SQP for the non-linear analysis of masonry double curvature structures, *I. J. Solids & Structures* 49, pp.808-834.

DETERMINATION OF PLANE HETEROGENEOUS PRESTRESS FIELD IN PLATE

R. Nedin and A. Vatulyan

*Faculty of Mathematics, Mechanics and Computer Sciences, Department of Theory of Elasticity,
Southern Federal University, Rostov-on-Don, Russia*

1. General

At present the development and perfection of the prestress identification techniques are important problems of solid mechanics. Over the last two decades we may see an evident tendency for the prestress identification techniques to shift away from semi-destructive methods towards promising non-destructive method. One of the most efficient nondestructive methods is acoustical method. Even in the limits of the linearized model, the solving of the identification problem of the heterogeneous prestress state can be realized only on the basis of solving the inverse elasticity theory problem with variable characteristics, which is non-linear and ill-posed problem. At that even for the influence estimation calculations, the elasticity theory problems with variable characteristics must be solved, and that is possible only with use of computing techniques, for example the finite element method. In the present paper the direct and inverse problems of the steady-state vibration of a thin elastic isotropic plate with heterogeneous prestress field are studied.

On the basis of the general problem formulation for the 3-dimensional prestressed body [1] the various direct problems formulations for the thin plate are constructed; at that the in-plane and the out-of-plane vibration regimes are considered. The frequency response functions for different plate points are obtained. The investigation of the prestress level influence on the frequency response functions is made. The discrepancy of the frequency response functions turned out to be sufficient to reconstruct the prestresses; the discrepancy is most significant nearby the resonant frequencies [4].

The inverse problem on the identification of the heterogeneous 2-dimensional residual stress state (i.e. of the three components $\sigma_{11}^0(x_1, x_2)$, $\sigma_{22}^0(x_1, x_2)$, $\sigma_{12}^0(x_1, x_2)$ of the prestress tensor satisfying the equilibrium equations) in the rectangular plate is regarded. As the additional information the data on the displacement field on the contour part under the loading was used, in the set of points, for several vibration frequencies [3].

The new technique of the plane heterogeneous prestress state is proposed which lies in expression of the unknown prestress components in terms of Airy stress function which is presented as a combination of the mutually orthogonal biharmonic polynomials in the area of the plate section. The inverse problem solving is reduced to the iterative process. At every step of the process the direct problem and the ill-conditioned system of linear algebraic equations are solved. For solving this system the Tikhonov regularization procedure was used [2].

The numerical calculations of the direct and inverse problems solving were made using the Finite Element Method in the package "FreeFem++" and programming language "Fortran". The series of numerical experiments on the identification of the 2-dimensional heterogeneous prestress state in the rectangular plate is conducted. The most auspicious loading regimes and frequency ranges for the identification procedure are given.

2. Acknowledgments

The present work is done with the support of Russian Foundation of Basic Research "Development of new methods for identification of localized and dispersed heterogeneity in solid bodies" (project code 10-01-00194-a) and Federal Target Program "Scientific and research-and-educational staff of innovation Russia" on 2009 - 2013 years (state contract P596).

3. References

- [1] R.D. Nedin and A.O. Vatulyan (2011). On the Reconstruction of Inhomogeneous Initial Stresses in Plates. *Advanced Structured Materials. Shell-like Structures – Nonclassical Theories and Applications*, Springer-Verlag, **15**, 165-182.
- [2] A. N. Tikhonov and V. Ya. Arsenin (1979). *Methods of ill-posed problems solving*. Nauka, Moscow, 288p.
- [3] A.O. Vatulyan (2007). *The Inverse Problems in Solid Mechanics*. Phizmatlit, Moscow.
- [4] A.O. Vatulyan and R.D. Nedin (2011). On the Identification of the Non-homogeneous Initial Stresses. *Bulletin of Saint-Petersburg State University*, **1**, 38-44.

MODELING OF SHOCK WAVE-LOADED PLATES USING A GRADIENT-ENHANCED DAMAGE MODEL

A.D. Nguyen, M. Stoffel and D. Weichert

Institute of General Mechanics, RWTH Aachen, Templergraben 64, 52062 Aachen, Germany

1. Introduction

During impulsive loading of metallic thin-walled structures, material damage on micro-structural levels can develop leading to loss of integrity. Excessive localization and dependence of mechanical response on substructure sizes (i.e. size effects) caused by softening and damage can be captured by introducing gradients of either plastic strain or damage parameter fields. Adapted from the approach for plastic continuum by Dimitrijevic and Hackl [1], a gradient-enhanced damage model [2] for dynamic finite element computation of viscoplastic thin-shell structures is proposed. Void nucleation and growth within substructures will be taken into account via a free energy function, which is enhanced phenomenologically in terms of a non-local damage variable and its gradient on the mid-surface of the structures. This makes necessary to introduce gradient parameters in terms of a substructure-related intrinsic length-scale and a relationship between non-local and local damage variable.

In this paper, a dynamic thin-shell elastic theory proposed in [3, 4] is chosen to integrate the presented gradient-enhanced model into the finite element program FEAP [5] to capture large displacements and finite rotations. Local constitutive laws considering viscoplastic behavior, isotropic hardening and isotropic ductile damage leading to softening in Velde et al. [6] are employed. The performance of the proposed approach is demonstrated through some numerical simulations of shock-wave loaded plates, which are validated by comparison with the experimental results [7]. The influence of spatial gradient of loading on the material behavior within a macroscopic continuum element will be also discussed.

2. Non-local damage of shell structures

It is assumed that the dynamic effect due to non-local variable can be neglected. Consequently, the kinetic energy is defined in the standard manner. The enhanced free energy $\tilde{\Psi}$ is then defined by

$$(1) \quad \tilde{\Psi}(\Phi) = \mathbf{r} : \mathbf{e} + \frac{1}{2}c_d \|\nabla\varphi\|^2 + \frac{\beta_d}{2} \left(\varphi - \gamma_d \int d d\xi \right)^2, \quad \text{with } \varphi = \int_{h^-}^{h^+} \tilde{d} d\xi$$

where $\Phi := (\mathbf{x}; \mathbf{t}, \varphi), \mathbf{x}, \mathbf{t}, \varphi$ denote respectively a position vector on the mid-surface, a director, a non-local variable; c_d, β_d, γ_d denote parameters; \mathbf{r}, \mathbf{e} denote vectors of effective resultants and strain measures respectively.

With this, the potential energy writes

$$(2) \quad P(\Phi) = \int_{\mathcal{A}_0} \tilde{\Psi}(\Phi) d\mathcal{A}_0 - P_{ext}(\Phi)$$

where $P_{ext}(\Phi)$ is the potential energy of the external loads.

Following [1], an evolution equation of non-local variable φ can be derived as

$$(3) \quad \beta_d [\varphi - \gamma_d \bar{d}] - c_d \nabla^2 \varphi = 0, \quad \text{with } \bar{d} = \int_{h^-}^{h^+} d d\xi$$

For local constitutive laws, St. Venant-Kirchhoff law of non-linear hyperelasticity and a ductile damage model coupled with isotropic hardening and viscoplasticity given in [6] are used, assuming strains to be small.

3. Numerical results

An aluminium plate with 553 mm diameter and 2 mm thickness is subjected alternately three times to shock waves until failure occurs in the plate centre. The deflections of the plate center in Figure 1 are calculated for two different finite element meshes. The damage parameter and equivalent plastic strain evolutions at the bottom of the plate center are depicted in Figure 2. The preliminary numerical results match well with experimental ones observed in Stoffel (2007).

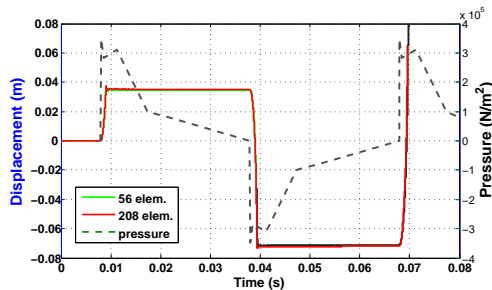


Figure 1. Deflections at plate center.

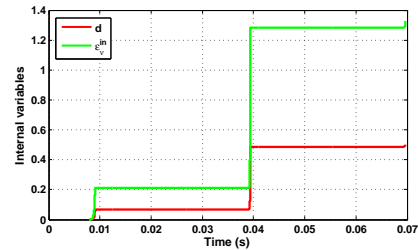


Figure 2. Damage and equivalent plastic strain at the bottom of the plate center.

4. Conclusion

This work proposes a non-local damage model for viscoplastic thin-shell structures subjected to shock waves. The presented approach allows to remove pathological mesh dependence and with this numerical difficulties occurring in softening and damage phenomena.

5. References

- [1] B.J. Dimitrijevic , K. Hackl (2008). A method for gradient enhancement of continuum damage models. *Tech. Mech.*, **28(1)**, 43-52.
- [2] A.D. Nguyen, M. Stoffel, D. Weichert (2012). A gradient-enhanced damage approach for viscoplastic thin-shell structures subjected to shock waves, *Comp. Meth. Appl. Mech. Engng.*, accepted, DOI link: <http://dx.doi.org/10.1016/j.cma.2012.01.017>.
- [3] J.C. Simo, N. Tarnow (1994). A new energy and momentum conserving algorithm for the non-linear dynamics of shells. *Int. J. Numer. Meth. Engng.*, **37**, 2527-2549.
- [4] Y. Basar, D. Weichert (2000). Nonlinear continuum mechanics of solids, fundamental mathematical and physical concepts, *Springer*.
- [5] FEAP-8.2.k, Finite Element Analysis Program (2008). University of California.
- [6] J. Velde, U. Kowalsky , T. Zümendorf, D. Dinkler (2009). 3D-FE-analysis of CT-specimens including viscoplastic material behavior and nonlocal damage. *Comp. Mat. Sci.*, **46**, 532-357.
- [7] M. Stoffel (2007). An experimental method for validating mechanical models. *Habilitation thesis*, RWTH-Aachen.

A SECOND GRADIENT REISSNER-MINDLIN PLATE MODEL VIA THE ASYMPTOTIC EXPANSIONS METHOD

M. Serpilli¹, F. Krasucki² and G. Geymonat³

¹*Departement of Civil and Buinding Engineering, and Architecture,
Università Politecnica delle Marche, Ancona, Italy*

²*Institut de Mathématique et de Modélisation de Montpellier,
Université Montpellier II, Montpellier, France*

³*Laboratoire de Mécanique des Solides,
École Polytechnique, Palaiseau, France*

1. Introduction

Higher order gradient continuum theories in linear and nonlinear elasticity have recently raised the interest on many scientists, since modern technologies involving multi-scale materials exhibit size effects and a strong dependence on internal (material) lengths. A possible generalization of Cauchy model has been proposed in the pioneering works by Germain, see [5], in which the stored energy is assumed to depend both on the strain and on the strain-gradient.

In this paper we derive a second gradient plate model starting from the three-dimensional second gradient linearized elasticity by means of the asymptotic expansion method.

The asymptotic analysis is a widely used technique for the formal derivation and justification of classical theories of thin structures, starting from the classical three-dimensional elasticity, see, for instance, [3]. In order to derive the Reissner-Mindlin plate model through an asymptotic analysis or variational convergence, it has been proved that we need to generalize the stored elastic energy adding some appropriate second gradient terms, see [6], or use a different continuum model as starting point, like the micropolar continuum, see [1].

2. Statement of the problem and main results

Let ω be a domain in \mathbb{R}^2 and let $\gamma_0 = \partial\omega$. Let $0 < \varepsilon < 1$ be a dimensionless *small* real parameter which will tend to zero. We define $\Omega^\varepsilon := \omega \times \left(-\frac{\varepsilon h}{2}, \frac{\varepsilon h}{2}\right)$, $\Gamma_0^\varepsilon := \gamma_0 \times \left[-\frac{\varepsilon h}{2}, \frac{\varepsilon h}{2}\right]$, $\Gamma_\pm^\varepsilon := \omega \times \left\{\pm\frac{\varepsilon h}{2}\right\}$. We note with $x^\varepsilon = (\tilde{x}^\varepsilon, x_3^\varepsilon) \in \Omega^\varepsilon$, with $\tilde{x}^\varepsilon = (x_\alpha^\varepsilon)$. We assume that the set $\bar{\Omega}^\varepsilon$ is the reference configuration of a second gradient linearly elastic plate of thickness εh and middle surface $\bar{\omega}$. We study the physical problem corresponding to the mechanical behaviour of a second gradient plate. The plate is completely clamped on Γ_0^ε , i.e., $u_i^\varepsilon = 0$ and $\partial_n^\varepsilon u_i^\varepsilon = 0$ on Γ_0^ε , where ∂_n^ε is the outward normal derivative along the boundary Γ_0^ε . Moreover, we suppose that the plate is subjected to body forces $f_i^\varepsilon \in L^2(\Omega^\varepsilon)$ and surface forces $g_i^{\pm, \varepsilon} \in L^2(\Gamma_\pm^\varepsilon)$. We assume that the plate is constituted by an isotropic homogeneous second gradient linearly elastic material, characterized by seven elastic moduli, see [4]. The displacement field $\mathbf{u}^\varepsilon = (u_i^\varepsilon)$ satisfies the following variational problem defined over the variable domain Ω^ε :

$$(1) \quad \int_{\Omega^\varepsilon} \left\{ \sigma_{ij}^\varepsilon(\mathbf{u}^\varepsilon) e_{ij}^\varepsilon(\mathbf{v}^\varepsilon) + p_{ijk}^\varepsilon(\mathbf{u}^\varepsilon) \partial_k^\varepsilon e_{ij}^\varepsilon(\mathbf{v}^\varepsilon) \right\} dx^\varepsilon = \int_{\Omega^\varepsilon} f_i^\varepsilon v_i^\varepsilon dx^\varepsilon + \int_{\Gamma_\pm^\varepsilon} g_i^{\pm, \varepsilon} v_i^\varepsilon d\Gamma^\varepsilon,$$

for all $\mathbf{v}^\varepsilon \in V(\Omega^\varepsilon) := \{v_i^\varepsilon \in H^2(\Omega^\varepsilon; \mathbb{R}^3); \mathbf{v}^\varepsilon = \mathbf{0}, \partial_n^\varepsilon \mathbf{v}^\varepsilon = \mathbf{0} \text{ on } \Gamma_0^\varepsilon\}$, where $(\sigma_{ij}^\varepsilon)$ is the Cauchy stress tensor, (p_{ijk}^ε) is the double stress tensor and $e_{ij}^\varepsilon(\mathbf{u}^\varepsilon) := \frac{1}{2}(\partial_i^\varepsilon u_j^\varepsilon + \partial_j^\varepsilon u_i^\varepsilon)$.

In order to study the asymptotic behaviour of the solution of (1) when ε tends to zero, we apply the usual change of variables (see [3]) and we rewrite the so-called rescaled problem on a fixed

domain $\bar{\Omega} := \omega \times \left[-\frac{h}{2}, \frac{h}{2}\right]$. We look for the formal a priori asymptotic expansion of the solution: $\mathbf{u}(\varepsilon) = \mathbf{u}^0 + \varepsilon^2 \mathbf{u}^2 + \varepsilon^4 \mathbf{u}^4 + \dots$. The limit displacement field \mathbf{u}^0 takes the following form:

$$u_\alpha^0(\tilde{x}, x_3) = x_3 \varphi_\alpha(\tilde{x}), \quad u_3^0(\tilde{x}, x_3) = w(\tilde{x}),$$

which represents, from a mechanical point of view, the Reissner-Mindlin plate kinematics. The primary unknowns w and $\varphi = (\varphi_\alpha)$ satisfy the limit variational coupled problems:

$$(2) \quad \begin{aligned} \int_\omega h [-(C_1 \partial_{\beta\beta} w + C_2 \partial_\beta \varphi_\beta) \partial_{\alpha\alpha} \eta_3 + 2\mu(\partial_\alpha w + \varphi_\alpha) \partial_\alpha \eta_3] d\tilde{x} &= \int_\omega q \eta_3 d\tilde{x}, \\ \int_\omega h [(C_3 \partial_{\beta\beta} w + C_4 \partial_\beta \varphi_\beta) \partial_\alpha \eta_\alpha + (C_4(\partial_\beta \varphi_\alpha + \partial_\alpha \varphi_\beta) + 2C_5 \partial_{\alpha\beta} w) (\partial_\beta \eta_\alpha + \partial_\alpha \eta_\beta) + \\ &+ 2\mu(\partial_\alpha w + \varphi_\alpha) \eta_\alpha] d\tilde{x} = 0 \end{aligned}$$

for all $\boldsymbol{\eta} \in V(\omega) := \{\boldsymbol{\eta} = (\eta_i) \in H^2(\omega; \mathbb{R}^3); \boldsymbol{\eta} = \mathbf{0}, \partial_\nu \boldsymbol{\eta} = \mathbf{0} \text{ on } \gamma_0\}$, where $q(\tilde{x}) := \int_{-h/2}^{h/2} f_3(\tilde{x}, x_3) g_3^+(\tilde{x}) + g_3^-(\tilde{x})$ and the constants C_i depend on the second gradient elastic moduli.

Remark. By using the simplified second gradient isotropic constitutive law proposed by E. Aifantis (see [2]), who considers only two constants λ and μ and an internal length ℓ , equations (2) reduce to the classical equations of the Reissner-Mindlin plate model.

3. References

- [1] I. Aganović, J. Tambača and Z. Tutek (2006). Derivation and justification of the models of rods and plates from linearized three-dimensional micropolar elasticity, *J. Elasticity*, **84**, 131-152.
- [2] E. Aifantis (1999). Strain gradient interpretation of size effects, *Int. J. Fract.*, **95**, 299-314.
- [3] P.G. Ciarlet (1997), *Mathematical Elasticity, vol. II: Theory of Plates*, North-Holland, Amsterdam.
- [4] F. dell'Isola, G. Sciarra and S. Vidoli (2009). Generalized Hooke's law second gradient materials, *Proc. R. Soc. A*, **465**, 2177-2196.
- [5] P. Germain (1973). La méthode des puissances virtuelles en mécanique des milieux continus. I. Théorie du second gradient, *J. Mécanique*, **12**, 235-274.
- [6] R. Paroni, P. Podio-Guidugli and G. Tomassetti (2007). A justification of the Reissner-Mindlin plate theory through variational convergence, *Analysis and Applications*, **5**, 165-182.

EXPERIMENTAL AND NUMERICAL STUDIES OF FOAM-FILLED CIRCULAR TUBES

A. Tobota, J. Karliński, A. Niechajowicz, P. Kaczyński
Wrocław University of Technology, Wrocław, Poland

1. General

The use of thin-walled tubular structures as an energy absorbing elements designed to improve passive safety, especially in automotive industry has been studied over three decades. The great majority of research works on thin-walled energy absorbing structures is focused on the influence of the structure material mechanical properties, absorber geometry and specific deformation mode on specimen crashworthiness parameters. The comprehensive review of existing experiment results can be found in articles [1-3].

2. Paper topic

Following paper is focused on experimental and numerical studies of both: quasi static and dynamic axial crushing of thin-walled cylindrical tubes filled with foam. Two types of profiles were used in this study: single-walled and double-walled specimens. Single walled tubes were cut out from commercial mild steel tubing (R35) 60 mm in diameter and 1,0 mm in thickness. In case of double-walled specimens outer material remained the same, while inner profile was cut out from aluminium solid drawn tube (PA38) 30 mm in diameter and 1,0 mm in thickness. The D/t ratio of steel and aluminium tubes amounted correspondingly to: 60 and 30. Total length of single-walled and double-walled specimens was 200 mm. The specimens geometry is depicted in fig. 1. Dimensions were selected in accordance to previous results [4], which showed that for these ratios, steel tubes should deform in diamond mode and aluminium tubes should collapse in axisymmetric (concertina) mode.

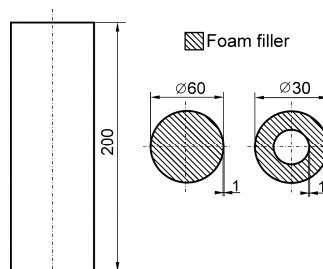


Fig 1. Specimen geometry.

The polyurethane foam (ISO foam RR 3040) was used to fill the tubes. After the mass of foam reagents required to obtain given density was poured into a tube, its ends were sealed to prevent the expanding foam from free discharge. Described methodology allowed to obtain average densities of polyurethane foam used as filler at the level between 50 and 240 kg/m³.

3. Results

Dynamic and static experiments were compared. Following parameters were analyzed: mean crushing force, relative crushing distance and specific energy absorption. Two main deformation modes were identified: diamond (asymmetric) and concertina (axisymmetric). The deformation

mode is an effective indicator of energy efficiency, which result from strong connection between their formation and energy dissipation mechanism. The first mode was observed for empty and for the low density foam-filled specimens. The second mode occurred for specimen with foam density $\rho > 80 \text{ kg/m}^3$. Mixed deformation mode, e.g.: two diamond folds, and four concertina folds, occurred for the filler density range $50 - 80 \text{ kg/m}^3$ (fig. 2).



Fig 2. Specimen deformation modes.

a) diamond (symmetric); b) concertina (axisymmetric); c) mixed

4. Conclusion

Conducted experiments allowed to draw conclusion, that crashworthiness ability increase with foam density. The investigation of the experimental data revealed, that double walled tubes have greater energy absorbing ability. The dynamic non-linear simulations were carried out by means of PAM-CRASH™ explicit code. For a better understanding of the crushing process real and numerical experiments were compared (fig. 3) Computational crushing force, plastic hinges locations and specimens post-crushed geometry found to be compatible with the real experiments.



Fig 3. The comparison of numerical and real specimen deformation mode

The task is co-financed by the European Union under the European Social Fund.

6. References

- [1] A.A. Alghamdi (2001). *Collapsible impact energy absorbers: an overview*, Thin-Walled Structures, Vol. 39, No. 2, 189-213.
- [2] N. Jones (1989). *Structural Impact*, Cambridge University Press, Cambridge, UK.
- [3] S.R. Reid (1993). *Plastic deformation mechanisms in axially compressed metal tubes used as impact energy absorbers*, International Journal of Mechanical Sciences, Vol. 35, No. 12, 1035 - 1052.
- [4] K.R. Andrews, G.L. England, E. Ghani (1983). *Classification of the axial collapse of cylindrical tubes under quasi-static loading*, International Journal of Mechanical Sciences, Vol. 25, No.5, 687-696.

DUAL-MIXED hp FINITE ELEMENT MODEL FOR ELASTODYNAMIC PROBLEMS OF CYLINDRICAL SHELLS

B. Tóth

Department of Mechanics, University of Miskolc, Miskolc-Egyetemváros, Hungary

1. Preliminary

In finite element analyzes of linear elasticity problems, significant numerical difficulties can be expected within the context of the primal-mixed and standard displacement-based methods. These conventional methods exhibit especially poor numerical performances, for example when the plate and shell problem becomes bending dominated for small thicknesses and when the Poisson ratio is close to the incompressibility limit of 0.5. These phenomena are known as numerical lockings (membrane-, shear-, incompressibility locking and so on). The complementary energy-based dual-mixed finite element models are free from these locking problems and give reliable numerical solutions especially in the computed stresses. The development for linear elastodynamic problems has been motivated by the fact that we managed to construct robust and effective multi-field dual-mixed hp plate and axisymmetric shell elements [1, 2, 3].

2. Variational formulation

The main objective is the derivation of a new dimensionally reduced cylindrical shell model, based on a three-field dual-mixed variational principle, for elastodynamic problems. In the linear theory of elasticity its functional takes the form [4]

$$(1) \quad \mathcal{F}(\sigma^{k\ell}, u_k, \phi^s) = \int_{t_0}^{t_1} \left(\mathcal{H} \mathcal{R}_d - \widehat{\mathcal{K}} \right) dt,$$

where

$$(2) \quad \widehat{\mathcal{K}}(\dot{u}_k) = \int_V \widehat{\mathcal{T}} dV = \frac{1}{2} \int_V \rho \dot{u}^k \dot{u}_k dV$$

is the complementary kinetic energy of the whole elastic body and

$$(3) \quad \begin{aligned} \mathcal{H} \mathcal{R}_d(\sigma^{k\ell}, u_k, \phi^s) &= - \int_V \widehat{\mathcal{U}} dV + \int_{S_u} \widetilde{u}_k \sigma^{k\ell} n_\ell dS \\ &\quad - \int_V [u_k (\sigma^{k\ell}{}_{;\ell} + b^k) - \phi^s \epsilon_{k\ell s} \sigma^{k\ell}] dV \end{aligned}$$

is the three-field dual-mixed Hellinger–Reissner functional of elastostatics [3]. Here V denotes the volume of the body in the undeformed configuration, the surface $S = S_p \cup S_u$, with $S_p \cap S_u = \emptyset$, is the boundary of V , $\epsilon_{k\ell s}$ is the covariant permutation tensor and \widetilde{u}_k is the displacement vector prescribed on the surface part S_u with outward unit normal n_ℓ , as well as b^p and ρ stand, respectively, for the density of the body forces and the material, and $t \in [t_0, t_1]$ defines a closed time interval (t_0 and t_1 are two arbitrary instants of time). The fundamental variables of the functional (1) are the not *a priori* symmetric stress tensor $\sigma^{k\ell}$, the displacements u_p and the rotations ϕ^s . The complementary strain energy density function $\widehat{\mathcal{U}}$ is defined by

$$(4) \quad \widehat{\mathcal{U}}(\sigma^{k\ell}) = \frac{1}{2} \sigma^{pq} \varepsilon_{pq}(\sigma^{k\ell}).$$

For linearly elastic materials the symmetric strain tensor ε_{pq} can be obtained from the inverse stress-strain relations (Hooke's law)

$$(5) \quad \varepsilon_{pq} = C_{pqkl} \sigma^{kl} \quad \text{in } V ,$$

where the fourth-order tensor C_{pqkl} with symmetry properties $C_{pqkl} = C_{pqlk} = C_{k\ell pq}$ is the elastic compliance tensor. This three-field dual-mixed method can be considered as a generalization of the Hellinger–Reissner-type variational principle [4]. The solution of the linear elastodynamic problem can be characterized as the unique stationary point of the functional (1) over the space of all vector-fields u_p , ϕ^s and all *a priori* non-symmetric stress fields σ^{kl} satisfying the stress boundary conditions

$$(6) \quad \tilde{p}^k = \sigma^{kl} n_\ell \quad \text{on } S_p ,$$

where \tilde{p}^k are prescribed surface tractions on S_p with outward unit normal n_ℓ . The initial conditions to (1) are

$$(7) \quad u_k(t=0) = u_k(t_0) = {}^0u_k, \quad \dot{u}_k(t=0) = v_k(t_0) = {}^0\dot{u}_k = {}^0v_k \quad \text{in } V ,$$

as well as $\delta u_k(t_0) = \delta u_k(t_1) = 0$ are valid (δ denotes the variational operator).

3. Cylindrical shell model

The three-field dual-mixed functional (1) is applied to elastodynamic problems of axisymmetrically loaded thin cylindrical shells. Employing truncated power series expansions, the independent variables, i.e., the stresses, the rotations and the displacements are approximated by polynomials of first- and second-degree in the thickness direction. An important property of the shell model is that the classical kinematical hypotheses regarding the deformation of the normal to the shell mid-surface are not applied.

The number of the independent stress components is reduced by *a priori* satisfaction of the prescribed surface loads on the inner and outer surfaces of the shell and by the elimination of the rotations. This procedure results in a modified dual-mixed variational principle for the time-dependent displacements and stresses with weakly imposed symmetry in the transverse direction.

A dual-mixed *hp* finite element model with stable polynomial stress- and displacement interpolation and C^0 continuous normal components of stresses is constructed for bending-shearing problems, using unmodified three-dimensional inverse stress-strain relations for linearly elastic materials.

Acknowledgements: The published work was carried out as part of the TÁMOP-4.2.2/B-10/1-2010-0008 project in the framework of the New Hungarian Development Plan. The realization of this project is supported by the European Union, co-financed by the European Social Fund.

- [1] E. Bertóti (2005). Derivation of plate and shell models using the Fraeijs de Veubeke variational principle, *Proceedings of the 5th International Conference on Computation of Shell and Spatial Structures*, E. Ramm, W. A. Wall, K.-U. Bletzinger and M. Bischoff, editors, 1–4 June 2005, Salzburg, Austria, pp. 1–4.
- [2] L.G. Kocsán (2011). Derivation of a dual-mixed *hp*-finite element model for axisymmetrically loaded cylindrical shells, *Archive of Applied Mechanics*, **81**, 1953-1971.
- [3] B. Tóth (2012). Dual-mixed *hp* finite element model for elastic cylindrical shells, *ZAMM, Zeitschrift für Angewandte Mathematik und Mechanik*, **92**, 236-252.
- [4] B. Tóth (2010). Dual-mixed Hellinger–Reissner functional for elastodynamics, *microCAD 2010 XXIV. International Scientific Conference*, Section G. Applied Mechanics, 18–20 March 2010, Miskolc, Hungary, pp. 73-77.

LOW-ORDER MEMBRANE AND SHELL ELEMENTS: THE ASSUMED CENTRICAL STRAIN METHOD AND ITS RELATION TO ENHANCED AND MIXED METHODS

R. Winkler

INTALES GmbH, Natters/Innsbruck, Austria

1. Introduction

Low-order plate bending and shell elements are known to suffer from transverse shear locking. That is, shear strain components derived from interpolated nodal displacements contain parasitic contributions, which may lead to an excessive overestimation of the element stiffness. *Assumed strain* fields obtained from specific strain interpolation schemes are employed to reduce the parasitic portion of strain energy. Dealing with distorted (non-rectangular) elements, a decisive feature is to apply *natural* strain components $\varepsilon_{\alpha\beta}^{(g)}$ (with respect to the natural element base vectors $\mathbf{g}_\alpha(\xi, \eta)$) for interpolation [1]. Modified interpolation schemes have been used for the elimination of in-plane shear locking [2].

2. Strain interpolation

These former approaches are recast to obtain new four node (linear and non-linear) membrane and shell elements. To pass the in-plane patch test, we apply *central* strain components $\varepsilon_{\alpha\beta}^{(o)}$ (with respect to the base vectors $\mathbf{o}_\alpha = \mathbf{g}_\alpha(0, 0)$ at the element center) instead of natural ones in connection with *skew* coordinates¹ $\bar{\xi}^\gamma$. The latter derive from natural curvilinear coordinates ξ^γ via $d\bar{\xi}^\gamma \mathbf{o}_\gamma = d\xi^\gamma \mathbf{g}_\gamma$. This leads to an assumed strain field,

$$(1) \quad \begin{cases} \bar{\varepsilon}_{11}^{(o)}(\bar{\xi}^1, \bar{\xi}^2) = \gamma_1 + \gamma_4 \bar{\xi}^2 \\ \bar{\varepsilon}_{22}^{(o)}(\bar{\xi}^1, \bar{\xi}^2) = \gamma_2 + \gamma_5 \bar{\xi}^1 \\ \bar{\varepsilon}_{12}^{(o)}(\bar{\xi}^1, \bar{\xi}^2) = \gamma_3 \end{cases}$$

The coefficients γ_n are derived from displacement compatible strain components $\varepsilon_{\alpha\beta}^{(o)}$,

$$(2) \quad \gamma_{1,4} = \frac{1}{2} [\varepsilon_{11}^{(o)}(0, 1) \pm \varepsilon_{11}^{(o)}(0, -1)], \quad \gamma_{2,5} = \frac{1}{2} [\varepsilon_{22}^{(o)}(1, 0) \pm \varepsilon_{22}^{(o)}(-1, 0)], \quad \gamma_3 = \varepsilon_{12}^{(o)}(0, 0)$$

3. Enhanced and mixed formulations

In some sense, the formulation is complementary to the enhanced assumed strain approach of Andelfinger & Ramm [4]. Translated to the concept of skew coordinates, their enhanced strain field reads

$$(3) \quad \begin{cases} \bar{\varepsilon}_{11}^{(o)}(\bar{\xi}^1, \bar{\xi}^2) = \alpha_1 \bar{\xi}^1 + \alpha_6 \bar{\xi}^1 \bar{\xi}^2 \\ \bar{\varepsilon}_{22}^{(o)}(\bar{\xi}^1, \bar{\xi}^2) = \alpha_2 \bar{\xi}^2 + \alpha_7 \bar{\xi}^1 \bar{\xi}^2 \\ \bar{\varepsilon}_{12}^{(o)}(\bar{\xi}^1, \bar{\xi}^2) = \alpha_3 \bar{\xi}^1 + \alpha_4 \bar{\xi}^2 + \alpha_5 \bar{\xi}^1 \bar{\xi}^2 \end{cases}$$

Together, (1) and (3) constitute complete bilinear polynomials. Consequently, for linear problems and regular meshes, both approaches yield coincident results. In the nonlinear regime, substantial

¹Skew coordinates have been introduced in the context of hybrid stress membrane elements [3].

improvements can be achieved employing a modified mixed approach. That is, the assumed strain field (1) is supplemented by an assumed stress field

$$(4) \quad \begin{cases} \sigma_{11}^{(o)}(\bar{\xi}^1, \bar{\xi}^2) = \beta_1 + \beta_4 \bar{\xi}^2 \\ \sigma_{22}^{(o)}(\bar{\xi}^1, \bar{\xi}^2) = \beta_2 + \beta_5 \bar{\xi}^1 \\ \sigma_{12}^{(o)}(\bar{\xi}^1, \bar{\xi}^2) = \beta_3 \end{cases}$$

According to the Pian-Sumihara approach [5], stress parameters β_n are obtained from a coupled equilibrium condition deriving from the Hellinger-Reissner variational principle. Conventional mixed formulations make use of equilibrium conditions deriving from the Hu-Washizu principle to calculate stress (β_n) and strain parameters (γ_n) in turn of the equilibrium iteration, see [6] and [7] and referenced therein. In contrast, we calculate γ_n directly from (2) which appears to be computationally significantly more efficient.

4. Results

Numerical results are obtained from a total Lagrangian shell element implementation oriented at [7] and applied to a common set of benchmark examples involving smooth and non-smooth membrane and bending dominated problems with regular and distorted meshes. The in-plane components of the Green-Lagrange strain tensor are treated according to the assumed central strain (ACS) scheme (1), the enhanced assumed strain (EAS) scheme (3), the mixed approach of reference [7], and the modified mixed approach. The increased accuracy of the skew coordinates approach with respect to in-plane deformations of distorted meshes has already been reported in [6] and is reproduced here. For regular and moderately distorted meshes, ACS and EAS elements yield virtually coincident results and a similar convergence behavior. The computational efficiency of mixed formulations in geometrically nonlinear problems is demonstrated in [7]. That is, mixed elements tolerate significantly larger load steps compared to enhanced and assumed strain elements and exhibit a superior convergence behavior. However, due to the large number of internal parameters (14 stress and 14 strain parameters are used in [7]), each single equilibrium iteration is time and memory consuming. This is in contrast with the modified mixed formulation. Its simplest implementation involves just 5 stress parameters.

5. References

- [1] T.J.R. Hughes and T.E. Tezduyar (1981). Finite elements based upon Mindlin plate theory with particular reference to the four-node bilinear isoparametric element, *J. Appl. Mech.* **48**, 587-596.
- [2] E.N. Dvorkin and S.I. Vassolo (1989). A quadrilateral 2-D finite element based on mixed interpolation of tensorial components, *Eng. Comp.* **6**, 217-224.
- [3] K.-Y. Yuan, Y.-S. Huang, and T.H.H. Pian (1993). New strategy for assumed stress for 4-node hybrid stress membrane element, *Int. J. Num. Meth. Eng.* **36**, 1747-1763.
- [4] U. Andelfinger and E. Ramm (1993). EAS-elements for two-dimensional, three-dimensional, plate and shell structures and their equivalence to HR-elements, *Int. J. Num. Meth. Eng.* **36**, 1311-1337.
- [5] T.H.H. Pian and K. Sumihara (1984). A rational approach for assumed stress finite elements, *Int. J. Num. Meth. Eng.* **20**, 1685-1695.
- [6] K. Wiśniewski and E. Turska (2009). Improved 4-node HuWashizu elements based on skew coordinates, *Comput. Struct.* **87**, 407-424.
- [7] W. Wagner and F. Gruttmann (2005). A robust non-linear mixed hybrid quadrilateral shell element, *Int. J. Num. Meth. Eng.* **64**, 635-666.

VIBRATIONS OF PERIODICALLY STRATIFIED UNBOUNDED THICK PLATES

Cz. Woźniak, J. Jędrzyak, B. Michalak

Department of Structural Mechanics, Technical University of Łódź, Łódź, Poland

1. Introduction

In this note the main objects under consideration are periodically layered thick plates. It is assumed that every layer is made of two various components being linear-elastic homogeneous and isotropic materials, cf. Figure 1.

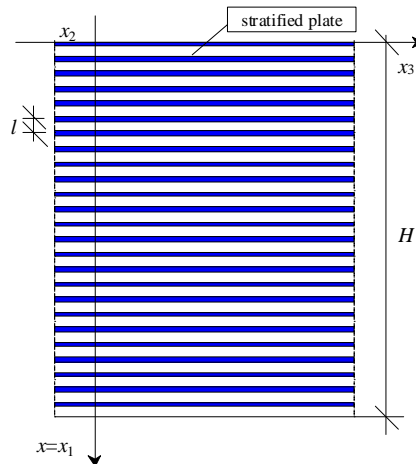


Figure 1. A fragment of a periodically stratified thick plate.

Let us assume that the plate under consideration is described in the coordinate system $Ox_1x_2x_3$. Denote: the time coordinate t ; $x \equiv x_1$; $\partial_\alpha \equiv \partial/\partial x_\alpha$, $\alpha=2, 3$; $\partial \equiv \partial/\partial x$; $\mathbf{x} \equiv (x_2, x_3)$. Let H be the constant plate thickness along the x -axis. It is assumed that the plate is unbounded along the x_α -axes. The plate occupies the region $\Omega \equiv (0, H) \times R^2$. The plate under consideration consists of p layers, $1/p \ll 1$, with thicknesses l . Every layer is made of two homogeneous, isotropic materials, which have material properties (E_R, G_R, ρ_R) for a reinforcement and (E_M, G_M, ρ_M) for a matrix. The thickness of the reinforcement part of the layer is described by l_R and of the matrix part – by l_M , cf. Figure 2. Hence, denote parameters $\varphi_R \equiv l_R/l$, $\varphi_M \equiv l_M/l$.

The main aim of this contribution is to consider a problem of longitudinal vibrations along Ox_1 -axis of the periodically stratified thick plates under consideration. Hence, our considerations are restricted only to the displacement along $x \equiv x_1$ -axis, denoted by w . Governing equations of a proposed model are PDEs with constant coefficients. This model is formulated under assumptions of the tolerance modelling developed for periodic or/and functionally graded laminates, (cf. [1,2,3]).

2. Modelling concepts and assumptions

In the modelling some introductory concepts as: a slowly varying function ($SV_d^1([0, H])$), an averaging operation ($\langle \cdot \rangle$), shape functions, are used.

To arrive at equations having constant coefficients, we introduce the following assumptions.

The *micro-macro decomposition* is the first modelling assumption, in which it is assumed that displacements of the plate can be decomposed by

$$(1) \quad w(x,t) = u(x,t) + g(x)v(x,t), \quad (x,t) \in R^2,$$

where the new basic unknowns u and v are called the *macrodisplacements* and the *fluctuation amplitudes*, respectively, and satisfy the condition $u(\cdot,t), v(\cdot,t) \in SV^1_\rho([0,H])$.

Let us introduce a *residual field* for the above decomposition $r \equiv \partial_1[K(\partial_1 u + \partial_1(gv))] - \rho \partial_{tt}(u + gv)$.

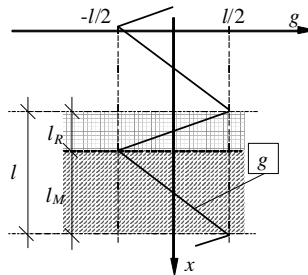


Figure 2. A periodicity cell of the plate with a diagram of shape function g .

The *tolerance averaging assumption* is the second modelling assumption, in which some conditions on this residual field are formulated:

$$(2) \quad \langle r \rangle_T(x) = 0, \quad \langle rg \rangle_T(x) = 0,$$

for a.e. $x \in R$ and $t \in R$.

3. Model equations

Using the aforementioned concepts and assumptions, after some manipulations and denoting $K \in \{E, G\}$, $K_R \in \{E_R, G_R\}$, $K_M \in \{E_M, G_M\}$, the following averaged equations are obtained:

$$(3) \quad \begin{aligned} &\langle K \rangle \partial_{11} u + (K_M - K_R) \partial_1 v = \langle \rho \rangle \partial_{tt} u, \\ &\underline{\frac{1}{12} l^2 \langle K \rangle \partial_1 v - \left(\frac{K_R}{\phi_R} + \frac{K_M}{\phi_M} \right) v} + (K_M - K_R) \partial_1 u = \underline{\frac{1}{12} l^2 \langle \rho \rangle \partial_{tt} v}. \end{aligned}$$

These equations stand with conditions (1) the *tolerance model of vibrations for periodically stratified thick plates* under consideration. It can be observed that neglecting the underlined terms in equation (3)₂ we obtain governing equations of the asymptotic model.

4. Remarks

Using the proposed modelling method the governing equations of vibrations of the plates under consideration with non-continuous periodic coefficients can be replaced by the equations of the tolerance model (3) with constant coefficients.

Applications of this model equations will be shown separately.

5. References

- [1] Cz. Woźniak (ed) (2010). *Mathematical Modelling and Analysis in Continuum Mechanics of Microstructured Media*, Wyd. PŚI, Gliwice, Poland.
- [2] Cz. Woźniak, B. Michalak and J. Jędrzyński (eds) (2008). *Thermomechanics of Heterogeneous Solids and Structures. Tolerance Averaging Approach*, Wyd. PŁ, Łódź, Poland.
- [3] Cz. Woźniak and E. Wierzbicki (2000). *Averaging techniques in thermomechanics of composite solids*, Wyd. PCz, Częstochowa, Poland.

A MODEL OF A THICK FUNCTIONALLY GRADED LAMINATED PLATE WITH INTERLAMINAR DEFECTS

Cz. Woźniak¹, M. Wągrow ska² and O. Szlachetka²
¹ *Technical University of Łódź, Łódź, Poland*
² *Warsaw University of Life Sciences, Warsaw, Poland*

The object of analysis is a thick functionally graded laminated plate made of two materials. The scheme of the plate is shown in Fig. 1.

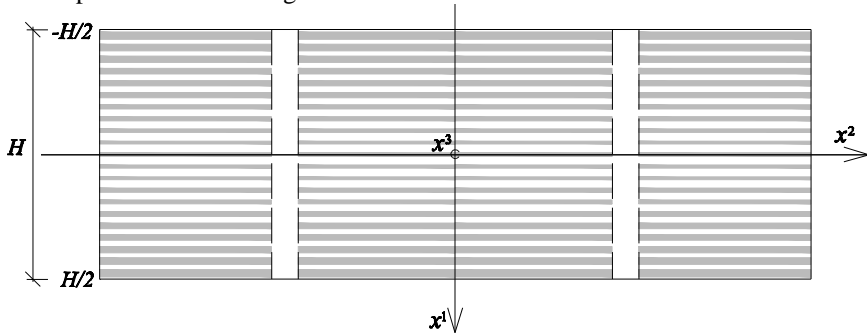


Fig. 1. A cross section of a thick functionally graded laminated plate

The plate occupies region $\left(-\frac{H}{2}, \frac{H}{2}\right) \times \Xi$ in three space $Ox^1x^2x^3$, where Ξ its midplane. It is assumed that H is smaller when compared to the smallest characteristic length dimension of Ξ .

From the formal point of view the plate can be divided into thin layers with a constant thickness $l = \frac{H}{2p+1}$, $\frac{1}{p} \ll 1$. Each layer has a symmetry plane $x^1 = x_n = 0 \pm nl$, $n = 0, \pm 1, \pm p$.

In order to describe a distribution of component materials (matrix and reinforcement) we introduce two smooth even fraction functional coefficients, $\varphi_R \in C^1\left(\left[-\frac{H}{2}, \frac{H}{2}\right]\right)$, $\forall x^1 \in \left(-\frac{H}{2}, \frac{H}{2}\right) \varphi_R(x^1) \in (0,1)$ and $l|\partial_1 \varphi_R(x^1)| \ll 1$, and $\varphi_M \equiv 1 - \varphi_R$. The distribution of components in the n -th layer is given by $\varphi_R(x_n)$, $\varphi_M(x_n)$, $n = 0, \pm 1, \dots, \pm p$.

For the sake of simplicity all subsequent considerations will be restricted to the heat conduction problem.

The heat conduction coefficients for both reinforcement and matrix materials are assumed to be orthotropic. Their principal values being denoted by k_R^α , k_M^α in reinforcement and matrix material respectively, $\alpha = 1, 2, 3$.

The contact between adjacent laminas is assumed to be non-perfect. In contrast to the approaches described in [1] and in a large number of the related papers, we shall deal with a continuous distribution of interlaminar defects.

The defects between adjacent laminas will be modeled by a very thin interlaminar layers with thickness δ made of a certain isotropic material different then the lamina materials. Neither the unilateral contact between adjacent lamina analyzed in [3], nor material failure effects [2] are considered. Term “very thin” has to be understood, in the asymptotic sense, it means that under the

formal asymptotic limit passage $l \rightarrow 0$ and also $\delta \rightarrow 0$ quotient $\frac{\delta}{l} \rightarrow \nu$, where ν is assumed to be positive ($\nu > 0$) and such that $\nu \ll \inf_{x^1 \in \left(-\frac{H}{2}, \frac{H}{2}\right)} \{\varphi_R(x^1), \varphi_M(x^1)\}$. Obviously constant ν represents the

fraction of the interlaminar material.

The aim of this contribution is twofold. First setting aside the effect of interlaminar defects, we propose an asymptotic approach to the modelling of functionally graded thick laminated plates introducing the concept of the local layer. In this case we arrive at the heat conduction model of a laminated plate in the form of PDEs with smooth functional coefficients depending on smooth fractional coefficients $\varphi_R(\cdot)$, $\varphi_M(\cdot)$. Secondly we introduce the effect of interlaminar defects by a homogenization of the reinforcement material with an interlaminar defect material. The similar procedure is also applied to homogenization of the matrix material with an interlaminar defect material.

On this way we obtain a new laminated structure which is functionally graded and consists of new reinforcement and matrix material, properties of which are modified by an interlaminar defect material.

The last step for the modelling procedure is the same as that in the procedure outlined above and leads to the model of a functionally graded material without defects.

On this way we arrive finally to the PDEs with functional smooth coefficients depending on argument $x^1 \in \left(-\frac{H}{2}, \frac{H}{2}\right)$. These coefficients represent the local effective modules for a laminated thick plate which is functionally graded and takes into account the effect of defects.

It has to be emphasized that the resulting smooth functional coefficients which can be referred to as local effective modules depend on:

- (1) Heat conduction orthotropic coefficients k_R^α , k_M^α in reinforcement and matrix material, $\alpha = 1, 2, 3$, specific heats c_R , c_M in reinforcement and matrix material, respectively.
- (2) Fraction coefficients $\varphi_R(x^1)$, $\varphi_M(x^1)$, $x^1 \in \left(-\frac{H}{2}, \frac{H}{2}\right)$.
- (3) Heat conduction isotropic coefficient k_I in interlaminar defects and specific heat c_I in interlaminar defects.
- (4) Constant fraction coefficient ν of the interlaminar defects.

2. References

- [1] A.Kaczyński, S. J Matysiak, V. J Pauk, (1995), Stress intensity factors for an interface penny-shaped crack in laminated elastic layer, *Mechanika Teoretyczna i Stosowana* 2, **33**, 361-373,
- [2] Z. Naniewicz, Cz. Woźniak, (1989), On the quasi-stationary models of debonding process, in layered composites, *Ing. Archiv* **60**, 31-40,
- [3] M.Woźniak, (1995), On the dynamic behaviour of micro-damaged stratified media, *Jnt. J. Fraction.*, **73**, 223-232.

Smart Materials and Structures

PIEZOELECTRIC ACTUATION OF A PNEUMATIC ADAPTIVE SHOCK ABSORBER

G. Mikułowski, R. Wiszowaty and J. Holnicki-Szulc

Institute of Fundamental Technological Research, Warsaw, Poland

1. Introduction

The recent material technology developments provide to the market a number of new types of materials per year, which encourage designers and constructors to utilize them in a broad variety of engineering branches. One of the more interesting group of materials, which are under extensive development, are functional materials. The functional materials are defined as having coupling between the mechanical properties and non-mechanical fields i.e. electrical field, magnetic field, thermal field. Examples of such materials are: electrorheological fluids, magnetorheological fluids, magnetostrictive materials, shape memory alloys. This category contains also piezoelectric ceramics, which is utilized for several decades for high frequency actuation in medicine, electronics and military industries [1]. One of relatively new, and still under intensive study, topic is using the piezo-ceramics as mechanical actuators in the range of low frequencies (up to 25 kHz) characteristic for structural dynamics range.

The piezo material has several advantages that make it very useful in the context of actuation of mechanical structures (high forces, wide frequency range) but also it has some drawbacks (diminutive stroke, high voltage requirements) that must be carefully analysed when a system is to be designed.

At the beginning the piezo ceramic was offered by the manufacturers as monolithic material able to convert mechanical energy into electrical and vice versa (straight and counter piezo-electric effect) which was characterised by requirement for voltage in range of 2 kV [1]. During the past two decades the progress in the technology of piezo materials allowed to fabricate multilayer piezo actuators where the piezo material is in the shape of thin layers isolated from each other by layers of isolating material i.e. polymer or conventional ceramic [2]. The main advantage of these materials is the electrical supply level limited to 200 V. This voltage range allowed to consider the material as an actuator for engineering applications that might be safe for potential users.

2. Scope of the work

In this paper a development of an piezo actuated gas shock-absorber is presented. The main idea is to dissipate the kinetic energy of impact in the way that incorporates compressing gas in the absorber. Therefore, the energy is converted into internal energy of the gas. And the second step is to convert the accumulated energy into an irreversible form by releasing the pressure of the compressed gas. In order to make the device reusable, the pressurised gas is transferred to a chamber inside of the absorber, instead of releasing the gas out of the system. Another mode of operation of the device is preserving the pressure difference between both sides of the piston on a predefined level and in this way to provide a shock absorber with a controllable reaction force [3], ready to be implemented as a part of a semi-active suspension of a wheel vehicle or an air vehicle.

3. Conducted research

This research program consisted of the following stages: 1. development of the concept of the pneumatic shock absorber and numerical analysis, 2. design and tests of the piezo activated valve dedicated to the considered application, 3. design and fabrication of the pneumatic shock absorber, 4. design and implementation of a control module 5. testing of the shock absorber under periodic kinematic excitation, 6. testing of the absorber under impact loading.

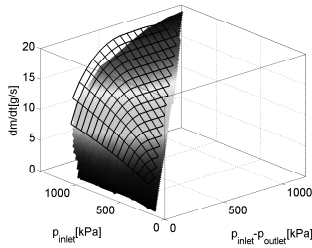


Figure 1. Mass flow rate vs inlet pressure and pressure drop, numerics and experiment

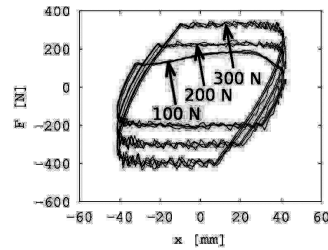


Figure 2. Reaction force vs piston displacement for various reference signals

4. Development of the piezo electric valve

The piezo electric valve [3] was designed in accordance to the requirements defined on the stage of the numerical analysis of the case. The analysis of the valve was conducted in the field of dynamics and thermodynamics of compressible fluid with the assumption of one dimensional flow in stationary conditions. Figure 1 depicts the mass flow rate of the gas through the valve in the domain of inlet pressure and the pressure drop on the valve. The value defined on the conceptual stage was demanded as the design parameter on the numerical stage and accomplished in the experiment.

5. Control system and operation of the absorber under periodic excitation

The control system for the shock absorber realized the "on-off" algorithm where the reference signal was pressure of the gas in the absorber's chambers [4]. The control algorithm was executed in real-time. Figure 2 depicts the results of the absorber's operation acquired during periodic tests.

6. Concluding remarks

This paper described the results of a pneumatic adaptive shock absorber development. The presented data acquired during tests of the piezo actuated valve and test of the absorber under periodic excitation can be treated as proof of the concept.

7. References

- [1] N. Setter ed. (2002). *Piezoelectric materials in devices*, Ceramics Laboratory EPFL, Lausanne.
- [2] S. Takahashia, A. Ochia, M. Yonezawaa, T. Yanob, T. Hamatsukic I. Fukuib (1983), Internal electrode piezoelectric ceramic actuator, *Ferroelectrics*, **50**, 181-190.
- [3] G. Mikułowski, W. Rogoźnicki, R. Wiszowaty (2010), Zawór płytowy, *Pat pend*, No P392368.
- [4] R. Wiszowaty, J. Biczuk, C. Graczykowski, G. Mikułowski (2011), Method of impact energy dissipation by the use of the pneumatic impact absorber with a piezo-valve, *Proc. 5th ECCOMAS Thematic Conference on Smart Structures and Materials SMART'11*, July 6 - 8, 2011, Saarbrcken.

8. Acknowledgements

The support of Structural Funds in the Operational Programme Innovative Economy (IE OP) financed from the European Regional Development Fund 'Projects Modern material technologies in aerospace industry' (POIG.0101.02-00-015/08) and Smart technologies for safety engineering SMART and SAFE' (TEAM/2008-1/4, Foundation for Polish Science Team Programme) is gratefully acknowledged.

MODELING OF A SANDWICH BEAM WITH UNDERPRESSURE GRANULAR STRUCTURE

J. M. Bajkowski¹, R. Zalewski², M. Pyrz²

¹ *Institute of Vehicles,* ² *Institute of Machine Design Fundamentals, Warsaw, Poland*

1. Introduction

Despite the prevalence of granular materials in the nature and in the industry, the physics of bulk materials still fails to explain many phenomena connected with their seemingly simple behaviour. The potential fields of application of their unique properties still remain highly unexplored.

The proposed construction of a sandwich beam incorporates granular structure, that allows to change the damping characteristics of the beam, by varying the negative pressure value inside the structure (Fig. 1). An elastic sleeve filled with granules that covers the steel beam, allows to trigger the so-called jammed state of the material, by controlling the value of the partial vacuum. The intensified effect of the interlocking leads to forming the force chains and increase in an overall rigidity and hardness of the structure [2]. The distinctive feature of such a beam is the ability to control the dissipation energy value by varying the control signal, hence it enables for vibrations reduction.

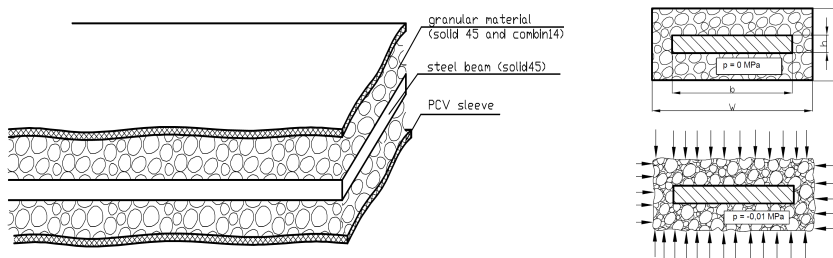


Fig. 1 Model of the beam with granular structure and it's behaviour for different pressures

2. Experiments and model

The paper presents experimental and simulation results of the concerned beam. The model is intended for utilizing the control algorithms of vibrations. The influence of the underpressure value on the behaviour of the granular material was extensively examined during experiments.

Granular beam free vibrations tests were additionally supported by uniaxial experiments carried out on specially performed cylindrical samples [3]. Basing on experimentally acquired hardening curves, Young's modulus values were estimated for various values of generated underpressures. It is worth mentioning that special granular structures behave different according to the applied loading direction. Such phenomenon additionally complicates controlling processes of damping properties.

Typical experimental characteristic describing variations of the Young's modulus values for different underpressures is depicted in Fig. 2. Basing on the depicted data we can observe reasonable possibilities of controlling the elastic range deformations of considered special granular structure. Similar phenomenon was also observed in the inelastic range [3].

The beam model was simplified to 3 layers: steel core (solid45), upper and lower granular structure covered with sleeve (solid45 with additional combin14 elements).

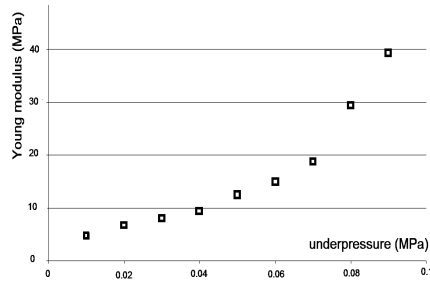


Fig. 2. ABS special granular structure Young's modulus variation for different underpressure values

As a preliminary approach to the problem it was assumed that the granular layers will be simulated as nonlinear, elastic material subjected to deflections, resulting in a stresses greater than the yield strength. The multilinear stress-strain relationship allows to more accurately model the plastic deformation of the material [1]. The tip displacement results for different values of underpressures and examined beam's lengths are presented in Fig. 3.

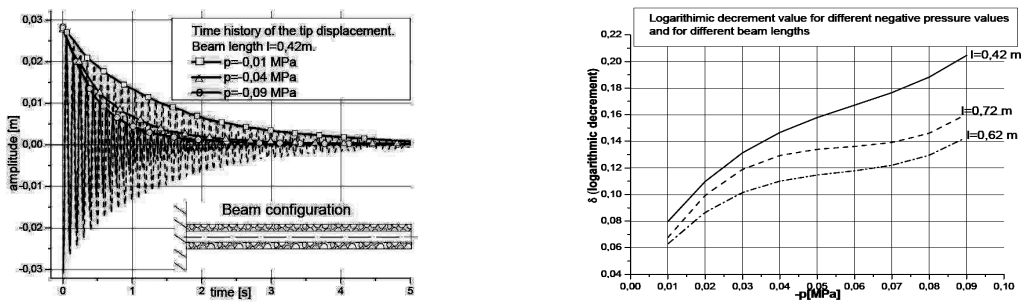


Fig. 3. Displacement of the tip of the beam and logarithmic decrement value.

3. Summary

Utilizing the properties of the underpressured bulk materials, mainly the possibility of adopting any shape depending on the boundaries, we can build a low-cost, efficient dampers of different shapes. The proposed finite element model is consistent with the modified mathematical model of the beam free vibrations, covered by the equation

$$(1) \quad \frac{\partial^4 y(x,t)}{\partial x^4} + \mu(p) \frac{\partial^5 y(x,t)}{\partial x^4 \partial t} + \sqrt{\frac{\rho A(x)}{E_z(p) J_z(x)}} \frac{\partial^2 y(x,t)}{\partial t^2} = 0$$

where internal damping $\mu(p)$ and resultant Young modulus $E_z(p)$ are the functions of the underpressure value.

4. References

- [1] J. Atkinson (1993). *An Introduction to the mechanics of soils and foundations*, McGraw Hill International, Berkshire, 23–35.
- [2] D. Mueth, M. Jaeger, S. R. Nagel (1998). Force Distribution in a Granular Medium. *Physical Review E*, Volume 57, No. 3.
- [3] R. Zalewski (2005). *Analysis of the mechanical properties of structures, built on the basis of the granular materials, placed in a tight space with underpressure*, Ph.D Thesis (In Polish) Warsaw University of Technology.

HIGH PERFORMANCE VALVE FOR ADAPTIVE PNEUMATIC IMPACT ABSORBERS

J. Holnicki-Szulc¹, C. Graczykowski¹, P. Pawłowski¹ and I. Ario²

¹ *Institute of Fundamental Technological Research, Warsaw, Poland*

² *Department of Civil and Environmental Engineering, Hiroshima University*

Dissipation of the energy in mechanical systems is a vitally important engineering and scientific problem. Current stringent safety requirements enforce substantial change of methods of structural design and application of new solutions and technologies which ensure structural integrity.

Currently applied passive safety systems are typically not equipped with control devices. Their dynamic characteristics remains unaltered and thus it is well adjusted to a narrow range of actual loadings. In case of impact loading, it is highly advantageous to apply systems of Adaptive Impact Absorption (AIA) [1], which are capable of fast change of the dynamic characteristics. Recent fast development of the material technologies and, in particular, development in the field of functional (smart) materials and electronic measurement and control systems had created new possibilities of practical applications of the AIA systems.

During the adaptation process the choice of optimal control strategy is followed by adjustment of the dynamic characteristics of adaptive elements of the absorber. These elements can entirely made of functional materials (as e.g. shape memory alloys) or, alternatively, they can be equipped with controllable devices, so-called structural fuses, which provide controlled response of the element. Depending on type of applied control, the changes of structural parameters occur only once (usually before impact) or they are controlled in real time during the impact process.

The systems of Adaptive Impact Absorption can be effectively used to increase the level of safety during the action of the impact loading. In particular, very promising results are obtained with the use of adaptive inflatable structures [2]. However, the possibilities of their practical applications are limited due to the lack methods allowing for the efficient and fast control of the gas flow during impact.

The presented work focuses on the pneumatic adaptive impact absorbing system equipped with a novel (patent application), high performance valve, which utilizes bistable snap-through effect. Snap-through effects are mainly the subject of theoretical analysis and they do not find many practical engineering applications. The classical example of snap-through behaviour is the two-bar von Mises truss. The extension of the above effect to multilayered structure (multifolding system, c.f. Fig. 1) providing multiple folding sequences and equilibrium paths, which could be potentially applied in smart pneumatic structures, was a subject of earlier investigations presented e.g. in [3].

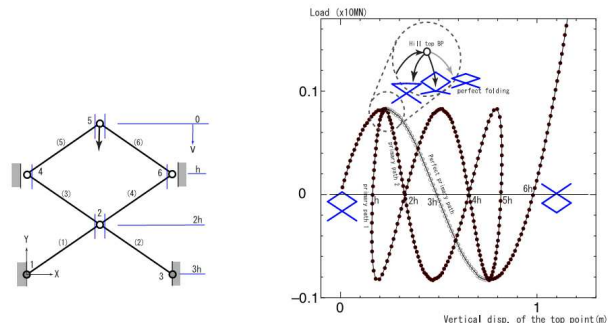


Fig.1. The multi-folding system and its equilibrium paths.

The controllable valve which utilizes bistable snap-through effect is equipped with two independent elastic shell elements with two stable configurations, which are aligned in the initial configuration such that the flow of the gas is totally closed. Opening of the valve is performed by controllable snap-through (e.g. evoked by a the use of piezoelectric fibers) of the first shell element which creates the flow channel. Closing of the valve is performed by controllable snap-through of the second shell element which causes alignment of the both shells and blocks the gas flow. The examples of the preliminary analyses of the snap-through effect of shell elements are depicted in Fig.2.

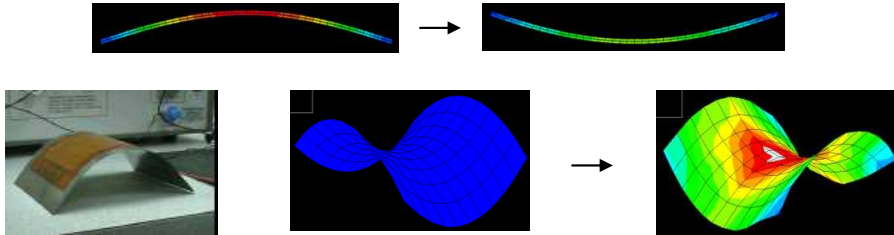


Fig. 2. Stable configurations obtained as a result of the snap-through of shall element shaped as part of the cylinder or hyperbolic paraboloid.

The above concept can be also used to design a multi-stage valve in the form of matrix of elastic shell elements, which are aligned in the initial configuration such that they totally block the gas flow (Fig.3). Control of the valve opening is performed by the sequentially controlled snap-through of chosen shell elements which allows for opening or closing of the appropriate number of flow channels. Recovering the initial configuration is conducted by controllable snap-back of shell elements or rotation of the valve assembly.

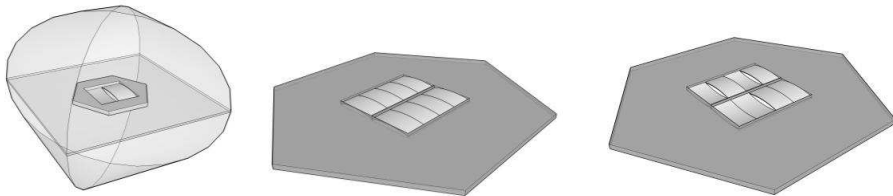


Fig. 3. General view: absorber equipped with bistable valve, the valve composed of a matrix of shell elements.

The proposed solution is characterized by large mass flow rate of the gas, small total mass and inertia of the device providing the possibility of fast opening and closing, which is required for realization of the optimal control strategy for the pneumatic absorbers.

References

- [1] J. Holnicki-Szulc (Ed.) (2008). *Smart Technologies for Safety Engineering*, Wiley.
- [2] C. Graczykowski (2011). *Inflatable Structures for Adaptive Impact Absorption*, Ph.D. Thesis, IPPT PAN.
- [3] I. Ario, P. Pawlowski, J. Holnicki-Szulc (2007). *Local/Global Structural Instability Based on Multi Folding Microstructure Theory*. Proc. of the 21st Canadian Congress of Applied Mechanics, Toronto, Canada, June 3-7.

MAGNETORHEOLOGICAL COMPOSITES BASED ON THERMOPLASTIC MATRICES. MANUFACTURE, MODELLING, EXPERIMENT

J. Kaleta, D. Lewandowski, M. Królewicz, M. Przybylski, P. Zając

*Institute of Materials Science and Applied Mechanics, Wrocław University of Technology,
Mariana Smoluchowskiego 25, 50-370 Wrocław, Poland*

1. Introduction

Magnetorheological elastomers, also known as solid matrix-based magnetorheological composites, are a relatively new group of SMART materials. They are characterized by a reversible change of selected mechanical and rheological properties under the influence of an external magnetic field, a phenomenon called magnetorheological effect. These materials are particularly predisposed to applications connected with vibration damping and controlled energy dissipation. Recently, magnetorheological elastomers are often used as active vibration dampers [1]. If such an application is to be effective, one should develop a constitutive model which describes the relations between mechanical and magnetic quantities. The most popular and simultaneously the simplest model used to describe MR elastomers is the Kelvin-Voigt model for a viscoelastic body [1]. The dependence on magnetic field is achieved by defining function of selected parameters (viscosity and stiffness). The authors proposed such a model and performed its identification.

2. Material and sample manufacture

The authors focused on examining the properties of a selected magnetorheological composite. MR composites belong to the material group which is vast and diverse because there are various possibilities of choosing the matrix material, the ferromagnetic filler and additives. The material presented in this paper is based on the thermoplastic polymer matrix and the ferromagnetic filler in the form of iron powder (several dozen micrometres in size). The components are mixed together in controlled conditions and the resulting material is shaped into plates which serve as the basis for test samples. The procedure is described in greater detail in the authors' previous works [2].

3. Test stand

The investigations of mechanical and magnetic properties of the selected magnetorheological elastomer were performed on a dedicated test stand. The test stand made it possible to load the samples in the way which can be described (approximated) as uniaxial pure shear (Figure 1.)

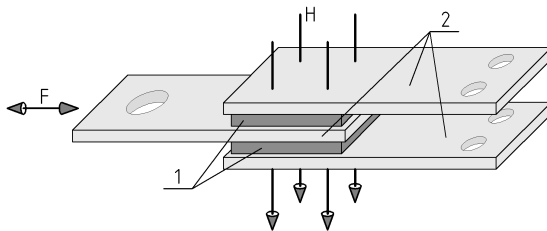


Figure 1. A scheme of the test specimen. The directions of forces and magnetic field are visible.

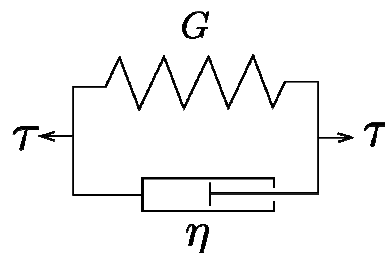


Figure 2. Kelvin-Voigt model.

4. Results of experiments – comparison with model

The samples were subjected to cyclic shearing at various magnetic field values, for a constant frequency of 1 Hz and strain amplitude $\gamma_a=0.025$. The results were registered in the form of hysteresis loops in the τ - γ system (Figure 3).

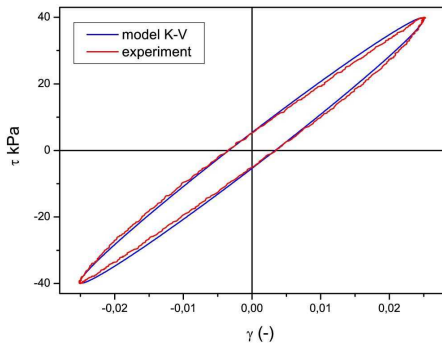


Figure 3. Comparison of the hysteresis loops obtained from the experiment and from the Kelvin-Voigt model.

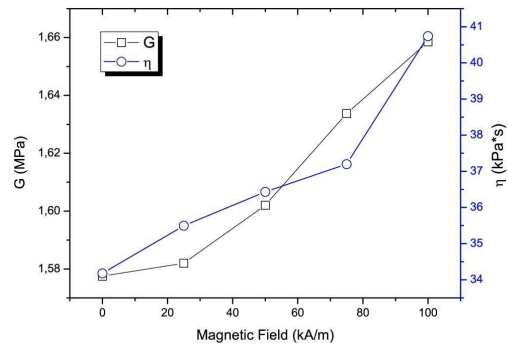


Figure 4. The graph showing how η and G parameters change as a function of magnetic field.

The experimental results were used to identify the viscoelastic body model (Kelvin-Voigt model - Figure 2). The model parameters were identified as G – elasticity and η – viscosity, these values depend on the magnetic field intensity. The identification results are shown in Figure 4. The comparison of the hysteresis loops obtained from experiments and calculated using the chosen model are presented in Figure 3.

5. Summary

The primary goal of the work was to analyse the magnetomechanical properties of magnetorheological elastomers, paying special attention to the possibility of their description using simple viscoelastic body model. The parameters of this model depended on the magnetic field strength H . It was proved that for the applied range of strain amplitude change γ_a and magnetic field intensities H , the Kelvin-Voigt model – with parameters dependent on the magnetic field – corresponds well to the results of experimental investigations.

6. Acknowledgment

The research was supported by Wrocław Research Centre EIT+ within the project “The Application of Nanotechnology in Advanced Materials” – NanoMat (POIG.01.01.02-02-002/08) financed by the European Regional Development Fund (Innovative Economy Operational Programme, 1.1.2).

7. References

- [1] M. Lokander. *Performance of Magnetorheological Rubber Materials*. PhD thesis, KTH, Stockholm, 2004.
- [2] P. Zajac, J. Kaleta, D. Lewandowski, and A. Gasperowicz. Isotropic magnetorheological elastomers with thermoplastic matrices: structure, damping properties and testing. *Smart Materials and Structures*, 19:045014, 2010.

OPTIMAL PIEZOELECTRIC LOCATION FOR COMPOSITE STRUCTURES

P. Kędziora, A. Muc

Institute of Machine Design, Cracow University of Technology, Cracow, Poland

1. Introduction

Elastic waves are generated by an actuator (one of the grid piezoelectric transducers (PZT)) and recorded using the remaining PZT transducers (from the same grid - Figure 1). The shape of system of PZT transducers, shape and number of PZT influence on the quality (sensitivity) and accuracy of detection of defects in the test of composite structures. An additional issue is the control and detection of failure sensors, which is discussed among other in the works [1, 2].

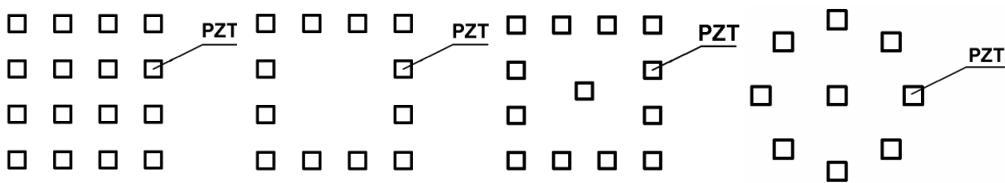


Figure 1. Examples of systems of PZT transducers.

2. Detection of damage

Figure 2 shows a comparison of the wave signal for the structure without any damage and disturbance in the propagation of the wave induced by delamination. The location of this damage is defined as follows:

$$(1) \quad d = \frac{v_g \Delta T}{2}$$

where v_g is the velocity of wave propagation, ΔT is the difference between the signal of the incident wave and the wave disturbed by the damage.

The correlation coefficient between the original and distorted signals was calculated for individual sensing paths in the time domain to get the perception to damage near the sensing paths. The damage index (D) is defined as: $D = 1 - \rho_{ab}$

3. Optimization problems

Optimization problems deal with the analysis of structures with some response (denoted by R) requirements. In general structures with actuators can be optimized using three computationally different strategies. In the first, the most common optimization problem the objective function to be minimized is the response of the system, i.e.:

$$(2) \quad \text{Min}_s R(s)$$

The vector s denotes the set of design variables.

The response tuning is the second problem. It can be treated as the alternative or sometimes equivalent optimization problem to the above:

$$(3) \quad \underset{s}{\text{Min}} [R_l(s) - R_{l-1}(s)], l = 2, 3, \dots$$

In addition, as the third problem volume or weight minimization of a structure has been considered here, in which:

$$(4) \quad \underset{s}{\text{Min}} V(s)$$

The problem of shape optimization of piezoelectric transducers has been discussed among others in the work [3, 4].

Optimal location of sensors concerns the best location of sensors and their required number. To solve this problem, the optimization procedures have been applied. In addition, the information of composite structures and wave propagation in the material has been used.

Simple methods have been used to find the best configuration of transducers. This is done by adding or removing one or more sensors and evaluated the relationship between the transducers, signal quality and accuracy of fault location in order to find the best combination. Development of methods of combinatorial optimization based on biological and physical analogy allows the use of such genetic algorithms, neural networks, simulated annealing, etc.

Optimal location of sensors and actuators over a structure can be different for different criteria based upon: maximization of modal forces/moments applied by the PZT actuator, maximization of deflection of the host structure, minimal change in host structural dynamics, desired host structural dynamics, minimization of control effort/maximizing energy dissipated, minimization of host vibrations, maximization of degree of controllability/observability of modes of interest, etc.

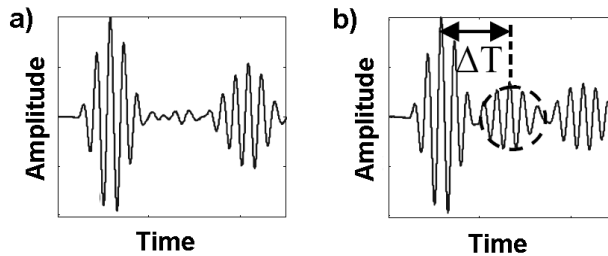


Figure 2. The determination of damage location.

4. References

- [1] K. Worden and W.J. Staszewski and G.R. Tomlinson (1997). Smart systems – the role of signal processing, In: *CEAS International Forum on Aeroelasticity and Structural Dynamics*, Rome, Italy, 17–20 June 1997.
- [2] W.J. Staszewski (2002). Intelligent signal processing for damage detection in composite materials, *Composites Science and Technology*, **62**, 941-950.
- [3] A. Muc and P. Kędziora (2008). Variational approach in optimal design of piezoelectric sensors & actuators, *Advanced Materials Research*, **47-50**, 1258-1261.
- [4] P. Kędziora and A. Muc (2012). Optimal shapes of PZT actuators for laminated structures subjected to displacement or eigenfrequency constraints, *Composite Structures*, **94**, 1224-1235.

DEFECT DETECTION AND SIZING IN PIPES USING TORSIONAL GUIDED WAVES

M. Kharrat, M.N. Ichchou, O. Bareille and W. Zhou

Laboratory of Tribology and Systems Dynamics, Ecole Centrale de Lyon, Lyon, France

1. The inspection system

Long pipelines are often used in petro-chemical industry for transporting liquid and gaseous substances. These pipes need to be regularly monitored and inspected for both safety reasons and environmental impact control. Guided waves have been increasingly used in nondestructive evaluations. Many researchers have been interested in the application of ultrasonic guided waves for the nondestructive inspection of pipes [1, 2, 3]. Axisymmetric modes are preferred for the detection of defects in pipes. Among these waves, the torsional one $T(0,1)$ is the only one whose velocity remains constant with frequency. All the others suffer speed variations as the frequency changes which is a major disadvantage for wave generators that could only generate longitudinal or flexural waves. Besides, it keeps its speed constant and it propagates through pipes filled with liquid without much leakage.

In this work, an inspection system has been designed and developed to excite the pipe under test with well-defined waves that propagate along the structure; and also to receive reflected signals from features and damages encountered. The torsional mode was chosen to be generated by the system. The generation of torsional waves is operated by using a number of piezoelectric transducers clamped around the circumference of the pipe. The design process of the torsional waves inspection system is presented. Time responses were examined for intact and damaged pipes. Then, experimental tests have been performed on two pipes with different materials: PVC and steel. Some defects have been machined on these pipes. Their interaction with torsional waves has been proven by analyzing experimental time responses. Subsequently, the Wave Finite Element Method (WFEM) has been used to construct a database of reflection coefficients from a rectangular defect with variable axial, circumferential and thickness extents. Calculations were made depending on the excitation frequency with the torsional mode $T(0,1)$ as incident wave. This aims to approximate defect sizes that were already detected.

2. Experimental tests

The actuator and the sensor are mounted on a straight 3 m-long, 5 mm-thick, 140 mm outer diameter PVC pipe without any defect. The actuator is attached at one end of the pipe; the sensor is placed at 1 meter from the actuator. Fig. 1(a) shows the time record for a pipe with a defect. This defect is a single 60 mm radial cut. It is located half way from both ends of the pipe. When a 3m-long steel pipe is used, the wave can travel back and forth, reflecting itself several times at each end of the pipe. This effect is visible on Fig. 1(b), with the same kind of pulse as for the previous example.

3. Defect sizing by WFEM

The Wave Finite Element Method (WFEM), which is a simple spectral method based on the standard finite element (FE) formulation, can be applied to examine the wave interaction with the local defects and the structural features [4, 5]. To approximate the size of the defect, the idea was to build a digital database containing the different probabilities of defect sizes that could exist while assuming that it was modeled with a form similar to that shown in Figure 2. The parameters that characterize the defect are ' a, b, c ', which are axial extent, depth, and circumferential extent respectively. Calculations were made by varying these three parameters. The axial extent sweeps the interval [4-20] mm in steps

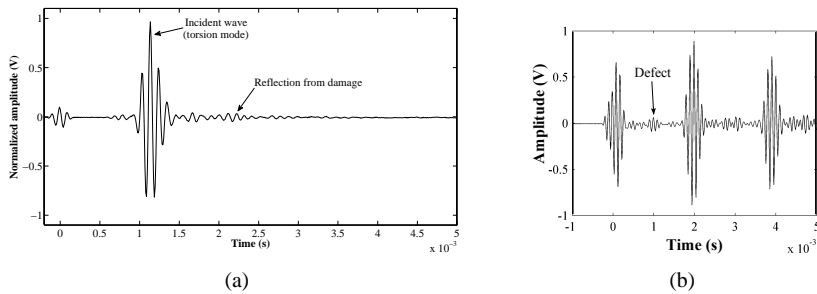


Figure 1. Time signal recorded : (a) from damaged PVC pipe, and (b) from damaged steel pipe.

of 4 mm. The circumference of the pipe was divided to 44 elements, the circumferential extent was varied by eliminating an element in every step. Knowing that the pipe diameter is of 168 mm, each element measures 12 mm in the circumferential direction. Finally, the depth of the defect varies from 2 mm with a step of 3 mm until the whole pipe thickness which is 11 mm. Reflection coefficient calculation was made depending on the frequency in the range [5-15] kHz. This latter corresponds practically to the signal frequency at which the pipe under test was excited. The torsion mode was considered in the calculation process.

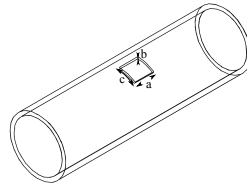


Figure 2. Damaged pipe with defect dimensions.

4. References

- [1] J.L. Rose. A baseline and vision of ultrasonic guided wave inspection potential. *Transactions-American society of mechanical engineers journal of pressure vessel technology*, 124(3):273–282 2002.
- [2] RB Thompson, GA Alers, and MA Tennison. Application of direct electromagnetic lamb wave generation to gas pipeline inspection. In *1972 Ultrasonics Symposium*, pages 91–94 IEEE, 1972.
- [3] MG Silk and KF Bainton. The propagation in metal tubing of ultrasonic wave modes equivalent to lamb waves. *Ultrasonics*, 17(1):11–19 1979.
- [4] M.N. Ichchou, J.-M. Mencik, and W. Zhou. Wave finite elements follow and mid-frequency description of coupled structures with damage. *Computer Methods in Applied Mechanics and Engineering*, 198(15-16):1311–1326 2009.
- [5] W.J. Zhou and M.N. Ichchou. Wave propagation in mechanical waveguide with curved members using wave finite element solution. *Computer Methods in Applied Mechanics and Engineering*, 199(33-36):2099–2109 2010.

NUMERICAL MODELING OF HARDENING AND COOLING OF CONCRETE STRUCTURES

G. Knor, J. Holnicki-Szulc

Institute of Fundamental Technological Research, Warsaw, Poland

1. Introduction

A numerical and experimental investigation on thermal behavior of young concrete is presented. The proposed model of temperature distribution in hardening concrete is based on the non-linear IHTP (inverse heat transfer problem) solution. Changes in properties of concrete during setting and hardening are included in the model. The proposed approach consists of several stages. First the temperature measurements in a one-dimensional form are performed and method of lines is used to solve one dimensional heat equation. This data and solution are treated as an input to IHTP. Next IHTP, which is used for determination of thermal properties: specific heat capacity, thermal conductivity and heat of hardening, is solved. To solve this problem pattern search method is used, which does not require the calculation of the gradient of the objective function. At the third step direct heat conduction problem is solved. Own, based on finite element method, software TMC (Thermal & Mechanical modeling of Concrete, [1]) to predict the temperature field is used. Additionally the heat equation in the concrete can be coupled with a heat equation for the water temperature in cooling pipes, which are used to remove hydration heat from concrete blocks during its hardening. The obtained numerical results are compared with measured temperatures in the experiment. The advantage of proposed method is that it can be used for any type of concrete (e.g. with calcium fly ash, blast-furnace slag etc.), because it does not assume anything about the composition.

2. Governing equations

The equation describing heat transfer in concrete can be written in the following form [2]:

$$\rho_c c_c(t_e) \frac{\partial T}{\partial t} = \frac{\partial}{\partial x} \left(k_{cx}(t_e) \frac{\partial T}{\partial x} \right) + \frac{\partial}{\partial y} \left(k_{cy}(t_e) \frac{\partial T}{\partial y} \right) + \frac{\partial}{\partial z} \left(k_{cz}(t_e) \frac{\partial T}{\partial z} \right) + S(t_e)$$

where ρ_c – density, c_c – specific heat capacity of concrete, T – temperature of concrete, t – time, k_{cx} , k_{cy} , k_{cz} – thermal conductivity in direction x , y , z , respectively, S – heat source (heat of hydration) and t_e is an equivalent age which is defined as:

$$t_e = \int_0^t e^{\frac{E}{R} \left(\frac{1}{293} - \frac{1}{T+273} \right)} dt'$$

and E/R (activation energy / gas constant):

$$\frac{E}{R} = \begin{cases} 4000 \left[\frac{1}{K} \right] & T > 20^\circ C \\ 4000 + 175(20 - T) \left[\frac{1}{K} \right] & T \leq 20^\circ C \end{cases}$$

Similarly, for water in the pipes heat transfer equation can be written as:

$$\rho_w c_w \left(\frac{\partial \theta}{\partial t} + \mathbf{u} \cdot \nabla \theta \right) = k_w \nabla^2 \theta$$

where the index w denotes coefficients for water, θ is a temperature of water and \mathbf{u} denotes water velocity.

The interaction between the two media takes place at the boundary, where the cooling condition is fulfilled [3]:

$$k_w \frac{\partial \theta}{\partial r} \Big|_{r=r_{pipe}} = H (T \Big|_{r=r_{pipe}} - \theta)$$

where r is a radius, r_{pipe} is the pipe radius and H (heat transfer coefficient) depends on type of the pipe.

As mentioned before to develop individual parameters for a particular concrete mixture an inverse heat transfer problem must be solved. To solve this problem the following objective function E (given by the ordinary least squares norm) is formulated [4]:

$$E = (T^e - T^n)^T (T^e - T^n) = \sum_{m=1}^M \sum_{i=1}^I (T_{im}^e - T_{im}^n)^2$$

where T^e is measured temperature and T^n is estimated temperature. M denotes number of sensors and I is a number of samples.

3. Results

Figures 1 and 2 show the sample result of the numerical simulations. Solid line shown in Fig. 1 denotes simulated target heat generation function and squares indicate estimated by IHTP values. Fig. 2 shows comparison between measured concrete temperature and modeled value for three sensors in selected concrete construction.

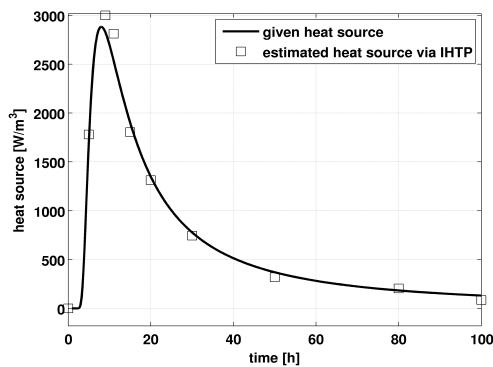


Figure 1: Result of an inverse problem.

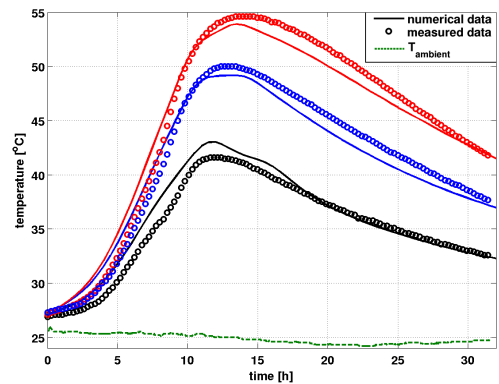


Figure 2: Measured concrete temperature compared to the modeled values.

4. Acknowledgments

The authors acknowledge the financial support from the project "Innovative cement binders and concretes using calcium fly ash" - POIG 01.01.02.-24-005/09 and the project "Monitoring of Technical State of Construction and Evaluation of its Lifespan"- MONIT – POIG 01.01.02-00-013/08-00 from the EU.

5. References

- [1] G. Knor, J. Holnicki-Szulc (2011), *Identify heat of hardening and transient thermal properties in concrete structures*, ECCOMAS Thematic Conference on Smart Structures and Materials - SMART11, July 6-8, Saarbrücken, Germany
- [2] H. S. Carslaw, J.C. Jaeger (1959), *Conduction of Heat in Solids (2nd edition)*, Oxford University Press, New York
- [3] T. G. Myers, N. D. Fowkes and Y. Ballim (2009), *Modeling the Cooling of Concrete by Piped Water*, J. Eng. Mech. 135, 1375
- [4] M. N. Özisik and H. R. B. Orlande (2000), *Inverse Heat Transfer: Fundamentals and Applications*, Taylor & Francis

TiNi SMA SUBJECTED TO COMPRESSION - THERMOMECHANICAL EFFECTS INVESTIGATED WITH IR TECHNIQUE

K. Kulasiński¹, E.A. Pieczyska¹, H. Tobushi² and K. Takeda²

¹ *Institute of Fundamental Technological Research, Warsaw, Poland*

² *Department of Mechanical Engineering, Aichi Institute of Technology, Toyota-city, Japan*

1. Introduction

Superelastic properties and transformation bands are often studied recently in shape memory alloys (SMA) under tension test. There are also some studies on SMA in compression, however the accompanying temperature changes were seldom taken into account [1]. In this research, quasistatic compression tests were carried out in room conditions on small bar specimens, in the vicinity of the A_f temperature, being very close to ambient one. The mechanical characteristics and the average specimen temperature variation were measured in a contact-less manner by a sensitive infrared camera. An influence of the strain rate and related temperature changes on the SMA thermomechanical loading-unloading behaviour including “cooling” stage is discussed.

2. Experimental results - mechanical and temperature characteristics

An exemplary stress, strain and temperature dependence for a TiNi SMA specimen compressed with 10^{-2}s^{-1} strain rate is shown in Fig. 1. One can infer looking at the mechanical and temperature loops (left) that both the stress and the specimen average temperature increase as the material is loaded, which is directly caused by the martensitic forward transformation (reorientation) being exothermic. As the strain rate increases, one can notice a widening of the stress range and an increase in the peak temperature. Moreover, higher strain rate makes the temperature loops narrower, in such a way that in the case of the highest strain rate applied not shown here (10^{-1}s^{-1}), the both sections almost overlaps. During the unloading, the stress and the temperature obviously decrease, as the result of the endothermic reverse transformation.

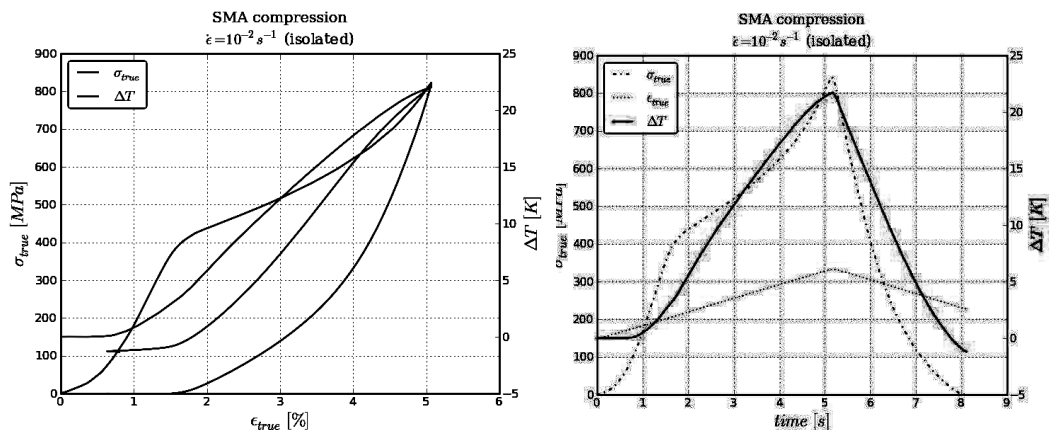


Fig. 1. TiNi SMA in compression cycle with 10^{-2}s^{-1} strain rate. Stress and temperature vs. strain (left) and time dependence (right).

Another part of the experiment was the TiNi SMA compression with cooling down to the ambient temperature imposed between loading and unloading. The goal was to investigate the run

of the reverse transformation, independently of the thermodynamical influence of the forward transformation. An exemplary mechanical loop coupled with the specimen temperature variation, obtained for the same strain rate equal to 10^{-2} s^{-1} is shown in Fig. 2. Once the loading ends, the specimen is kept in the machine with constant strain and after 5 min. the specimen is unloaded.

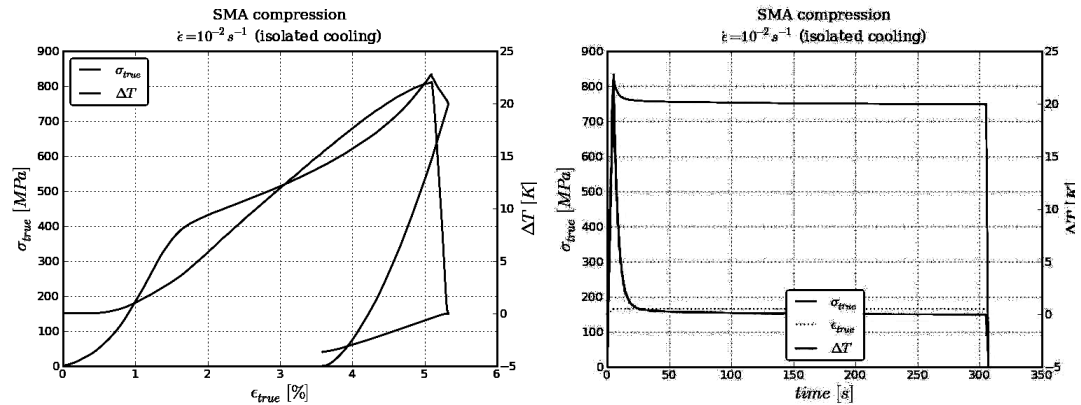


Fig. 2. TiNi SMA in compression cycle with 10^{-2} s^{-1} strain rate, cooled at maximal strain. Mechanical (left) and time (right) characteristics.

3. Discussion.

During the experiment, the surrounding's temperature remained very close to the A_f which results in the mechanical loop's profile (Fig. 1,2). Namely, the specimen shape recovery is not perfect and therefore what we do encounter is a combination of superelasticity (SE) and shape-memory effect (SME). The strain rate has a strong impact on SE-SME superposition; i.e., the higher the strain rate, the better the shape recovery and the greater participation of SE in favour of SME was observed. If we compare the residual strain in Fig. 1 and Fig. 2 we can say that the cooling strongly influences the shape recovery being in this case much smaller due to the thermomechanical coupling. The temperature profile tells us also that, despite constant strain rate, the martensitic transformation does not develop in the same manner: it slows down at the advanced stage of the forward transformation, which is particularly visible in the case of lower strain rates. The final temperature is different (usually smaller) than that at the beginning of the process which is enhanced if the compression is performed with cooling before unloading. This difference is probably caused by the fact that the heat of forward and reverse transformation is comparable but the heat outflux related to the elastic unloading and the exponential temperature drop during the cooling needs to be taken into account, too [2]. The discussed thermomechanical behaviour creates a new opportunity for shape memory alloys to be implemented as radiators.

ACKNOWLEDGMENTS: This work was partially supported by the MNiSW project 501220837, and the NCN project 2011/01/M/ST8/07754. Assistance of L.Urbanski and J.Luckner in obtaining experimental data is appreciated. The infrared measurements were performed by M.Maj to whom the authors wish to express their gratitude.

4. References

- [1] E.A. Pieczyska, J. Dutkiewicz, F. Masdeu, J. Luckner, R. Maciak (2011). Investigation of thermomechanical properties of ferromagnetic NiFeGa shape memory alloy subjected to pseudoelastic compression test, *Archives of Metallurgy and Materials*, **56**, 401-408.
- [2] E.A. Pieczyska, Activity of stress-induced martensite transformation in TiNi shape memory alloy studied by infrared technique, *Journal of Modern Optics*, **57**, 18, 1700-1707, 2010.

INFLUENCE OF NITROGEN ION IMPLANTATION ON DEFORMATION AND FATIGUE PROPERTIES OF TiNi SHAPE-MEMORY ALLOY WIRE

K. Mitsui¹, K. Takeda¹, H. Tobushi¹, N. Levintant-Zayonts² and S. Kucharski²

¹ *Aichi Institute of Technology, 1247 Yachigusa, Yakusa-cho, Toyota, 470-0392, Japan*

² *Institute of Fundamental Technological Research, Polish Academy of Sciences, Pawinskiego 5B, 02-106, Warsaw, Poland*

1. Introduction

Shape memory alloy (SMA) is expected to be applied as intelligent materials since it shows the unique characteristics of the shape memory effect (SME) and superelasticity (SE). Most SMA elements with using these characteristics perform cyclic motions. In these cases, fatigue of SMA is one of the important properties in view of evaluating functional characteristics as SMA elements. Fatigue properties of SME and SE are complex since they depend on stress, strain, temperature and time which are related to the martensitic transformation (MT). If SMA is implanted by high energy ions, the thermomechanical properties may change, resulting in long fatigue life. In the present paper, the nitrogen ion implantation was applied to modify TiNi SMA wire surface and the influence of implantation treatment on the tensile deformation and bending fatigue properties is investigated.

2. Transformation temperature

The TiNi SMA wire of a diameter of 0.5 mm was implanted from two opposite directions by nitrogen ion beam with acceleration energy of 50 keV (See directions C_i in Fig. 4). The total doses of implanted ion were 5×10^{16} J/cm² and 1×10^{18} J/cm². The DSC thermograms for three kinds of wires with non-implanted surface, implanted with 5×10^{16} J/cm² dose and implanted with 1×10^{18} J/cm² dose are shown in Fig. 1. If the dose of ion implantation increases, the reverse transformation temperatures A_s and A_f increase.

3. Tensile deformation property

The stress-strain curves of three kinds of wires obtained by the tension test at room temperature are shown in Fig. 2. The stress-strain curve with non-implanted draws a hysteresis curve during loading and unloading, showing the SE. The curve with 5×10^{16} J/cm² dose shows the partial SE. The curve with 1×10^{18} J/cm² dose shows the SME. As observed in Fig. 1, if higher dose of implantation is applied, the reverse transformation temperatures increase. Both upper and lower yield stresses therefore decrease and the SME appears in place of the SE.

4. Bending fatigue property

The relationships between the maximum bending strain and the number of cycles to failure for three kinds of wires obtained by the alternating-plane bending fatigue test at room temperature are shown in Fig. 3. The larger the maximum bending strain, the shorter the fatigue life is. If the maximum bending strain is 4 %, the fatigue lives of all materials are almost the same. If the maximum bending strain is small, the fatigue life becomes longer in the case of higher dose implantation.

5. Fatigue fracture surface

Figure 4 shows a microscope photograph of a fracture surface of a wire obtained by the fatigue test. In Fig. 4, C_i denotes the center of ion implantation and the point of the maximum bending strain. F_c denotes the initiation point of the fatigue crack. The crack nucleates at a certain point F_c on the surface of the wire and propagates towards the center in a sinuous radial pattern. Although small

cracks are observed in both sides of the wire, one single crack grows preferentially. Following the appearance of fatigue crack with a fan-shaped surface, unstable fracture finally occurs. For non-implanted samples, the point F_c coincides with the point C_i and the fatigue life is short.

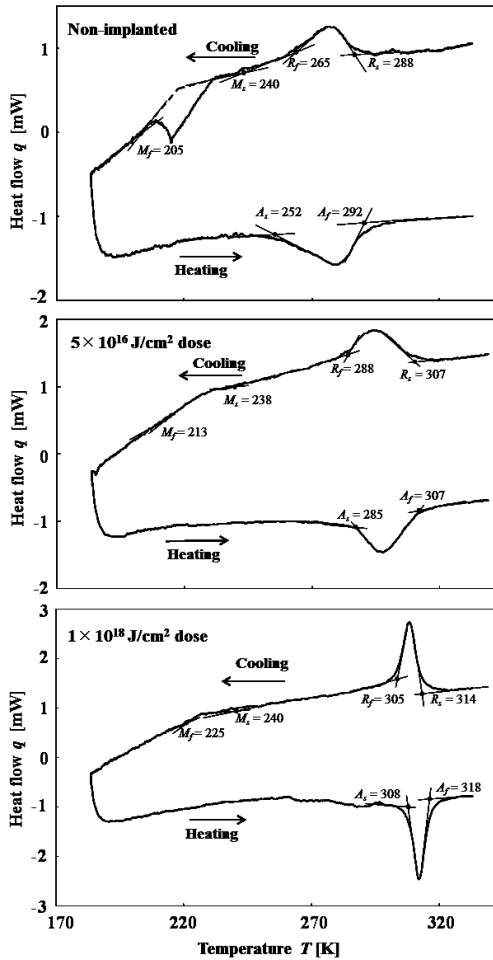


Fig. 1 DSC thermograms for three kinds of wires with non-implanted, $5 \times 10^{16} \text{ J/cm}^2$ dose and $1 \times 10^{18} \text{ J/cm}^2$ dose

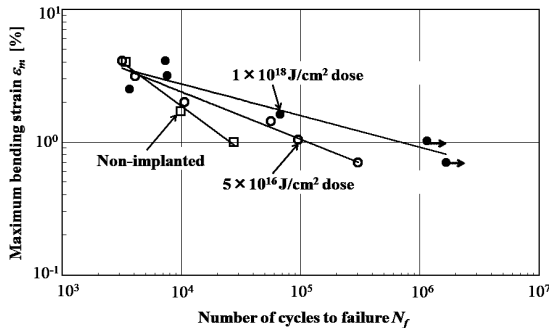


Fig. 3 Relationships between the maximum bending strain and the number of cycles to failure for three kinds of wires obtained by the alternating-plane bending fatigue test

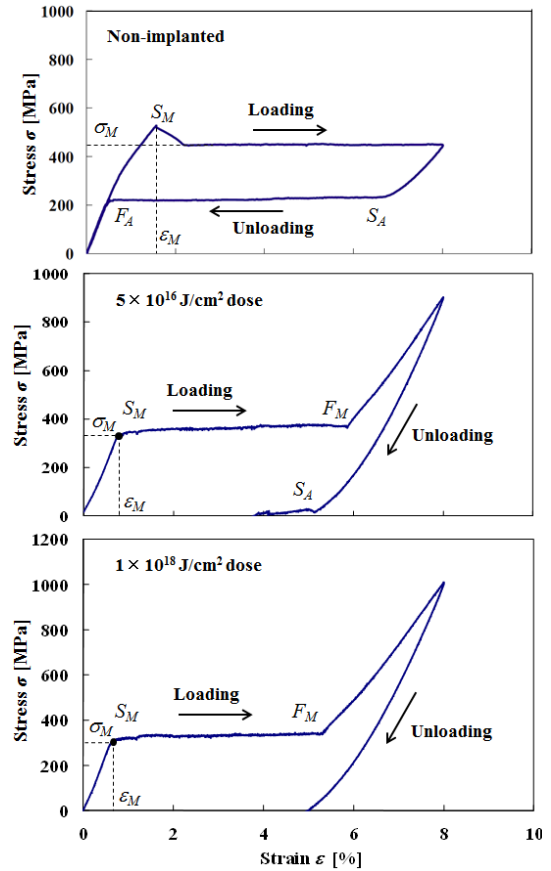


Fig. 2 Stress-strain curves of three kinds of wires obtained by the tension test at room temperature

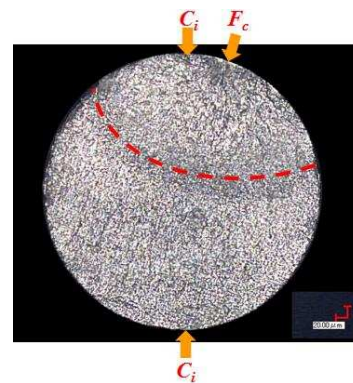


Fig. 4 Microscope photograph of a fracture surface of a wire ion-implanted by $5 \times 10^{16} \text{ J/cm}^2$ dose and 2 % of maximum bending strain obtained by the fatigue test

ACTIVE VIBROACOUSTIC CONTROL OF BEAMS AND PLATES WITH GENERAL BOUNDARY CONDITIONS

L. Nowak and T. G. Zieliński

Institute of Fundamental Technological Research, Warsaw, Poland

1. Introduction

Active vibroacoustic control of beam and plate structures with arbitrary boundary conditions is considered. The goal is to develop a method of minimizing sound radiation efficiency of such structures. Primary sound field arise as a result of vibrations, due to external disturbances. It is assumed that the control system is compact - it does not contain any additional, ambient microphones. Piezoelectric transducers, mounted on the surface of the controlled object, are used as sensors and actuators. Accurate numerical model of the considered structure is needed to determine optimal parameters of the control system. Theoretical background and the results of numerical and experimental research are briefly introduced.

Due to the fact that it is not possible to give an analytical solution of such problem in general case, it is solved numerically. Eigenfrequencies and the corresponding mode shapes are found using the finite element method. Basing on the derived results and the actuator/sensor equations, the piezotransducers locations that ensure optimal sensing/actuating abilities for specific vibration modes of the structure are determined. The modes are selected taking into account fact that the main purpose of the described study is to minimise acoustic field generated by the vibrating element. It is assumed, that the piezotransducers are rectangle-shaped and their dimensions are given. The resultant radiation efficiency of controlled, vibrating structure is estimated using the Rayleigh integral, assuming that the element is placed in an infinite rigid baffle. Similar analysis is carried out for the beam structures, but, instead of using FEM for modal analysis, one dimensional analytical solutions are applied.

2. Acoustic radiation of vibrating beam and plate structures

Due to the undertaken assumptions, classical thin beam and thin plate theories are used for modelling. It is assumed, that vibrations of the structures are caused by external disturbances, that consist of finite number of harmonic forces with different spatial distribution. The response of the structure can be written as a sum of equivalent frequency components, each of which shape is modelled as a finite sum of the eigenmodes. Radiated sound power is calculated independently for each frequency. According to the initial assumptions described in the previous section, the Rayleigh integral is used to calculate the far-field acoustic pressure distribution. Taking into account decomposition of the spatial velocity distribution on the surface of the considered structure into the eigenmode vectors, following expression for the radiated sound power at frequency $f = \frac{\omega}{2\pi}$ may be written:

$$(1) \quad \Pi = \frac{\rho_o \omega^2}{2\pi c_0} \left| \sum_{n=1}^N \left[\int_0^{2\pi} \int_0^{\frac{\pi}{2}} \hat{W}_n \left(\iint_S \phi_n e^{-jkx \sin \phi \cos \theta} e^{-jky \sin \phi \sin \theta} dS \right) \sin \phi d\phi d\theta \right] \right|^2,$$

where ρ_o and c_0 are the density and the speed of sound of surrounding medium (air), respectively, S denotes the area of considered structure in x and y coordinates, N is the number of considered structural modes and the \hat{W}_n is complex amplitude of mode n whereas ϕ_n denotes its normalized shape function.

In the considered low-frequency range and for plate dimensions much lower than the acoustic wavenelgh in air, radiation patterns of structural modes (considered separately) are quite regular,

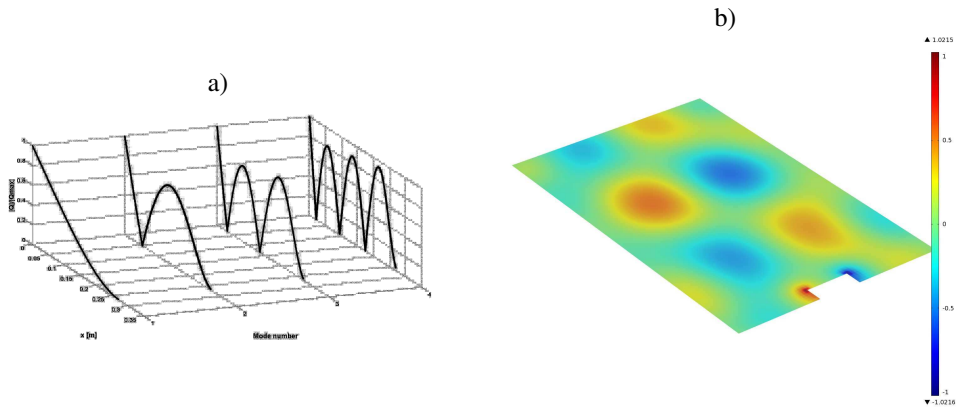


Figure 1. Normalized amplitude of electric charge induced on a **a)** rectangle-shaped piezosensor, as a function of its location on the surface of cantilevered beam for the first four vibration modes **b)** point sensor on a plate surface for an example single vibration mode

close to monopole or dipole source patterns. The „dipole” modes are found to be very weak acoustic radiators. Those observations are important while developing the optimal strategy for the active control system.

3. Determining the optimal parameters of the control system and experimental verification

To minimize radiation efficiency of the controlled structure the following steps need to be executed. First, the parameters of the primary disturbance have to be estimated. Piezosensors are used to determine the frequency components and corresponding complex amplitudes of their decomposition into the structure eigenmodes. Then, the optimal feedback gain factors need to be computed for all piezoactuators. The goal is to minimize the total radiated sound power, given by the Eq. (1).

The location of the piezoelectric components on the surface of the controlled structure determines the ability of the active control system to sense and control specific structural modes. For that reason it is very important to properly choose positions of sensors and actuators, while developing system geometry. Results of an example analysis of sensitivity of different located piezoelectric sensors to specific vibration modes is presented on Figure 1.

Different beam and plate structures with piezoelectric elements mounted on the surfaces were used to verify experimentally conclusions obtained with theoretical and numerical investigations.

4. References

- [1] C.R. Fuller, S.J. Elliot and P.A. Nelson (1996). *Active Control of Vibration*, Academic Press, London.

Acknowledgment

Financial support of Structural Funds in the Operational Programme - Innovative Economy (IE OP) financed from the European Regional Development Fund - Project „Modern material technologies in aerospace industry”, Nr POIG.01.01.02-00-015/08-00 is gratefully acknowledged.

Financial support of Structural Funds in the Operational Programme Innovative Economy (IE OP) financed from the European Regional Development Fund - Project „Smart technologies for safety engineering SMART and SAFE” (No TEAM/2008-1/4, operated within the Foundation for Polish Science Team Programme) is gratefully acknowledged.

CREEP BEHAVIOR UNDER STRESS-CONTROLLED SUBLOOP LOADING IN TINI SHAPE MEMORY ALLOY

K. Takeda¹, H. Tobushi¹ and E. A. Pieczyska²

¹ *Aichi Institute of Technology, 1247 Yachigusa, Yakusa-cho, Toyota, 470-0392, Japan*

² *Institute of Fundamental Technological Research, Polish Academy of Sciences, Pawinskiego 5B, 02-106, Warsaw, Poland*

1. Introduction

Shape memory alloys (SMAs) are remarkable materials characterized by the thermomechanical properties of shape memory and superelasticity. The functional properties of an SMA appear based on the martensitic transformation (MT), and since the MT is sensitive to variations in temperature and stress and to their hysteresis, the deformation properties due to the MT are complex. Research up to now in this area has been mainly concerned with a full loop (or perfect loop) of the MT completion. But in practical applications, temperature and stress are likely to vary in various ranges. If SMA elements are subjected to loads with a subloop (or partial loop, internal loop) in which temperature or stress varies in an incomplete MT range, the conditions for the start and finish of the MT as in a full loop are not satisfied. It can be recognized from this that the subloop deformation behaviour of an SMA is of great importance for an accurate evaluation of the functional properties of SMA elements and for the design of such elements for practical applications. The present study investigates superelastic deformation behavior of TiNi alloy, in subloop loading test, in particular the characteristics of transformation-induced creep deformation in the stress plateau region under constant stress. Variations in the stress-induced martensitic transformation (SIMT) bands during deformation are observed using a microscope, and a thermograph is used to identify the temperature distributions on the surface of the tape specimen. The subloop creep deformation behavior is discussed in terms of the local deformations due to the SIMT.

2. Transformation-induced creep deformation

Figure 1 shows the stress-strain curve obtained from the creep test under a constant stress rate of 0.5 MPa/s up to a strain of 2 % at the upper stress plateau, followed by a constant stress. In Fig. 1, the SIMT starts at a strain of 1.3 % (point A) in the loading process, under a constant stress rate. If stress is controlled so as to remain constant at its level for 2 % (point B), it initially fluctuates slightly before settling down to a constant 438 MPa at a strain of 3.5 % (point C). Strain then continues to increase to about 8 % (point D). This phenomenon of strain increase under constant stress is similar to what is

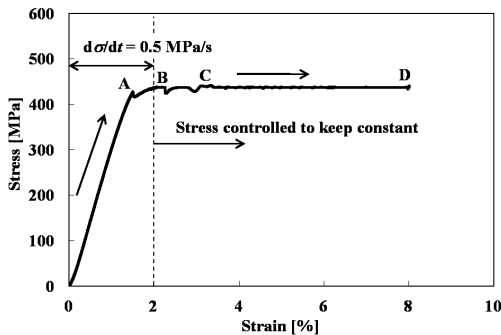


Fig. 1 Stress-strain curve under stress rate of $d\sigma/dt = 0.5$ MPa/s till strain of 2 % followed by stress controlled to remain constant

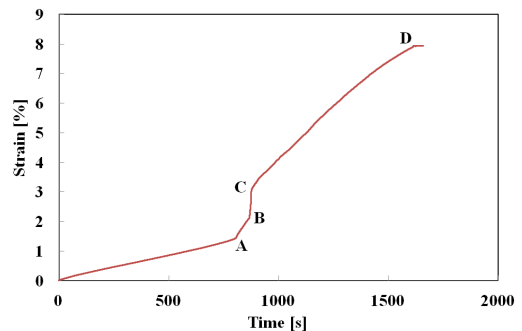


Fig. 2 Variation in strain with passing of time in creep test

found with normal creep deformation. The explanation in this case would be that the SIMT causes the temperature to increase during loading up to a strain of 2 %, after which it decreases under a constant stress. Conditions are therefore satisfied for the SIMT to progress and strain increases.

The relationship between strain and time is shown in Fig. 2. As can be seen in Figs. 1 and 2, the rate of increase in the strain rises sharply at the level of 1.3 %, following the start of the SIMT. Stress fluctuates slightly between strain levels 2 % and 3.5 % while strain increases rapidly. After a strain of 3.5 % is reached, stress settles down to be constant and strain increases at an almost constant rate of $6.5 \times 10^{-5} \text{ s}^{-1}$. Strain goes on increasing to about 8% before finally becoming constant.

3. Progress of creep strain

Figure 3 shows thermograms of the temperature distributions on the surface of a specimen, and Fig. 4 shows photographs of the SIMT bands.

As can be seen from the temperature distributions, the SIMT process due to the exothermic reaction first appears at the two ends during loading at a strain level of 2 %, and then spreads toward the center where the bands combine into one, completing the SIMT. When the stress is held constant at the level reached for 2 % strain, the SIMT bands spread due to a decrease in temperature. Transformation heat is generated at each new point of advance in the SIMT process, which leads to a chain reaction in the SIMT, resulting in creep deformation.

In Fig. 4, the SIMT bands in the photographs are tinted blue to enhance the visibility of the propagation progress. After first appearing at the two ends, the bands spread toward the center as stress is held constant. All of the SIMT bands photographed in Fig. 4 also appear in the same positions on the reverse surface of the specimen and can be considered as continuing throughout the cross section of the tape. This means that the area fraction occupied by the M-phase on each surface must be equivalent to the volume fraction occupied in the body as a whole. In this way, the volume fraction of the M-phase can be estimated from the measured area fraction of the SIMT bands. The relationship between the volume fraction of the M-phase and strain is shown in Fig. 5. The volume fraction of the M-phase increases in proportion to an increase in strain.

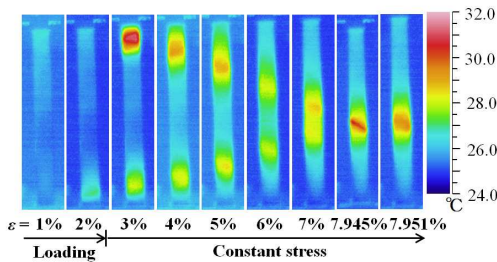


Fig. 3 Thermograms of temperature distribution on the specimen surface under $d\sigma/dt = 0.5 \text{ MPa/s}$ up to a strain ϵ of 2 % followed by constant stress

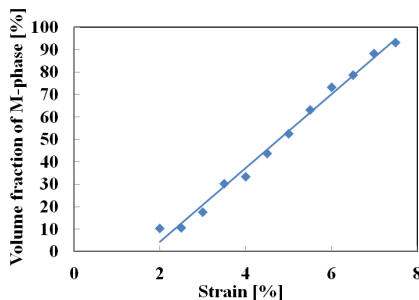


Fig. 5 Relationship between volume fraction of M-phase and strain during creep deformation

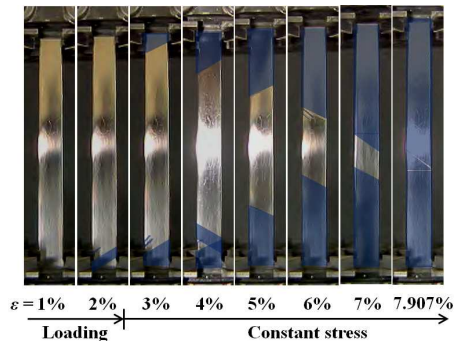


Fig. 4 Photographs of specimen surface at various strains ϵ under stress rate of $d\sigma/dt = 0.5 \text{ MPa/s}$ up to a strain ϵ of 2 % followed by constant stress

Structural Mechanics, Optimization and Reliability

STOCHASTIC MODEL REDUCTION TECHNIQUES APPLIED TO INVERSE PROBLEMS IN STRUCTURAL ENGINEERING

T. Garbowski, A. Knitter-Piatkowska and D. Jaskowska
Institute of Structural Engineering, Poznan, Poland

1. Introduction

In the present paper the stochastic programming technique based on Gaussian Processes [1, 2] applied to inverse problems in structural engineering, e.g. material parameters characterization and damage detection is presented. The inverse analysis often uses a numerical model as an counterpart of experiment in order to build the discrepancy function between experimentally measured and numerically computed quantities, such as displacements, reaction forces, strains, accelerations, etc. If the numerical model is complex the iterative minimization procedure becomes very expensive, therefore not attractive from practical point of view or when the test has to be performed 'in situ' (i.e. without a computer which can handle heavy computations). The alternative is to use a surrogate which approximates the behavior of the numerical model but is much simpler thus less expensive. The surrogate is usually constructed as a 'black box' where for the approximation the following methods, among others, are commonly used: Radial Basis Functions (RBFs), Polynomials, Proper Orthogonal Decomposition (POD) combined with RBFs, Artificial Neural Networks (ANNs) or Gaussian Processes (GP).

All listed here approximation techniques require the numerically computed responses (i.e. training samples) in order to build a smooth and accurate analytical approximation of the sought solution. Ideally would be to use a method which need the smallest possible number of 'training' points and in the same time is precise and robust. The approximation method based on GP satisfies all above mentioned requirements: it gives very good results when the number of training examples is limited. Another important feature of GP is that it gives not only the approximation of the mean value of sought parameter but also its standard deviation. This feature gives a possibility of automatic and systematic improvement of the solution, because the computed standard deviation of the model prediction provides a localization where the approximation is weak, (and therefore it points out where, in the parameter space, the additional experimental or numerical data are necessary to improve the approximation).

An important problem during the construction of the surrogate is usually a big number of data, i.e. control parameters (e.g. material, geometrical features) and state parameters (measurable quantities). The probable correlations between the control variables as well as between the state variables can be computed, and consequently used to reduce the number of model parameters, by the application of Principal Component Analysis (which is a part of the proposed method). The presented stochastic algorithm is formulated within Bayesian framework thus provides additional information about the magnitude of correlation between state and control variables, i.e. the relevance of input-output correlation. This is very important if one would like to exclude from the model the parameters which not influence the measurable quantities (i.e. the measurable quantities are not sensitive to those parameters).

The stochastic model reduction techniques based on GP have, however, one significant disadvantage, namely the Gaussian Processes are usually parameterized in terms of their covariance functions. This makes it difficult to deal with multiple outputs, because ensuring that the covariance matrix is positive definite is problematic. An alternative formulation is to treat Gaussian processes as white noise sources convolved with smoothing kernels, and to parameterize the kernel instead (see [3]). Using this approach, one can extend Gaussian Processes to handle multiple, coupled outputs.

2. Application

In the present communication two examples are used to show the application of above described model reduction techniques. The first example shows the application of multi-output GP to damage detection in the structural elements (as beams and plates) through Wavelet Transformation [4, 5] and Inverse Analysis. The second application shows the use of GP as numerical model surrogate in characterization of glass and foil parameters in SGP and PVP laminated glasses [6, 7] through Digital Image Correlation and Inverse Analysis [8].

In both examples GP based approximation serves as a surrogate of numerical model, which in combination with iterative minimization algorithm (e.g. trust-region algorithm) gives very fast and accurate results, both in damage detection and material model parameters identification. By iterative comparing of experimental data to data obtained from the multi-output GP approximation model the discrepancy is minimized and sought parameters (i.e. damage localization and size, as well as material constants in laminated glass) can be vary fast identified, provided the surrogate is appropriate constructed.

3. Summary

The GP approximation model which serve as a numerical model reduction is used here in combination with Inverse Analysis to solve structural engineering problems, e.g. damage detection and constitutive models identification. The work is mainly focus on the proper construction of the GP model, namely on: (1) training process based on minimal number of training samples, by making use of automatic samples selection through computed standard deviation of model prediction; (2) control and state parameters compression based on PCA techniques; (3) control parameters reduction based on input-output correlation; (4) proper construction of multi-output GP.

4. References

- [1] C.M. Bishop (2007). *Pattern Recognition and Machine Learning*, Springer.
- [2] C.E. Rasmussen, C.K.I. Williams (2006). *Gaussian Processes for Machine Learning*, MIT Pres.
- [3] M.A. Alvarez, N.D. Lawrence (2011). Computationally Efficient Convolved Multiple Output Gaussian Processes *Journal of Machine Learning Research*, **12**, 1459-1500.
- [4] M. Rucka, K. Wilde (2006). Application of continuous wavelet transform in vibration based damage detection method for beams and plates, *Journal of Sound and Vibration*, **297**, 536-550.
- [5] A. Knitter-Piatkowska, Z. Pozorski, A. Garstecki (2006) Application of discrete wavelet transformation in damage detection. Part I: Static and dynamic experiments. *Computer Assisted Mechanics and Engineering Sciences*, **13**, 21-38.
- [6] J. Belis, J. Depauw, D. Callewaert, D. Delince, R. Van Impe (2009). Failure mechanisms and residual capacity of annealed glass/SGP laminated beams at room temperature, *Engineering Failure Analysis*, **16**, 1866-1875.
- [7] L. Biolzi, S. Cattaneo, G. Rosati (2010). Progressive damage and fracture of laminated glass beams, *Construction and Building Materials*, **24**, 577-584.
- [8] T. Garbowski, G. Maier, G. Novati (2011). On calibration of orthotropic elastic-plastic constitutive models for paper foils by biaxial tests and inverse analyses, *Structural and Multidisciplinary Optimization*, DOI: 10.1007/s00158-011-0747-3.

CELLULAR AUTOMATA AS EFFICIENT GENERATOR OF OPTIMAL TOPOLOGIES

B. Bochenek, K. Tajs-Zielińska

Institute of Applied Mechanics, Cracow University of Technology, Cracow, Poland

1. Introduction

Heuristic evolutionary methods are gaining nowadays widespread popularity among researchers because they are easy for numerical implementation, do not require gradient information, and one can easily combine this type of algorithm with any finite element structural analysis code. Among such techniques are also Cellular Automata. Cellular Automata (CA) are mathematical idealization of a physical systems in which the design domain is divided into a lattice of cells, states of which are updated synchronously in discrete time steps according to some local rules. The principle of the CA is that global behavior of the system is governed by cells that only interact with their neighbors. CA have attracted researchers from various disciplines. This concept has been found attractive also in optimal design because of its simplicity and versatility and since CA methodology can be adopted both to optimal sizing and topology optimization. The aim of this paper is to present a novel CA approach which can be used in topology optimization. The new efficient local update rules are proposed and the performance of the numerical algorithm based on the presented concept is discussed.

2. Local design rules for topology optimization

The idea of Cellular Automata is to replace a complex problem by a sequence of relatively simple decision making. In engineering implementation this leads to decomposition of considered domain into a set of cells which build an uniform lattice. The particular cell together with cells to which it is connected form neighborhood, and it is assumed that the interaction between cells takes place only within the neighborhood. The special local rules are selected in order to control evolution of each neighborhood state. The rules are identical for all neighborhoods and are applied simultaneously to each of them. The rules operate over a large number of cells that carry on only local information. By applying the rules repetitively to locally updated physical quantities the process converges to a description of the global behavior of the system. In topology optimization one searches for a distribution of material within a design domain that is optimal in some sense. The design process consists in redistribution of a material and parts that are not necessary from objective point of view are selectively removed. Topology optimization usually ends up in finding material/void distribution that is visualized by black and white regions over the design domain. The power law approach defining solid isotropic material with penalization (SIMP) proposed for example by Bendsoe [1] can easily be adapted here with design variables being relative densities of a material. The elastic modulus of each cell element is modelled as a function of relative density d_i using power law: $E_i = d_i^p E_0$, $d_{min} \leq d_i \leq 1$. This power p penalizes intermediate densities and drives design to a black-and-white structure. One of the proposed design rules includes information gathered within an individual cell neighborhood, as well as carries additional supplementary information influenced by all neighborhoods:

$$d_i^{(t+1)} = d_i^{(t)} \left(1 + \alpha \frac{\bar{U}_i^{(t)} - \beta \bar{U}^{(t)}}{U_i^{(t)}} \right)$$

In the above $\bar{U}_i^{(t)}$ represents average value of strain energy density found for cell neighborhood and $\bar{U}^{(t)}$ stands for the global average. By modifying values of tuning parameters α , β it is possible to weigh these two items of information, hence control and modify performance of the numerical

algorithm. It is worth noting that some other local rules proposals have been presented in former authors' papers e.g. [2].

3. Optimal topologies

Selected Cellular Automata optimal topologies obtained within the framework of this paper illustrate the proposed concepts. Two examples are presented below: in the Figure 1 a cantilever with square-shaped line support, and a spatial chair-like structure in the Figure 2.

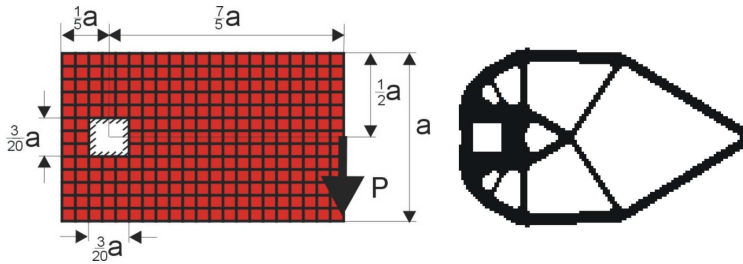


Figure 1. 128×40 cells ($1\text{mm} \times 1\text{mm}$), $P=100\text{ N}$, $a=40\text{ mm}$. Iteration 40, compliance 152.1 Nmm , volume fraction 0.25

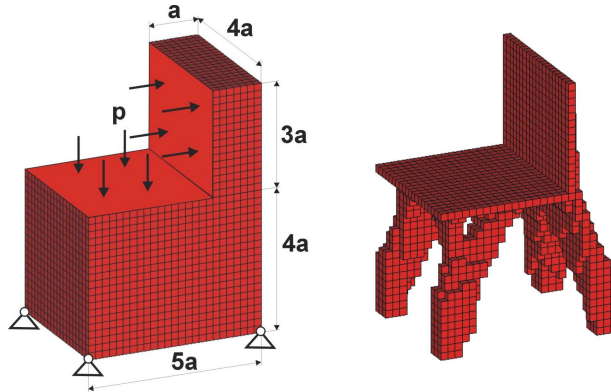


Figure 2. $5 \times 20 \times 15 + 25 \times 20 \times 20$ cells ($1\text{mm} \times 1\text{mm} \times 1\text{mm}$), $a=5\text{ mm}$, $p=100\text{ N/mm}^2$. Iteration 33, compliance 119.6 Nmm , volume fraction 0.18

4. Closing remarks

The main advantage of the developed CA algorithm is that it is a fast convergent technique and usually requires far less iterations as compared to other approaches to achieve the solution. What is also important it does not require any additional density filtering. There are not many parameters to adjust, and it is very easy to implement parallel computations in Cellular Automata algorithms. Finally, for topology optimization problems changing mesh density does not influence resulting topologies and solutions are free from checkerboard effect.

5. References

- [1] M.P. Bendsoe (1995). *Optimization of structural topology, shape and material*, Springer, Berlin/Heidelberg/NewYork.
- [2] B. Bochenek and K. Tajs-Zielińska (2012). Novel local rules of Cellular Automata applied to topology and size optimization, *Engineering Optimization*, **44**, 1, 23-35.

SHAKEDOWN LIMIT LOADS FOR PERIODIC HETEROGENEOUS STRUCTURAL ELEMENTS

M. Chen, A. Hachemi and D. Weichert

Institute of General Mechanics, RWTH-Aachen, Germany

Direct methods, namely shakedown and limit analysis, are used effectively for the prediction of structure failure behavior under variable loads with unknown evolution in time. The extension of the classical shakedown theorems to thermal loadings are mainly applied in homogeneous materials [1]. In this work, a numerical method is presented to determine the shakedown and limit loads of periodically heterogeneous structures under thermal and structural loading.

Shakedown analysis of heterogeneous materials generally concerns two scales [2, 3]. On microscopic scale, the Melan's lower-bound shakedown theorem is applied to representative volume element (RVE). The difficulty here lies on the implementation of periodic boundary conditions. According to the type of the prescribed loading condition, either a strain approach or a stress approach can be adopted for structural loading [4]. By thermal loading, periodic coupling boundary conditions of RVE must be considered and the quadratic yield condition of von Mises type, has to be satisfied [5]

$$F(\alpha\sigma^E + \bar{p}, \sigma_T(\vartheta)) < 0 \quad \text{in } V$$

It means that shakedown may happen if there exist a safety factor α and a time-independent and periodic residual stress field \bar{p} in the RVE, so that the total stress field $\alpha\sigma^E + \bar{p}$ does not violates the yield condition at associated temperature field ϑ .

On the macroscopic scale, the global response of the composites is investigated. The link between local stress field in RVE and global admissible stress field is made by means of homogenization theory [6]. In the shakedown theory for composite materials with periodic microstructure, the macroscopic stress is decomposed as follows

$$\Sigma = \frac{1}{V} \int_V (\alpha\sigma^E + \bar{p}) dV = \frac{1}{V} \int_V \alpha\sigma^E dV + \frac{1}{V} \int_V \bar{p} dV \quad \text{with} \quad \frac{1}{V} \int_V \bar{p} dV = 0$$

The effective properties of the composite are determined from geometrical and material data available from the study of a RVE. For periodic composites, these data are completely specified from geometrical and mechanical properties of a unit cell which generates by periodic repetition the whole microstructure of the composite.

The use of Melan's shakedown theorem in composites leads to a nonlinear convex optimization problems, which is characterized by large number of variables and constraints. The numerical implementation mainly involves two tools: finite element method and large scale nonlinear optimization method. In term with principle of virtual work, the discretization is carried out for the purely elastic stress field σ^E and the residual stress field \bar{p} . The use of solid non-conforming elements, constructed from bilinear shape functions and enriched by internal second-order polynomials, may not only increase the basic accuracy of shakedown and limit analysis of composites, but also reduce the scale of optimization problem [7]. For the solution of such large scale convex mathematical programming, an interior-point-algorithm based optimization software package is adopted [8], which is proved to be reliable and efficient [1].

In this paper, this methodology is illustrated by the application to a structure made of composites under variable pressure and temperature loads. The proposed method provides a direct numerical approach to evaluate the macroscopic properties of heterogeneous materials with periodic micro- or meso-structure as a useful tool for the design of structures.

- [1] J.W. Simon, M. Chen and D. Weichert (2012). Shakedown analysis combined with the problem of heat conduction. *J. Pressure Vessel Technol.*, **134**, 021206_1-8.
- [2] D. Weichert, A. Hachemi and F. Schwabe (1999). Application of shakedown analysis to the plastic design of composites, *Arch. Appl. Mech. (Struct. Mech.)*, **69**, 623-633.
- [3] D. Weichert and A. Ponter (2009). *Limit states of Materials and Structures*. Springer, Wien/New-York.
- [4] P.Suquet (1982). *Plasticité et homogénéisation*. PhD. Thesis, Université Pierre et Marie Curie, Paris VI.
- [5] J. A. König (1987). *Shakedown of elastic-plastic structures*. Amsterdam-Oxford-New York-Tokyo, Elsevier.
- [6] H. Magoaric, S. Bourgeois and O. Débordes (2004). Elastic plastic shakedown of 3d periodic heterogenous media: a direct numerical approach, *Int. J. Plasticity*, **20**, 1655-1675.
- [7] M. Chen, A. Hachemi and D. Weichert (2010). A non-conforming finite element for limit analysis of periodic composites, *Proc Appl Math Mech*, **106**, 405-406.
- [8] A. Wächter and L. Biegler (2006). On the implementation of an interior-point filter line-search algorithm for large-scale nonlinear programming, *Math Program*, **106**, 25-57.

ONLINE LOCAL STRUCTURAL HEALTH MONITORING USING THE SUBSTRUCTURE ISOLATION METHOD

J. Hou¹, Ł. Jankowski² and J. Ou^{1,3}

¹ *School of Civil Engineering, Dalian University of Technology, Dalian 116024, P. R. of China*

² *Institute of Fundamental Technological Research (IPPT PAN), Warsaw, Poland*

³ *School of Civil Engineering, Harbin Institute of Technology, Harbin 150090, P. R. of China*

1. Introduction

This paper proposes a Substructure Isolation Method (SIM) for online local health monitoring at the substructural level. The SIM [1] includes two key steps: isolation of the substructure, and its local identification. Isolated substructure is an independent virtual structure, which is isolated from the global structure with virtual supports placed in the interface DOFs. Its response is constructed by such a linear combination of time series of measured local responses that the desired boundary conditions are satisfied and all outside influences are removed. Given the combined response, the substructure is locally identified using any of the standard methods aimed originally at global analysis. This is unlike other substructuring methods, see e.g. [2,3], which require dedicated methods in order to deal simultaneously with structural damages and generalized interface forces.

The SIM has been originally [1] used in off-line analysis and required zero initial conditions. Here, it is used for local online monitoring by a repeated application to successively extracted measurement time series. Non-zero initial conditions are allowed; they are reflected in a free vibration component of the constructed responses of the isolated substructure.

2. Sensors, excitations and measurement time series

The substructure is virtually isolated from the global structure by placing virtual supports in all its interface DOFs. These supports are implemented by physical interface sensors x_i , $i=1, \dots, I_B$, and used for the purpose of isolation only. Besides, there are I_S internal sensors y_i , $i=1, \dots, I_S$, which are placed inside the substructure in order to measure its response. The isolation process consists of altering the readings y_i of the internal sensors (using the reading of the interface sensors x_i) in such a way that the result equals their reading *as if* they were placed in a physically isolated substructure.

Here, no intentionally applied excitations of the substructure are considered. That is, the sensors measure only its free response to operational excitations occurring in the outside structure, such as wind, traffic, modal hammer, running engines, etc.

For the purpose of online monitoring, it is assumed that the responses x_i and y_i are measured continuously. The time series measured this way $\{x_i(t_k)\}_k$ and $\{y_i(t_k)\}_k$ are divided into N successive and possibly overlapping time sections each of length K , $\mathbf{x}_i^n = \{x_i^n(t_k)\}_{k=1, \dots, K}$ and $\mathbf{y}_i^n = \{y_i^n(t_k)\}_{k=1, \dots, K}$, where k indexes the time steps anew within each section, n is the number of the time section and $t_1^{n-1} < t_1^n < t_1^{n+1}$ for all n . In each time section, the readings of all the interface sensors \mathbf{x}_i^n , $i=1, \dots, I_B$, are combined into a single interface response vector \mathbf{X}^n . The readings of all the internal sensors \mathbf{y}_i^n , $i=1, \dots, I_S$, are combined into a single internal response vector \mathbf{Y}^n , too.

3. The combined response and isolation

Assume that the measurement vectors \mathbf{X}^n and \mathbf{Y}^n for $n=1, \dots, N+1$ are extracted from the measured time series and available. Consider the following combined response vectors:

$$(1) \quad \mathbf{C}_X = \mathbf{X}^{N+1} + \sum_{n=1}^N \alpha_n \mathbf{X}^n = \mathbf{X}^{N+1} + \mathbf{X}\alpha, \quad \mathbf{C}_Y = \mathbf{Y}^{N+1} + \sum_{n=1}^N \alpha_n \mathbf{Y}^n = \mathbf{Y}^{N+1} + \mathbf{Y}\alpha$$

where the vector $\boldsymbol{\alpha}$ collects is combination coefficients α_n , and \mathbf{X} and \mathbf{Y} are matrices composed of column vectors \mathbf{X}^n and \mathbf{Y}^n . If the substructure is assumed to be linear, the combined response vectors \mathbf{C}_X and \mathbf{C}_Y are its valid responses (solutions to its equation of motion), and they can be thus used for monitoring. Moreover, if the combination coefficients are selected in such a way that the combined interface response vanishes,

$$(2) \quad \mathbf{C}_X = \mathbf{X}^{N+1} + \mathbf{X}\boldsymbol{\alpha} = \mathbf{0}, \quad \boldsymbol{\alpha} = -\mathbf{X}^{-1}\mathbf{X}^{N+1},$$

then the corresponding combined internal response vector \mathbf{C}_Y ,

$$(3) \quad \mathbf{C}_Y = \mathbf{Y}^{N+1} - \mathbf{Y}\mathbf{X}^{-1}\mathbf{X}^{N+1},$$

is the response of the isolated substructure (the actual substructure, *as if* it was physically isolated from the outside structure).

4. Online local structural health monitoring

The response \mathbf{C}_Y of the isolated substructure can be used with any general SHM approach aimed originally at global monitoring [4]. Online monitoring is possible by repetitive (1) updating of the set of N time sections used to construct \mathbf{X}^n and \mathbf{Y}^n with new measurements, (2) application of the SIM to the updated set, and (3) application of an SHM method to the constructed response.

5. Numerical and experimental examples

The isolation approach was verified experimentally using an aluminum cantilever beam and a virtual pinned support, which was implemented by a transverse velocity sensor and a strain sensor. The damage was identified by fitting the natural frequencies of the modeled substructure [5] to the identified frequencies of the isolated substructure [6]. Due the space constraints of this abstract, the results will be presented during the conference.

6. Acknowledgements

The authors gratefully acknowledge the support of National Natural Science Foundation of China (NSFC) (51108057, 51108066), of the Project of National Key Technology R&D Program (China) (2011BAK02B01, 2011BAK02B03) and of China Postdoctoral Science Foundation (20110490142). Financial support of Structural Funds in the Operational Programme—Innovative Economy (IE OP) financed from the European Regional Development Fund—Projects ‘Modern material technologies in aerospace industry’ (POIG.0101.02-00-015/08) and ‘Health monitoring and lifetime assessment of structures’ (POIG.0101.02-00-013/08-00) is gratefully acknowledged.

6. References

- [1] J. Hou, Ł. Jankowski and J. Ou (2012). Experimental study of the substructure isolation method for local health monitoring. *Struct. Control Hlth.* Doi: 10.1002/stc.443
- [2] K.F. Tee, C.G. Koh and S.T. Quek (2009). Numerical and experimental studies of a substructural identification strategy. *Struct. Health Monit.*, **8**(5):397–410.
- [3] C. Koh and K. Shankar (2003). Substructural identification method without interface measurement. *J. Eng. Mech.*, **129**(7):769–776.
- [4] W. Fan and P. Qiao (2011). Vibration-based Damage Identification Methods: A Review and Comparative Study. *Struct. Health Monit.*, **10**(1):83–111.
- [5] P. Vanhonacker (1980). Differential and difference sensitivities of natural frequencies and mode shapes of mechanical structures. *AIAA Journal*, **18**(12):1511–1514.
- [6] R.A. De Callafon, B. Moaveni, J.P. Conte, X. He and E. Udd (2008). General realization algorithm for modal identification of linear dynamic systems. *J. Eng. Mech.*, **134**(9):712–722.

IMPLEMENTATION OF OPTIMIZATION TECHNIQUES IN DETERMINING ELASTIC-PLASTIC AND VISCO-PLASTIC PROPERTIES FROM INSTRUMENTED INDENTATION CURVES

J.J. Kang, A.A. Becker and W. Sun

*Department of Mechanical, Materials and Manufacturing Engineering
University of Nottingham, Nottingham NG7 2RD UK*

Instrumented indentation techniques at micro or nano-scales have become more popular for determining mechanical properties from small samples of material [1]. These techniques can be used not only to obtain and to interpret the hardness of the material but also to provide information about the near surface mechanical properties and deformation behaviour of bulk solids and/or coating films. In particular, various approaches [1, 2] have been proposed to evaluate the elastic-plastic properties of power-law materials from the experimental loading-unloading curves. In order to obtain a unique set of elastic-plastic properties, many researchers have proposed to use more than one set of loading-unloading curves obtained from different indenters [3, 4].

A combined Finite Element (FE) analysis and optimisation approach [5] developed by the authors, using three types of (single) indenter (Conical, Berkovich and Vickers), for determining the elastic-plastic material properties, using one set of ‘simulated’ target FE loading-unloading curves and one set of real-life experimental loading-unloading curves, will be described. The results obtained have demonstrated that excellent convergency can be achieved with the ‘simulated’ target FE loading-unloading curve, but less accurate results have been obtained with the real-life experimental loading-unloading curve. This combined technique has been extended to determine the elastic and visco-plastic material properties using only a single indentation ‘simulated’ loading-unloading curve based on a two-layer viscoplasticity model [6].

A combined dimension analysis and optimisation approach [7] has been developed and used to determine the elastic-plastic material properties from loading-unloading curves with single and dual indenters. The dimension functions have been established based on the parametric study using FE analyses and the loading and linearised unloading portions of the indentation curves. It has been demonstrated that the elastic-plastic material properties cannot be uniquely determined by the test curves of a single indenter, and the unique or more accurate results can be obtained using the test curves from dual indenters.

Since the characteristic loading-unloading responses of indenters can be approximated by the results of dimensional analysis, a simplified approach [8] has been used to obtain the elastic-plastic mechanical properties from loading-unloading curves, using a similar optimisation procedure. It is assumed that the loading-unloading portions of the curves are empirically related to some of material properties, which avoids the need for time consuming FE analysis in evaluating the load-deformation relationship in the optimization process. This approach shows that the issues of uniqueness have been raised by using a single indenter and more accurate estimation of material properties with dual indenters can be obtained by reducing the bound range of mechanical parameters.

This paper highlights some recent development of optimization techniques, for use in determining elastic-plastic and visco-plastic properties from instrumented indentation loading-unloading curves. The optimization approaches based on FE analysis, dimension analysis and a simplified empirical method are briefly described. The general performance and the applicability of those techniques are evaluated and some of limitations and areas that need to be exploited in the future are briefly addressed.

References

- [1] W. C. Oliver and G. M. Pharr (1992). An improved technique for determining hardness and elastic modulus using load and displacement sensing indentation experiments. *J. Mater Res.*, **7**, 1564-1583.
- [2] M. Dao, N. Chollacoop, K. J. Van Vliet, T. A. Venkatesh and S. Suresh (2001). Computational modelling of the forward and reverse problems in instrumented sharp indentation, *Acta Mater.*, **49**, 2899-2918.
- [3] J. Luo and J. Lin (2007). A study on the determination of plastic properties of metals by instrumented indentation using two sharp indenters, *Int. J. Solids Struct.*, **44**, 5803-5817.
- [4] N. Chollacoop, M. Dao and S. Suresh (2003). Depth-sensing instrumented indentation with dual sharp indenters, *Acta Mater.*, **51**, 3713-3729.
- [5] J. J. Kang, A. A. Becker and W. Sun, Determining elastic-plastic properties from indentation data obtained from finite element simulations and experimental results, *Int. J. Mech. Sci.* (Under Review)
- [6] J. J. Kang, A. A. Becker and W. Sun, Determination of elastic and visco-plasticity material properties from indentation tests using a combined finite analysis and optimization approach. *Computation material science* (Under Review)
- [7] J. J. Kang, A. A. Becker and W. Sun (2011). A combined dimensional analysis and optimization approach for determining elastic-plastic properties from indentation tests. *J. Strain Analysis*, **46**, 749-759.
- [8] J. J. Kang, B. Martin, A. A. Becker and W. Sun, Using indentation tests to obtain elastic-plastic material properties based on finite element simulation and simplified dimensional equations. *11th Int. Conf. on Computational structures Technology, 4-7 Sept, 2012, Dubrovnik, Croatia.* (Abstract accepted)

STRUCTURAL DAMAGE DETECTION THROUGH WAVELET DECOMPOSITION AND SOFT COMPUTING

A. Knitter-Piatkowska, T. Garbowski and A. Garstecki
Institute of Structural Engineering, Poznan, Poland

1. Introduction

Damage identification belongs to the field of problems connected with structural health monitoring and safety assessment. Safety of the structure can be decreased by defects evolving in the structure which may take the form of cracks, voids, decohesions etc. It is expected that various methods of damage identification provide information whether damage exists or not. Among a large number of non-destructive testing one can propose for example X rays, vibration, acoustic emission, heat transfer, etc. These methods of inspection allow to identify the position of damage and possibly also its form and magnitude. In this work methods of damage identification based on measurement of structural response to the actual actions or actions specially planned and applied to the existing defective structure are proposed. Different types of structural response namely displacements, velocities or accelerations can be monitored. By the comparison of the response of the existing structure with the response of its computer model containing expected damage parameters one can construct the discrepancy function. Minimization of the differences between measurable quantities computed by the numerical model and recorded on the real defective structure allows to obtain the information on the defects. Recently alternative approaches have been developed where data processing techniques are applied to the response signal of the damaged structure only, therefore the time-consuming optimization procedures can be avoided. At present the great potential is assigned to methods of artificial intelligence e.g. Artificial Neural Networks (ANNs) [1] or methods of signal processing e.g. Fast Fourier Transform (FFT) and Wavelet Transform (WT) in continuous (CWT) or discrete (DWT) form.

In this work the attention is focused on Wavelet Transformation in its discrete form. The most fundamental challenge is the fact that damage is typically local phenomenon and may not significantly influence the global response of structures. Signal decomposition using WT allows to detect and localize the damage [2] because wavelets demonstrate strong disturbance in a place where the damage is localized. To assess the magnitude of the damage Lipschitz exponent for example can be used. However, data processing of the structural response signal using WT proved to be rather ineffective in identification of the type or shape of a defect. Therefore, the possibility of using a new approach of more precise damage identification based on Artificial Neural Networks is studied. Here the attention is focused on Radial Basis Function Networks (RBFNs).

2. Description of the proposed method

The proposed method uses both Discrete Wavelet Transformation and Artificial Neural Networks as a damage detection tools which, in combination, gives possibility to detect not only the localization of damage [3] but also its shape and/or size. All geometrical features of defect together with its localization in the structure form a vector of parameters \mathbf{x} to be identified. In order to verify if such identification can be done in the real experiment, it is commonly accepted to build first a computer model which mimic the examined structure and perform on it the numerical identification procedure. Usually a pseudo-experimental validation analysis consist of two steps: (1) first a reference model with a-priori chosen parameters \mathbf{x}^* is computed and all necessary signals are stored; (2) later the numerous of identification procedures are performed starting from different values of $\mathbf{x}_i \neq \mathbf{x}^*$

in order to check if convergence to known solution \mathbf{x}^* can be obtained. Alternative to (2) is to use, instead of iterative solver, the ANN for \mathbf{x}^* prediction. ANNs provides a very fast identification tool which can be used 'in situ' on a portable computer without any time-consuming computations nor sophisticated software. However ANNs require to be trained, which, in general, is an expensive process if many training examples need to be generated, yet the training is done once-for-all in the preliminary phase (i.e. not during the identification phase). Here the training samples are computed by the Finite Element (FE) model, which for various damage parameter vectors \mathbf{x}_i computes the response signals (displacement and acceleration fields). Then the signal is transformed through DWT and the wavelet coefficients are computed; all coefficients form a vector \mathbf{c} , and together with corresponding damage parameters gathered in \mathbf{x} , are used as training data for ANNs (each training sample consists of damage parameter vector \mathbf{x} as ANNs' output and wavelet transformation coefficient vector \mathbf{c} as an input).

In the first step of validation the different types of damage (e.g. inclusions, voids, stiffness or cross-section reduction, etc.) are employed in the numerical model in order to check which defect type perturbs the most the measurable signals and therefore the sensitivity of the signal with respect to damage parameters. The recorded signals are the deformations and accelerations of various points in the structure (here beams and plates are investigated). In beams defect is modeled as a step-wise reduction of cross-section on a small area and/or stiffness reduction whereas in plate structures defects have the form of voids or inclusions (also reduction of cross-section and stiffness is checked).

In the later stage the attention is focus on proper training techniques of ANNs and reduction of input data (wavelet transformation coefficients vector \mathbf{c}) through principal component analysis. The minimum number of ANNs training samples (i.e. the number of damage scenarios) necessary in appropriate construction of model approximation is also studied here in order to reduce the number of experiments to be performed.

3. References

- [1] Z. Waszczyszyn and L. Ziemiański (2001). Neural networks in mechanics of structures and materials - new results and prospects of applications, *Computers and Structures*, **79**, 2261-2276.
- [2] A. Knitter-Piatkowska, Z. Pozorski and A. Garstecki (2006). Application of discrete wavelet transformation in damage detection. Part I: Static and dynamic experiments, *Computers Assisted Mechanics and Engineering Sciences*, **13**, 21-38.
- [3] M. Rucka and K. Wilde (2010). Neuro-wavelet damage detection technique in beam, plate and shell structures with experimental validation, *Journal of Theoretical and Applied Mechanics*, **48**, 579-604.

DESIGN AND ANALYSIS OF COMPLIANT MECHANISMS WITH FLEXURE HINGES

R. Lammering, F. Dirksen, and M. Rösner

*Institut für Mechanik, Helmut-Schmidt-Universität / Universität der Bundeswehr Hamburg
Holstenhofweg 85, 22043 Hamburg*

1. Introduction and motivation

In order to create machine tools for small-scale applications, compliant mechanisms have become quite popular in recent years as an alternative to rigid body systems connected by conventional pin joints. Compliant mechanisms are flexible, monolithic structures whose overall motion is a result of the elastic deformation of certain components, so called flexural hinges. Compliant mechanisms are potentially more accurate, have superior scalability, are cleaner, less noisy and, most important, less expensive to manufacture and maintain than conventional devices.

However, designing compliant mechanisms is difficult and non-intuitive due to their inherent complex overall deformation. Therefore, a topology optimization algorithm based on a continuum design domain is applied to maximize the motion on a user-specified output path. Fatigue effects on the flexural hinges can lead to premature failure of the entire CM under dynamic loading conditions.

To describe the mechanical behavior of a feed unit in an accurate way, very large and sparse finite element models arise. Thus, the numerical simulations require an unacceptable amount of time and memory space. This fact and the need for efficient control algorithms motivate the introduction and application of model order reduction methods.

2. Topology optimization for compliant mechanisms

A topology optimization procedure is used for the design of large-displacement, path-following compliant mechanisms possessing optimized flexure hinges. It is based on a continuum design domain is applied to maximize the motion $\mathbf{u}_{\text{out}}(\mathbf{x})$ on a user-specified output path $\mathbf{u}_{\text{out}}^{\text{spec}}$, as shown in the upper box of Fig. 1. Non-linear geometric effects are taken into account to ensure proper modelling of large displacements occurring in compliant mechanisms. A robust and efficient staggered optimization scheme, based on optimality criteria method and globally convergent method of moving asymptotes, is implemented to solve the optimization problem \mathbb{P} written as

$$\mathbb{P} = \begin{cases} \underset{X}{\text{minimize}} & f(\mathbf{x}) = -\|\mathbf{u}_{\text{out}}(\mathbf{x})\| \\ \text{subject to} & g_1(\mathbf{x}) = \|\mathbf{u}_{\text{out}}(\mathbf{x}) - \mathbf{u}_{\text{out}}^{\text{spec}}\| - \epsilon \leq 0 \\ & g_2(\mathbf{x}) = x_i - x^{\text{spec}} \leq 0, i = 1, \dots, n \\ & \mathbf{K}(\mathbf{u})\mathbf{u} = \mathbf{f} \\ & \mathbf{x} \in X = \{\mathbf{x} \in \mathbb{R} : \underline{x}_i \leq x_i \leq \bar{x}_i, i = 1, \dots, n\}, \end{cases}$$

with x_i as the design variables (i.e. densities of n elements), x^{spec} as its specified maximum value, and $\mathbf{K}(\mathbf{u})$, \mathbf{u} and \mathbf{f} as the stiffness matrix, displacement vector and external load vector, respectively. The obtained final topology of the compliant mechanism is able to follow the specified motion path within the given precision limit ϵ .

This procedure yields final topologies of compliant mechanism that include the *positions* of artificial (flexure) hinges but not their *optimal shape* leaving doubts on the physical meaning as well as an uncertainty in the manufacturing process. To overcome this drawback, artificial hinges are replaced by real flexure hinges meeting the performance specifications given by the compliant mechanism's kinematics and/or by the intended application. Different flexure hinges were investigated beforehand

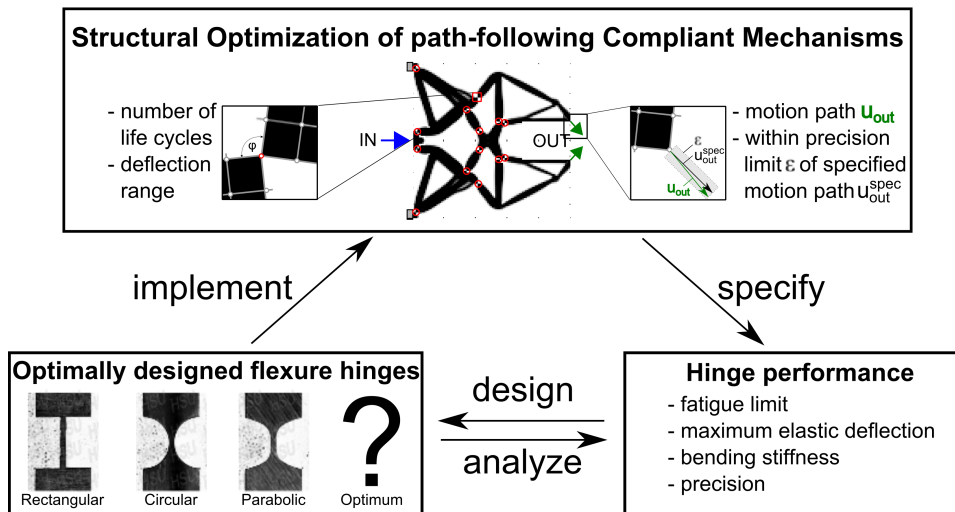


Figure 1. Scheme of the optimization procedure for compliant mechanisms

in terms of relevant performance criteria such as maximum deflection range, bending stiffness, natural frequency and, most importantly, fatigue life. Explicit analytical expressions are derived for common rectangular and circular as well as customizable parabolic hinge geometries for static and dynamic loading conditions and are validated by experimental data (cf. [1]).

3. Model order reduction for compliant mechanisms

Model order reduction is an established method in many technical fields for the approximation of large-scale linear time-invariant dynamical systems described by ordinary differential equations. Based on system theory, underlying representations of the dynamical system are introduced from which the general reduced order model is derived by projection. During the last years, numerous new procedures were published and investigated appropriate to simulation, optimization and control. Singular value decomposition, condensation-based and Krylov subspace methods representing three order reduction methods are reviewed and their advantages and disadvantages are outlined with respect to compliant mechanisms. Moreover, the requested attributes for order reduction as a future research direction meeting the characteristics of compliant mechanisms are commented.

4. Acknowledgement

This work is supported by the Deutsche Forschungsgemeinschaft (DFG) within the priority programme SPP1476 "Small tools for small workpieces".

5. References

- [1] F. Dirksen and R. Lammering (2011). On mechanical properties of planar flexure hinges of compliant mechanisms, *Mechanical Sciences*, **1**, Volume 2, 109–117.
- [2] M. Rösner and R. Lammering (2011). Basic principles and aims of model order reduction in compliant mechanisms, *Mechanical Sciences*, **1**, Volume 2, 197–204.

THE OPTIMAL DESIGN OF BOLTED CONNECTIONS BY APPLYING FINITE ELEMENT METHOD

F. Lisowski

Faculty of Mechanical Engineering, Cracow University of Technology, Poland

1. Introduction

The paper presents an approach to the optimal design of bolted joints using the finite element method. It was discussed how to create the parametric models of such connections. Particular attention was paid to their practical use for stress analysis involving optimization procedure. For the optimization process where the number of iterations is not known in advance, reducing computational time for each set of optimization is undoubtedly beneficial.

Besides, the paper takes up the question of how to form the mesh within the notch area due to reducing computational time of optimization process. The author also pays attention to the way of accepting the objective function depending on the geometry of studied element. Practical application of the issues raised in the article is presented on the example of the stress analysis and geometric optimization for two types of nuts. These are the nut with supporting ring and the nut with undercut.

2. Parametric models of bolted connections

To perform the optimization problem two-dimensional axysymmetric finite element models of bolted connections were used. Such models are sufficient for stress analysis and optimization due to obtaining the minimum of stress on the thread of bolt [1],[2]. Geometry of studied nuts and their design variables for geometrical optimization are shown in the Fig.1 and Fig.2.

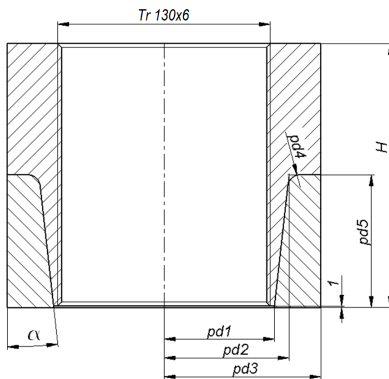


Fig. 1. Design variables and dimensions for parametric model of nut with supporting ring

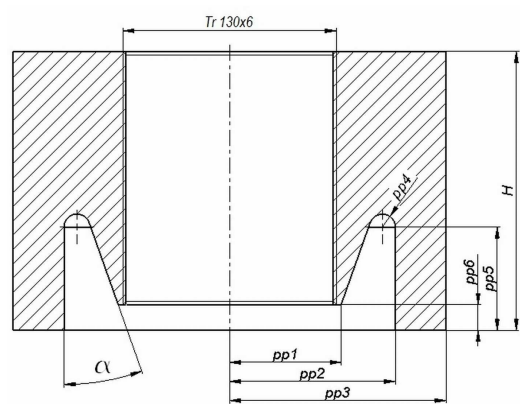


Fig. 2. Design variables and dimensions for parametric model of nut with undercut

3. Modeling the radius of notch fillet by using proper size of finite element

In bolted connections the thread is a structure consisted of serial notches. Fillet radius at the root of thread has at best few millimeters. Therefore to obtain the sufficiently approximated outline of curvature, it is necessary to use very fine mesh within the notch area. This in turn results in a rapid increase in the number of finite elements and elongates the computational time. Optional way to obtain correct solution may be modelling the notch radius as a sharp notch and accepting the size of finite element within the notch area so that obtained result will be convergent. According to [2] decrease in the finite element number for axisymmetric model of trapezoidal thread Tr100x12 can

reach 82% (2-D, 8-Node element) while the percentage relative error of maximum stress is less than 1% (compare fig.1 and fig.2). Applying of this method for modeling the radius of notch fillet can significantly reduce the computational time for optimization set. However, it requires choosing the proper size of finite element depending on angle and radius of the notch.

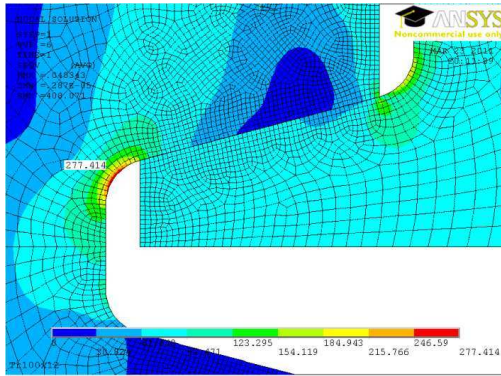


Fig. 1. σ_{HMH} stress map of 2-D axisymmetric model of bolted joint Tr100x12 with rounded notches

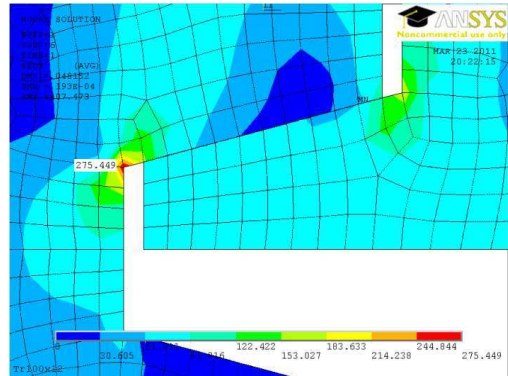


Fig. 2. σ_{HMH} stress map of 2-D axisymmetric model of bolted joint Tr100x12 with sharp notches

4. Acceptance of the objective function

For studied nuts, it was assumed that the height H and the outer diameter $pd3/pp3$ are constant. In that case for nut with supporting ring the mass is also constant, so the objective function was accepted as a Huber-Mises-Hencky reduced stress on the thread of bolt. Whereas for nut with undercut, the objective function can be formulated as given by equation 1. Such a formulation of the objective function allows to take into account stress and area (mass) criterions simultaneously. Significance of mass criterion can be controlled by f and n factors.

$$(1) \quad Q(x) = \frac{\sigma_{HMH}^{\max_B SET}}{\sigma_{HMH}^{\max_B SP}} + f \left(\frac{A_N^{SET}}{A_N^{SP}} \right)^n$$

$\sigma_{HMH}^{\max_B SP}$ – maximum σ_{HMH} stress in the thread of bolt for starting point [MPa], $\sigma_{HMH}^{\max_B SET}$ – maximum σ_{HMH} stress in the thread of bolt for current optimization set [MPa], A_N^{SP} – surface area of nut for starting point [mm²], A_N^{SET} – surface area of nut for current optimization set [mm²]

5. References

- [1] Chen J-J, Shih Y-S (1999). A study of the helical effect on the thread connection by three dimensional finite element analysis, Nuclear Engineering and Design, Vol.19, pp. 109-116
- [2] Pai N.G., Hess D.P. (2002). Three-dimensional finite element analysis of threaded fasteners loosening due to dynamic shear load, Engineering Failure Analysis, Vol.9, pp.383-402
- [3] Lisowski F. (2011). FEM modelling of structures with serial notches, Czasopismo Techniczne Politechniki Krakowskiej, Vol.7, pp.341-348
- [4] Stadnicki J. (2006). Teoria i praktyka rozwiązywania zadań optymalizacji z przykładami zastosowań technicznych, Warszawa, WNT

NUMERICAL MODEL OF ALN-BASED BULK ACOUSTIC HIGH-FREQUENCY RESONATORS

E. Postek¹, C. Caliendo² and P. Massimiliano Latino²

¹*Institute of Fundamental Technological Research, Warsaw, Poland*

²*Istituto dei Sistemi Complessi, ISC-CNR, Area della Ricerca di Roma 2, Italy*

1. Introduction

Thin film bulk acoustic resonators (TFBAR) have been adopted as alternatives to high-frequency SAW resonators, due to their inherent advantages, such as low insertion loss, low cost, high power handling capability and small size. TFBAR consists of a piezoelectric layer sandwiched between two metal electrodes. The electric field of the signal across the electrodes sets the piezoelectric film into vibration. For example, they are analysed in [1]. The crystallographic orientation of the piezoelectric film (*c-axis* oriented normal to the film surface) is such that the device work in the fundamental thickness-extensional mode. Vibrations propagates in the thin Si_3N_4 membrane mechanically coupled to the bottom electrode. The resonance frequency is mainly determined by the thickness of the piezoelectric layer (several 100 nm) and they are suitable for mobile communication systems operating in the 1 to 10 GHz range.

2. Numerical model

The TFBARs are realized on a Si_3N_4 membrane, 200 nm thick, chemically etched on a Si substrate. The AlN film is grown on a metal (Al or Pt) bottom electrode previously sputtered on the Si_3N_4 diaphragm; then an Al or Pt metal top electrode is deposited on the AlN free surface, being the active area of the device in the range from 500×500 to $500 \times 200 \text{ m}^2$.

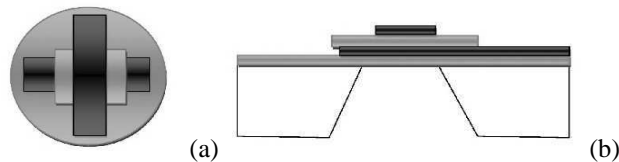


Fig. 1. The resonator, top view (a), cross-section (b)

The important modes for the resonator are the thickness modes. The thickness mode is evaluated on sample of AlN. The test example is prepared for $1000 \times 1000 \times 1000 \text{ nm}$ cube (Fig. 2a) with the sliding boundary conditions along the 4 walls of the cube. The cube was discretized with 1000 8-nodes brick elements. We have obtained the thickness mode as mode 9 and the corresponding natural frequency 5.55GHz which matches the analytical solution for Masons resonator [2].

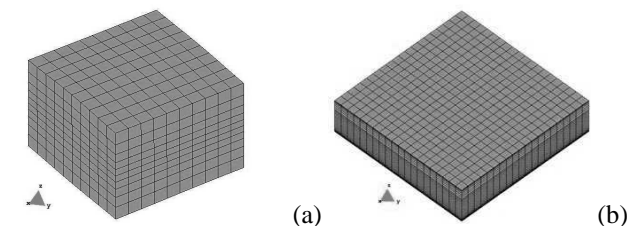


Fig. 2. Test example (a), active part, thickness mode (b)

It is shown the analysis of the thickness mode of the following resonator Al(100nm)/ AlN(1000n Al(100nm)/ SiN(200nm) and the active area of 0.5x0.5 mm. The corresponding thickness mode is shown in Fig. 2b.

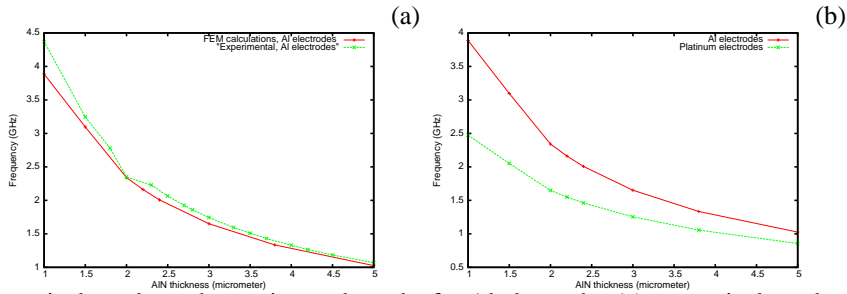


Fig. 3. Numerical results and experimental results for Al electrodes (a), numerical results for Al and Pt electrodes (b)

The thickness mode is identified as 4222 with the corresponding frequency of 3.889 GHz. Further, the analysis of different AlN resonators of the thicknesses between 1.0 and 5.0 μm is carried out and compared with the experiment. The results are shown in Fig. 3a. It has been found that the difference between the experiment and the numerical results is in the range of 3% up to 10%. The higher difference appears for thinner layers of AlN. The results of the analysis of the resonators with Pt electrodes is given in Fig. 3b.

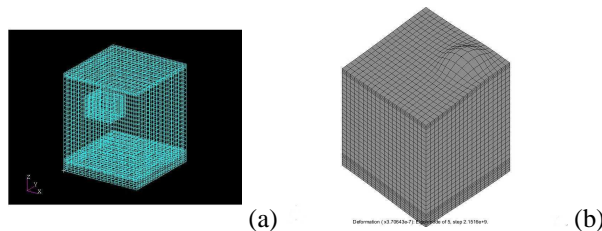


Fig. 4. Considered void (a), imperfect mode (b)

We consider an imperfect system with void, Fig. 4a. The system without void vibrates in thickness mode. This is in contrast to the imperfect one, Fig. 4b. First of all, the general mode is skewed and we can see a bulge on top. We may note, that the FEA is useful to capture the effect of tiny voids and impurities.

3. Acknowledgements

The research has been performed in the frame of the cooperation between Consiglio Nazionale delle Ricerche and Polska Akademia Nauk. The numerical results are obtained in the HPC-Centre of the Interdisciplinary Centre for Mathematical and Computational Modelling University of Warsaw.

4. References

- [1] C. Caliendo (2008). Analysis of the acoustoelectric behavior of microwave frequency, temperature-compensated AlN-based multilayer coupling configurations, *Journal of Applied Physics*, **104**.
- [2] R. Lerch (1990), Simulation of Piezoelectric Devices by Two- and Three-Dimensional Elements, *IEEE Transactions on Ultrasonics, Piezoelectrics and Frequency Control*, **37**, 233-247.

Index of Authors

- Adamowicz A., 138
Alevras P., 220
Altenbach H., 244
Altmeyer G., 160
Ario I., 280
Avalishvili G., 230
Avalishvili M., 230
- Badur J., 22
Bajkowski J.M., 278
Bajolet J., 192
Balevičius R., 180
Balzani D., 212
Baranowski P., 40
Bareille O., 286
Barski M., 232
Bauer S., 234
Becker A., 308
Bednarek T., 42, 44
Bertram A., 120
Białas M., 162
Bilotta A., 52
Bizoń K., 164
Bochenek B., 302
Bochniak W., 146
Boso D.P., 190
Brands D., 212
Bulgariu E., 76
Burczyński T., 48
- Caliendo C., 316
Celigueta M.A., 10
Chen M., 304
Chinchaladze N., 236
Chmielewski M., 206
Cieszko M., 44, 194, 196
Czechowicz K., 22
- Damaziak K., 40
dell'Isola F., 13
Denina O., 46
Derezin S.V., 238
Dietrich L., 146
- Dirksen F., 312
Długosz A., 48
Dodla S., 120
Dubois F., 28
Dziatkiewicz J., 64
- Egner H., 78, 166
Egner W., 78
Eremeyev V.A., 244
Ermakov A., 240
- Fernández-Canteli A., 154
Fernández-Sáez J., 132, 154
Fernández-Zúñiga D., 154
Fialko S., 50
Formica G., 242
Fournier Dit Chabert F., 80
Fraś T., 92, 122
Fukalov A., 82
Fukuda N., 118
- Gadzała P., 196
Ganghoffer J.F., 20
Garbowski T., 300, 310
Garcea G., 52
Garstecki A., 310
Gaubert A., 80
Genoese A., 52
German M., 54
Geymonat G., 262
Giner E., 154
Girchenko A., 244
Graczykowski C., 280
Grosman F., 108, 172
- Hachemi A., 304
Haghighat E., 178
Hashemian A., 56
Hernik Sz., 24
Hoffman J., 204
Holnicki-Szulc J., 276, 280,
288
Hou J., 306
- Huynen K., 192
Hyrca-Michalska M., 84
- Ichchou M.N., 286
Idelsohn S.R., 10
Inoshita D., 124
Ito H., 118
Iwamoto T., 124
Iwankiewicz R., 222
- Jacques N., 14
Jakubowicz A., 26
Jankowski Ł., 306
Jaśkowiec J., 36
Jaśkowska D., 300
Javili A., 198
Jędrysiak J., 270
- Kačianauskas R., 206, 210
Kaczyński A., 168
Kaczyński P., 264
Kaleta J., 282
Kaliński D., 206
Kang J., 308
Kaplunov J., 246
Karamshina L., 234
Karczmarzyk S., 248
Karliński J., 264
Kempiński M., 196
Kędziora P., 284
Kharrat M., 286
Khorshidi A., 98
Kneć M., 126
Knitter-Piątkowska A., 300,
310
Knor G., 288
Kochanowski K., 138
Kocsán L.G., 250
Kolesnikov A.M., 252
Kopernik M., 90
Kosiński W., 86
Kostecki M., 146

- Kowalczyk-Gajewska K., 88, 96
Kowalczyk P., 42, 68
Kowalewski Z., 128
Kowalewski Z.L., 16, 130, 134, 136, 146
Kozicki J., 182
Kozioł P., 224
Krasucki F., 262
Kret S., 204
Królewicz M., 282
Krzyżyński T., 224
Kucharski S., 204, 292
Kuczma B., 200
Kuczma M., 200
Kulasiński K., 290
Kuramae H., 214
Kurpisz D., 110
Kutergin A., 82

Laengler F., 170
Lammering R., 312
Larese A., 10
Latino P.M., 316
Lefik M., 190
Leindl M., 58
Lembo M., 242
Lengiewicz J., 202
Leśniewska D., 184
Levintant-Zayonts N., 292
Lewandowski D., 282
Lipinski P., 192
Lisowski F., 314
Longuet A., 80
Loya J., 132
Loya J.A., 154
Lumelskyy D., 172

Łodygowski T., 30

Majchrzak E., 60
Maj M., 140
Makowska K., 134, 146
Małachowski J., 40
Mao T., 170
Maurice G., 20
Mazurkiewicz Ł., 40
Maździarz M., 204
McBride A., 198
Mercier S., 14

Michalak B., 270
Miedzińska A.D., 62
Mikhasev G., 254
Mikułowski G., 276
Milani G., 256
Milenin A., 90
Mitsui K., 292
Mochnacki B., 64
Moćko W., 128, 136
Mohr D., 2
Molinari A., 14
Monastyrskyy B., 168
Mozul R., 28
Mróz Z., 114, 180, 208
Muc A., 232, 284

Naess A., 220
Nalepka K., 74, 204
Nalepka P., 204
Narkiewicz K., 22
Nedin R., 258
Nguyen A.D., 260
Niechajowicz A., 264
Niedostatkiwicz M., 184
Niezgoda T., 62
Nishida M., 118
Nosewicz Sz., 206
Nowak Ł., 294
Nowak M., 92, 174
Nowak Z., 92, 94, 128, 174

Oberaigner E.R., 58
Oliferuk W., 138, 140
Olszyna A., 146
Oñate E., 10
Ostrowska-Maciejewska J., 96, 106
Ou J., 306

Pączelt I., 208
Pamin J., 36, 54, 70
Pawlicki J., 108
Pawłowski P., 280
Perduta A., 66
Pereira A., 38
Perzyna P., 86, 94, 156
Petryk H., 4
Pęcherski R., 92, 106, 122, 172, 174
Philippon S., 192

Pieczyńska E.A., 290, 296
Pietraszkiewicz W., 8
Pietruszczak S., 178
Pietrzak K., 146, 206
Pietrzyk M., 26
Pilkavičius S., 210
Pluciński P., 36
Płochocki Z., 138
Podio-Guidugli P., 242
Postek E., 28, 316
Potoczek M., 174
Prikazchikov D.A., 246
Przybylski M., 282
Putanowicz R., 36, 66
Pyrz M., 278

Quilici S., 80

Rimša V., 210
Rittel D., 112
Rodríguez-Martínez J.A., 112
Rösner M., 312
Rojek J., 172, 206, 210
Rossi R., 10
Roškowicz M., 142
Rudolph H.-D., 144
Rusinek A., 122
Rutecka A., 146
Ryś M., 166

Sadowski T., 126
Salat J., 192
Salazar F., 10
Scarpa F., 12
Scheunemann L., 212
Scholz A., 170
Schröder J., 212
Serpilli M., 262
Sheiko A., 254
Shodja H., 56
Shodja H.M., 98
Skoczeń B., 100, 166
Słuszniaik A., 44
Smal T., 142
Stankiewicz A., 36
Staroszczyk R., 186
Steinmann P., 198
Stoffel M., 260
Stręk A.M., 148

- Stupkiewicz S., 4, 202
Sulich P., 24
Sumelka W., 102
Sun W., 308
Svanadze M., 104
Szajek K., 30
Szczepański Z., 196
Szelażek J., 134
Szeptyński P., 106
Szlachetka O., 272
Szymański Z., 204
Szymczak T., 130
- Śliwa R., 174
- Tabin J., 150
Tajs-Zielińska K., 302
Takeda K., 290, 292, 296
Tejchman J., 182, 184
Tkocz M., 108, 172
- Tobota A., 264
Tobushi H., 290, 292, 296
Tóth B., 266
Tralli A., 256
Tsuchiya K., 214
Tsukrov I., 90
Turska E., 228
- Uetsuji Y., 214
- Vatulyan A., 258
Voronkova E., 234
- Watanabe H., 118
Wawrzyk K., 68
Wągrowka M., 272
Wcisło B., 70
Wegner T., 110
Weichert D., 6, 260, 304
Wierszycki M., 30
Winkler R., 268
- Wiszowaty R., 276
Wiśniewski K., 228
Wojciechowski M., 190
Wosatko A., 36
Woźniak Cz., 270, 272
Woźniak J., 146
Wróblewski G., 32
- Yamanaka S., 124
Yurchenko D., 220
- Zaera R., 112
Zaitsev A., 82
Zajac P., 282
Zalewski R., 278
Zembrzycki K., 140
Zhou W., 286
Zieliński T.G., 216, 294
Ziętek G., 114
Zubov L.M., 238